bERLin
2019

HZB Helmholtz
Zentrum Berlin

ICFA

ERL2019

63rd ICFA Advanced Beam Dynamics Workshop on Energy Recovery Linacs, 15th-20th September 2019

hosted by Helmholtz-Zentrum Berlin

WORKSHOP TOPICS

- ERL facilities
- ERL beam dynamics and instrumentation
- Electron sources and injectors
- Superconducting RF
- ERL applications

CONTACT

Helmholtz-Zentrum Berlin für Materialien und Energie
Mail: **erl2019@helmholtz-berlin.de** | Web: **hz-b.de/erl2019**

VENUE

WISTA Building, Volmerstr. 2, 12489 Berlin

Online registration will be available from 15TH JANUARY

hz-b.de/erl2019

LOCAL ORGANIZING COMMITTEE

- Jennifer Bierbaum
- Hartmut Ehmler
- Aleksandr Matveenko (SPC Chair)
- Meghan McAteer
- Atoosa Meseck (ERL2019 Chair & LOC Chair)
- Roswitha Schabardin
- Jens Völker

INTERNATIONAL ORGANIZING COMMITTEE

- Kurt Aulenbacher (Mainz)
- Sergey Belomestnykh (FNAL)
- Stephen Benson (JLAB)
- Ilan Ben-Zvi (BNL)
- Yong Ho Chin (KEK)
- Ryoichi Hajima (QST)
- Georg Hoffstaetter (Cornell)
- Erk Jensen (CERN)
- Kwang-Je Kim (ANL)
- Jens Knobloch (HZB)
- Kexin Liu (PKU)
- Atoosa Meseck (HZB)
- Tsukasa Miyajima (KEK)
- Oleg Shevchenko (BINP)
- Susan Smith (STFC)

SCIENTIFIC PROGRAM COMMITTEE

- Michael Abo-Bakr (HZB)
- Deepa Angal-Kalinin (ASTeC)
- André Arnold (HZDR)
- Michaela Arnold (SDALINAC)
- Kurt Aulenbacher (U Mainz)
- Ivan Bazarov (Cornell)
- Alex Bogacz (JLAB)
- Oliver Brüning (CERN)
- Andrew Burrill (SLAC)
- Yong Ho Chin (KEK)
- Pavel Evtushenko (HZDR)
- Frank Gerigk (CERN)
- Georg Hoffstaetter (Cornell)
- Walid Kaabi (LAL)
- Thorsten Kamps (HZB)
- Dmitry Kayran (BNL)
- Ivan Konoplev (ADAMS)
- Georgios Kourkafas (HZB)
- Matthias Liepe (Cornell)
- Kexin Liu (Peing U.)
- Aleksandr Matveenko (HZB)
- Peter McIntosh (STFC)
- Axel Neumann (HZB)
- Houjun Qian (PITZ)
- Bob Rimmer (JLAB)
- Hiroshi Sakai (KEK)
- Daniel Schulte (CERN)
- Oleg Shevchenko (BINP)
- Achille Stocchi (LAL)
- Christopher Tennant (JLAB)
- Nikolay Vinokurov (BINP)
- Erdong Wang (BNL)
- Jiuqing Wang (IHEP)
- Masahiro Yamamoto (KEK)

Program ERL 2019

Sunday, 15th September 2019		
16:00	Registration	HZB Foyer
18:00	Welcome Reception	HZB Foyer
20:00	End	

Monday, 16th September 2019		
08:00	Registration	WISTA Building
09:00	**Opening** *Atoosa Meseck (Helmholtz-Zentrum Berlin)*	WISTA - Bunsen Saal
09:10	**Welcome** *Jan Lüning (Helmholtz-Zentrum Berlin)*	WISTA - Bunsen Saal
	ERL facilities (Chair: M. Abo-Bakr)	
09:25	**CBETA, a 4-turn ERL Based on SRF Linacs: construction and commissioning** *Georg Hoffstaetter (Cornell, USA)*	WISTA - Bunsen Saal
09:55	**Compact ERL (cERL), stable 1 mA operation with a small beam emittance at KEK** *Tsukasa Miyajima (KEK, Japan)*	WISTA - Bunsen Saal
10:30	Coffee Break	WISTA - Einstein-Newton-Kabinett
	ERL facilities (Chair: M. Arnold)	
10:45	**ERL Operation of S-DALINAC** *Norbert Pietralla (TU Darmstadt, Germany)*	WISTA - Bunsen Saal
11:10	**Status of Novosibirsk ERL** *Nikolay Vinokurov (BINP, Novosibirsk, Russia)*	WISTA - Bunsen Saal
11:35	**The bERLinPro Project** *Andreas Jankowiak (HZB, Germany)*	WISTA - Bunsen Saal
12:00	**The MESA ERL Project** *Florian Hug (Mainz University, Germany)*	WISTA - Bunsen Saal
12:30	Lunch on your own	
	ERL applications (Chair: N. Vinokurov)	
14:00	**PERLE: A High Power Energy Recovery Facility at Orsay** *Walid Kaabi (IN2P3, France)*	WISTA - Bunsen Saal
14:25	**A hard X-ray FEL and Nuclear Physics facility based on a Multi-pass re-circulating superconducting CW Linac with Energy Recovery** *Peter Williams (STFC, UK)*	WISTA - Bunsen Saal
14:50	**Nuclear photonics with an ERL-based hard X-ray source** *Norbert Pietralla (TU Darmstadt, Germany)*	WISTA - Bunsen Saal
15:15	**Electrodisintegration of 16O and the Rate Determination of the Radiative Alpha Capture on 12C at Stellar Energies** *Ivica Friscic (MIT, USA)*	WISTA - Bunsen Saal
15:45	Coffee Break	WISTA - Einstein-Newton-Kabinett
	ERL applications (Chair: D. Angal-Kalinin)	
16:00	**The Use of ERLs to Cool High Energy Ions in Electron-Ion Colliders** *Stephen Benson (Jlab, USA)*	WISTA - Bunsen Saal
16:30	**Industrial Applications of cERL** *Hiroshi Sakai (KEK, Japan)*	WISTA - Bunsen Saal
17:00	**Recent Advances in Terahertz Photonics and Spectroscopy at Novosibirsk Free Electron Laser** *Yulia Choporova (BINP, Novosibirsk, Russia)*	WISTA - Bunsen Saal
17:30	**ERL as a versatile SRF test facility** *Erk Jensen (CERN, Switzerland)*	WISTA - Bunsen Saal
18:00	End	

Tuesday, 17th September 2019		
	ERL beam dynamics and instrumentation (Chair: A. Bogacz)	
09:00	**Longitudinal Phase Space Dynamics in ERLs** *Stephen Benson (JLAB, USA)*	WISTA - Bunsen Saal
09:30	**Beyond the limits of 1D coherent synchrotron radiation** *Peter Williams (ASTeC, UK)*	WISTA - Bunsen Saal
10:00	**CSR phase space dilution in ERLs** *William Lou (Cornell, USA)*	WISTA - Bunsen Saal
10:30	Coffee Break	WISTA - Einstein-Newton-Kabinett
	ERL beam dynamics and instrumentation (Chair: G. Hoffstaetter)	
10:45	**Beam Halo in Energy Recovery Linacs** *Olga Tanaka (KEK, Japan)*	WISTA - Bunsen Saal
11:10	**Beam timing and cavity phasing** *Rosalyn Koscica (Cornell, USA)*	WISTA - Bunsen Saal
11:35	**The LHeC ERL - Optics and Performance Optimizations** *Alex Bogacz (JLab, USA)*	WISTA - Bunsen Saal
12:00	**Beam dynamics layout of the MESA ERL** *Florian Hug (Mainz University, Germany)*	WISTA - Bunsen Saal
12:30	Lunch on your own	
	Superconducting RF (Chair: A. Neumann)	
14:00	**KEK ERL SRF Operation Experience** *Hiroshi Sakai (KEK, Japan)*	WISTA - Bunsen Saal
14:25	**Superconducting Twin-Axis Cavity for ERL Applications** *Jean Delayen (ODU, USA)*	WISTA - Bunsen Saal
14:50	**Integration of the MESA modules to bERLinPro for high power beam tests** *Sebastian Thomas (KPH, Germany)*	WISTA - Bunsen Saal
15:15	**Time for discussion**	WISTA - Bunsen Saal
15:45	Coffee Break	WISTA - Einstein-Newton-Kabinett
	Superconducting RF (Chair: H. Sakai)	
16:00	**Cryomodules for the Mainz Energy-recovering Superconducting Accelerator (MESA)** *Florian Hug (KPH, Germany)*	WISTA - Bunsen Saal
16:20	**A ferroelectric Fast Reactive Tuner (FRT) to combat microphonics** *Alick Macpherson (CERN, Switzerland)*	WISTA - Bunsen Saal
16:45	**Characterization of Microphonics in the cERL main linac superconducting cavities** *Feng Qiu (KEK, Japan)*	WISTA - Bunsen Saal
17:10	**LLRF ERL experience at the S-DALINAC** *Manuel Steinhorst (TU Darmstadt, Germany)*	WISTA - Bunsen Saal
17:35	**Time for discussion**	WISTA - Bunsen Saal
18:00	End	
18:30	**Scientific Opportunities of bERLinPro 2020+** *Satellite Workshop "Barcamp"* *Starts with a light Dinner, Barcamp starts 19:00*	Magnusstr. 2, 12489 Berlin near WISTA Building & HZB

Wednesday, 18th September 2019		
	Electron sources and injectors (Chair: E. Wang)	
09:00	**Vertical test results and preparation for horizontal test of the KEK SRF gun #2** *Taro Konomi (KEK, Japan)*	WISTA - Bunsen Saal
09:30	**Using a protective layer for alkali cathodes** *John Smedley (LANL, USA)*	WISTA - Bunsen Saal
10:00	**High current polarized electron source development** *Luca Cultrera (Cornell, USA)*	WISTA - Bunsen Saal
10:30	Coffee Break	WISTA - Einstein-Newton-Kabinett
	Electron sources and injectors (Chair: L. Cultrera)	
10:45	**Photocathode preparation and charcaterization at HZB** *Sonal Mistry (HZB, Germany)*	WISTA - Bunsen Saal
11:10	**Cathode preformance for high current operation in LEReC** *Mengjia Gaowei (BNL, USA)*	WISTA - Bunsen Saal
11:35	**Bench Test Results of CW 100 mA Electron RF Gun for Novosibirsk ERL based FEL** *Vladimir Volkov (BINP, Russia)*	WISTA - Bunsen Saal
11:55	**Time for discussion**	WISTA - Bunsen Saal
12:30	Lunch on your own	
14:00	Postersession	WISTA - Einstein-Newton-Kabinett
15:45	Coffee Break	WISTA - Einstein-Newton-Kabinett
	Mixed session (Chair: O. Shevchenko)	
16:00	**Asymmetric SRF dual axis cavity for ERLs: studies and design for ultimate performance and applications** *Yarosloav Shashkov (JAI, UK)*	WISTA - Bunsen Saal
16:30	**ERL with Fixed Field Altrernating Gradient Linear Gradient Role in EIC** *Dejan Trbojevic (BNL, USA)*	WISTA - Bunsen Saal
16:50	**High-Efficiency Broadband THz Emission via Diffraction-Radiation Cavity** *Miho Shimada (KEK, Japan)*	WISTA - Bunsen Saal
17:20	**Applying Machine Learning Approaches to bERLinPro** *Bettina Kuske (HZB, Germany)*	WISTA - Bunsen Saal
17:40	**Time for discussion**	WISTA - Bunsen Saal
18:00	End	
19:00	Workshop Dinner (Shuttle departs 18:30 in front of the WISTA - Building)	
23:00	End (Shuttle departs 22:00 & 23:00 in front of the Dinner Location)	

Thursday, 19th September 2019		
	Superconducting RF (Chair: F. Gerigk)	
09:00	**System Identification Procedures for Resonance Frequency Control of SC Cavities** *Sebastian Orth (TU Darmstadt, Germany)*	WISTA Bunsen-Saal
09:20	**Passive and active control of microphonics at CBETA and elsewhere** *Nilanjan Banerjee (Cornell, USA)*	WISTA Bunsen-Saal
09:45	**The development of HOM-damped 166.6MHz SRF cavities for High Energy Photon Source in Beijing** *Pei Zhang (IHEP, China)*	WISTA Bunsen-Saal
10:10	**Beam breakup limit estimations and HOM characterisation for MESA** *Christian Stoll (KPH, Germany)*	WISTA Bunsen-Saal
10:30	Coffee Break	WISTA - Einstein-Newton-Kabinett
	Superconducting RF (Chair: P. McIntosh)	
10:45	**Waveguide HOM loads for high current elliptical cavities** *Jiquan Guo (JLAB, USA)*	WISTA Bunsen-Saal
11:10	**Development of HOM coupler with C-shaped waveguide for ERL operation** *Masaru Sawamura (QST, Japan)*	WISTA Bunsen-Saal
11:35	**Degradation and Recovery of Cavity Performance in Compact-ERL Injector Cryomodule at KEK** *Eiji Kako (KEK, Japan)*	WISTA Bunsen-Saal
12:00	**High Q 704 MHz cavity tests at CERN** *Alick Macpherson (CERN, Switzerland)*	WISTA Bunsen-Saal
12:30	Lunch on your own	
	Electron sources and injectors (Chair: J. Knobloch)	
14:00	**Metal/ semiconductor photocathode in HZDR SRF gun** *Rong Xiang (HZDR, Germany)*	WISTA Bunsen-Saal
14:30	**Peking Univ. DC-SC/SRF gun progressing** *Huamu Xie (Peking U., China)*	WISTA Bunsen-Saal
15:00	**High charge high current beam from BNL 112MHz SRF gun** *Igor Pinayev (BNL, USA)*	WISTA Bunsen-Saal
15:30	**Time for discussion**	WISTA - Bunsen Saal
15:45	Coffee Break	WISTA - Einstein-Newton-Kabinett
	Electron sources and injectors (Chair: D. Kayran)	
16:00	**Injector development at KeK** *Tsukasa Miyajima (KEK, Japan)*	WISTA Bunsen-Saal
16:30	**Novosibirsk ERL injector** *Oleg Shevchenko (BINP, Russia)*	WISTA Bunsen-Saal
17:00	**Status of SRF Gun for bERLinPro** *Axel Neumann (HZB, Germany)*	WISTA Bunsen-Saal
17:30	**Magnetized beam generated from DC gun for JLEIC Electron Cooler** *Stephen Benson (JLAB, USA)*	WISTA Bunsen-Saal
18:00	End	

Friday, 20th September 2019		
	ERL beam dynamics and instrumentation (Chair: P. Evtushenko)	
09:00	**Essential instrumentation for the characterization of ERL beams** *Nilanjan Banerjee (Cornell, USA)*	WISTA Bunsen-Saal
09:30	**Design and commissioning experience with state of the art MPS for LEReC accelerator** *Sergei Seletskiy (BNL, USA)*	WISTA Bunsen-Saal
10:00	**Beam Commissioning Experience at Low Energy RHIC Electron Cooler (LEReC)** *Dmitry Kayran (BNL, USA)*	WISTA Bunsen-Saal
10:30	Coffee Break	WISTA - Einstein-Newton-Kabinett
	ERL beam dynamics and instrumentation (Chair: T. Kamps)	
10:45	**Electronic modulation of the FEL-oscillator radiation power driven by ERL** *Oleg Shevchenko (BINP, Russia)*	WISTA Bunsen-Saal
11:10	**Adjusting bERLinPro optics to commissioning needs** *Bettina Kuske (HZB, Germany)*	WISTA Bunsen-Saal
11:35	**Beam dynamics simulations for the twofold ERL mode at the S-DALINAC** *Felix Schließmann (TU Darmstadt, Germany)*	WISTA Bunsen-Saal
12:00	**Status of the Control System for the Energy Recovery Linac bERLinPro at HZB** *Thomas Birke (HZB, Germany)*	WISTA Bunsen-Saal
12:30	Lunch on your own	
	WG reports and close out (Chair: A. Matveenko)	
14:00	**Report WG1: ERL facilities** *Michael Abo-Bakr / Michaela Arnold*	WISTA Bunsen-Saal
14:20	**Report WG2: ERL beam dynamics and instrumentation** *Georg Hoffstaetter / Pavel Evtushenko*	WISTA Bunsen-Saal
14:40	**Report WG3: Electron sources and injectors** *Erdong Wang / Luca Cultrera*	WISTA Bunsen-Saal
15:00	**Report WG4: Superconducting RF** *Frank Gerigk*	WISTA - Bunsen Saal
15:20	**Report WG5: ERL applications** *Deepa Angal-Kalinin / Oliver Bruning*	WISTA - Bunsen Saal
15:45	Coffee Break	WISTA - Einstein-Newton-Kabinett
16:00	bERLinPro/BESSY II tour (Albert-Einstein-Str. 15, 12489 Berlin)	HZB
18:00	End	

ERL2019

Workshop Committees

Workshop Chair

Atoosa Meseck (HZB)

Local Organizing Committee (LOC)

- Jennifer Bierbaum
- Hartmut Ehmler
- Aleksandr Matveenko (SPC Chair)
- Meghan McAteer
- Atoosa Meseck (ERL2019 Chair & LOC Chair)
- Roswitha Schabardin
- Jens Völker

International Organizing Committee (IOC)

- Kurt Aulenbacher (Mainz)
- Sergey Belomestnykh (FNAL)
- Stephen Benson (JLAB)
- Ilan Ben-Zvi (BNL)
- Ryoichi Hajima (QST)
- Ingo Hoffmann (TU Darmstadt)
- Georg Hoffstaetter (Cornell)
- Erk Jensen (CERN)
- Kwang-Je Kim (ANL)
- Jens Knobloch (HZB)
- Kexin Liu (PKU)
- Atoosa Meseck (HZB)
- Tsukasa Miyajima (KEK)
- Oleg Shevchenko (BINP)
- Susan Smith (STFC)

Scientific Program Committee (SPC)

- Michael Abo-Bakr (HZB)
- Deepa Angal-Kalinin (ASTeC)
- André Arnold (HZDR)
- Michaela Arnold (SDALINAC)
- Kurt Aulenbacher (U Mainz - SPC Co-Chair)
- Ivan Bazarov (Cornell)
- Alex Bogacz (JLAB)
- Oliver Brüning (CERN)
- Andrew Burrill (SLAC)
- Luca Cultrera (Cornell)
- Pavel Evtushenko (HZDR)
- Frank Gerigk (CERN)
- Ingo Hoffmann (TU Darmstadt)
- Georg Hoffstaetter (Cornell)
- Walid Kaabi (LAL)
- Thorsten Kamps (HZB)
- Dmitry Kayran (BNL)
- Ivan Konoplev (ADAMS)
- Matthias Liepe (Cornell)
- Kexin Liu (Peking U.)
- Aleksandr Matveenko (HZB)
- Peter McIntosh (STFC)
- Axel Neumann (HZB)
- Houjun Qian (PITZ)
- Bob Rimmer (JLAB)
- Hiroshi Sakai (KEK)
- Daniel Schulte (CERN)
- Oleg Shevchenko (BINP)
- Achille Stocchi (LAL)
- Christopher Tennant (JLAB)
- Nikolay Vinokurov (BINP)
- Erdong Wang (BNL)
- Jiuqing Wang (IHEP)
- Masahiro Yamamoto (KEK)

Contents

ISBN: 978-3-95450-217-2 doi:10.18429/JACoW-ERL2019-MOCOXBS02

ERL OPERATION OF S-DALINAC*

M. Arnold†, T. Bahlo, M. Dutine, R. Grewe, J. Hanten, L. Jürgensen, J. Pforr, N. Pietralla,
F. Schließmann, M. Steinhorst, S. Weih, Technische Universität Darmstadt, Darmstadt, Germany

Abstract

The S-DALINAC is a thrice-recirculating superconducting electron accelerator which can be either used in conventional accelerating operation or, since a major upgrade was installed in 2015/2016, as an energy recovery linac (ERL) alternatively. A once- or twice-recirculating ERL operation is possible due to the layout of the accelerator. During the commissioning phase the once-recirculating ERL operation was demonstrated in August 2017. Measurement data and an analytical model for the radio-frequency power behaviour due to changes in the beam loading are presented.

INTRODUCTION

The material discussed in this oral presentation is based upon the content of a scientific article which we have submitted on 4th of October 2019 to *Physical Review Accelerators and Beams*. Our present contribution to these conference proceedings, hence, contains descriptions of our work in the way which we were able to formulate them best.

S-DALINAC

The S-DALINAC is in operation since 1991 at TU Darmstadt [1]. A floorplan is shown in Fig. 1.

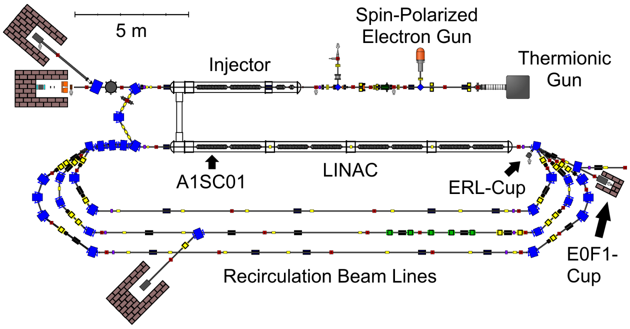

Figure 1: Floorplan of the S-DALINAC. The first main accelerator cavity A1SC01 and the two beam dumps being relevant for the measurement explained in section ”Once-Recirculating ERL Operation” are indicated.

The beam is either produced in a thermionic gun with a pre-acceleration of 250 keV or in a spin-polarized electron gun with a pre-acceleration of up to 125 keV. The beam is prepared for further acceleration with 3 GHz in the normal-conducting chopper-prebuncher section. The superconducting (sc) injector linac is able to accelerate the beam up to 10 MeV (7.6 MeV for recirculating operation). The beam is bent into the main accelerator, providing an energy gain of 30.4 MeV. The maximum design energy is 130 MeV at currents of 20 µA.

A New Recirculation Beam Line

In 2015/2016 a third recirculation beam line was installed, enabling higher end-energies and energy-recovery linac (ERL) operation due to a path-length adjustment system in the new beam line with a stroke of up to 360° [2, 3]. The beam line elements have been aligned with a laser tracker [4], achieving a global 1D positioning precision in the order of 200 µm.

Operational Modes and Commissioning

The lattice of the S-DALINAC allows different operation schemes:

- Injector operation
- Single pass mode (one passage through the main linac)
- Once-recirculating mode (two passages through the main linac)
- Thrice-recirculating mode (four passages through the main linac)
- Once-recirculating ERL mode (one accelerating and one decelerating passage through the main linac, see Fig. 2(a))
- Twice-recirculating ERL mode (two accelerating and two decelerating passages through the main linac, see Fig. 2(b)), not demonstrated yet

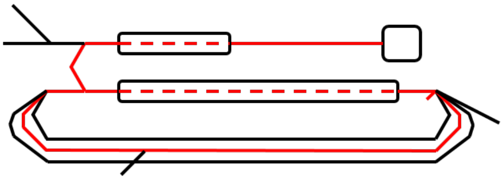

(a) Once-recirculating ERL mode.

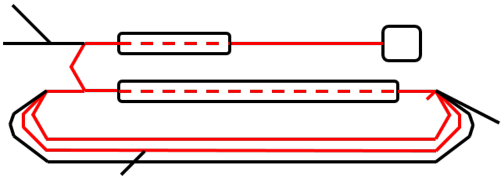

(b) Twice-recirculating ERL mode.

Figure 2: The S-DALINAC lattice is capable of a once- or twice-recirculating ERL operation. The 180° phase shift is done in the second recirculation beam line.

---

* Work supported by DFG through GRK 2128

† marnold@ikp.tu-darmstadt.de

The commissioning of the modes started at the end of 2016 with an injector and the first single pass setting. In 2017 the focus was set to the once-recirculating modes (conventional and ERL). Both have been achieved in 2017, the ERL operation is presented in a later section. A major refurbishment of the cryo-plant was done in 2018. During the remaining year the thrice-recirculating mode was operated for the first time. The twice-recirculating ERL mode is in preparation.

ERL Efficiencies

The efficiency of an ERL is an important quantity, judging on the success of the operation. There are several ways to define an efficiency, either based on the beam or the radio-frequency (RF) powers. One of them is the *beam-recovery efficiency* defined by

$$\mathcal{E}_\mathrm{b} = \frac{E_\mathrm{b,max} I_\mathrm{b,dump} - P_\mathrm{b,dump}}{P_\mathrm{b,max}} \tag{1}$$

where $E_\mathrm{b,max}$ ($I_\mathrm{b,dump}$) are the beam energy (beam intensity) at maximum energy (at the beam dump) and where $P_\mathrm{b,max} = E_\mathrm{b,max} I_\mathrm{b,max}$ ($P_\mathrm{b,dump} = E_\mathrm{b,dump} I_\mathrm{b,dump}$) is the beam power at top energy (at the beam dump). The beam-recovery efficiency can only be finite if the beam energy at the dump is lower than maximum and if a finite transmission to the dump is achieved. The ideal beam-recovery efficiency of 100 % is obtained by a complete deceleration of the entire beam current available at maximum energy, *i.e.*, $I_\mathrm{b,dump} = I_\mathrm{b,max}$ and $E_\mathrm{b,dump} = 0$. In general, decelerating to zero energy is not possible, so the efficiency of an ERL is limited by the injector energy, usually chosen at a few MeV level to reach close to ultra-relativistic electron motion before the main linac. For optimum transmission the beam-recovery efficiency is then limited to

$$\mathcal{E}_\mathrm{b,max} = 1 - \frac{E_\mathrm{b,dump}}{E_\mathrm{b,max}}. \tag{2}$$

The beam-recovery efficiency, however, does not allow to judge directly the technological gain provided by the deceleration process due to the reduction of external RF power required for the machine operation. For that purpose, the *RF-recovery effect*

$$\mathcal{E}_\mathrm{RF} = \frac{P_\mathrm{RF,acc.} - P_\mathrm{RF,ERL}}{P_\mathrm{RF,acc.}} \tag{3}$$

is more useful, where the RF beam loading is compared in situations when the beam is either blocked externally at its maximum energy ($P_\mathrm{RF,acc.}$) or when its energy is recovered by out-of-phase recirculation to the RF cavities ($P_\mathrm{RF,ERL}$) at the same absolute amplitude of the RF field. The optimum RF-recovery effect is obtained when the beam loading in ERL mode vanishes completely.

ONCE-RECIRCULATING ERL OPERATION

An ERL machine time took place during the commissioning phase of the upgraded S-DALINAC (see subsection ”Operational Modes and Commissioning”) in August 2017 [5]. The goals of this ERL run have been to achieve once-recirculating ERL operation and to study the low-level radio-frequency system and its performance during ERL operation [6]. A summary of all main parameters of the ERL measurement is listed in Table 1. The energy gain of the injector was small, thus phase slippage effects in the 20-cell accelerating structures are strongly present. For this reason the change in phase in comparison to conventional acceleration resulted in 186° (setpoint of path length adjustment system) for an optimized operation.

Table 1: Main Parameters of the Once-Recirculating ERL Operation.

Parameter	**Value**
Energy gain injector	2.5 MeV
Energy gain linac	20.0 MeV
Current (before injector)	1.2 μA
Total change in phase (setpoint)	186°
RF recovery effect $\mathcal{E}_\mathrm{RF}$	(90.1 ± 0.3) %
Beam-recovery efficiency $\mathcal{E}_\mathrm{b,max}$	88.9 %

During the ERL machine time, data on RF power measurements of the first main accelerating cavity A1SC01, and on the beam current at the two corresponding beam dumps (ERL mode: ERL-Cup, conventional mode: E0F1-Cup), were taken. The data was acquired for four different settings that refer to the following color code:

1. No beam in the main accelerator. (red)
2. Single pass: one beam is accelerated in the main accelerator. (grey)
3. Once-recirculating mode: two beams are accelerated in the main accelerator. (blue)
4. ERL mode: one beam is accelerated, another beam is decelerated in the main accelerator. (green)

Figure 3 gives an overview on the complete measurement. This data was taken shortly after an access to the accelerator hall was needed for maintenance work at the path length adjustment system. The measured powers (raw data) are increasing over time, being an effect during the first hours of RF operation. The increase occurs due to thermal heating of the input coupler caused by RF losses at the coupler during the operation and a corresponding change of the coupling resulting in an additional change of the length of the self-excited loop over time. This change can in common beam operation be corrected by the operators using a loop phase shifter, when the coupler temperatures have reached equilibrium. In the presented experiments this correction hasn’t been applied as temperatures were still drifting. Therefore, we need to take the drifts into account for the analysis. For this reason a drift-correction was done for all powers, resulting in $\Delta\widetilde{P}_i$ (i: forward and reverse power).

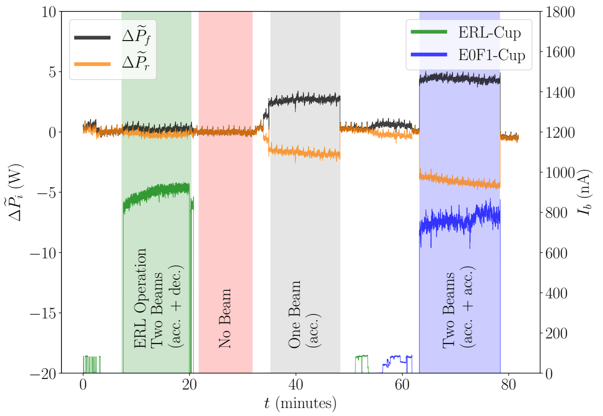

Figure 3: During four different settings (ERL: green, no beam: red, single pass: grey, twice accelerating: blue) the changes in forward (black curve) and reverse (orange curve) RF power of the first main accelerating cavity (A1SC01, see Fig. 1) have been monitored. The beam current on the corresponding faraday cups (ERL-Cup: green, E0F1-Cup: blue, see Fig. 1) was measured [5].

The forward (black curve) and reverse power (orange curve) of the first main accelerating cavity (A1SC01) have been measured and normalized to the time without beam but with electromagnetic field in the cavity (red band in Fig. 3). During the single pass setting (grey shading in Fig. 3) both powers changed with respect to the situation without beam due to the beam loading: the forward power increased while the reversed power dropped to a lower level. The absolute changes amount to about 2 W in both cases. If a second beam for acceleration is put into the cavity, the beam loading further increases (once-recirculating mode, blue shading in Fig. 3). Both, the forward power and the reverse power, change again by about the same amount as observed before. In case of the ERL operation (green shading, Fig. 3), the effective beam loading of the cavity A1SC01 was found to almost fully cancel out. The power levels were equivalent to a beam-free linac while still the beam was transported to the ERL beam dump (green curve) after having intermediately been transported through the recirculation arcs with an energy of 22.5 MeV. This is a clear evidence for operation of the S-DALINAC in ERL mode.

The current measurement is a further evidence that the beam was transported to the ERL beam dump (green curve) in the ERL mode phase (green shading) as well as to the extraction beam dump (blue curve) during the once-recirculating mode (blue shading).

More details on the evaluation of the measurement can be found in [5].

Analytical Model

The drop in reverse power, when increasing the number of beams accelerated in the cavities, can be explained with the beam being an additional external load which couples to the electric acceleration field. In absence of the amplitude control of the RF control system the forward power would stay constant. In this case the power transferred to the beam would only be measurable in the reverse power. The presence of the amplitude control causes an increase in forward power to keep the accelerating field constant despite of the beam loading. With higher beam coupling the reflection coefficient r decreases resulting in a drop of the reverse power level. It is given by the input coupling β_1, output coupling β_2 and beam coupling β_b. P_0 is the dissipated power in the cavity, P_f and P_r are the forward respectively reverse powers:

$$r = \frac{\beta_1 - (1 + \beta_2 + \beta_\mathrm{b})}{\beta_1 + (1 + \beta_2 + \beta_\mathrm{b})} = \sqrt{\frac{P_\mathrm{r}}{P_\mathrm{f}}}. \tag{4}$$

Both effects mentioned above cause the steps in the corresponding powers. In the following, an analytical model to the power data will be applied to show the expected behaviour of the reverse power. An expression for the forward power P_f is given by

$$P_\mathrm{f}(t) = P_0 \frac{[\beta_1(t) + (1 + \beta_2(t) + \beta_\mathrm{b})]^2}{4\beta_1(t)}, \tag{5}$$

The reverse power P_r can be expressed as:

$$P_\mathrm{r}(t) = P_0 \frac{[\beta_1(t) - (1 + \beta_2(t) + \beta_\mathrm{b})]^2}{4\beta_1(t)}. \tag{6}$$

The different coefficients have been obtained by fits to the data in the different situations: first with no beam loading, second with fits to the data on the forward power in presence of beam (ERL, single linac pass, double linac pass). Figure 4 shows the achieved curves. More details on the analytical model can be found in [5].

SUMMARY AND OUTLOOK

The S-DALINAC was extended by a third recirculation beam line, allowing a phase shift of up to 360°. During the commissioning process of all machine operation modes the once-recirculating ERL operation was achieved in August 2017. An RF recovery effect of (90.1 ± 0.3) % in the first main accelerating structure was reached. An analytical model was found, that predicts the behaviour of the reverse power for measured and fitted forward power.

The twice-recirculating ERL operation is in preparation. Investigations on the effect of phase slippage are ongoing [7]. A crucial aspect for a twice-recirculating ERL operation is the diagnostics, as two beams of the same energy are travelling through the same beam line. Different possibilities to measure both beams are under investigations [8]. The twice-recirculating ERL operation will be worked on during an upcoming beam time.

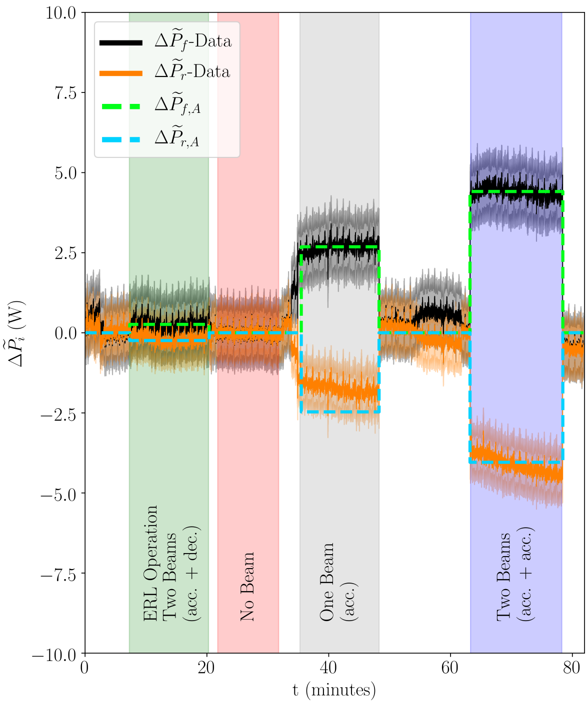

Figure 4: Curves of the forward (black) and reverse (orange) power data including uncertainties marked as areas. The dashed lines show the curves extracted from the analytical model via curve fitting. The analytical curves show the theoretical behaviour of forward (green) and reverse power (blue) in absence and presence of the beam (steps) [5].

REFERENCES

[1] N. Pietralla, "The Institute of Nuclear Physics at the TU Darmstadt", in *Nuclear Physics News*, vol. 28, no. 2, p. 4-11, 2018. `doi:10.1080/10619127.2018.1463013`

[2] M. Arnold, C. Eschelbach, R. Grewe, F. Hug, T. Kürzeder, M. Lösler, J. Pforr, N. Pietralla, "Construction and Status of the Thrice Recirculating S-DALINAC", *Proc. IPAC 2017*, Copenhagen, Denmark, May 2017, pp. 1384-1387. `doi:10.18429/JACoW-IPAC2017-TUPAB030`

[3] M. Arnold, C. Burandt, C. Eschelbach, R. Grewe, F. Hug, M. Lösler, J. Pforr, N. Pietralla. M. Steinhorst, "First ERL Operation of S-DALINAC and Commissioning of Path Length Adjustment System", *Proc. IPAC 2018*, Vancouver, BC, Canada, May 2018, pp. 4859-4862. `doi:10.18429/JACoW-IPAC2018-THPML087`

[4] M. Lösler, M. Arnold. H. Bähr, C. Eschelbach, T. Bahlo, R. Grewe, F. Hug, L. Jürgensen, P. Winkemann, N. Pietralla, "Hochpräzise Erfassung von Strahlführungselementen des Elektronenlinearbeschleunigers S-DALINAC", Fachbeitrag in *zfv* Ausgabe 6/2015 140. Jg. (2015) pp. 346-356. `doi:10.12902/zfv-0090-2015`

[5] M. Arnold, J. Birkhan, F. Hug, J. Pforr, N. Pietralla, F. Schließmann, M. Steinhorst, "First operation of the superconducting Darmstadt linear electron accelerator as an energy recovery linac", submitted for publication.

[6] M. Steinhorst, M. Arnold, T. Bahlo, R. Grewe, L. Jürgensen, J. Pforr, N. Pietralla, F. Schließmann, S. Weih, "Low Level RF ERL Experience at the S-DALINAC", presented at ERL'19, Berlin, Germany, September 2019, paper TUCOZBS05, this conference.

[7] F. Schließmann, M. Arnold, M. Dutine, J. Pforr, N. Pietralla, M. Steinhorst, "Beam Dynamics Simulations for the Twofold ERL Mode at the S-DALINAC", presented at ERL'19, Berlin, Germany, September 2019, paper FRCOXBS03, this conference.

[8] M. Dutine, M. Arnold, T. Bahlo, R. Grewe, L.E. Jürgensen, N. Pietralla, F. Schließmann, M. Steinhorst, "Concept of a Beam Diagnostics System for the Multi-Turn ERL Operation at the S-DALINAC", *Proc. IBIC 2019*, Malmö, Sweden, September 2019, pre-release. `http://ibic2019.vrws.de/papers/wepp004.pdf`

ISBN: 978-3-95450-217-2 doi:10.18429/JACoW-ERL2019-MOCOXBS03

STATUS OF NOVOSIBIRSK ERL

N. A. Vinokurov[†,1], Budker Institute of nuclear physics SB RAS, Novosibirsk, Russia
[1]also at Novosibirsk State University, Novosibirsk, Russia

Abstract

The Novosibirsk ERL is dedicated electron beam source for three free electron lasers operating in the wavelength range 8 – 240 micron at average power up to 0.5 kW and peak power about 1 MW. Radiation users works at 8 user stations performing biological, chemical, physical and medical research. The Novosibirsk ERL is the first and the only four-turn ERL in the world. Its peculiar features include the normal-conductive 180 MHz accelerating system, the DC electron gun with the grid thermionic cathode, three operation modes of the magnetic system, and a rather compact (6×40 m2) design. The facility has been operating for users of terahertz radiation since 2004. The status of the installation and plans are described.

INTRODUCTION

The Novosibirsk free electron laser (FEL) facility [1] has three FELs, installed on the first, second and fourth orbits of the dedicated energy recovery linac (ERL). The first FEL covers the wavelength range of 90 – 240 μm at an average radiation power of up to 0.5 kW with a pulse repetition rate of 5.6 or 11.2 MHz and a peak power of up to 1 MW. The second FEL operates in the range of 40 - 80 μm at an average radiation power of up to 0.5 kW with a pulse repetition rate of 7.5 MHz and a peak power of about 1 MW. These two FELs are the world’s most powerful (in terms of average power) sources of coherent narrow-band (less than 1%) radiation in their wavelength ranges. The third FEL was commissioned in 2015 to cover the wavelength range of 5 – 20 μm. The Novosibirsk ERL is the first and the only multiturn ERL in the world. Its peculiar features include the normal-conductive 180 MHz accelerating system, the DC electron gun with the grid thermionic cathode, three operation modes of the magnetic system, and a rather compact (6×40 m^2) design. The facility has been operating for users of terahertz radiation since 2004 [2].

ERL

All the FELs use the electron beam of the same electron accelerator, a multi-turn ERL. A simplified scheme of the four-turn ERL is shown in Fig. 1. Starting from low-energy injector 1, electrons pass four times through accelerating radio frequency (RF) structure 2. After that, they lose part of their energy in FEL undulator 4. The used electron beam is decelerated in the same RF structure, and the low-energy electrons are absorbed in beam dump 5.

The electron source is a 300-kV electrostatic gun with a grid cathode. It provides 1-ns bunches with a charge of up to 1.5 nC, a normalized emittance of about 20 μm, and a repetition rate of zero to 22.5 MHz. After the 180.4-MHz bunching cavity the bunches are compressed in the drift space (about 3 m length), accelerated in the two 180.4-MHz accelerating cavities up to 2 MeV, and injected by the injection beamline and the chicane into the main accelerating structure of the ERL (see Fig. 2).

The accelerating structure consists of 16 normal-conducting RF cavities, connected to two waveguides. The operation frequency is 180.4 MHz. Such a low frequency allows operation with long bunches and high currents.

The Novosibirsk ERL has three modes, one mode for operation of each of the three FELs. The first FEL is installed under the accelerating (RF) structure (see Figs. 2 and 3). Therefore, after the first passage through the RF structure, the electron beam with an energy of 11 MeV is turned by

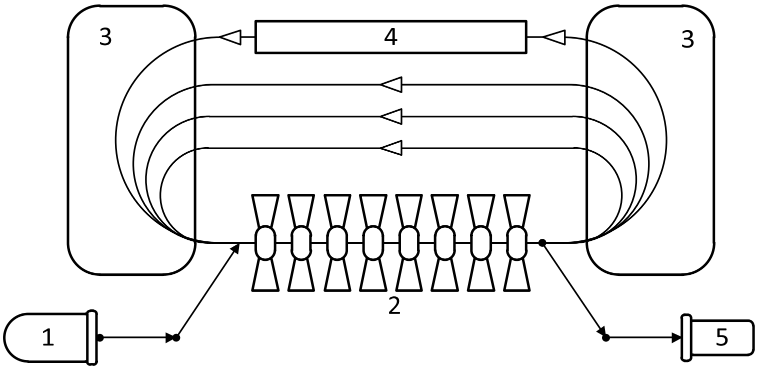

Figure 1: The simplified scheme of Novosibirsk ERL. 1 – injector, 2 – main accelerating structure, 3 – bending magnets, 4 – FEL, 5 – beam dump.

[†] vinokurov@inp.nsk.su

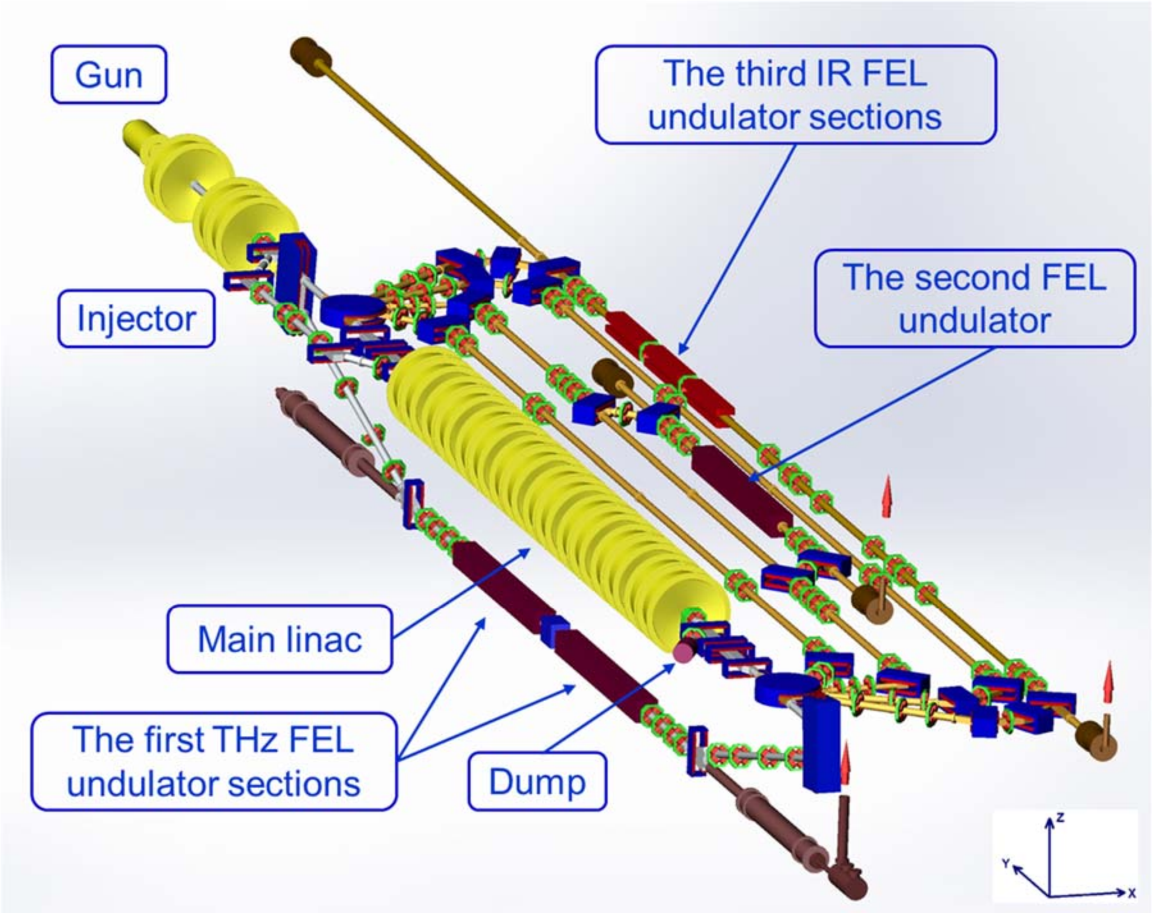

Figure 2: The Novosibirsk ERL with three FELs (top view).

180 degrees in the vertical plane. After the use in the FEL, the beam returns to the RF structure in the decelerating phase. In this mode, the ERL operates as a single-orbit installation.

For operation with the second and third FELs, two round magnets (a spreader and a recombiner) are switched on. They bend the beam in the horizontal plane, as shown in Fig. 2. After four passes through the RF accelerating structure, the electron beam gets in the undulator of the third FEL. The energy of electrons in the third FEL is about 42 MeV. The used beam is decelerated four times and goes to the beam dump.

If the four magnets on the second track (see Fig. 2) are switched on, the beam with an energy of 20 MeV passes through the second FEL. After that, it enters the accelerating structure in the decelerating phase due to the choice of the length of the path through the second FEL. Therefore, after two decelerations the used beam is absorbed in the beam dump.

A photo of the accelerator hall with the accelerating RF cavities and the FELs is shown in Fig. 3.

It is worth noting that all the 180-degree bends are achromatic (even second-order achromatic on the first and second horizontal tracks,) but non-isochronous. It enables beam longitudinal “gymnastics” to increase the peak current in the FELs and to optimize deceleration of the used beam.

The current of the Novosibirsk ERL is now limited by the electron gun. A new RF gun was built and tested recently. It operates at a frequency of 90 MHz. An average beam current of more than 100 mA was achieved [3]. The injection beamline for the RF gun is manufactured and installed to the beam test facility.

CONCLUSION

Novosibirsk ERL is in operation for more than 15 years. It provides the beam for three FELs of the Novosibirsk FEL user facility in the collective research center “Siberian Synchrotron and Terahertz Radiation Centre”. Several upgrades are planned to improve radiation parameters.

Figure 3: Acclelerator hall with the accelerating RF cavities (upper left side) and the FELs (lower left and upper right sides).

REFERENCES

[1] Vinokurov N. A. and Shevchenko O. A., "Free electron lasers and their development at the Budker Institute of Nuclear Physics",*Physics-Uspekhi,* **61**, 5, 435 (2018). `doi:10.3367/UFNe.2018.02.038311`

[2] Knyazev B.A. *et al*., "Recent experiments at NovoFEL user stations", *EPJ Web of Conferences*. **195**, 00002 (2018). `doi:10.1051/epjconf/201819500002`

[3] Volkov V.N. *et al*., "Latest Results of CW 100 mA Electron RF Gun for Novosibirsk ERL Based FEL", *Proc. 29th Lin. Accel. Conf. LINAC 2018*. 598 (2018). `doi:10.18429/JACoW-LINAC2018-WE1A03`

ISBN: 978-3-95450-217-2 doi:10.18429/JACoW-ERL2019-MOCOXBS04

THE BERLIN ENERGY RECOVERY LINAC PROJECT bERLinPro – STATUS, PLANS AND FUTURE OPPORTUNITIES*

M. Abo-Bakr†, N. Al-Saokal, W. Anders, A. Büchel, K. Bürkmann-Gehrlein, A. Bundels, Y. Bergmann, P. Echevarria, A. Frahm, H.-W. Glock, F. Glöckner, F. Göbel, S. Heling, J.-G. Hwang, H. Huck, A. Jankowiak, C. Kalus, T. Kamps, G. Klemz, J. Knobloch, J. Kolbe, J. Kühn, B. Kuske, J. Kuszynski, A. Matveenko, M. McAteer, A. Meseck, S. Mistry, R. Müller, A. Neumann, N. Ohm-Krafft, K. Ott, L. Pichl, F. Pflocksch, J. Rahn, O. Schüler, M. Schuster, Y. Tamashevich, J. Ullrich, A. Ushakov, J. Völker,
Helmholtz-Zentrum Berlin für Materialien und Energie GmbH, Berlin, Germany.

Abstract

The Helmholtz-Zentrum Berlin is constructing the Energy Recovery Linac Project bERLinPro, a demonstration facility for the science and technology of ERLs for future light source applications. bERLinPro was designed to accelerate a high current (100 mA, 50 MeV), high brilliance (norm. emittance below 1 mm mrad) cw electron beam. Given the recent prioritization of the BESSY II light source upgrade to the BESSY VSR variable pulse length storage ring, HZB is forced to draw on resources originally allocated to bERLinPro so that the full project goals can no longer be reached within the current project period. As a result, bERLinPro had to be descoped within the present boundary conditions, with the goal to maximize its scientific impact . We report on the adjusted project goals, on the progress and status of the building, the warm and cold infrastructure and on the time line of the remaining project.

INTRODUCTION

bERLinPro [1] is an Energy Recovery Linac Project, currently under construction at the Helmholtz-Zentrum Berlin (HZB), Germany. Application of superconducting radio frequency (SRF) systems will allow cw operation of all RF systems and thus to accelerate high currents. The layout is shown in Fig. 1, the project's basic set of parameters is listed in Table 1.

The bERLinPro injector, consisting of an photo injector cavity (1.4 cell), followed by a Booster module containing three SRF cavities (2 cells), generates a high brilliant beam with an energy of 6.5 MeV.

The beam from the injector is merged into the linac section by means of a dogleg chicane. Two beams then pass the main linac to be accelerated and decelerated respectively. Through a racetrack magnetic lattice, the accelerated beam will be recirculated to demonstrate effective energy recovery, while the decelerated one is sent into the dump line with a high power (650 kW, designed for 100 mA operation) beam dump at its end.

Space in the return arc is provided to install future experiments or insertion devices to demonstrate the potential of ERLs for user applications. Various of these options have been discussed on a satellite workshop [2] of the ERL2019. Due to schedule, resources and budget reasons a major descope of the project became necessary. As one of the two major consequences, the high current gun, planned for up to 100 mA beam operation in a later phase of the project was canceled. Thus bERLinPro will be operated with a medium current gun only, expected to generate a maximum current of about 5 mA, limited by the installed TTF III RF power couplers. The second major project descope is the cancellation of the bERLinPro main linac, which will not be part of the project anymore. However, acceleration and energy recovery is still planned in bERLinPro, due to a collaboration with the Johann Gutenberg University Mainz. With the so called MESA option [3] the temporal test operation of one of the two MESA project [4] main linacs will give the chance to characterize the MESA module with beam and to accelerate the beam in bERLinPro to an energy of about 32 MeV and to demonstrate energy recovery.

Table 1: bERLinPro's main target parameters, initial project goals before descoping parenthesized.

parameter	**value**
maximum beam energy / MeV	32 (50)
maximum average current* / mA	5 (100)
RF freq. & max. rep. rate / GHz	1.3
reference bunch charge / pC	77
normalized emittance / μm rad	1.0
bunch length (standard mode) / ps	2.0
bunch length (short pulse mode**) / fs	100
maximum losses	$< 10^{-5}$

* limited by the gun maximum coupler power or to lower values by beam break up (BBU)
** at reduced bunch charge

The accelerator installation was planned in two stages, to subsequently commission the various SRF modules and machine parts. Stage-I, being the entire low energy beam path from the gun to the high power beam dump, is completed now: all girders and magnets as well as the vacuum system components including all the diagnostics hardware are placed and aligned, RF and cryogenic installations are finished. The only exception are the two SRF modules (gun

---

* Work supported by the German Bundesministerium für Bildung und Forschung, Land Berlin and grants of Helmholtz Association.
† Michael.Abo-Bakr@helmholtz-berlin.de

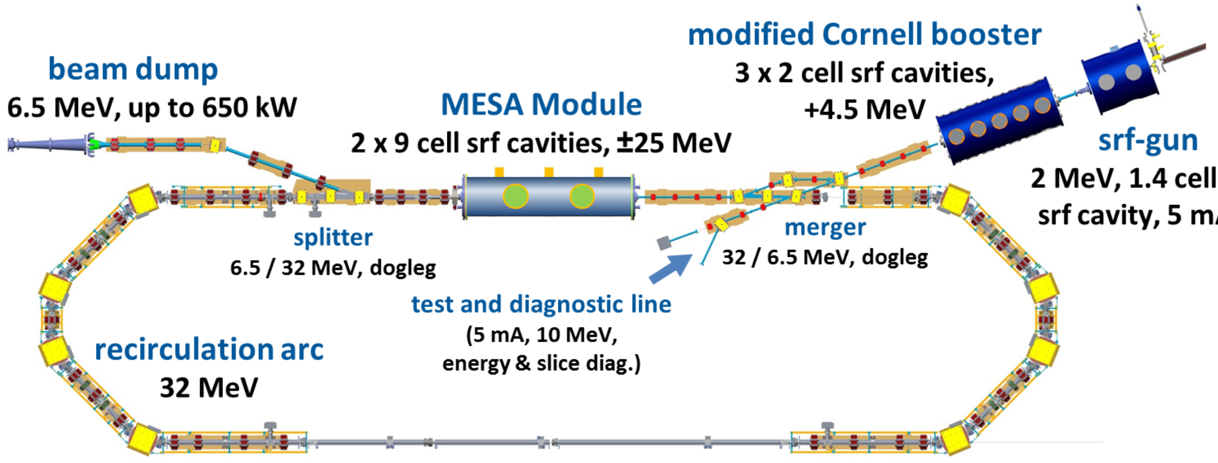

Figure 1: bERLinPro - with a MESA module as main linac.

& Booster), where still major components to start the cold string and module assembly are missing. Several production problems at the vendors, both with the gun cavity as well as with the Booster high power input couplers caused significant delivery delays. These directly determine the duration of Stage-I operation, since its end is set by the installation of the recirculator vacuum system, needed to start in October 2020 to hold the schedule for the remaining project phase, Stage II, running until the end of 2022 (with the MESA module at least until 6/2022). With the most recent delays, accumulated over the last year the Stage-I operation period shrunk to zero and will be not longer possible within the given time constraints. For that reason the installation of the whole machine for Stage II, including Gun, Booster & MESA module and the recirculator vacuum system will be completed, before bERLinPro commissioning and beam operation will start in mid of 2021.

BUILDING

The major construction of the building (Fig.: 2) was completed in 2016 so that machine component installation could begin. Two issues still need to be completed: first, the smoke exhaust system had to be modified to guarantee the requested volume flow, so far limited by under designed ventilation shafts. After installing a more powerful exhaust the incoming air flow was found to be insufficient. A solution has been worked out and is awaiting its official authority permit from an external air conditioning expert. Second, after more than one year operating the cooling water system severe corrosion at welding seams were found in routine checks. After a full system inspection it became clear that the majority of seams had not been adequately welded. Moreover wrong types of steel (V2A instead of V4A) have been found, so that most of the pipes needed to be disassembled and have to be repaired or even replaced.

The work on both issues is ongoing and expected to be finished until the end of this year, so that the formal hand over of the building to the HZB may be expected in early 2020.

Figure 2: bERLinPro-Building in summer 2019

WARM MACHINE

All girders and magnets were delivered and installed in 2017 [5]. The Stage I magnets were precisely aligned after the installation of the vacuum chamber in the low energy machine part last year. The recirculator magnets will be reopened for vacuum chamber installation and heating by the end of next year, closed again and finally aligned. The dump has been installed also in 2017 - an additional lead block enclosure for local radiation protection has been erected this year.

The Stage I diagnostics components were installed together with the vacuum chamber. Cabling is ongoing and first hardware test have been started. The Control System is set up in its basic conception [6]. It is EPICS based and adopted from the other accelerator facilities operated at HZB, so that most solution for device communication and control as well as a variety of operation software is available.

The personal interlock system will become operational in the beginning of next year [7].

SRF COMPONENTS

A comprehensive overview on the status of the bERLinPro SRF Gun cavity can be found in [8], RF properties of all systems are shown in e.g. [9].

RF and Cryo System

RF Systems: all three 270 kW amplifiers are installed now, four solid state 15 kW amplifiers are ordered. Also all circulators and wave guides were completely delivered and have been partly assembled already. The water cooled high power loads are partly delivered - one of them was already in use during the first 270 kW amplifier tests in full power operation (still before the loss of cooling water).

Cryogenics: Infrastructure: a L700-type, 4K Helium refrigerator was moved to bERLinPro accelerator hall. A 1.8 K cold compressor box, warm vacuum pumps, all cryogenic lines and three feedboxes for the cryomodules are delivered, installed and cabled. All leak tests have successfully been passed. The system is now awaiting commissioning, starting as soon as the cooling water is available again.

Electron Source

Two gun versions were initially planned: Gun1.0 (with TTF type couplers) for the first medium current project phase. In the second project stage a high power version - Gun 2.0 with KEK type couplers and capable to generate a 100 mA beam of up to 2.3 MeV energy - was planned to replace the first gun. With the descope of the project Gun2.0 had to be canceled, so that the maximum beam current will coupler limited remain at about 5 mA.

Cathode

A codeposition growth procedure has been developed at HZB to deliver high quantum efficiency (QE) Cs-K-Sb photo cathodes for bERLinPro [10]. Furthermore, upgrades have been made in the photo cathode laboratory to bring the production and analysis system (PAS) closer to a robust production system, namely with the installation of a new manipulator [11], see Fig. 3.

The thermal contact experiment (TCX, [12]) has been established to recreate the conditions inside the photo injector with respect to the cathode cooling system. Initial tests have been conducted using LN2 as a cooling medium. It was found, that a heat load of 30 W on the plug, would bring the plug up to room temperature. This could be reproduced in several cycles of assembling and disassembling the cathode plug to the holder. Further tests using He (g) have now begun which better simulate cooling in the gun.

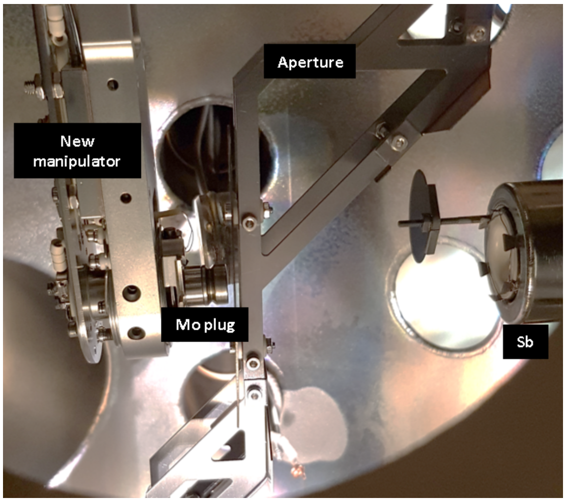

Figure 3: New manipulator in the cathode preparation chamber.

Laser

Two lasers systems, running on 50 MHz and 1.3 GHz, are being developed and will be installed at the HZB by the Max Born Institute.

The 50 MHz laser in addition will deliver single bunches within a set of repetition rates in the Hz to 100 kHz range. It will be operational by the end of 2019. Starting in the NIR ($\lambda \approx 1\ \mu$m) after frequency doubling in a nonlinear conversion crystal the required wavelength in the green is generated. Synchronization with the RF system has been demonstrated down to the sub-picosecond level. The 1.3 GHz laser is under construction, expected to become operational in mid 2020.

The beam line from the laser hutch to the cathode in the gun module has a length of about 36 m. All optical components have been delivered. Due to the limited accessibility of major beam line parts (e.g. in the vicinity of the ceiling) some of the mirrors and lenses will be remotely adjustable. By operating about 24 m of the beam line under fine vacuum conditions ($p \sim 1$ mbar) degradation of the pointing stability of the laser spot on the cathode surface will be strongly reduced. The remaining distance needs to be accessible for alignment and diagnostic purposes and will be contained in tubes placed in air.

1.4 Cell Gun Cavity & Module

The SRF prototype gun cavity was an in-house development [13] in a collaboration with Thomas Jefferson Laboratory and Helmholtz Zentrum Dresden and used in a dedicated test facility called GunLab to demonstrate first beam generation with a high QE Cs-K-Sb photo cathode. The main idea was to fully characterize the photo injector's beam properties before installing it into bERLinPro. An overview of the limited beam program is presented in [14].

During assembly and testing of the SRF gun module in GunLab valuable experience was gained with the operation of this demanding technology in combination with a diagnostic beam-line and especially integrating a normal conducting, thermal-electrically isolated cathode into the cavity. By that, all surrounding vacuum systems have to maintain an ISO 5 cleanroom norm to avoid contamination and thus limitation of the SRF gun cavity. While the cavity's performance was maintained during the cleanroom assembly of the cold string, some level of contamination started to limit the usable field range by field emission once operating in the module. The reason might be caused by several obstacles, as a breaking of the first view-screen in the beam-line and some accidental venting of the SRF cavity via the cathode transfer system.

Nevertheless, with the first transferred cathode made of solid Copper a limited beam program was performed, measuring QE maps, longitudinal phase-space of both, laser emitted electron beam and unwanted beam or dark current. Also, the cathode positing measurement system was commissioned and cross-checked, as the information of final cathode position with reference to the cathode cell's backplane is crucial for survival of this system. In the following, the holding system got damaged by over-heating and RF sputtering caused by a gap between Cu cathode plug and holder. This led finally to a loss of the next cathode of Cs-K-Sb type and the GunLab program was stopped.

In parallel a second cavity was manufactured, but before delivery to rebuild the gun module for bERLinPro got damaged on the inner RF surface at the vendor's site. Using both, the cavity operated at GunLab and the new one, a repair program was developed to mechanically remove the inner damages followed by chemical etching using standard buffered chemical polishing. This process is underway and the first cavity acts as a pilot in this refurbishment method, before it will be applied to the second cavity for bERLinPro. In case - this process is finalized in November this year, RF commissioning of the module can start autumn 2020. In the meantime, module assembly is being prepared in the accelerator hall.

Booster Module

The HZB Booster module is based on the Cornell design using three instead of five cavities and the first in zero-crossing operation for longitudinal phase space manipulation. Thus, for the two high power cavities new couplers had to be designed for up to 120 kW in cw regime to reach the envisaged voltage of 2.2 MV per cavity. For that also the coupling section of the cavities was modified. New fundamental power couplers were developed which are based on a design by KEK for their cERL project, but modified with respect to increased coupling and minimized coupler kick by a specially shaped antenna tip [15].

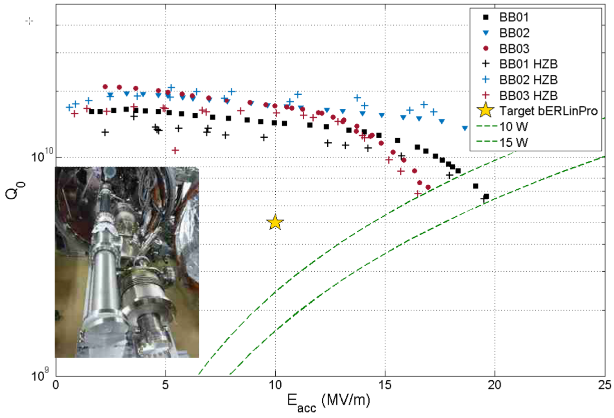

Figure 4: Quality factor versus accelerating field measurement reproducing the vertical test results from JLab at HZB in horizontal set up, see insert picture.

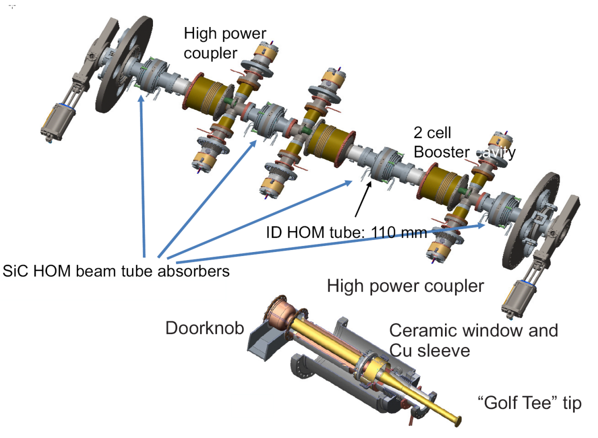

Figure 5: Scheme of the Booster module cold string and a cut-view of the fundamental power coupler.

Cavities

All cavities were retested at HZB and still fulfilled by far the specifications as shown in Fig. 4, similar to the post production tests done at JLab. Recently cavity one was retested with the blade tuner system installed and the results are unchanged, whereas the tuner system meets the required specifications.

Fig. 5 shows an overview of the Booster module cold string comprised of three 2-cell cavities with a Cornell style SiC higher oder mode absorber on both sides of each cavity. To limit the power load per coupler and reduce beam deterioration caused by coupler field distortions, each cavity is powered by a pair of opposite fundamental power couplers as shown in the sketch below the cold string.

Coupler

The modification of the KEK design to adapt it to the bERLinPro project requirements is described in detail in the following publications: [15–17].

Currently all eight coupler cold parts were received and also some pair of preliminary warm parts, so that assembly of the RF conditioning test stand was finished recently, see Fig. 6. Once radiation safety permit is issued and final installations are done, the conditioning will start about in Q1/2020, with the full power test envisaged around Q2/2020, when the final warm coupler parts are received. For the 5 mA operation regime, the fixed power coupling will be adjusted by spacers to increase external quality factor from $1.05{\cdot}10^5$ to about $1.8{\cdot}10^6$. Once full power operation is foreseen, those will be removed by reassembling the couplers. This reduces the required power from 60 kW to 13 kW at this beam current.

Module

In Fig. 7 a cut view of the module is shown. It will have a 80K Helium gas cooled thermal shielding and 2 layers of Cryoperm$^{\mathrm{TM}}$ magnetic shielding, whereas the first layer is between Helium tank and tuner of each cavity, the outer shielding is still locally around the cavity. That was done for

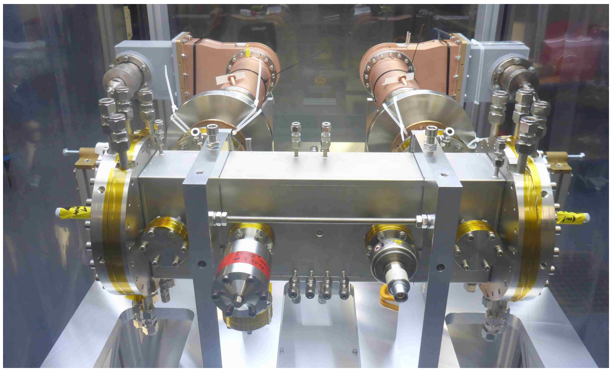

Figure 6: First pair of high power couplers installed for RF conditioning.

cost reasons, so that small vertical steering magnets are to be installed around the HOM absorbers to compensate for earth magnetic field which will act on the beam between the shielded areas via the normal conducting beam pipes.

Besides the HOM absorbers all cold string parts are in house, as well as magnetic shields, tuners, etc. The cryo-piping, thermal shielding and cryostat are currently being procured. It is planned to start string assembly after coupler conditioning around Q3/2020 and in the following complete the module. First cooldown and RF commissioning will thus happen within the bERLinPro's accelerator hall.

Linac Module / MESA Module

The revaluation of the project goals for now have stopped any further development of the bERLinPro main linac cavity and module. Still, for future upgrade the design is ready to being built [9, 18]. Currently all work is focused on integrating the MESA module into bERLinPro, see e.g. [3]. The main adjustments neccessary, are the adoption of the bERLinPro cryo-system to the pressure level and safety valve settings of the MESA linac module. Also a vacuum adapter with emphasis on particulate free assembly is designed which fits the bERLinPro vacuum system and beam pipe to the MESA module's geometry. Currently, a plan how to define acceptance tests to compare the performance of the module before and after operation with bERLinPro is being worked out. Anyhow, the MESA module will be the first linac to be operated with bERLinPro in ERL mode and eventually studies about beam break up can be performed [19].

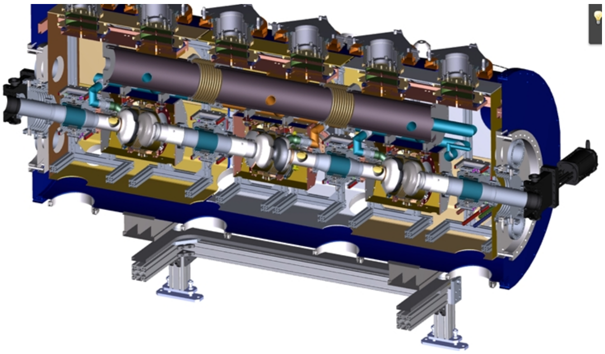

Figure 7: Cut view of the Booster module design.

OPTICS & THEORY

While the descoping of the project does not affect the injector design, the change of the main linac has some influence on the recirculator. The varied linac layout and the reduced accelerating gradients require moderate adjustments of the beam optics.

The change of strength and position of RF focusing in the main linac leads to modified matching conditions into the recirculator. With the reduced recirculation energy also the velocity decreases so that the path length had to be adjusted by about 5 mm. Also with the reduced recirculation energy the bump amplitude of the merger and splitter chicanes grows, but still will not limit the horizontal machine acceptance. However, a reduction of the injection energy remains possible though not favored. At reduced energy the beam becomes more sensitive to space charge (SC) and coherent synchrotron radiation (CSR) effects. Although of acceptable amount, an increased emittance dilution is seen in the simulation as well as indications for micro bunching [20]. After all recirculator adjustments also a re-tuning of the dump line including SC forces becomes necessary.

BBU threshold calculations using the measured MESA cavity HOM spectra with the updated bERLinPro lattice still have to be done. Beside these activities, commissioning planning is ongoing and tests of measurement routines have started.

TIMELINE

The proposed bERLinPro timeline for the remaining project time is summarized in Table 2. The operation period will start in mid of 2021 and includes all steps from commissioning to recirculation and energy recover. It is limited by the date, the MESA module needs to be returned to Mainz, currently assumed for the second half of 2022. VSR module tests in bERLinPro hall are delayed too and will most likely not happen during the foreseen operation period. The funding for a 2000 h/a operation of bERLinPro is secured until the end of 2022.

Table 2: bERLinPro - Present Project Planning

06/2020	Gun1 cool down and RF commissioning (no beam tests)
10/2020	start installation of recirculator vacuum (to be finished 03/2021)
12/2020	Booster module installed
01/2021	MESA module installed (collaboration JGU Mainz, 2 x 9 cell)
06/2021	First beam possible, with subsequent recirculation & recovery

REFERENCES

[1] M. Abo-Bakr *et al.*, “Status Report of the Berlin Energy Recovery Linac Project BERLinPro”, in *Proc. 9th Int. Particle Accelerator Conf. (IPAC’18)*, Vancouver, Canada, Apr.-May 2018, pp. 4127–4130. `doi:10.18429/JACoW-IPAC2018-THPMF034`

[2] T. Kamps *et al.*, “Scientific opportunies for bERLinPro 2020+, report with ideas and conclusions from bERLinProCamp 2019”, ERL 2019, arXiv:1910.00881.

[3] B.C. Kuske, W. Anders, K. Aulenbacher, F. Hug, A. Jankowiak, A. Neumann, *et al.*, “Incorporation of a MESA Linac Modules into BERLinPro”, in *Proc. IPAC’19*, Melbourne, Australia, May 2019, pp. 1449–1452, `doi:10.18429/JACoW-IPAC2019-TUPGW023`

[4] F. Hug *et al.*, “Status of the MESA ERL Project”, presented at the 63rd Advanced ICFA Beam Dynamics Workshop on Energy Recovery Linacs (ERL’19), Berlin, Germany, Sep. 2019, paper MOCOXBS05, this conference.

[5] A. N. Matveenko *et al.*, “The Magnets of BERLinPro: Specification, Design, Measurement and Quality Analysis”, in *Proc. 8th Int. Particle Accelerator Conf. (IPAC’17)*, Copenhagen, Denmark, May 2017, pp. 4124–4126. `doi:10.18429/JACoW-IPAC2017-THPIK012`

[6] T. Birke *et al.*, “Status of the Control System for the Energy Recovery Linac bERLinPro at HZB”, presented at the 63rd Advanced ICFA Beam Dynamics Workshop on Energy Recovery Linacs (ERL’19), Berlin, Germany, Sep. 2019, paper FRCOXBS04, this conference.

[7] L. Pichl, Y. Bergmann, A. Bundels, and K. Ott, “Radiation Protection Instrumentation of bERLinPro”, presented at the 63rd Advanced ICFA Beam Dynamics Workshop on Energy Recovery Linacs (ERL’19), Berlin, Germany, Sep. 2019, paper WEPNEC06, this conference.

[8] A. Neumann *et al.*, “Status of SRF Gun for bERLinPro”, presented at the 63rd Advanced ICFA Beam Dynamics Workshop on Energy Recovery Linacs (ERL’19), Berlin, Germany, Sep. 2019, paper THCOZBS02, this conference.

[9] A. Neumann *et al.*, “Update on SRF Cavity Design, Production and Testing for BERLinPro”, in *Proc. 17th International Conference on RF Superconductivity (SRF2015)*, Whistler, BC, Canada, 13-18, 2015, paper THPB026, pp. 1127–1131, `doi:10.18429/JACoW-SRF2015-THPB026`, 2015.

[10] M.A.H. Schmeißer, et al. ”Towards the operation of Cs-K-Sb photocathodes in superconducting rf photoinjectors.” Physical Review Accelerators and Beams 21.11 (2018): 113401. `doi:10.1103/PhysRevAccelBeams.21.113401`

[11] S. Mistry, A. Jankowiak, T. Kamps, and J. Kuehn, “Photocathode Preparation and Characterization at HZB.”, presented at the 63rd Advanced ICFA Beam Dynamics Workshop on Energy Recovery Linacs (ERL’19), Berlin, Germany, Sep. 2019, paper WECOXBS01, this conference.

[12] N. Al-Saokal *et al.*, “Thermal Load Studies on the Photocathode Insert with Exchangeable Plug for the bERLinPro SRF-Photoinjector”, presented at the 63rd Advanced ICFA Beam Dynamics Workshop on Energy Recovery Linacs (ERL’19), Berlin, Germany, Sep. 2019, paper WEPNEC03, this conference.

[13] A. Neumann et al., ”Photoinjector SRF Cavity Development for BERLinPro”, Proceedings of LINAC2012, Tel-Aviv, Israel THPB066, pp. 993-995

[14] A. Neumann *et al.*, “The BERLinPro SRF Photoinjector System - From First RF Commissioning to First Beam”, in *Proc. IPAC’18*, Vancouver, BC, Canada, Apr. 4,, pp. 1660–1663, `doi:10.18429/JACoW-IPAC2018-TUPML053`

[15] A. Neumann *et al.*, “Booster Cavity and Fundamental Power Coupler Design Issues for BERLinPro”, in *Proc. IPAC’14*, Dresden, Germany, June 2014, pp. 2490–2492, `doi:10.18429/JACoW-IPAC2014-WEPRI007`

[16] V.F. Khan, W. Anders, A. Burrill, J. Knobloch, and A. Neumann, “High Power RF Input Couplers and Test Stand for the BERLinPro Project”, in *Proc. IPAC’14*, Dresden, Germany, June 2014, pp. 2487–2489, `doi:10.18429/JACoW-IPAC2014-WEPRI006`

[17] B.D.S. Hall, V. Dürr, F. Göbel, J. Knobloch, and A. Neumann, “120kW RF Power Input Couplers for BERLinPro”, in *Proc. 8th Int. Particle Accelerator Conf. (IPAC’17)*, Copenhagen, Denmark, May 2017, paper MOPVA046, pp. 960–963, `doi:10.18429/JACoW-IPAC2017-MOPVA046`, 2017.

[18] A. Neumann, K. Brackebusch, T. Flisgen, T. Galek, J. Knobloch, B. Riemann, U. van Rienen and T. Weis “Final Design for the BERLinPro Main Linac Cavity”, in *Proc. 27th Int. Linear Accelerator Conf. (LINAC’14)*, Geneva, Switzerland, September 2014, paper MOPP070, pp. 217–220, `http://accelconf.web.cern.ch/AccelConf/LINAC2014/papers/mopp070.pdf`, 2014.

[19] C.P. Stoll and F. Hug, “Beam Breakup Simulations for the Mainz Energy Recovering Superconducting Accelerator MESA”, in *Proc. IPAC’19*, Melbourne, Australia, May 2019, pp. 135–138, `doi:10.18429/JACoW-IPAC2019-MOPGW025`

[20] B.C. Kuske and A. Meseck, “Numerical Calculation of Micro Bunching in BERLinPro Due to Space Charge and CSR Effects”, in *Proc. IPAC’19*, Melbourne, Australia, May 2019, pp. 116–119, `doi:10.18429/JACoW-IPAC2019-MOPGW020`

STATUS OF THE MESA ERL-PROJECT*

F. Hug†, K. Aulenbacher[1], S. Friederich, P. Heil, R.G. Heine, R. Kempf, C. Matejcek, D. Simon
Johannes Gutenberg-Universität Mainz, Mainz, Germany
[1]also at Helmholtz Institut Mainz, Germany and
GSI Helmholtzzentrum für Schwerionenforschung, Darmstadt, Germany

Abstract

MESA is a recirculating superconducting accelerator under construction at Johannes Gutenberg-Universität Mainz. It can be operated in either external beam or ERL mode and will be used for high precision particle physics experiments. The operating cw beam current and energy in EB mode is 0.15 mA with polarized electrons at 155 MeV. In ERL mode a polarized beam of 1 mA at 105 MeV will be available. In a later construction stage of MESA the beam current in ERL-mode shall be upgraded to 10 mA (unpolarized). Civil construction and commissioning of components like electron gun, LEBT and SRF modules have been started already. We will give a project overview including the accelerator layout, the current status and an outlook to the next construction and commissioning steps.

INTRODUCTION

The Mainz Energy-recovering Superconducting Accelerator (MESA) (layout see Fig. 1) will be a low energy continuous wave (cw) recirculating electron linac for particle and nuclear physics experiments. In the first phase of operation it will serve mainly three experiments.

The main experiment of MESA, run in external beam (EB) mode, where the beam needs to be dumped after being used, will be the fixed target setup P2 [1], whose goal is the measurement of the weak mixing angle (Weinberg angle) by measuring parity violation asymmetry with highest accuracy. Required beam current for P2 is 150 µA with spin-polarized electrons at a maximum energy of 155 MeV.

Additionally, a so called beam-dump experiment (BDX) is planned to run in parallel to P2 [2]. This experiment will be located outside of the accelerator hall in line with the beam dump and is dedicated for searching dark particles, which might be generated dumping the beam of the P2 experiment, benefiting from the massive radiation shielding of the dump, which reduces background to a minimum. The third experimental setup will be the high resolution two-arm spectrometer facility MAGIX [3], which uses a gas jet target [4] and can be run in ERL mode.

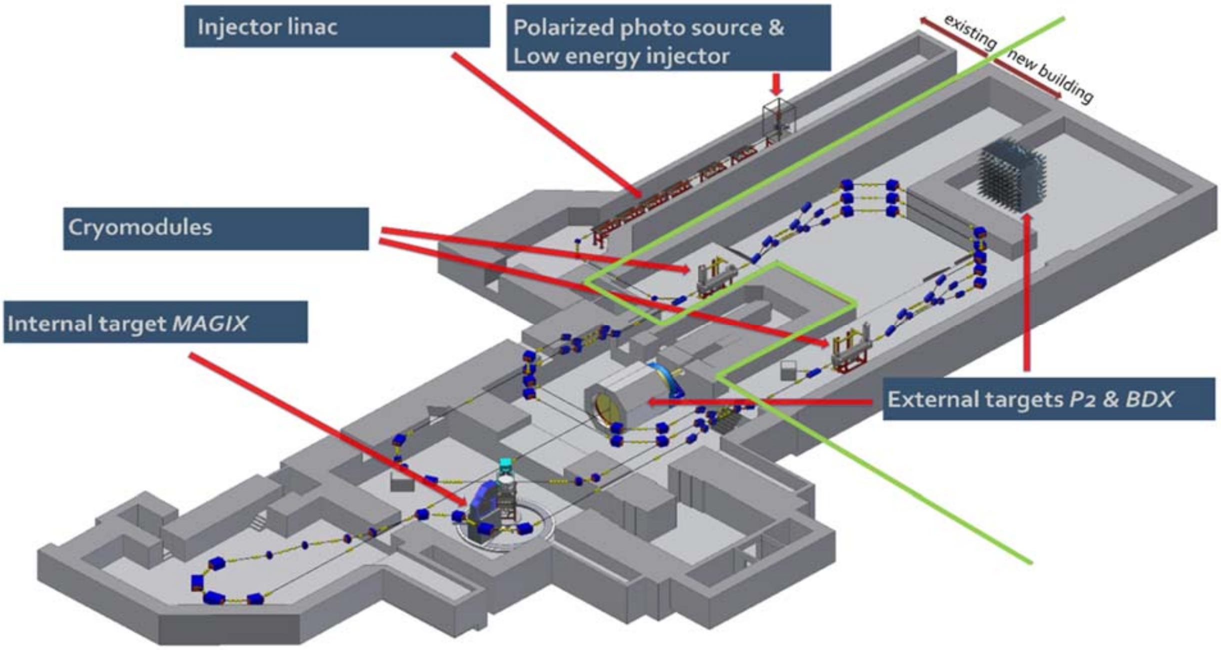

Figure 1: Layout of the MESA accelerator and the planned experimental setups. The accelerator will be located in existing and newly constructed underground halls. The boundary between the old and new parts of the building is marked by a green line. The injector will be constructed and commissioned first as it is located in an existing building part. Civil construction work for the new underground hall has started and will last until end 2021. Afterwards, construction of main linac and experiments will start as well (courtesy of drawing: D. Simon).

---

* This work has been supported by DFG through the PRISMA$^+$ cluster of excellence EXC 2118/2019 and by the European Union's Horizon 2020 Research and Innovation programme under Grant Agreement No 730871.

†.flohug@uni-mainz.de

The maximum beam energy in ERL mode is limited to 105 MeV as up to two recirculations can be used only in contrary to the external mode with up to three recirculations. Nevertheless, the beam current in ERL mode is not limited by rf power installed at the superconducting main linac anymore and is planned to be 1 mA in the beginning of MESA operation Later, this current shall be upgraded to 10 mA, which is the maximum available current from the normal-conducting injector linac MAMBO [5]. The MAGIX facility can be used for different experiments on gas targets in ERL operation. Highlights will be the precise measurement of the proton radius at low momentum transfer or the search for dark photons, both on a Hydrogen gas jet target. In addition, the experiment can be run in an external mode as well, then restricted to lower beam current comparable to P2.

MESA LAYOUT

Underground Halls

The MESA accelerator has been designed since approx. 2009 [6] and its construction was funded in 2012 in course of the cluster of excellence “PRISMA”. Since that date, it has undergone several design changes as the detailed layouts and requirements of the experiments have been optimized as well [7-9]. By now the layouts of both, MESA floorplan and experimental sites, have been finalized. The latest version is presented in Fig. 1. MESA will be constructed partly inside of existing underground halls, which have been used by one experimental setup (A4) at the microtron cascade MAMI [10]. Since A4 has been decommissioned, the existing halls are available now and can be used by MESA. MAMI nevertheless will continue operation in parallel. In addition, the German research foundation DFG funded the erection of an additional experimental hall adjacent to the existing halls in June 2015. Construction of the new hall, which will enlarge the underground area for the accelerator as well as for the experiments, started already. In course of the construction work the existing halls will be refurbished as well. Until start of the refurbishment of the existing underground halls in August 2019, a test setup for the polarized electron gun STEAM [11,12] and the low energy beam transport system MELBA [13] has been located there and produced first low energy electron beams for MESA.

Accelerator Layout

The MESA accelerator will consist of a polarized dc photogun on an extraction voltage of 100 kV followed by a low energy beam transport system (MELBA) containing a spin manipulation system and a chopper-buncher section for longitudinal matching into the normal-conducting booster linac MAMBO. In addition, the LEBT is used for transverse matching into the accelerating structures of the injector and for extensive beam diagnostics. In MAMBO the electrons can be further accelerated by four normal-conducting injector cavities to energies of up to 5 MeV and beam currents of up to10 mA (cw) [5,14]. After the injector the beam is transferred into the main linac through a 180° arc, which can be used as a bunch compressor to reach shortest possible bunches at the position of the first SRF cavity of the main linac [15,16]. The recirculating main linac follows the concept of a double sided accelerator design with vertical stacking of return arcs. Acceleration is done by in total four SRF cavities located in two cryomodules [17]. In the following sections we will present experimental results from the injector test setup (Fig. 2) and give an outlook to the timeline of MESA construction and commissioning. The status of beam optics and cryomodules are presented in [18,19] and will not be discussed in this contribution.

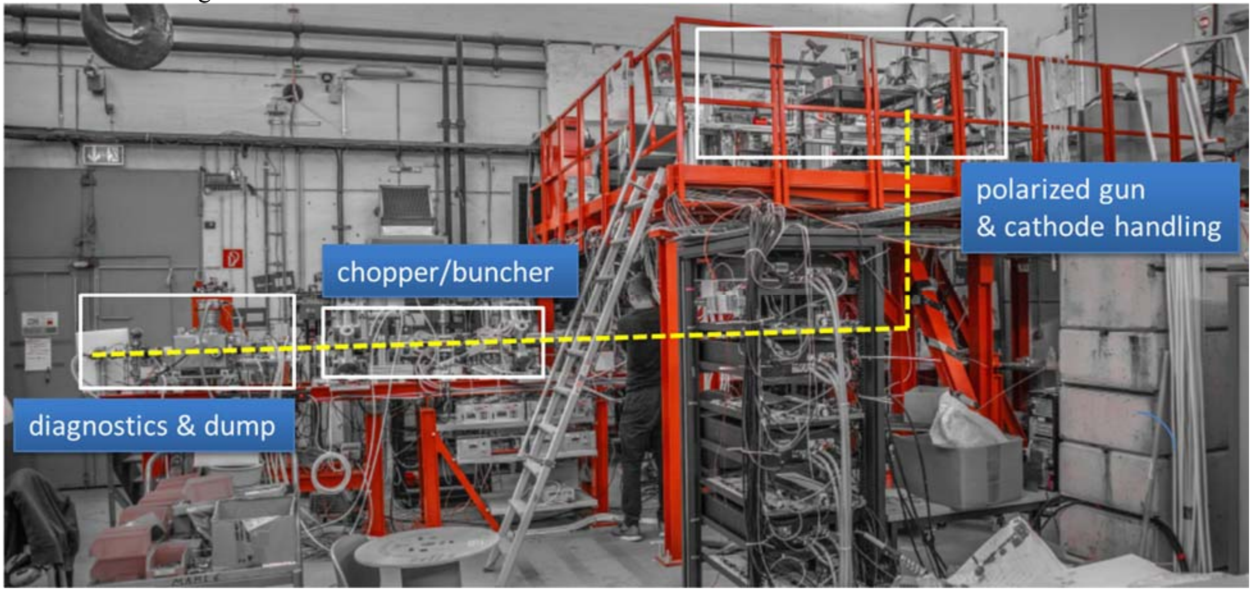

Figure 2: Injector test setup as run until July 2019. The test beamline consisted of the polarized inverted dc gun STEAM and parts of the MELBA LEBT system (chopper, buncher and beam transport). Extensive longitudinal and transverse diagnostics have been set up and used for beam characterization. The way of the electron beam along the beamline is illustrated by the yellow dashed line (photography: MELBA group).

ISBN: 978-3-95450-217-2 doi:10.18429/JACoW-ERL2019-MOCOXBS05

INJECTOR TEST RESULTS

MELBA

The low energy part of the injector has been tested successfully already producing the first MESA beams at 100 keV (and up to higher energies >150 keV for testing reasons) [12,13]. The setup (see Fig. 2) could be used for first tests of the crucial components and for extensive beam diagnostics. During the operation of the MELBA test setup the performance of the dc photo-gun and of the bunching system could be investigated. In addition, a new bunch length diagnostic device [20] and a cavity for future beam stabilization at P2 [21] could be qualified as well. It was possible to demonstrate the extraction of 10 mA beam current from the gun, which already satisfies the goal for MESA stage 2. The results of emittance measurements performed during the beam tests are shown in Fig. 3. Even though the measured emittance deviates from simulations depending on the type of laser used, the required transverse emittance for the 150 µA external MESA beam has been achieved already [13].

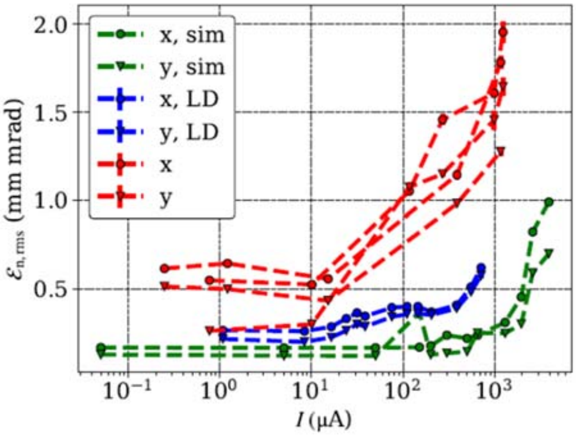

Figure 3: Measurement of beam emittance at different extracted beam current produced by different lasers and compared to simulation results [13]. The emittance goal for the external beam experiment P2 could be achieved already.

MAMBO

The 5 MeV booster linac MAMBO consists of two main components: four normal-conducting cavities, the first one β-graded, and four solid state amplifiers providing the required rf power. For qualifying the cw solid state technology at the MESA operation frequency of 1.3 GHz, a prototype has been produced by industry and tested successfully at HIM [22]. This prototype amplifier could be used for the cryomodule acceptance tests as well [19]. The design of the normal-conducting linac cavities follows the MAMI linac design but needed to be adapted for frequency and for suppressing multipacting in presence of longitudinal magnetic field needed for space-charge compensation at the high current MESA beam. Therefore, a prototype was ordered and tested at Helmholtz Institut Mainz (HIM, see Fig. 4). Both parts performed well and the design of the booster cavities could be verified. The four cavities for the complete MESA booster linac have been ordered from industry and will be delivered to Mainz in fall 2020. Right afterwards the injector construction can start, as the injector will be located in an existing building part and can be constructed independently from the civil construction work of MESA underground halls.

Figure 4: Photography of the MAMBO test cavity inside of the HIM rf test bunker. (photography: R. Heine).

CONCLUSION AND TIMELINE

The MESA accelerator under construction at JGU Mainz will serve nuclear and particle physics experiments with cw electron beams. The experiments are planned and will be run within the framework of PRISMA^{+}. Civil construction work for MESA underground halls is ongoing and planned to be finalized until end 2021. Afterwards accelerator construction and commissioning can start. Nevertheless, important parts of the accelerator have been designed already and tested successfully. In this contribution we concentrated on results of test measurements for the normal-conducting injector at MESA. The dc photogun and LEBT system worked properly and the experimental results gathered in the testing runs will be very useful for beam commissioning of the final injector. The rf tests on the normal-conducting booster cavity prototype using the newly developed solid state amplifier could verify the simulation results.

The timeline for completing the MESA facility is mainly determined by the civil construction work on the underground building. Therefore, construction start of the MESA main accelerator and of the experiments is postponed to end 2021. Construction and commissioning of the injector will start much earlier, as the injector will be located in an existing building part. It is envisaged to have the injector set up and start commissioning before construction of the underground halls is finished. First beam to the experiments is expected in 2023.

REFERENCES

[1] D. Becker *et al.*, "The P2 Experiment - A future high-precision measurement of the electroweak mixing angle at low momentum transfer", *Eur. Phys. J. A* **54** (2018) 208. `doi:10.1140/epja/i2018-12611-6`

[2] M. Christmann *et al.*, "Instrumentation and optimization studies for a beam dump experiment (BDX) at MESA – DarkMESA", *NIM A* (2019), accepted. `doi:10.1016/j.nima.2019.162398`

[3] A. Denig, "Recent results from the Mainz Microtron MAMI and an outlook for the future", *AIP Conf. Proc.* **1735** (2016) 020006. `doi:10.1063/1.4949374`

[4] S. Grieser *et al.*, "A Cryogenic Supersonic Jet Target for Electron Scattering Experiments at MAGIX@MESA and MAMI", *NIM A* **906** (2018) 120. `doi:10.1016/j.nima.2018.07.076`

[5] R. Heine, K. Aulenbacher, "Injector for the MESA Facility", *Proc. IPAC'13*, Shanghai, China, (2013) 2150. Paper: WEPWA011

[6] K. Aulenbacher, A. Jankowiak, "Polarized Electrons and Positrons at the MESA Accelerator", *Proc. of PST 2009*, Ferrara,Italy (2009) 49.

`doi:10.1142/9789814324922_0006`

[7] R. Heine, K.. Aulenbacher, R. Eichhorn, "MESA-Sketch of an Energy Recover Linac for Nuclear Physics Experiments at Mainz", *Proc. of IPAC '12*, New Orleans, Louisiana, USA (2012) 1993. Paper: TUPPR073

[8] D. Simon, K. Aulenbacher, R. Heine, F. Schlander, "Lattice and Beam Dynamics of the Energy Recovery Mode of the Mainz EnergyRecovering Superconducting Accelerator MESA", *Proc. of IPAC '15*, Richmond, Virginia, USA (2015) 220 `doi:10.18429/JACoW-IPAC2015-MOPWA046`

[9] F. Hug, K. Aulenbacher, R.G. Heine, B. Ledroit, D. Simon, "MESA - an ERL Project for Particle Physics Experiments", *Proc. LINAC'16*, East Lansing, MI, USA, (2016) 313.

[10] M. Dehn, K. Aulenbacher, R. Heine, H.J. Kreidel, U. Ludwig-Mertin, A. Jankowiak, "The MAMI C accelerator: The beauty of normal conducting multi-turn recirculators", *Eur.Phys.J.ST,* **198** (2011) 19-47.

[11] S. Friederich, K. Aulenbacher, "Test Electron Source for Increased Brightness Emission by Near Band Gap Photoemission" , *Proc. of IPAC '15*, Richmond, Virginia, USA (2015) 1512. `doi:10.18429/JACoW-IPAC2015-TUPWA044`

[12] S. Friederich, K. Aulenbacher, C. Matejcek, "Vacuum Lifetime and Surface Charge Limit Investigations Concerning High Intensity Spin-Polarized Photoinjectors", *Proc. of IPAC'19* (2019) 1954. `doi:10.18429/JACoW-IPAC2019-TUPTS011`

[13] C. Matejcek, K. Aulenbacher, S. Friederich, "Low Energy Beam Transport System for MESA", *Proc. of IPAC'19* (2019) 1461. `doi:10.18429/JACoW-IPAC2019-TUPGW028`

[14] R. Heine, K. Aulenbacher, L. Hein, C. Matejcek, "Current Status of the Milliampere Booster for the Mainz Energy-recovering Superconducting Accelerator", *Proc. of IPAC '16*, Busan, Korea (2016) 1743. `doi:10.18429/JACoW-IPAC2016-TUPOW002`

[15] F. Hug, R. Heine, "Injector linac stability requirements for high precision experiments at MESA", *J. Phys.: Conf. Ser.* **874** (2017) 012012. `doi:10.1088/1742-6596/874/1/012012`

[16] A. Khan, O. Boine-Frankenheim, F. Hug, C. Stoll, "Beam matching with space charge in energy recovery linacs", *NIM A* **948** (2019) 162822. `doi:10.1016/j.nima.2019.162822`

[17] T. Stengler, K. Aulenbacher, R. Heine, F. Schlander, D. Simon, M. Pekeler, D. Trompetter, "Modified ELBE Cryomodules for the Mainz Energy-Recovering Superconducting Accelerator *MESA", Proc. of SRF '15*, Whistler, Canada (2015) 1413. Paper: THPB116

[18] F. Hug *et al.*, presented at ERL'19, Berlin, Germany, September 2019, paper TUCOXBS03, this conference.

[19] T. Stengler *et al.*, presented at ERL'19, Berlin, Germany, September 2019, paper TUCOZBS06, this conference.

[20] P. Heil, K. Aulenbacher, "Smith-Purcell Radiation for Bunch Length Measurements at the Injection of MESA", *Proc. of IPAC'18*, Vancouver, BC, Canada (2018) 4213. `doi:10.18429/JACoW-IPAC2018-THPMF062`

[21] R. Kempf, K. Aulenbacher, J. Diefenbach, "High Precision Beam Parameter Stabilization for P2 at MESA", *Proc. of IPAC'18*, Vancouver, BC, Canada (2018) 2209. `doi:10.18429/JACoW-IPAC2018-WEPAL024`

[22] R.G. Heine, F. Fichtner, "The MESA 15 kW cw 1.3 GHz Solid State Power Amplifier Prototype", *Proc. of IPAC'18*, Vancouver, BC, Canada (2018) 4216. `doi:10.18429/JACoW-IPAC2018-THPMF063`

ISBN: 978-3-95450-217-2 doi:10.18429/JACoW-ERL2019-MOCOYBS04

ELECTRODISINTEGRATION OF ^{16}O AND THE RATE DETERMINATION OF THE RADIATIVE α CAPTURE ON ^{12}C AT STELLAR ENERGIES

I. Friščić *, T. W. Donnelly, R. G. Milner
Massachusetts Institute of Technology, Cambridge, Massachusetts 02139, USA

Abstract

For over five decades one of the most important goals of experimental nuclear astrophysics has been to reduce the uncertainty in the S-factor of radiative α capture on ^{12}C at stellar energies. We have developed a simple model, which relates the radiative capture reaction and the exclusive electrodisintegration reaction. We then show that by measuring the rate of electrodisintegration of ^{16}O in a high luminosity experiment using a state-of-the-art jet-target and a new generation of energy-recovery linear (ERL) electron accelerators under development, it is possible to significantly improve the statistical uncertainty of the radiative α capture on ^{12}C in terms of E1 and E2 S-factors in the astrophysically interesting region, which are the key inputs for any nucleosynthesis and stellar evolution models. The model needs to be validated experimentally, but, if successful, it can be used to improve the precision of other astrophysically-relevant, radiative capture reactions, thus opening a significant avenue of research that spans nuclear structure, astrophysics and high-power accelerator technology.

INTRODUCTION

During the stellar evolution, the helium burning stage is dominated by two reactions: radiative triple-α capture and radiative α capture on ^{12}C, *i.e.* ^{12}C$(\alpha,\gamma)^{16}$O. The values of the individual rates will determine the ^{12}C/^{16}O abundance at the end of the helium burning stage, which highly influences the subsequent nucleosynthesis [1]. The current uncertainty in triple-α capture at stellar energies is known with an uncertainty of ~10%, but for the ^{12}C$(\alpha,\gamma)^{16}$O rate the situation is much worse [2]. In the modeling of the stellar evolution, the large uncertainty of the measured ^{12}C$(\alpha,\gamma)^{16}$O rate translates into large range of rates and because of this models give different outcomes in terms of nuclei abundance inside a star of a given mass [1, 2]. Thus, for many decades, the goal of experimental nuclear physics was to improve the precision of measurements of the ^{12}C$(\alpha,\gamma)^{16}$O rate at stellar energies [3]. Attempts were made to constrain the ^{12}C$(\alpha,\gamma)^{16}$O rate using the models and the observed solar abundances [1], implicating that the experimental rate needs to be measured with an uncertainty ≤10% [4]. Such a level of precision has still not been achieved..

At typical helium burning temperature for massive stars ~$2\cdot10^8$ K, the equivalent Gamow energy E_g is ~300 keV and due to large Coulomb barrier the cross section of the ^{12}C$(\alpha,\gamma)^{16}$O reaction is extremely small ~10^{-5} pb, making the direct measurements infeasible. The strategy is to measure the cross section, which is usually expressed in terms of the astrophysical S-factor as a function of α-particle center-of-mass (cm) kinetic energy E_α^{cm}:

$$S = \sigma E_\alpha^{cm} e^{2\pi\mu} \tag{1}$$

where μ is the Sommerfeld parameter, at several larger energies and then to extrapolate to stellar energies. The extrapolation is complicated due the structure of ^{16}O [5] and involves dealing with the interference of subthreshold and above threshold E1/E2 states.

In the past, many different experimental methods have been developed and used to measure the ^{12}C$(\alpha,\gamma)^{16}$O rate, including the direct reaction measurements [6–19], elastic scattering ^{12}C$(\alpha,\alpha)^{12}$C [20, 21], and β−delayed α-decay of ^{16}N [22–24]. Below $E_\alpha^{cm} < 2$ MeV the data points are increasingly dominated by the statistical uncertainties, due to rapidly falling of the cross section as it approaches the Gamow energy. Recently, researchers have started to investigate the inverse reaction induced by real photons (the photodisintegration of ^{16}O), in order to improve the statistics of low-energy data. One concept uses a bubble chamber [25, 26] and the other an optical time projection chamber [27]. More details about the specific experiments and the astrophysical implications of the ^{12}C$(\alpha,\gamma)^{16}$O rate can be found in the most recent review [2].

Contrary to photodisintegration, where the real photon beam is involved $|\vec{q}| = q = E_\gamma$, the electrodisintegration uses an electron beam with an exchange of a virtual photon $(\omega,\vec{q})$, for details see [28]. In the past, the potential astrophysical application of the electrodisintegration of ^{16}O was discussed in [29] and an storage ring based experiment was proposed in [30], but was never carried out. More recent discussions [31, 32] are motivated by development of a new generation of high intensity (≈ 10 mA) low-energy (≈ 100 MeV) energy-recovery linear (ERL) electron accelerators [33, 34] and which together with modern jet gas targets [35], can deliver luminosity $>10^{35}$ cm^{-2} s^{-1}. By measuring the final state of the scattered electron it is possible to define and fix the α+^{12}C excitation energy, but at the same time control the three-momentum of the virtual photon $\vec{q}$ either by selecting the electron scattering angle θ_e or the beam energy E_e, see Fig 1. The real photon result can be recovered by taking the limit $q/\omega \to 1$.

In this paper, we briefly present a new method to improve the precision of the ^{12}C$(\alpha,\gamma)^{16}$O reaction at stellar energies based on electrodisintegration of ^{16}O, *i.e.* ^{16}O$(e,e'\alpha)^{16}$C. The full description of this method can be found in [36].

---

* friscic@mit.edu

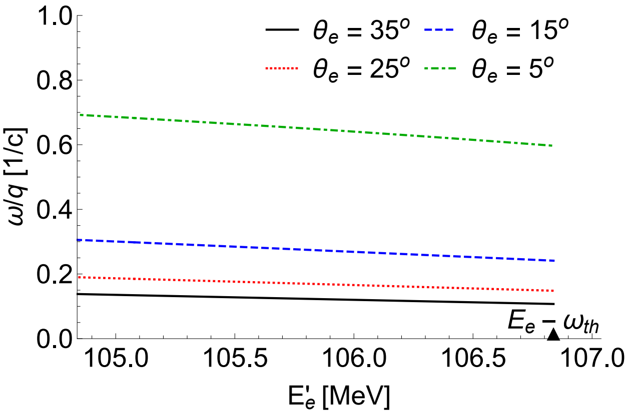

Figure 1: The dependence of the ratio of the transferred energy to the transferred three-momentum ω/q on the scattered electron energy E'_e for kinematics corresponding to 2 MeV above threshold for electron beam energy $E_e = 114$ MeV, ω_{th} denotes the energy of the photon at the threshold.

DIFFERENTIAL CROSS SECTION FOR THE ELECTRODISINTEGRATION

The differential cross section for the reaction $^{16}O(e,e'\alpha)^{12}C$ reaction in the *cm* frame can be expressed as [36]:

$$\left[\frac{d\sigma}{d\omega d\Omega_e d\Omega_\alpha^{cm}}\right]_{(e,e'\alpha)} = \frac{M_\alpha M_{^{12}C}}{8\pi^3 W}\frac{p_\alpha^{cm}\sigma_{Mott}}{(\hbar c)^3}$$
$$\times\left(\widetilde{v}_L R_L + \widetilde{v}_T R_T + \widetilde{v}_{TL} R_{TL} + \widetilde{v}_{TT} R_{TT}\right). \quad (2)$$

where σ_{Mott} is the Mott cross section. In case of the unpolarized exclusive electron scattering we have four nuclear response functions R_K: the longitudinal R_L and transverse R_T components (L and T with respect to the direction of the virtual photon $\vec{q}$), and two interference responses, transverse-longitudinal R_{TL} and transverse-transverse R_{TT}. The functions $\widetilde{v}_K$ are electron kinematic factors [28].

A big advantage of measuring the electrodisintegration reaction over the photodisintegration reaction is, that one can be in the astrophysical interesting region in terms of ω, and at same time transfer enough three-momentum q to the final state α-particles, which can then exit the jet target and be detected. By measuring the angular distribution of produced α-particles, for both reactions, it is possible to separate contributions from various multipoles. In real photon processes close to threshold and involving exclusively ground states of 0^+ nuclei only E1 (electric dipole) and E2 (electric quadrupole) multipole are assumed [6]. By measuring the final state of the scattered electron in coincidence with the final state of the produced α-particle it is possible to determine the final state of the unobserved ^{12}C and separate any excited state. In case of electrodisintegration, both electric and Coulomb multipoles contribute, therefore we are considering C0, C1, C2, E1 and E2 multipoles.

At low values of the momentum transfer q, compared with a typical nuclear momentum q_0 (order of 200–250 MeV/c), each multipole is dominated by its low-q behavior which enters as a specific power of q [36]. Again, by fixing ω and increasing q one may vary the contribution of a particular multipole and thus eventually explore the potential C3/E3 contributions.

In case of real photons only the transverse R_T response function contributes to the cross section and eventually R_{TT} if there are linearly polarized real photons involved (see Sect. III of [36] for more details). R_T and R_{TT} response functions only contain EJ multipoles, longitudinal R_L response function only CJ multipoles, and interference transverse-longitudinal R_{TL} contains combinations of both EJ and CJ multipoles. Their form as functions of α-particle angles θ_α^{cm} (angle between α-particle and momentum $\vec{q}$) and ϕ_α are described in detail in [36].

DEFINITION OF THE MODEL AND MONTE-CARLO SIMULATION

At this point we have developed the general differential cross section formula and from now we are continuing with development of a model for the electrodisintegration reaction. First, we determine the leading-order contribution to the E1 and E2 multipoles by fitting the second order polynomial to all S_{E1} and S_{E2} data from the direct reaction experiments having $E_\alpha^{cm} < 1.7$ MeV. By using current conservation in the low-q limit it is possible to relate the leading-order of the EJ an CJ multipoles (J > 0). For the next-to-leading (NLO) order q-dependence in the C1/E1 and C2/E2 multipoles cannot be related using current conservation, therefore we made assumptions for the q-dependence and similarly in the C0 multipole (see [36] for details). The goal here is to develop a reasonable model in order to study the feasibility of performing the electrodisintegration measurements in the astrophysical interested region. In a real experiment higher-order q-dependences will also be measured and then one will determine the region where the used parameterization can be applied.

Using the described model and assuming the experimental parameters given in Table 1 we have used Monte-Carlo simulation to calculate the rate of the electrodisintegration of ^{16}O. We have assumed a 2 mm wide oxygen cluster-jet target [35] capable of achieving a thickness of 5×10^{18} atoms/cm^2.

We also need an high current (40 mA) electron accelerator which can deliver a beam energy of around 100 MeV. For example MESA, which should be able to deliver a beam current of 10 mA [33] and CBETA which should reach 40 mA [37] for beam energies of 42, 78, 114 and 150 MeV (all energies in between are also possible). Assuming a beam current of 40 mA and a jet target as described above the luminosity amounts to 1.25×10^{36} cm^{-2}s^{-1}.

For the identification of events originating from electrodisintegration of ^{16}O the scattered electron needs to be detected in coincidence with the produced α-particle. Fig. 2 shows a schematic layout of a possible experiment. The

ISBN: 978-3-95450-217-2 doi:10.18429/JACoW-ERL2019-MOCOYBS04

Table 1: Summary of the experimental parameters for the rate calculations used in [36].

Acceptance	Electron	α-particle
In-plane	±2.08°	60°
Out-of-plane	±4.16°	360°
Solid angle	10.5 msr	3.14 sr
Oxygen Target	Thickness	$5{\times}10^{18}$ atoms/cm^2
	Density	$6.65{\times}10^{-4}$ g/cm^3
Electron Beam	Current	40 mA
	Energies (E_e)	78, 114, 150 MeV
Luminosity		$1.25{\times}10^{36}$ cm^{-2}s^{-1}
Integrated Lumi. (100 days)		$1.08{\times}10^{7}$ pb^{-1}
Central electron scatt. angles θ_e		15°, 25°, 35°
E_α^{cm}-range of interest		$0.7{\le}E_\alpha^{cm}{\le}1.7$ MeV

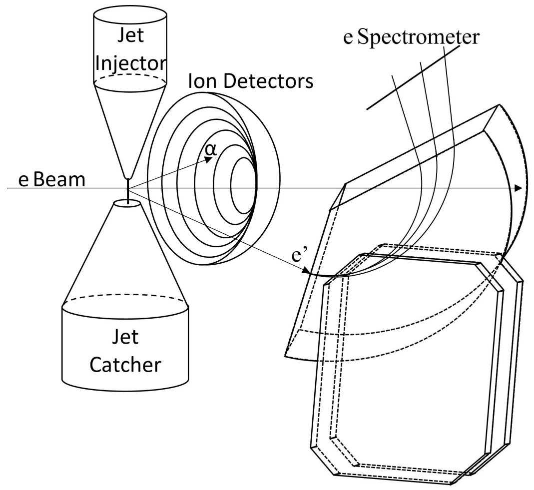

Figure 2: Schematic layout of simulated $^{16}O(e,e'\alpha)^{12}C$ experiment: ^{16}O is disintegrated by the electron beam into an α-particle and ^{12}C nuclei. The scattered electron is detected in an electron spectrometer and the produced α-particle in large acceptance ion detectors [36].

scattered electron is detected by a high precision magnetic spectrometer. We assumed that the spectrometer has an in-plane acceptance of ±2.08° and out-of-plane acceptance of ±4.16°. This corresponds to a solid angle of 10.5 msr.

The large acceptance ion detectors should be based on time-of-flight (ToF) detection in order to be able to distinguish the background α-particles originating from the electrodisintegration of ^{17}O and ^{18}O, as well as the proton background from the electrodisintegration of ^{14}N, as shown in Fig. 3. Furthermore, ion detectors should be centered around the direction of the virtual photon $\vec{q}$ in order to be detect particles having the largest kinetic energy (or lowest ToF like on Fig. 3) and subsequently having the smallest angular spread. For these detectors we assumed that the solid angle is large enough to accept all α-particles having the in-plane scattering angle θ_α^{cm} in range from 0° to 60° and to have the full acceptance for the out-of-plane angle ϕ_α from 0° to 360°.

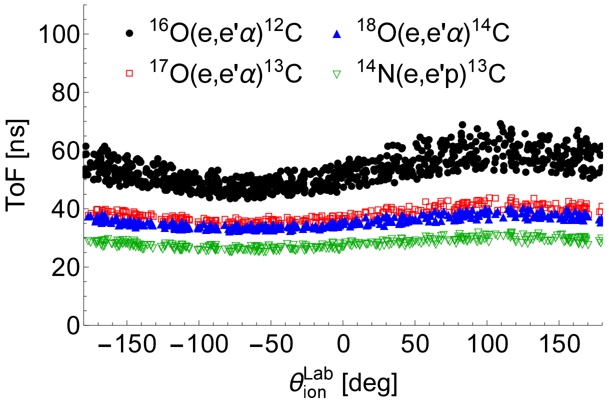

Figure 3: Energy-loss corrected time-of-flight ToF as functions of laboratory ion production angle θ_{ion}^{Lab} assuming that the ions were produced by electrons involved in the electrodisintegration of ^{16}O, at E_e = 114 MeV and θ_e = 15° with a cut on $1.0 \le E_\alpha^{cm} \le 1.1$ MeV. The energy-loss of the α-particles and the protons inside the ^{16}O gas jet was simulated by using the SRIM-2013 software [38, 39].

RESULTS AND DISCUSSION

Monte Carlo simulation was used to calculate the number of events after 100 days of running, which were subsequently used to calculate statistical uncertainties, which were then propagated all the way back to S-factors and the corresponding projected statistical uncertainties. The result of one simulation from [36] for the beam energy E_e = 114 MeV and the electron scattering angle θ_e = 15° is shown in figure 4. One can clearly see a significant improvement in terms of the statistical uncertainties when comparing the electrodisintegration projected data with the previous experiments.

The full set of Monte-Carlo simulations for beam energies E_e = 74, 114 and 150 MeV, electron scattering angles θ_e = 15°, 25° and 35°, and two values of modeling of C0 multipole can be found in [36]. The overall conclusion is that when comparing the results from [36] with the most accurate measurements from [14] and [17], the uncertainties in the determination of S_{E1} and S_{E2} at a given energy above threshold are improved by at least ×5.6 and ×23.9, respectively. The significant uncertainty improvement for the S_{E2} comes from two contributions. The dominant one is the fact that C2/E2 matrix elements, compared to C1/E1, enter in response functions $R_{L,T,TL,TT}$ are enhanced by factor q/ω, which for given E_e = 114 MeV and θ_e = 15° amounts to ~3.6 (in real photon experiments $q/\omega = 1$). The other contribution comes from the angular distribution of the multipoles for the selected range of θ_α^{cm} from 0° to 60°, the angular distributions of C2/E2 are larger in magnitude compared to the C1/E1 angular distributions. In the case of

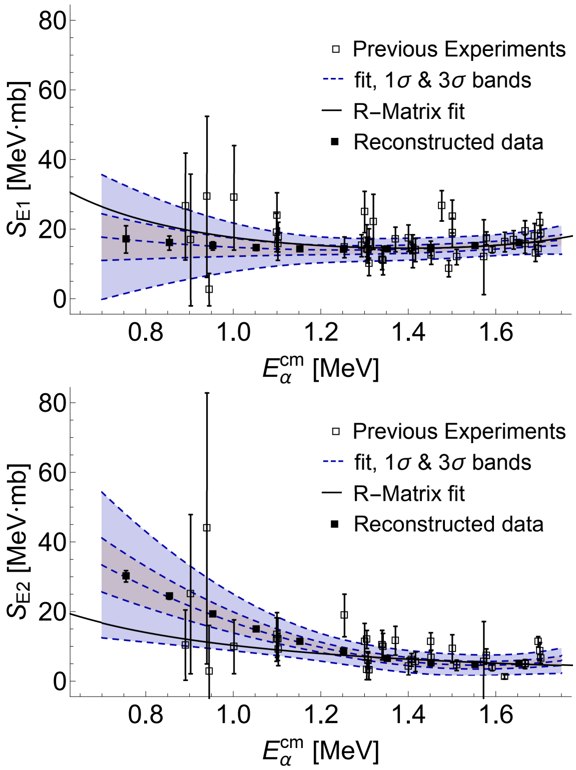

Figure 4: Projected S_{E1}- and S_{E2}-factors with statistical error bars (represented by solid squares) for simulation with $E_e = 114$ MeV and $\theta_e = 15°$ from [36], and previous experiments [6–14, 16, 17, 19]. The solid line represents the AZURE2 [40] R-Matrix fit of the world data set.

real photon experiments, the angular distributions of E1 and E2 behave the same, for example see figure 5. in [2].

OUTLOOK AND CONCLUSION

We have developed a simple model, which allowed us to relate the electrodisintegration of ^{16}O and the α-particle capture on ^{12}C reactions. By considering the optimal kinematics for the electrodisintegration of ^{16}O in terms of the electron beam energy, oxygen jet-target density, the electron spectrometer, and the low-energy α-particle detectors for suppressing the chemical and isotopic background. We showed that the new ERLs are essential to achieve high luminosity, in order to have a high statistics electrodisintegration measurement, which can be used to determine the ^{12}C$(\alpha, \gamma)^{16}$O reaction rate with unprecedented precision.

The running of α-detectors in close proximity of the Megawatt electron beam will be very challenging, but it was already demonstrated that such high power ERL beams can be achieved with a minimal halo [41].

We propose an initial run of ^{16}O(e, e′α)^{12}C using an ERL with a beam energy of ~100 MeV. This experiment would be focused on higher energies E_α^{cm}, in the region where the reaction rates are relatively high and the running time would be few weeks long. The first milestone would be to experimentally validate the extrapolation to real photon limit and to determine the rate contributions of the different multipoles. If successful, it would pave the way for a longer experiment with the highest beam current available to determine the ^{12}C$(\alpha, \gamma)^{16}$O reaction rate with unprecedented precision at the stellar energies.

ACKNOWLEDGMENTS

We acknowledge valuable discussions with E. Tsentalovich and H. Weller. This research was supported by the U.S. Department of Energy Office of Nuclear Physics under grant No. DE-FG02-94ER40818.

REFERENCES

[1] T. A. Weaver and S. E. Woosley, *Phys. Rep.*, vol. 227, pp. 65–96, 1993. DOI: `10.1016/0370-1573(93)90058-L`.
[2] R. J. deBoer *et al.*, *Rev. Mod. Phys.*, vol. 89, p. 035 007, 2017. DOI: `10.1103/RevModPhys.89.035007`.
[3] S. E. Woosley *et al.*, *Nucl. Phys. A*, vol. 718, p. 3c, 2003. DOI: `10.1016/S0375-9474(03)00673-0`.
[4] S. E. Woosley, A. Heger, and T. A. Weaver, *Rev. Mod. Phys.*, vol. 74, p. 1015, 2002. DOI: `10.1103/RevModPhys.74.1015`.
[5] D. R. Tilley, H. R. Weller, and C. M. Cheves, *Nucl. Phys. A*, vol. 565, pp. 1–184, 1993. DOI: `10.1016/0375-9474(93)90073-7`.
[6] P. Dyer and C. Barnes, *Nucl. Phys. A*, vol. 233, p. 495, 1974. DOI: `10.1016/0375-9474(74)90470-9`.
[7] A. Redder *et al.*, *Nucl. Phys. A*, vol. 462, p. 385, 1987. DOI: `10.1016/0375-9474(87)90555-0`.
[8] R. M. Kremer *et al.*, *Phys. Rev. Lett.*, vol. 60, p. 1475, 1988. DOI: `10.1103/PhysRevLett.60.1475`.
[9] J. M. L. Ouellet *et al.*, *Phys. Rev. C*, vol. 54, p. 1982, 1996. DOI: `10.1103/PhysRevC.54.1982`.
[10] G. Roters, C. Rolfs, F. Strieder, and H. Trautvetter, *Eur. Phys. J. A*, vol. 6, p. 451, 1999. DOI: `10.1007/s100500050369`.
[11] L. Gialanella *et al.*, *Eur. Phys. J. A*, vol. 11, p. 357, 2001. DOI: `10.1007/s100500170075`.
[12] R. Kunz *et al.*, *Phys. Rev. Lett.*, vol. 86, p. 3244, 2001. DOI: `10.1103/PhysRevLett.86.3244`.
[13] R. W. Kunz, PhD thesis, Univ. of Stuttgart, 2002.
[14] M. Fey, PhD thesis, Univ. of Stuttgart, 2004.
[15] D. Schürmann *et al.*, *Eur. Phys. J. A*, vol. 26, pp. 301–305, 2005. DOI: `10.1140/epja/i2005-10175-2`.
[16] M. Assunção *et al.*, *Phys. Rev. C*, vol. 73, p. 055 801, 2006. DOI: `10.1103/PhysRevC.73.055801`.
[17] H. Makii *et al.*, *Phys. Rev. C*, vol. 80, p. 065 802, 2009. DOI: `10.1103/PhysRevC.80.065802`.
[18] D. Schürmann *et al.*, *Phys. Lett. B*, vol. 703, pp. 557–561, 2011. DOI: `10.1016/j.physletb.2011.08.061`.
[19] R. Plag *et al.*, *Phys. Rev. C*, vol. 86, p. 015 805, 2012. DOI: `10.1103/PhysRevC.86.015805`.
[20] R. Plaga *et al.*, *Nucl. Phys. A*, vol. 465, pp. 291–316, 1987. DOI: `10.1016/0375-9474(87)90436-2`.
[21] P. Tischhauser *et al.*, *Phys. Rev. C*, vol. 79, p. 055 803, 2009. DOI: `10.1103/PhysRevC.79.055803`.
[22] L. Buchmann *et al.*, *Phys. Rev. Lett.*, vol. 70, p. 726, 1993. DOI: `10.1016/j.nima.2015.01.060`.
[23] R. E. Azuma *et al.*, *Phys. Rev. C*, vol. 50, p. 1194, 1994. DOI: `10.1103/PhysRevC.50.1194`.

[24] X. D. Tang *et al.*, *Phys. Rev.C*, vol. 81, p. 045 809, 2010. DOI: `10.1103/PhysRevC.81.045809`.

[25] B. DiGiovine *et al.*, *Nucl. Instrum. Methods Phys. Res. A*, vol. 781, pp. 96–104, 2015. DOI: `10.1016/j.nima.2015.01.060`.

[26] R. J. Holt *et al.*, 2018. arXiv: `1809.10176 [nucl-ex]`.

[27] M. Gai *et al.*, *JINST*, vol. 5, P12004, 2010. DOI: `10.1088/1748-0221/5/12/P12004`.

[28] A. S. Raskin and T. W. Donnelly, *Ann. Phys.*, vol. 191, pp. 78–142, 1989. DOI: `10.1016/0003-4916(89)90337-0`.

[29] T. W. Donnelly, "Electron scattering and the nuclear many-body problem," in *The Nuclear Many-Body Problem 2001*, W. Nazarewicz and D. Vretenar, Eds. Dordrecht: Springer Netherlands, 2002, pp. 19–26. DOI: `10.1007/978-94-010-0460-2_3`.

[30] E. Tsentalovich *et al.*, MIT-Bates PAC proposal 00-01, 2000.

[31] I. Friščić, *Electrodisintegration of* ^{16}o *as a tool for investigating the* $^{12}c(\alpha,\gamma)^{16}o$ *reaction*, Conf. Abstracts EINN2017, 2017. `%7Bhttp://einnconference.org/2017/wp-content/uploads/2017/10/EINN-2017-Conference-Abstracts-2810.pdf%7D`

[32] S. Lunkenheimer, *Studies of the nucleosynthesis* $^{12}c(\alpha,\gamma)^{16}o$ *in inverse kinematics for the MAG-IX experiment at MESA*, 650. WE-Heraeus-Seminar, 2017.

[33] F. Hug *et al.*, *Proc. of Linear Accelerator Conference (LINAC'16)*, vol. 28, pp. 313–315, 2017. DOI: `10.18429/JACoW-LINAC2016-MOP106012`.

[34] G. H. Hoffstaetter *et al.*, 2017. arXiv: `1706.04245 [physics.acc-ph]`.

[35] S. Grieser *et al.*, *Nucl. Instrum. Methods Phys. Res. A*, vol. 906, pp. 120–126, 2018. DOI: `10.1016/j.nima.2018.07.076`.

[36] I. Friščić, T. W. Donnelly, and R. G. Milner, *Phys. Rev. C*, vol. 100, p. 025 804, 2019. DOI: `10.1103/PhysRevC.100.025804`.

[37] D. Trbojevic *et al.*, *Proc. of International Particle Accelerator Conference (IPAC'17)*, vol. 8, pp. 1285–1289, 2017. DOI: `10.18429/JACoW-IPAC2017-TUOCB3`.

[38] J. F. Ziegler, M. D. Ziegler, and J. P. Biersack, *Nucl. Instrum. Methods Phys. Res. B*, vol. 268, pp. 1818–1823, 2010. DOI: `10.1016/j.nimb.2010.02.091`.

[39] `http://www.srim.org/`.

[40] R. E. Azuma *et al.*, *Phys. Rev. C.*, vol. 81, p. 045 805, 2010. DOI: `10.1103/PhysRevC.81.045805`.

[41] R. Alarcon *et al.*, *Phys. Rev. Lett.*, vol. 111, p. 164 801, 2013.

BEAM HALO IN ENERGY RECOVERY LINACS

O. A. Tanaka[†], High Energy Accelerator Research Organization (KEK), Tsukuba, Japan

Abstract

The beam halo mitigation is a very important challenge for reliable and safe operation of a high energy machine. Since Energy Recovery Linacs (ERLs) are known to produce high energy electron beams of high virtual power and high density, the beam halo and related beam losses should be properly mitigated to avoid a direct damage of the equipment, an unacceptable increase in the vacuum pressure, a radiation activation of the accelerator components etc. To keep the operation stable, one needs to address all possible beam halo formation mechanisms, including those unique to each machine that can generate beam halo. Present report is dedicated to the beam halo related activities at the Compact ERL at KEK, and our operational experience with respect to the beam halo.

INTRODUCTION

Beam halo studies and halo mitigation schemes are of the great importance at each stage of accelerator R&D. For those machines that are at their design stage, beam halo studies are limited simply by the absence of the real equipment to perform some tests. Nevertheless, several halo formation mechanisms and processes impacting into the halo could be modeled and estimated prior the machine construction. Here are some of them:

- A space charge effect causes emittance blow-up and bunch lengthening that finally could lead to the formation of the beam halo and consequent beam losses. Examples of space charge effect studies for ERL machines could be found in [1] – [4].
- Effects of the CSR (Coherent Synchrotron Radiation). CSR related issues are in trend nowadays, and addressed in numerous studies (see, for example, [4] – [5]).
- Dark current from the electron gun and longitudinal bunch tails originated at the photocathode [6] – [7].

Other mechanisms could be studied only after the machine construction. One of the examples of the processes enhancing the halo that could not be investigated beforehand is a dark current from RF cavities. Recent results could be found in [8]. Another example is those halo formation mechanisms that are unique for each machine. Thus at the Compact ERL (cERL) at KEK such a unique process was detected and explained for the essential vertical beam halo observed in the end of the injector section and at several locations of the recirculation loop [9]. However, this study was done for the low bunch charge operation (1 pC/bunch, [10]), while the next step operational goal was to achieve a high bunch charge operation (60 pC/bunch, [11]).

Recent industrialization of the cERL beam line [12] imposed new requirements to the beam operation. During last run in June 2019, we optimized injector to the energy 4 MeV [13]. Design parameters dedicated to this run and achieved parameters are listed in the Table 1. Next operational step is to develop the method of beam tuning to control space charge effect. Thus, to be able to produce mid-infrared Free Electron Laser (IR-FEL) light in May 2020, we need to tune the machine for high charge CW operation, while the normalized rms emittance should be kept less than 3π mm mrad, bunch length should be of order of 4 ps, and the energy spread should be minimized to less than 0.062%. These considerations motivated several halo related activities at cERL.

IR-FEL upgrade requires a high bunch charge CW operation. Accordingly, the energy spread should be minimized to improve the FEL-light quality. The halo influence should be studied in this respect. Then, bunch length and beam emittance should be controlled, and we need to exclude the beam halo impact (or reduce as much as possible). Also a reasonable collimation is required to protect the beam line components from its unnecessary activation and to lower the overall beam losses. Collimators should be tested and approved towards the CW operation. Present report is dedicated to these activities and our operational experience with respect to the beam halo.

Table 1: Typical Parameters of CERL Run in June, 2019

Parameter	Design	In operation
Beam energy [MeV]:		
Injector	4	4.05
Recirculation loop	17.6	17.5
Bunch charge [pC]	60	60
Repetition rate [GHz]	1.3	1.3
Bunch length (rms) [ps]	4	4.5
Energy spread [%]	<0.06	0.12
Normalized emittance (rms) in injector [μm·rad]:		
Horizontal	< 3	2.89±0.09
Vertical	< 3	1.99±0.20

HALO TRACKING THROUGH THE INJECTOR

After the injector optics was updated for the energy of 4 MeV, a high bunch charge (60 pC/bunch) beam with a longitudinal bunch tail was tracked through it to compare with observed profiles. To introduce the longitudinal bunch tail into simulations, the initial longitudinal distribution of the bunch was generated in accordance with the curve shown in Figure 1. The core of the bunch is 50 ps FWHM flat-top Gaussian. The backward tail includes 20% of the core intensity. A small (1.5% of the core) forward tail was also added similarly to how it was done in previous beam halo studies [9]. The cutoff of the longitudinal distribution was set to 100 ps. The initial trans-

---

[†] olga@post.kek.jp.

ISBN: 978-3-95450-217-2 doi:10.18429/JACoW-ERL2019-TUCOXBS01

verse distribution is assumed to be uniform of 2 mm diameter. Other input parameters for simulations are listed in Table 2. Then, the bunch distribution was tracked with General Particle Tracer code [14] through the injector lattice. The tracking output is compared with measured profiles at Figure 2. We have got a good agreement. One can observe that for a 60 pC bunch the effect of the longitudinal halo is diminished by the beam blow-up due to the space charge effect. Some signs of the horizontal halo could be found at SM#8 location due to nonzero dispersion. Another interesting observation is that tracking without longitudinal tail (only 50 ps rms flat-top Gaussian core) yields exactly same profiles, except at SM#1-2, 8. In that case a central spots disappear. One can conclude that observed central spots are due to the longitudinal bunch tail that is produced at GaAs photocathode.

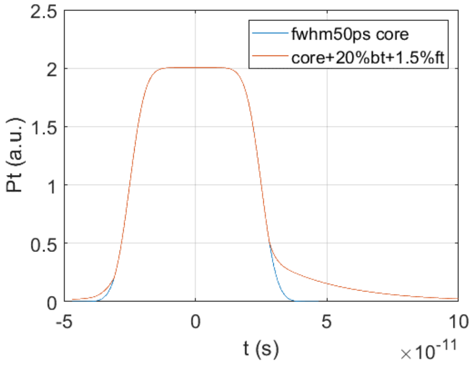

Figure 1: Initial longitudinal distribution at the cathode.

Table 2: Initial Parameters for Injector Tracking

Parameter	Value
Number of particles	25000
Beam energy	4 – 17.5 MeV
Total charge	60 pC / bunch
RF frequency	1.3 GHz
Longitudinal distribution:	
Core	FWHM 50 ps flat-top Gaussian
Tail	Back & forward tails of 100 ps length
Transverse distribution	Uniform φ= 2 mm

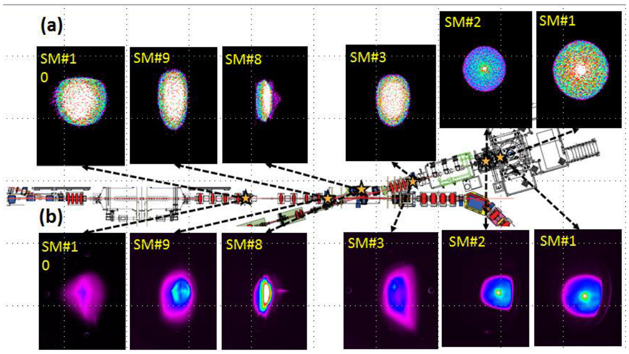

Figure 2: Beam profiles at all injector screen monitor locations: a). Simulated profiles; b). Measured profiles.

COLLIMATOR WAKE STUDY

When the high intensity particle beam passes through locations with narrow apertures, such a collimator's rods, it leads to the creation of the unwanted wake fields. The transverse wake field may affect the beam emittance and the longitudinal wake field can cause the energy loss and the energy spread. The cERL has five collimators (one in the injector section, one in the merger section and three in the recirculation loop, see Fig. 3) to remove the beam halo and to localize the beam loss. An operation at 10 mA average beam current and 1.3 GHz repetition rate is planned in the near future, thus an impact to the collimators together with beam loss reduction issues will become crucial.

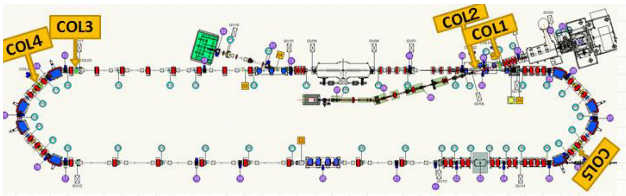

Figure 3: The layout of cERL with collimator's locations.

All cERL collimators consist of four cylindrical rods of 7 mm radius made of copper. They could be independently inserted from the top, bottom, left and right sides of the beam chamber. Collimators COL1 – 3 were designed for the straight sections, therefore they have a round chamber 50 mm radius made of stainless still. Its schematic is given at Fig. 4. Note that the energy at collimators COL 1 – 2 is 4 MeV, while the energy at rest of them is 17.6 MeV. Collimators COL4 – 5 are dedicated to the arc section, thus their chambers are elliptical 70 x 40 mm diameter (Fig. 4).

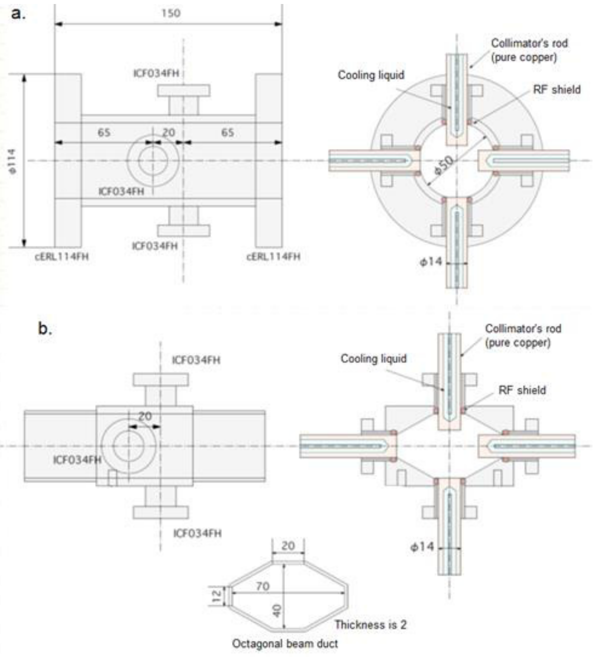

Figure 4: A schematic of the collimators: a). Collimators COL 1 – 3 for the straight sections; b). Collimators COL 4 – 5 for the arc sections.

Transverse Wake and Emittance Growth

Let us consider first transverse wake fields created by the vertical rods of the collimator. The summary of CST Particle Studio [15] simulation results together with analytical calculations for 2 ps bunch length is demonstrated at Fig. 5. We have estimated the emittance blow-up for the 60 pC electron bunch at cERL using analytical expression [16]:

$$\frac{\Delta\varepsilon_y}{\varepsilon_{y0}} = \sqrt{1+\frac{\beta_y\sigma_\omega^2}{\varepsilon_{y0}}}-1, \qquad (1)$$

where the value $\Delta\varepsilon_y$ is the transverse emittance growth with respect to the initial emittance ε_{y0}. The rms of the centroid kicks caused by the longitudinally varying field σ_ω could be found as follows [17]:

$$\sigma_\omega = \frac{Q}{E/e}k_\perp^{rms}y_0. \qquad (2)$$

In Eq. (2) the value E is the beam energy at the location of collimator. The value $Q = 60\,pC$ is the bunch charge. The value y_0 is the beam centroid offset, and lastly, the value $k_\perp^{rms}$ is the rms kick factor, estimated for the bunch head-tail difference in the kick. For Gaussian bunch $k_\perp^{rms} = k_\perp/\sqrt{3}$.

Expected values of the emittance blow-up due to the collimator half gap 1.5 mm are summarized in Table 3.

Since for 60pC per bunch and burst mode of the operation the emittance growth effect is expected to be small, let us treat longitudinal wake.

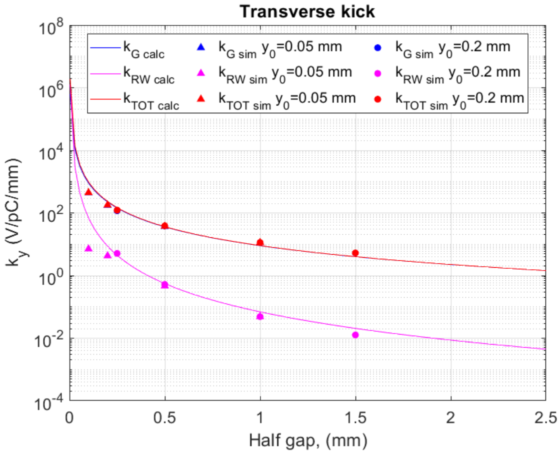

Figure 5: A summary of the transverse wake kick factors of the collimators.

Table 3: Expected Values of the Emittance Blow-Up for the Collimator Half Gap 1.5 mm

Collimator	**ε_{y0} [μm×rad]**	**β_y [m]**	**$\Delta\varepsilon_y/\varepsilon_{y0}$ [%]**
COL1 E=4 MeV	1.15	27.47	1.05
COL2 E=4 MeV	1.25	19.23	0.84
COL3 E=17.6 MeV	0.954	34.76	3.82
COL4 E=17.6 MeV	0.954	6.99	1.61
COL5 E=17.6 MeV	0.954	6.99	1.61

Longitudinal Wake and Energy Spread

Now, let us consider a problem of longitudinal wake fields excited by collimators. The values of the wake-loss factor were evaluated numerically through the CST simulation for half-gap values in the range from 0.1 to 1.5 mm. The dependence of the energy spread on the collimator's half gap for the designed (2 ps) and current (4.5 ps) bunch length is demonstrated at Fig. 6. For the analytical description, the following equation was considered [18]:

$$k_\parallel = \frac{Z_0 c}{2\pi^{3/2}\sigma_z}\ln\left(\frac{b}{a}\right). \qquad (3)$$

In Eq. (3) the value $Z_0=120\pi$ is the impedance of the free space, $c = 3\cdot10^8$ m/s is the speed of light, σ_z is the bunch length, b = 25 mm is the vacuum duct's half aperture, and a is the collimator's half gap.

The energy loss per whole bunch at one collimator for the 60 pC per bunch burst mode at the bunch length 2 ps, and for the collimator half gap 1.5 mm is:

$$\Delta E = k_\parallel Q^2 = 46.86V/pC\times(60pC)^2 = 168.7nJ. \qquad (4)$$

The voltage received by the electrons is $\Delta V=k_\parallel\times Q=2812$ V. The energy change in one electron is reduced by eΔV=2812 eV. If E=17.6 MeV, the change of energy peak is eΔV/E=2816 eV/17.6 MeV=0.016%. For Gaussian bunch the energy spread due to one collimator is $\sigma E=0.4\times k_\parallel\times Q=1124$V. With respect to the beam energy E=17.6 MeV the wake-induced energy spread reads $\sigma E/E=1124$ eV/17.6 MeV=0.0063%. Unfortunately estimated values are beyond the limits of the resolution of our monitors, and it is unlikely we could detect them.

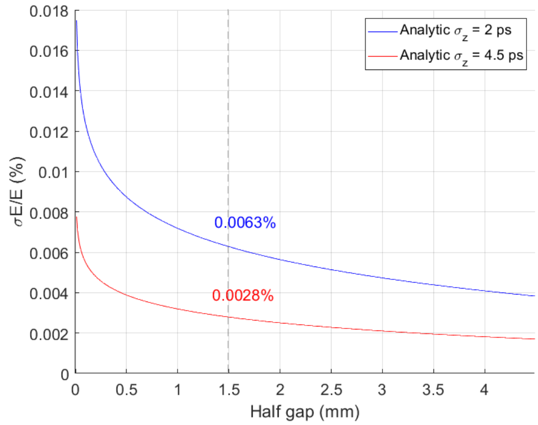

Figure 6: A wake-induced energy spread for different values of the collimator half gap and bunch lengths 2 ps (blue line) and 4.5 ps (red line).

BEAM-BASED MEASUREMENTS

Energy Spread Measurement

For the measurement of the energy spread caused by the collimator's longitudinal wake, we used COL3 located before first arc entrance, SM#13 located between COL3 and the entrance of the are section and SM#15 located just in the middle of the arc (see Fig. 3). SM#13 needed to monitor the beam spot, which was successively cut by collimator's rods. The measurement itself was done by SM#15. To do so, first, we have restored the history of the quadrupole magnets to have the best beam spot at the COL3 location. Then we have degaussed all quadrupoles of the first arc between SM#13 and SM#15 to make the dispersion maximized. We have measured the dispersion to be 2.41 m. The default energy spread was $\sigma E/E_{default}=\sigma_x/\eta=0.117\%$. It is a ratio of the rms beam size to the dispersion. However, in the following we care only the change of the energy spread, not its default value.

Next step was to insert the collimator COL3. We used two horizontal rods, because the beam spot at the collimator location is known for its vertical beam halo. Therefore, we have avoided an influence of the halo on our energy spread measurement. We have performed the measurement for the half gap values 2 mm, 1.5 mm, 2 mm, 2.5 mm, 4 mm, COL out correspondingly. Related rms beam sizes and beam profile peak positions were recorded at SM#15. The raw data of the beam profile was fitted by Gaussian fitting routine and weight analysis. An example of the measurement data processing could be found at Fig. 7. Here the upper image is a SM#15 beam spot, the blue curve at the bottom plot is the raw data, the red line is its Gaussian fitting, and the magenta mark denotes the peak position with respect to the data weight.

Weight analysis [19] gives the following expression for the profile peak position:

$$x_c = \frac{1}{N}\sum_{i=1}^{659} x_i N_i, \quad where \quad N = \sum_{i=1}^{659} N_i. \tag{5}$$

Here N is the number of data points, and x_i is the value of the ith data point. The rms beam size is given by:

$$\sigma_x = \sqrt{\frac{1}{N}\sum_{i=1}^{659} N_i \left(x_i - x_c\right)^2}. \tag{6}$$

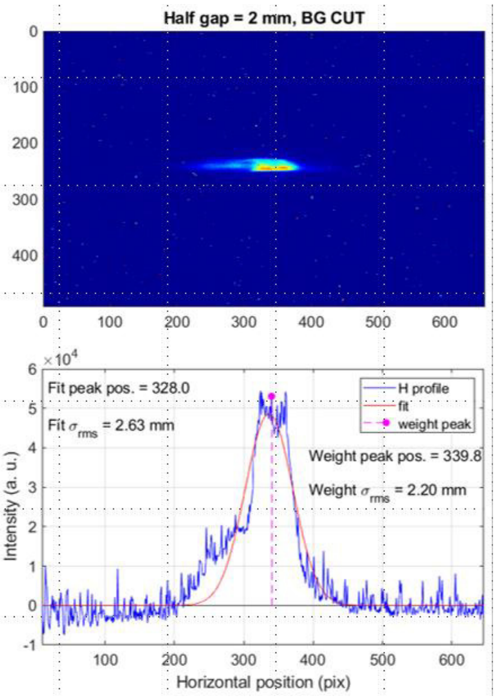

Figure 7: Energy spread measurement data at SM#15: beam spot (top), raw data and its fitting (bottom).

Results of the processing of all six measurements are demonstrated at Fig. 8. The rms beam size is not changed significantly within the error bar except in the case of the 1.5 mm half gap. It was a prediction by simulation and calculation. The beam size drop at the half gap 1.5 mm indicates that the beam core was damaged by the collimator's rod.

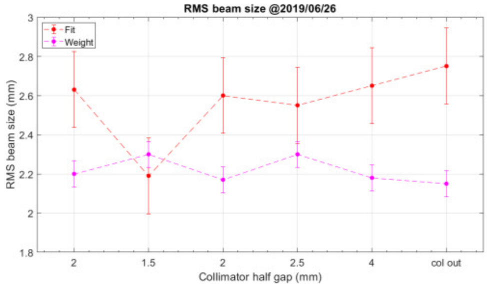

Figure 8: A horizontal beam size at SM#15 with respect to the horizontal collimation: fitting result (red), weight analysis result (magenta).

Beam Halo Influence

The location of the collimator COL3 (before the arc entrance, Fig. 3) is known for the considerable vertical beam halo [7]. The correspondent beam spot at SM#13 is shown at Fig. 9. Thus, by inserting vertical rods of the collimator COL3, one can study the beam halo influence on the energy spread and consequently manage the beam quality by removing the halo by the collimator.

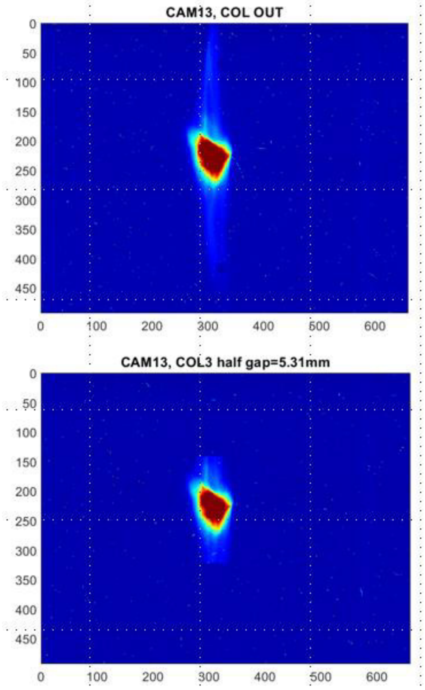

Figure 9: A beam spot at CAM13: without (top), and with (bottom) the collimation.

To study this effect, we performed the same measurements as was described in the previous section. Although the vertical collimation was allowed. A series of four measurements was done. The collimator's half gap was set to 5.31 mm, 5.75 mm, 6.25 mm, and COL3 out correspondingly. Then the proper data processing gave results, presented at Fig. 10. One can see the horizontal beam size is slightly decreased with the cutting away the vertical beam halo. The energy spread also became smaller.

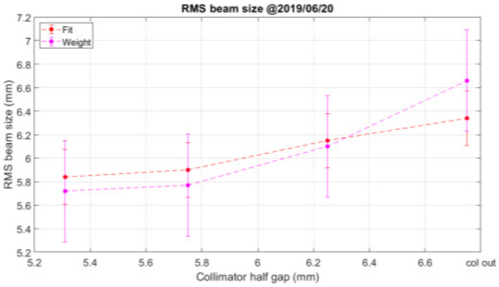

Figure 10: Horizontal beam size at SM#15 with respect to the vertical collimation: fitting result (red), weight analysis result (magenta).

CONCLUSION AND OUTLOOK

Halo related discussion does not seem to be a trend nowadays. Nevertheless, the problem of the beam halo addresses to a numerous issues at all stages of accelerator machine R&D.

Experimentally we have found, that for current beam parameters (bunch charge is 60 pC (burst mode), bunch length is 4.5 ps, energy spread is ~0.12%, beam energy is 17.5 MeV (injector energy is 4.05 MeV)) even if one put the half gap of the collimator up to 2 mm, the emittance and energy spread are not affected so much. Thus we approved the beam collimation at cERL.

The additional energy spread due to collimator's wake at cERL is found to be 0.0028 % at 17.5 MeV, which is negligibly small.

Considering future cERL upgrade to the IR-FEL, a possibility of consequent degradation of the FEL performance should be taken into account. Correspondent power loss was obtained as 13.7 W (81.25 MHz, 5 mA, 2 ps).

At cERL like at any other ERL facility, we have to consider the halo seriously for the beam current increase (up to 10 mA at cERL), since without due care the beam loss problem would be unavoidable.

ACKNOWLEDGEMENTS

This research is carried out with the support of NEDO project "Development of next generation laser technology with high brightness and high efficiency".

REFERENCES

[1] `https://arxiv.org/pdf/1706.04245.pdf`

[2] `https://arxiv.org/pdf/1705.08783.pdf`

[3] B. Kuske, "Adjusting bERLinPro optics to commissioning needs", presented at the 60th ICFA Advanced Beam Dynamics Workshop on Energy Recovery Linacs (ERL19), Berlin, Germany, September 2019, this conference.

[4] M. Abo-Bakr, "Beam dynamics and optics challenges of bERLinPro", presented at the 59th ICFA Advanced Beam Dynamics Workshop on Energy Recovery Linacs (ERL17), Geneva, Switzerland, Jun. 2017, paper WEIBCC003, unpublished.

[5] W. Lou *et al.*, "Coherent synchrotron radiation simulation for CBETA", in *Proc. IPAC'19*, Melbourne, Australia, May 2019, pp. 406-409. `doi:10.18429/JACoW-IPAC2019-MOPGW124`

[6] M. McAteer, "Dark current and halo tracking in ERLs", presented at the 59th ICFA Advanced Beam Dynamics Workshop on Energy Recovery Linacs (ERL17), Geneva, Switzerland, Jun. 2017, paper THIACC002, unpublished.

[7] O. Tanaka, "Beam halo study at the KEK compact ERL", presented at the 59th ICFA Advanced Beam Dynamics Workshop on Energy Recovery Linacs (ERL17), Geneva, Switzerland, Jun. 2017, paper THICCC001, unpublished.

[8] A. Neumann *et al.*, "The bERLinPro SRF photo injector system – from first RF commissioning to first beam", in *Proc. IPAC'18*, Vancouver, BC, Canada, Apr.-May 2018, pp. 1660-1663. `doi:10.18429/JACoW-IPAC2018-TUPML053`

[9] O. Tanaka *et al.*, "New halo formation mechanism at the KEK compact energy recovery linac", *Phys. Rev. Accel. Beams*, vol. 21, p. 024202, Feb. 2018. `doi:10.1103/PhysRevAccelBeams.21.024202`

[10] M. Akemoto *et al.*, "Construction and commissioning of the compact energy-recovery linac at KEK", *Nucl. Instrum. Methods*, vol. 877, pp. 197-218, 2018. `doi: 10.1016/j.nima.2017.08.051`

[11] T. Miyajima, "Higher bunch charge operation in Compact ERL at KEK", presented at the 59th ICFA Advanced Beam Dynamics Workshop on Energy Recovery Linacs (ERL17), Geneva, Switzerland, Jun. 2017, paper THIACC001, unpublished.

[12] H. Sakai, "Industrial applications of cERL", presented at the 60th ICFA Advanced Beam Dynamics Workshop on Energy Recovery Linacs (ERL19), Berlin, Germany, September 2019, this conference.

[13] T. Miyajima, "Injector development at KEK", presented at the 60th ICFA Advanced Beam Dynamics Workshop on Energy Recovery Linacs (ERL19), Berlin, Germany, September 2019, this conference.

[14] S. B. van der Geer and M. J. de Loos, *The General Particle Tracer code: Design, Implementation and Application*, Technische Universiteit Eindhoven, Eindhoven, 2001.

[15] CST-Computer Simulation Technology, CST PARTICLE STUDIO. `http://www.cst.com/Content/Products/PS/Overview.aspx`

[16] M. Dohlus, T. Limberg, "Impact of Optics on CSR-Related Emittance Growth in Bunch Compressor Chicanes", in Proc. of 21st Particle Accelerator Conference (PAC05), Knoxville, USA, May. 2005.

[17] S. Di Mitri, "Geometric efficiency of a two-stage fully absorbing collimation system in single-pass linacs", *Phys. Rev. ST Accel. Beams,* vol. 13, p. 052801, May 2010. `doi: 10.1103/PhysRevSTAB.13.052801`

[18] S. Heifets and S. Kheifets, "Coupling impedance in modern accelerators", *Rev. Mod. Phys.* vol. 63, p. 631, Jul. 1991. `doi:10.1103/RevModPhys.63.631`

[19] P. R. Bevington and D. K. Robinson, *Data Reduction and Error Analysis for the Physical Sciences*, McGraw-Hill, 1992.

BEAM DYNAMICS LAYOUT OF THE MESA ERL*

F. Hug†, K. Aulenbacher[1], D. Simon, C.P. Stoll, S.D.W. Thomas
Johannes Gutenberg-Universität Mainz, Mainz, Germany
[1]also at Helmholtz Institut Mainz, Germany and
GSI Helmholtzzentrum für Schwerionenforschung, Darmstadt, Germany

Abstract

The MESA project is currently under construction at Johannes Gutenberg-Universität Mainz. It will be used for high precision particle physics experiments in two different operation modes: external beam (EB) mode (0.15 mA; 155 MeV) and energy recovery (ERL) mode (1 mA; 105 MeV). The recirculating main linac follows the concept of a double sided accelerator design with vertical stacking of return arcs. Up to three recirculations are possible. Acceleration is done by four TESLA/XFEL 9-cell SRF cavities located in two modified ELBE cryomodules. Within this contribution the recirculation optics for MESA will be presented. Main goals are achieving best energy spread at the experimental setups in recirculating ERL and non-ERL operation and providing small beta-functions within the cryomodules for minimizing HOM excitation at high beam currents.

INTRODUCTION

The Mainz Energy-recovering Superconducting Accelerator (MESA) is a low energy continuous wave (cw) recirculating electron linac for particle and nuclear physics experiments under construction at Johannes Gutenberg-Universität Mainz [1-3]. The first phase of operation foresees to serve mainly three experiments, two of them running in external beam mode (EB) and one in energy recovering mode (ERL). MESA construction was funded in 2012. The facility and its experiments [4-6] have undergone several design changes since then. The latest change of layout has been applied in spring 2019 and was presented already in [7]. Therefore, start to end tracking simulations for the complete machine [8] are still based on an older layout version and need to be repeated for the new one. Nevertheless, the main design of MESA has been kept up throughout the changes of accelerator layout. MESA will be constructed in a double sided accelerator layout with two superconducting linacs and vertically stacked return arcs. In EB mode, up to three linac passes are possible and maximum beam energy and current yield 155 MeV and 150 µA respectively. In ERL operation only two passes can be used for acceleration and after experimental use of the beam for deceleration again. The maximum beam energy reduces to 105 MeV but the maximum beam current is not limited by installed rf power anymore and can go up to 1 mA. In a later stage of MESA operation, the beam current shall be increased to the maximum available current from the injector linac (10 mA) [9].

All MESA experiments rely on excellent beam quality in order to perform precision experiments on nuclear and particle physics searching for dark particles and beyond standard model physics. Therefore, a relative energy spread of the beam of approx. 10^{-4} (RMS) or better is required for not being the main source of error in electron scattering experiments. In addition, beam quality needs to be kept stable for long time measurement runs. In particular, in ERL mode reaching these conditions can be quite challenging, as high beam intensities can deteriorate the bunches and decrease beam quality. Furthermore, instabilities due to high beam current like beam break-up (BBU) have to be considered when designing the MESA optics. In the following sections we will present the MESA optics layout and will discuss the possibility to achieve best energy spread by application of certain non-isochronous longitudinal working points.

MESA LAYOUT

General Layout

The MESA beam is produced at a polarized dc photogun on an extraction voltage of 100 kV [10]. The gun injects the beam into the low energy beam transport system (MELBA) [11]. Here, spin manipulation can be applied and a chopper-buncher section is used for longitudinal matching into the normal-conducting booster linac MAMBO. In the booster linac the electrons are further accelerated by four normalconducting injector cavities up to 5 MeV beam energy up to10 mA cw beam current [12,13]. The simulated transverse and longitudinal phase space from MAMBO has been used in simulations presented within this contribution [14]. The 5 MeV beam is transferred into the main linac through a 180° arc afterwards, which can also be used as bunch compressor in order to reach shortest possible bunches at the position of the first SRF cavity of the main linac [14,15]. The recirculating main linac is using a double sided accelerator design with two superconducting linac modules [16], each on either side, containing in total four SRF cavities and providing an energy gain of 25 MeV per turn. Recirculation arcs are stacked vertically. Figure 1 illustrates the MESA layout.

Vertical Spreaders and Combiners

The vertical spreader and combiner sections need to separate the beams of different energies to their return arcs. In addition, vertical dispersion needs to be cancelled out at the end of each spreading or combining section. Longitudinal dispersion, also known as momentum compaction, adding

---

* This work has been supported by DFG through the PRISMA$^+$ cluster of excellence EXC 2118/2019 and by the European Union's Horizon 2020 Research and Innovation programme under Grant Agreement No 730871.

†flohug@uni-mainz.de

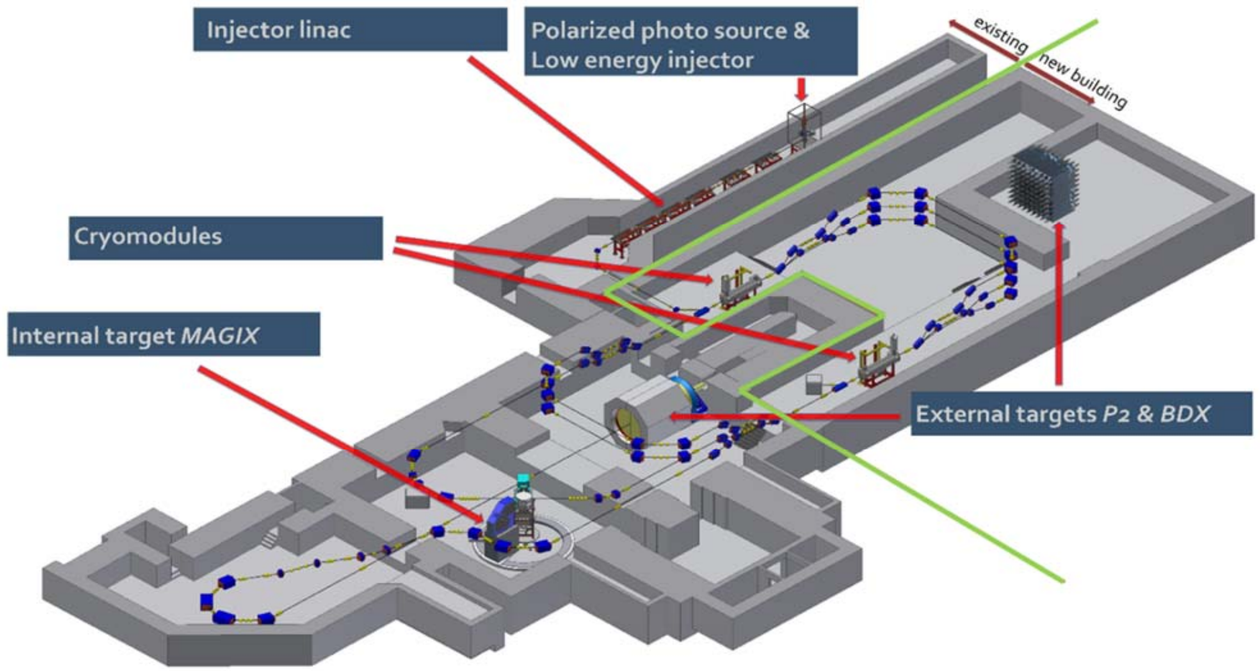

Figure 1: Layout of the facility [7]. The accelerator will be located in existing and newly constructed underground halls. The boundary between the old and new parts of the building is marked by a green line. The layout comprises of two main linac cryomodules and vertically stacked return arcs. The internal experiment MAGIX can be run in multi-turn ERL mode (courtesy of drawing: D. Simon).

up inside the spreader sections can be corrected and adapted in the subsequent horizontal return arc. The spreader design uses a symmetric sequence of dipole magnets with parallel yokes cancelling out any transverse dispersion at the end of the section (see Fig. 2). Furthermore, the two highest energy beams can receive an extra kick from additional dipole magnets. This setup can be used for running MESA on different beam energies than the designed maximum energy. This flexibility in maximum energy is required by the experiments in order to perform electron scattering on variable momentum transfer. The additionally added dipoles enable fine tuning of the allowed energy ratios between injector linac and main linac. In ERL mode the only top two beamlines are used. This setting allows to focus the beam to very low transverse beta functions inside the cryomodules and is beneficial for mitigating BBU. Actually, simulated BBU threshold currents using the MESA optics lay above 10 mA [17,18].

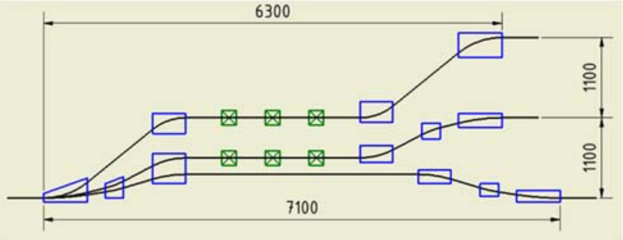

Figure 2: Layout and size of the MESA spreader sections. The beam with lowest energy will be transported to the top beamline and the one with highest energy on the bottom. The design follows a double dogleg for the lowest two energies and a chicane for the highest energy (courtesy of drawing: D. Simon).

Return Arcs

Return arcs for MESA consist of two double bends with a long straight section in between. Within each double bend three quadrupole magnets are located, which can be used to manipulate dispersion functions and transverse focusing. Along the long straight line, the transverse dispersion is still present but angular dispersion is set to zero. The optics of a complete arc is symmetric with respect to the middle of the long straight line having $\alpha = 0$ in the middle. The return arcs are highly flexible in providing variable amounts of momentum compaction, which is beneficial for running the accelerator on different longitudinal working points in the future. This topic will be further discussed in the next section. By adjusting the quadrupole settings, the longitudinal dispersion R_{56} can be varied by approx. 1 m without imposing any transverse dispersion. The complete arc including spreader and combiner sections is set to zero horizontal and vertical dispersion to have each beam free of transverse dispersion on each linac section. At present, no sextupole magnets are considered yet within the return arcs but may be in the future for longitudinal phase space linearization. As MESA will be run on different beam energies, a path length manipulation system for each return arc will be necessary. At least 40 deg of RF phase will be needed meaning a minimum path length adjustability of 2.6 cm. Such a system can be either realized by integrating chicanes into the long straight section of the return arcs or by using movable magnets. Figure 3 illustrates the optics for one complete MESA arc.

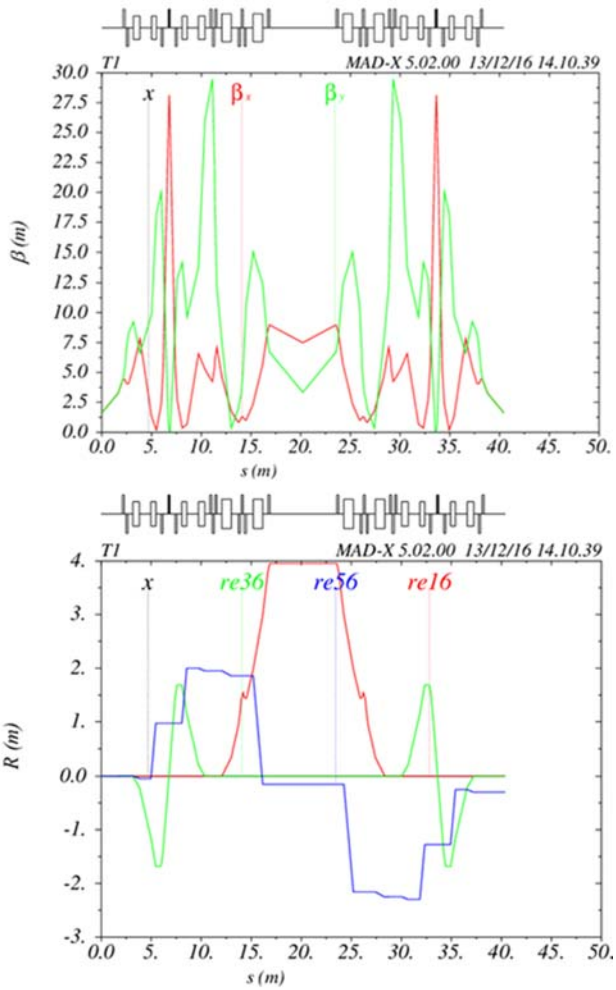

Figure 3: MESA arc optics. On top: Horizontal and vertical β-functions. The symmetry of the arcs can be seen. At the beginning and the end the beam coming from or travelling to the cryomodules is round and convergent having its focus in the middle of the modules. On bottom: Dispersion functions along the arc. Vertical and horizontal dispersion vanish at the end. Longitudinal dispersion is set to the design value for external beam mode (simulations by D. Simon).

LONGITUDINAL BEAM DYNAMICS

Non-Isochronous Multi-Turn Operation

Short recirculating electron linacs and in particular energy recovering linacs (ERLs) are commonly operated with on crest acceleration when aiming for smallest energy spread. In few-turn recirculators, this requires to keep the bunch length constantly small (< ± 1°) using achromatic and isochronous recirculation arcs. Isochronicity is a property of beam optics meaning all electrons of different energies have the same time of flight through the optics ($dt/dE = 0$). It is also known as the momentum compaction factor of the recirculating lattice. In the special case of ultra-relativistic electrons ($v \approx c$) isochronicity is achieved when the path length of all electrons is equally long represented by having a longitudinal dispersion matrix element of $R_{56} = 0$. The resulting energy spread is mainly determined by the short bunch length for an electron linac operated on crest, if the amplitude and phase jitters of the accelerating cavities are uncorrelated. In superconducting few-turn linacs, like most smaller ERLs, these jitters can add up coherently throughout the small number of linac passages due to the large time constant of field changes compared to the short travelling time of the electrons through the complete machine. This can be overcome by changing the longitudinal working point to a non-isochronous one like first described in [19,20]. On a non-isochronous longitudinal working point off crest acceleration and finite longitudinal dispersion of return arcs are combined. Now the electrons perform synchrotron oscillations in longitudinal phase space, which additionally increases operational stability if the oscillations are bound. In contrary to synchrotrons, small integer multiples of synchrotron oscillations are desired [20]. In fact, half or full integer numbers of synchrotron oscillations lead to the best energy resolution of the extracted beam as resulting energy spread at extraction is only determined by the energy spread at injection and all errors caused by RF jitters of the main linac cavities are cancelled out completely [19,20]. In addition, the linac is much less sensitive for external errors like e.g. path length errors. For few turns this concept has been tested already successfully by tuning the three pass superconducting linac S-DALINAC [21] on a non-isochronous working point with a half rotation in longitudinal phase space reducing its energy spread and enhancing its stability significantly [22,23]. This experiment and the simulation methods are described in more detail in [22-24]. The resulting energy spread improvement can be seen in Fig. 4. For the EB mode of MESA an optimized working point has been calculated as well, again running on a half rotation in longitudinal phase space along the three turns recirculating acceleration process. By setting the return arcs to R_{56} = -0.26 m and choosing an acceleration phase off crest by ϕ_S = -5.8°, a relative energy spread at the experiment of $\Delta E_{\mathrm{rms}}/E = 5.5 \cdot 10^{-5}$ can be expected [25].

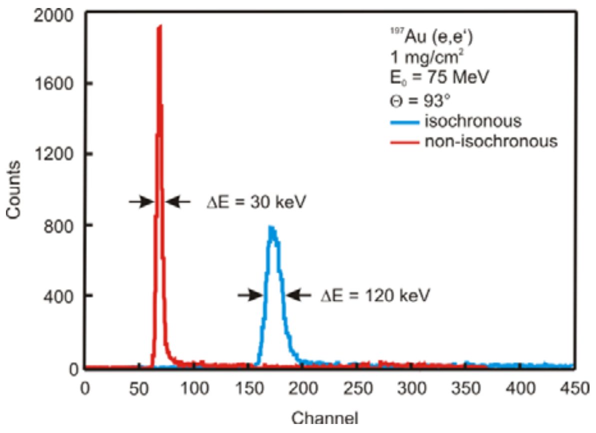

Figure 4: Energy spread of an electron beam from a three pass linac measured by elastic scattering on a thin gold target [22]. Blue: isochronous; Red: non-isochronous longi-

ISBN: 978-3-95450-217-2 doi:10.18429/JACoW-ERL2019-TUCOXBS03

tudinal working point. For better visibility the blue spectrum has been shifted in horizontal direction. The energy spread could be reduced significantly.

Non-Isochronous Beam Dynamics in ERLS

In ERLs not only the acceleration process but also the deceleration process needs to be considered while operating on non-isochronous working points. If the beam quality is reduced too much within the deceleration process, beam loss can occur making an ERL operation impossible. Nevertheless, off crest acceleration and deceleration is rather common in single turn ERLs but mostly for inducing an energy chirp to the beam allowing bunch compression afterwards and therefore the production of short pulses, which is of greatest interest in radiation experiments like FELs [26]. The decelerating phase though has to be chosen at a phase shift close to 180°, in order to reach optimum ERL efficiency. When applying such a 180° phase shift to a non-isochronous multi-turn lattice like presented in the section before, the slope of the RF curvature is changing its sign from acceleration to deceleration while the longitudinal dispersion of the arcs stays constant as the same beamline is passed by the beam again in the deceleration process. This results in an unbound longitudinal motion and therefore in an increasing energy spread throughout the complete deceleration process. The beam would be lost finally before reaching the beam dump [27]. A phase shift of $\delta\phi = 180° - 2\cdot\phi_S$ could mitigate the problem of increasing energy spread in deceleration but efficiency of energy recovery would decrease drastically (see Fig. 5). On the other hand, one could discuss implementing individual return arcs for accelerating and decelerating particles, which would allow to manipulate each turn independently but also would result in doubling the reqired amount of arc magnets [26].

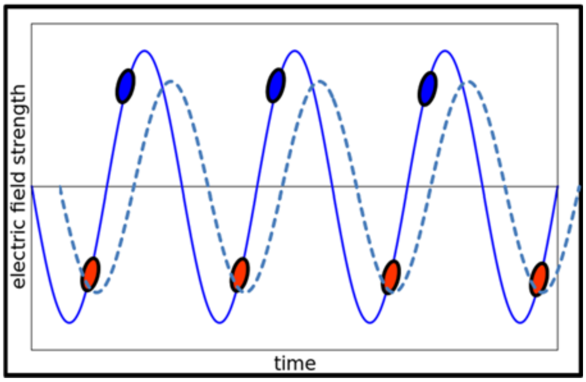

Figure 5: Bunches in non-isochronous ERL operation mode set on a different phase shift than 180° between acceleration and deceleration [25]. The accelerated bunches are plotted in blue, the decelerating bunches in red. Injecting the decelerating bunches on the optimum position regarding energy spread, the ERL efficiency reduces (illustrated by the dashed line for the excited RF wave by the decelerated particles, which is completely different in phase and amplitude to the desired RF wave).

Nevertheless, the double sided layout of the MESA accelerator with two acceleration linacs on each side followed by a return arc allows considering a different non-isochronous operation mode for ERLs. At MESA, the total number of linac passes and recirculation arcs each add up to a number of four. So the phase space can be rotated half way throughout the first two linac passes already having an optimum energy spread. Afterwards, the beam is transferred to the next linac section by an isochronous arc and the second two linac passes can be used to rotate the phase space back to its initial orientation by accelerating on the other crest of the acceleration field, now requiring a different sign of longitudinal dispersion as well. This acceleration scheme combines two benefits: it allows to apply the stabilization methods mentioned above [19-24] but now distributes two bunches on either crest of the RFwave in acceleration as well as in deceleration, not implying a deterioration of RF phase anymore (see Fig. 6). The decelerated bunches start on a phase of $\delta\phi = 180° - 2\cdot\phi_S$ and profit from a bound oscillation passing the high energy arcs at the right slope of R_{56} first. Afterwards the sign of both, RF slope and R_{56} changes again and the bound oscillation continues. This results in having best energy spread at the experimental setup as well as on the way to the beam dump. The additional RF power needed for such an ERL operation only compensates the increased dynamic losses of the RF cavities due to the required field overshoot. It should be mentioned, that some margin in cryogenic power is needed to run the accelerator this way, indeed. First results of tracking simulations for MESA non-isochronous ERL operation show an improved energy spread of $\Delta E_{rms}/E = 8.9\cdot10^{-5}$ [24]. The simulated optics parameters for the best setting now have different signs due to the changing rotation direction in longitudinal phase space: $R_{56}(1^{st}) = +0.155$ m; $R_{56}(2^{nd}) = 0$, $R_{56}(3^{rd}) = -0.645$ m and $\phi_S = -5.8°$ [25].

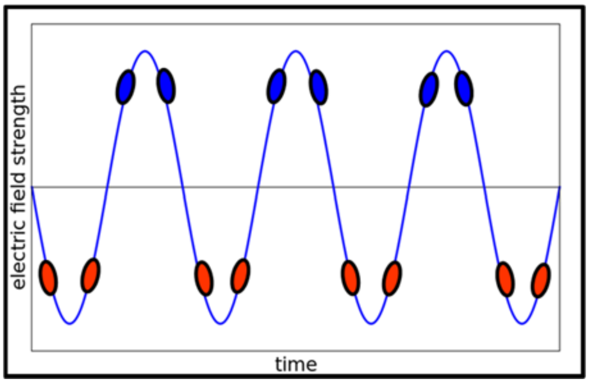

Figure 6: Non-isochronous ERL operation mode with acceleration and deceleration on either side of the accelerating/decelerating field [25]. Here the excited wave is in phase with the required one.

SUMMARY AND OUTLOOK

Within this contribution the current MESA layout and beam optics have been presented with emphasis on the dispersive spreaders and return arcs. Both need to provide great flexibility for matching the requirements of different

MESA operation modes. As the design of MESA changed very recently [7], all optics need to be re-evaluated. This work is in process. Nevertheless, the general layout of the recirculator has been kept throughout the latest design change. Therefore, only minor corrections will be necessary. New start-to-end tracking simulations will follow soon.

A non-isochronous longitudinal working point with half-integer phase advance can reduce the energy spread of the electron beam in few-turn recirculators significantly. For MESA, such an operation will be applied in external beam operation and is under further investigation for ERL operation as well. Here the acceleration on both crests of the RF wave show promising results. Beam experiments on flexible multi-turn ERL setups, like S-DALINAC, in the future would be beneficial to study the behavior of the RF system at such a bunch distribution scheme. The non-isochronous ERL operation will be investigated more precisely in the future. The presented longitudinal dynamics indeed shows some similarity with longitudinal manipulation for providing short bunches like presented during this conference, so called chirp flipping [26,28]. A collaborative approach in investigating such optics has been started already.

REFERENCES

[1] K. Aulenbacher, A. Jankowiak, “Polarized Electrons and Positrons at the MESA Accelerator”, *Proc. of PST 2009*, Ferrara, Italy (2009) 49. doi:10.1142/9789814324922_0006

[2] R. Heine, K. Aulenbacher, R. Eichhorn, “MESA-Sketch of an Energy Recover Linac for Nuclear Physics Experiments at Mainz”, *Proc. of IPAC’12*, New Orleans, Louisiana, USA (2012) 1993. Paper: MOP106012

[3] F. Hug, K. Aulenbacher, R.G. Heine, B. Ledroit, D. Simon, “MESA - an ERL Project for Particle Physics Experiments”, *Proc. of LINAC’16*, East Lansing, MI, USA, (2016) 313. doi:10.18429/JACoW-LINAC2016-MOP106012

[4] D. Becker *et al.*, “The P2 Experiment - A future high-precision measurement of the electroweak mixing angle at low momentum transfer”, *Eur. Phys. J. A* **54** (2018) 208. doi:10.1140/epja/i2018-12611-6

[5] M. Christmann *et al.*, “Instrumentation and optimization studies for a beam dump experiment (BDX) at MESA – DarkMESA”, *NIM A* (2019), accepted. doi:10.1016/j.nima.2019.162398

[6] A. Denig, “Recent results from the Mainz Microtron MAMI and an outlook for the future”, *AIP Conf. Proc.* **1735** (2016) 020006. doi:10.1063/1.4949374

[7] F. Hug *et al.*, presented at ERL’19, Berlin, Germany, September 2019, paper MOCOXBS05, this conference.

[8] D. Simon, K. Aulenbacher, R. Heine, F. Schlander, “Lattice and Beam Dynamics of the Energy Recovery Mode of the Mainz EnergyRecovering Superconducting Accelerator MESA”, *Proc. of IPAC’15*, Richmond, Virginia, USA (2015) 220. doi:10.18429/JACoW-IPAC2015-MOPWA046

[9] R. Heine, K. Aulenbacher, “Injector for the MESA Facility”, *Proc. IPAC’13*, Shanghai, China, (2013) 2150. paper: WEPWA011

[10] S. Friederich, K. Aulenbacher, C. Matejcek, “Vacuum Lifetime and Surface Charge Limit Investigations Concerning High Intensity Spin-Polarized Photoinjectors”, *Proc. of IPAC’19* (2019) 1954. doi:10.18429/JACoW-IPAC2019-TUPTS011

[11] C. Matejcek, K. Aulenbacher, S. Friederich, “Low Energy Beam Transport System for MESA”, *Proc. of IPAC’19* (2019) 1461. doi:10.18429/JACoW-IPAC2019-TUPGW028

[12] R. Heine, K. Aulenbacher, L. Hein, C. Matejcek, “Current Status of the Milliampere Booster for the Mainz Energy-recovering Superconducting Accelerator”, *Proc. of IPAC’16*, Busan, Korea (2016) 1743. paper: TUPOW002

[13] R.G. Heine, F. Fichtner, “The MESA 15 kW cw 1.3 GHz Solid State Power Amplifier Prototype”, *Proc. of IPAC’18*, Vancouver, BC, Canada (2018) 4216. doi:10.18429/JACoW-IPAC2018-THPMF063

[14] F. Hug, R. Heine, “Injector linac stability requirements for high precision experiments at MESA”, *J. Phys. Conf. Ser.* **874** (2017) 012012. doi:10.1088/1742-6596/874/1/012012

[15] A. Khan, O. Boine-Frankenheim, F. Hug, C. Stoll, “Beam matching with space charge in energy recovery linacs”, *NIM A* **948** (2019) 162822. doi:10.1016/j.nima.2019.162822

[16] T. Stengler *et al.*, presented at ERL’19, Berlin, Germany, September 2019, paper TUCOZBS06, this conference.

[17] C.P. Stoll, F. Hug, “Beam Breakup Simulations for the Mainz Energy Recovering Superconducting Accelerator MESA”, *Proc. of IPAC’19*, Melbourne, Australia (2019) 135. doi:10.18429/JACoW-IPAC2019-MOPGW025

[18] C.P. Stoll *et al.*, presented at ERL’19, Berlin, Germany, September 2019, paper THCOWBS06, this conference.

[19] H. Herminghaus, “The polytron as a cw electron accelerator in the 10 GeV range”, *NIM A* **305** (1991) 1. doi:10.1016/0168-9002(91)90511-N

[20] H. Herminghaus, “On the inherent stability of non-isochronous recirculating accelerators”, *NIM A* **314** (1992) 209. doi:10.1016/0168-9002(92)90516-7

[21] N. Pietralla, “The Institute of Nuclear Physics at the TU Darmstadt”, *Nuclear Physics News* Vol. **28/2** (2018) p.4.

[22] R. Eichhorn, A. Araz, J. Conrad, F. Hug, M. Konrad, T. Quincey, “Reducing the Energy Spread of Recirculating Linac by Non-isochronous Beam Dynamics”, *Proc. of LINAC’10*, Tsukuba, Japan (2010) 64. paper:MOP008

[23] F. Hug, C. Burandt, R. Eichhorn, M. Konrad, N. Pietralla, “Measurements of a Reduced Energy Spread of a Recirculating Linac by Non-Isochronous Beam Dynamics”, *Proc. of LINAC’12*, Tel Aviv, Israel (2012) 531. paper: SUPB010

[24] F. Hug, M. Arnold, T. Kürzeder, N. Pietralla, R. Eichhorn, “Improving Energy Spread and Stability of a Recirculating Few Turn Linac”, Proc. of IPAC’16, Busan, Korea (2016) 3222. doi: 10.18429/JACoW-IPAC2016-THPMB004

[25] F. Hug, “Application of Non-Isochronous Beam Dynamics in ERLs for Improving Energy Spread and Stability”, *Proc. of IPAC’17*, Copenhagen, Denmark (2017) 873. doi:10.18429/JACoW-IPAC2017-MOPVA013

[26] P.H. Williams., presented at ERL'19, Berlin, Germany, September 2019, paper TUCOWBS02, this conference.

[27] R. Eichhorn, J. Hoke, Z. Mayle, "Energy Stability of ERLs and Recirculating Linacs", *Proc. of LINAC'16*, East Lansing, MI, USA, (2016) 304. `doi:10.18429/JACoW-LINAC2016-MOP106001`

[28] P.H. Williams *et al*., presented at ERL'19, Berlin, Germany, September 2019, paper WEPNEC17, this conferen

THE LHeC ERL – OPTICS AND PERFORMANCE OPTIMIZATION*

S.A. Bogacz†, Jefferson Lab, Newport News, VA, USA

Abstract

Unprecedently high luminosity of 10^{34} cm^{-2}s^{-1}, promised by the LHeC accelerator complex poses several beam dynamics and lattice design challenges [1]. Here we present beam dynamics driven approach to accelerator design, which in particular, addresses emittance dilution due to quantum excitations and beam breakup instability in a large scale, multi-pass Energy Recovery Linac (ERL) [2]. The use of ERL accelerator technology to provide improved beam quality and higher brightness continues to be the subject of active community interest and active accelerator development of future Electron Ion Colliders (EIC). Here, we employ current state of though for ERLs aiming at the energy frontier EIC. The main thrust of these studies was to enhance the collider performance, while limiting overall power consumption through exploring interplay between emittance preservation and efficiencies promised by the ERL technology [3].

ERL ARCHITECTURE

The ERL layout is sketched in Fig. 1. The machine is arranged in a racetrack configuration hosting two superconducting linacs in the parallel straights and three recirculating arcs on each side. The linacs are 1 km long and the arcs have 1 km radius, additional space is taken up by utilities like spreading, matching and compensating sections. The total length is 9 km: 1/3 of the LHC circumference. Each of the two linacs provides 10 GV accelerating field, therefore a 60 GeV energy is achieved in three turns. After the collision with the protons in the LHC, the beam is decelerated in the three subsequent turns. The injection and dump energy has been chosen at 500 MeV.

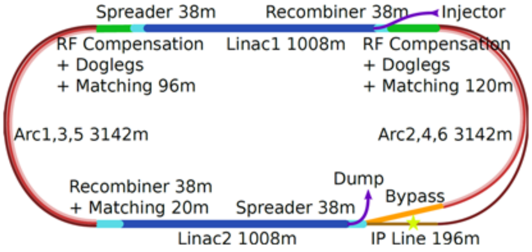

Figure 1: Scheme of the LHeC ERL layout.

Linac Design and Optimization

Each 1 km long linac hosts 72 cryo-modules, each containing 8 cavities for a total of 576 cavities per linac operating at 802 MHz. In the baseline design a quadrupole is placed every two cryomodules providing a FODO configuration. Note that the optics of a high gradient linac can be substantially perturbed by the additional focusing coming from the RF [4]. It is therefore important to make sure that it is properly modelled.

Energy recovery in a racetrack topology explicitly requires that both the accelerating and decelerating beams share the individual return arcs. This in turn, imposes specific requirements for TWISS function at the linacs ends: the TWISS functions have to be identical for both the accelerating and decelerating linac passes converging to the same energy and therefore entering the same arc.

To visualize beta functions for multiple accelerating and decelerating passes through a given linac, it is convenient to reverse the linac direction for all decelerating passes and string them together with the interleaved accelerating passes, as illustrated in Fig. 2. This way, the corresponding accelerating and decelerating passes are joined together at the arcs entrance/exit. Therefore, the matching conditions are automatically built into the resulting multi-pass linac beamline.

The optics of the two linacs are symmetric, the first being matched to the first accelerating passage and the second to the last decelerating one. In order to maximize the BBU threshold current, the optics is tuned so that the integral: is minimized. The resulting phase advance per cell is close to 130°. Non-linear strength profiles and more refined merit functions were tested, but they only brought negligible improvements.

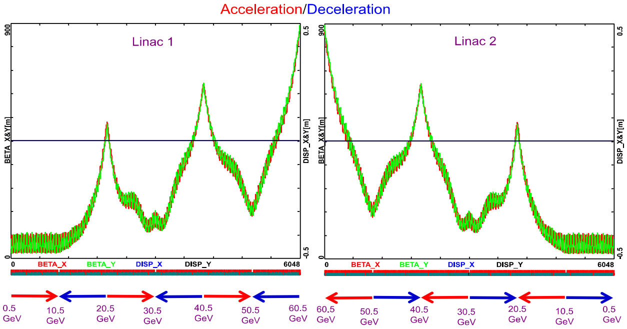

Figure 2: Beta function in the optimized LHeC Linacs during the acceleration. The linac contains 576 cavities.

Recirculating Arcs

All six arcs (three on each side) are accommodated in a tunnel of 1 km radius. Their lattice cell adopts a flexible momentum compaction layout that presents the very same footprint for each arc. This allows us to stack magnets on top of each other or to combine them in a single design. The dipole filling factor of the cell is 76%; therefore, the effective bending radius is 760 m.

The tuning of each arc takes into account the impact of synchrotron radiation at different energies. At the highest

---

* Work has been authored by Jefferson Science Associates, LLC under Contract No. DE-AC05-06OR23177 with the U.S. Department of Energy.

† bogacz@jlab.org

energy, it is crucial to minimize the emittance dilution; therefore, the cells are tuned to minimize the dispersion in the bending sections, as in a theoretical minimum emittance lattice. At the lowest energy, it is possible to compensate for the bunch elongation with a negative momentum compaction setup which, additionally, contains the beam size. The intermediate energy arcs are tuned to a double bend achromat (DBA)-like lattice, offering a compromise between isochronicity and emittance dilution. Figure 3 illustrates all three settings of the arc cells. Tapering will be required in particular for Arc 6, where the beam loses more than 1% of its total energy.

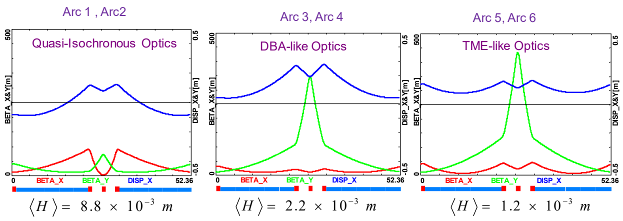

Figure 3: Different tunings of the arc cells at different energies. From left to right: low energy quasi-isochronous, middle energy DBA-like, high energy TME-like.

Before and after each arc a matching section adjusts the optics from and to the linac. Adjacent to these, additional cells additional cells are placed, hosting the RF compensating sections. The compensation makes use of a second harmonic field to replenish the energy lost by synchrotron radiation for both the accelerating and the decelerating beam, therefore allowing them to have the same energy at the entrance of each arc.

Path length-adjusting chicanes were also foreseen to tune the beam time of flight in order to hit the proper phase at each linac injection. Later investigations proved them to be effective only with the lowest energy beam, as these chicanes triggers unbearable energy losses if applied to the higher energy beams. A possible solution may consist in distributing the perturbation along the whole arc with small orbit excitations.

An alternative design based on FFA (Fixed Field Alternating Gradient) have been proposed and explored. It allows one to transport multiple energies in the same beam pipe, although only a very specific energy is bent with a constant radius. A drop-in FFA arc tuned to the 60 GeV energy showed promising results when substituted in the lattice, mainly because of the much higher bending filling factor, which mitigates synchrotron radiation. Nevertheless the LHeC would still need at least two FFA arcs on each side and it is not yet clear if the benefits compensate for the added complexity.

Spreaders and Recombiners

The spreaders are placed after each linac, and they separate bunches at different energies in order to route them to the corresponding arcs. The recombiners do just the opposite, merging the beams into the same trajectory before entering the next linac.

The spreader design consists of a vertical bending magnet, common for all beams, that initiates the separation. The highest energy, at the bottom, is brought back to the horizontal plane with a chicane, as illustrated in Fig. 4. The lower energies are captured with a two-step vertical bending adapted from the CEBAF design [5].

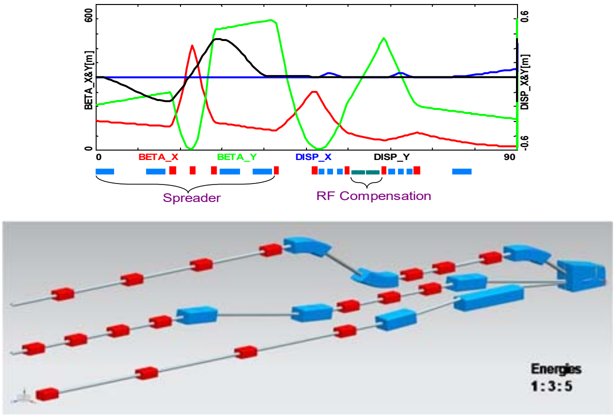

Figure 4: Spr/Rec Optics (top) and configuration (bottom)

The Bypass

While after the last spreader the 60 GeV beam can go straight to the interaction region, the lower energies beams, at 20 and 40 GeV, needs to be further separated in order to avoid interference with the detector. Different design options for the bypass section were explored and the one that minimizes the extra bending has been chosen and installed in the lattice.

Ten arc-like dipoles are placed very close to the spreader, to provide an initial bending, which results in 10 m separation from the detector located 150 m downstream. The straight section of the bypass is approximately 300 m long. In order to join the footprint of Arc 6, 10 of the 60 standard cells in Arc 2 and Arc 4 are replaced with seven higher field cells. The number of junction cells is a compromise between the field strength increase and the length of additional bypass tunnel, as can be inferred from the scheme in Fig. 5.

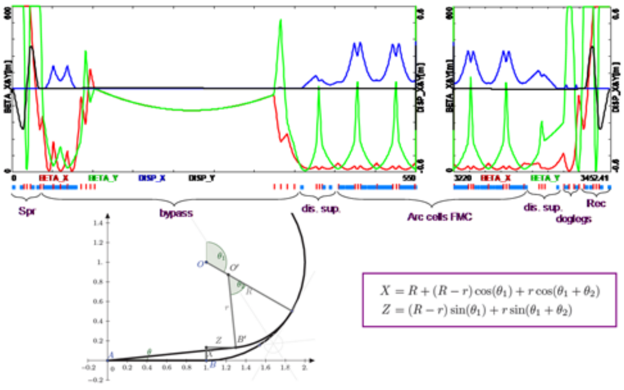

Figure 5: Layout of the bypass and optics. Featuring: the matching section from the linac, the initial bending, the long straight, the dispersion suppressor, cells with higher bending field and regular arc cells.

The stronger bending in the junction cells creates a small mismatch which is corrected by adjusting the strengths of

ISBN: 978-3-95450-217-2 doi:10.18429/JACoW-ERL2019-TUCOXBS04

the quadrupoles in the last junction cell and in the first regular cell.

Synchrotron Radiation Effects

Scaling of energy recovery to multi-GeV energies also encounters incoherent synchrotron radiation energy loss and spread, which asymmetrize accelerated and decelerated beam energies and profiles. These asymmetries substantially complicate multi-pass energy recovery and matching, and ultimately they limit the energy reach of the ERL due to recirculating arc momentum acceptance.

Table 1 lists arc-by-arc dilution of the longitudinal and transverse emittances due to quantum excitations. High luminosity colder requirements put very stringent limits on the allowed emittance increase. This can be met by design, employing low emittance optics arcs implemented in our design.

Table 1: Emittance Dillution Due to Synchrotron Radiation

Arc #	E [GeV]	ΔE [MeV]	$\Delta\varepsilon_n{}^{\mathrm{arc}}$ [m rad]	$\Delta\varepsilon_n$ [m rad]	$\Delta^{\mathrm{arc}}\sigma_{\Delta E/E}$	$\Delta\ \ \sigma_{\Delta E/E}$
1	10.5	1	2.7e-9	2.7e-9	3.9e-6	3.9e-6
2	20.5	11	1.5e-7	1.5e-7	2.1e-5	2.4e-5
3	30.5	51	4.1e-7	5.6e-7	5.6e-5	8.0e-5
4	40.5	160	2.2e-6	2.8e-6	1.1e-4	1.9e-4
5	50.5	387	4.6e-6	7.4e-6	2.0e-4	3.9e-4
6	60.5	797	1.4e-5	2.1e-5	3.1e-4	7.0e-4
5	50.5	387	4.6e-5	2.5e-5	2.0e-4	8.9e-4
4	40.5	160	2.2e-5	2.8e-5	1.1e-4	1.0e-5
3	30.5	51	4.1e-7	2.81e-5	5.6e-5	1.06e-5
2	20.5	11	1.5e-7	2.82e-5	2.1e-5	1.08e-5
1	10.5	1	2.7e-9	2.825e-5	3.9e-6	1.09e-5
Dump	0.5			2.825e-5		1.09e-5

‘DOGBONE’ TOPOLOGY ERL

So far, we have considered a ‘Racetrack’ configuration for an ERL. However, there are certain advantages of an alternative ‘Dogbone’ topology, which was first considered for rapid acceleration of fast decaying muons, as part of Neutrino Factory design [6]. Here, we propose a multi-pass electron ERL consisting of a single superconducting linac configured with elliptical twin axis cavities [7], capable of accelerating (or decelerating) beams in two separate beam pipes (see Fig. 6a). Such cavity, features opposite direction longitudinal electric fields in the two halves of the cavity, as illustrated schematically in Fig. 6b.

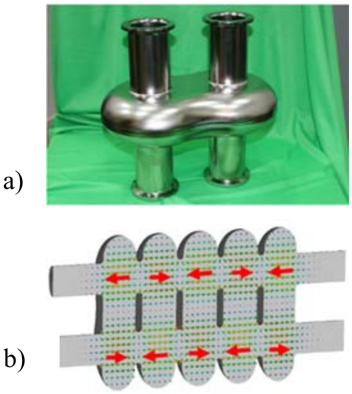

Figure 6: Elliptical twin axis cavity: a) Single cell Niobium cavity; b) Configuration of electric fields with opposing directions in two halves of a multi-cell cavity.

As illustrated in Fig. 7, the beam is injected via a fixed field chicane at the middle of the linac to minimize the effect of phase slippage for the lowest energy beam accelerated in the linac, which is phased for the speed-of-light particle. At the linac ends the beams need to be directed into the appropriate energy-dependent (pass-dependent) ‘droplet’ arc for further recirculation [8] (a pair of droplet arcs at each end of the linac). Reusing the same linac for multiple (3.5) beam passes provides for a more compact and efficient accelerator design and leads to significant cost savings [9]. Furthermore, this scheme is well suited to operate in the energy recovery mode.

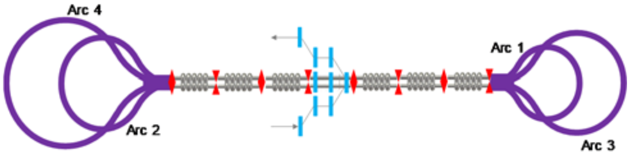

Figure 7: Multi-pass ‘Dogbone’ ERL – Schematic view of the accelerator layout; featuring a single SRF linac based on elliptical twin axis cavities, four return ‘droplet’ arcs and a pair of injection/extraction chicanes.

Multi-pass Linac

The focusing profile along the linac was chosen so that energy recovered beams with a large energy spread could be transported within the given aperture. Since the beam is traversing the linac in both directions (as being accelerated, or decelerated) two consecutive passes are accommodated in different ‘halves’ of elliptical twin axis cavities. To assure adequate focusing for counter propagating beams a ‘bisected’ focusing profile was chosen for the multi-pass linac [10]. Here, the quadrupole gradients were set to scale up with momentum to maintain 90° phase advance per cell for the first half of the linac and then they were mirror reflected in the second half to mitigate the beta beating resulting from under-focusing for the first full pass through the linac, as illustrated in Fig. 8. Multi-pass linac optics for all 3.5 passes is illustrated in Fig. 9.

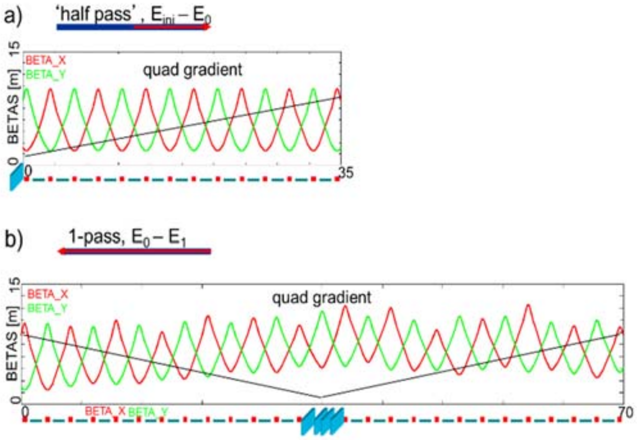

Figure 8: “Bisected” linac optics: (a) periodic FODO structure set for the lowest energy ‘half-pass’ through the linac; (b) linac optics for the first ‘full pass’; the under focusing

effects in the first half of the linac are mitigated by reversing the focusing profile in the second half.

One can notice the 'bisected' linac optics naturally supports energy recovery, providing an extra path length delay of one half of the RF wavelength is added to the highest energy arc (Arc 4), which will put the beam into a decelerating mode. The linac optics for 3.5 decelerating passes (energy recovery) follows a mirror symmetric optics to the one illustrated in Fig. 9.

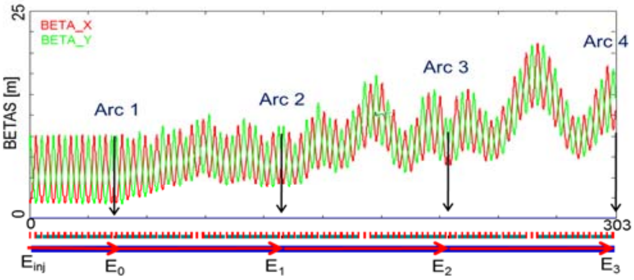

Figure 9: Multi-pass linac optics for all passes, with mirror symmetric arcs inserted as point matrices (arrows). The virtue of the optics is the appearance of distinct nodes in the beta beat-wave at the ends of each pass (where the arcs begin), which limits the growth of initial betas at the beginning of each subsequent droplet arc (Arc 1–4), hence eases linac-to-arc matching.

'Droplet' Arcs

At the ends of the RLA linac, the beams need to be directed into the appropriate energy-dependent (pass-dependent) droplet arc for recirculation. The entire droplet-arc architecture [8] is based on 90° phase-advance cells with periodic beta functions. For practical reasons, horizontal rather than vertical beam separation has been chosen. Rather than suppressing the horizontal dispersion created by the spreader, it has been matched to that of the outward arc. This is partially accomplished by removing one dipole (the one furthest from the spreader) from each of the two cells following the spreader. To switch from outward to inward bending, three transition cells are used, wherein the four central dipoles are removed. The two remaining dipoles at the ends bend the same direction as the dipoles to which they are closest. The transition region, across which the horizontal dispersion switches sign, is therefore composed of two such cells. To facilitate subsequent energy recovery following acceleration, a mirror symmetry is imposed on the droplet arc optics. This puts a constraint on the exit/entrance Twiss functions for two consecutive linac passes, namely: $\beta_{n\ out} = \beta_{n+1\ in}$ and $\alpha_{n\ out} = -\alpha_{n+1\ in}$, where n = 0, 1, 2... is the pass index.

The complete droplet arc optics for the lowest-energy pair of arcs is shown in Fig. 10. All higher arcs are based on the same principle as Arc 1, with gradually increasing cell length (and dipole magnet length) to match naturally to the increasing beta functions dictated by the multi-pass linac. The quadrupole strengths in the higher arcs are scaled up linearly with momentum to preserve the 90° FODO lattice. The physical layout of the above pair of droplet arcs is illustrated in Fig. 11.

One additional requirement to support energy recovery in a linac configured with elliptical twin axis cavities is that the path-length of Arcs 1-3 has to be a multiple of the RF wavelength. Conversely, Arc 4 path-length should be a multiple plus one half of the RF wavelength to switch the beam from the 'accelerating' to 'decelerating' phase in the linac.

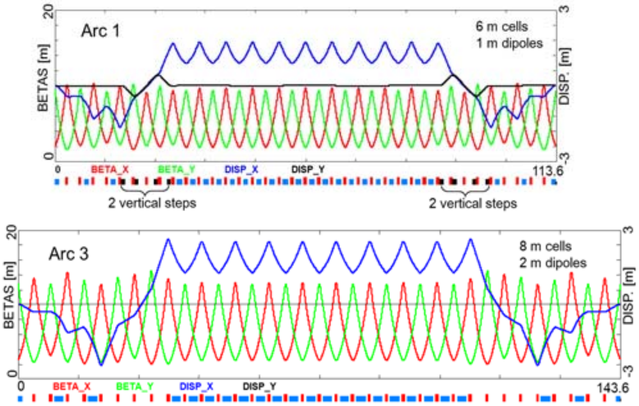

Figure 10: 'Droplet' arc optics for a pair of arcs on one side of the 'Dogbone'; Arc 1 and Arc 3.

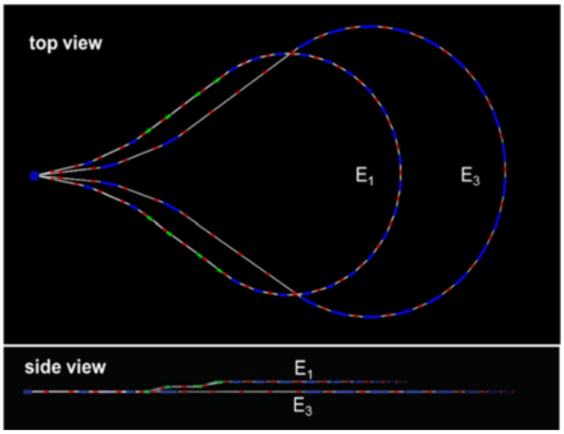

Figure 11: Layout of a pair of arcs on one side of the 'Dogbone' RLA, Top and side views, showing vertical two-step 'lift' of the middle part of lower energy droplet arc to avoid interference with the larger droplet (1 meter vertical separation).

OUTLOOK

The maximum number of passes through the RLA's linac is often limited by design considerations for the switchyard, which first spreads the different energy passes to go into the appropriate arcs and then recombines them to align the beam with the linac axis. To reduce complexity of the above single energy return arcs, we have recently proposed a novel multi-pass arc design based on linear combined function magnets with variable dipole and quadrupole field components, which allows two consecutive passes with very different energies (factor of two, or more) to be transported through the same string of magnets [11]. Such a solution combines compactness of design with all the advantages of a linear, non-scaling FFA (Fixed Field Alternated Gradient) optics [12], namely, large dynamic aperture and momentum acceptance essential for energy recovery, no need for complicated compensation of non-linear effects, and one can use a simpler combined-function magnet design with only dipole and quadrupole field components. The scheme utilizes only fixed magnetic fields, including those for injection and extraction.

SUMMARY

Here, we discussed novel approach to meet the LHeC challenges of adding new accelerator capabilities (ERL with multiple-passes, tens of GeV at high current, tens of mA). They were addressed through exploration of innovative lattice solutions. Effective implementation of Energy Recovering Linac technology requires: proper design of multi-pass optics, fine control of beam stability and losses (halo), preservation of 6D bunch quality, energy recovery efficiency, multiple-beam diagnostic devices, and development of ERL-specific commissioning and optics tuning procedures[13], [14].

Presented unique design of the IR optics gives the impression that luminosity of 10^{34} cm^{-2}s^{-1} is within reach.

The key advantage of a multi-pass RLA is its very efficient use of an expensive SRF linac. That efficiency can be further enhanced by configuring an RLA in a ‘Dogbone’ topology, which almost doubles the RF efficiency (compare to a corresponding racetrack). Furthermore, the ‘Dogbone’ RLA is well suited for operation in the energy recovery mode. Finally, we have presented a-proof-of-principle lattice design of a multi-pass energy recovery linac (ERL) in a ‘Dogbone’ topology.

REFERENCES

[1] D. Pellegrini, A. Latina, D. Schulte and S.A. Bogacz, “Beam-dynamics Driven Design of the LHeC Energy Recovery Linac”, *Phys. Rev. ST-AB*, 121004 (2015). doi:10.1103/PhysRevSTAB.18.121004

[2] D. Pellegrini, “Beam Dynamics Studies in Recirculating Machines”, Ph.D. Thesis, EPFL, Switzerland, 2016.

[3] O. Brüning *et al,* “Development of an ERL Based TeV Energy ep and eA Collider at CERN” *ICFA Beam Dynamics Newsletter* No 68, December 2015.

[4] J. Rosenzweig and L. Serafini, “Transverse particle motion in radio-frequency linear accelerators”, *Phys. Rev. E*, vol. 49, Feb 1994. doi:10.1103/PhysRevE.49.1599

[5] “12 GeV CEBAF Upgrade”, Reference Design, www.jlab.org/12GeV

[6] S.A. Bogacz, “Beam Dynamics of Muon Acceleration for Neutrino Factory’, *Journal of Physics G: Nuclear and Particle Physics*, 29, 1723 (2003). doi:10.1088/0954-3899/29/8/338

[7] H. Park, S. U. De Silva, J. R. Delayen, F. Marhauser, A. Hutton, ‘First Test Results of Superconducting Twin Axis Cavity for ERL Applications’, *Proceedings of LINAC 2018*, Beijing, China (2018). doi:10.18429/JACoW-LINAC2018-TUPO032

[8] C. Ankenbrandt *et al.*, “Low Energy Neutrino Factory Design”, Phys. Rev. ST-AB **12**, 070101 (2009). doi:10.1103/PhysRevSTAB.12.070101

[9] J.S. Berg *et al.*, “Cost-effective Design for a Neutrino Factory”, *Phys. Rev. ST-AB* **9**, 011001(2006). doi:10.1103/PhysRevSTAB.9.011001

[10] S.A. Bogacz, “Muon Acceleration Concepts for NuMAX: ‘Dual-use’ Linac and ‘Dogbone’ RLA”, *JINST*, 13, P02002 (2018). doi:10.1088/1748-0221/13/02/P02002

[11] V.S. Morozov, S.A Bogacz, Y.R. Roblin, K.B. Beard, “Linear Fixed-field Multi-pass Arcs for Recirculating Linear” *PRST-AB*,**15**, 060101 (2012). doi: 10.1103/PhysRevSTAB.15.060101

[12] V.S. Morozov, S.A Bogacz, K.B. Beard, “Muon Acceleration with RLA and Non-scaling FFA Arcs”, in *Proc. IPAC’10*, Kyoto, Japan (2010). Paper: WEPE084

[13] A.B. Temnykh, “Beam Losses Due to Intra-Beam and Residual Gas Scattering for Cornell’s Energy Recovery Linac”, in *Proc. EPAC08*, MOPC064, pp. 214-216, Genoa, Italy (2008).

[14] P. Evtushenko, “Large Dynamic Range Beam Diagnostics for High Average Current Electron Linacs”, in *Proc. IPAC2014*, WEYB01, pp. 1900-1905, Dresden, Germany, (2014). doi:10.18429/JACoW-IPAC2014-WEYB01

ISBN: 978-3-95450-217-2 doi:10.18429/JACoW-ERL2019-TUCOXBS05

BEAM TIMING AND CAVITY PHASING

R. Koscica*, N. Banerjee, G. H. Hoffstaetter, W. Lou, G. Premawardhana
Cornell University (CLASSE), Ithaca, NY 14853, USA

Abstract

In a multi-pass Energy Recovery Linac (ERL), each cavity must regain all energy expended from beam acceleration during beam deceleration. The beam should also achieve specific energy targets during each loop that returns it to the linac. To satisfy the energy recovery and loop requirements, one must specify the phase and voltage of cavity fields, and one must control the beam flight times through the return loops. Adequate values for these parameters can be found by using a full scale numerical optimization program. If symmetry is imposed in beam time and energy during acceleration and deceleration, the number of parameters needed decreases, simplifying the optimization. As an example, symmetric models of the Cornell BNL ERL Test Accelerator (CBETA) are considered. Energy recovery results from recent CBETA single-turn tests are presented, as well as multi-turn solutions that satisfy CBETA optimization targets of loop energy and zero cavity loading.

INTRODUCTION

The Energy Recovery Linac (ERL) is designed to create high-quality, high-current beams at a lower energy cost than conventional linacs. Energy transferred to the beam during acceleration is later recovered by the system. In an ERL where the beam accelerates and decelerates through the same linac, full energy recovery is achieved when each radio-frequency (RF) cavity in the linac recovers the energy that it originally expended: a beam ideally causes zero net power load on the system. In multiturn ERLs, the beam enters the linac at different speeds during each accelerating or decelerating pass. As a result, the beam may experience phases slipped away from the ultrarelativistic case, and this phase slippage can result in incomplete energy recovery.

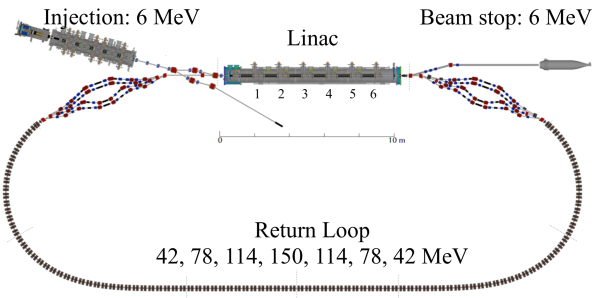

Figure 1: CBETA layout [1]. CBETA has a single linac with 6 RF cavities. The return loop has 4 independent beam paths shared by accelerating and decelerating beams of corresponding energy.

The Cornell BNL ERL Test Accelerator (CBETA) is a single-linac ERL with four independent loops that return the beam to the linac (Fig. 1). A 6 MeV beam accelerates to 150 MeV over four passes of the main linac, where it may be used for experiments. The beam then decelerates to 6 MeV over four more passes, using the same set of loops to return to the linac as during acceleration. The intended beam will have a current of 40 mA [1]. In Summer 2019, CBETA was tested in a 1-turn configuration. A beam of under 0.1 μA accelerated from 6 MeV to 42 MeV, then decelerated back to 6 MeV. Better than 99.8% energy recovery was achieved in each cavity.

CBETA has not yet been tested in multiturn operation, where energy recovery may be more challenging to achieve due to the increased complexity of the system. If a 4-turn CBETA model is simulated with RF phase and loop length settings that give energy recovery when $v = c$ everywhere, then a 40 mA beam of expected non-ultrarelativistic speed incurs up to 46 kW power load in a single cavity. However, the CBETA cavities only have 2 kW power allotted for beam acceleration; assuming a beam speed of $v = c$ would result in unfeasible power consumption.

Optimization of RF phase and loop timing is needed to reduce the simulated beam load during multi-turn operation. Direct optimization would require a large system of variables and constraints, but the system size can be greatly reduced if RF phases are chosen for a symmetric accelerating and decelerating energy configuration. The ERL symmetry strategy presented here is further discussed in [2] and [3].

OPTIMIZATION SYSTEM

Suppose a single-linac ERL with shared accelerating and decelerating return loops (*e.g.* CBETA) has M linac passes and N cavities. For CBETA, $M = 8$ and $N = 6$. The optimization system must have N constraints to minimize each cavity load. An additional ($M - 1 = 7$) constraints are needed to ensure that the beam has the correct energy during return loops, such that the shared loops can direct both accelerating and decelerating beams identically, and the central loop can achieve the correct maximum energy for experiments. To achieve these goals, one can vary the length of the $\frac{M}{2} = 4$ independent return loops, or the RF phase and voltage of the N cavities. This optimization system will have a total of ($N + M - 1 = 13$) constraints and ($2N + \frac{M}{2} = 16$) possible variables.

If the ERL is made symmetric, then the accelerating time-energy profile of a single-particle ideal beam is experienced in exactly reverse order during deceleration. This mirrored energy profile causes the load on each pair of cavities equidistant from the linac center, *e.g.* the first and last, to be correlated: only $\frac{N}{2} = 3$ load constraints are needed. The symmet-

---

* rmk275@cornell.edu

ric energy also causes identical beam energy during each pair of return loops, *e.g.* the first and last; only 1 energy constraint is needed for the central loop, as the maximum energy must be accurate for experiments. The phase and voltage variables are halved by the cavity pairing effect, but the return loops remain free to vary. The symmetric ERL yields a total of ($\frac{N}{2}+1 = 4$) constraints and ($N+1 = 7$) variables.

SYMMETRIC ERL CONDITIONS

Consider a small ERL with $N = 1$ cavity of length L, and $M = 2$ linac passes. The accelerating first encounter is designated A, and the decelerating second encounter is D. Suppose the cavity has an electric field $\mathcal{E}_A$ with spatial symmetry about the center,

$$\mathcal{E}_A(s,t) = \mathcal{E}_{A0}(s)\sin\left(\omega(t - t_{\text{in,A}}) + \phi_{\text{in},A}\right), \tag{1}$$

where $\phi_{\text{in},A}$ is the RF phase when the beam enters the cavity, ω is the RF frequency, s is the spatial coordinate, t is time, and $t_{\text{in},A}$ is the time when the beam enters A. For a deceleration profile that reverses the beam energy increase of acceleration, encounter D must have a field satisfying,

$$\mathcal{E}_D(L - s, t_{\text{total}} - t) = \mathcal{E}_A(s,t), \tag{2}$$

where t_{total} is the time between entering A and exiting D. This is only satisfied when the input phase of D follows the condition,

$$\begin{aligned} \phi_{\text{in},D} &= -\phi_{\text{in},A} - \omega T_A = -\phi_{\text{out},A} && \text{[odd]} \\ \phi_{\text{in},D} &= \pi - \phi_{\text{in},A} - \omega T_A = \pi - \phi_{\text{out},A}. && \text{[even]} \end{aligned} \tag{3}$$

where T_A is the time between entering and exiting A. The equations for cavities with even or odd cells differ by π due to the symmetry or antisymmetry of the spatial electric fields.

In a larger ERL, let n and m be cavity or pass indices, where $1 \le n \le N$ and $1 \le m \le M$. Each accelerating cavity of encounter (m,n) has a decelerating pair $(M - m, N - n + 1) = (m', n')$ that delivers an equal, opposite energy change to the beam. Since the pair could be chosen from any pass pair m and m', it is useful to write RF phases ϕ_0 at time of injection $t = 0$,

$$\phi_{0,n} = \phi_{\text{in},mn} - \omega t_{\text{in},mn} = \phi_{\text{out},mn} - \omega t_{\text{out},mn}. \tag{4}$$

Hence Eq. (3) for a multiturn ERL becomes,

$$\begin{aligned} \phi_{0,n} &= -\phi_{0,n'} - \omega t_{\text{total}} && \text{[odd]} \\ \phi_{0,n} &= \pi - \phi_{0,n'} - \omega t_{\text{total}}. && \text{[even]} \end{aligned} \tag{5}$$

When these phase conditions are applied to all $\frac{N}{2} = 3$ cavity pairs, symmetric electric fields should occur during beam-cavity encounters. However, the selected value of t_{total} must first match the total time over which the beam traverses the ERL. The return loop that switches from acceleration to deceleration must have the time of flight,

$$t_{\text{loop},\frac{M}{2}} = t_{\text{total}} - 2t_{\text{out},\frac{M}{2}N}, \tag{6}$$

If Eq. (5) and Eq. (6) are satisfied, the ERL will have symmetric time-energy profiles.

Table 1: Objectives after Optimization of Symmetric CBETA Models. Ranges indicate the closest and furthest values from targets across all model solutions. Loads assume a 40 mA beam current. Note, beam energies in loops 1-3 are not used as optimization parameters.

ERL Output (Objective)	**Optimized Value**	**Target**
Power load	28 pW - 32 μW	0 W
Peak energy offset	37 μeV - 0.9 eV	0 eV
Loop 1 (MeV)	42.00 - 42.18	42.00
Loop 2 (MeV)	78.01 - 78.20	78.00
Loop 3 (MeV)	114.00 - 114.23	114.00
Loop 4 (MeV)	150.00	150.00

SYMMETRIC CBETA MODELS

Optimization of energy recovery in a symmetric system is tested in models of CBETA. For the purpose of speed, Newton's Method and Levenberg-Marquardt optimization algorithms are used in the *Mathematica* or *Bmad* softwares. Since RF field modeling can be computationally intensive, the CBETA optimizations use simulated cavities of varying complexity.

(i) Thin Lens (TL) cavities. The simulated cavity delivers an instantaneous delta-function energy kick to a particle passing the center of the physical cavity location. This simulation optimizes the most quickly, although it is also the least physical model.

(ii) Ultrarelativistic (UR) cavities. Inside the cavity region, the particle experiences a time of flight and energy change consistent with the $v = c$ case, regardless of actual energy.

(iii) Finite Time-tracked (FT) cavities. Inside the cavity region, time evolution is estimated by an average velocity, and energy is delivered based on this time of flight.

(iv) Runge Kutta (RK) cavities. The particle is integrated through a grid of time-varying field intensities. This is the most realistic model, but it also optimizes the most slowly.

Energy recovery and load values are optimized to within machine precision for all models, although the RK model is slightly farther from target due to the higher numerical noise of its optimization. Solution ranges are located in Table 1, where a 40 mA beam is assumed for load calculations. Optimization of the symmetric CBETA models indeed converges upon phase and loop length settings that minimize load and achieve the correct maximum energy.

LONGITUDINAL BEAM TILT

The conditions from Eq. (5) and Eq. (6) indeed result in an energy-symmetric system for a beam with phase space coordinates of the ideal particle. However, for a beam with nonzero spread in time and energy, the injected and final distributions do not display the same energy symmetry as the ideal particle experiences (Fig. 2, Left). If extension of ERL symmetry to non-ideal beams is desired, the input

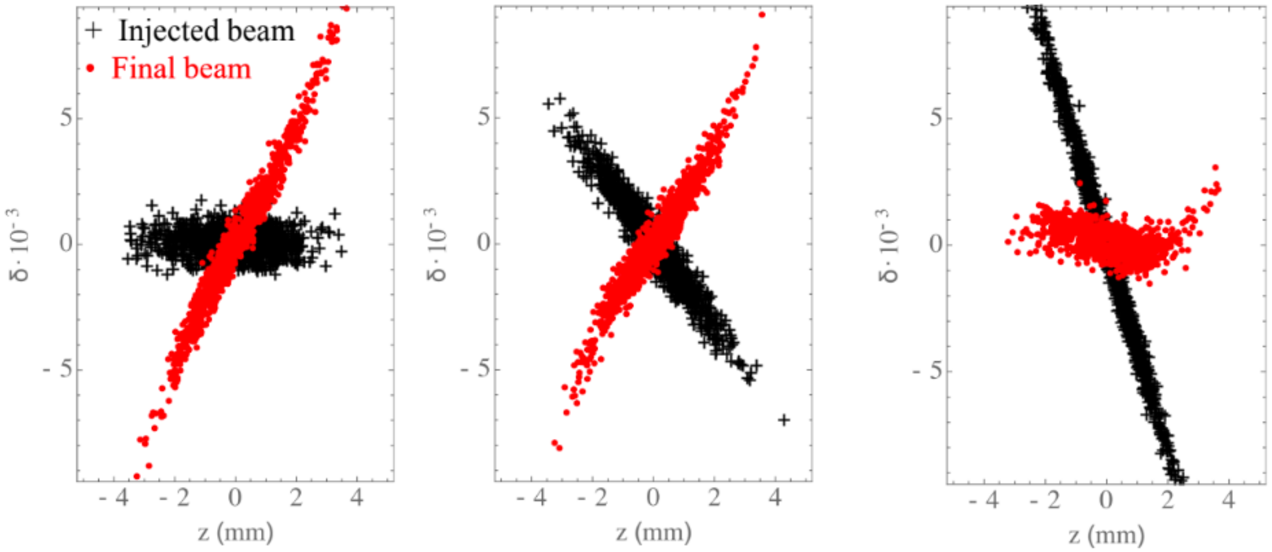

Figure 2: Longitudinal Phase Space at Injection and Beam Stop. Left: an injected Gaussian distribution ends with a positive slope. Center: a Gaussian superposed with a linear injection tilt ends with an equal energy spread. Right: a Gaussian superposed with a large linear injection tilt gives a minimized energy spread.

distribution can be tilted in longitudinal phase space using off-crest injector phases; the appropriate injected beam will result in visually symmetric input and output distributions with equal energy spreads (Fig. 2, Center).

In some ERL systems, it may be preferred to minimize the energy spread at beam stop (beam dump). This may be the case if, for instance, beam stop has a narrow range of energy acceptance. In this case, an even more extreme tilt can minimize the energy spread of the final distribution (Fig. 2). Appropriate tilt patterns can be identified by scanning through a range of simulated injector phases, or by calculating the transport matrix for the full ERL; further details on the analytical calculation of tilt angle can be found in [2].

CONCLUSION

Phase slippage poses one major challenge to achieving energy recovery in multiturn ERLs. This effect can be reduced by optimizing the cavity RF phases, voltages, and loop lengths to minimize power load on each cavity. However, this results in a large and computationally intensive optimization system. The method of ERL symmetry reduces the size of the required optimization system by guaranteeing identical time and energy steps during acceleration and deceleration. In this way, the power loads of cavity pairs are correlated, reducing the total number of independent optimization constraints. By applying ERL symmetry to models of CBETA, phase and loop length settings have been identified to minimize power load and achieve the correct maximum beam energy. Symmetry optimization and beam tilting appear effective in CBETA simulations, but these strategies can also be extended to the optimization of other single-linac, shared return loop ERL systems with N cavities and M passes.

ACKNOWLEDGEMENTS

We thank Dr. David Sagan for assistance with the Bmad simulation software. We thank Dr. Christopher Mayes for assistance with the RF cavity fields. This work was supported by Brookhaven National Labs and the New York State Energy Research and Development Agency (NYSERDA).

REFERENCES

[1] G. H. Hoffstaetter, D. Trbojevic, C. Mayes, N. Banerjee, J. Barley, I. Bazarov, *et al.*, "CBETA Design Report, Cornell-BNL ERL Test Accelerator," Jun. 2017, `arXiv:1706.04245`

[2] R. Koscica, N. Banerjee, G.H. Hoffstaetter, W. Lou, and G. Premawardhana, "Energy and rf cavity phase symmetry enforcement in multiturn energy recovery linac models", *Phys. Rev. ST Accel. Beams*, vol. 22, p. 091602, Sept. 2019, `doi:10.1103/PhysRevAccelBeams.22.091602`

[3] R.M. Koscica, N. Banerjee, C.M. Gulliford, G.H. Hoffstaetter, W. Lou, "Energy and RF cavity phase symmetry enforcement in multi-turn ERL models", in *Proc. 10th Int. Particle Accelerator Conf. (IPAC'19)*, Melbourne, Australia, May 2019, pp. 1606-1608, `doi:10.18429/JACoW-IPAC2019-TUPGW086`

A FERROELECTRIC FAST REACTIVE TUNER (FE-FRT) TO COMBAT MICROPHONICS*

N. Shipman, J. Bastard, M. Coly, F. Gerigk, A. Macpherson, N. Stapley,
CERN, Geneva, Switzerland
I. Ben-Zvi, Brookhaven National Laboratory, Upton NY, USA
C. Jing, A. Kanareykin, Euclid Techlabs LLC, Gaithersburg MD, USA
G. Burt, A. Castilla, Lancaster University, Lancaster, UK
E. Nenasheva, Ceramics Ltd, St.Petersburg, Russia

Abstract

FerroElectric Fast Reactive Tuners (FE-FRTs) are a novel type of tuner that may be able to achieve near perfect compensation of microphonics in the near future. This would eliminate the need to design over-coupled fundamental power couplers and thus significantly reduce RF power, particularly for low beam current applications.

The recently tested proof of principle FE-FRT is discussed and the theory and practice of FE-FRT operation are developed. These theoretical methods are then used to explore the potential benefits of using an FE-FRT with specific ERL proposals, which are seen as one of the major use cases. Specifically the ERLs considered are: eRHIC ERL, PERLE, LHeC ERL and the Cornell Light Source. Particular attention is given to the substantial peak and average RF power reductions which could be achieved; in many cases these are shown to be approximately an order of magnitude.

INTRODUCTION

Energy Recovery Linacs (ERLs) are designed to operate with virtually no beam loading. In principle, the only forward power that must be supplied to an ERL cavity is that needed to replace the power lost on the cavity walls. For super conducting cavities this is rather small.

Unfortunately, even with well designed cryomodules, frequency excursions caused by microphonics are typically orders of magnitude larger than the natural bandwidth of the cavity and as a result almost all of the supplied forward power is reflected and lost.

Significant effort has been made in recent years to design fast mechanical piezo-electric tuners to combat microphonics. Whilst important progress has been made in this direction[1–3], it is an extremely difficult challenge. Although piezo-electric crystals are intrinsically fast, the speed of a piezo-electric tuner is limited by how fast a deformation can be applied to the cavity wall. A cavity also has its own mechanical resonances which imply complicated transfer functions between piezo actuator input and cavity resonant frequency. In addition, any applied mechanical deformation will invariably excite additional unwanted mechanical vibrations which will themselves affect the frequency.

Recent progress in ferroelectric (FE) material properties[4–6] have now made an entirely new method of combatting microphonics viable. An FE-FRT is a device containing FE material which is coupled to the cavity via an antenna and transmission line. By applying a voltage to the FE, its permittivity and therefore the reactance coupled to the cavity is altered, which changes the cavity's resonant frequency.

FE-FRTs have no moving parts, do not act on the cavity mechanically and do not excite unwanted mechanical vibrations. They also operate outside of cryomodules avoiding the cryogenic cost of dissipating power in liquid helium.

For ERLs and low beam loading machines FE-FRTs could soon offer significant power and cost savings.

PROTOTYPE FE-FRT

A proof of principle (PoP) FE-FRT was designed by S. Kazakov, built by Euclid and successfully tested on an SRF cavity at CERN[7]. A photograph and 3D rendering are shown in Fig. 1. It connects to the cavity on the left via a co-axial cable and to a high voltage source on the right.

The PoP FE-FRT was tested with a superconducting cavity and preliminary results were presented in [7]. The (measurement limited) response of the cavity to the tuner was found to be $< 50\,\mu$s, the true response may be much faster as the FE material itself responds in ~ 10s ns[8, 9].

Whilst the response time estimation was measurement limited, it is already possible to draw two key conclusions. Firstly the cavity response to an FE-FRT is not limited by the time constant of the cavity. Secondly the response time is certainly fast enough to easily correct for microphonics which are typically not significant above $\approx$ 1kHz [3, 10].

Predictions of PoP FE-FRT impedance as a function of frequency were made with a transmission line model (TLM), and compared to CST simulations[11] and VNA measurements in Fig. 2. Close agreement is seen around the intended operating frequency (≈ 400 MHz), validating the TLM.

MECHANISM OF ACTION

Theory of an FE-FRT has already been presented in [7]. Here the most important results are reviewed and behaviour in anticipated paradigmatic scenarios is explored.

Theoretical Overview

The cavity is modelled as a conductance G_c, capacitance C_c and inductance L_c connected in parallel. The cavity-tuner or FE-FRT coupler is modelled as a lossless trans-

---

[*] This work was supported in part by the DOE SBIR grant: DE-SC0007630.

ISBN: 978-3-95450-217-2 doi:10.18429/JACoW-ERL2019-TUCOZBS02

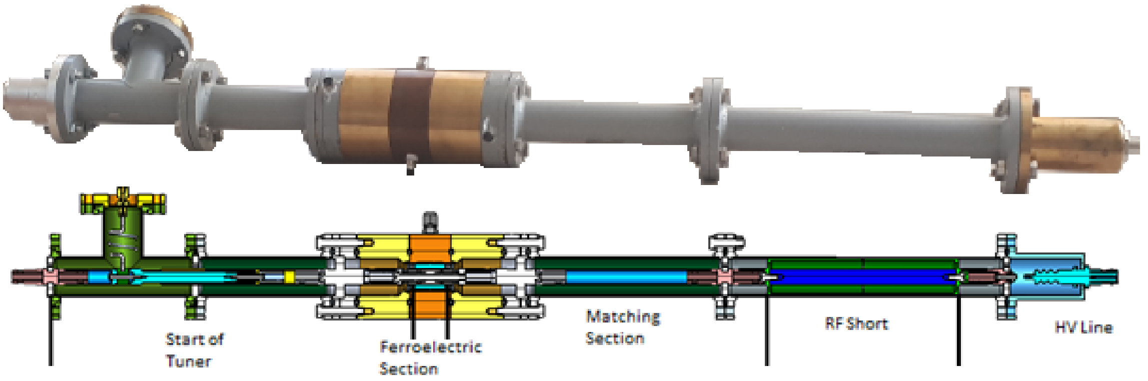

Figure 1: A photograph and cut away 3D rendering of the PoP FE-FRT.

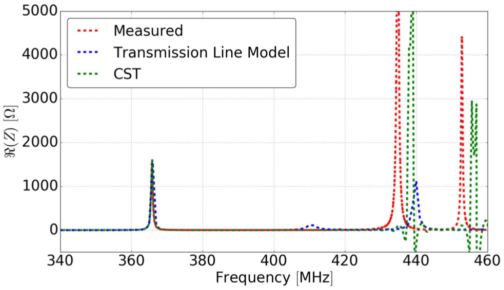

(a) Real part of impedance.

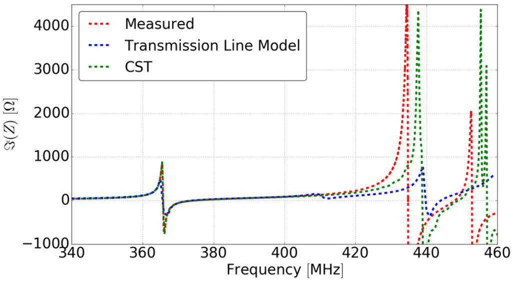

(b) Imaginary part of impedance.

Figure 2: Impedance of the PoP FE-FRT vs. frequency measured with a VNA (red); derived from a Transmission Line Model (blue); and simulated with CST (green).

former of ratio N. The tuner and transmission line (TL) connecting it to the cavity, has an admittance Y'_t; with real and imaginary parts G'_t (conductance) and B'_t (susceptance) respectively.

The tuner admittance as seen by the cavity is:

$$Y_t = G_t + iB_t = \frac{Y'_t}{N^2} \tag{1}$$

A prime indicates a tuner quantity before it is ‘coupled into the cavity’ through the transformer. A subscript can indicate the corresponding tuner state[1] [7], with ‘n’ denoting an arbitrary state and ‘1’ and ‘2’ denoting the ‘end’ states with minimum and maximum FE permittivities respectively.

Table 1 shows the theoretical expressions developed in [7]. $\Delta\omega_{12}$ is the tuning range effected by the FE-FRT, with $\Delta B'_{t12}$ the change in FE-FRT susceptance between the end

Table 1: Review of Theoretical Results

Description	**Symbol**	**Equation**
Tuning range	$\Delta\omega_{12}$	$\frac{-\omega_0 \Delta B'_{t12}\sqrt{L_c/C_c}}{2N^2}$
Dissipated Power	P_{tn}	$U_c\frac{G'_{tn}}{N^2C_c}$
Reactive Power	$\mathcal{P}_{tn}$	$U_c\frac{B'_{tn}}{N^2C_c}$
Increase in Bandwidth	$\Delta\mathrm{BW}_n$	$\frac{G'_{tn}}{N^2C_c}$
State Ratio	SR_n	$\frac{\Delta\omega_{12}}{\Delta\mathrm{BW}_n}$
Figure of Merit	FoM	$\frac{2\lvert\sin\frac{\Delta\theta_{12}}{2}\rvert}{\sqrt{(1-\lvert\Gamma_1\rvert^2)(1-\lvert\Gamma_2\rvert^2)}}$

states. P_{tn} and $\mathcal{P}_{tn}$ are the dissipated and reactive power in the FE-FRT, with U_c the cavity’s stored energy. $\Delta\mathrm{BW}_n$ is the increase in cavity bandwidth due to the FE-FRT. SR_n is the ’State Ratio’ and FoM the ‘Figure of Merit’. Γ_1 and Γ_2 are the reflection coefficients in states 1 and 2 respectively and $\Delta\theta_{12}$ the difference in phase between them.

SR_n can be calculated from equivalent circuit parameters and enables the calculation of $\Delta\mathrm{BW}_n$ from $\Delta\omega_{12}$ independent of N. As it depends on the state and TL length, it is not a useful figure of merit, which we instead define as the geometric average of SR_1 and SR_2. The FoM allows easy comparison of different FE-FRT designs via simulation and evaluation of FE-FRT performance via VNA measurements. A higher FoM gives greater tuning range with reduced losses.

Examples of Operation

The theory in the previous section is now used to study different operational scenarios for a hypothetical cavity and FE-FRT operating at 800 MHz. Figure 3 shows the Smith chart position, frequency change and the dissipated and reactive power in the FE-FRT vs. FE permittivity, for three TL lengths. For each TL length the coupling ratio N is chosen such that $\Delta\omega_{12}$ is 100Hz.

In the ‘Open’ scenario the TL length is such that possible Γ_ns are centered on the Smith chart’s open position. In this scenario $\mathcal{P}_{tn}$ is minimised. P_{tn} varies slightly between

---

[1] The state of an FE-FRT, for example, would be different for different FE permittivities resulting from voltages applied to it.

ISBN: 978-3-95450-217-2 doi:10.18429/JACoW-ERL2019-TUCOZBS02

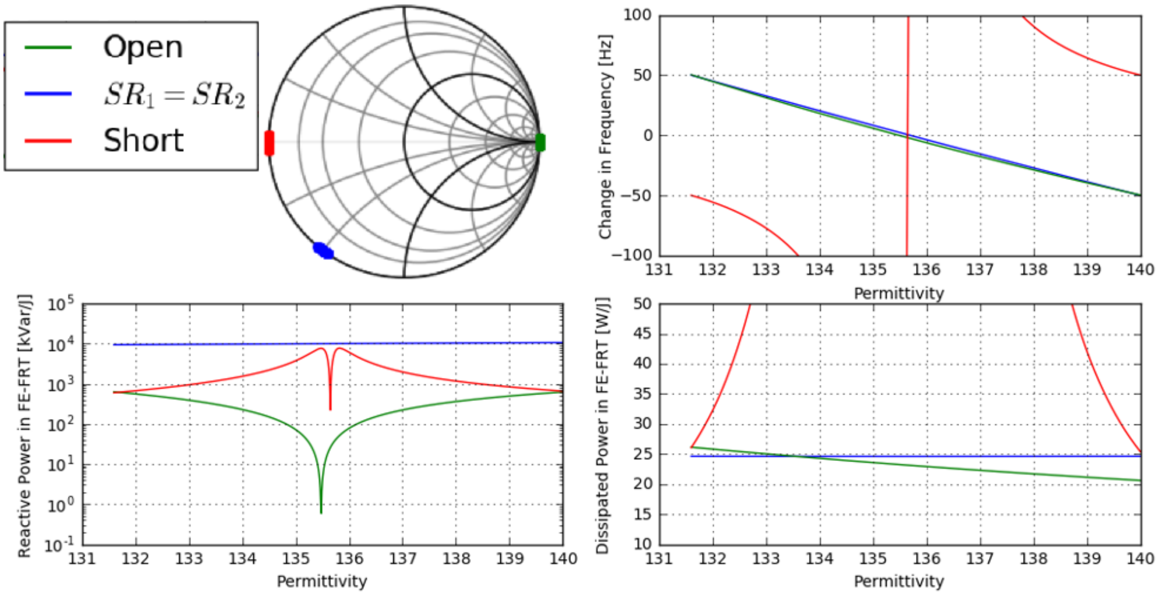

Figure 3: Operational scenarios for three TL lengths. Each antenna is chosen so the frequency shift between end states is 100 Hz. Smith chart position is shown top left. The frequency change (relative to central tuning frequency), dissipated, and reactive power in the FE-FRT vs. FE permittivity are shown top right, bottom left and bottom right respectively.

states, and therefore the cavity loaded-Q (Q_L) and required forward power (P_{RF}) also show a slight variation. This position also requires the most strongly coupled FE-FRT antenna which means the antenna will protrude further into the cavity and see increased losses on its surface. This is still likely to be close to the optimal scenario in the majority of use cases.

In the ‘SR$_1$ = SR$_2$’ scenario the TL length is such that SR$_1$ and SR$_2$ are equal. In this case, as seen in Fig. 3 the dissipated power is, to a good approximation, state independent. This is an attractive feature as both Q_L and P_{RF} are then also only weakly dependent on the FE-FRT state. However in this scenario the reactive power is large which may be a precluding factor for high U_c or $\Delta\omega_{12}$ applications.

In the ‘Short’ scenario the possible Γ_ns are centered on the Smith chart’s short position. As ΔB_{t12} is greatest here, this scenario requires the weakest antenna coupling. However, G_{tn} and B_{tn} diverge at the short, resulting in large variations of ω_n, $\mathcal{P}_{tn}$ and P_{tn} rendering continuous tuning impossible. This scenario could only be used for switching between two distinct frequencies. Note: reducing the permittivity range diminishes performance; the frequency shift is larger, but the dissipated power is larger still which decreases the FoM.

Table 2 shows the TL length and Q_{eq} of the FE-FRT antenna for each scenario in Fig. 3. We define Q_{eq} as the external Q-factor (Q_e^{FRT}) the antenna would have if terminated by a 50 Ω load. As the impedance of the FE-FRT is usually far from 50 Ω, Q_{eq} is far from Q_e^{FRT}. However, Q_{eq} gives a good intuitive idea of the required antenna size for readers more familiar with Q-factors than coupling ratios.

Table 2: Example Tuner Setup vs. Smith Chart Position

Position	Q_{eq}	**Line Length**
Open	1.26×10^{5}	0.283λ
SR$_1$ = SR$_2$	1.01×10^{6}	0.475λ
Short	2.94×10^{8}	0.533λ

APPLICABILITY TO ERLS

As an ERL has almost no beam loading, the forward RF power required to maintain the cavity voltage is[12]:

$$P_{RF} = \frac{V_c^2}{4 R/Q\, Q_L}\,\frac{\beta+1}{\beta}\left[1+\left(2Q_L\frac{\Delta\omega_\mu}{\omega_0}\right)^2\right] \tag{2}$$

With no FE-FRT, the Q_L of an ERL cavity is dominated by the external Q-factor of the fundamental power coupler (Q_e). In this case it can be shown from Eq. (2) that the optimal Q_e (Q_e^{opt}) to minimise the peak forward power (P_{RF}^{peak}) is:

$$Q_e^{\text{opt}} \approx \frac{\omega_0}{2\Delta\omega_\mu^{\text{peak}}} \tag{3}$$

where $\Delta\omega_\mu^{\text{peak}}$ is the peak detuning due to microphonics. From Eq. (3) and Eq. (2) it can be shown that if $Q_e = Q_e^{\text{opt}}$:

$$P_{RF}^{\text{peak}} \approx U\Delta\omega_\mu^{\text{peak}} \tag{4}$$

If microphonics induced frequency deviations are normally distributed and $\Delta\omega_\mu^{\text{peak}}$ is defined as greater than $5\sigma(\Delta\omega_\mu)$ then the average forward power is given by:

$$\overline{P}_{RF} \approx \frac{U\Delta\omega_{\mu\,\text{peak}}}{2} = \frac{P_{RF}^{\text{peak}}}{2} \tag{5}$$

If an FE-FRT is used, P_{tn} will contribute to Q_L. For full

ISBN: 978-3-95450-217-2 doi:10.18429/JACoW-ERL2019-TUCOZBS02

microphonics compensation $\Delta\omega_{12}$ must be set to $2\Delta\omega_{\mu}^{\text{peak}}$ and in this case, for a realistic FoM, $Q_0 >> Q_{FRT}$, with:

$$Q_{FRT} = \frac{\omega_0}{\Delta BW} \tag{6}$$

and ΔBW is defined as:

$$\Delta BW = \sqrt{\Delta BW_1 \Delta BW_2} \tag{7}$$

We assume the tuner is not in the 'Short' scenario and:

$$\Delta BW_1 \approx \Delta BW_2 \tag{8}$$

With FE-FRT use as described above $Q_e^{\text{opt}} = Q_{FRT}$ and it can be shown that both peak and average forward power are:

$$P_{RF}^{\text{FRT}} \approx \frac{\omega_0 U}{Q_{FRT}} \approx \frac{2U\Delta\omega_{\mu\,\text{peak}}}{\text{FoM}} \tag{9}$$

From Eq. (9), Eq. (4) and Eq. (5) it can be seen that:

$$\frac{P_{RF}^{\text{peak}}}{P_{RF}^{\text{FRT}}} \approx \frac{\text{FoM}}{2} \tag{10}$$

and that

$$\frac{\overline{P}_{RF}}{P_{RF}^{\text{FRT}}} \approx \frac{\text{FoM}}{4} \tag{11}$$

An FE-FRT therefore reduces the required peak and average forward power by a factor of $\frac{FoM}{2}$ and $\frac{FoM}{4}$ respectively.

FREQUENCY DEPENDENCE OF FOM

The dielectric α_d and conductive α_c losses in a copper coaxial cable at frequency f are given by[13]:

$$\alpha_d = 9.11 \times 10^{-8} f \sqrt{\epsilon_r} \tan\delta \text{ dB/m} \tag{12}$$

$$\alpha_c = 2.98 \times 10^{-7} \sqrt{f} \frac{1}{b}(1 + \frac{b}{a}) \frac{\epsilon}{\ln \frac{b}{a}} \text{ dB/m} \tag{13}$$

with b and a the outer and inner radii respectively, ϵ_r the relative permittivity of the dielectric and $\tan\delta$ its loss tangent.

The $\tan\delta$ of microwave ceramics including FEs scale linearly with frequency over a wide range of $\approx$ 100 MHz – 100s GHz [5, 14, 15]. If we restrict b such that only the principle TEM mode can propagate, then $b \propto f$ and therefore:

$$\alpha_c \propto f^{3/2} \tag{14}$$

$$\alpha_d \propto f^2 \tag{15}$$

With the above considerations a TLM and Monte-Carlo method similar to that presented in [7] were used to estimate the highest achievable FoM for frequencies between 400 and 1600 MHz. The results are shown in Fig. 4.

CASE STUDIES

The benefit of using an FE-FRT with specific ERL projects is now explored, using the parameter values in table 3. A black font indicates a value taken from a reference[12, 16–21], an orange font a value calculated from a referenced value and a red font an estimated parameter which could neither be found nor calculated from referenced values. Equation (2) is used to calculate all required powers.

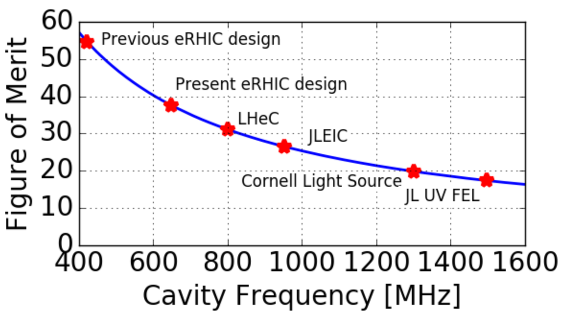

Figure 4: Expected FoM vs. Frequency

For all average powers a normal microphonics distribution is assumed. Also, in the non-FE-FRT case we assume all frequency correction is done via RF power and no other fast tuner (such as a piezo device) is used.

In the FE-FRT case, Q_0, which forms part of Q_L and β in Eq. (2), is necessarily replaced with the expression: ${}^{1}/_{Q_0} + {}^{1}/_{Q_{\text{FRT}}}$. The peak and average powers in the FE-FRT case are treated as identical, but this is only strictly true in the '$\text{SR}_1 = \text{SR}_2$' scenario. In the 'open' scenario for example, the peak power would be $\approx$ 10% higher than shown.

eRHIC

The eRHIC project[16] recently decided to pursue a Ring-Ring over an ERL based Linac-Ring design. However examining the benefits an FE-FRT could have brought to the ERL design is still informative.

Figure. 4 shows an expected FoM of $\approx$ 38 at the proposed ERL frequency of 647.4 MHz[22]. No value for the expected microphonics level could be found so a value of 20 Hz was estimated, from which we calculate Q_e based on Eq. (3).

By using an FE-FRT, peak power is reduced by a factor $\approx$ 19, and average powers by a factor $\approx$ 9. The results are shown in Fig. 5. Both electrical powers assume a grid conversion efficiency of 70 %.

PERLE and LHeC

Both PERLE and the LHeC plan to use an 801.58 MHz cavity[19, 20], whilst several designs exist, here we consider the updated CERN cavity design[21]. At this frequency Fig. 4 gives an expected FoM of $\approx$ 30. LHeC appears to use a more optimistic grid conversion efficiency and peak detuning (calculated form the specified total electrical power assuming $Q_e = Q_e^{opt}$ as per Eq. (3)) than PERLE.

For both PERLE and LHeC, peak power is reduced by a factor $\approx$ 15 and average power by a factor $\approx$ 7.5. The results for PERLE are shown in Fig. 6 and for the LHeC in Fig. 7.

Cornell Light Source

Whilst the 'maximum' expected peak detuning for the Cornell Light Source[12] is 20 Hz, Q_e was optimised instead for a 'typical' expected peak detuning of 10 Hz. This decreases $\overline{P}_{RF}$ but increases P_{RF}^{peak}. As a consequence, an FE-FRT decreases the average and peak power by a smaller ($\approx$ 3) and greater ($\approx$ 12) factor respectively than shown in Eq. (10) and Eq. (11). The results are shown in Fig. 8

ISBN: 978-3-95450-217-2 doi:10.18429/JACoW-ERL2019-TUCOZBS02

Table 3: Machine Parameters

Parameter	**eRHIC**	**PERLE**	**LHeC**	**Cornell**
Frequency	647.4 MHz	801.58 MHz	801.58 MHz	1.3 GHz
Cavity Voltage – V_c	26.88 MV	18.7 MV	18.7 MV	13.1 MV
External Q-Factor of FPC – Q_e	1.60×10^7	1.00×10^7	1.56×10^7	6.5×10^7
Intrinsic Q-Factor – Q_0	2.00×10^{10}	2.00×10^{10}	2.00×10^{10}	2.00×10^{10}
$^R/_Q$	502 Ω	393 Ω	393 Ω	387 Ω
Peak Detuning – $\Delta\omega_{\mu peak}$	20.0 Hz	40.0 Hz	26.2 Hz	20.0 Hz
RMS Detuning – $\sigma(\Delta\omega_\mu)$	3.33 Hz	6.67 Hz	4.36 Hz	3.33 Hz
Accelerating Gradient – E_{acc}	16 MV/m	20 MV/m	20 MV/m	16.2 MV/m
Cavity Length	1.68 m	0.935 m	0.935 m	0.81 m
Final Beam Energy	20 GeV	0.9 GeV	60 GeV	5 GeV
ERL Passes	12	3	3	1
Number of Cavities	62	16	1069	384
Grid to RF conversion efficiency	≈ 70%	≈ 50%	≈ 70%	≈ 50%
Total Electrical Power for microphonics control	1.37 MW	732 kW	22.2 MW	734 kW

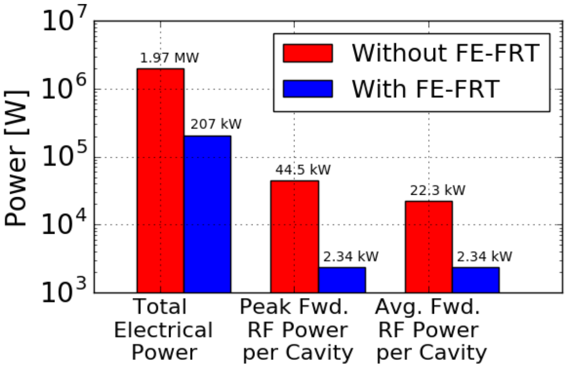

Figure 5: Power savings with FE-FRT use for eRHIC.

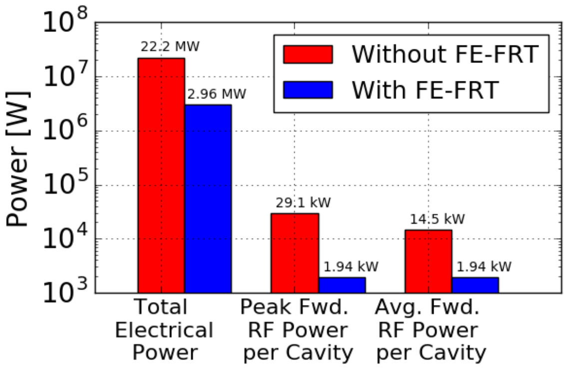

Figure 7: Power savings with FE-FRT use for LHeC.

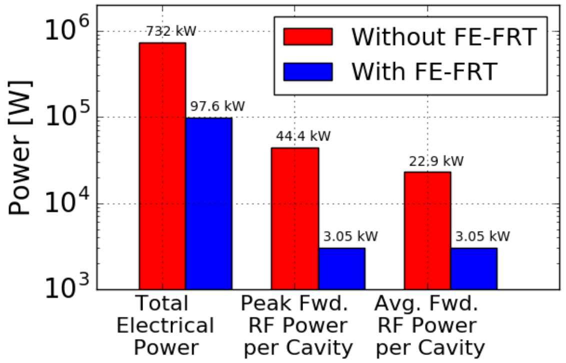

Figure 6: Power savings with FE-FRT use for PERLE.

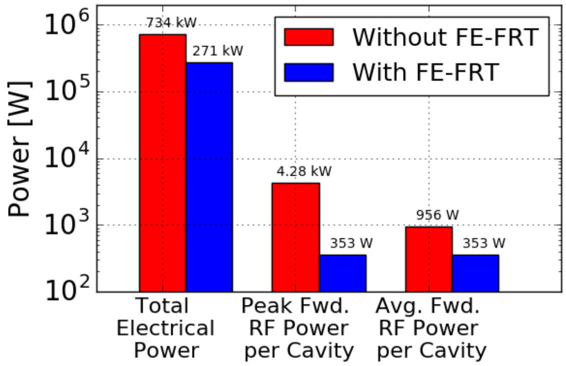

Figure 8: Power savings with FE-FRT use for Cornell.

CONCLUSION

The measured speed at which an FE-FRT can change a cavity's frequency is fast enough to easily correct for microphonics, but full microphonics compensation must still be verified experimentally. In addition, for future FE-FRT development, losses on the FE brazing must be addressed, as presently these cause a rather low FoM for the PoP FE-FRT. If these two key criteria can be demonstrated however, FE-FRTs would offer power and cost savings for ERLs to an extent that could significantly affect the feasibility and financial viability of large scale projects.

FE-FRTs require their own port and a large coupler which can handle sizeable reactive power, however the cost of implementing this would likely be more than offset by: a large reduction in required grid power; and a decrease in size and cost of RF infrastructure and fundamental power couplers.

FE-FRTs are likely to have a significant impact on a project's parameter optimisation considerations (for instance operating frequency and cavity design) and would ideally therefore be 'designed in' from the beginning.

REFERENCES

[1] N. Banerjee, G. Hoffstaetter, M. Liepe, P. Quigley, and Z. Zhou, “Active suppression of microphonics detuning in high Q_L cavities,” *Physical Review Accelerators and Beams*, vol. 22, pp. 052 002–17, 2019. doi: 10.1103/PhysRevAccelBeams.22.052002.

[2] Y. Pischalnikov *et al.*, “Operation of an SRF Cavity Tuner Submerged into Liquid Helium,” in *FERMILAB-CONF-19*, 2019. https://lss.fnal.gov/archive/2019/conf/fermilab-conf-19-294-td.pdf

[3] A. Neumann, W. Anders, O. Kugeler, and J. Knobloch, “Analysis and active compensation of microphonics in continuous wave narrow-bandwidth superconducting cavities,” *Physical Review Special Topics - Accelerators and Beams*, vol. 13, no. 8, 2010. doi: 10.1103/PhysRevSTAB.13.082001.

[4] A. B. Kozyrev, A. D. Kanareykin, E. A. Nenasheva, V. N. Osadchy, and D. M. Kosmin, “Observation of an anomalous correlation between permittivity and tunability of a doped ferroelectric ceramic developed for microwave applications,” *Appl. Phys. Lett*, vol. 95, p. 12 908, 2009. doi: 10.1063/1.3168650.

[5] E. Nenasheva *et al.*, “Low loss microwave ferroelectric ceramics for high power tunable devices,” *Journal of the European Ceramic Society*, vol. 30, no. 2, pp. 395–400, Jan. 2010, issn: 09552219. doi: 10.1016/j.jeurceramsoc.2009.04.008.

[6] A. Kanareykin, S. Kazakov, A. Kozyrev, E. Nenasheva, and V. Yakovlev, “Ferroelectric based high power tuner for L-band accelerator applications,” in *Proc. IPAC13*, Shanghai: JACoW, paper:WEPWO082, 2013, pp. 2486–2488.

[7] N. Shipman *et al.*, “A Ferroelectric Fast Reactive Tuner for Superconducting Cavities,” in *SRF2019*, Dresden, paper:WETEB7, 2019.

[8] A. Kanareykin *et al.*, “Fast switching ferroelectric materials for accelerator applications,” *AIP Conference Proceedings*, vol. 877, no. December 2006, pp. 311–319, 2006, issn: 0094243X. doi: 10.1063/1.2409151.

[9] S. Y. Kazakov, S. V. Shchelkunov, V. P. Yakovlev, A. Kanareykin, E. Nenasheva, and J. L. Hirshfield, “Fast ferroelectric phase shifters for energy recovery linacs,” *Physical Review Special Topics - Accelerators and Beams*, vol. 13, no. 11, p. 113 501, Nov. 2010, issn: 1098-4402. doi: 10.1103/PhysRevSTAB.13.113501.

[10] S. Simrock, “Control of Microphonics and Lorentz Force Detuning with a Fast Mechanical Tuner,” in *Proc. SRF 2003*, Lübeck, 2003, 254–257, paper:TUO09.

[11] *CST Studio Suite*. https://www.3ds.com/products-services/simulia/products/cst-studio-suite/

[12] E. G. H. Hoffstaetter *et al.*, “Cornell Energy Recovery Linac Science Case and Project Definition Design Report,” Cornell, Tech. Rep., 2013, p. 518.

[13] T. Moreno, *Microwave Transmission Design Data*, ser. Dover books on physics, engineering. McGraw-Hill Book Company, 1948.

[14] J. Petzelt and S. Kamba, “Submillimetre and infrared response of microwave materials: Extrapolation to microwave properties,” *Materials Chemistry and Physics*, 2003. doi: 10.1016/S0254-0584(02)00269-9.

[15] J. L. Hirshfield, “Fast 704 MHz Ferroelectric Tuner for Superconducting Cavities,” Chicago Operations Office, Argonne, IL (United States), Tech. Rep., Apr. 2012, pp. 1–34. doi: 10.2172/1038253.

[16] E. C. Aschenauer *et al.*, “eRHIC Design Study: An Electron-Ion Collider at BNL,” Tech. Rep., Sep. 2014. arXiv:1409.1633[physics.acc-ph]

[17] W. Xu *et al.*, “RF and Mechanical Design of 647 MHz 5-CELL BNL4 Cavity for ERHIC ERL,” in *Proceedings of IPAC2016*, Busan, 2014. doi: 10.18429/JACoW-IPAC2016-WEPMR041.

[18] W. Xu *et al.*, “Progress of 650 MHz SRF cavity for eRHIC SRF linac,” in *18th International Conference on RF Superconductivity*, Lanzhou: JACoW Publishing, 2017, pp. 64–66. doi: 10.18429/JACoW-SRF2017-MOPB009.

[19] D. Angal-Kalinin *et al.*, “PERLE. Powerful energy recovery linac for experiments. Conceptual design report,” *Journal of Physics G: Nuclear and Particle Physics*, vol. 45, no. 6, p. 065 003, Jun. 2018. doi: 10.1088/1361-6471/aaa171.

[20] J. L. Abelleira Fernandez *et al.*, “A Large Hadron Electron Collider at CERN Report on the Physics and Design Concepts for Machine and Detector,” *Journal of Physics G: Nuclear and Particle Physics*, vol. 39, no. 7, p. 075 001, Jul. 2012. doi: 10.1088/0954-3899/39/7/075001.

[21] R. Calaga, “A design for an 802 MHz ERL Cavity,” no. CERN-ACC-NOTE-2015-0015, 2015.

[22] W. Xu, I. Ben-Zvi, T. Roser, and V. Ptitsyn, “Frequency choice of eRHIC SRF linac,” Brookhaven National Laboratory (BNL), Upton, NY (United States), Tech. Rep., Jan. 2016. doi: 10.2172/1335380.

ISBN: 978-3-95450-217-2 doi:10.18429/JACoW-ERL2019-TUCOZBS04

CHARACTERIZATION OF MICROPHONICS IN THE cERL MAIN LINAC SUPERCONDUCTING CAVITIES

F. Qiu[1,2,†], S. Michizono[1,2], T. Miura[1,2], T. Matsumoto[1,2], D. Arakawa[1], H. Katagiri[1], E. Kako[1,2],
H. Sakai[1,2], K. Umemori[1,2], T. Konomi[1,2], M. Egi[1,2]
[1]High Energy Accelerator Research Organization (KEK), Tsukuba, Ibaraki 305-0801, Japan
[2]The Graduate Univiersity for Advanced Studies (Sokendai), Hayama, Kanagawa 240-0193, Japan

Abstract

In the main linac (ML) of the KEK-cERL, two superconducting cavities with high loaded Q ($Q_L \approx 1\times10^7$) are operated in continuous wave (CW) mode. It is important to control and suppress the microphonics detuning owing to the low bandwidth of the cavities. We evaluated the background microphonics detuning by the low level radio frequency system during the beam operation. Interestingly, a "field level dependence microphonics" phenomenon was observed on one of the cavities in the ML. Several frequency components were suddenly excited if the cavity field is above a threshold field (~3 MV/m). We found that this threshold field is probably related with the cavity quench limits despite the unclear inherent physical mechanism. Furthermore, in order to optimize the cavity resonance control system for better microphonics rejection, we have measured the mechanical transfer function between the fast piezo tuner and cavity detuning. Finally, we validated this model by comparing the model response with actual system response.

INTRODUCTION

At KEK, a compact energy recovery linac (cERL) was constructed to study the feasibility of the future 3 GeV ERL based light source in 2009 [1]. It is a 1.3 GHz superconducting (SC) facility that operated in continuous-wave (CW) mode. In the main linac (ML) of the cERL, two nine-cell cavities (ML1 and ML2) were installed for energy recovery [2]. These two cavities have a high loaded Q (Q_L) of about 1×10^7, with the corresponding cavity half-bandwidth ($\omega_{0.5}$) of about 65 Hz. The lower bandwidth makes the cavity phase very sensitive to the microphonics detuning. A low level radio frequency (LLRF) system is usually required to reduce the microphonics effects.

Figure 1(a) compares the cumulative microphonics detuning as a function of the vibration frequency of the ML cavities in the past 5 years (indicated by different colors). In 2015, a 50 Hz component caused by scroll pumps was observed in both cavities (especially ML2). This components were disappeared after inserting a rubber sheet under the pumps. From 2016 to 2019, we have observed that the microphonics conditions gradually deteriorated in the ML1 cavity. Roughly, the RMS micrphonics detuning in 2019 (blue) is 2.5 times of the detuning in 2016 (red). On the other hand, such a phenomenon was not observed in the ML2 cavity. Figure 1(b) shows the corresponding RF stability (left: ML1, right: ML2) in the past 5 years. After 2016, according to Fig. 1(b), the RF stabilities for ML1 cavity were, unfortunately, getting worse due to the deteriorated microphonics conditions. Whereas the stabilities of ML2 cavity always performed well due to its similar microphonics conditions in the past five years.

In view of this situation, we have investigated the background microphonics of these two cavities carefully. Interestingly, a "field level dependence microphonics" phenomenon was observed in cavity ML1 [3]. We found that if the cavity field in the ML1 is larger than a threshold filed of 3 MV/m, several high frequency components were suddenly excited. This threshold field is probably related with quench limits according to the experimental results. Furthermore, in order to optimize the current resonance control, we measured the transfer function (TF) model between the piezo tuner and the cavity detuning, and then demonstrated the validation of the model in the beam commissioning. This paper will present our studies in 2019.

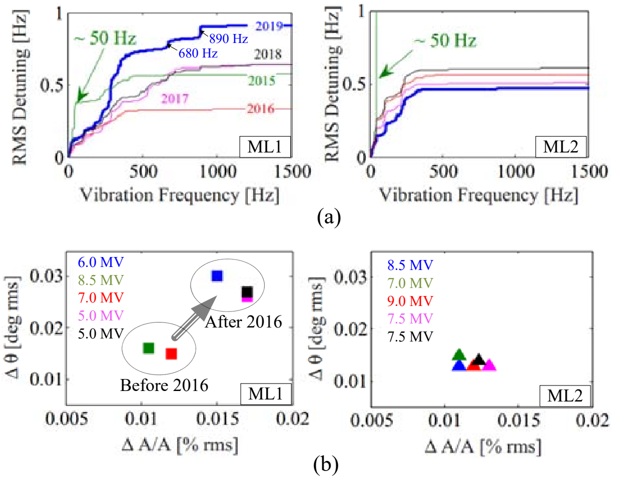

(a)

(b)

Figure 1: Five years comparison of (a) cumulative RMS detuning (in a function of vibration frequency) and (b) amplitude and phase stabilities (under feedback operation) of the ML1 (left) and ML2 (right). The cavity voltages in each operation are also marked in Fig. 1(b).

LLRF SYSTEM

Figure 2 shows the digital LLRF systems (indicated by red block) and frequency tuner system (indicated by blue block) of the ML cavities. The detailed information of these two systems can be found in [4-5] and [6], respectively. The phase differences ($\Delta\varphi$) between cavity pick-up and cavity incident (Pf) are calculated in both two systems. In LLRF system, this $\Delta\varphi$ will be further filtered

---

[†] qiufeng@post.kek.jp

by a first order low-pass filter with 2.5 kHz bandwidth to reduce the background noise. The microphonics detuning $\Delta\omega$ is then calibrated based on the $\Delta\varphi$ by the equation

$$\Delta\omega = \omega_{0.5} \cdot \tan\left(\Delta\varphi\right), \tag{1}$$

where $\omega_{0.5}$ represents the half-bandwidth of the cavity. In the tuner system, the $\Delta\varphi$ is first regulated by an integral (I) controller and then combined with a feedforward model (FF2 in Fig.2). This combined signal will finally drives a piezo tuner which tune the cavity resonance frequency.

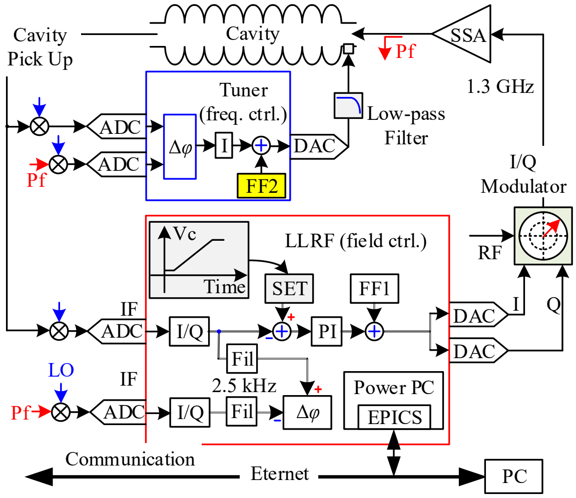

Figure 2: Schematic of the digital LLRF system (indicated by red block) and frequency tuner system (indicated by blue block) of the cERL ML cavity.

MICROPHONICS OF ML CAVITIES

In 2019, the operational field of ML1 was limited to 6 MV/m due to the degradation of the cavity performance [2]. We found that some high frequency components such as 680 Hz and 890 Hz were excited under 6 MV/m operation (see the accumulative RMS detuning plot at Fig.1). However, these components were disappeared when we operate the ML1 with lower field (e.g. 2 MV/m). It seems that the microphonics detuning is related with the field level in the ML1. To evaluate whether there is a field dependence of the microphonics detuning, we gradually increased the cavity voltage (V_c) by changing the set value of the LLRF system under feedback (FB) operation (see Fig. 2). The field-detuning map was then obtained by performing Fourier analysis of $\Delta\omega$ under different cavity field.

Figure 3 shows the measured field-detuning maps of ML1 (upper) and ML2 (lower) cavities. The color code here represents the detuning spectrum power. Interestingly, an unexpected boundary, corresponding to a threshold V_c of approximately 3.1 MV, was observed in the map of the ML1. Noted that the relationship between V_c and the cavity field (E_{acc}) is expressed as V_c [MV] = 1.038 [m]×E_{acc} [MV/m], i.e. the value of V_c and E_{acc} is almost same in our cavity [7]. In the field-detuning maps of the ML2, such a “field dependence microphonics” phenomenon did not appeared.

We scanned this field-detuning maps by several times under different LLRF conditions (switching on/off the LLRF FB control loops or the frequency tuner feedback loop). The threshold voltage was reproduced almost on the same value for all of these cases. We therefore ruled out the possibility of the FB loops that caused the “field dependency microphonics” phenomenon. On the other hand, we found the value of the threshold voltage is probably related with quench limits. The cavity quench limit field of ML1 was increased from 5.9 MV/m to 6.3 MV/m by the pulse (PS) aging processing. It is interesting to see that the threshold field was also increased from 3.0 MV/m to about 3.2 MV/m. After one week beam operation, we observed that the quench limits level was reduced slightly, as well as the corresponding threshold field. Table 1 has summarized the quench limits field and the corresponding threshold field under different stage [3].

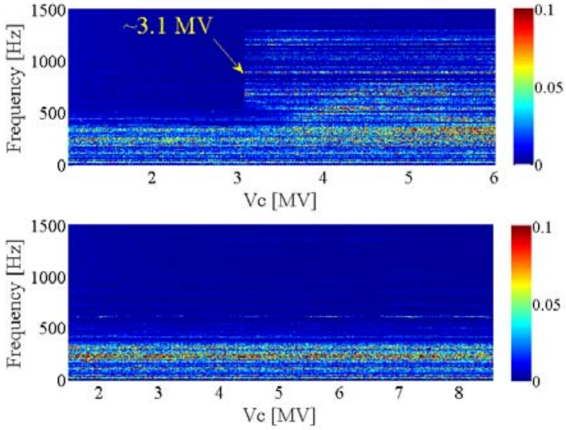

Figure 3: Field-detuning maps of ML1 (upper) and ML2 (lower) cavity. The color in the figure presents the intensity of the microphonics detuning. A threshold voltage of 3.1 MV appeared on the map of the ML1.

Table 1: Threshold Field versus Quench Limit Field

Cavity Conditions	**Threshold E_{acc}**	**Quench Limits**
Before PS aging	3.0 MV/m	5.9 MV/m
After PS aging	3.2 MV/m	6.3 MV/m
After one week operation	3.1 MV/m	6.1 MV/m

TRANSFER FUNCTION MEASUREMENT

In the current frequency tuner system based on I controller, the bandwidth of the closed system is less than several Hz. However, as shown in Fig. 3, the microphonics components are distributed from DC to several hundred Hz. That is to say, the current I controller is not capable of suppressing the microphonics detuning. To achieve a better performance of the tuner FB system, advanced control method such as active compensation method with adaptive finite impulse response filter or active noise control method are candidate approaches [8-9]. In such methods,

ISBN: 978-3-95450-217-2 doi:10.18429/JACoW-ERL2019-TUCOZBS04

prior measurement of the tuner TF model is necessary (or helpful) for the controller design.

The TF model of piezo tuner system with *N* modes is given by [8]

$$H(s)=\left(\frac{M_0}{\tau s+1}+\sum_{k=1}^{N}\frac{\omega_k^2 M_k}{s^2+2\xi_k\omega_k s+\omega_k^2}\right)e^{-T_d s}. \qquad (2)$$

The parameter M_0 is the steady state gain and τ a time constant of a low-pass filter. The parameter T_d represents the group delay of the system. The parameters ω_k, M_k and ξ_k represent the frequency, magnitude, and damping constant of the k$^{\text{th}}$ mode, respectively.

In cERL, inspired by the successful experience of a disturbance observer (DOB)-based method in the LLRF field control system [5], we also estimated the possibility of extending this method to the tuner control system in 2016 [6]. A tuner system model is also required in the design of the DOB-based controller. However, due to the time limitation in the beam commissioning, we did not have enough time to measure the complete TF model of the tuner system at that time. We only considered that the tuner system is a simple first-order model [see the first order model in (2)] with a group delay, and then used this simplified model for controller design. The experiment is not fully successful due to the oscillation of a 340 Hz mechanical mode [6].

In 2019, we have measured the tuner TF by exciting the tuner system with the sinusoidal signal from FF2 (see the yellow block in Fig. 3). The response of the cavity detuning was then calculated by LLRF system. We recorded the response of the tuner system from 5 Hz to about 340 Hz which covers the main vibration components. The frequency step is set to 1 Hz, and for each frequency point, up to 5 seconds measurements was conducted to achieve a steady state response.

The amplitude and phase response of the tuner system of ML1 (blue) and ML2 (red) are shown Fig. 4. From the amplitude response of ML1, a 340 Hz mechanical mode is easily found. This mode is in good consistence with the result in Ref. [6]. In addition, for ML1 tuner system, the steady state gain M_0 is approximately 2.6 according to Fig. 4. This result is also in good agreement with the result in Ref. [6], which has a M_0 of 2.7. By fitting a linear curve to the phase response plot, we can identified the system group delay of 0.11 ms by the slope of the linear curve. The other parameters in each mechanical mode can be identified by modern system identification method.

To validate the identified TF model, we have compared the response of the TF model and actual tuner system in the ML1 cavity. Firstly, we operated the tuner system and LLRF system with the open-loop. In the next step, we excited the tuner system with two types of signals, type-A and type-B. In the case of the type-A, the excited signal is a 50 Hz square wave signal with amplitude a_1. In the case of the type-B, the excited signal is a 20 Hz square-wave with the amplitude $4{\cdot}a_1$. Finally, we measured the corresponding cavity detuning response of this two cases. Figure 5(a) has compared the response of the type-A signal of the actual system (indicated by blue color) and the TF model (indicated by red color). Similarly, Figure 5(b) compared the responses of the type-B signal. The results are in good agreement in both of these two cases.

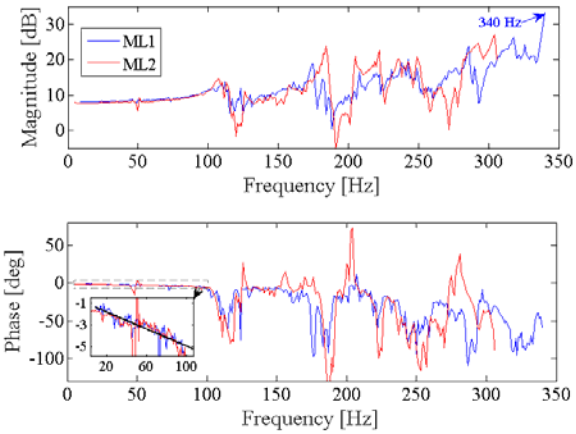

Figure 4: Tuner amplitude (upper) and phase (lower) response as a function of exciting frequency of ML1 (blue) and ML2 (red).

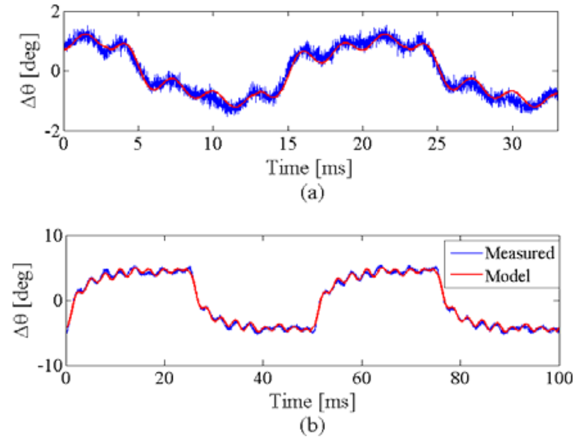

(a)

(b)

Figure 5: Comparison of the square-wave response of the transfer function model (red) and actual tuner system (blue). We have applied two types of square wave. (a) Type-A, 50 Hz and amplitude = a_1, (b) Type-B, 20 Hz and amplitude = $4{\cdot}a_1$.

SUMMARY

The microphonics detuning is increased in the past five years in one of the ML cavities. After investigating the cavity back-ground microphonics carefully, a "field level dependency microphonics" phenomenon was observed. Several components were suddenly appeared if the cavity field is above a threshold field of 3 MV/m. This threshold field is probably related with the quench limits although the internal mechanism is still not well understood. Furthermore, we have measured the TF model of the tuner system, and then validate the model by comparing the model response with the measured system response. For the future work, we will optimize our tuner control with the identified TF model.

REFERENCES

[1] M. Akemoto *et al.*, "Construction and commissioning of compact energy-recovery linac at KEK", *Nucl. Instr. Meth.*, vol. 877, pp. 197-219, 2018. doi:10.1016/j.nima.2017.08.051

[2] H. Sakai *et al.*, "Long-term operation with Beam and Cavity Performance Degradation in Compact-ERL Main Linac at KEK", in *Proc. LINAC'18*, Beijing, China, Sep. 2018, pp. 695-698. doi: 10.18429/JACoW-LINAC2018-THPO008

[3] F. Qiu *et al.*, "Status of microphonics on cERL nine-cell cavities" in *Proc. PASJ2019*, Kyoto, Japan, July-Aug. 2019, paper: WEPH010.

[4] T. Miura *et al.*, "Low-Level LLRF system for cERL", in *Proc. IPAC'10*, Kyoto, Japan, May 2010, pp. 1440-1442, paper: TUPEA048

[5] F. Qiu *et al.*, "Application of disturbance observer-based control in low-level radio-frequency system in a compact energy recovery linac at KEK", *Phys. Rev. ST Accel. Beams*, vol. 18, p. 092801, Sep. 2015. doi: 10.1103/PhysRevSTAB.18.092801

[6] F. Qiu *et al.*, "Progress in the work on the Tuner control system of the cERL at KEK", in *Proc. IPAC'16*, Busan, Korea, May 2016. Pp.2742-2745. doi: 10.18429/JACoW-IPAC2016-WEPOR033

[7] H. Sakai *et al.*, "Field emission studies in vertical test and during cryomodule operation using precise x-ray mapping system", *Phys. Rev. Accel. Beams*, vol. 22, p. 022002, Feb. 2019. doi: 10.1103/PhysRevAccelBeams.22.022002

[8] A. Neumann *et al.*, "Analysis and active compensation of microphonics in continuous wave narrow-bandwidth superconducting cavities", *Phys. Rev. ST Accel. Beams*, vol. 13, p. 082001, Aug. 2010. doi: 10.1103/PhysRevSTAB.13.082001

[9] N. Banerjee *et al.*, "Active compensation of microphonics detuning in high Q_L cavities", *Phys. Rev. Accel. Beams*, vol. 22, p. 052002, May 2019. doi: 10.1103/PhysRevAccelBeams.22.052002

ISBN: 978-3-95450-217-2 doi:10.18429/JACoW-ERL2019-TUCOZBS05

LOW LEVEL RF ERL EXPERIENCE AT THE S-DALINAC*

M. Steinhorst†, M. Arnold, T. Bahlo, R. Grewe, L. Juergensen, J. Pforr, N. Pietralla,
F. Schließmann, S. Weih
Institut für Kernphysik, TU Darmstadt, Darmstadt, Germany

Abstract

In 2011 the present digital low-level RF (LLRF) control system was set into operation. The first successful one-turn ERL operation was set up in August 2017. The RF control performance was investigated during this new possible operation mode in comparison to other modes that were conventional already before at the S-DALINAC.
The efficiency of the ERL operation can be determined by measurement of the beam loading in the cavities. This could only be done for the first main accelerator cavity. Therefor, an alternative way to determine the ERL efficiency from the already done RF control stability measurements was done to have a good estimate for this measurement. To quantify the ERL efficiency via beam loading measurement an RF power measurement system was developed which is able to measure the RF powers and hence the beam loading for all cavities simultaneously.

RF STABILITY

Introduction

The recirculating superconducting Darmstadt linear accelerator S-DALINAC [1] is one of the main research instruments at the institute for nuclear physics at the TU Darmstadt. It is operating in cw mode at beam currents of up to 20 µA with energies of up to 130 MeV using a thrice recirculating scheme. The current in-house digital LLRF control system of the S-DALINAC was developed in 2011 [2]. Since 2017 the S-DALINAC can be used as an energy recovery linac (ERL). The ERL mode is adjusted by shifting the phase of the beam by 180° in the second recirculation beam line. A first succesful ERL operation was conducted in August 2017 with an injector energy of 2.5 MeV [3, 4]. To state if the current digital LLRF control system is sufficient for a stable ERL operation, it have to be tested in this operation mode and the results have to be compared with stabilities in other modes that are conventional at the S-DALINAC.

Measurement

The investigation of the stability of the current RF control system was done by measuring the residual amplitude and phase errors of all cavities in four different operation modes at a beam current of about 1 µA during an about two hours measurement run. Figure 1 shows an overview of the different operation modes. For RF stability investigation the amplitude error and phase error data of the RF signal was measured in the time domain using the RF control electronics [2, 5]. The data was then Fourier-transformed to the

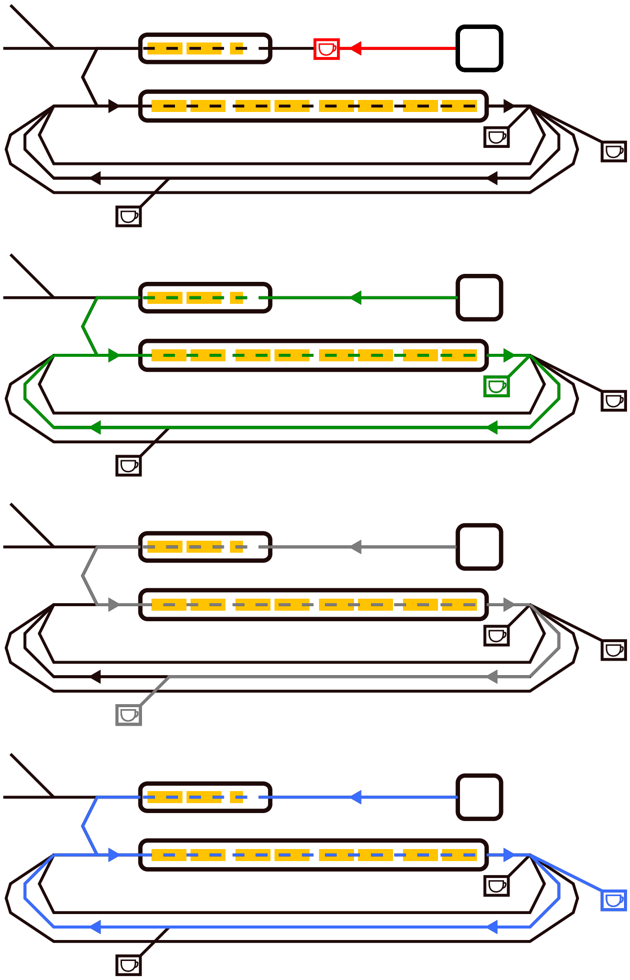

Figure 1: Schematic overview of the four different operation modes of the S-DALINAC during the ERL run. Top: Operation without beam. The beam was stopped at a Faraday cup in front of the injector (beam path indicated in red). Second: Once recirculated ERL operation. The beam was accelerated once in the main accelerator, decelerated in a second pass and dumped in a dedicated cup (green). Third: Once accelerated beam operation. After the first pass through the main accelerator the beam was dumped in a cup in the second recirculation beam line (grey). Fourth: Twice accelerated (once recirculated) beam operation. The beam was accelerated two times in the main accelerator (blue).

---

[*] Supported by DFG (GRK 2128)

[†] msteinhorst@ikp.tu-darmstadt.de

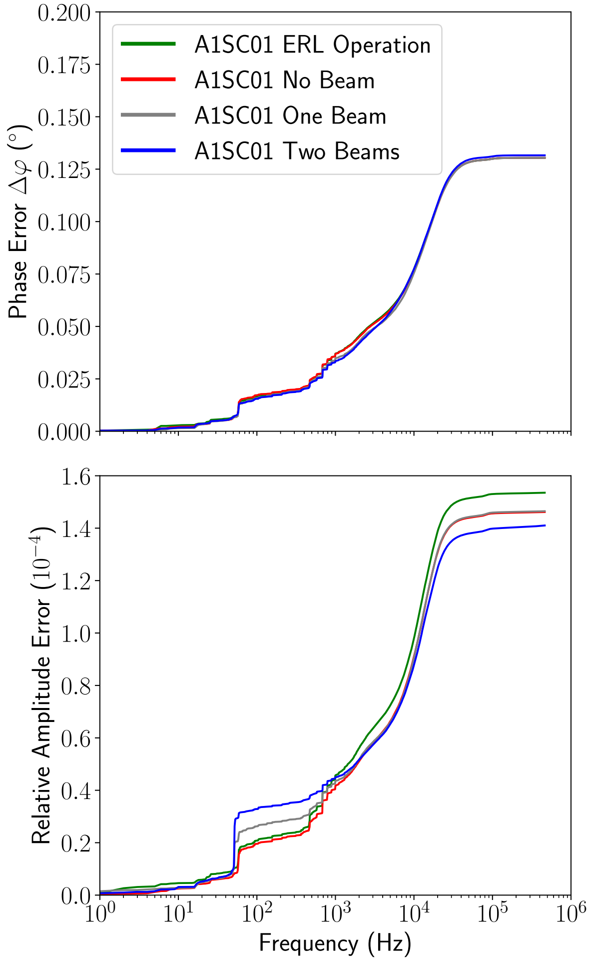

Figure 2: Integrated Fourier spectra of the phase error (top) and the relative amplitude errors (bottom) at the four different operation modes. The contribution of the frequency-dependent disturbances to the total residual errors are visible by the height of the increases [5].

frequency domain. The extracted Fourier spectrum contains information about the frequency-dependent disturbances of the whole RF control loop including cavity, amplifiers and transfer line. Via integration of the Fourier spectrum the contribution of the perturbations to the total residual errors of the system are determined by the step heights at the different frequencies. The higher the step height the higher the contribution of the disturbances at a given frequency. The integrated Fourier data for the four different operation modes is shown in Fig. 2 for the first main accelerator cavity A1SC01.

The integrated Fourier spectra of the phase error do not show significant differences between the four different operation modes. For the integrated Fourier spectra of the relative amplitude error, the final values as well as step sizes in the region of 1 Hz to 1 kHz differ for the four modes.

The RF control stability of ERL operation, hence lowest beam loading (except no beam operation), and once-recirculated operation, i.e. highest beam loading, are compared in Table 1. The estimated relative uncertainty of the measurement is about 5 %.

Table 1: RF stability comparison the total residual errors at ERL operation and at once-recirculated operation with two accelerated beams in the main accelerator. These two modes differ in beam loading in the cavities. The data of all eight main linac cavities is shown with an estimated uncertainty of 5 %.

Cavity	Relative Amp. Error (10^{-4})		Phase Error (°)	
	ERL	Two Beams	ERL	Two Beams
A1SC01	1.5	1.4	0.13	0.13
A1SC02	4.4	4.3	0.43	0.41
A1SC03	1.9	4.0	0.13	0.14
A1SC04	3.4	3.7	0.11	0.11
A1SC05	2.4	2.1	0.17	0.17
A1SC06	1.1	1.2	0.14	0.14
A1SC07	0.9	0.9	0.13	0.13
A1SC08	1.7	1.3	0.12	0.12

In comparison with the specified absolute phase stability of 0.7° and relative amplitude stability of 8×10^{-5}, the phase errors are better than specified and the relative amplitude errors do not fullfill the specifications. For the ERL run, the control parameters of the LLRF system have been optimized to minimize the phase error resulting in a slight increase of the relative amplitude error at the same time.

The phase errors in the two operation modes are similar to each other with a maximum relative difference of about 8 % for cavity A1SC03 (see Table 1). Except A1SC03 the relative amplitude errors differ at maximum by about 20 % for A1SC08Some of the main linac cavities had some general RF issues and have shown far higher relative amplitude errors and phase errors in comparison to others. The cavity A1SC02 had a problem with one of the piezoelectric eigenfrequency tuners which was exchanged by now.

For the cavity A1SC03 the reason for much higher relative amplitude errors is not fully known. The main contribution to this errors is a beam induced disturbance at 52 Hz (see Sec. *ERL Efficiency*). There is evidence that the cavity is detuned in respect to field flatness. This cavity quenches at a relativly low RF forward power but had an unloaded quality factor $Q_0 = (1.23 \pm 0.07) \times 10^9$ which is comparable to the other cavities. This leads to the conclusion that the field in some cells is much higher than in others leading to a quench. It is assumed that the field at the end cells of the cavity was relativly small in comparison to the front cells, i.e. the impact of the beam and hence the beam induced disturbance is higher at the end cells. There the RF control signal is extracted which was then measured for the RF control stability.

Despite these RF issues it could be assumed in general that the current RF control system is sufficient for a once-

ISBN: 978-3-95450-217-2 doi:10.18429/JACoW-ERL2019-TUCOZBS05

recirculating ERL operation at the S-DALINAC. To increase RF stability generally, the RF control loop has to be tuned with a focus on decreasing the relative amplitude errors. The RF stability in a multi-turn ERL operation at the S-DALINAC has to be proven in future. The behaviour at beam loading exceeding 1 µA will be studied in upcoming measurements.

ERL Efficiency

During the ERL machine time just the RF forward and reverse powers of the first main accelerator cavity could be measured. This measurement is needed to quantify the energy recovery efficiency for all cavities. The efficiency $\mathcal{E}_{\mathrm{RF}}$ via RF beam power measurement is given by

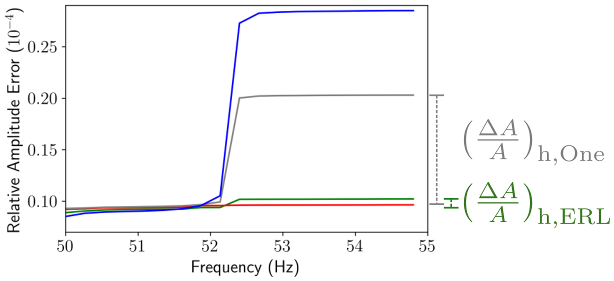

Figure 3: Extract of the relative amplitude error spectrum around the 52 Hz disturbance induced by the electron beam for the first main accelerator cavity. The step height is in first order proportional to the beam loading in the cavity. Using the step heights of ERL operation and once accelerated operation the ERL efficiency of all main accelerator cavities can be estimated.

$$\mathcal{E}_{\mathrm{RF}} = \frac{P_{\mathrm{b,Acc}} - P_{\mathrm{b,ERL}}}{P_{\mathrm{b,Acc}}} \tag{1}$$

with $P_{\mathrm{b,Acc}}$ being the beam power corresponding to the beam loading in once accelerating mode and $P_{\mathrm{b,ERL}}$ as the beam power corresponding to the effective beam loading in ERL operation. The beam loading power P_{b} in cw operation is determined via

$$P_{\mathrm{b}} = P_{\mathrm{f}} - P_{\mathrm{r}} - P_0 - P_{\mathrm{t}}. \tag{2}$$

with P_f and P_r as forward and reverse power, P_0 as the dissipated cavity power and P_t the transmitted power. At zero beam loading ($P_{\mathrm{b}} = 0\,\mathrm{W}$) $P_0 + P_{\mathrm{t}}$ can be quantified with a measurement of P_{f} and P_{r}. The beam loading can then be determined assuming the beam loading does not affect $P_0 + P_{\mathrm{t}}$.

Every cavity in the main accelerator had shown a disturbance at 52 Hz in the residual relative amplitude errors of the RF control. The step height at 52 Hz is zero and the step heights of the once accelerated operation and twice accelerated operation scaled with the beam current in the cavities which was measured in Faraday cups. Therefore, it is assumed that the disturbance step height in the spectra is proportional to the beam loading in the respective cavity. The relative effective beam loading in ERL operation can be measured indirectly with this method. Analog to the RF efficiency determination the efficiency can be estimated with the step heights $\left(\frac{\Delta A}{A}\right)_{\mathrm{h}}$ in the relative amplitude errors by

Table 2: Estimated efficiencies for all main accelerator cavities with an estimated uncertainty of about 10 %.

Cavity	$\mathcal{E}'_{\mathrm{RF}}$
A1SC01	92 %
A1SC02	73 %
A1SC03	92 %
A1SC04	98 %
A1SC05	96 %
A1SC06	100 %
A1SC07	100 %
A1SC08	60 %

$$\mathcal{E}'_{\mathrm{RF}} = \frac{\left(\frac{\Delta A}{A}\right)_{\mathrm{h,One}} - \left(\frac{\Delta A}{A}\right)_{\mathrm{h,ERL}}}{\left(\frac{\Delta A}{A}\right)_{\mathrm{h,One}}}. \tag{3}$$

The corresponding steps are illustrated in Fig. 3. The estimated efficiencies $\mathcal{E}'_{\mathrm{RF}}$ for all cavities are shown in Table 2. $\mathcal{E}'_{\mathrm{RF}}$ for the first cavity A1SC01 is in accord with the measured $\mathcal{E}_{\mathrm{RF}}$ of (90.1 ± 0.3) % [3]. The explanation for the drop of efficiency for A1SC08 is the presence of phase slippage due to the low injection energy of 2.5 MeV. At this low energy the beam is not in the ultrarelativistic regime. The main accelerator cavities are designed for ultrarelativistic particles. This mismatch results in a phase slip during the transit of the particles which has to be compensated. This was done by adjusting the RF field from on-crest to off-crest acceleration in the first main accelerator cavity. All other cavities were operated on-crest. Therefor, the cavity A1SC08 were adjusted for an ultrarelativistic beam leading to a phase slip at deceleration because the particles are not ultrarelativistic anymore. The drop of efficiency for A1SC02 has to be further investigated. In all other cavities a high recovery of at least 92 % could be achieved.

NEW RF POWER MEASUREMENT SYSTEM

The test setup used during this ERL beamtime is based on Schottky-diodes mounted directly in the accelerator hall. The diodes can be damaged due to the RF and beam induced radiation. Additionally the setup was not temperature stabilized. Therefore, a new power measurement system was developed in-house and setup at the S-DALINAC which is also compatible with the EPICS-based control system [6]. Figure 4 shows a new RF power board. It contains three RF inputs each with a 65 dB wide dynamic range power detector [7]. In the power detectors the RF signals are rectified.

The digitization and averaging of the DC-voltage is done on a microcontroller [8] comunicating via CAN-bus protocol. Ten power measurement boards are currently in usage allowing up to thirty RF powers to be measured simultaneously. For the superconducting cavities 22 RF powers are measured including forward and reverse power.

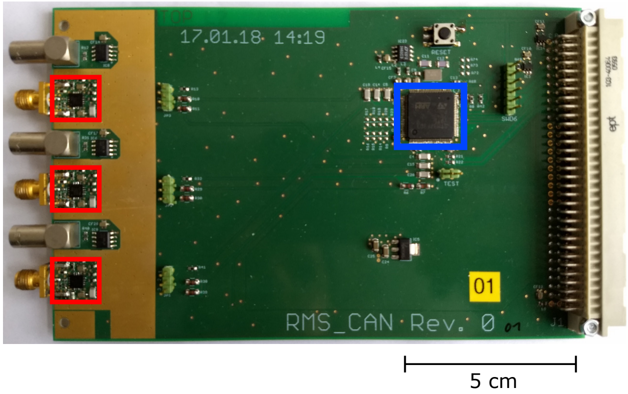

Figure 4: Photography of an in-house developed power measurement board. The power detectors are marked in red and the microcontroller is marked in blue. The board contains three RF-inputs where the RF-signal is rectified in the power detectors. The DC-voltage is digitized in the microcontroller and send to the EPICS-based control system via CAN-bus protocol.

SUMMARY AND OUTLOOK

In August 2017 the first ERL operation was achieved at the S-DALINAC. During this machine time four different operation modes where set up to measure beam loading and RF control stability in respect to relative amplitude and phase errors. The RF control system showed comparable results in all four different operation modes which differ in general in the amount of beam loading in the main accelerator.

Additionally a beam induced disturbance was found in the superconducting cavities at 52 Hz. The disturbance is assumed to be approximately proportional to the amount of beam loading. Because of that the origin of the disturbance is presumed to be a modulation with the netfrequency in the electron gun. With the beam loading proportionality the energy recovery efficiency for all main accelerator cavities can be estimated. This is favourable because the efficiency could be measured directly only in the first main accelerator cavity. The approximated value fits the measured efficiency for this case.

For the next ERL beamtimes, a new RF power measurement system was set up to directly measure energy recovery efficiencies via beam loading quantification in all cavities simultaneously. The system was already used as diagnostic tool and is ready for upcoming ERL machine times.

REFERENCES

[1] Norbert Pietralla, “The Institute of Nuclear Physics at the TU Darmstadt”, *Nuclear Physics News 2018*, 28:2, 4-11. `doi:10.1080/10619127.2018.1463013`

[2] M. Konrad *et al.*, “Digital base-band rf control system for the superconducting Darmstadt electron linear accelerator”, *Phys. Rev. ST Accel. Beams*, vol. 15, p. 052802, 2012. `doi:10.1103/PhysRevSTAB.15.052802`

[3] M. Arnold *et al.*, “First Operation of Superconcuting Darmstadt Linear Electron Accelerator as an Energy Recovery Linac”, submitted for publication.

[4] M. Arnold *et al.*, “First ERL operation of S-DALINAC and commissioning of a path length adjustment system”, *in Proc. IPAC’18*, Vancouver, British Columbia, Canada, May 2018, pp. 4859-4862. `doi:10.18429/JACoW-IPAC2018-THPML087`

[5] M.Steinhorst *et al.*, “First Energy Recovery Operation at the S-DALINAC: RF Control Stablitiy Measurements”, *in Proc. LINAC’18*, Beijing, China, September 2018, pp. 706-709. `doi:10.18429/JACOW-LINAC2018-THPO011`

[6] C. Burandt *et al.*,“The EPICS-based Accelerator Control System of the S-DALINAC”, *Proc. of ICALEPCS 2013*, San Francisco, CA, USA, p. 332-335 (2013). paper: MOPPC098

[7] Analog Devices, TruPwr$^{\mathrm{TM}}$ detector ADL5902, Retrieved September 30, 2019, from `http://www.analog.com/en/products/adl5902.html`

[8] STMicroelectronics: *Microcontroller STM32F303VD*, Retrieved September 30, 2019, from `https://www.st.com/resource/en/datasheet/stm32f303vd.pdf`

ISBN: 978-3-95450-217-2 doi:10.18429/JACoW-ERL2019-TUCOZBS06

CRYOMODULES FOR THE MAINZ ENERGY-RECOVERING SUPERCONDUCTING ACCELERATOR (MESA)*

T. Stengler†, K. Aulenbacher[1], F. Hug, D. Simon, C.P. Stoll, S.D.W. Thomas
Johannes Gutenberg-Universität Mainz, Mainz, Germany
[1]also at Helmholtz Institut Mainz, Germany and
GSI Helmholtzzentrum für Schwerionenforschung, Darmstadt, Germany

Abstract

Two superconducting radio frequency acceleration cryomodules for the new multiturn ERL facility MESA (Mainz Energy Recovering Superconducting Accelerator) at Johannes Gutenberg-Universität Mainz have been fabricated by industry and are undergoing rf tests at the Helmholtz Institut Mainz (HIM) currently. The modules for MESA are modified versions of the ELBE modules at Helmholtz Center Dresden-Rossendorf. The design energy gain per module and turn is set to 25 MeV. Acceleration is done by in total four TESLA/XFEL cavities, which have been vertically tested at DESY, Hamburg, Germany before being integrated in the MESA modules. In order to validate the performance of the fully dressed cryomodules a test stand has been set up at HIM. Within this contribution we report on the necessary modifications of the modules for high current ERL operation as well as on vertical and horizontal rf test results.

INTRODUCTION

For the main linac of the Mainz Energy-Recovering Superconducting Accelerator MESA [1-3], currently under construction at Johannes Gutenberg Universtität Mainz, two ELBE/Rossendorf-type [4] cryomodules have been produced by industry in Germany [5]. Each module consists of two TESLA/XFEL cavities running on an operation frequency of 1.3 GHz in continuous wave (cw) mode. For electron acceleration a gradient of 12.5 MV/m in each cavity is required to suit the experimental needs of the MESA facility. The dynamic losses of the cavities are limited due to the maximum available cooling power of the cryo-plant. Therefore, the unloaded quality factor of each cavity running on the operating gradient of 12.5 MV/m needs to exceed a value of 10^{10} at the operating temperature of 1.8 K. If MESA is run in ERL mode, a beam current of up to 1 mA needs to be accelerated and decelerated two turns each, yielding to a total sum of 4 mA electron beam in cw inside the accelerating cavities. To suit these needs of MESA, modifications on the module needed to be applied. In particular, the cooling of the HOM antennas was optimized and a fast eigenfrequency tuner (XFEL/Saclay type) based on Piezo actuators for an optimized microphonics compensation has been integrated [6,7].

MESA CAVITIES

Specifications

The performance goals for the MESA cavities and cryomodules have been specified beforehand and the vendor guaranteed parameters for the total energy gain per cryomodule and the static and dynamic cryogenic losses. Table 1 gives an overview on the target values to be verified in the horizontal acceptance tests at HIM.

Table 1: Specifications of fully dressed cryomodule performance in horizontal test operated at 2 K [8]

Variable	**Specified Value**
Energy Gain	25 MeV
Static Losses	< 15 W
Dynamic Losses @ 25 MeV (cw)	< 25 W
$\propto Q_0$ @12.5 MV/m	$> 1.25\cdot 10^{10}$

Vertical Test Results

After cavity production a XFEL standard treatment procedure has been applied to the cavities. To check the performance of each cavity after being welded into their Helium vessels, a vertical test at DESY has been carried out. Goals of this test have been the measurement of the quality factors at 2 K and 1.8 K and the determination of maximum gradients and performance limits. The test results have already been discussed in detail in [7,8]. Nevertheless, for giving the possibility to compare the results with the horizontal ones, the results will be presented briefly again. All cavities have achieved test results within specification at 2 K (see Fig. 1).

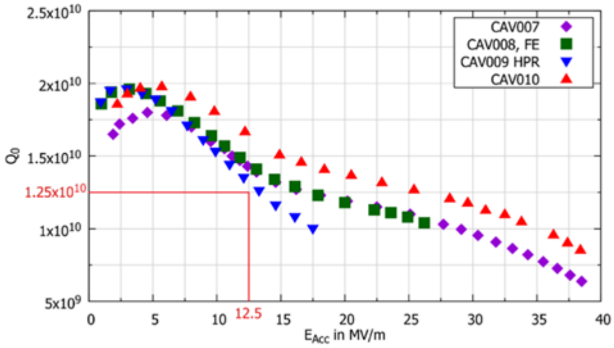

Figure 1: Vertical test results at 2 K operation for all MESA cavities. The measurements have been done at DESY AMTF. All cavities are above specification (red box). CAV 008 showed field emission above 26 MV/m [8].

---

* This work has been supported by DFG through the PRISMA⁺ cluster of excellence EXC 2118/2019.
†.tstengle@uni-mainz.de

Two out of four cavities have shown an excellent behaviour (CAV 007 and CAV 010). The third one (CAV 008) performed acceptable but suffered from light field emission above 26 MV/m. The fourth cavity (CAV 009) fulfilled the specification but needed an additional high pressure rinsing treatment. The quench limit has been measured to 16 MV/m which is lower than the limits of the other three cavities but still exceeding the acceptance limit for full MESA gradient (12.5 MV/m). After vertical testing, the cavities have been integrated into two cryomodules. Cryomodule 1 consists of CAV007 and CAV008, while cryomodule 2 is equipped with CAV009 and CAV010.

MESA CRYOMODULES

HOM Antenna Cooling

If MESA is operated in ERL mode, every cell of each cavity is filled with two bunches, either accelerating or decelerating. The high beam current aimed for at ERL operation (1 mA initially, later 10 mA) interacts with the cavity fields and can excite higher order modes (HOMs), which may be rather long living due to the high quality factor of the SRF cavities. Due to the recirculating design of the accelerator, the beam is sensitive to field disturbances and may close a feedback loop with any of the HOMs, which can cause beam break up (BBU) in the worst case. BBU threshold current depends on the HOM spectra and recirculation optics. BBU limitations have been simulated for MESA using the measured HOM spectra from vertical and horizontal tests of all four cavities. Threshold current for BBU at MESA exceeds 10 mA and BBU is not considered to be the limiting factor for MESA beam current [9,10].

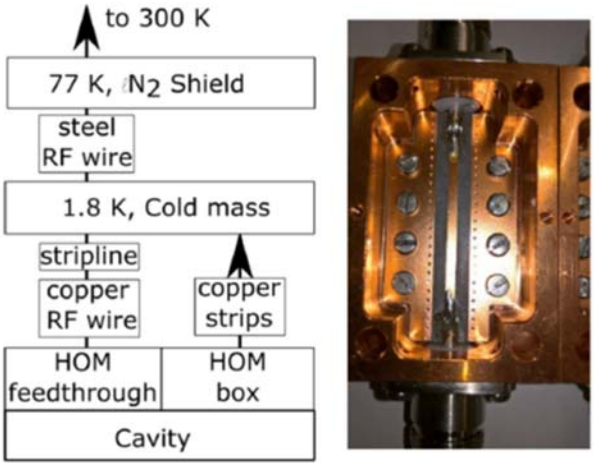

Figure 2: Left side: cooling concept for the inner conductor of the MESA HOM absorbers. Right side: stripline coupler allowing the thermal attachment to the cold mass of the module at 2 K [6,7].

On the other hand, HOMs excited by the high intensity beam need to be damped by the installed HOM absorbers and can result in heating of the antennas. If the cooling of the antennas is not sufficient, a quench can occur and cause the complete cavity to quench. For that reason, the thermal connection of the inner conductor of the antennas to the cold mass have been improved by two measures. First, the feedthrough has been replaced with a version using sapphire as insulator instead of a ceramic with poorer heat conductivity. Second improvement is the use of a stripline coupler for direct cooling of the inner conductor [6,7]. For benchmarking the new system, extensive temperature diagnostics has been integrated to the MESA cryomodules. Cooling concept and a photography of the stripline coupler can be seen in Fig. 2. During cold rf tests no heating of the HOM antennas could be observed. But for a concluding evaluation of the system high current beam tests are necessary as foreseen in the MESA@bERLinPro collaboration [11].

RF Coupling and Horizontal Test Setup

Each MESA cavity will be driven by a 15 kW solid state power amplifier (SSPA) running in cw at 1.3 GHz [12]. For horizontal testing at HIM one SSPA, designed as prototype for rf generation at MESAs normal-conducting and superconducting cavities, was used. The input couplers are capable to accept full power of the amplifier in cw and have been conditioned up to 20 kW in cw operation before module integration [7]. External coupling of the input couplers has been chosen to $Q_L = 1.38 \cdot 10^7$ suiting both MESA operation modes, external beam and ERL [7]. After module completion the resulting coupling at operation temperature has been measured. The values at 2 K range from $Q_L = 1.15 \cdot 10^7$ to $Q_L = 1.66 \cdot 10^7$, which is acceptable for MESA operation. With the maximum power from SSPA, an additional microphonic reserve of 5 kW and the given coupling, the maximum gradient for each cavity can be calculated (see Fig. 3) [8]. Without beamloading, which is the case in ERL operation, the cavities can be stable operated at maximum gradients between 21 MV/m and 25 MV/m using 15 kW forward power and considering the reserve for microphonic detuning, which is well above the 12.5 MV/m design gradient. For rf tests using a phase locked loop (PLL) setting and thus not needing a microphonic reserve, the cavities can be tested up to a range of 25 MV/m to 30 MV/m using the maximum allowed forward power [8]. Therefore, only cavities CAV 008 and CAV 009 can reach their quench field limits from vertical testing in cw in the present horizontal setup.

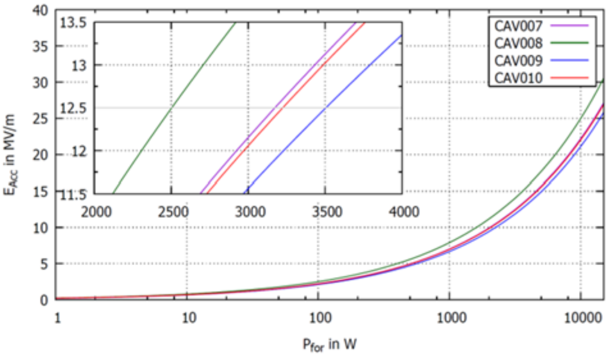

Figure 3: Acceleration gradient at given forward power [8]. The solid state amplifier is limited to 15 kW. The different curves take the measured Q_L for each cavity into account.

ISBN: 978-3-95450-217-2 doi:10.18429/JACoW-ERL2019-TUCOZBS06

Horizontal Test Results

Due to the strongly over coupled cavities, the cw measurement of unloaded Q_0 in the horizontal tests needed to be done using calorimetric methods. Therefore, two approaches for measuring the dissipated power through the amount of evaporated helium have been applied. In the first method the helium flow rate has been detected and compared to measurements with calibrated heaters. For the second method the pressure rise inside the Helium vessel has been measured and again calibrated with runs on defined heater settings. At the time of each measurement all inlet valves into the helium vessel have been closed for creating stable conditions. The Helium flow rate dependent of the accelerating gradient was measured over a period of 5 min in each run and can be compared with a series of heater measurements for flow calibration. The calibration measurement has been used to determine static losses of the modules as well by evaluating the fit function of the calibration run data.

To measure dissipated power by pressure rise, the exhaust valves of the Helium vessel have been closed and the pressure rise inside of the closed volume was measured and again compared to heater measurements for calibration. This method has been described in [13] already. The time per measurement is set to 30 sec. In that time the pressure rise is clearly detectable but not as high as corrections on Helium temperature need to be applied. The dissipated power in each measurement method can be calculated by:

$$P_{Diss} = \left(\frac{x_{RF}-x_{static}}{x_{heater}-x_{static}}\right) P_{heater} \qquad (1)$$

Here, the value x can stand for the pressure rise (dp/dt) or the measured flow rate ϕ respectively. The unloaded quality factor Q_0 can be calculated by inserting the results for the dissipated power from Eq. 1 at each accelerating gradient into the following formula:

$$Q_0 = \frac{E_{acc}^2}{\frac{R}{Q} P_{Diss} L^2} \qquad (2)$$

The known values [14] for normalized shunt impedance (R/Q = 1030 Ω) and the active resonator length (L = 1.038 m) of the TESLA resonators needed to be inserted as well. In the following figures we present the horizontal test results of both cryomodules.

Cryomodule 1 The resulting quality factors for both cavities can be found in Fig. 4. The horizontal test results of CAV 007 are in compliance with the vertical test results. No field emission has been observed while running the cavity in cw. The measurements of CAV 008 assume to show a higher Q_0 in module test than in vertical test on the first glance. At a detailed revision of the test set-up an unwanted interference of a newly installed µTCA LLRF test set-up [15] with the PLL used for the measurement have been identified. Therefore, the quality factor measurement of CAV 008 need to be done again. Nevertheless, no field emission was present at any time and the Helium flow rates clearly indicated a quality factor above specification at design gradient. The static losses of the module yielded P_{static} = 9.0(23) W, which is within specification.

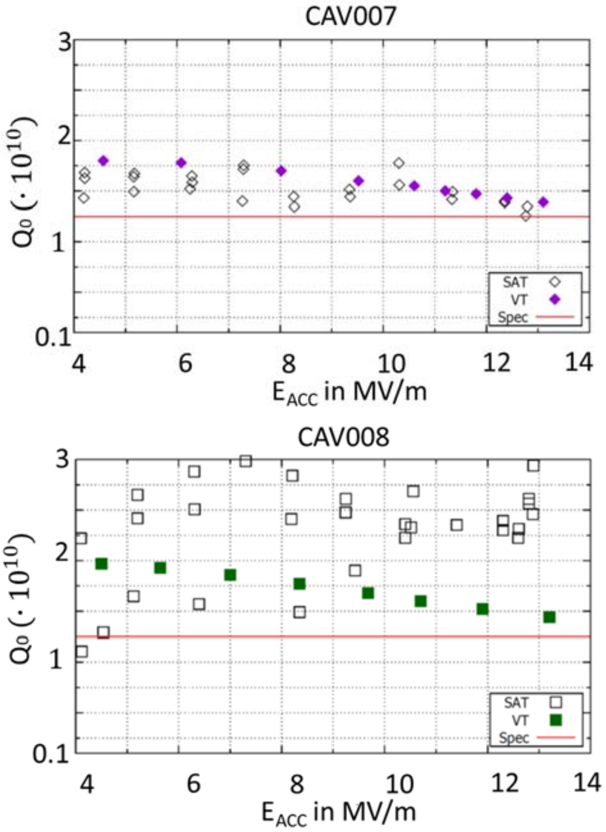

Figure 4: Horizontal test results for the first MESA module [8]. The achieved values for CAV 007 are compliant to the vertical test results and above specification. During measurements on CAV 008 interferences on the rf system caused an uncertainty on the measurement of the accelerating gradient and therefore of the quality factor. These measurements need to be repeated [8].

Cryomodule 2 During measurement of the quality factors of the cavities in cryomodule 2 severe problems with radiation showed up. The test results are plotted in Fig. 5. Both cavities showed radiation from field emission starting with 2 mSv/h at 2 MV/m up to several Sv/h at 10 MV/m [8]. Radiation measured inside and outside of the test bunker limited the operating gradient in cw to below 10 MV/m. A pulsed processing was tried to mitigate the radiation, but a processing effect couldn't be observed. Tests to identify a single field emitter with a matrix of dosimeters attached on the outside of the vacuum vessel showed no pint like source of radiation but a scattered radiation. So a single field emitter could be ruled out to be the reason for the observed radiation [8]. One hypothesis for the unexpected behaviour can be particulate contamination. After delivery of the module a not correctly closed valve between cavity string and a blind flange has been found at visual inspection. This valve at the cavity vacuum was in an indifferent state. After applying pressured air, it closed.

Due to the vibrations during the transport from the vendor to JGU Mainz, an unwanted movement of the valve disk could have produced particles. Those particles may spread through the nitrogen atmosphere all over both cavities and act as a diffuse pattern of field emitters in the tests. One indicator for this hypothesis is the slightly higher Q_0 of CAV 010. This cavity is located farther away from valve. Static losses of the cryomodule 2 are calculated to P_{static} = 5.61(35) W, which is within specification again. The module is under refurbishment at present including a complete disassembly. Therefore, the static losses have to qualified again in course of the next horizontal acceptance tests.

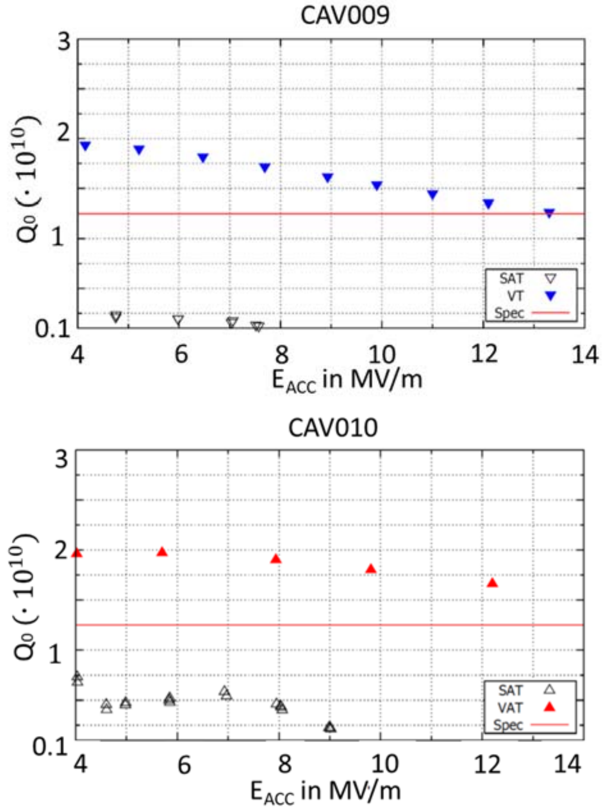

Figure 5: Horizontal test results for the second MESA module [8]. Strong field emission limited operating gradients and resulted in a significant reduced quality factor compared to the vertical tests for both cavities. The module is under refurbishment at the vendor currently. Next horizontal tests are envisaged to take place in end 2019.

CONCLUSION AND OUTLOOK

Both cryomodules for the MESA facility have been fabricated by industry and were tested at 2 K at HIM. Cryomodule 1 could be accepted already showing test results above specification. Nevertheless, further tests are planned in the future on that module up to higher operating cw gradients. Cryomodule 2 showed severe radiation from field emission in both cavities starting at low fields already and was sent back to the vendor for refurbishment. As a possible particulate source, a loose valve disk was identified. Because of the shipping under nitrogen atmosphere, the particulates could float all over the cavities and produced a diffuse radiation pattern. A future shipment under vacuum condition could reduce the risk of particulate transportation inside the cavity vacuum.

In order to verify the improved HOM antenna cooling, experiments with high current electron beam would be necessary. Such tests are planned to happen in course of the MESA@bERLinPro collaboration [11].

ACKNOWLEDGEMENTS

We kindly thank the Helmholtz Institut Mainz, in particular the groups ACID 1 and ACID 2 for providing their rf testing infrastructure for the horizontal tests.

REFERENCES

[1] R. Heine, K.. Aulenbacher, R. Eichhorn, “MESA-Sketch of an Energy Recover Linac for Nuclear Physics Experiments at Mainz”, *Proc. of IPAC’12*, New Orleans, Louisiana, USA (2012) 1993. paper: TUPPR073

[2] F. Hug, K. Aulenbacher, R.G. Heine, B. Ledroit, D. Simon, “MESA - an ERL Project for Particle Physics Experiments”, *Proc. of LINAC’16*, East Lansing, MI, USA, (2016) 313. doi:10.18429/JACoW-LINAC2016-MOP106012

[3] F. Hug *et al.*, presented at ERL’19, Berlin, Germany, September 2019, paper MOCOXBS05, this conference.

[4] J. Teichert *et al.*, “RF status of superconducting module development suitable for CW operation : ELBE cryostats”, NIM A 557 (2006) 239. doi:10.1016/j.nima.2005.10.077

[5] T. Stengler, K. Aulenbacher, R. Heine, F. Schlander, D. Simon, M. Pekeler, D. Trompetter, “Modified ELBE Cryomodules for the Mainz Energy-Recovering Superconducting Accelerator MESA”, *Proc. of SRF’15*, Whistler, Canada (2015) 1413. paper:THPB116

[6] T. Stengler, K. Aulenbacher, F. Hug, D. Simon, P. Weber, N. Wiehl, F. Schlander, “Status of the Superconducting Cryomodules and CryogenicSystem for the Mainz Energy-Recovering Superconducting Accelerator MESA”, *Proc. IPAC’16*, Busan, Korea, (2016) 2134. doi:10.18429/JACoW-IPAC2016-WEPMB009

[7] T. Stengler, K. Aulenbacher, F. Hug, D. Simon, T. Kuerzeder, “Cryomodule Fabrication and Modification for High Current Operation at the Mainz Energy Recovering Superconducting Accelerator MESA”, *Proc. of SRF’17*, Lanzhou, China (2017) 297. doi:10.18429/JACoW-SRF2017-MOPB101

[8] T. Stengler, K. Aulenbacher, F. Hug, S.D.W. Thomas, “SRF testing for Mainz Energy Recovering Superconducting Accelerator MESA”, *Proc. of SRF’19*, Dresden, Germany (2019). doi:10.18429/JACoW-SRF2019-TUP041

[9] C.P. Stoll, F. Hug, “Beam Breakup Simulations for the Mainz Energy Recovering Superconducting Accelerator MESA”, *Proc. of IPAC’19*, Melbourne, Australia (2019) 135. doi:10.18429/JACoW-IPAC2019-MOPGW025

[10] C.P. Stoll et al., presented at ERL’19, Berlin, Germany, September 2019, paper THCOWBS06, this conference.

[11] B.C. Kuske, W. Anders, A. Jankowiak, A. Neumann, K. Aulenbacher, F. Hug, T. Stengler, C.P. Stoll, “Incorporation of a MESA Linac Modules into bERLinPro”, P*roc. of IPAC’19*, Melbourne, Australia (2019) 1449. doi:10.18429/JACoW-IPAC2019-TUPGW023

[12] R.G. Heine, F. Fichtner, “The MESA 15 kW cw 1.3 GHz Solid State Power Amplifier Prototype”, *Proc. of IPAC’18*, Vancouver, BC, Canada (2018) 4216. `doi:10.18429/JACoW-IPAC2018-THPMF063`

[13] T. Powers, “Theory and Practice of Cavity RF Test Systems”, Proc. of SRF’05, Ithaca, NY, USA (2005) 40. paper:SUP02

[14] B. Aune et al., “The Superconducting TESLA Cavities”, (2000). `arXiv:physics/0003011v1`, `doi:10.1103/PhysRevSTAB.3.092001`

[15] J.N. Bai, K. Aulenbacher, J. Diefenbach, F. Fichtner, P. Echevarria, R.G. Heine, “MESA - Status of the Implementation of the MicroTCA.4-based LLRF Control System”, *Proc. of LINAC’18*, Beijing, China (2018) 691. `doi:10.18429/JACoW-LINAC2018-THPO007`

ISBN: 978-3-95450-217-2 doi:10.18429/JACoW-ERL2019-WECOXBS02

High Current Performance of Alkali Antimonide Photocathode in LEReC DC Gun *

M. Gaowei†, E. Wang, J. Cen, A. Fedotov, D. Kayran, R. Lehn, C. J. Liaw,
T. Rao, J. Tuozzolo, J. Walsh
Brookhaven National Laboratory, Upton, NY 11973, U.S.A

Abstract

The bi-alkali antimonide photocathode are chosen as the electron source material for the Low Energy RHIC electron Cooling (LEReC) project at RHIC, BNL based on its requirement for high bunch charge and long-time beam operation. This report presents the design and operation of the cathode deposition and transportation systems for the LEReC photocathodes, the cathode performance under the high current operation in the LEReC DC gun, as well as the characterization of the damaged cathodes from the long-time operation. *In situ* x-ray characterization results for the growth recipe of the alkali antimonide photocathodes prepared for the LEReC is also presented and discussed.

INTRODUCTION

The bunched beam electron cooler (LEReC) at the Relativistic Heavy Ion Collider (RHIC) has been built to provide luminosity improvement for Beam Energy Scan II (BES-II) physics program BES-II at RHIC. The photocathode DC gun in the LEReC accelerator is designed to provide an average current of up to 100 mA, with a required quantum efficiency of 2% ~ 10% from the photocathode material. In the LEReC 2018 operation, the photocathode DC gun has generated an average current of 30 mA and operated non-stop for several hours, with cathode lifetime fitted to be ~ 100 hours. [1-4] In this paper we report the *in situ* x-ray characterization results for the growth recipe of the alkali antimonide photocathodes prepared for the LEReC operation. Cathode performance in the 9.3MHz CW operation of LEReC is also reported. Post operation characterization has been performed and results are discussed in the last section of this paper.

CATHODE DEPOSITION

The LEReC cathode deposition has been switched from the effusion cell deposition back to the sequential 3 step deposition using SEAS getter sources since 2018. The deposition procedure we used for the bi-alkali antimonide photocathode was well developed for the ERL and CeC projects. [5] Compared to the CeC system, the LEReC deposition chamber differs slightly in geometry and does not have an active cooling capacity for the substrate. Therefore, the growth procedure in the LEReC deposition chamber has been optimized for this specific application. The detailed design of the LEReC deposition chamber was described in [6].

As was described in [6], the recipe we decided to use for the LEReC cathode is the well-established sequential growth recipe where 10 nm of Sb was deposited onto the substrate at 80 ˚C, followed by K and subsequent Cs deposition. The K step was performed at 135 ˚C to 140 ˚C, while the Cs step is performed between 130 ˚C to 70 ˚C, while the sample heater is turned off and the substrate cools down. Photocurrent generated by green light was monitored for both the K and the Cs step.

The temperature profile of the substrate with respect to the QE evolution through the K and the Cs step are plotted in Fig. 1. The inset photocurrent during the K step has been shown in × 5 scale for better display and the Cs QE was scaled by post QE calibration with a green laser with known power from the characterization chamber. For the LEReC cathode, we decided to seize the K deposition at an early stage, shortly after the QE rise and before its maximum. The Cs growth is stopped after substrate temperature drops below 70 ˚C, which is the known temperature for maintaining the stable stoichiometry of K_2CsSb. [7]

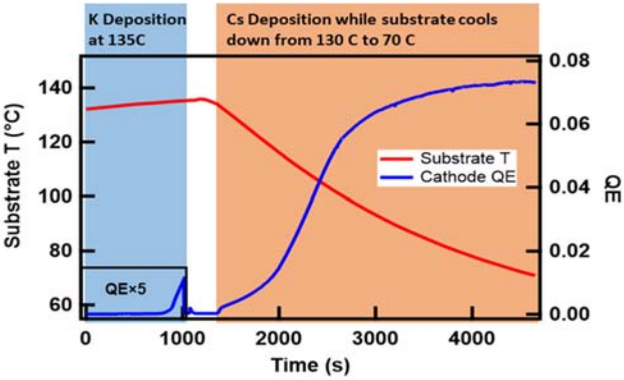

Figure 1: The temperature profile of the substrate with respect to the QE evolution in the Cs step.

The full deposition process takes ~ 2 hrs, while the whole deposition cycle for one cathode is typically 12 hrs, including the substrate heating cleaning, cathode cool down, QE mapping and puck exchange. The production rate for this deposition system is therefore 2 cathodes per day.

In 2018, we have produced 28 cathodes using this system. In 2019, the produced cathodes increased to 38, with an average deposition QE increased from 5.41% to 6.25%. Figure 2 and Table 1 listed all the as measured deposition QE from the LEReC cathodes in 2018 and 2019. The optimized deposition procedure for the LEReC deposition system has yielded ~ 1% higher average QE and an overall

---

*This work was carried out at Brookhaven Science Associates, LLC under contract DE-SC0012704 with the U.S. DOE.

† mgaowei@bnl.gov

stable output. The QE vitiation within a run is commonly observed due to the variation in the outgassing rates and deposition rates of individual alkali source. Cathode QE measured in the LEReC DC gun is typically 10 % ~ 20% higher than the deposition QE, due to the difference in the QE measuring scheme.

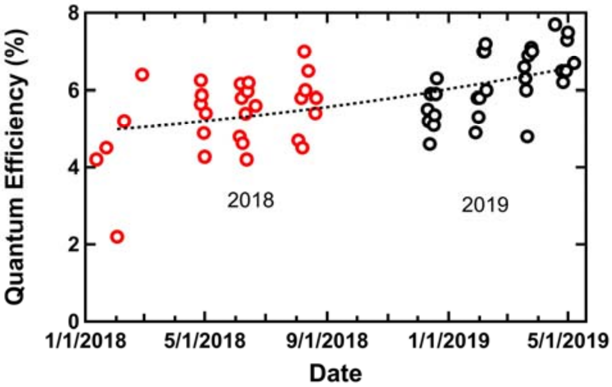

Figure 2: The cathode QE summary of LEReC run 2018 (red circles) and run 2019 (dark circles)

Table 1: The Cathode QE Summary of LEReC Run 2018 and 2019

	Run 2018	**Run 2019 (to May)**
# of cathodes	28	34
RMS Deposition QE (%)	5.41	6.25 (+0.87)
SDEV of QE (%)	0.97	0.85 (-0.08)

X-RAY CHARACTERIZATION OF LEREC CATHODE

The recipe of LEReC photocathode was duplicated in the UHV characterization chamber at beamline 4-ID, NSLS2, BNL, where real time, *in situ* x-ray characterization was performed to record the structural and chemical evolution of the LEReC photocathode, with detailed post analysis of x-ray fluorescence (XRF) and x-ray diffraction (XRD). In this report, the XRF and the XRD results are presented and discussed.

At beamline 4-ID, the photon energy of the incident x-ray was 11.4 keV (λ = 1.09 Å) with a nominal beam diameter of 50 μm focused at the sample position. The x-ray diffraction pattern was collected via two Dectris Eiger R 1M X-ray cameras mounted in-axis (75 cm away from the sample) and 30 ° off-axis (27 cm away from the sample) with the sample plane, respectively. The XRF signal was collected through a vortex multi-cathode x-ray detector mounted 45 ° with respect to the sample surface normal and ~ 30 cm away from the sample. Note that instead of the Moly puck used in the DC gun, the growth recipe was duplicated on an HF rinsed Si (100) substrate heated to 600 °C and then cool down to 80 °C for deposition. The detailed description of the UHV characterization chamber and illustration of experimental set up can be found in [8-11].

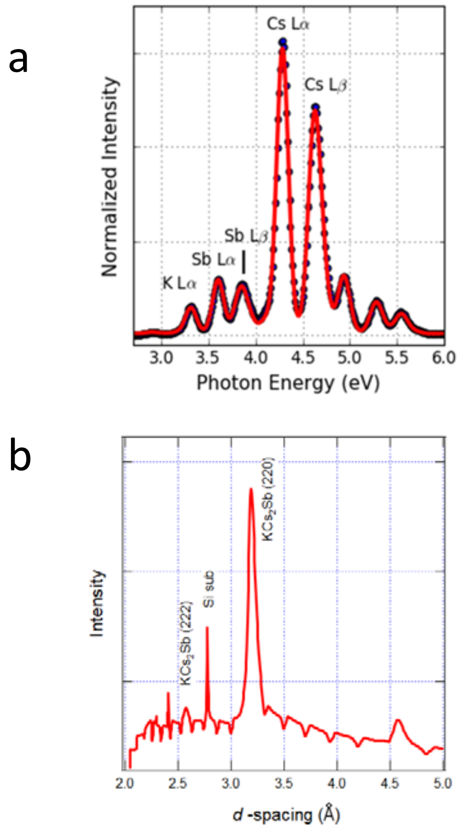

Figure 3: a) XRF spectrum and b) XRD spectrum of K-Cs-Sb cathode prepared with LEReC recipe.

Table 2: Atomic Mass Fraction of LEReC Photocathode

	Atomic Ratio
K/Sb	1.14
Cs/Sb	2.08

After the completion of the photocathode growth as was described in the beginning of this report, a final XRF and XRD was performed to determine the cathode stoichiometry and crystal structure. The fluorescence peaks of the 3 composite elements labeled are shown in Fig. 3a. The fitted atomic mass fraction is listed in Table 2. From the fitting results we can determine that the photocathode film prepared by the LEReC recipe is KCs_2Sb, instead of K_2CsSb, which is commonly obtained with the sequential recipe [12]. Similar cathode stoichiometry was observed by elsewhere. [13]

The *in situ* XRD pattern of the LEReC photocathode is shown in Fig. 3b. The results were compared with simulated powder diffraction patterns calculated using cubic structure and lattice parameters established in [14], namely 8.61 Å for K_2CsSb and 8.88 Å for KCs_2Sb. The dominant peak at d = 3.19 Å is identified as KCs_2Sb (220), which agrees with the fitted stoichiometry from the fluorescence spectrum. [13] Grain size estimated for this film is ~ 14 nm.

CAHTODE LIFETIME IN CW OPERATION

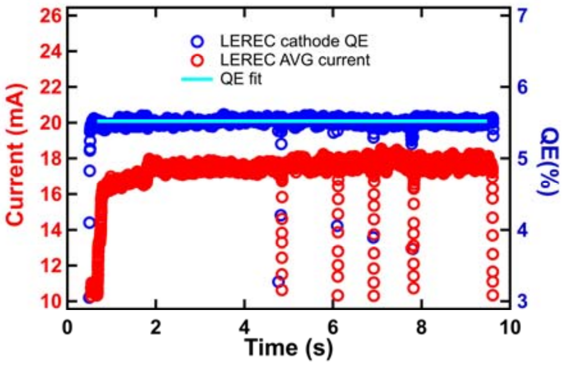

Figure 4: LEReC average beam current (red circles) and cathode QE (blue circles) monitored in CW operation.

In the run of 2019, the LEReC CW operation was kept under 20 mA to ensure better beam performance. Figure 4 shows the recorded average beam current (in red) and the calculated cathode QE (in blue) with the laser power kept ~ 0.7 W. During the 10 hr CW operation with an average beam current at 17 mA, despite multiple MPS trips, there was no QE decay observed for this cathode. The detailed description of the LEReC high current operation was described in [15].

CONCLUSION

The LEReC cathode production system has demonstrated its capability of stably and repeatedly producing high QE and uniform bi-alkali antimonide photocathodes in a timely manner. These cathodes show great lifetime in high current operation. LEReC cathode has been studied by x-ray characterization at synchrotron light source. The Results show that this bi-alkali antimonide photocathode is KCs_2Sb with good crystallinity, which explains the high QE.

ACKNOWLEDGEMENT

Special thanks are given to D. Asner, R. Begay, B. Walsh and many staff from Instrumentation Division, Brookhaven national Lab for their essential support on the LEReC deposition system. Authors would also like to thank K. Decker, C. Degen, J. Ditta, D. Gassner, X. Gu, P. Inacker, J. Jamilkowski, J. Kewisch, M. Minty, M. Mapes, L. Nguyen, M. Paniccia, J. Sanfilippo, L. Smart, S. Seletskiy, K. Sinclair, D. Vonlintig, H. Zhao, Z. Zhao and many staff from Collider-Accelerator Department, Brookhaven National Laboratory for their devoted work on the LEReC project.

The authors would like to acknowledge John Smedley, Anna Alexander and Vitaly Pavlenko from Los Alamos National Laboratory, David Juarez-Lopez from the Cockcroft Institute of Accelerator Science, STFC Daresbury Laboratory and John Sinsheimer from NSLS2 and staff at beamline 4-ID for their valuable assistance in the experiment.

Work was supported by Brookhaven Science Associates, LLC, under Contract No. DE-SC0012704 with the U.S. Department of Energy. The use of National Synchrotron Light Source II at Brookhaven National Laboratory is supported by U.S. Department of Energy (DOE) Office of Science under Contract No. DE-AC02-98CH10886.

REFERENCES

[1] A. Fedotov *et al.,* "Accelerator physics design requirements and challenges of RF based electron cooler LEReC", *Proceedings of the North American Particle Accelerator Conference 2016*, Chicago, IL, USA, 2016. `doi:10.18429/JACoW-NAPAC2016-WEA4CO05`

[2] E. Wang *et al.*, "Multi-alkali photocathodes production for LEReC DC gun", USDOE Office of Science (SC), Nuclear Physics (NP) (SC-26), 2018. `doi:10.2172/1438329, 2018`

[3] D. Kayran *et al.*, "First results from commissioning of low energy RHIC electron cooler (LEReC)", in *Proc. 10th Int. Particle Accelerator Conf. (IPAC2019)*, Melbourne, Australia, May 2019, pp. 770-772. `doi:10.18429/JACoW-IPAC2019- MOPRB085`

[4] A. Fedotov, "Bunched beam electron cooling for Low Energy RHIC operation", *ICFA Beam Dynamics letter*, No. 65, p. 22, December 2014. `https://icfa-usa.jlab.org/archive/newsletter.shtml`

[5] E. Wang *et al.,* "Enhancement of photoemission from and postprocessing of K_2CsSb photocathode using excimer laser" *Phys. Rev. ST Accel. Beams*, vol. 17, p. 023402, 2014. `doi:10.1103/PhysRevSTAB.17.023402`

[6] E. Wang *et al.,* "Multi-alkali photocathodes production for LEReC DC gun", in *Proc. 10th Int. Particle Accelerator Conf. (IPAC'19),* Melbourne, Australia, May 2019. `doi:10.18429/JACoW-IPAC2019- MOPRB085`

[7] Z.H. Ding *et al.,* "Temperature-dependent quantum efficiency degradation of K-Cs-Sb bialkali antimonide photocathodes grown by a triple-element codeposition method", *Phys. Rev. Accel. Beams*, vol. 20, p. 113401 (2017). `doi:10.1103/PhysRevAccelBeams.20.113401`

[8] M. Gaowei *et al.,* "Co-deposition of ultra-smooth and high QE cesium telluride photocathodes", *Phys. Rev. Accel. Beams* 22, 073401, (2019). `doi:10.1103/PhysRevAccelBeams.22.073401`

[9] S. Schubert *et al.,* "Bi-alkali antimonide photocathode growth: An X-ray diffraction study," *Journal of Applied Physics* 120, 035303 (2016). `doi:10.1063/1.4959218`

[10] Z. Ding *et al.* , "In-situ synchrotron x-ray characterization of K2CsSb photocathode grown by ternary co-evaporation", *Journal of Applied Physics* 121, 055305 (2017); `doi:10.1063/1.4975113`

[11] H. Yamaguchi *et al.*, "Photocathode: Free-standing bialkali photocathodes using atomically thin substrates," *Adv. Mater. Interfaces*, vol. 5(13), 1870065, (2018). `doi:10.1002/admi.201870065`

[12] J. Q. Xie *et al.*, "Synchrotron x-ray study of a low roughness and high efficiency K2CsSb photocathode during film growth", *J. Phys. D*, vol. 50, 205303 (2017). `doi:10.1088/1361-6463/aa6882`

[13] M. Gaowei *et al.*, “Synthesis and x-ray characterization of sputtered bi-alkali antimonide photocathodes”, *APL Materials* 5, 116104 (2017). `doi:10.1063/1.5010950`

[14] A.R.H.F. Ettema *et al.*, “Electronic structure of Cs2KSb and K2CsSb,” *Physical Review B*, 66, 115102, (2002). `doi:10.1103/PhysRevB.66.115102`

[15] X. Gu *et al.*, “Stable operation of a high-voltage high-current DC gun for the bunched beam electron cooler in RHIC,” unpublished.

ISBN: 978-3-95450-217-2 doi:10.18429/JACoW-ERL2019-WECOXBS03

BENCH TEST RESULTS OF CW 100 mA ELECTRON RF GUN FOR NOVOSIBIRSK ERL BASED FEL *

V. N. Volkov †, V. Arbuzov, E. Kenzhebulatov, E. Kolobanov, A. Kondakov, E. Kozyrev, S. Krutikhin, I. Kuptsov, G. Kurkin, S. Motygin, A. Murasev, V. Ovchar, V.M. Petrov, A. Pilan, V. Repkov, M. Scheglov, I. Sedlyarov, S. Serednyakov, O. Shevchenko, S. Tararyshkin, A. Tribendis, N. Vinokurov, BINP SB RAS, Novosibirsk, Russia

Abstract

Continuous wave (CW) 100 mA electron rf gun for injecting the high-quality 300-400 keV electron beam in Novosibirsk Energy Recovery Linac (ERL) and driving Free Electron Laser (FEL) was developed, built, and commissioned at BINP SB RAS. The RF gun consists of normal conducting 90 MHz rf cavity with a gridded thermionic cathode unit. Bench tests of rf gun is confirmed good results in strict accordance with our numerical calculations. The gun was tested up to the design specifications at a test bench that includes a diagnostics beam line. The rf gun stand testing showed reliable work, unpretentious for vacuum conditions and stable in long-term operation. The design features of different components of the rf gun are presented. Preparation and commissioning experience is discussed. The latest bench test beam results are reported.

INTRODUCTION

Recent projects of advanced sources of electromagnetic radiation [1] are based on the new class of electron accelerators where the beam current is not limited by the power of rf system – energy recovery linacs (ERLs). Such accelerators require electron guns operating in continuous wave (cw) mode with high average current. The only solution is an rf gun, where the cathode is installed inside the rf cavity. There are no back bombardment ions in rf guns so there are no cathode degradation, and the vacuum condition does not critical there (see Table 1). The most powerful Novosibirsk FEL [2] can be more powerful by one order on magnitude with this rf gun [3-5].

RF GUN AND DIAGNOSTIC STAND

The rf gun and diagnostic stand are presented in Fig. 1.

The RF gun cavity is made on the base of standard bimetallic cavity of Novosibirsk ERL. Detailed information can be found in [3-5]. Only the insert with the thermionic cathode-grid unit is built into the cavity. The gridded thermionic dispenser cathode is driven by special modulator with GaN rf transistor. The modulator generates a launch pulse voltage of up to 150 V and the duration of about 1 ns in any series with repetition frequencies of 0.01 - 90 MHz.

The insert focusing electrode has a concave form to decrease the electric RF field at the grid surface down to 1 MV/m (by one order on magnitude). Due to this the fields before the grid and after it becomes equal to each other so the laminarity of the electron beam flow through the grid remains higher and beam emittance lower. Furthermore, the insert focusing electrode executes the strong rf focusing on the beam just near the cathode that ensures the beam emittance compensation at the relatively low electric field at the cathode. Also it ensures the absence of dark currents in the beam.

There are in the stand: 30 kW water cooled beam dump with 5 cm lead radiation shield, wideband Wall Current Monitor (WCM2) inserted into the replaceable target, Transition Radiation Sensor, the pair of standard WCM, three focusing solenoids, and the special testing cavity.

Table 1: Measured RF Gun Characteristics

Average beam current, mA	≤100
Cavity Frequency, MHz	90
Bunch energy, keV	100 ÷ 400
Bunch duration (FWHM), ns	0.06 ÷ 0.6
Bunch emittance, mm mrad	10
Bunch charge, nC	0.3 ÷ 1.12
Repetition frequency, MHz	0.01 ÷ 90
Radiation Doze Power, mR/h	100/2m
Operating pressure, Torr	$10^{-9}…10^{-7}$
Cavity RF loses, kW	20

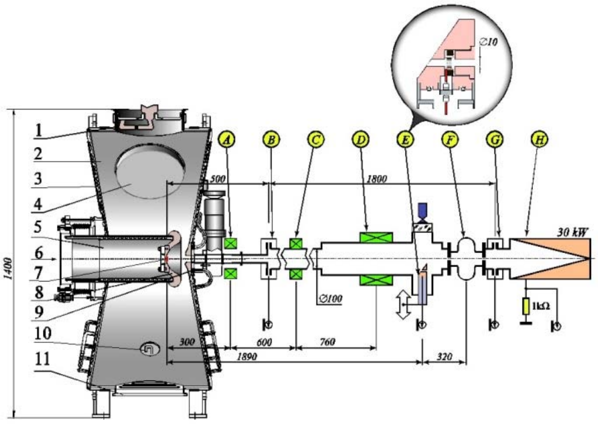

Figure 1: Rf gun and stand layout: 1-Power input coupler; 2- Cavity shell; 3-Cavity back wall; 4-Sliding tuner; 5-Insert; 6-Cathode injection/extraction channel; 7-Thermionic cathode-grid unit; 8-Concave focusing electrode; 9-Cone like nose; 10-Loop coupler; 11-Vacuum pumping port; A-Emittance compensation solenoid; B-First Wall Current Monitor (WCM); C, D - Solenoids ; E-Wideband WCM and transition radiation

---

* Work supported by Russian Science Found- n (project N 14-50-00080)
† v.n.volkov@inp.nsk.su

target; F – Test Cavity; G-third WCM; H-Faraday cup and Water-cooled beam dump.

BENCH TESTING RESULTS

Beam Current Regulation

There is the problem of thermionic dispenser cathodes that the thermionic current emission ability depends on the emission current. This is demonstrated in Figure 2 where the beam current from the cathode is increased due to increasing of repetition frequency. To preserve the bunch charge to be stable we have to change the bias voltage (V_{bias}) also if the launch pulse voltage (V_{launch}) is stable.

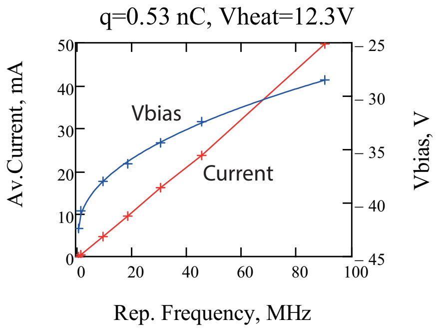

Figure 2: Beam current rising due to repetition frequency increasing (V_{launch}=100 V).

There are some methods of beam current increasing: decreasing of the grid bias voltage (V_{bias}), increasing of the modulator pulse voltage (V_{puls}), and increasing of the repetition frequency. Also there must be increased the cathode heating voltage (V_{heat}) to compensate the cathode emission ability derating. The applying of these methods is demonstrated in Fig.3.

In the beginning of the operation with the large beam current of 100 mA there have made the processing procedure. A rising the beam current by 10-20 mA steps in each day was made during one week to normalize the vacuum condition in the beam dump. It is interesting that the deteriorated vacuum condition after the each step was being low during all day without changing but in the next day we can make a new current increasing step while the vacuum deteriorates down to the previous level.

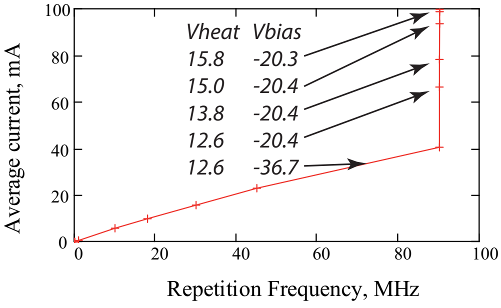

Figure 3: Typical method current rising (V_{launch}=120V).

Calibration of Cavity Voltage Meter

To measure the beam energy there is used the measuring of time delay between two wall current monitors. Since the particle velocities at the relatively low energy are lower than speed of light. It is demonstrated in Fig.4 where the measured data are fitted by the theory curve obtained from relativistic equations. This effect was used for the calibration of the cavity voltage meter. The calibration has a high accuracy not more than 1 %. There have to take into account that bunch energy also differ from the cavity voltage of about -1… -1.3 % in the range of 100-400 keV energies.

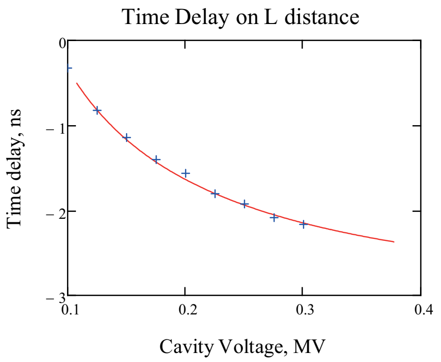

Figure 4: Measured data fitting by theory curve.

Cavity Testing up to 400 kV

To test the cavity for a high voltage the cavity voltage was increased with step by step method. After each step there required 1/2 an hour to normalize the vacuum condition (see Fig. 5).

Maximum beam current at 400 kV (see Fig. 6) was being limited by the beam dump permissible power and deteriorating of vacuum condition in it that requires some days to normalize the vacuum condition.

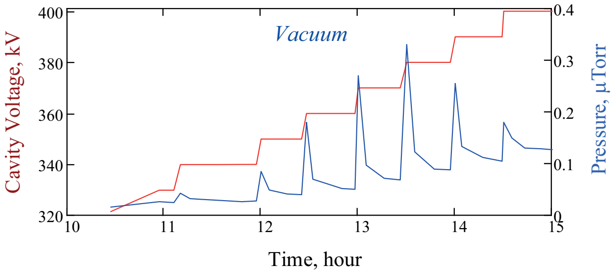

Figure 5: Cavity testing process behavior.

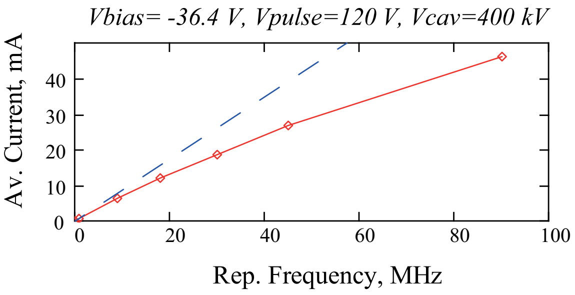

Figure 6: Beam current testing at 400 kV cavity voltages.

Launch Phase Functions

Energy distribution along the bunch is changed due to the launch phase changing. The energy of head particles becomes lower than the tail one at lower launch phases as shown in Fig. 7. The minimal launch phase value of 31° is limited by the duration of the launch pulse of 1 ns. At launch phases of more than 120° there are appeared back accelerated electrons that can corrupt the cathode quality.

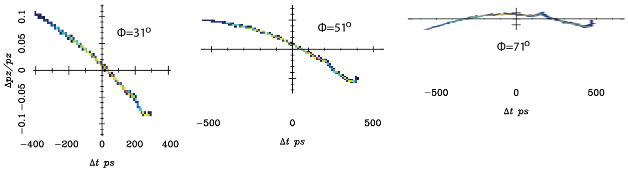

Figure 7: Energy distributions of particles along the bunch just after the rf gun for different launch phases.

Also there is changed the bunch energy as it shown in Fig. 8. The maximal bunch particle energy is at 68°, and minimal bunch length at 31°. It is used for velocity bunching on a drift space and for the phase instability (jitter) compensation.

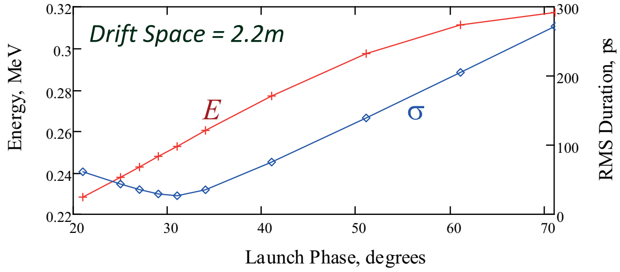

Figure 8: Launch phase functions.

Direct Bunch Length Measurement

There are complex particle distributions along the bunch due to plasma oscillation into a cathode-grid unit. On the drift space this distribution are changed significantly. The example of this at the launch phase of 31° is shown in Fig. 9. Current distributions along the bunch are shown for those coordinates where wall current monitors are placed in the stand. Frontal spike is formed into cathode-grid gap of 80 micron length. Then it grows and becomes short of about 20 ps FWHM while traveling along the drift space.

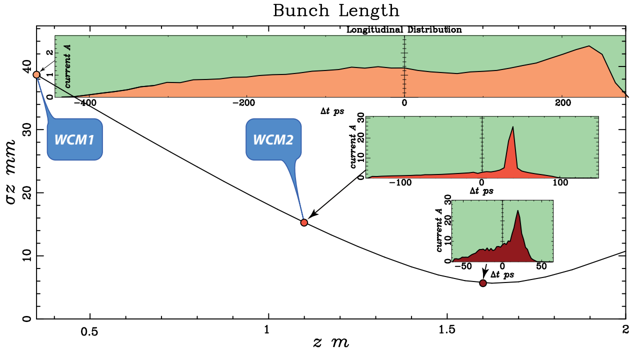

Figure 9: Bunch duration behaviour on the drift space.

The direct measurements of these distributions are difficult because the frequency bend of our 6 m coaxial lines with our 4 GHz oscilloscope are limited. Only measured values of more than 200 ps are possible in this configuration (see Fig.10). But we have found another method to determine the unique particle distribution and the bunch length with help of a special test cavity. This method will be described in the next chapter.

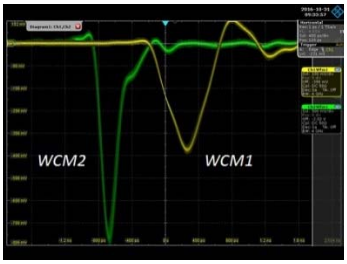

Figure 10: Measured bunch distributions by oscilloscope.

Cathode-Grid Plasma Oscillation Effect

Calculations and experiments have shown the plasma oscillation effect into the cathode grid gup of 80 microns depends on the cathode emission ability. That is demonstrated in Fig. 11 where the amount of frontal spikes due to the emission ability increasing is enlarged.

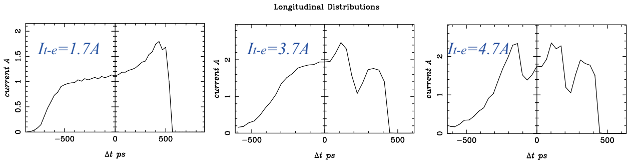

Figure 11: The enlarging of frontal spike amounts in bunch current distributions due to increasing of cathode emission ability ($I_{t\text{-}e}$).

This effect can be explained as follows. There are known that cathode current of endless beam is limited by the beam space charge according to "law of 3/2". Before the launch pulse comes to the cathode the cathode grid gup is empty so for the frontal particles that appeared after the pulse has been come this law does not work and the beam current is large in view of the spike that is limited only by the cathode emission ability and by the frontal slope of the launch pulse. So due to beam plasma oscillation some amount of current spikes is appeared in the current distribution.

For a low emission ability the bunch at the end of the drift space becomes having two parts unlike to the bunch comes with large emission as shown in Fig. 12. The excitation of a testing cavity by such a double bunch will be having anomalous behaviour due to interfere effect between these parts. ^

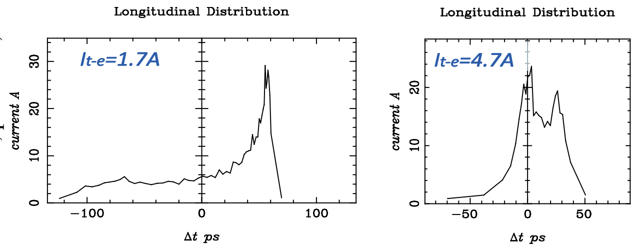

Figure 12: Particle distributions transformed to the drift space end.

Numerical modeling of the excitation and experiments are made with a special cavity having the main mode frequency of 1.4 GHz. In the frequency bend of up to 4 GHz for our oscilloscope there are many HOMs in the cavity. But only two of them (3674 and 4046 MHz) have enough coupling impedances with the beam and with pickups.

The simulated excitation amplitudes of these HOMs by bunch of Fig.11 depending on the launch phase are shown in the upper of Fig. 13. We see the shorter bunch length the large excitation amplitudes. Only the excitation with low emission bunch have the anomalous excitation behaviour due to the interfere effect. The same effect is observed in the experiments shown at the bottom of Fig. 13 where the emission ability was regulated by changing of cathode heating voltage.

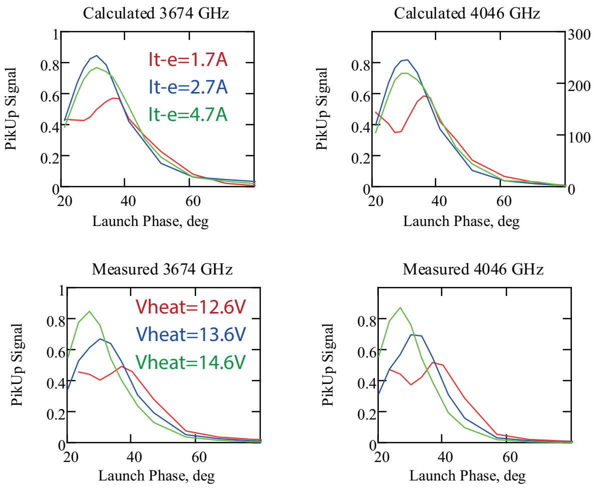

Figure 13: Excitations of test cavity HOMs. Calculations (at the top) and experiment (at the bottom) shows the interference for the low cathode emission bunches.

So we can conclude the numerical simulation of beam dynamics in cathode grid units [4] has enough accuracy to describe beam behaviors and to determine the minimal bunch rms length in the RF gun as 20 ps.

Launch Phase Jitter Compensation

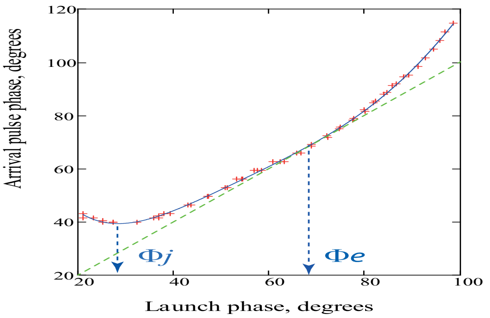

Figure 14: Arrival pulse phase behavior.

The jitter compensation effect has measured between two WCMs with 1.2 m distance between them (see Fig. 14). At the launch phase of 27 degrees the arrival time is independent on launch phase so the jitter is compensated there. I.e. the requirement to the phase stability of the modulator pulses is not high at the launch phase of 27°.

Emittance Measurements

Bunch emittance was measured by solenoid focusing method when the spot size of the beam focussed to a target is measured through CCD camera registering the transition radiation.

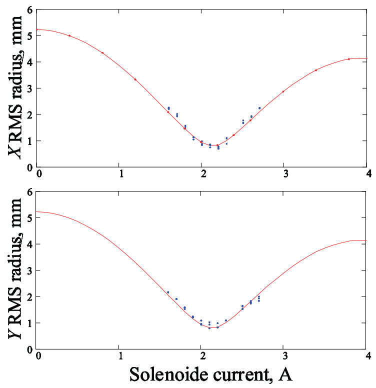

Figure 15: Measured and calculated beam behaviors.

The measured data behaviour on the focusing solenoid strength confirms to ASTRA [6] numerically calculated behaviour (see Fig. 15) with the accuracy of 9%. It corresponds to beam emittance of 15 mm mrad. As simulation shows the emittance can be compensated by proper focusing down to 10 mm mrad.

Dark and Leakage Particle Contaminations

Two spots in the RF gun cavity with peak surface field of 10-14 MV/m are the sources of field emitted dark currents (see Fig. 16). There are no dark currents in the beam since dark current trajectories are far from the beam.

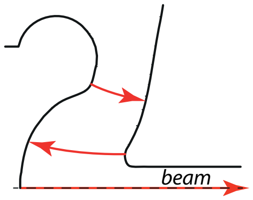

Figure 16: Dark current trajectories in the RF gun cavity.

The leakage current may be appeared in the cathode grid unit under the field of the cavity percolated through the grid. Dependencies of this current on the bias voltage and on the heating voltage are shown in Fig. 17. So to exclude the leakage current from the beam we have to choose the proper bias voltage.

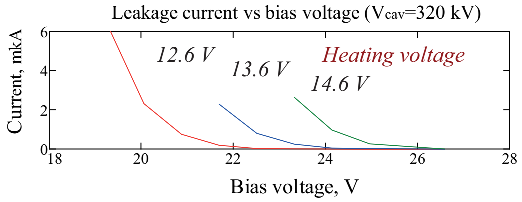

Figure 17: Leakage current from the cathode grid unit.

Radiation Background

The source of bremsstrahlung radiation is the field emission current described by Fouler-Nordheim equation

$$I \approx (\beta E)^{2.5} exp\left(-\frac{B\varphi^{1.5}}{\beta E}\right) \qquad (1)$$

Radiation background was measured behind the cavity wall with the thickness of 15 mm. The enhancement factor measured is found to be β=628 for one of sensors (see Fig. 18, red line).

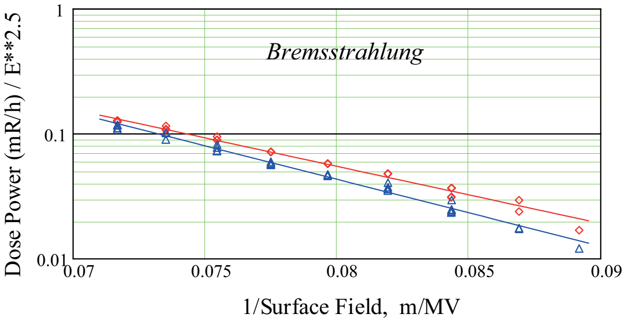

Figure 18: Measured radiation background by two different sensors in different places of the stand.

It was used as the base for simulation of enhancement factors for different shield thickness (10, 5, 3 mm), for bremsstrahlung power, for field emission particle power, and for field emission current (see Fig. 19). The enhancement factor for emission current is found to be β_I=*1250* (see Table 2). For the comparison, it is large by one order on magnitude than enhancement factors of superconducting cavities preparing with a perfect modern technology.

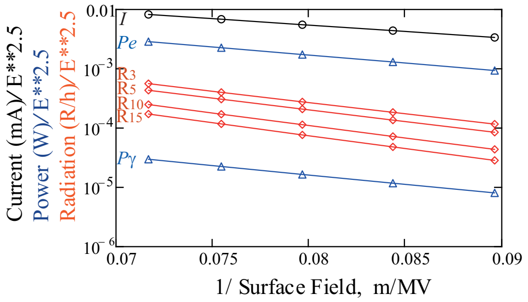

Figure 19: Calculated and measured (R15) field emission process.

Table 2: Simulated Enhancement Factors for Different Parameters of the Radiation Process in the RF Gun

Name		label	β
Dark Current of Field Emission		I	1264
Dark Current Power		Pe	1003
Bremsstrahlung Power		Pγ	865
Cu Shielded Dose Power	d=3 mm	R3	721
	d=5 mm	R5	695
	d=10mm	R10	649
	d=15mm	R15	628

There is interesting that all parameters in the radiation process are confirmed to F-N equation and have different enhancement factors.

REFERENCES

[1] N. A. Vinokurov and E. B. Levichev, "Undulators and wigglers for the production of radiation and other applications", Physics-Uspekhi, 58, 2015, pp. 850–871. doi: 10.3367/UFNe.0185.201509b.0917

[2] G. N. Kulipanov *et al.*, "Novosibirsk Free Electron Laser—Facility Description and Recent Experiments", IEEE TRANSACTIONS ON TERAHERTZ SCIENCE AND TECHNOLOGY, 5, doi:10.1109/ TTHZ.2015.2453121.

[3] V.N. Volkov *et al.*, "First test results of RF gun for the Race-Track Microtron Recuperator of BINP SB RAS" in *Proc. RuPAC'12*, Saint-Petersburg, Russia, 2012. paper:TUPPB049

[4] V. Volkov *et al.*, "Thermionic cathode-grid assembly simulations for rf guns", in *Proc. PAC'09*, Vancouver, Canada, 2009. paper:MO6RFP087

[5] V. Volkov *et al.*, "Thermocathode Radio-Frequency Gun for the Budker Institute of Nuclear Physics Free-Electron Laser", ISSN 1547-4771, Physics of Particles and Nuclei Letters, Vol. 13, No. 7, 2016, pp. 827–830. doi:10.1134/S1547477116070517

[6] K. Floettmann, ASTRA User`s Manual, http://www.desy.de~mpyflo/Astra_docomentation.

STATUS AND FUTURE PERSPECTIVE OF THE TRIUMF E-LINAC

S.D. Rädel*, M. Alcorta, F. Ames, E. Chapman, K. Fong, B. Humphries, O. Kester, D. Kishi,
S.R. Koscielniak, R.E. Laxdal, Y.Y. Ma, T. Planche, M. Rowe, V.A. Verzilov,
TRIUMF, Vancouver, Canada

Abstract

The currently installed configuration of TRIUMF's superconducting electron linac (e-linac) can produce an electron beam up to 30 MeV and 10 mA. Low beam power commissioning of the e-linac spanning the section from the electron gun to the high energy dump took place in summer 2018 and 2019 with an achieved beam energy of 30 MeV. As the driver of the Advanced Rare Isotope Laboratory (ARIEL[1]) project, the e-linac will deliver electrons to a photo-converter target station to produce neutron-rich rare isotope beams (RIB) via photo fission. The e-linac will have sufficient beam power to support the demands of other user community as well. This driver accelerator could serve as a production machine for high field THz radiation and as irradiation centre. A recirculation of the beam would be beneficial for RIB production at higher beam energy and would allow for high bunch compression to generate THz radiation. Such a system would also allow for the investigation of a high beam intensity energy recovery linac. To this end, TRIUMF is investigating the design of an alternate circulation path and the beam dynamics as a first step.

INTRODUCTION

TRIUMF's e-linac is a driver accelerator established within the ARIEL project which was proposed in 2008 [1]. The description of the scientific program can be found in [2, 3].

The layout of the e-linac is shown in Figure 1, including DC gun, bunch compressor and third cryomodule EACB. Currently still in the commissioning phase, the e-linac is operating in a continuous wave (cw) mode with 100 W beam power. This is limited by the present license for beam energies above 10 MeV.

With its final beam specification of 30 MeV and 10 mA the e-linac is an ideal test driver for a high power, high intensity THz photon source. Application for THz radiation are of high-field nonlinear spectroscopy, imaging (including microscopy), biology and medicine as well as in industrial applications.

The Canadian photon science community has a high demand and needs for light sources, therefore the e-linac is a potential drive for a high brilliance source for an IR-FEL. [4]

COMMISSIONING UPDATE

This year TRIUMF continued commissioning the e-linac. In 2018 the commissioning team achieved several milestones while guiding the beam from the source to the main high energy dump with a low power beam, see Figure 1. A detailed description of 2018 commissioning can be found in [5]. Also, during the commissioning the machine protection system (MPS) along the beamline has been commissioned step-by-step to the entrance of EACA.

Electron Gun

The e-linac uses a 300 kV RF-modulated thermionic electron source. The source has been commissioned and operating parameters have been verified. More detailed results can be found in [6, 7]. The origin of recent high voltage problems, which prevented operation above 270 kV, has been identified. They are caused by discharges along a high voltage cable, which connects the power supply to the source. An improvement of the design is being implemented.

Machine Protection System

The e-linac beam loss monitors (BLM) of the MPS are undergoing commissioning [8]. Currently the BLMs in the low and medium energy sections of the e-linac (300 keV and 10 MeV) have been commissioned with a combination of BGO scintillator coupled to a Photo-Multiplier Tube and long ionization chambers. The BLM commissioning in the high-energy section (300 MeV) is underway. Once the BLMs have been commissioned, the power will be slowly increased above 100 W to test the various components of the accelerator, including the 100 kW beam dump.

RF

After passing an injection cryo module that boost the electron beam energy to 10 MeV, the main acceleration happens in the main superconducting acceleration module equipped with two 1.3 GHz nine-cell radio frequency (rf) cavities. Both cavities are driven by one single klystron in a self-excited loop (SEL) in vector sum control [9]. During the 2018 commissioning both cavities were locked and successfully driven together. Instabilities seeded by microphonics and sustained by ponderomotive effects (internal electromagnetic pressure [5]) limited the beam acceleration to an energy of up to 25 MeV with a beam energy stability outside specification.

This year environmental vibration and consequent microphonic effects were reduced at most frequencies by passive means. This was accomplished by adding damping materials or modifying design of several systems including the LN2 cryogenic system and the interfaces to the rf waveguide

---

* sradel@triumf.ca

[1] ARIEL is funded by the Canada Foundation for Innovation, the Provinces AB, BC, MA, ON, QC, and TRIUMF. TRIUMF receives funding via a contribution agreement with the National Research Council of Canada.

ISBN: 978-3-95450-217-2 doi:10.18429/JACoW-ERL2019-WEPNEC01

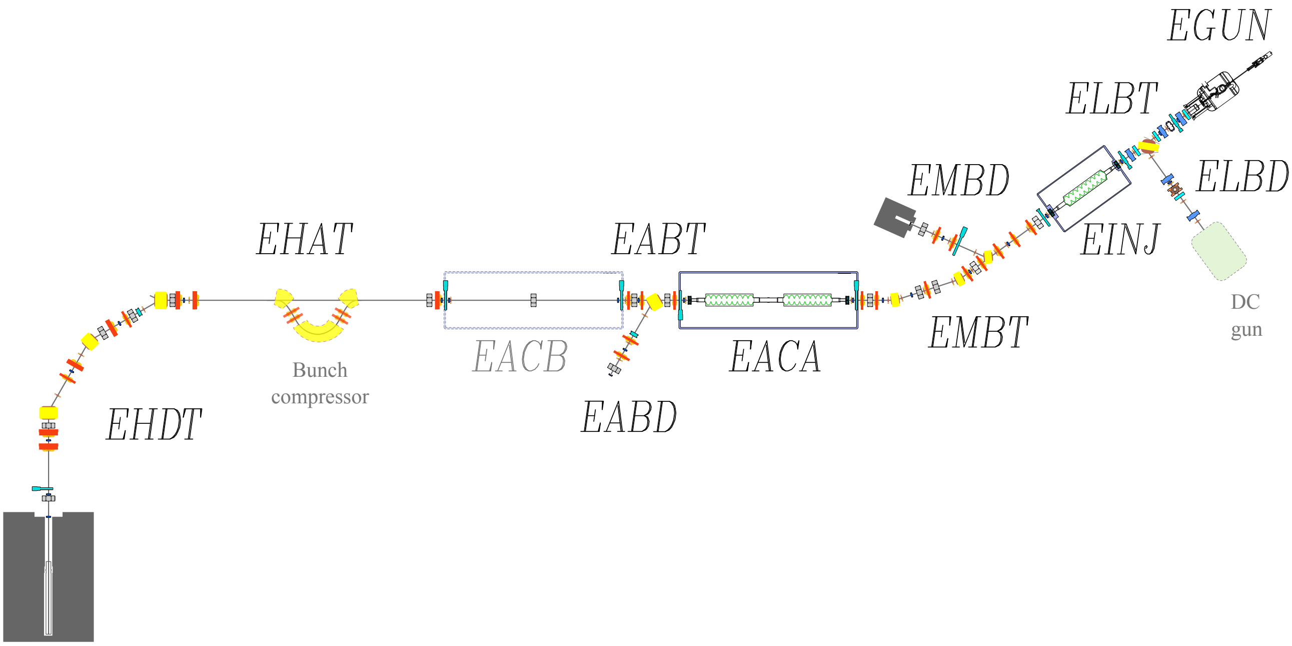

Figure 1: Sketched plan of e-linac including a potential second cryo module (EACB) and feasible position for a bunch compressor and a DC gun delivering beam for THz radiation production.

system. However, additional migration is required to reduce vibrations another order of magnitude.

The theoretical understanding of ponderomotive instability with two cavities under SEL vector sum control has been improved [10–16]. With the new understanding and more stable mechanical systems an operating regime has been identified and 30 MeV acceleration was reached but still limited by oscillation instability. The beam stability in this new configuration will be tested in November 2019.

THZ PRODUCTION BASED ON E-LINAC

When an ultra-relativistic electron bunch is bent on a curves path, a broad spectrum of radiation is emitted. To produce high power, high-intensity THz radiation coherent synchrotron radiation is the key [17]. Therefore the electron bunch length must be short enough so the electrons emit in phase. Thus, the electrons emit radiation with the same wavelength at the same time when synchronous emission is achieved. The power of the emitted light is quadratic to the number of electrons taking part of the process. Such a short bunch is ideally produced at the source and can be further compressed by a magnetic compressor as discussed in [18].

The idea using the e-linac as a photon source at TRIUMF in a recirculating linac configuration with FEL option was considered from its very first beginning [1, 19]. So far the built beamline consists of the electron gun, low, medium and high energy sections with corresponding beam dumps as well as the main dump at the very end. This layout is shown in Figure 1, excluding DC gun, bunch compressor and third acceleration module EACB. In the last couple of years the interest of the Canadian scientific community changed towards THz based light sources. Spearheaded by the University of Waterloo the community is preparing to submit a proposal to the Canadian Foundation of Innovation (CFI) to construct a national FEL program. TRIUMF has been asked to support this program using the existing e-linac.

Table 1: General Beam Requirements

Beam parameter	THz mode	RIB mode	Unit
Bunch rep. rate	0.001 – 1	130	MHz
Charge per bunch	> 200	26	pC
Beam energy	20	30	MeV
Bunch length	< 50	10	ps
Trans. emittance	< 50	< 10	mm mrad
Beam power	< 5	100	kW
Energy stability	10^{-4}	10^{-3}	

To utilize the e-linac as a test driver for such a program, it must be upgraded and key technologies need to be explored. To be capable of producing short and high charge bunches a new electron source is necessary. Therefore a 500 keV DC photocathode with accompanying driver laser must be designed and built. The design of such a DC gun can be modelled on existing gun designs, e.g. [20, 21]. To secure the e-linac's main purpose being the driver for ARIEL a new photocathode gun will be installed in addition to the existing thermionic electron source. To compress the bunch to even shorter bunch lengths a magnetic bunch compressor will be designed and built. Both DC gun and bunch compressor will be integrated at a feasible position in the current e-linac. The complete layout is shown in Figure 1. In addition, a second accelerator cryo module is included as well. Thus it would be possible to accelerate the beam to higher energy up

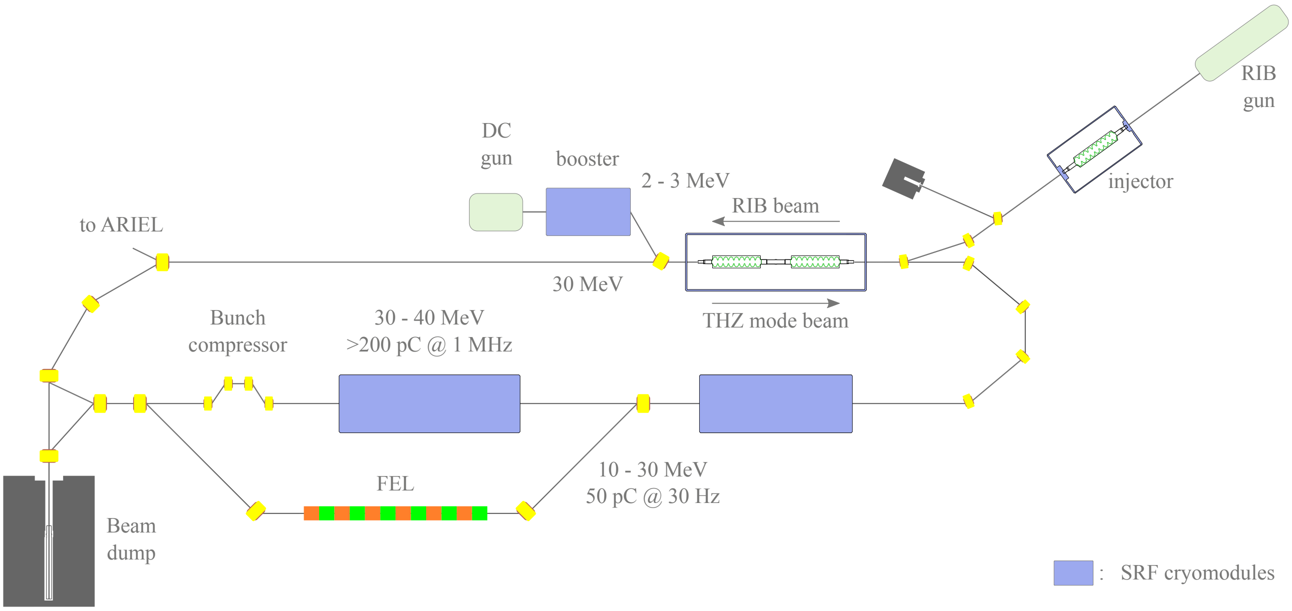

Figure 2: Sketched overview of a potential future layout for the e-linac to provide simultaneous operation of THz mode beam and beam for ARIEL (RIB beam).

to 50 MeV as well as give the beam a desired energy spread for the bunch compression. Necessary corresponding beam dynamic simulations of the e-linac with integrated DC gun will be started in January 2020. The beam requirements of the DC photocathode for both, the electron beam delivered to ARIEL and the electron beam for the THz radiation production are presented in Table 1.

Another part of the e-linac upgrade is the construction of the required THz light infrastructure. The laser light to the photocathode gun and the THz radiation must be transported between the e-linac vault and the optical laboratory that houses the laser and THz radiation equipment. Ideally the laser supplies green light to the NaKSb cathode. Ideally diagnostics will be foreseen to characterize the produced THz radiation in situ.

POSSIBLE FUTURE DEVELOPMENTS

In the future TRIUMF will explore the use of the e-linac for users using THz radiation for pump-probe experiments. Once demonstrated future capabilities of the TRIUMF e-linac can be expanded with the construction of an infrared Free Electron Laser (IR FEL) and expanding towards a users program. A potential layout for this e-linac expansion is shown in Figure 2. The design includes two possible radiation production paths, THz radiation as well as IR radiation produced by an undulator, in a recirculation setup. Thus TRIUMF would be able to explore ERL beam physics and technologies. Hereby the design is chosen in a way to combine two different beam modes and to be flexible and adapt to users needs. For the THz FEL beam mode the bunch charge should be increased to a range from 500 pC to 1 nC. Within the presented layout the operation of the RIB beam and the beam for THz radiation or IR FEL radiation can be simultaneous.

CONCLUSION

The TRIUMF e-linac is an ideal machine to support several research areas. Aside driving the ARIEL electron target station, it can serve as a source for high field THz radiation and in a recirculation set-up also for high intensity ERL studies. During this year commissioning progress in many areas has been made. The MPS was recommissioned in the low and medium energy section while the commissioning in the high energy section is ongoing. Vibration and microphonic amplitudes were reduced by passive means. Due to the improved theoretical understanding of ponderomotive instabilities together with a more stable mechanical system, a 30 MeV acceleration was reached but still limited by oscillation instability.

The e-linac will be expanded by a DC photocathode, a bunch compressor and a potential second cryo module with two cavities to produce THz radiation. This radiation production is a first stage to a possible future THz FEL in a recirculating setup.

REFERENCES

[1] S.R. Koscielniak *et al.*, “Accelerator Design for a 1/2 MW Electron Linac for Rare Isotope Beam Production”, in *Proc. 11th European Particle Accelerator Conf. (EPAC’08)*, Genoa, Italy, June 23 – 27, 2008, paper WEPP090, pp. 2728–2730.

[2] J. Bagger *et al.*, “TRIUMF in the ARIEL Era”, in *Proc. 9th International Particle Accelerator Conf. (IPAC’18)*, Vancouver, Canada, April 29 – May 4, 2018, paper MOXGB2, pp. 6–11, doi: 10.18429/JACoW-IPAC2018-MOXGB2.

[3] J. Dilling, R. Krücken, L. Merminga, *ISAC and ARIEL: The TRIUMF Radioactive Beam Facilities and the Scientific Pro-*

ISBN: 978-3-95450-217-2 doi:10.18429/JACoW-ERL2019-WEPNEC01

gram. Springer Netherlands, 2014, doi: 10.1007/978-94-007-7963-1.

[4] W.S. Hopkins *et al.*, “Establishing A Canadian Free Electron Laser Research Program”, in *Canadian Journal of Physics*, submitted for publication.

[5] S.R. Koscielniak *et al.*, “Status and Issues (Microphonics, LFD, MPS) with TRIUMF ARIEL e-Linac Commissioning”, in *Proc. 29th Linear Accelerator Conf. (LINAC’18)*, Beijing, China, September 16 – 21, paper TU1A03, pp. 286–291, doi: 10.18429/JACoW-LINAC2018-TU1A03.

[6] F. Ames *et al.*, “Operation of an RF Modulated Thermionic Electron Source at TRIUMF”, in *Proc. 9th International Particle Accelerator Conf. (IPAC’18)*, Vancouver, Canada, April 29 – May 4, 2018, paper THPML025, pp. 4705–4707, doi: 10.18429/JACoW-IPAC2018-THPML025.

[7] F. Ames *et al.*, “The TRIUMF ARIEL RF Modulated Thermionic Electron Source”, in *Proc. The 28th International Linear Accelerator Conf. (LINA’16)*, East Lansing, MI USA, September 25 – 30, 2016, paper TUPRC020, pp. 458–461, doi: 10.18429/JACoW-LINAC2016-TUPRC020.

[8] M. Alcorta *et al.*, “Commissioning of the ARIEL e-Linac Beam Loss Monitor System”, present at the *Proc. 8th International Beam Instrumentation Conf. (IBIC’19)*, Malmö, Sweden, September 8 – 12, 2019, talk TUAO04, pp. 0–3.

[9] Y.Y. Ma *et al.*, “First RF Test Results of Two-Cavities Accelerating Cryomodule for ARIEL eLinac at TRIUMF”, in *Proc. 9th International Particle Accelerator Conf. (IPAC’18)*, Vancouver, Canada, April 29 – May 4, 2018, paper THPMK090, pp. 4512–4515, doi: 10.18429/JACoW-IPAC2018-THPMK090.

[10] Y.Y. Ma *et al.*, "Microphonics Suppression In ARIEL ACM1 Cryomodule", in *Proc. 10th International Particle Accelerator Conf. (IPAC’19)*, Melbourne, Australia, May 19 – 24 2019, paper MOPGW004, pp. 65–68, doi: 10.18429/JACoW-IPAC2019-MOPGW004.

[11] K. Fong and R. Leewe, "Parametric Pumped Oscillation By Lorentz Force In Superconducting RF Cavity", in *Proc. 10th International Particle Accelerator Conf. (IPAC’19)*, Melbourne, Australia, May 19 – 24 2019, paper WEPRB003, pp. 2798–2800, doi: 10.18429/JACoW-IPAC2019-WEPRB003.

[12] S.R. Koscielniak, "Ponderomotive Instability of Self-Excited Cavity", in *Proc. 10th International Particle Accelerator Conf. (IPAC’19)*, Melbourne, Australia, May 19 – 24 2019, paper THPRB007, pp. 3808–3811, doi: 10.18429/JACoW-IPAC2019-THPRB007.

[13] S.R. Koscielniak, "Ponderomotive Instability of Two Self-Excited Cavities", in *Proc. 10th International Particle Accelerator Conf. (IPAC’19)*, Melbourne, Australia, May 19 – 24 2019, paper THPRB008, pp. 3812–3815, doi: 10.18429/JACoW-IPAC2019-THPRB008.

[14] S.R. Koscielniak, "Vector Sum & Diffference Control of SRF Cavities", in *Proc. 10th International Particle Accelerator Conf. (IPAC’19)*, Melbourne, Australia, May 19 – 24 2019, paper THPRB009, pp. 3816–3819, doi: 10.18429/JACoW-IPAC2019-THPRB009.

[15] S.R. Koscielniak, "Ponderomotive Instability of Generator-Driven Cavity", in *Proc. 10th International Particle Accelerator Conf. (IPAC’19)*, Melbourne, Australia, May 19 – 24 2019, paper THPRB010, pp. 3820–3823, doi: 10.18429/JACoW-IPAC2019-THPRB010.

[16] S.R. Koscielniak, "Ponderomotive Instability of RF Cavities with Vector Sum, and Cure by Difference Control", in *9th Low-Level RF Workshop (LLRF’19)*, Chicago, USA, September 29 – October 03, 2019, e-Print: arXiv:1910.07106.

[17] A. Novokhatski, “Coherent synchrotron radiation: Theory and simulations”, *International Committee for Future Accelerators: Beam Dynamics Newsletter*, vol. 57, pp. 127–144, 2012. SLAC-PUB-14893

[18] M. Dohlus, T. Limberg, and P. Emma, “Coherent synchrotron radiation: Theory and simulations”, *International Committee for Future Accelerators: Beam Dynamics Newsletter*, vol. 38, pp. 15–37, 2005.

[19] L. Merminga *et al.*, “ARIEL: TRIUMF’s Advanced IsotopE laboratory”, in *Proc. 11th International Particle Accelerator Conf. (IPAC’11)*, San Sebastián, Spain, September 4 – 9, 2011, paper WEOBA01, pp. 1917–1919

[20] J. Maxson *et al.*, “Design, conditioning, and performance of a high voltage, high brightness dc photoelectron gun with variable gap”, *Review of Scientific Instruments*, vol. 85, no. 9, p. 093306, Sep. 2014, doi: 10.1063/1.4895641.

[21] R. Nagai *et al.*, “High-voltage testing of a 500-kV dc photocathode electron gun”, *Review of Scientific Instruments*, vol. 81, p. 033304, 2010, doi: 10.1063/1.3354980.

ISBN: 978-3-95450-217-2 doi:10.18429/JACoW-ERL2019-WEPNEC08

DISPERSION MATCHING WITH SPACE CHARGE IN MESA

A. Khan*, O. Boine-Frankenheim, Technische Universität Darmstadt, Germany
K. Aulenbacher, Johannes Gutenberg-Universität Mainz, Germany

Abstract

For intense electron bunches traversing through bends, as for example the recirculation arcs of an Energy-Recovery Linac (ERL), dispersion matching with space charge of an arc into the subsequent radio-frequency (RF) structure is essential to maintain the beam quality. We show that beam envelopes and dispersion along the bends and recirculation arcs of an ERL, including space charge forces, can be matched to adjust the beam to the parameters of the subsequent section. The present study is focused on a small-scale, double-sided recirculating linac Mainz Energy-recovering Superconducting Accelerator (MESA). MESA is an under construction two pass ERL at the Johannes Gutenberg-Universität Mainz, which should deliver a continuous wave (CW) beam at 105 MeV for physics experiments with a pseudo-internal target. In this work, a coupled transverse-longitudinal beam matrix approach for matching with space charge in MESA is employed.

INTRODUCTION

For intense electron bunches at low to medium energy traversing through bends, it is essential to understand the details of space-charge-induced effects to maintain beam quality throughout the ERL operation [1]. Particularly, current dependent dispersion matching of an arc into the subsequent RF section has been found to be essential to preserve the beam quality. Dispersion matching with space charge has been discussed mostly in the context of high intensity beams in conventional synchrotrons [2]. For example, [3,4] outlined the concept of two different dispersion functions, one for the beam center, which is not affected by space charge, and one for the off-center particles. Experiments related to space charge and dispersion with low energy proton beams were performed in the CERN PS Booster, matching the beam from the linac into the synchrotron. Although the space charge was found to be relevant, it was sufficient to use the zero-intensity dispersion for the matching of the beam center, in order to improve the injection efficiency [5]. In this work, we show that the space-charge-modified dispersion plays a key role for the adjustment of the R_{56} required for both the isochronous and the non-isochronous recirculation mode of an ERL.

An important role of the recirculation arc in an ERL is to provide path length adjustment options to set the accurate required RF phase of 0° to 180° for acceleration and deceleration. Transverse space charge modifies the dispersion function along the arc and so the momentum compaction which is the transport matrix element R_{56} for the individual particles. In case the arc settings are chosen for zero-intensity, one would end up with a dispersion and bunch length different from the design values at a subsequent RF structure [6]. It is therefore necessary to understand the modification of dispersion due to space charge along the arc in order to do proper matching into the next lattice section. Longitudinal space charge also plays an important role, especially for short bunches and small momentum deviations. Longitudinal space-charge-induced variations in the bunch length or momentum deviation also affect the transverse space charge force by varying the local current density and the transverse beam size through the dispersion.

DISPERSION WITH SPACE CHARGE

In the presence of bending magnets, the horizontal displacement x of a particle from the reference particle is written as [6]

$$x\left(s\right) = x_{\beta}\left(s\right) + D_0\left(s\right)\delta, \tag{1}$$

where x_β is the betatron oscillation amplitude, $D_0 \equiv D_0(s)$ is the dispersion function, and $\delta = \Delta p/p_0$ is the fractional momentum deviation. The linear dispersion function without space charge $D_0(s)$ is the solution of the equation [2]:

$$D_0''(s) + \kappa_x(s)D_0(s) = \frac{1}{\rho(s)}, \tag{2}$$

which gives the local sensitivity of the particle trajectory to the fractional momentum deviation δ, and the prime denotes derivative with respect to distance s along the beamline. ρ is the bending radius and κ_x is the linearized horizontal external focusing gradient.

With space charge, we can write:

$$x_{\mathrm{sc}}\left(s\right) = x_{\mathrm{sc},\beta}\left(s\right) + D\delta, \tag{3}$$

where $D \equiv D\left(s\right)$ is the dispersion function with space charge.

Taking the average of Eq. (1) and Eq. (3) and subtracting them over the symmetrical phase space distribution, such that $\langle x_\beta\rangle = \langle x_{\mathrm{sc},\beta}\rangle = 0$, we obtain (see also [4]):

$$\langle x_{\mathrm{sc}}\rangle - \langle x\rangle = (D - D_0)\langle\delta\rangle. \tag{4}$$

For a beam with a momentum distribution centered at the design momentum the dispersion describing the position of the beam centroid is space charge independent. This also explains the experimental results obtained in the CERN PS Booster [5]. There the dispersion was measured and matched by changing the beam momentum and recording the displacement of the beam center.

To observe the effect of space charge on the individual particle dispersion, we have to compute the second moments of the beam distribution. Using the assumption that the momentum deviation is uncorrelated to the betatron oscillations,

---

* khan@temf.tu-darmstadt.de

ISBN: 978-3-95450-217-2 doi:10.18429/JACoW-ERL2019-WEPNEC08

such that $\langle x_\beta \delta \rangle = \langle x_{\mathrm{sc},\beta} \delta \rangle = 0$, we get the expression for D by multiplying Eq. (3) by δ and taking the average over the phase space. Following a similar procedure for D' [6]:

$$D = \frac{\langle x_{\mathrm{sc}} \delta \rangle}{\langle \delta^2 \rangle} = \frac{\sigma_{16}}{\sigma_{66}}, \quad D' = \frac{\langle x'_{\mathrm{sc}} \delta \rangle}{\langle \delta^2 \rangle} = \frac{\sigma_{26}}{\sigma_{66}}. \tag{5}$$

where the last equalities are written in terms of the beam sigma matrix [3, 6] as explained following.

Instead of individual particle tracking, we track the rms beam envelope defined as [3, 7, 8]:

$$\sigma_{ij} = \langle u_i u_j \rangle \tag{6}$$

where the averages are taken over the phase space variables and the subscripts i, j run from 1 to 6 representing x, x', y, y', z, z'. The time evolution of a beam matrix σ_s from s_0 to s_1 along the longitudinal position s is given by [3, 8]

$$\sigma_{s_1} = R(s_0 \rightarrow s_1)\, \sigma_{s_0}\, R^T(s_0 \rightarrow s_1), \tag{7}$$

where R is the transport matrix. The space charge kick is implemented as $R(s_0, s_0 + \Delta s) = R_{\Delta s} R^{\mathrm{sc}}$, where $R_{\Delta s}$ is a drift of length Δs and R^{sc} is the space charge kick as described in Ref. [3, 8, 9].

The effective transverse rms beam radii X and Y including dispersion are:

$$X^2 = \sigma_x^2 + D_x^2 \sigma_\delta^2, \quad Y^2 = \sigma_y^2 + D_y^2 \sigma_\delta^2, \tag{8}$$

where $\sigma_x = \sqrt{\langle x^2 \rangle} = \sqrt{\sigma_{11}}$, $\sigma_y = \sqrt{\langle y^2 \rangle} = \sqrt{\sigma_{33}}$ are the rms betatron amplitudes, and $\sigma_\delta = \sqrt{\langle \delta^2 \rangle} = \sqrt{\sigma_{66}}$ is the rms momentum deviation.

The momentum compaction R_{56} is the variation of the path length with momentum deviation for a relativistic beam:

$$R_{56} = \frac{\Delta L}{\delta} = \int_0^L \frac{D_x + D_y}{\rho} \mathrm{d}s, \tag{9}$$

which also is the (5,6)th component of the 6 × 6 transport matrix of the beamline elements. Where L is the total path length of the beamline.

In a beamline with dispersion D, space charge modifies the path length or time of flight of individual particles following the space charge dependent phase slip factor η:

$$\eta = \left. \frac{R_{56}}{L} \right|_{s=L} \tag{10}$$

In this work, we use above discussed beam matrix approach to obtain the optical functions along a beamline with bends, including the self-consistent space charge force.

OVERVIEW OF MESA

An overview of the MESA facilities is shown in Fig. 1. The electron source provides up to 1 mA of a polarized beam at 100 keV. In the next planned stage of MESA, the electron source will provide 10 mA of unpolarized beam current. This electron source is followed by a spin manipulation system containing two Wien filters. A chopper and two buncher cavities prepare the bunches for the normal-conducting milliampere booster (MAMBO), which accelerates them to 5 MeV. In MESA electrons will be accelerated by two ELBE-type cryomodules each housing two superconducting TESLA-type cavities with an accelerating gradient of 12.5 MeV, which results in 25 MeV per pass. There are four spreader sections for separating and recombining the beam and two chicanes for injection and extraction of the 5 MeV beam.

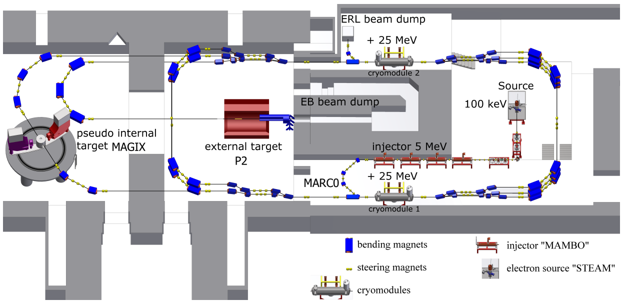

Figure 1: A schematic layout of MESA.

MESA is planned to operate in two modes: external beam (EB) mode and energy-recovery (ER) mode. In EB mode, the electron beam will gain 155 MeV with up to 150 µA beam current by circulating thrice around the accelerator. The beam is planned to be used for high-precision fixed-target experiments. The main experiment in the EB mode will be the measurement of the electroweak mixing angle at the P2 setup [10]. Similarly in ER mode, the CW electron beam will gain 105 MeV with 1(10) mA beam current by circulating twice around the accelerator. The main experiments in the ER mode will be pseudo-internal target (PIT) experiments in a search for dark photons with high luminosity [11]. In ER mode, 100 MeV of the beam energy can be recovered by decelerating the beam in the superconducting cavities and using this recovered energy to accelerate further bunches [12]. Both operational modes set high demands on beam quality and stability. Mainly, a low momentum deviation is required to achieve higher precision of experiments. The main prerequisite for sustaining beam quality is a proper beam transport through the injection arc (MARC0), which is a 5 MeV, 180°, first-order achromat with flexible 1st order momentum compaction R_{56} required for the different isochronous and non-isochronous recirculation modes.

SIMULATION RESULTS

In this section, we present the solutions for the beam envelopes, dispersion and momentum compaction with space charge in MESA. Estimation of space charge effects is done for a typical set of beam parameters listed in Table 1 [6]. Note that we are using an idealized lattice for the MESA beamline ignoring magnet misalignments and multipole er-

ISBN: 978-3-95450-217-2 doi:10.18429/JACoW-ERL2019-WEPNEC08

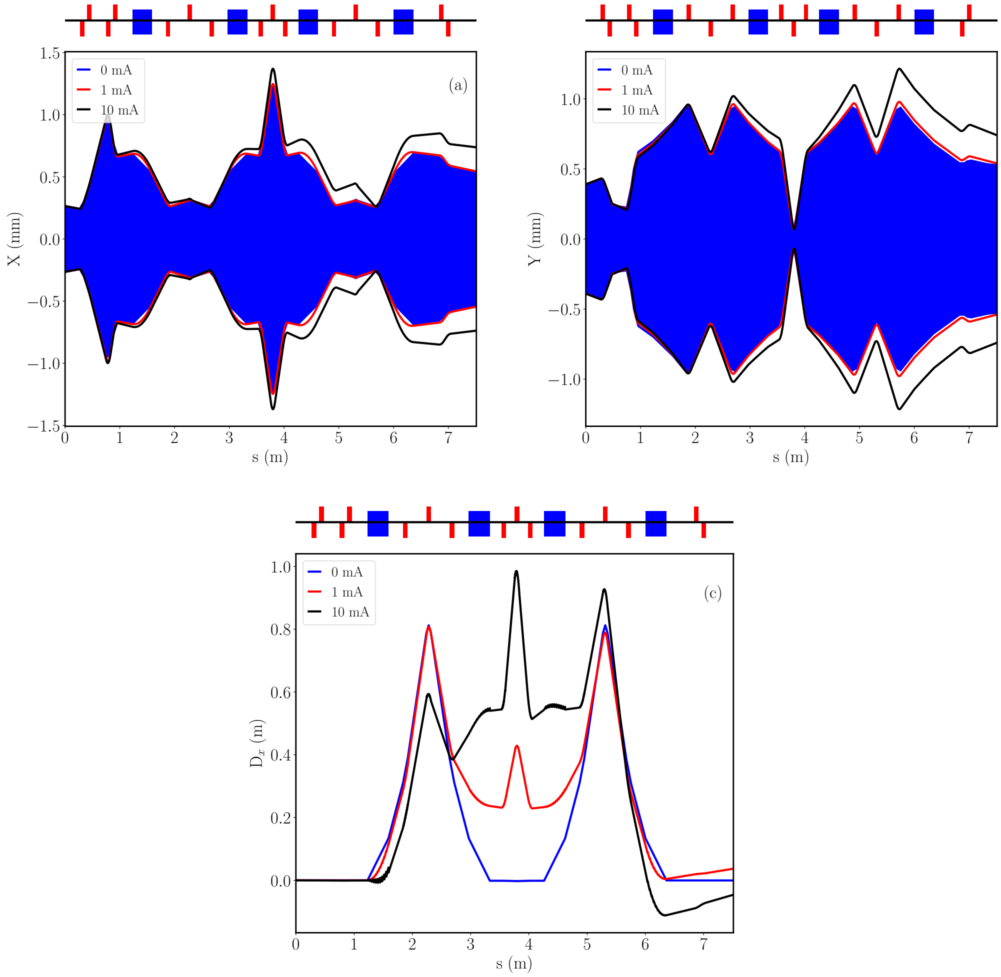

Figure 2: Evolution of (a) horizontal beam envelope, (b) vertical beam envelope, (c) dispersion, and (d) momentum compaction along the MARC0 beamline for I = 0, 1, 10 mA including transverse and longitudinal space charge.

rors for the simulations. Additional studies are required to include these effects.

First, we compute the horizontal and vertical beam envelope, and dispersion profile along the MARC0 arc for "zero", 1, and 10 mA current and an rms momentum deviation of 10^{-4}, accounting for coupled transverse-longitudinal space charge. The injection arc of MESA (MARC0) is suppose to be a dual purpose 5 MeV arc with finite momentum compaction R_{56} for energy recovery and external beam mode. A nominal design of arc should deliver fixed beam parameters with zero dispersion after first cryomodule for energy recovery operation. Figures 2 (a)–(b) show the variation of horizontal and vertical transverse envelopes along s, for $I =$ 1, and 10 mA in MARC0. It can be seen from Fig. 2 (c) that with longitudinal and transverse space charge the dispersion is significantly modified for non-zero currents. The sign reversal of D_x may contribute to phase mismatch at the entrance of the RF section due to changes in the time of flight of particles (see Eq. (9) and Eq. (10)). Thus, it is important to consider both longitudinal and transverse space charges for optimal matching.

Table 1: Beam Parameters for the Injection Arc of MESA.

Parameters [unit]	Symbol	Value
Kinetic energy [MeV]	E_k	5
Bunch charge [pC]	Nq	0.77/7.7
RF frequency [GHz]	f_{rf}	1.3
RMS momentum deviation [%]	σ_δ	0.01
Half bunch length [ps]	z_m	4.2
Normalized emittance [π mm mrad]	$\epsilon_{nx,ny}$	2/6
Momentum compaction [m]	R_{56}	0.14

Second, we compute the beam envelopes and dispersion along the full MESA beamline to observe the effect of space charge mismatch. Figure 3 (a)-(b) shows the horizontal and vertical beam envelopes with space charge for I = "zero", 1, and 10 mA in MESA. It can be seen from Fig. 3 (c)-(d) that dispersion with space charge is significantly modified

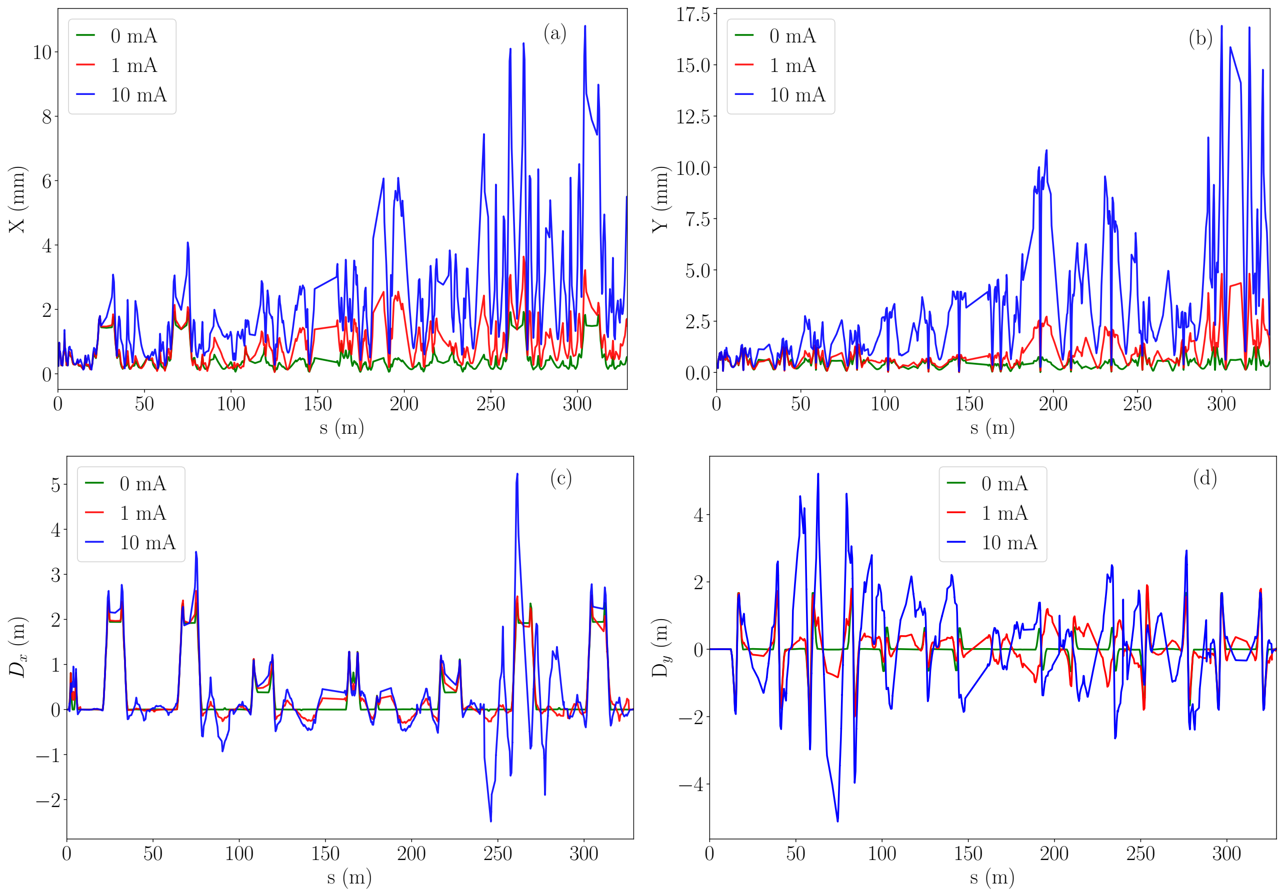

Figure 3: Evolution of (a) horizontal beam envelope, (b) vertical beam envelope, (c) horizontal dispersion function, and (d) vertical dispersion function along the MESA beamline for I = 0, 1, 10 mA including transverse and longitudinal space charge.

for non-zero currents from the designed values. Also, there appears to be a strong mismatch in the beam envelopes and dispersion near PIT experiment at s = 175 m and in the further arcs. This strong effect of space charge at high-energy arc (105 MeV) can be expected from Fig. 2 results that space charge induces a mismatch between the beam envelopes and non-zero dispersion at the end of the 5 MeV low energy injection arc which leads to the strong mismatch in the beam envelopes in the further arcs during acceleration and deceleration and distorts the phase space.

In this work, we optimize the lattice parameters of MARC0 to get fixed values of $\beta_{x,y}, \alpha_{x,y}, D_x, D'_x$ and R_{56} at the end so we can estimate the mismatch in the beam envelopes and dispersion in the further arcs. While the transverse dispersion functions D_x and D'_x need to be zero at the end of the arc, the longitudinal dispersion is fixed at a finite value of $R_{56} = 0.14$ m in order to use the arc as part of a bunch compressor to achieve a short bunch length at the start of the first superconducting RF section.

As can be seen from Fig. 2, MARC0 consists of two double-bend achromats (DBA) [13]. It controls both transverse beam confinement and longitudinal phase space to compress the bunch. A set of four quadrupoles at the start of the arc matches the first DBA to the MAMBO injector. The central part of the arc between the two DBAs contains three quadrupoles to again match the Twiss parameters. A total of 15 quadrupole gradients are available knobs to optimize the lattice.

Table 2: Example current, the horizontal and vertical beta functions mismatch respectively, and the horizontal dispersion mismatch from the design value at the end of MARC0 with space charge [6].

I (mA)	$\frac{\Delta\beta_x}{\beta_x}$ (%)	$\frac{\Delta\beta_y}{\beta_y}$ (%)	ΔD_x(m)
1	3.0	2.6	0.037
5	17.5	17.3	-0.017
10	39.7	41.0	-0.046
10 (matched)	0	0	0

Table 2 illustrates the horizontal beta function mismatch $\Delta\beta_x/\beta_x$ and the vertical beta function $\Delta\beta_y/\beta_y$ mismatch from the design value respectively, and the horizontal dispersion mismatch ΔD_x from the design value at the end of MARC0 with space charge for 1, 5 and 10 mA. Here, $\Delta\beta_x = \beta_{\text{sc},x} - \beta_x$, $\Delta\beta_y = \beta_{\text{sc},y} - \beta_y$, and $\Delta D_x = D_{\text{sc},x} - D_x$. We can see from the last column of Table 2 that current de-

ISBN: 978-3-95450-217-2 doi:10.18429/JACoW-ERL2019-WEPNEC08

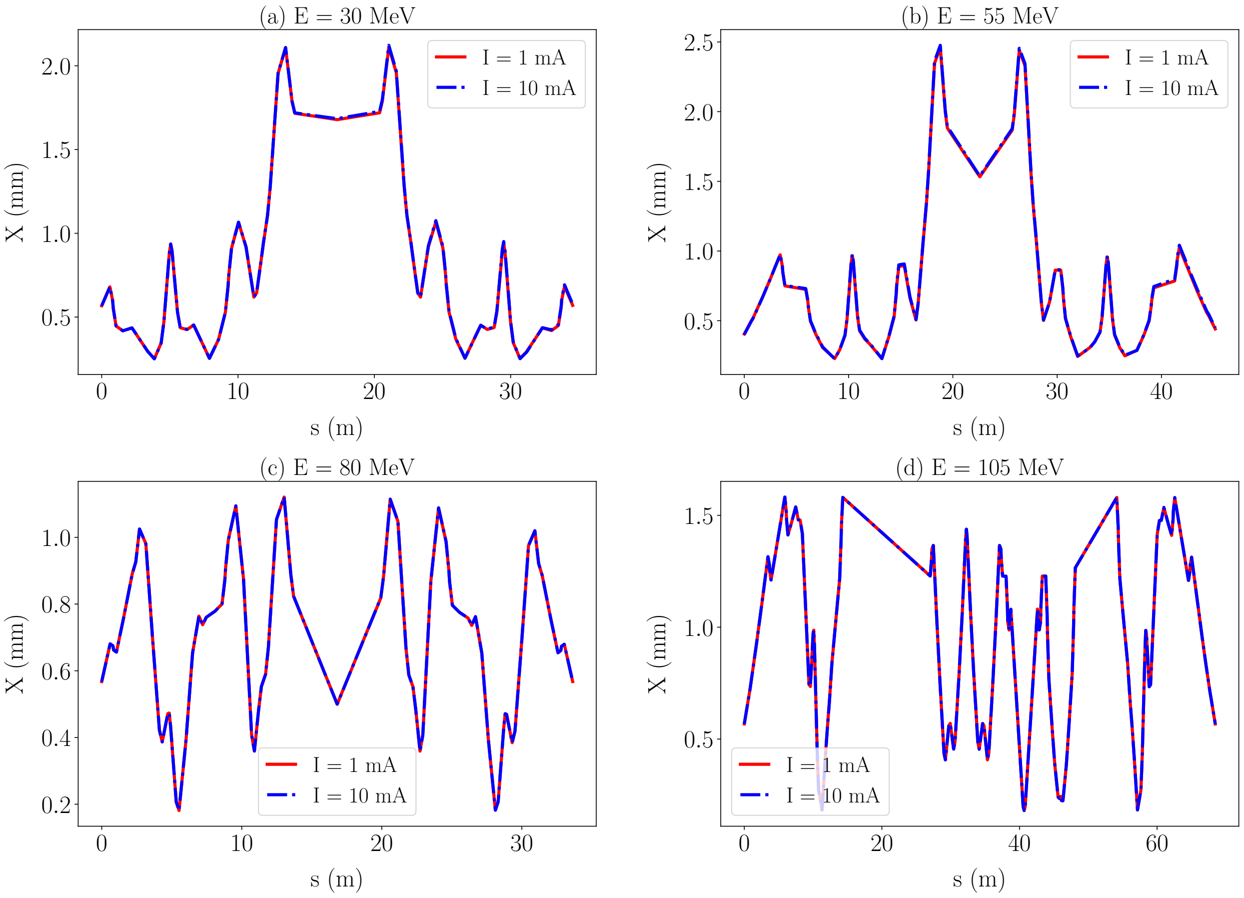

Figure 4: Horizontal beam envelopes along the (a) 30 MeV recirculation arc (b) 55 MeV recirculation arc (c) 80 MeV recirculation arc, (d) 105 MeV internal arc of MESA for I = 1, 10 mA when the beam is matched with space charge in the 5 MeV injection arc MARC0.

pendent dispersion is non-zero at the end of MARC0 which might lead to emittance growth in the RF section because of longitudinal-transverse phase space coupling.

We use a simple "random walk" routine to optimize all lattice parameters to get the matched solution of MARC0 with space charge. Note that D' should be considered for optimization of D in the beamline with space charge. D' must be zero at the central quadrupole of the achromat to achieve zero dispersion at the end of the last dipole. A new set of quadrupole strengths is obtained with corrections of up to 15% in the original quadrupole to get the matched solution.

The above results show the beam envelopes and dispersion mismatch from the design values due to space charge effects. Thus, to estimate the intensity limitations due to space charge in MESA, first we match the beam in the MARC0 using the random walk scheme as discussed above, and then track that matched beam through high energy recirculation arcs. Figure 4 shows the horizontal beam envelopes along the 30, 55, 80, and 105 MeV recirculation arcs of MESA for I = 1, 10 mA when the beam is matched with space charge in the MARC0. It can be seen that if all the lattice parameters of the beamline are matched properly with the subsequent RF structure in the presence of space charge at the injection, there is no mismatch between the beam envelopes due to space charge in the high-energy recirculations arcs of MESA.

CONCLUSION

This study shows that the proper matching of the injection arc into the RF section of an ERL is important with space charge. We showed how space charge modifies the dispersion function along the arc and so the momentum compaction which leads to change in the path length of electrons. A "random walk" scheme was employed to get the matched parameters with space charge at the subsequent RF section of an arc. In subsequent recirculation arcs of MESA, the beam energy is much higher than the injection energy. It is shown that MESA has no intensity limitations due to space charge if the beam is properly matched with space charge at the injection. The future application of this work is to predict the longitudinal space-charge-induced microbunching instability in MESA, which depends on the details of the dispersion function along the arcs [14].

REFERENCES

[1] Aamna Khan, Kurt Aulenbacher, and Oliver Boine-Frankenheim. “Study of microbunching instability in MESA”. In *59th ICFA Advanced Beam Dynamics Workshop on Energy Recovery Linacs (ERL’17)*, 2018. doi:10.18429/JACoW-ERL2017-THICCC002.

[2] Martin Reiser. “ Theory and design of charged particle beams”. John Wiley & Sons, 2008. ISBN: 978-3-527-40741-5.

[3] Tomohiro Ohkawa and Masanori Ikegami. “Dispersion matching at the injection from a high-intensity linac to a circular accelerator”. *Nuclear Instruments and Methods in Physics Research Section A*, 576(2-3):274–286, 2007. doi:10.1016/j.nima.2007.03.015.

[4] S. Bernal, B. Beaudoin, T. Koeth, and P. G. O’Shea. “Smooth approximation model of dispersion with strong space charge for continuous beams”. *Physical Review Special Topics - Accelerators and Beams*, 14(10):1–15, 2011. doi:10.1103/PhysRevSTAB.14.104202.

[5] K. Hanke, J. Sanchez-Conejo, and R. Scrivens. “Dispersion matching of a space charge dominated beam at injection into the CERN PS Booster”. *Proceedings of the 2005 Particle Accelerator Conference*, p. 3283, 2005, paper: TPAT054.

[6] Aamna Khan, Oliver Boine-Franenheim, Florian Hug, and Christian Stoll. “Beam matching with space charge in energy recovery linacs”. *Nuclear Instruments and Methods in Physics Research Section A*, 948, p. 162822, 2019. doi:10.1016/j.nima.2019.162822.

[7] Thomas P Wangler. “RF Linear accelerators”. John Wiley & Sons, 2008. ISBN:978-3-527-40680-7.

[8] Kenneth R Crandall. “TRACE 3D documentation”. Technical report, Los Alamos National Lab., 1987.

[9] Christopheer K Allen and N Pattengale. “Theory and technique of beam envelope simulation”. Los Alamos National Laboratory, Internal Report LA-UR-02-4979, 2002.

[10] Dominik Becker, Razvan Bucoveanu, Carsten Grzesik, and et al. “The P2 experiment”. *The European Physical Journal A*, 54(11):208, Nov 2018. doi:10.1140/epja/i2018-12611-6.

[11] Achim. Denig. “Recent results from the Mainz Microtron MAMI and an outlook for the future”. *AIP Conf.Proc.*, 1735. 020006, 2016. doi:10.1063/1.4949374.

[12] Kurt Aulenbacher. “Opportunities for parity violating electron scattering experiments at the planned MESA facility”. *Hyperfine Interactions*, 200(1-3):3–7, 2011. doi:10.1007/s10751-011-0269-9.

[13] Helmut Wiedemann. “Particle accelerator physics”. Springer, 2015. doi:10.1007/978-3-319-18317-6.

[14] A. Khan, O. Boine-Frankenheim, and C. Stoll. “Space charge and microbunching studies for the injection arc of MESA” In *Journal of Physics: Conference Series*, 1067, p. 062022, 2018. doi:10.1088/1742-6596/1067/6/062022.

63th ICFA Advanced Beam Dynamics Workshop on Energy Recovery Linacs ERL2019, Berlin, Germany JACoW Publishing
ISBN: 978-3-95450-217-2 doi:10.18429/JACoW-ERL2019-WEPNEC10

INVESTIGATION ON THE ION CLEARING OF MULTI-PURPOSE ELECTRODES OF BERLINPRO

G. Pöplau*, Universität zu Lübeck, Lübeck, Germany
A. Meseck, HZB, Berlin, and Johannes Gutenberg-Universität, Mainz, Germany

Abstract

High-brightness electron beams provided by modern accelerators require several measures to preserve their high quality and to avoid instabilities. The mitigation of the impact of residual ions is one of these measures. It is particularly important if high bunch charges in combination with high repetition rates are aimed for. This is because ions can be trapped in the strong negative electrical potential of the electron beam causing emittance blow-up, increased beam halo and longitudinal and transverse instabilities. One ion-clearing strategy is the installation of clearing electrodes. Of particular interest in this context is the performance of multi-purpose electrodes, which are designed such that they allow for a simultaneous ion-clearing and beam-position monitoring. Such electrodes will be installed in the bERLinPro facility. In this contribution, we present numerical studies of the performance of multi-purpose clearing-electrodes planned for bERLinPro, i.e. we investigate the behavior of ions generated by electron bunches while passing through the field of the electrodes. Hereby, several ion species and configurations of electrodes are considered.

INTRODUCTION

The Energy Recovery Linac bERLinPro is currently being set up at the Helmholtz-Zentrum Berlin. Based on superconductive RF (SRF) technology, it aims to deliver high current, low emittance cw beams, and to demonstrate energy recovery at unprecedented parameters [1].

In general, Energy Recovery Linacs place very high demands on maintaining beam brightness and reducing beam losses. Ions in vicinity of the electrons have a ruinous impact on the brightness and stability of the beam. This also applies to bERLinPro. Hence counter measures such as clearing electrodes and their performance is of highest importance for the project. For bERLinPro multi-purpose electrodes, that enable simultaneous ion-clearing and beam position monitoring were developed and built at the HZB [2].

They consist of four rectangular electrode-plates, which can in principle be biased independently with a voltage up to 1000V resulting in different voltage-configurations. The different voltage-configurations naturally have different distributions of the electric field. In this paper, we evaluate the performance of the bERLinPro multi-purpose electrodes for four different voltage-configurations. We relate the difference in performance for different voltage-configurations to the motion of the ions within the corresponding clearing fields.

Table 1: Nominal Parameters of bERLinPro.

bERLinPro Bunch	
Nominal Beam Energy	50 MeV
Nominal Beam Charge Q	77 pC
Maximum Repetition Rate	1.3 GHz
Transv. RMS Bunch Size $\sigma_{x,y}$	300 μm
Bunch Length σ_t	2 ps
Vacuum Pressure	$5 \cdot 10^{-10}$mbar

SIMULATION SETUP AND SIMULATION TOOLS

In this section a short introduction to the simulation setup and the simulation tools are provided. Since the applied models and simulation tools coincide with those used for former studies, more details can be found in [2, 3]. The nominal parameters of bERLinPro that are relevant for the simulations are summarized in Table 1.

The Multi-Purpose Electrode

A description of the technical details of the bERLinPro multi-purpose electrode was given in [2]. Here we only provide the information relevant for the presented simulation studies. The multi-purpose electrodes are constructed of four rectangular stripes (electrode-plates) with a size of 10 mm x 38 mm. These stripes are placed pairwise in parallel with a distance of 24.72 mm along the elliptical beam pipe of bERLinPro (70 mm x 40 mm).

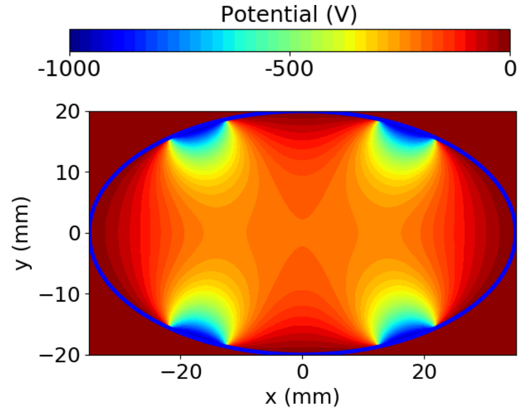

Figure 1: The potential of the bERLinPro multi-purpose electrode with a voltage of −1000 V supplied to all four electrode-plates.

Figure 1 shows the potential of the electrodes with the typical voltage-configuration, where a voltage of −1000 V is

---

[*] poeplau@math.uni-luebeck.de

ISBN: 978-3-95450-217-2 doi:10.18429/JACoW-ERL2019-WEPNEC10

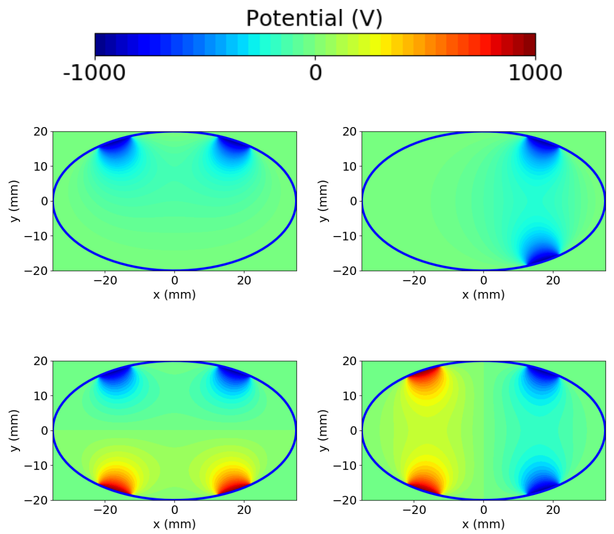

Figure 2: Potential of the bERLinPro multi-purpose electrode in transversal cross-section: voltage-configuration 1 (top, left), voltage-configuration 2 (top, right), voltage-configuration 3 (bottom, left) and voltage-configuration 4 (bottom, right).

supplied to all four electrode-plates. In [2] it was shown that this voltage-configuration has a poor clearing performance, because in this case the strength of the electric field at the position of the electron beam is rather low.

In this paper we investigate the clearing performance of voltage-configurations that provide a high field gradient at the pipe centre, i.e. at the position of the electron beam. The clearing performance and rates in the case of the bERLinPro multi-purpose electrodes were examined for the following voltage-configurations:

- *voltage-configuration 1*: the negative voltage is supplied to the two upper stripes and zero voltage to the two lower stripes of the clearing electrode.
- *voltage-configuration 2*: the negative voltage is supplied to the two right stripes and zero voltage to the two left stripes of the clearing electrode.
- *voltage-configuration 3*: the negative voltage is supplied to the two upper stripes and the positive voltage to the two lower stripes of the clearing electrode.
- *voltage-configuration 4*: the negative voltage is supplied to the two right stripes and the positive voltage to the two left stripes of the clearing electrode.

Figure 2 shows the potentials in transversal cross-section with a voltage of +/-1000 V applied to the electrodes. It has to be mentioned that the voltage-configurations 1 and 3 were already studied in [2] with a voltage of 1000 V. We repeat these results here in order to give a direct comparison to the voltage-configurations 2 and 4.

The Ion Model

In order to allow the comparison of the simulation results presented in this paper to former results we apply two different mixtures of residual gas introduced in [3]. Both mixtures are compositions of H_2^+, CH_4^+ and CO^+, where Gas A consists mainly of the light H_2^+-ions and gas B consists roughly of 50% H_2^+-ions and 50% of the much heavier CH_4^+- and CO^+-ions. Within the present simulations the ions are generated due to collisions with the electrons of the bunch, where the production rate R_j of ion j is described by the following model [4]:

$$R_j = c N_e \sigma_j \frac{P}{k_B T}. \tag{1}$$

Hereby c denotes the speed of light, N_e the number of electrons in the bunch, σ_j the ionization cross-section of ion species j (see [5]), P the vacuum pressure, k_B the Boltzmann constant and T the temperature.

The resulting number of bunch passages after which a new ion per cm is generated is given in Table 2 for the bERLinPro case. Furthermore, within the simulations the ions are generated at a length of 4 cm. This is approximately the length of the electrode-plates. For a more detailed picture also the total number of ions generated after a simulation time of 10 ms (1.3 million bunch passages) at a length of 4 cm is added to Table 2.

Table 2: Mixtures of Ionized Residual Gas and the Corresponding Ionization Process for the bERLinPro Case

ion species	**%**	**ion gener. after bunch no.**	**total no. of ions** (10 ms) **4 cm**
Gas A			
H_2^+	98	18,500	2,812
CH_4^+	1	282,500	188
CO^+	1	330,000	160
Gas B			
H_2^+	48	37,000	1,388
CH_4^+	26	11,000	4,728
CO^+	26	13,000	4,000

Simulation Tools

The ions once generated are tracked further due to the equations of motion under the influence of the attracting field of the passing bunches and the field of the multi-purpose electrode. Once an ion hits the electrode or wall of the beam pipe the ion is neutralized and will be tracked no longer. This approach enables a detailed study of the built-up of the ion cloud (accumulation) and the level of the established equilibrium.

The tracking and the generation of ions was performed with the code CORMORAN [3]. Here also the potential of the bunch is computed. The potential of the multi-purpose electrode is pre-computed by means of the Python Poisson

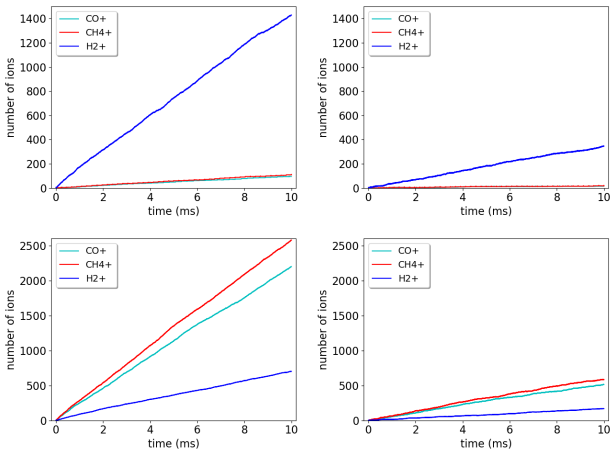

Figure 3: Comparison of electrode 1 (left) and 2 (right) at a voltage of 1000 V: the number of remaining ions is shown as a function of clearing time for gas mixture A (top) and B (bottom).

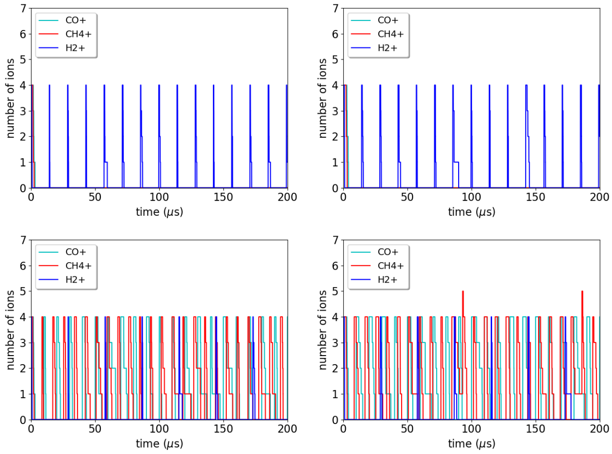

Figure 4: Comparison of electrode 3 (left) and 4 (right) at a voltage of 1000 V: the number of remaining ions is shown as a function of clearing time for gas mixture A (top) and B (bottom).

Solver [6]. More details about the simulation model and parameters can be found in [3, 6].

The time for a bunch passage was set to 200 ps due to an interaction region of 4 cm with a step size of 2 ps. The remaining time between two bunches was discretized by 10 equal time steps.

SIMULATION RESULTS

First, let us examine the four voltage-configurations with a voltage of 1000 V. The corresponding potentials are depicted in Figure 2. Figure 3 presents the results for voltage-configuration 1 and 2. It can be observed, that in both cases the ions accumulate, but the accumulation rate for voltage-configuration 2 is four times less than for voltage-configuration 1. With voltage-configuration 2 nearly 90%

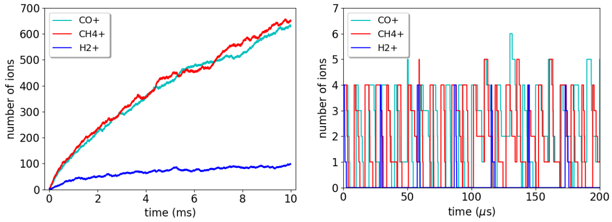

Figure 5: Comparison of electrode 3 (left) and 4 (right) at a voltage of 600 V: the number of remaining ions is shown as a function of clearing time for gas mixture B.

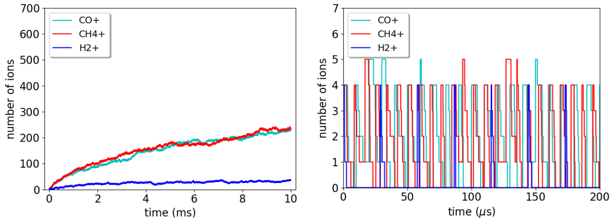

Figure 6: Comparison of electrode 3 (left) and 4 (right) at a voltage of 700 V: the number of remaining ions is shown as a function of clearing time for gas mixture B.

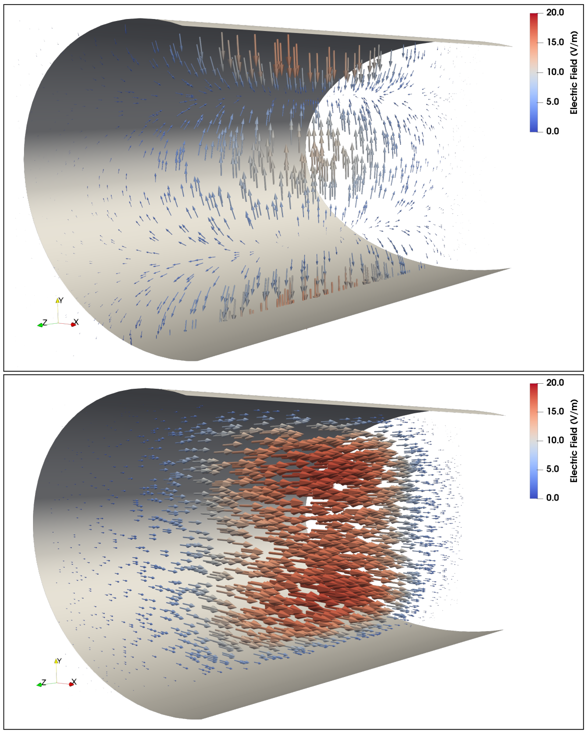

Figure 7: Electric field of the multi-purpose electrode: voltage-configuration 3 with a voltage of 1000 V (top) compared to voltage-configuration 4 (bottom); the longitudinal cross-sections at $x = 0$ are shown.

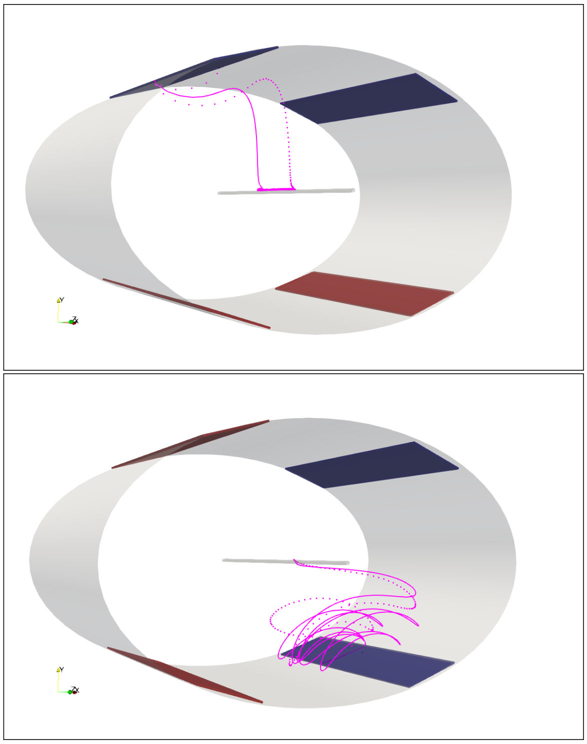

Figure 8: Path of an ion in the field of the multi-purpose electrode with a voltage of 700 V (solid line) and with a voltage of 1000 V (dashed line): voltage-configuration 3 (top) compared to voltage-configuration 4 (bottom).

of the generated ions are cleared after 10 ms, whereas only around 50% are cleared with voltage-configuration 1.

In the case of the voltage-configuration 3 and 4 all ions are cleared almost immediately after the generation, see Figure 4. Therefore, we investigated these two voltage-configurations with lower voltages of 600 V and 700 V. The simulation results for gas mixture B are presented in the Figures 5 and 6, respectively. It turns out that the ions are immediately cleared for voltage-configuration 4. This happens even at lower voltages. This is not the case with voltage-configuration 3, where the ions accumulate more as the voltage decreases. The reason seems to be that the electric field at the centre of the pipe is much higher for voltage-configuration 4 than for voltage-configuration 3 as shown in Figure 7. As a consequence an ion lingers much longer in the vicinity of the beam in the case of voltage-configuration 3, whereas it is kicked out from the centre of the pipe with voltage-configuration 4, see Figure 8. Similar considerations can be made for the difference between voltage-configuration 1 and 2.

CONCLUSIONS

Using numerical codes we have evaluated the performance of the bERLinPro multi-purpose clearing electrodes for four different voltage-configurations. We have observed that voltage-configurations that have the stripes biased with the same voltage on the left and right side perform far better than voltage-configurations that have the stripes biased with the same voltage on top and bottom. Although the stripes may be in principal independently biased, configurations 2 and 4 may not be possible at bERLinPro for a technical reason. This needs to be checked.

REFERENCES

[1] M. Abo-Bakr *et al.*, “Status report of the berlin energy recovery linac project bERLinPro,” in *Proc. IPAC’18*, Vancouver, BC, Canada, Apr. 4,, pp. 4127–4130, `doi:10.18429/JACoW-IPAC2018-THPMF034`

[2] G. Pöplau, M. Meseck, F. Falkenstern, M. Markert, and J. Bartilla, “Investigation on the ion motion towards clearing electrodes in high-brightness electron accelerators,” `arXiv: 1910.04025`, 2019.

[3] G. Pöplau and M. Meseck, “Investigation on the ion motion towards clearing electrodes in an accelerator,” in *Proc. IPAC2017*, Copenhagen, Denmark, May 2017, paper THPAB016, pp. 3723–3726. `doi:10.18429/JACoW-IPAC2017-THPAB016`

[4] A. Poncet, “Ions and neutralization,” in *Frontiers of Particle Beams: Intensity Limitations* (M. Dienes, M. Month, and S. Turner, eds.), vol. 400 of *Lecture Notes in Physics*, pp. 488–508, Springer Berlin / Heidelberg, 1992. `doi:10.1007/3-540-55250-2_41`

[5] F. F. Rieke and W. Prepejchal, “Ionization cross sections of gaseous atoms and molecules for high-energy electrons and positrons,” *Phys. Rev. A*, vol. 6, pp. 1507–1519, Oct 1972. `doi:10.1103/PhysRevA.6.1507`

[6] G. Pöplau and C. Potratz, “A python poisson solver for 3D space charge computations in structures with arbitrary shaped boundaries,” in *Proc. IPAC 2014* (5th International Particle Accelerator Conference), Dresden, Germany, pp. 406–408, 2014. `doi:10.18429/JACoW-IPAC2014-MOPME013`

63th ICFA Advanced Beam Dynamics Workshop on Energy Recovery Linacs ERL2019, Berlin, Germany JACoW Publishing
ISBN: 978-3-95450-217-2 doi:10.18429/JACoW-ERL2019-WEPNEC11

X-RAY ICS SOURCE BASED ON MODIFIED PUSH-PULL ERLS

I. Drebot*, A. Bacci, A. Bosotti, F. Broggi, S. Cialdi, L. Faillace, D. Giannotti,
D. Giove, P. Michelato, L. Monaco, R. Paparella, F. Prelz, M. Rossetti Conti, A. R. Rossi, L. Serafini,
D. Sertore, M. Statera, V. Torri, INFN, Milano, Italy
V. Petrillo, Universitá degli Studi di Milano & INFN, Milano, Italy
G. Galzerano, E. Puppin, Politecnico di Milano, Milano, Italy
A. Esposito, A. Gallo, C. Vaccarezza, INFN/LNF, Frascati Roma, Italy
G. Mettivier, P. Russo, A. Sarno, Universitá di Napoli, Napoli, Italy
P. Cardarelli, M. Gambaccini, G. Paternó, A. Taibi, Universitá di Ferrare & INFN, Ferrara, Italy

Abstract

We present the conceptual designs of BriXS and BriXsinO (a minimal test-bench demonstrator of proof of principle) for a compact X-ray Source based on innovative push-pull ERLs. BriXS, the first stage of the Marix project, is a Compton X-ray source based on superconducting cavity technology with energy recirculation and on a laser system in Fabry-Pérot cavity at a repetition rate of 100 MHz, producing 20-180 keV radiation for medical applications. The energy recovery scheme based on a modified folded push-pull CW-SC twin Linac ensemble allows to sustain MW-class beam power with almost just one hundred kW active power dissipation/consumption.

INTRODUCTION

BriXS (Bright and compact X-ray Source) [1] is a twin Compton X-ray source based on superconductive cavities technology for the electron beam with energy recirculation and on a laser system in Fabry-Pérot cavity at a repetition rate of 100 MHz, producing 20-180 keV radiation.

It has been conceived as the first acceleration stage of the X-ray FEL MariX [2,3]. MariX is an X-ray FEL based on the innovative design of a two-pass two-way superconducting linear electron accelerator, equipped with an arc compressor to be operated in CW mode at 1 MHz.

The double Compton X-ray sources will operate at very high repetition rate 100 MHz, with 200 pC electron bunches that means very high average current 20 mA.

These Compton sources are designed to operate with an electron energy range of 30-100 MeV, which for a 20 mA of current means 2 MW. Such a high beam power cannot be dumped without deceleration, and together with the CW (Continuous Wave) regime, it justifies to foresee an ERL (Energy Recovery Linac) machine, like in the CBETA ERL projecct [4].

The focus on enabled applications by such an energy range and brilliance is on medical oriented research/investigations, mainly in the radio-diagnostics and radio-therapy fields [5,6], exploiting the unique features of monochromatic X-rays, as well as in micro-biological studies, and, within this mainstream, material studies, crystallography and museology for cultural heritage investigations. In this paper, the layout and the typical parameters of the BriXS X-ray source will be discussed.

MACHINE LAYOUT

The BriXS layout, shown in Figure 1, consists of two symmetric beam lines, fed by two independent photoinjectors, where two equal and coupled Energy Recovery Linacs (ERL) accelerate the electron beams. Electron trains are extracted from the photo-cathodes Inj1 and Inj2 at the left side of in Figure 1. The two ERLs (named ERL1 and ERL2 in the Figure) accelerate and decelerate the electron trains in an unconventional push-and-pull scheme. Bunches from Guns and travelling right away in the Figure are accelerated, those coming back from the interaction points (IPs) are decelerated during the energy recovery phase and brought simultaneously to a single beam-dump. Each Linac is therefore traversed by two counter-propagating trains of electron beams, both gaining and yielding energy. This push-and-pull coupled scheme permits to concurrently drive two Compton X-ray sources with the same degrees of freedom, in terms of energy and electron beam quality, as a Linac driven source, with the advantage that the coupled ERLs scheme, fed by two independent RF, systems is more stable. CW electron Guns, capable to produce such an average beam current, are not yet state of the art. Some of the most promising photo cathode Guns [7] as the Cornell DC Gun [8] and the RF-CW Apex Gun [9] have been therefore compared by simulations. Considering the simulations results was chosen the APEX one. Partial modifications of the beam lines to host additional Compton interaction points are under study. BriXs should be considered as a single folded ERL running two beams. This scheme is more compact than two independent ERLs, with the necessity of less magnetic elements and, therefore, a minor cost. An important advantage is that the present scheme provides two knobs for adjusting the phases at the entrance of the linacs in the recovery stage, thus circumventing the necessity of additional matching lines for running one single ERL at different energies.

INJECTOR

Two twin injectors are present in BriXS. The injector layout of the BriXS/MariX common acceleration beam-line, as sketched in Figure 2, is composed of the following accelerating and focusing elements: 1. The CW RF Gun; 2.

---

* illya.drebot@mi.infn.it

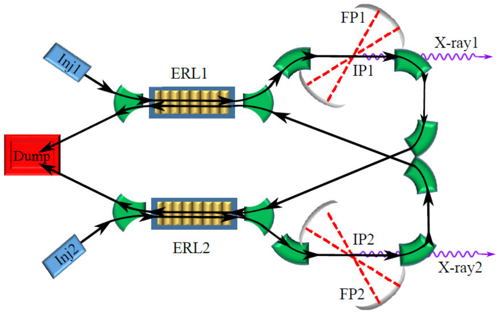

Figure 1: Pictorial view of the BriXs layout: From the left side: Inj1 and Inj2: photocathodes. ERL1 and ERL2: Superconducting Linacs. FP1 and FP2: Fabri-Pérot cavities. IP1 and IP2: interaction points. X-ray1 and X-ray2: X rays beams, going towards Compton users areas.

Two focusing solenoids; 3. One RF buncher; 4. Two linear accelerators; 5. One RF linearizing cavity. Being two identical beamlines, we show and discuss only one from here on for simplicity. The RF power source for each component of the BriXS injector operates in CW, since the high repetition rate (100 MHz) electron beam reaches an average power of 120 kW at the exit, i.e. energy up to 6 MeV and average current of 20 mA. Therefore, the choice of the RF system is based on the maximum average RF power that can be handled by the RF devices. The CW RF-Gun and the RF Buncher are based on normal conducting (NC) technology, since the RF power dissipated inside the cavities, required to accelerate and to bunch the electron beam with an energy of about 800 keV at the beginning, can be still handled by using standard water-cooling systems. The APEX Gun [9] has already shown operation at about 87 kW of average dissipated RF power with the possibility to operate even up to 100 kW . As for the two linacs and the RF linearizer, where the high rep-rate beam is accelerated up to at least 6 MeV, we have decided to use superconducting (SC) technology since standard copper structures are not able to dissipate the high average RF power that would be required. Indeed, the cavity wall power consumption inside a SC structure is lower than a NC one by a factor of $10^5 - 10^6$.

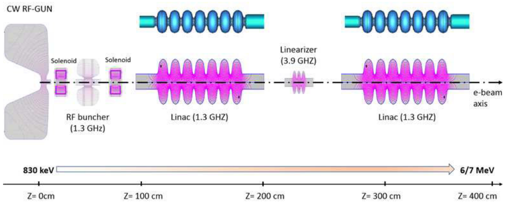

Figure 2: Injector layout for 1 beam-line, SuperFish 2D model.

ACCELERATOR SECTION

The requirement for a CW beam structure imposes the choice of the Superconducting technology for the accelerating section, in order to save in capital and operational cost because we want to operate at an accelerating gradient of at least 15 MV/m. This technology has been developed over the past thirty years and has now reached a mature status. The latest most important high repetition rate or CW accelerator facilities (E-XFEL, LCLS-II, ESS, etc.) are now based on this consolidated technology.

To provide the required 100 MeV maximum energy, we need to consider two important aspects for the selection of the accelerating structure, namely the requirement for RF operation and the effect of the induced High Order Modes on the beam quality. The choice of the BriXS accelerating structure is determined by the above considerations and by the performance already achieved in structures used in installations similar to BriXS. We have evaluated, for this case, two experimentally tested different cavity/module designs:

- Compact ERL(KEK), 100 mA current target still to be demonstrated. The based accelerating unit is a cryomodule with two 9-cells cavity design to suppress HOM-BBU up to the nominal current (theoretical limit is 200 mA). It has demonstrated an up to 1 mA CW operation with a 100.0 ± 0.03 % energy recovery and providing a 15 MV/m accelerating gradient. The TESLA-geometry cavity has been modified to accommodate two HOM absorber able to dissipate up to 150 W. These cavities are operated at 2.0 K.

- CBETA (Cornell), multi-pass ERL demonstrator, linac module tested, Design Report. Each module consists of six 7-cell cavities, designed to operate in CW mode at 16 MV/m with a HOM-BBU limit at 100 mA. Specifically designed HOM absorbers installed on both side are able to handle up to 400 W of dissipated power. These absorbers are isolated from the cavity and they are eventually cooled with liquid nitrogen. The module has been successfully tested and has reached the designed performances. The cryogenic operation temperature for this project is 1.8 K.

In order to contain the overall module footprint, a solution adopting a single cryomodule hosting the required number of cavities is preferable. This would suggest to explore the opportunities offered by the six-cavities CBETA cryomodule given its demonstrated performance. However, with a 0.81 m single cavity active length, the CBETA cryomodule would yield a 77.8 MeV energy gain when operated at 16 MV/m accelerating gradient. An eight 7-cells cavities geometry CBETA cryomodule appears to be needed to fulfill the energy gain requirements for BriXS. It is clear that, while the CBETA cryomodule remains a reference design , dedicated developments are needed for the current project.

Dealing with the cryogenics losses we need to include the dynamic losses as well as the HOM power. The cryogenic dynamic losses per single cavity, based on the previous parameter set, are expected to be 9.3 W. For the HOM power, in the non-resonant monopole case, the CBETA cavity has a longitudinal loss factor of 14.7 V/pC [4]. Based on this

Table 1: BriXS Cavity Operational Parameters

Parameter	Value
Accelerating structure	Standing Wave
Accelerating mode	$TM_{0,1,0}\ \pi$
Fundamental frequency [GHz]	1.3
Energy gain per cavity [MeV]	12.5
Accelerating gradient E_{acc} [MV/m]	15.6
Intrinsic quality factor Q_0	2×10^{10}
Loaded quality factor Q_{load}	3.25×10^7
Cavity half bandwidth at Q_{load} [Hz]	20
Operating temperature [K]	1.8 (2.0)
Number of cells	7
Active length [m]	0.810
R/Q (fundamental mode) [Ohm]	774
RF power per cavity [kW]	2.85
Dynamic cryogenic losses per cavity [W]	9.3
HOM cryogenic losses per cavity [W]	117
Cavity total longitudinal loss factor for σ = 0.6 mm [V/pC]	14.7
Q [pC]	200.0
f_{bunch} [MHz]	100
Average current [mA]	20

parameter, the estimated loss power is 117 W per cavity. This value can be reasonably handled by a CBETA-like solution for the HOM absorber made of SiC material and with a cooling jacket held at 80 K.

It is then clear that, if we opt to start from a proofed and operating cavity and cryomodule design, the CBETA layout guarantees these points and allows a smaller total length with respect to a solution like ERL(KEK). It is worth noting that modifications of the original CBETA design are necessary to reach the requested 100 MeV energy gain by implementing an 8 cavities per module structure. On the cavity side, we should keep in mind that the 2×10^{10} unloaded quality factor is achieved by operating the cavity at 1.8 K, while we are now aiming at operating BriXS at 2.0 K. While the CBETA cavity has shown to reach our specification also at 2.0 K, we are now considering to introduce an Electro Polishing process in the cavity treatment procedure (well established in the XFEL production). This will help achieving BriXS higher Q_0 values and will give us more confidence in reaching the design unloaded Q value. In Table 1, we summarize the BriXS requirements and the accelerating section design parameters.

ELECTRON BEAM LINES

The top view projection of the BriXs scheme, in the present configuration with two interaction points (IP) is shown in Figure 1. Each branch of the two BriXs beam lines, depicted in Figure 3, includes the following sections:

1. a quadrupole triplet, located downstream the SC Linac ERL1, matches the beam to the first chicane and allows for quadrupole-scan emittance diagnostic; electron bunches travel through these elements in both directions, outgoing from the accelerator or backwards from the specular path;
2. a dog-leg chicane, composed of two 20° dipoles and three quadrupole lenses closing the chicane dispersion, transports the beam to the IP line;
3. the IP region includes two strong focusing triplets, symmetrically installed w.r.t. the IP, and the about 1 m long Fabri-Pérot Optical Cavity. This section has identity transport matrix, so different focusing settings at IP can be adopted without affecting the magnetic elements downstream.
4. a double bend achromat (DBA) section with two 90° dipoles and three quadrupoles deflects the beam by 180° and closes the dispersion at its end;
5. a long dog-leg chicane with two 20° dipoles translates the beam to the second SC Linac; the triplets provide control the clearance of the first quads to avoid interference at the X-cross of the two beam lines;
6. the triplets "1" in Figure 3 are identical and specular structures.

Each of the electron beam lines has been designed so that the dispersion is closed at the IP region, at the exit of the DBA (4), where a diagnostic station will be installed, and at the exit of the second chicane (5) in order to optimize the beam injection in the ERL.

The IP region is designed with possibility to install second IP what open a possibility to operate BriXs as two-colour X-ray source [10, 11].

The transport of the electron beam from the exit of the first ERL, through the IP to the entrance of the second ERL has been performed by Elegant [12] and is part of start to end simulations.

The main electron beam parameters at the IP are collected in Table 2.

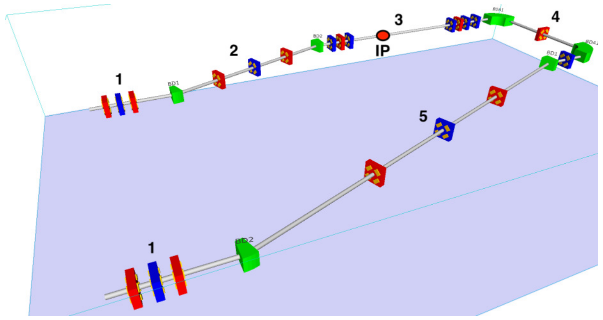

Figure 3: Scheme of the magnetic elements of a single BriXs beam line.

ISBN: 978-3-95450-217-2 doi:10.18429/JACoW-ERL2019-WEPNEC11

Table 2: Electron Beam Parameters at the Compton IP

Parameter	**Value**
Electrons mean energy [MeV]	30-100
Bunch charge [pC]	100-200
Emittance ϵ_{nx}, ϵ_{ny} [mm mrad]	0.6-1.5
Relative energy spread σ_e [%]	$10^{-2} - 10^{-1}$
Focal spot size σ_x,σ_y [μm]	19.4-23.4
Bunch length rms [μm]	400-900
Repetition rate [MHz]	100

Table 3: Parameters of Start to End Simulations for the High Energy WP

Electron beam Parameters			
Electrons mean energy (MeV)	100		
Bunch charge (pC)	200		
Normalized emittance ϵ_{nx}, ϵ_{ny} (mm mrad)	1.2, 1.2		
Relative energy spread σ_{E}/E	1.6×10^{-2}		
Bunch length rms (μm)	440		
Focal spot size σ_x, σ_y (μm)	19.4, 23.4		
Repetition rate (MHz)	100		
Laser Parameters			
Laser pulse energy (mJ)	7.5		
Laser wavelength (nm)	1030		
Laser pulse length (ps)	2		
Laser focal spot size $w_{0\mathrm{x}}$ (μm)	40		
Laser focal spot size $w_{0\mathrm{y}}$ (μm)	80		
Collision angle (deg)	7		
γ-ray Photon beam Parameters			
Relative bandwidth rms %	1	5	10
Absolute bandwidth rms (keV)	1.98	8.66	16.01
Absolute bandwidth FWHM (keV)	3.51	22.7	47.67
Collimation angle $\theta_{\max}$ (mrad)	0.6	2.08	3.3
Peak photon energy (keV)	183.4	182.4	180.4
Mean photon energy (keV)	181.0	170.4	158.7
Photon number per shot N_{Tot}	2.5×10^5		
Photon number per shot after collimation N_{ph}	5×10^3	4.7×10^4	8.4×10^4
Source rms size $\sigma_{\gamma\mathrm{x}}$, $\sigma_{\gamma\mathrm{y}}$ at IP (μm)	19.6, 16.7		
Source rms divergence $\sigma_{\gamma x'}$,$\sigma_{\gamma y'}$ (μrad)	0.3, 0.3	1.0, 1.0	1.6, 1.3
Source rms divergence θ_{rms} (μrad)	0.42	1.41	2.08
Spot Size at 10 m (mm)	3.0, 3.0	10.5, 9.44	16.3, 13.0
Rad. pulse length $\sigma_{\gamma\mathrm{z}}$ (ps)	1.35		

EXPECTED PERFORMANCE

The working point is the result of a full start-to-end simulation along all the BriXs electron beam line, from the photocathode to the radiation detector. The electron bunch parameters at IP used in this simulation, as well as the laser and the radiation characteristics, are presented in the first seven lines of Table 3. The Compton emission has been simulated using the Monte Carlo code CAIN [13].

Due to the boosted nature of the Compton back scattering process,

$$E_{\mathrm{ph}} = \frac{2E_{\mathrm{L}}\gamma^2\,(1+\cos\alpha_0)}{1+\gamma^2\theta^2}, \tag{1}$$

where γ is electron Lorentz factor, α_0 is interaction angle, θ is emission angle, the radiation exhibits an energy-angle correlation with the most energetic photons emitted on axis, while the outer regions are occupied by low energy photons. This feature makes possible to get monochromatic radiation by inserting irides or collimators along the path of the radiation, selecting therefore only the photons within a given collimation angle $\theta_{\max}$.

Figure 4 presents the spectrum of the radiation collimated respectively in the angles: $\theta_{\max} = 0.6$ mrad, leading to a bandwidth of 1%, $\theta_{\max} = 2.9$ mrad with $bw = 5\%$ and $\theta_{\max} = 3.9$ mrad with a corresponding bandwidth of 10%. The number of collimated photons per shot, about 5×10^3 in 1% bandwidth, increases to 4.7×10^4 for 5% of bandwidth and to 8.4×10^4 for 10% of bandwidth, giving respectively 5×10^{11}, 4.7×10^{12} and 8.4×10^{12} photons per second.

The dependence of the number of the scattered photons N_{ph}, bandwidth bw and average Stoke parameter $< S_x >$ on the collimation angle $\theta_{\max}$ is reported in Figure 5. The polarization [14] slightly decreases with increasing angles, but remains always in total well above 80% and even more in the collimated region. The photon intensity on a screen perpendicular to the electron beam at various distances are presented in Figure 6.

BRIXSINO

BriXsinO, as a reduced scale demonstrator of the modified push-pull folded ERL scheme with maximum energy of electrons 8-10 MeV. The layout of it presented in Figure 7. The specific goal of this demonstrator compact machine is to investigate RF mode stability issues in the CW energy recovery operating mode at high average current and very high repetition rate for the electron beam (up to 100 MHz), and related impacts on the electron beam quality (emittance, energy spread) due to beam break-up effects and beam loading. The main issues to be addressed by the test-bench demonstrator BriXsinO include: a) Achievement of electron beam quality (emittance, energy spread), as requested by an optimal luminosity in the ICS. b) Stability of RF, phasing

ISBN: 978-3-95450-217-2 doi:10.18429/JACoW-ERL2019-WEPNEC11

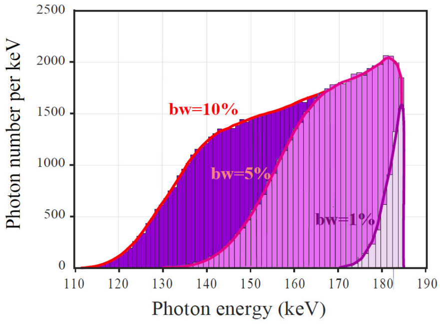

Figure 4: Spectrum of collimated scattered photons for the high energy case E_e = 100 MeV. Violet histogram: bw = 10%, $\theta_{\max}$ = 3.3 mrad; magenta histogram: bw = 5%, $\theta_{\max}$ = 2.08 mrad; grey histogram: bw = 1%, $\theta_{\max}$ = 0.6 mrad.

and timing of beam energy recovery in the folded push-pull ERL scheme. c) Photo-cathodes and RF-Gun capabilities to generate 100 MHz electron beams. d) Beam quality preservation with and without ERL (beam-breakup, beam loading). e) Options of two-color ICS generation. f) Radio-protection evaluation with deaccelerated beam after energy recovery.

CONCLUSIONS

In this paper the conceptual design of the compact X-ray Source BriXS (Bright and compact X-ray Source) is presented. BriXS , the first stage of Marix project, is a Compton X-ray source based on superconducting cavities technology for the electron beam with energy recirculation and on a laser system in Fabry-Pérot cavity at a repetition rate of 100 MHz, producing 20-180 keV radiation for medical applications. An energy recovery scheme based on a modified folded push-pull CW-SC twin Linac ensemble allows to sustain MW-class beam power with almost just one hundred kW active power dissipation/consumption. $5 \times 10^4 - 10^5$ collimated photons per shot in a bandwidth of $5 - 10\%$ are produced with 10^8 repetition rate for a total amount of more than 10^{13} photons per second, a performance comparable to the most advanced X-rays sources. An adjoint possibility is the production of two color radiation for imagine application.

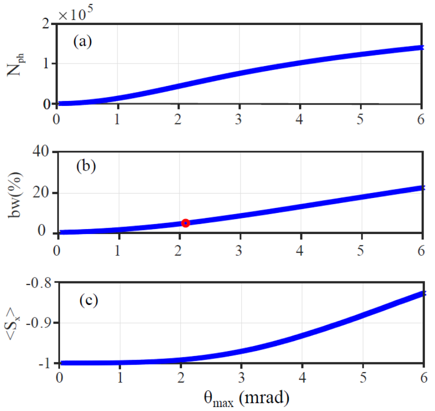

Figure 5: High energy case E_e = 100 MeV. (a) Number scattered photons, (b) bandwidth and (c) average Stoke parameter as function of collimator angular aperture $\theta_{\max}$.

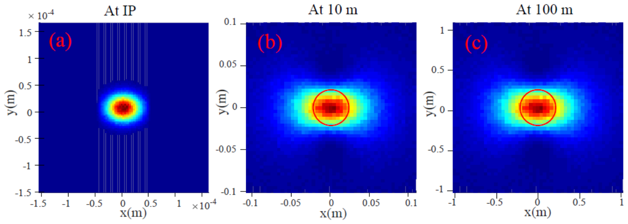

Figure 6: Photon intensity on a screen perpendicular to the electron beam. (a): at the interaction point (IP); (b): at 10 m from the source; (c) at 100 m. The red circle delimits the region inside the θ=1/γ acceptance angle.

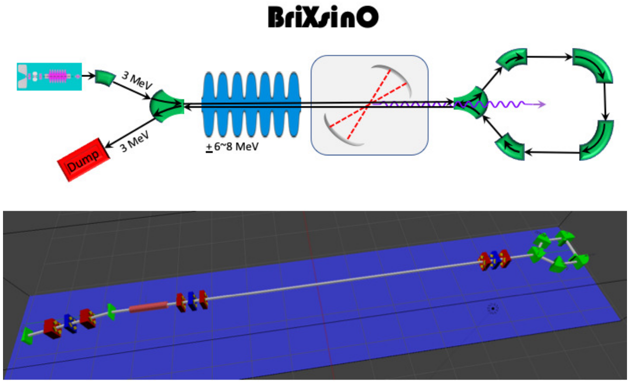

Figure 7: Layout of BriXsinO.

REFERENCES

[1] MARIX Conceptual Design Report, 2019, `www.marix.eu`

[2] L. Serafini, *et al.*, "MariX, an advanced MHz-class repetition rate X-ray source for linear regime time-resolved spectroscopy and photon scattering", NIM, A930, 2019, p 167-172. `doi:10.1016/j.nima.2019.03.096`

[3] L. Serafini *et al.*, "The MariX source (Multidisciplinary Advanced Research Infrastructure with X-rays)", in *Proceedings of IPAC2018*, Vancouver, Canada, 2018. `doi:10.18429/JACoW-IPAC2018-THPMF058`

[4] G. Hoffstaetter, *et al.*, "CBETA Design Report", USDOE - OSTI, BNL-114549-2017-IR, June 2017. `doi:10.2172/1412725`

[5] G. Mettivier, *et al.*, "[OA192] Kilovoltage rotational radiotheraphy with the marix/brixs source for partial breast irradiation", *Physica Medica*, Volume 52, Supplement 1, 2018, Page 74. `doi:10.1016/j.ejmp.2018.06.264`

[6] G Paternó, *et al.*, "Inverse Compton radiation: a novel x-ray source for K-edge subtraction angiography?", *Physics in Medicine & Biology*, V. 64, 2019. `doi:10.1088/1361-6560/ab325c`

[7] B. Dunham *et al.*, "Record high-average current from a high-brightness photoinjector", in *Applied Physics Letters* 102.3 (2013), p. 034105. `doi:10.1063/1.4789395`

[8] C. Gulliford *et al.*, "Demonstration of cathode emittance dominated high bunch charge beams in a DC gun-based photoinjector", in *Applied Physics Letters*, 106.9 (2015), p. 094101. `doi:10.1063/1.4913678`

[9] F. Sannibale *et al.*, "Upgrade Options Towards Higher Fields and Beam Energies for Continuous-Wave Room-Temperature VHF RF Guns", in *8th Int. Particle Accelerator Conf.(IPAC'17)*, Copenhagen, Denmark, 2017. `doi:10.18429/JACoW-IPAC2017-MOPIK019`

[10] I. Drebot, V. Petrillo, and L. Serafini, "Two-colour X-gamma ray inverse Compton back- scattering source", in *EPL (Europhysics Letters)*, 120.1 (2017), p. 14002. `doi:10.1209/0295-5075/120/14002`

[11] I. Drebot *et al.*, "Multi Colour X-Gamma Ray Inverse Compton Back-Scattering Source", in *Proceedings of IPAC2018*, Vancouver, Canada. `doi:10.18429/JACoW-IPAC2018-THPMF057`

[12] M. Borland, "Elegant: A flexible SDDS-compliant code for accelerator simulation", USDOE - OSTI, LS-287, 2000. `doi:10.2172/761286`

[13] P. Chen et al. "CAIN: Conglomerat d'ABEL et d'Interactions Non-lineaires". In: Nuclear Instruments and Methods in Physics Research Section A: Accelerators, Spectrometers, Detectors and Associated Equipment 355.1 (1995), pp. 107–110. `doi:10.1016/0168-9002(94)01186-9`

[14] V. Petrillo et al. "Polarization of x-gamma radiation produced by a Thomson and Compton inverse scattering". In: Physical Review Special Topics-Accelerators and Beams 18.11 (2015), p. 110701. `doi:10.1103/PhysRevSTAB.18.110701`

ISBN: 978-3-95450-217-2 doi:10.18429/JACoW-ERL2019-WEPNEC13

PRELIMINARY INVESTIGATIONS AND PRE-RESEARCH SCHEME OF HIGH AVERAGE CURRENT ELECTRON INJECTORS AT IMP

Q.T. Zhao†, Z.M. Zhang, J.C. Yang, H.W. Zhao
Institute of modern physics, Chinese academy of sciences, Lanzhou, China

Abstract

High average current electron injectors are desired by high average beam power SRF linacs. With respect to the different linac applications, different beam qualities are required. Two kinds of the electron guns are planned for future projects at IMP, one is thermionic electron gun dedicated for high average current, and another one is photocathode gun for high average current and high beam quality or even with high polarization. Current status and development of the high average current electron sources are investigated and summarized. The thermionic gun studies are planned and the feasible types of guns for the future Electron ion collider of China (EicC) project are also proposed. The pre-research of these required electron injectors is schemed, which will be the start of high average current and high-quality electron source development at Institute of modern physics (IMP), Chinese academy of sciences (CAS).

INTRODUCTION

High repetition rate, high average current electron injectors are required by many high average power superconducting radio frequency (SRF) electron linacs. These high average power SRF linacs are dedicated for different applications, such as high average power free-electron lasers (FEL) [1], medical isotope production [2], industry application [3], electron ion collider (EIC) [4], electron cooling for high energy heavy ions [5] and so on. With respect to different applications mentioned above, the requirements of the beam quality are different. The final beam quality required in the interaction region can be traced back to the requirements on the electron bunches from the injector, the first stage of the SRF linac. The electron injector, beginning with a cathode, is the source of the electrons. The quality, bunch length, and timing of the electrons injected into the first linac cavities are critical to determining the properties of the final high energy electron bunch.

Electron injectors can use several different types of cathodes to generate the electrons. One approach is to use a thermionic cathode, which can produce high average currents, but its shortage is hard to generate short bunch length and high repetition rate electron bunches, and the beam quality is mediate. Another approach is to use a photocathode, which is very popular and the promising method to produce high quality electron bunches and can be used for applications with high quality beam, such as FEL, EIC and electron cooling. However, the thermal issues, short lifetime, and drive-laser average power requirements currently present limitations for high average current photocathode injectors. Another unique advantage of the photocathode injector is capable to generate the polarization electron beam which is required for EIC. The electron gun can be classified into three types by the gun cavities and field modes, high voltage DC type, normal conducting RF and SRF type [6]. Due to the critical thermal loads for the normal conducting RF gun, it is not efficient and suitable for high average current and high average power electron source. Another issue of its poor vacuum condition, the normal conducting RF gun is not suitable for polarization electron source. Therefore, here we mainly talk about the high voltage DC gun and SRF gun.

The SRF linac projects are planned in IMP, one is dedicated with high average power application for medical isotope production and others are planned for EicC project [7], which has two SRF linacs, one requires polarized electron injectors with high beam quality and high polarization rate and another one needs high repetition rate, high bunch charge, high beam quality electron injectors for e-cooling of the high energy heavy ions. Different electron injectors are scheduled for the above projects based on the properties of the different types of the electron injectors. In this paper, we discussed the designed and required injectors' parameters for different application and proposed the solution and study plans of the injectors.

RF MODULATED THERMIONIC CATHODE HIGH VOLTAGE ELECTRON GUN

Due to the ability to generate high average current, long lifetime, and good stability and reliability, the thermionic cathode gun is preferred for many high average powers with mediate beam quality applications, like IR-FEL [8] and medical isotope production [9]. Normally, the thermionic cathode high voltage gun generates the direct current, which should be manipulated to short bunch with chopper and buncher devices, in order to match the RF acceleration. This method is inefficient and costly. Another method is gated the thermionic cathode high voltage DC gun with RF voltage, the generated electron bunch repetition rate is same with the frequency of the RF voltage, which is very convenient to generate the high repetition rate electron bunches, as high as 1 GHz [10]. This kind of gun is also considered to be the possible electron source for energy recovery linacs (ERLs) [11], like ERL based IR-FEL, electron cooling [12].

---

† Email address: zhaoquantang@impcas.ac.cn

ISBN: 978-3-95450-217-2 doi:10.18429/JACoW-ERL2019-WEPNEC13

The required electron gun parameters for medical isotope production are shown in table 1. With these parameters, the RF modulated thermionic cathode high voltage DC gun is selected due to its optimal properties mentioned above. In addition, it is already successfully used in other labs [13, 14].

Table 1: Designed RF Modulated Thermionic Cathode High Voltage DC Gun Parameters

Beam parameters	**Designed values**
Beam energy	300 keV
Average current	5 mA
Beam repetition rate (CW)	325 MHz
Bunch charge	16 pC
Energy spread	1%
Normalized rms emittance	<5 mm mrad

The sketch map of the RF modulated thermionic cathode high voltage DC gun is shown in figure 1(a). The voltage applied on the grid is Ug=Uc+Ub+Urf, where the Uc is the cathode voltage (-300 kV), Ub is the biased DC voltage to block the electrons extraction, Urf is the RF voltage used to extracting the electrons when the RF voltage is phased for positive polarization. Furthermore, the RF voltage can be designed with fundamental plus the high order harmonic RF voltage for generating the shorter bunches [15]. From figure 1(b), it is clearly shown that with this method it can generate the shorter bunch length electron beams (conducting angle is smaller).

For this gun design, except the normal challenges for high voltage DC gun, another big challenge is how to feed the RF voltage into the grid between the cathodes. Some lessons learned from TRUMF may be helpful [13]. One method is putting the RF voltage supply on the high voltage platform, which will make the gun body huge. Another method is putting the RF voltage supply on the ground and connected to the grid and cathode by ceramic wave guide and impedance matching network, which is not only used for feeding the RF voltage to the grid, but also for isolating the high voltage from the RF voltage generator. The gun body can be compact with this method. Currently, we planned to use the ceramic wave guide. The RF modulation test studies with 30 kV high voltages are under way. The gun structure design combined with beam dynamics simulation is studying with *SF* [16] and *GPT* [17] code.

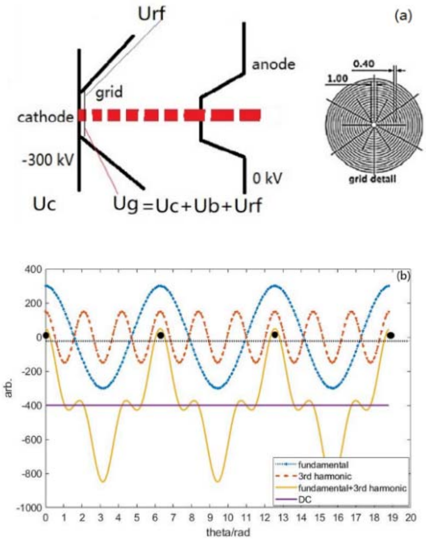

Figure 1: The sketch map and principle of RF modulated thermionic cathode high voltage DC electron gun: (a) principles (b) grid RF voltage for gating the shorter bunch electron emission.

PHOTOCATHODE INJECTORS

A project for a polarized electron-ion collider in China (EicC) is planned based on the high intensity heavy ion accelerator facility (HIAF) [18]. The HIAF is already starting construction. The preliminary design and layout the EicC are shown in figure 2. Two electron injectors are required for the EicC, one is polarized electron beam and another one is for ERL based electron cooling (e-cooler).

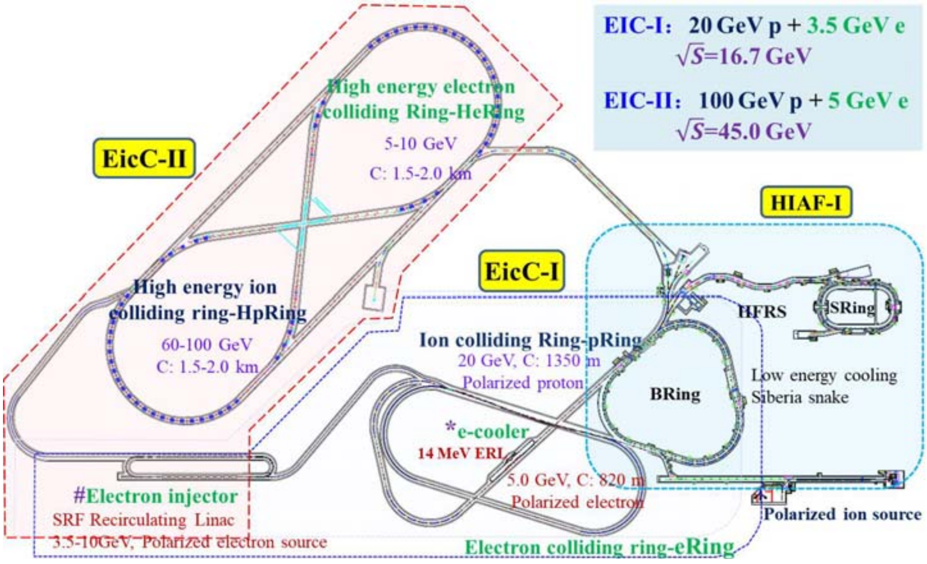

Figure 2: the preliminary blueprint of the EicC project and basic parameters. [Courtesy of J.C. Yang and G.D. Shen].

ISBN: 978-3-95450-217-2 doi:10.18429/JACoW-ERL2019-WEPNEC13

The preliminary electron injector parameters for the polarized electron beam are listed in table 2. Currently, for the polarized electron beam, due to its unique cathode material (GaAs) and some critical demands, especially for the high vacuum (10^{-10}pa) conditions, the high voltage DC photocathode electron gun is the most possible choice [19]. The photocathode for polarized beam is strained GaAs. Currently the QE, lifetime and polarization rate are still big challenges [20]. For high average current polarization electron gun, the cathode problem should be solved firstly. For the high voltage DC photocathode gun, the gun voltage higher is better for generating high quality beam, normally 500 kV is preferred. For polarized electron gun, 300-200 kV is chosen because of lower field emission and beam energy for longer cathode lifetime and easy polarization manipulation [21]. Here we choose 300 kV, the same with thermionic cathode gun. The SRF photocathode gun can produce high average current high-quality electron beam although the technology is not mature. The biggest challenge is the compatibility of the normal conducting cathode and the SRF cavity. The SRF gun for polarized electron source was proposed and tested by putting the GaAs photocathode in the SRF gun cavity but without beam commissioning [22]. There is still a long way to develop the SRF gun properly for polarization electron source.

Table 2: Preliminary Beam Parameters Requirement for EicC Electron Injector

Beam parameters	Required values
Beam energy	6-10 MeV
Bunch charge	0.1 – 0.5 nC
Micro-pulse repetition rate	30 MHz
Macro pulse length	50 us
Macro pulse repetition rate	20 Hz
Normalized rms emittance	<2 mm mrad
rms beam energy spread	<0.1%
rms bunch length	<50 ps
polarization	>80%

A high voltage DC photoemission electron gun followed by an SRF accelerating module is presently the best solution for generating high average power electron beams of moderate bunch charge, particularly for energy recovery linac. The general conceptual DC/SRF booster injector layout is shown in figure 3.

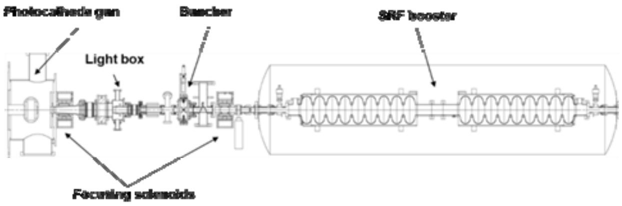

Figure 3: DC/SRF booster injector general layout [23].

The preliminary electron injectors' parameters for electron cooling ERL are listed in table 3. It requires high bunch charge, high repetition rate and high-quality CW operation mode specially. With high voltage DC photocathode gun, the bunch charge is mediate due to limited field gradient at cathode, normally the bunch charge less than 1 nC and currently the highest record is 2 nC [24]. Another potential type of electron source is SRF gun, which is capable to generate high bunch charge, for example BNL 112 MHz quarter ware resonator (QWR) SRF gun, the bunch charge can be as high as 10.7 nC [25, 26]. However, the SRF gun technology is still under development. Other critical parameters are the low emittance and small energy spread, which should be cared from beginning of the beam dynamics design. For electron cooling ERL injector, the QWR SRF photocathode gun is considered especially for high bunch charge. The "green" cathode is most promising for high average current electron source due to the high QE and high efficiency laser technology [27, 28]. Two types of photocathodes, GaAs (polarization and no polarization) and Cs-K-Sb are scheduled to be studied in the future.

Table 3: Preliminary Electron Injector Beam Parameters Requirement for EicC Electron Cooling

Beam parameters	Required values
Beam energy	6 MeV
Bunch charge	4 nC
rms bunch length	100 ps
Pulse repetition rate	0.3 – 3 MHz
Normalized rms emittance	<2.5 mm mrad
rms energy spread	$<5\times10^{-4}$

For the electron injector talked above, some common critical technologies are the same. For high voltage DC gun, thermionic cathode or photocathode, the high voltage supply and high voltage platform is same. For high voltage DC photocathode gun and SRF photocathode gun, photocathode fabrication and test system, laser system can be shared. Furthermore, for characteristic the injectors beam parameters, the test beam line is also proposed. Therefore, it is essential to set up an injector test facility for characteristic the beam parameters of different guns. The conceptual design and layout of the high average current electron injector lab is shown in figure 4, some auxiliary system can be reused for different gun test, such as booster, diagnostics, beam dump and so on.

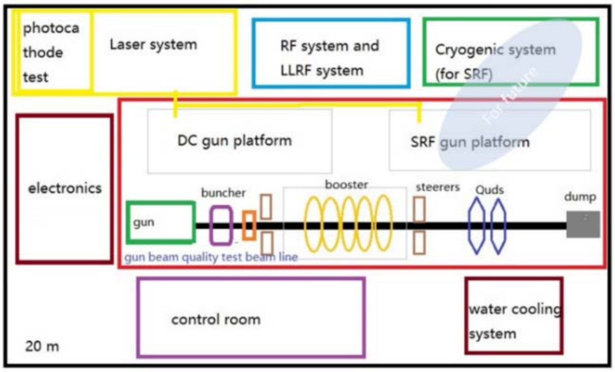

Figure 4: The conceptual design and layout of the high average current electron injector test lab.

SUMMARY

The high average current electron injectors' requirements for IMP projects are listed and discussed. The high voltage DC high average current injectors will be the first step to develop and start with RF modulated thermionic cathode type. The solution for polarized electron injector and electron cooling ERL injector is proposed and the difficulties to be conquered are also discussed. Furthermore, the high average current electron injector lab conceptual design and layout is shown and essential for test of different guns. The high voltage gun geometry design combined with beam dynamics optimization is under way and the design results will be reported soon.

REFERENCES

[1] D. Nölle, "COMMISSIONING OF THE EUROPEAN XFEL", *in Proc. of LINAC'18*, Beijing, Sep. 2018, pp. 994-999. doi:10.18429/JACoW-LINAC2018-FR2A02

[2] I. Bylinskii, *et al.*, "AN ELECTRON LINAC PHOTO-FISSION DRIVER FOR THE RARE ISOTOPE PROGRAM AT TRIUMF", *in Proc. of PAC09*, Vancouver, BC, Canada, 2009, pp. 1958-1960. paper:WE4PBC04

[3] G. Ciovati, *et al.,* "Design of a cw, low-energy, high-power superconducting linac for environmental applications", *Physical Review Accelerators and Beams* 21, 091601 (2018), doi: 10.1103/PhysRevAccelBeams.21.091601.

[4] V. Ptitsyn, *et al.*, "HIGH LUMINOSITY ELECTRON-HADRON COLLIDER ERHIC", *in Proc. of IPAC2011*, San Sebastián, Spain, pp. 3726-3728. paper: TUOAN2

[5] J. Kewisch *et al.*, "ERL FOR LOW ENERGY ELECTRON COOLING AT RHIC (LERC)", *in Proc. of ERL2015*, Stony Brook, NY, USA, pp.67-71. doi:10.18429/JACoW-ERL2015-WEICLH1058

[6] Triveni Rao and David H. Dowell, "AN ENGINEERING GUIDE TO PHOTOINJECTORS", 2013, https://arxiv.org/abs/1403.7539.

[7] X. Chen, "A Plan for Electron Ion Collider in China". Proceedings of science, https://arxiv.org/pdf/1809.00448.pdf.

[8] R.J. Bakker *et al.*, "1 GHz modulation of a high-current electron gun", *Nuclear Instruments and Methods in Physics Research A* 307 (1991) 543-552. doi:10.1016/0168-9002(91)90229-J

[9] S. Koscielniak *et al.*, "PROPOSAL FOR A ½ MW ELECTRON LINAC FOR RARE ISOTOPE AND MATERIALS SCIENCE", *in Proc. of EPAC08*, Genoa, Italy TUOCG03, pp. 985-987.

[10] A. Todd *et al.*, "HIGH-PERFORMANCE ACCELERATORS FOR FREE-ELECTRON LASER (FEL) AND SECURITY APPLICATIONS", *in Proc. of PAC2011*, New York, NY, USA, pp. 2196-2198 paper:THP034

[11] H. P. Bluem *et al.*, "HIGH BRIGHTNESS THERMIONIC ELECTRON GUN PERFORMANCE", *in Proc. of ERL2011*, Tsukuba, Japan, pp. 34-39. Paper:WG1010

[12] Vadim Jabotinski, Yaroslav Derbenev and Philippe Piot, "Thermionic Bunched Electron Sources for High-Energy Electron Cooling", MEIC Collaboration Meeting SPRING 2016, Jefferson Lab, March 29-31, 2016.

[13] F. Ames *et al.*, "OPERATION OF AN RF MODULATED ELECTRON SOURCE AT TRIUMF", in Proc. of IPAC2018, Vancouver, BC, Canada, pp. 4705-4707. doi:10.18429/JACoW-IPAC2018-THPML025.

[14] Wieland Schöllkopf, *et al.*, "The new IR and THz FEL facility at the Fritz Haber Institute in Berlin", http://fel.fhi-berlin.mpg.de/uploads/2015_SPIE_95121L.pdf .

[15] Phillip Sprangle *et al.*, "High average current electron guns for high-power free electron lasers", *Physical Review Special Topics - Accelerators and Beams* 14, 020702 (2011).

[16] Superfish (SF), https://laacg.lanl.gov/laacg/services/download_sf.phtml

[17] General Particle Tracking (GPT), http://www.pulsar.nl/index.htm

[18] http://hiaf.impcas.ac.cn/

[19] C. K. Sinclair, *et al.*, "Development of a high average current polarized electron source with long cathode operational lifetime", *Phys. Rev. STAB,* Vol.10, 023501 (2007). doi: 10.1103/PhysRevSTAB.10.023501

[20] Wei Liu, "Study of Advanced Photocathodes for Highly Polarized Electron Sources". doctor thesis (in Chinese), 2017.

[21] D Angal-Kalinin, *et al.*, "PERLE. Powerful energy recovery linac for experiments. Conceptual design report", *Journal of Physics G: Nuclear and Particle Physics* 45 (2018) 065003 (71pp). doi:10.1088/1361-6471/aaa171

[22] R. Xiang, *et al.*, "LOW EMITTANCE POLARIZED ELECTRON SOURCE BASED ON SUPERCONDUCTING RF GUN", *in Proc. of SRF2007*, Peking Univ., Beijing, China, TUP66, pp. 293-295.

[23] Ben Hounsell, "Design of the PERLE injector", LHeC/FCC-eh workshop, 27/06/2018-29/06/2018.

[24] Adam Bartnik, *et al.*, "Operational experience with nanocoulomb bunch charges in the Cornell photoinjector", *PHYSICAL REVIEW SPECIAL TOPICS—ACCELERATORS AND BEAMS* 18, 083401 (2015). doi:10.1103/PhysRevSTAB.18.083401

[25] T. Xin, *et al.*, "Design of a high-bunch-charge 112-MHz superconducting RF photoemission electron source", *Rev Sci Instrum* 87, 093303 (2016); doi:10.1063/1.4962682.

[26] Vladimir N Litvinenko, *et al.*, "Commissioning of CW FEL Amplifier for Coherent Electron Cooler (CeC)", https://fel2019.vrws.de/talks/moa06_talk.pdf.

[27] Martin A. H. Schmeißer *et al.*, "Towards the operation of Cs-K-Sb photocathodes in superconducting rf photoinjectors", *PHYSICAL REVIEW ACCELERATORS AND BEAMS* 21, 113401 (2018). doi:10.1103/PhysRevAccelBeams.21.113401

[28] W. Liu, *et al.*, "Record-level quantum efficiency from a high polarization strained GaAs/GaAsP superlattice photocathode with distributed Bragg reflector", *Appl. Phys. Lett.* 109, 252104 (2016). doi:10.1063/1.4972180

ISBN: 978-3-95450-217-2 doi:10.18429/JACoW-ERL2019-WEPNEC14

ELECTROMAGNETIC DESIGN OF A SUPERCONDUCTING DUAL AXIS SPOKE CAVITY*

Ya. V. Shashkov†, N. Yu. Samarokov
National Research Nuclear University MEPhI, Moscow, Russia
I.V. Konoplev, John Adams Institute, Department of Physics, University of Oxford, Oxford, UK

Abstract

Dual axis superconducting spoke cavity for Energy Recovery Linac application is proposed. Conceptual design of the cavity is shown and preliminary optimizations of the proposed structure have been carried out to minimize the ratio of the peak magnetic and electric fields to the accelerating voltage. The new design and future work are discussed.

INTRODUCTION

In order for the ERL based sources of coherent THz and X-ray radiation to be widely accepted a truly compact (10 m^3), high average current ERLs are required. The demand for the compactness and efficiency can be satisfied by superconducting RF Energy Recovery Linear accelerators (SRF ERL).

The application of two-axis cavity made of identical elliptical shaped RF superconducting accelerating cells for the ERLs applications was proposed by Noguchi and Kako in 2003 [1] and was revisited by Wang, Noonan, and Lewellen in 2007 [2, 3]. The advantage of the asymmetric dual axis system to localise HOMs was only recently realised [4-6] and it was suggested to use for a number of the ERL based applications.

The spoke cavity, originally invented for acceleration of ions and protons, can be used for electron acceleration and there is a growing interest in applications of the multispoke cavities [7]. In this paper, we present the conceptual design of the dual axis asymmetric spoke cavity, optimizations of the cavity shape and preliminary results of the cavity studies. The attractive features of RF superconducting spoke cavities include: 1) the operating frequency of the spoke cavity mainly depends on the spoke length; 2) high cavity stiffness reduces the fluctuation of the cavity resonant frequency due to microphonics; 3) the minimisation of the frequency fluctuations can decrease the required RF power and soften the tolerances required for the construction of the HP input coupler. The spoke cavity is compact as compared with conventional elliptical cavity and if the outer size of a spoke cavity is similar to that of the elliptical cavity, the operating frequency of the spoke cavity is nearly half of that the elliptical cavity. There are a number of advantages of using the low frequency including possibility of utilization of the solid-state power sources as well as operation at higher 4.2 K temperature. Cell coupling of the spoke cavity is stronger than that of elliptical cavity and higher coupling coefficient means robustness with respect to the manufacturing inaccuracy and higher mechanical stability. The fields on the outer surface of a spoke cavities can be relatively small allowing for both the fundamental power coupler and higher-order mode couplers to be located on the outer surface rather than on the beam line. This means better "packing" as couplers are on outer conductor. We note that the tuning of a spoke cavity is complex and demonstration of the ideal design is outside the scope of this work. The aim of this paper is to demonstrate conceptual design with the fields comparable to those observed for a single axis spoke cavity. We focus on a several concepts of the dual axis spoke cavity design and discussion of the advantages and disadvantages of the structures. The schematic diagrams showing merging of the two cavities into the dual axis spoke structure is presented on Fig. 1.

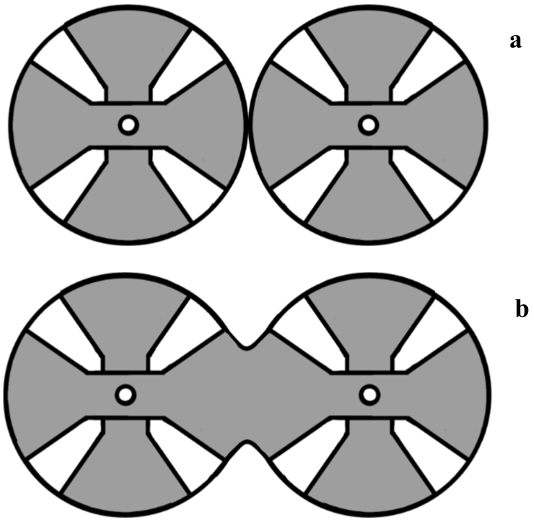

Figure 1: Schematic illustration of observing the dual axis spoke cavity via merging of two cavities (a) before merging and (b) after merging.

TUNING PROCESS

High surface fields in superconducting cavities are highly undesirable because of the detrimental effects on the cavity and ERL performance. At high surface magnetic fields, quenching can occur, and high surface electric fields can cause electron field emission and RF breakdown. As a result, when comparing the performance of the cavities, normalized surface fields are often discussed.

Spoke cavities have a large number of geometric parameters which often influence RF properties. The cavity optimization, therefore is multi-parametric process with a large parameter space to be explored. As a result, the tuning of the cavity to satisfy many parameters takes place in several stages.

---

* The reported study was funded by RFBR according to the research project 18-302-00990

ISBN: 978-3-95450-217-2 doi:10.18429/JACoW-ERL2019-WEPNEC14

Stage 1: Single Axis Spoke Cavity

In order to get initial geometrical parameters of the structure the tuning of a single period, single axis spoke cavity (Fig. 1a) has to be performed. In Fig. 2a the cell tuned. to frequency of 325 MHz is shown. One notes that at this frequency the solid-state RF power supplies are now available. Spoke parameters were optimized in order to achieve E_s/E_a and B_s/E_a values as in [7]. Distribution of electric and magnetic field on the cavity surface are presented in Figs. 2b and 2c. Electrodynamic characteristics of this structure are presented in Table 1.

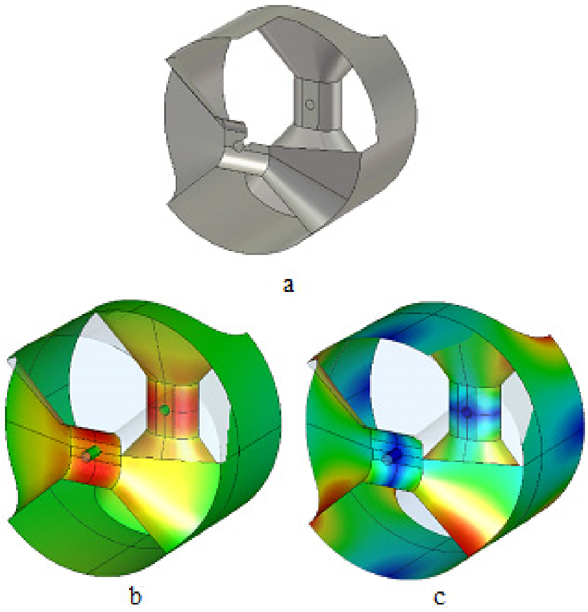

Figure 2: Single axis spoke cavity (a); distribution of electric (b) and magnetic (c) field on the cavity surface.

Stage 2: Bridge Region

The second goal was to tune the bridge region of the structure i.e. the region where the two cavities are merged. Distribution of the electric and magnetic fields on the cavity surfaces are presented on Figs. 3a and 3b.

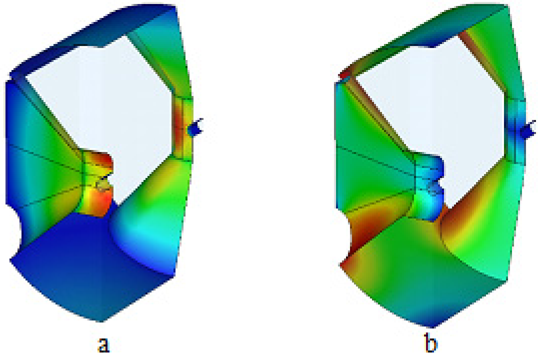

Figure 3: Distribution of electric (a) and magnetic (b) field on the cavity surface.

We note that the operating frequency of the merged structure is 3 MHz different from the initial structure but this can be compensated by changing geometry of the base of the spokes i.e. possible minor alteration without change of the main geometry. Electrodynamic characteristics of this structure are presented in Table 1.

Stage 3: Single Period of Dual Axis Spoke Cavity

The single axis spoke cavity and bridge region were connected to form a single period dual axis spoke cavity. The distributions of electric and magnetic fields on the cavity surfaces are presented on Figs. 4a and 4b.

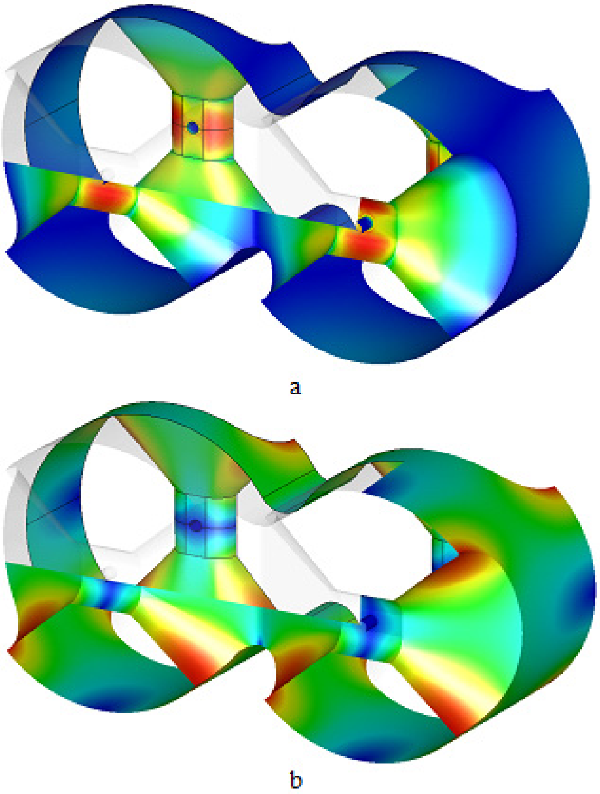

Figure 4: Distribution of the electric (a) and magnetic (b) fields on the cavity surfaces.

The EM characteristics of this structure are presented in Table 1.

Table 1: Electromagnetic (EM) Characteristics of the Single Cell Spoke Cavity, Bridge Region and the Single Period of Dual Axis Spoke Cavity

EDC	**Single**	**Bridge**	**Dual**
f, MHz	325	322.88	324.492
R/Q, Ohm	207.7	208.7	103.64
Es/Ea	2.84	2.84	2.81
Bs/Ea, mT/MV/m	7.82	7.85	7.78
V[*], MB	6.5e5	6.5e5	4.6e5

[*] At stored energy J = 1 W

It can be noted that E_s/E_a and B_s/E_a are almost the same for the single and dual axis spoke cavities.

Stage 4: End Cavities Tuning

After merging the sections, the tuning of the end cavity cells (Fig. 5) has been performed.

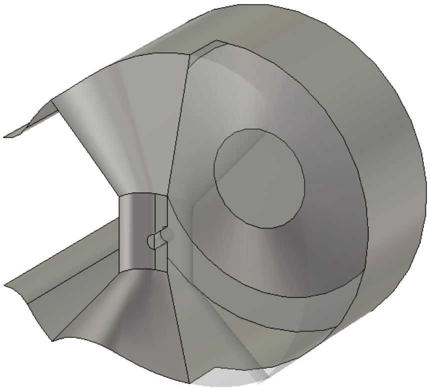

Figure 5: The end cell of the dual axis spoke cavity.

The EM characteristics of this structure are presented in Table 2.

Table 2: Electrodynamic Characteristics of End Cell of Dual Axis Spoke Cavity

Parameter	**End cell**
f, MHz	326.55
R/Q, Ohm	235.1
Es/Ea	2.69
Bs/Ea, mT/MV/m	6.63
V*, MB	6.9e5

*At stored energy J = 1 W

Stage 5: Final Assembly

Finally, to construct the cavity all the parts have been assembled (Fig. 6).

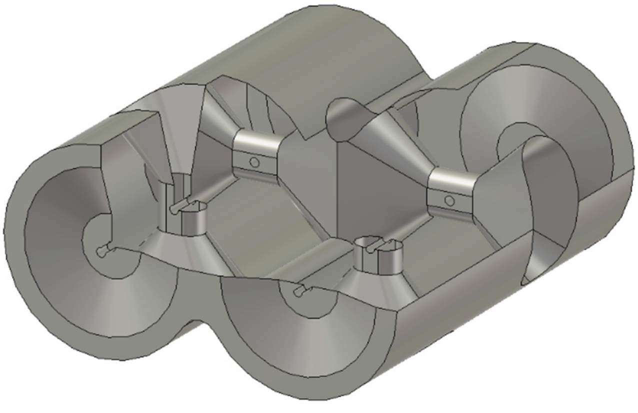

Figure 6: Dual axis spoke cavity.

The contour plots of the electric (a) and magnetic (b) fields in the dual axis spoke cavity are presented in Fig. 7.

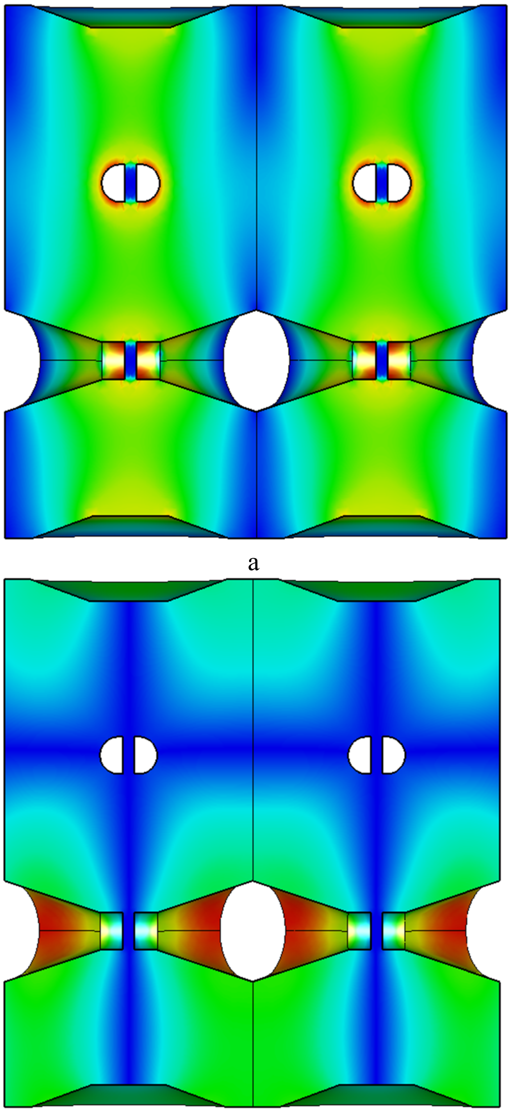

a

b

Figure 7: The contour plots illustrating the distribution of electric (a) and magnetic (b) field in dual axis spoke cavity.

The distributions of the electric fields on the both axis of the structure are presented on the Fig. 8.

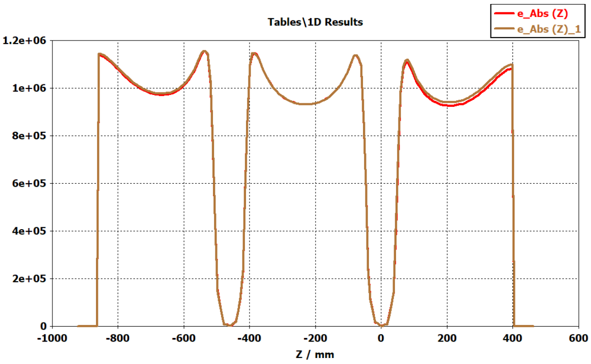

Figure 8: The distributions of the electric fields on the both axis of the structure.

The EM characteristics of the assembled cavity are presented in the Table 3:

Table 3: The EM Characteristics of the Cavity

Parameter	**Full cavity**
f, MHz	326.73
R/Q, Ohm	336.21
Es/Ea	2.82
Bs/Ea, mT/MV/m	7.38
V^*, MB	8.3e5
k_{cc}, %	5.8

*At stored energy J = 1 W

CONCLUSION

The concept of the dual axis spoke cavity is presented and the steps of its optimizations are shown. The cavity design is complex and requires gradual optimizations of all the parts. During the optimization the values of the E_s/E_a and B_s/E_a has been achieved to be almost the same as for a conventional single axis spoke cavity.

REFERENCES

[1] S. Noguchi and E. Kako, “Multi-Beam Accelerating Structures”, in *Proc. SRF'03*, Lübeck, Germany, Sep. 2003, paper TUP16, pp. 317-319.

[2] C. Wang, J. Noonan, and J. Lewellen, “Dual-Axis Energy Recovery Linac”, in *Proc. ERL'07*, Daresbury, UK, May 2007, paper 18, pp. 122-125.

[3] C.-X. Wang, “Conceptual design considerations of a 5-cell dual-axis SRF cavity for ERLs”, in *Proc. SRF'07*, Beijing, China, Oct. 2007, paper WEP59, pp. 641-645.

[4] S. U. De Silva, J. R. Delayen, A. Hutton, F. Marhauser, and H. Park, “Electromagnetic Design of a Superconducting Twin Axis Cavity”, in *Proc. LINAC'16*, East Lansing, MI, USA, Sep. 2016, pp. 203-205. `doi:10.18429/JACoW-LINAC2016-MOPLR030`

[5] R. Ainsworth, G. Burt, I. V. Konoplev, and A. Seryi, “Asymmetric dual axis energy recovery linac for ultrahigh flux sources of coherent x-ray and THz radiation: Investigations towards its ultimate performance”, *Phys. Rev. Accel. Beams*, vol. 19, p. 083502, Aug. 2016. `doi:10.1103/PhysRevAccelBeams.19.083502`

[6] I.V. Konoplev, K. Metodiev, A. J. Lancaster, G. Burt, R. Ainsworth, and A. Seryi, “Experimental studies of 7-cell dual axis asymmetric cavity for energy recovery linac”, *Phys. Rev. Accel. Beams*, vol. 20, p. 103501, Oct. 2017. `doi:10.1103/PhysRevAccelBeams.20.103501`

[7] C. S. Hopper and J. R. Delayen, “Superconducting spoke cavities for high-velocity applications”, *Phys. Rev. ST Accel. Beams,* vol. 16, p. 102001, Oct. 2013. `doi:10.1103/PhysRevSTAB.16.102001`

ELECTRON OUTCOUPLING SYSTEM OF NOVOSIBIRSK FREE ELECTRON LASER FACILITY– BEAM DYNAMICS CALCULATION AND THE FIRST EXPERIMENTS

Y.V. Getmanov[1,2†], O.A. Shevchenko[1], N.A. Vinokurov[1,2], A.S. Matveev[1,2]
[1] Budker INP SB RAS, 11 ac. Lavrentiev prosp., Novosibirsk, Russia, 630090
2 Novosibirsk State University, 1 Pirogova St., Novosibirsk, Russia, 630090

Abstract

The radiation power of the FEL with optical cavity can be limited by the overheating of reflecting mirrors. In the electron outcoupling scheme electron beam radiates the main power at a slight angle to the optical axis. For this, it is necessary to divide undulator by dipole magnet at least for two parts – the first for the electron beam bunching in the field of the main optical mode, and the second for the power radiation by deflected beam.

Electron outcoupling system is installed on the third FEL based on the multiturn energy recovery linac of the Novosibirsk Free Electron Laser facility (NovoFEL). It consists of three undulators, dipole correctors and two quadrupole lenses assembled between them. There are two different configurations of the system since the electrons can be deflected in either the second or the third undulator.

The electron beam dynamics calculations and the results of the first experiments are presented.

INTRODUCTION

Free electron lasers (FELs) are the unique source of monochromatic electromagnetic radiation. Radiation is generated due to motion of relativistic electron bunches into the magnetic field of undulator. In contrast to types of lasers, FEL allows to receive radiation of any given wavelength in the operating range, and this wavelength can be relatively quickly tuned [1]. The efficiency of FEL is tenths of a percent of the electron beam average power therefore the use of the energy recovery linacs (ERLs) seems to be the most optimal. The maximum achievable power of an FEL with an optical cavity, aside from the parameters of the electron beam, can be limited by the overheating of reflecting mirrors. To prevent this effect there was proposed the electron outcoupling system [2,3]. Numerical calculations of the such configurations were carried out by various groups of researchers [4-7].

The main idea of the electron outcoupling scheme is to radiate the main part of the power into the small angle to the FEL optical axis, thereby avoiding mirrors overheating. The principle of operation of the schemee is the following (Fig. 1): the electron beam (1) is turned by the dipole magnet (2) into the undulator (3); bunched by interaction with electromagnetic field of the fundamental mode (6) and then deflected by small angle (5) direct to the next undulator (4); emits the main power of the radiation (8). This radiation transported (7) to the user stations. Then the used electron bunch (9) is removed from the system by magnet (2).

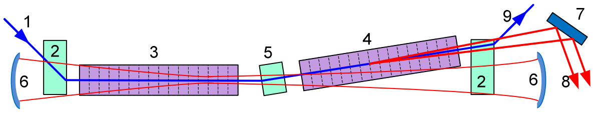

Figure 1: 1 – initial electron beam; 2 – bending magnets; 3 – bunching undulator; 4 – radiating undulator; 5 – beam rotation magnet; 6 – optical mirrors and fundamental mode; 7 – electron outcoupling mirror; 8 – main radiation power; 9 – used electron beam.

NOVOFEL FOUR-TRACK ERL

NovoFEL (Fig. 2) is the high-power terahertz and infrared radiation source [8]. Radiation can be generated by three different FELs using an electron beam of three different ERL configurations. The main parameters of the third FEL based on four-track ERL (Fig. 3) are presented in Table 1. The third FEL operates as user facility since 2015. It consists of three permanent magnet undulators with the variable gap (see Fig. 4) and an optical cavity. This undulator separation into three parts was made, in particular, for experiments with electron outcoupling system. For this purpose, the quadrupole lenses and additional dipole correctors are installed in the empty spaces between the undulators and at the ends of the undulators (Fig. 5). The feasibility study of using this scheme in the NovoFEL facility was described in [9].

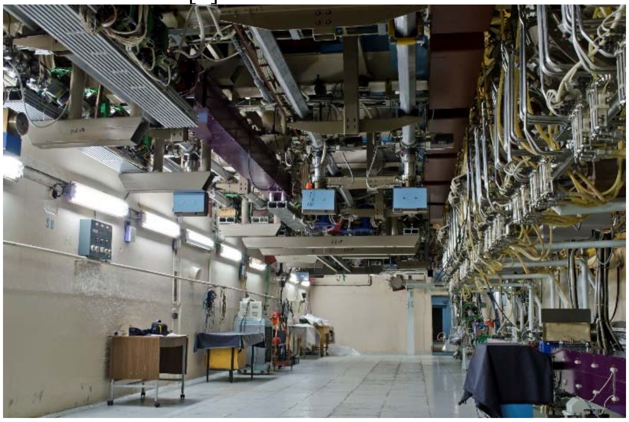

Figure 2: Accelerator hall and the tracks (on the ceiling) of the four-pass NovoFEL ERL.

---

† y_getmanov@mail.ru

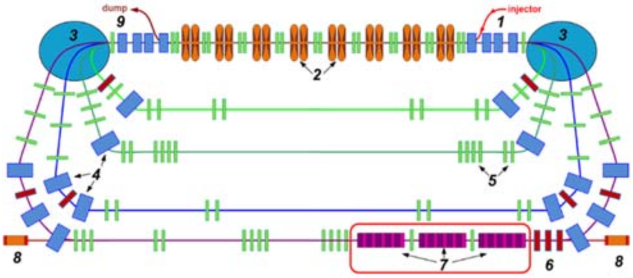

Figure 3: Scheme of NovoFEL installed on a four-track ERL:1- electron injector, 2 - NRF cavities, 3 – round dipole magnet, 4 - rectangular magnets, 5 – quadrupole lenses with dipole correctors, 6 - quadrupole lenses, 7 - undulators of the electron outcoupling system, 8 - mirrors of the optical cavity, 9 - electron dump.

Table 1: NovoFEL Facility Parameters

parameter	value
Electron energy	39 MeV
Average current	3 mA
Peak current	100 A
Norm. Emittance	30 μm×rad
Wavelength	~9 μm
Energy spread	~2%
Number of undualtors	3
Undulator periods	28
Period length	0.06 m
Outcoupling angles diapasons (horizontal. and vertical)	1.76 – 5.24 mrad -3.23 – 3.23 mrad
Optical cavity loss	0.135
Optical cavity length	40 m

Figure 4: Undulators of the third FEL (7 on the Fig. 3).

CONTINIOUS BENDING REGIME

In contrast with the scheme on the Fig.1 in the NovoFEL electron outcoupling system the electron bunches are supposed to turn out from the optical axis while the undulators are mounted on it. In this case, one of the important conditions for lasing into the outcoupling angle is the conservation of the electron bunching in the turn between bunching and radiating undulators. It can be achieved by using the achromatic bend.

The magnetic system of the bend in presented on Fig. 5. Since the quadrupole lens is not symmetrically with respect to the location of the dipole correctors and moreover, the reference trajectory of the electrons depends on deflecting angles, it is necessary to introduce an additional dipole component of the magnetic field in the quadrupole. In other words, to achieve achromatic constraints it is required to shift the quadrupole lens from optical axis. On the facility the lens was shifted by 2 cm. That displacement does not significantly affect the operation in ordinary laser regimes for users, since in such configurations the currents of quadrupole lenses between undulators are usually small.

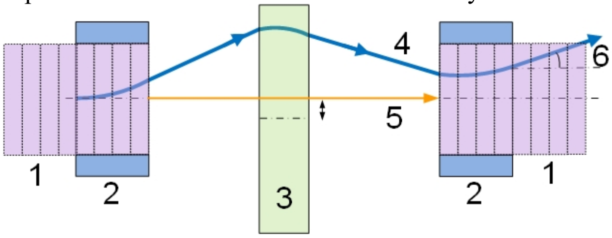

Figure 5: Electron bunch trajectory in the magnetic system between undulators: 1 – undulator, 2- dipole corrector, 3 – shifted quadrupole lens, 4 – electron bunch, 5 – light beam, 6 – outcoupling angle.

As well as electron bunch deflected from axis of symmetry, the additional dipole field component in quadrupole should be taken into account in achromatic conditions calculation. They form two equations for transport matrix elements

$$R_{16}(\alpha_1, \alpha_2(K_1, \alpha_1), \alpha_3, K_1\ ) = 0, \qquad (1)$$

$$R_{26}(\alpha_1, \alpha_2(K_1, \alpha_1), \alpha_3, K_1) = 0, \qquad (2)$$

where R – transport matrix between two undulators, α_1, α_3 – deflecting angles in dipole correctors and α_2 – in the dipole field component of the quadrupole. This field component depends of course on K_1 strength parameter of the lens, which itself influences on dispersion condition in the bend. The deflecting angels should give in total the outcoupling angle α_0

$$\alpha_0 = \alpha_1 + \alpha_2(K, \alpha_1) + \alpha_3. \qquad (3)$$

The outcoupling scheme can be realized by two different options. The electrons can be deflected in the second or in the third undulator (Fig. 6). In the case second undulator the bended electron beam should return back to the optical axis at the third undulator to enhance the main radiation mode of the optical cavity. This adds an additional condition to the system of equations (1-3), because the electron gets extra horizontal deviation while moving through the second undulator with outcoupling angle. It looks hard to satisfy all these limitations with today's magnetic fields of dipole correctors. Therefore, at this time, we concentrate on the outcoupling scheme from the third undulator.

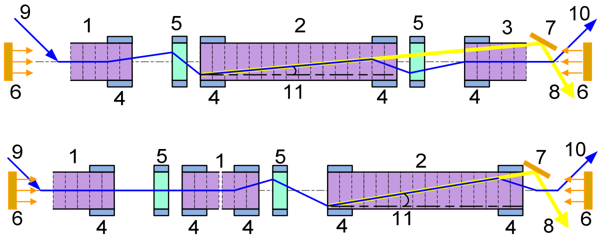

Figure 6: Two possible variants of electron outcoupling scheme – deflecting in the second (top figure) or in the third undulator (bottom figure): 1 – bunching undulator, 2 – radiation undulator, 3 – undulator, 4 – dipole correctors, 5 – quadrupole lenses, 6 – optical mirrors and fundamental mode, 7 – mirror for main radiation, 8 - main radiation, 9 – initial electron beam, 10 – used electron beam, 11 – deflection angle.

The experience in tuning the FEL regime with a deflected beam shows that lasing on two undulators is a feasible but rather difficult goal [10]. Since the Twiss parameters at the beginning of the undulator's system are not well defined the calculated optic regime may not provide enough amplification for lasing. Therefore, to facilitate the adjustment of the structure, it was proposed to make a continuous achromatic bend from zero to the angle of electron outcoupling (Fig. 5). In this case, the lasing starts in more simplified mode with three undulators then slightly tune to the regime with deflected electron beam at the last undulator. The continuous bend regimes were calculated by Elegant code (Fig. 7) [11]. As it shown by calculations to achieve the achromatic conditions the much higher magnetic fields of the dipole correctors are necessary than to obtain only deflection angle.

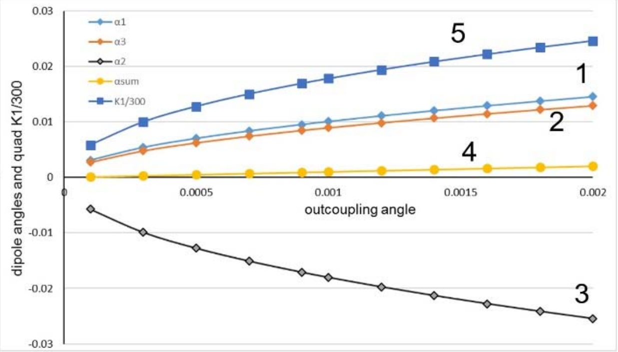

Figure 7: Achromatic bends parameters for the different outcoupling angles: 1,2 – dipole corrector's angles, 3 – angle of the shifted quadrupole, 4 – total angle, 5 – K_1 parameter of the quadrupole.

In the next experiments it is supposed to configure the optimal Twiss parameters by the beam diagnostic system using the pictures from radiation-resistant camera.

The beam profile after the lasing can be measured by detecting the synchrotron radiation from the dipole magnet [12]. The diagnostic system for the electron bunch longitudinal distribution measurements is currently under installation and launching [13].

ELECTRON BUNCHING AND RADIATION

The numerical simulation of the electron beam dynamics and radiation in the undulators was made in the Genesis code [14]. Firstly, in the mode of the continuous electron beam the optimal Twiss parameters calculated by Elegant code were set (Fig. 7). The achieved electron beam distribution after each undulator transformed by transport matrix from optic regime. It should be noted that dipole correctors are installed directly on undulators, therefore, the transport matrix, calculated separately for rotation, must be converted to real geometry (Fig. 5)

$$M_b = M_{Ld}^{-1} M_{bend} M_{Ld}^{-1}, \tag{4}$$

where M_b – transport matrix between undulator, M_{LD} – drift matrix with length of the dipole corrector, M_{bend} – matrix of the bend.

The light beam between the undulators flies along a straight path, while the electron beam moves along a curved, and also with a speed βc. Therefore, the electron beam should get additional phase to the light with the following value

$$\Delta\varphi = \frac{2\pi}{\lambda}\left(\frac{Ltr-2LD}{\beta} - Ldr\right), \tag{5}$$

where λ – radiation wavelength, Ltr – length of the electron trajectory in the bend, LD – length of the dipole corrector, Ldr – the distance between undulators. This phase shift can achieve the sufficient values, more than several pi, therefore the variation of the resonance radiation wavelength is necessary in the calculation.

The radiation obtained after the passage all three undulators was decomposed into the main mode of the optical cavity and the remaining field. The power of the fundamental mode was transferred to the beginning of the calculation (to the input of the first undulator) taking into account previously determined losses of the optical system [15]. This procedure was repeated until a stable radiation regime was achieved.

At the first, numerical simulation of the FEL lasing in ordinary operation modes was made (without deflection of the electron beam). The calculated angular distribution after third undulator is shown on the Fig. 8. Numerical simulations by Genesis code also confirm that the fundamental mode (1 at Fig. 8) does not effect on the outcoupling mirrors (area 3 at Fig. 8). In the opposite of the main radiation mode, the part of other high order modes (2 at Fig. 8) falls on the outcoupling mirror even without the electron deflection in undulator. These calculations are planned to be verified experimentally. In the special regime with short lasing pulses we are going to detect the radiation attenuation fronts after optical cavity and outcoupling mirror. Such FEL lasing mode is realized by special modulation regime of NovoFEL DC-gun [16].

ISBN: 978-3-95450-217-2 doi:10.18429/JACoW-ERL2019-WEPNEC16

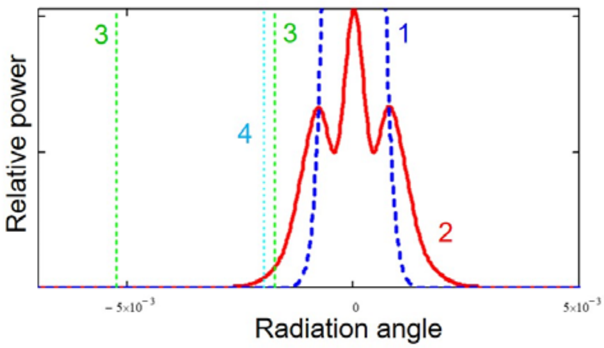

Figure 8: Angular power distribution of the electron beam in the FEL without deflecting in the undulator: 1 – fundamental mode, 2 – high order modes, 3 – area of the outcoupling mirror, 4 – electron outcoupling angle.

As already mentioned, the magnetic field of the dipole correctors should be much higher than requirements for total deflecting angle. Therefore, it is not possible to achieve the achromatic conditions at each angle. The obtainable outcoupling angle is 2 mrad. The angular power distribution in the regime with such deflection in the third undulator is shown on the Fig. 9. The enhancement of radiation power can be observed in the area of electron outcoupling mirror. However, the increasing is not significant relative to the rest of the power.

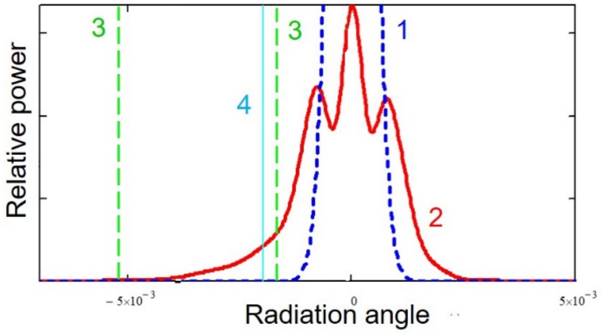

Figure 9: Angular power distribution of the electron beam in the FEL with deflecting in the third undulator: 1 – fundamental mode, 2 – high order modes, 3 – area of the outcoupling mirror, 4 – electron outcoupling angle.

The Fig. 10 shows the angular power distribution generated by electrons in the last undulator. The power is radiated to the desired angle, but it is much lower than scattered high order radiation modes from other two undulators. The possible reason is the electron bunching decreases rapidly while passing the last undulator (3 at Fig. 11). On the Fig. 11 is shown the bunching factor calculated by Genesis code along the optical axis (1, 2 and 4) and along the deflected beam trajectory (3). In spite of the achromatic bends, it changed at the areas 5 and 6 due to non-zero R_{56} elements of the transport matrix.

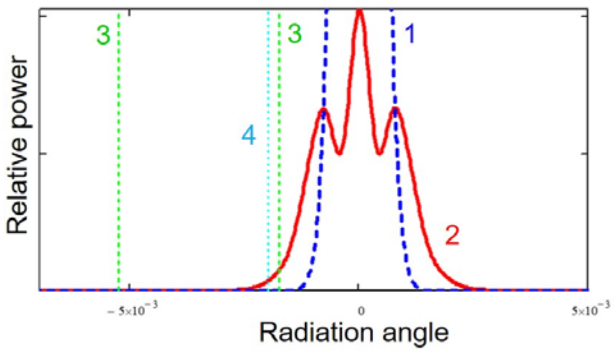

Figure 10: Angular power distribution: electron bunches achromatic bended before third undulator.

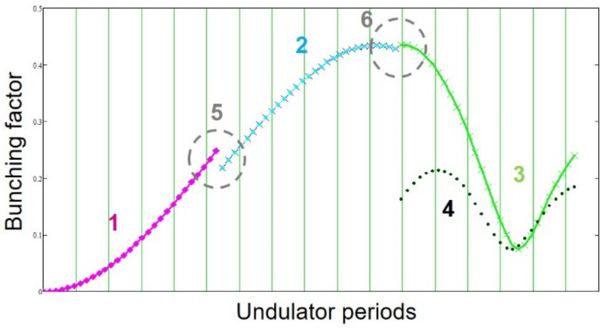

Figure 11: Bunching factor in the undulators system: 1 – first undulator, 2 –second undulator, 3 – bunching factor in the third undulator, calculated along the electron beam propagation axis, 4 – bunching factor, calculated along the optical axis by Genesis code, 5 – drift between 1-st and 2-d undulators, 6 – achromatic bend between 2-d и 3-d undulators.

CONCLUSION

The continuous achromatic bend from ordinary lasing regime to the desired deflected trajectory of the electron beam in the third undulator was calculated. Another issue related to this tuning is the compensation of the bunch perturbation due to the lasing the existing optics before the electrons return to the common track of the ERL.

The angular distribution of the radiation power in the system of electron outcoupling from the third undulator was calculated. It shows that the power of the high order modes from first and second undulators falling on the outcoupling mirror comparable with the radiation from deflected electron beam in the last undulator.

For ordinary FEL lasing regime with three undulators the radiation power of the high order modes at the outcoupling mirror is much higher than scattered on it fundamental optical cavity mode. The ration between these quantities is supposed to be checked in future experiments.

ACKNOWLEDGEMENT

This work was supported by the Russian Science Foundation grant 18-72-00123.

REFERENCES

[1] N. A. Vinokurov, O. A. Shevchenko "Free electron lasers and their development at the Budker Institute of Nuclear Physics, SB RAS" *Phys. Usp.,* vol. 61, pp. 435–448, Feb. 2018. `doi:10.3367/UFNe.2018.02.038311`

[2] N.G. Gavrilov *et al.*, "Observation of mutual coherence of spontaneous radiation from two undulators separated by an achromatic bend", *Nucl. Instr. and Meth.* A, Vol. 304, pp. 63-65, 1991. `doi:10.1016/0168-9002(91)90821-7`

[3] G.N. Kulipanov, A.S. Sokolov, N.A. Vinokurov "Coherent undulator radiation of an electron beam, microbunched for the FEL power outcoupling" *Nucl. Instr. and Meth.* A, Vol. 375, pp. 576-579, 1996. `doi:10.1016/0168-9002(96)00038-1`

[4] D.D. Quick, *et. al.*, "Phase space simulations of electron bunching and power output in the Novosibirsk / SELENE FEL", *Nucl. Instr. and Meth.* A, Vol. 341, pp. ABS92-ABS93, 1994. `doi:10.1016/0168-9002(94)90462-6`

[5] J. Blau, *et. al.*, "Three dimensional simulations of the Novosibirsk/SELENE FEL" *Nucl. Instr. and Meth.* A, Vol. 341, p. ABS94, 1994. `doi:10.1016/0168-9002(94)90463-4`

[6] S.J. Hahn, *et. al.*, "Time-dependent multi-dimensional simulation studies of the electron output scheme for high power FELs" *Nucl. Instr. and Meth.* A, Vol. 358, pp. 167-170, 1995. `doi:10.1016/0168-9002(94)01262-8`

[7] S.J. Hahn and W.M. Fawley, "Multidimensional simulation studies of the SELENE FEL oscillator/buncher followed by a radiator/amplifier output scheme", P*roc. of SPIE*, Vol. 2376, pp. 116-124, 1995. `doi:10.1117/12.208198`

[8] G.N. Kulipanov, *et al.* "Novosibirsk Free Electron Laser—Facility Description and Recent Experiments", *IEEE Trans. Terahertz Science and Tech*., Vol. 5 (5), pp. 798-809, 2015. `doi:10.1109/TTHZ.2015.2453121`

[9] A.N. Matveenko, *et al*. "Electron outcoupling scheme for the Novosibirsk FEL," *Nucl. Instr. Meth. A*, Vol. 603, pp. 38–41, 2009. `doi:101016/jnima200812228`

[10] Y.V. Getmanov, et al. "Comparing and Assessing the Efficiency of Lasing for Different Configurations of the Electron Outcoupling System of the Novosibirsk Free Electron Laser", Bulletin of the Russian Academy of Sciences: Physics, Vol. 83(2) pp 175-179, 2019. `doi:10.3103/S1062873819020138`

[11] M. Borland "Elegant: A Flexible SDDS-Compliant Code for Accelerator Simulation", *Advanced Photon Source* LS-287, 2000. `doi:10.2172/761286`

[12] V.M. Borin, *et al*. "Measurements of Beam Parameters at the Last Track of the ERL-Based Novosibirsk Free Electron Laser", *in Proc. IPAC'19*, Melbourne, Australia, May 2019, pp. 2632—2634. `doi:10.18429/JACoW-IPAC2019-WEPGW068`

[13] Meshkov O. *et al.* Picosecond dissector with crossed sweep and optimization of picosecond dissector parameters. *Proceedings of SPIE*, 11051, SPIE, 2019. `doi:10.1117/12.2524826`

[14] S. Reiche, "GENESIS 1.3: a fully 3D time-dependent FEL simulation code" *Nucl. Instr. Meth.* A, V. 429, pp. 243-248, 1999. `doi:10.1016/S0168-9002(99)00114-X`

[15] Kubarev, V.V., Doctoral (Phys.–Math) Dissertation, Novosibirsk: Budker Inst. of Nuclear Physics, 2015.

[16] Shevchenko O. *et a*l. "Electronic Modulation of THz Radiation at NovoFEL: Technical Aspects and Possible Applications", Materials, Vol. 12(19), p. 3063, 2019. `doi:10.3390/ma12193063`

ISBN: 978-3-95450-217-2 doi:10.18429/JACoW-ERL2019-WEPNEC17

PHOTOCATHODE R&D AT DARESBURY LABORATORY: NEW TRANSVERSE ENERGY SPREAD MEASUREMENTS AND THE DEVELOPMENT OF A MULTI–ALKALI PHOTOCATHODE PREPARATION FACILITY

L.B. Jones[1,3*], D.P. Juarez-Lopez[2,3], L.A.J. Soomary[2,3], B.L. Militsyn[1,3],
C.P. Welsch[2,3] & T.C.Q. Noakes[1,3]

[1] ASTeC[†], STFC Daresbury Laboratory, Warrington, WA4 4AD, United Kingdom
[2] Department of Physics, University of Liverpool, L69 7ZE, United Kingdom
[3] The Cockcroft Institute, Warrington, WA4 4AD, United Kingdom

Abstract

The minimum achievable emittance in an electron accelerator depends strongly on the intrinsic emittance of the photocathode electron source. This is measurable as the mean longitudinal and transverse energy spreads in the photoemitted electron beam from the cathode source.

ASTeC[†] constructed the Transverse Energy Spread Spectrometer (TESS) experimental facility to measure both the transverse and longitudinal electron energy spectra for III–V semiconductor, multi–alkali and metal photocathodes. Our R&D facilities also include in–vacuum quantum efficiency measurement, XPS, STM, plus ex–vacuum optical and STM microscopy for surface metrology.

Photocathode intrinsic emittance is strongly affected by surface roughness, and the development of techniques to manufacture the smoothest photocathode is a priority for the electron source community. Other factors such as crystal face, illumination wavelength and temperature have a significant effect on photocathode intrinsic emittance. We present an update on advances in our photocathode R&D capabilities and some preliminary results from new measurements.

INTRODUCTION

The intrinsic emittance of a photocathode is the combination of many physical attributes such as composition, crystal face, surface roughness, cleanliness, quantum efficiency (QE), work function (ϕ) and illumination wavelength (λ). Intrinsic emittance expressed in microns per mm of laser illumination spot diameter ($\mu m/mm$) defines the lower limit of emittance in a well–configured linear accelerator.

In the absence of space charge effects, the source emittance can be preserved throughout acceleration in machines of this class [1]. The impact of reducing intrinsic emittance is therefore significant, and can potentially reduce both the physical size and capital cost of a Free-Electron Laser (FEL) facility driven by such an accelerator [2] while also increasing the X–ray beam brightness and hence the FEL performance. This is the primary justification for our work in this area in support of the CLARA [3] linear accelerator project.

Our Transverse Energy Spread Spectrometer (TESS) [4] experimental facility measures the photocathode electron emission footprint for low–energy electrons (typically <100 eV) from which the transverse and longitudinal energy distribution curves (TEDC and LEDC respectively) can be extracted [5]. TESS is connected to our III–V Photocathode Preparation Facility (PPF) [6] which provides storage for up to 6 photocathode samples under XHV conditions and supports thermal and atomic hydrogen cleaning.

The factors which affect photocathode performance require a suite of diagnostic techniques so our R&D facilities also include XPS, LEED and AFM/STM in our SAPI (Surface Analysis, Preparation and Installation) system [7, 8], with ex–situ interferometric optical and AFM microscopes for surface roughness measurements. We have a range of laser and broadband light sources which permit QE measurements at various wavelengths on different cathode materials.

Recently the TESS experimental system has been further upgraded and we have constructed a vacuum suitcase system which facilitates the movement of up to 4 photocathode samples between our various experimental systems under UHV conditions. This vacuum suitcase can also be used to bring photocathodes from other laboratories for characterisation using our systems. Our photocathode manufacturing capabilities are also being expanded through the construction of a multi–alkali photocathode preparation facility.

TESS CRYOGENIC UPGRADE

The TESS detector was originally specified as a general–purpose instrument to image the photoemission footprint of semiconductor photocathodes under illumination by solid–state laser modules [4]. The detector combined 3 independent grid meshes with a microchannel plate (MCP) electron multiplier and a P43 ITO phosphor screen, using a sensitive camera to record the electron emission footprint.

The detector was recently upgraded and now uses a single demountable grid mesh which facilitates the same transverse and longitudinal energy spread measurements, but with increased sensitivity [9]. This upgrade included the installation of a broadband Energetiq EQ–99 laser plasma-driven light source coupled through nitrogen–purged off–

---

[*] lee.jones@stfc.ac.uk
[†] ASTeC: Accelerator Science and Technology Centre

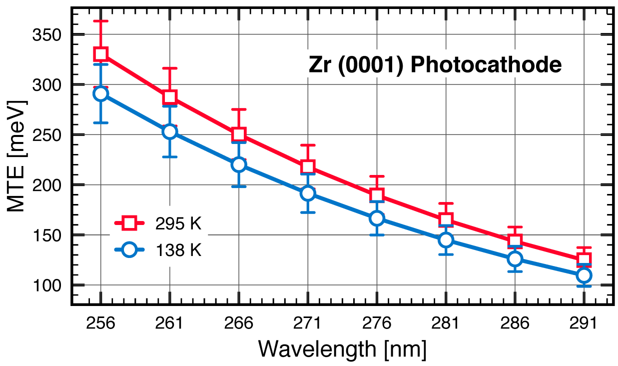

Figure 1: MTE as a function of illumination wavelength for a Zr (0001) photocathode at room and cryogenic temperatures.

axis parabola optics to a Bentham TMC300 $f/4$ monochromator which delivers considerably higher flux over the range $\lambda = (200 - 800)$ nm, but particularly at UV wavelengths.

The latest upgrade adds the ability to cool a photocathode using liquid nitrogen (LN_2), supporting MTE measurements at photocathode temperatures down to -140 °C ($\approx$ 135 K). FEA modelling at the TESS design phase some years ago had shown that the cooling method applied should allow the system to reach -196 °C (96 K). It is not known whether the present shortfall is due to an instrumentation issue, or if there is a significant heat leak which limits the cryogenic performance.

A commissioning measurement has been carried out using a Zr (0001) single–crystal supplied by MaTeck (4N purity, $> 99.99\%$) with a typical work function of $\phi = 4.05$ eV [10]. The results are listed below in Table 1 and shown in Fig. 1.

Table 1: Summary of Extracted MTE Values for a Zr (0001) Photocathode under Illumination at Various Wavelengths, λ

Illumination Wavelength	**MTE [meV]**	
λ [nm] / energy [eV]	**T = 300 K**	**T = 140 K**
256 / 4.84	330	291
261 / 4.75	287	253
266 / 4.66	250	220
271 / 4.58	218	191
276 / 4.50	189	167
281 / 4.41	164	145
286 / 4.34	143	126
291 / 4.26	125	110

SURFACE ANALYSIS FOR PHOTOCATHODES

To facilitate in–vacuum surface analysis, we constructed our Surface Analysis for Photocathodes Instrument (SAPI) [8], also known as *Multiprobe*.

The system operates at UHV and supports XPS, LEED and AFM/STM for samples mounted on the Omicron 'flag' sample plate. Sample loading is achieved via a fast–entry airlock or through our vacuum suitcase (described later). Sample cleaning can be carried out using a Thermo Fisher EX-05 ion source for ion bombardment and annealing or thermal cleaning by e-beam heating to around 1,300 °C.

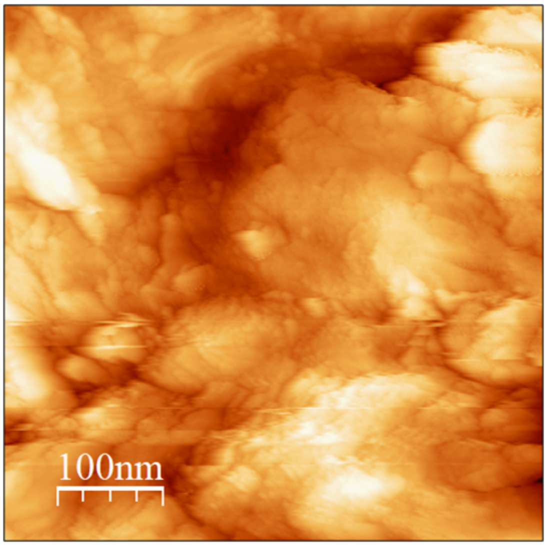

Figure 2: STM Surface image for an Nb (100) sample with a measured surface roughness of R_a =16.3 nm RMS.

The XPS capability combines a PSP CTX400 twin–anode X-ray source with a Thermo Fisher Alpha 110 hemispherical energy analyser. This combination can deliver an energy resolution of better than 5 meV under optimal conditions.

Sample microscopy is achieved using an Omicron UHV STM 1 which provides both AFM and STM functions. It features eddy current damping, in–vacuum I/V conversion, UHV sample and tip exchange from an in–vacuum storage carousel with capacity for up to 8 samples/tips at any one time. Fig. 2 shows a commissioning measurement for a Nb (100) single–crystal sample.

VACUUM SUITCASE

The requirement to move photocathodes under UHV/XHV conditions between our experimental systems and even laboratories at other sites has prompted us to build a vacuum suitcase. Our solution is based on a magnetic linear transfer arm supporting a magazine which accommodates up to 4 photocathode samples.

The magazine accepts sample plates which are directly compatible with our III-V PPF and TESS vacuum systems, or the combination of an Omicron 'flag' sample plate (compatible with our SAPI AFM/STM/XPS system and multi-alkali PPF) and a III-V PPF/TESS adapter. The 'flag' sample plate and its adapter are shown in Fig. 3. The suitcase is sealed with a VAT DN63 all–metal gate valve.

The suitcase includes a SAES NEXTorr D100-5 SIP/NEG pump which maintains a vacuum level below 1×10^{-10} mbar. The suitcase has a custom–made transit crate and the pump can be operated with a FerroVac LSA2.1 battery power pack

ISBN: 978-3-95450-217-2 doi:10.18429/JACoW-ERL2019-WEPNEC17

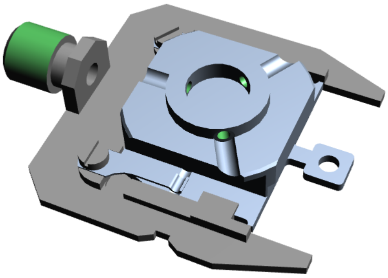

Figure 3: ‘Flag’ style photocathode sample holder (silver) and adapter plate (grey), designed for sample ‘pucks’ with dimensions 6 mm $\phi \times 2$ mm.

which can be driven from the 12 V accessory system in a car or van, making this suitcase portable over long distances.

The suitcase is shown in Fig. 4 coupled to the loading system of our multi–alkali photocathode preparation facility.

MULTI–ALKALI PPF

There has been a migration towards the use of alkali–telluride photocathodes illuminated at UV wavelengths around 266 nm or alkali–antimonides illuminated at visible wavelengths around 532 nm. This is driven by continual progress in techniques to manufacture such photocathodes which offer significantly increased QE over simple metallic photocathodes, coupled with superior temporal response characteristics and operational lifetime over semiconductor photocathodes. The alkali–antimonide photocathode family convey the additional benefit of operation at visible wavelengths, so reducing the complexity of the drive laser system and simplifying the application of transverse and longitudinal laser pulse shaping to improve electron beam quality.

We are constructing a multi–alkali photocathode preparation facility to provide multi–alkali electron sources for the CLARA accelerator [3]. The PPF shown in Fig. 4 is partly constructed, and will shortly receive a suite of alkali metal sources and a sample manipulator.

The initial configuration of the PPF includes a sample loading interface compatible with our vacuum suitcase. This will allow us to grow multi–alkali photocathode surfaces on a variety of substrate materials mounted on the ‘flag’ sample holder which can then be transferred under vacuum to our TESS and SAPI systems for further characterisation.

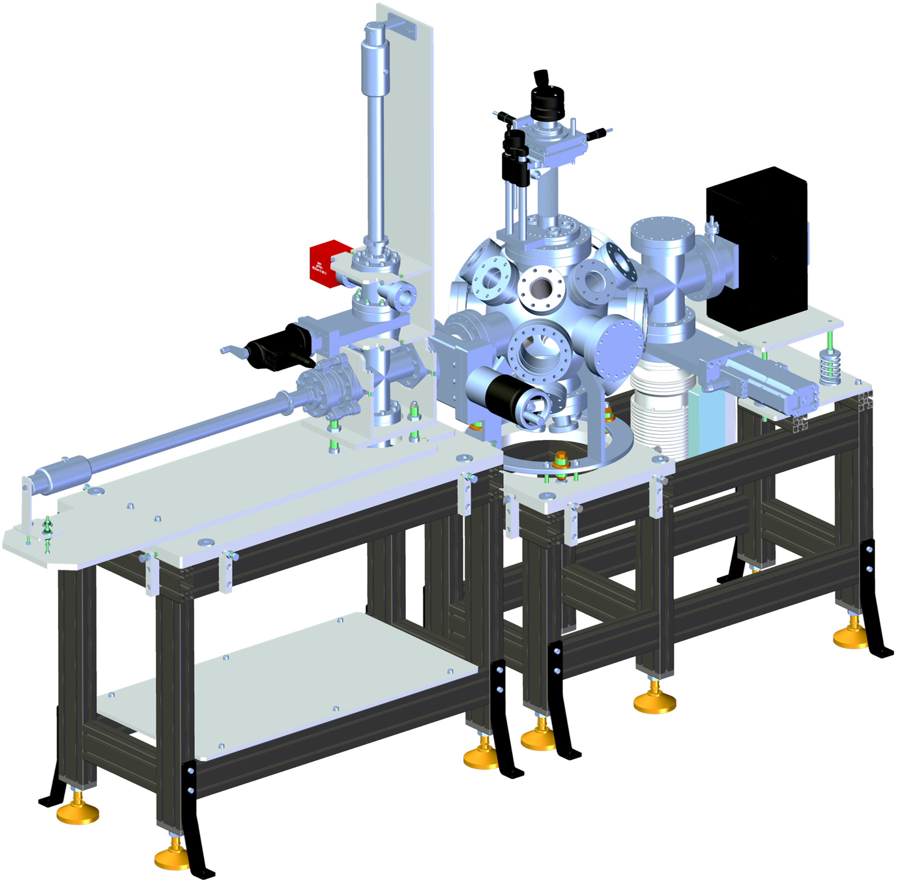

Figure 4: Engineering model of our multi–alkali photocathode preparation facility coupled to our vacuum suitcase. The photocathode preparation chamber, pumps and vacuum instrumentation are mounted on the right–hand table. The left–hand table supports the sample loading transfer arm (horizontal), to which is connected a UHV vacuum suitcase (vertical).

At a later date, an interface with an additional vacuum suitcase will be added to the side port of the preparation chamber to support the loading of an INFN-style photocathode puck [11] and its transport carriage such that our multi–alkali photocathodes can be prepared and transferred to the CLARA RF gun.

FUTURE WORK

We hope to be in a position to grow multi–alkali photocathodes by the middle of 2020, and plan to begin with Cs_2Te. The photocathodes grown will be transferred to our TESS and SAPI instruments using our vacuum suitcase to facilitate composition and performance analysis.

In the shorter term, our TESS and SAPI systems will be used to continue a programme of work to characterise various metal photocathodes with the aim of further evaluating the effect of surface roughness and operational temperature on photocathode performance.

ACKNOWLEDGEMENTS

The work is partly–funded by the Mexican government through the Consejo Nacional de Ciencia y Tecnologia (https://www.conacyt.gob.mx/).

The authors gratefully acknowledge Prof. A.S. Terekhov and Dr. H.E. Scheibler (both from the Institute for Semiconductor Physics, SB RAS, Novosibirsk) for their invaluable contributions in the development of the TESS instrument.

The authors also wish to acknowledge Barry Fell, Mike Cordwell and Ryan Cash (all from STFC's Technology Department) for their engineering solutions in support of our photocathode R&D.

REFERENCES

[1] C.P. Hauri, R. Ganter *et al.* "Intrinsic emittance reduction of an electron beam from metal photocathodes", *Phys. Rev. Lett.*, vol. 104, 234802 (2010). doi:10.1103/PhysRevLett.104.234802

[2] M.C. Divall, E. Prat, *et al.* "Intrinsic emittance reduction of copper cathodes by laser wavelength tuning in an RF photoinjector", *Phys. Rev. ST Accel. Beams*, vol. 18, 033401 (2015). doi:10.1103/PhysRevSTAB.18.033401

[3] J.A. Clark *et al.* "CLARA Conceptual Design Report", *JINST*, vol. 9, T05001 (2014). doi:10.1088/1748-0221/9/05/T05001

[4] L.B. Jones, H.E. Scheibler *et al.* "The commissioning of TESS: An experimental facility for measuring the electron energy distribution from photocathodes", in *Proc. FEL 2013*, New York, NY, USA, 2013, 290 – 293. paper: TUPSO33

[5] L.B. Jones, H.E. Scheibler *et al.* "Evolution of the transverse and longitudinal energy distributions of electrons emitted from a GaAsP photocathode as a function of its degradation state", *Journal of Applied Physics*, vol. 121, 225703 (2017). doi:10.1063/1.4984603

[6] B.L. Militsyn *et al.* "First results from the III-V photocathode preparation facility for the ALICE ERL photoinjector", in *Proc. IPAC 2010*, Kyoto, Japan 2010, paper: TUPE095.

[7] T.C.Q. Noakes *et al.* "Commissioning of the SAPI for operation with metal photocathodes", EuCARD-2, CERN-ACC-2014-0039.

[8] S. Mistry *et al.* "A comparison of surface properties of metallic thin film photocathodes", in *Proc. IPAC 2016*, Busan, Korea, May 2016. doi:10.18429/JACoW-IPAC2016-THPMY017

[9] L.B. Jones, D.P. Juarez-Lopez *et al.* "Transverse energy distribution measurements for polycrystalline and (100) copper photocathodes with known levels of surface roughness", in *Proc. IPAC 2018*, Vancouver, BC, Canada, 2018. doi:10.18429/JACoW-IPAC2018-THPMK062

[10] H.B. Michaelson "The workfunction of the elements and its periodicity", *J. Appl. Phys.*, vol. 48, p. 4729 (1977). doi:10.1063/1.323539

[11] P. Michelato, C. Gesmundo, D. Sertore "High quantum efficiency photocathode preparation system for TTF injector II", TESLA FEL-Report 1999-07.

OPTIMIZATION OF THE PERLE INJECTOR

B. Hounsell*[1, 2], M. Klein, C.P. Welsch[1], University of Liverpool, Liverpool, United Kingdom
W. Kaabi, Laboratoire de l'accélérateur Linéaire CNRS/IN2P3 Université Paris-Saclay, Orsay, France
B.L. Militsyn[1], UKRI STFC, Sci-Tech Daresbury, Warrington United Kingdom
[1]also at Cockcroft Institute, Warrington, United Kingdom
[2]also at Laboratoire de l'accélérateur Linéaire CNRS/IN2P3 Université Paris-Saclay, Orsay, France

Abstract

The injector for PERLE, a proposed electron Energy Recovery Linac (ERL) test facility for the LHeC and FCC-eh projects, is intended to deliver 500 pC bunches at a repetition rate of 40.1 MHz for a total beam current of 20 mA. These bunches must have a bunch length of 3 mm rms and an energy of 7 MeV at the entrance to the first linac pass while simultaneously achieving a transverse emittance of less than 6 mm·mrad. The injector is based around a DC photocathode electron gun, followed by a focusing and normal conducting bunching section, a booster with 5 independently controllable SRF cavities and a merger into the main ERL. A design for this injector from the photocathode to the exit of the booster is presented. This design was simulated using ASTRA for the beam dynamics simulations and optimized using the many objective optimization algorithm NSGAIII. The use of NSGAIII allows more than three beam parameters to be optimised simultaneously and the trade-offs between them to be explored.

INTRODUCTION

PERLE is a proposed three turn 500 MeV ERL intended as a test facility for the FCC-eh/LHeC projects [1]. The bunch repetition rate of PERLE is 40.1 MHz which means that to achieve an average beam current of 20 mA a bunch charge of 500 pC is required. The specification of PERLE requires also a transverse emittance of less than 6 mm·mrad at a bunch length of 3 mm to be delivered from the injector to the main ERL loop. The specifications of the PERLE injector are summarised in Table 1.

Table 1: A Summary of the Specification for the Bunch Properties Delivered from the PERLE Injector

Beam parameter	Required value
Bunch charge, pC	500
Bunch repetition rate, MHz	40.1
Average beam current, mA	20
RMS normalised transverse emittance mm·mrad	< 6
RMS bunch length, mm	3
Beam energy, MeV	7
Uncorrelated energy spread, keV	< 10
Operation mode	CW

The requirement of a CW operation mode and beam parameters of the injector means that there are three possible options for the electron source: a high voltage DC electron gun, an SRF CW gun or a VHF CW gun. The gun should operate with photocathode illuminated with laser light which is the only way of providing beams with the required time structure at the required quality.

The majority of pre-existing ERL projects have used DC gun based injectors. The possible operation mode with polarised electrons of PERLE would require a GaAs based photocathode. This kind of photocathode is extremely sensitive to the vacuum conditions and at the moment only DC guns are capable of achieving the vacuum quality required. Such a gun was used as electron source of ALICE ERL test facility at Daresbury Laboratory, UK [2]. In addition it has been experimentally demonstrated at Cornell University that DC gun based injectors can deliver bunches with bunch charges higher than the nominal value for PERLE and transverse emittances lower than required for the PERLE specification [3]. The history of successful use of DC electron guns on ERL projects, the possibilty of re-using the ALICE electron gun, the fact that they are the only technology which can provide polarised electron beams and their experimentally demonstrated performance at high bunch charges are all factors in why the injector for PERLE will be based on a DC electron gun.

INJECTOR LAYOUT

The PERLE injector follows the proven layout comprising of a 350 kV high voltage electron gun, focusing solenoid, a normal conducting buncher cavity, solenoid and then a superconducting booster linac. The booster linac consists of 5 SRF cavities with independently controllable phases and amplitudes. A sketch of the layout can been seen in Fig. 1.

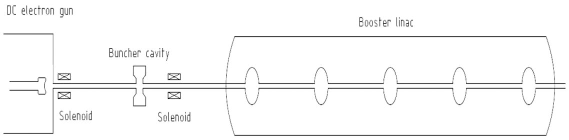

Figure 1: The layout of the PERLE injector.

The electron gun used for the PERLE injector will be an upgraded and modified ALICE electron gun operating with an antimonide based photocathode such as Cs_3Sb. The majority of the upgrade will be identical to that designed for ALICE itself [4]. However the electrode system has to

---

* ben.hounsell@cockcroft.ac.uk

be changed as much higher bunch charge is required. The geometry of the electrodes was obtained using a many objective optimization to minimise slice emittance and beam size at the position of the second solenoid and is a compromise design between 500 pC unpolarised operation at 350 kV and a 500 pC polarised operation at 220 kV [5]. To allow for the potential for an upgrade for polarised operation which would require operation at the lower gun voltage of 220 kV

The significant space charge forces of the 500 pC bunch cause a rapid increase in the bunch length shortly after emission. This means that irrespective of the initial laser pulse duration the bunch length at the buncher is long enough that RF induced non-linearities in the longitudinal phase space at the exit of the buncher are a concern. To mitigate this potential issue a 401 MHz subharmonic buncher is going to be used.

The booster comprises 802 MHz single cell cavities and their phases and amplitudes can be individually controlled. This allows for fine adjustment of the bunching proccess in the first two cells as well as control of the final chirp on the bunch using the last cavity of the booster.

OPTIMIZATION PROCCEDURE

The design of the PERLE injector is an optimization problem with multiple objectives, multiple constraints and a significant number of variables. The use of multi-objective optimization algorithms to optimise DC gun based injector is common. An example of this being the optimization of the Cornell University injector [6]. Multiobjective genetic algorithms are used because there are multiple competing requirements on the injector, complex space charge dominated beam dynamics and a sufficently large number of variables to make finding the optimal solution by hand challenging.

The PERLE injector optimization procedure uses 19 variables which are summarised with their permitted ranges in Table 2. There needs to be some distance between the components to allow for the placement of components such as diagnositcs, vacuum pumps and the mirror box for delivery of the photoinjector laser light. The minimum distances required for this were estimated using the distances in the ALICE injector

Four constraints were used in the optimization, one inequality and three equality. The inequality constraint was that the rms transverse beam size which must be less than 6 mm at all points along the injector beamline to ensure that the beam will fit through all of the apertures in the injector. The bunch length specification of 3 mm and the final energy of 7 MeV were both handled as equality constraints rather than objectives as a specific value is required at the injection point and consequently trading off between these parameters and the objectives is not required. The bunch length and energy constraints were handled by transforming them into inequality constraints with a variable tolerance decreasing linearly with generation from an intial tolerance of ±55% to a final tolerance of ±5%. The constraint that particle count equals zero was treated as an inequality constraint that the number of particles lost must be less than one. A summary of the constraints used in the optimization can be seen in Table 3.

Table 2: The Variables in the Optimization of the PERLE Injector with Their Permitted Ranges

Variable	Range
Laser spot diameter, mm	4 – 10
Laser pulse duration, ps	1 – 160
1st solenoid field, T	0.01 – 0.05
1st solenoid and buncher additional distance, m	0 – 0.4
Buncher amplitude, MV/m	0.5 – 4.0
Buncher phase, °	-110 – -70
Buncher and 2nd solenoid additional distance, m	0 – 0.4
2nd solenoid setting, T	0.01 – 0.05
2nd solenoid and booster addtional distance, m	0 – 0.4
1st booster cell amplitude, MV/m	0 – 25
1st booster cell phase, °	-50 – 50
2nd booster cell amplitude, MV/m	0 – 25
2nd booster cell phase, °	-50 – 50
3rd booster cell amplitude, MV/m	0 – 25
3rd booster cell phase, °	-50 – 50
4th booster cell amplitude, MV/m	0 – 25
4th booster cell phase, °	-50– 50
5th booster cell amplitude, MV/m	0 – 25
5th booster cell phase, °	-50 – 50

Table 3: The Constraints in the Optimization of the PERLE Injector

Constraints
RMS transverse beam size < 6 mm
Final RMS bunch length = 3 mm
Final energy = 7 MeV
Number of particles lost = 0

The optimization had five objectives which are summarized in Table 4. The cylindrical symmetry of the the injector was used to reduce the number of objectives as the transverse properties are the same in both the horizontal and vertical planes so only one of the planes needs to be considered. The first two objectives were the transverse and longitundinal emittance which serve as measures of the beam quality. The RMS energy spread factors in both the correlated and uncorrelated energy spread. The uncorrelated energy spread should be as low as possible. However the desired value of the correlated energy spread, which is essentially defined by the energy chirp which, in turn, depends on the merger and the longitudinal match of the main ERL loop. The correlated energy spread value required for these is not currently well defined. As the desired chirp is not known it was decided

ISBN: 978-3-95450-217-2 doi:10.18429/JACoW-ERL2019-WEPNEC19

to try and achieve as small a correlated energy spread as possible. The motivation for this was to try and maximize the flexibility and have an injector which didn't have a tendency towards either positive or negative chirps and which consequently should be able to achieve as wide a range as possible of both postive and negative chirps by adjusting the last cavity of the booster.

The transverse and longitudinal halo parameters as defined in [7] are used as a means to quanitfy the bunch shape. This is done as it is desirable to avoid bunches with significant temporal tails. The halo parameter has the advantage of being defined in 2d phase space which gives a more complete veiw of the behaviour of the bunch distribution.

Table 4: The Objectives in the Optimization of the PERLE Injector - the objectives are all minimised at the booster exit

Objectives
RMS transverse normalized emittance
RMS longitundinal normalized emittance
RMS energy spread
Transverse halo parameter
Longtidunal halo parameter

The number of objectives in this optimization is greater than three which means that NSGAII is no longer a suitable optimization algorithm. Above three objectives the non-dominated sorting approach used begins to lose its ability to provide selection pressure towards more optimial solutions. Consequentially a specialist many objective optimization algorithm NSGAIII was chosen. an algorithm related to the NSGAII but which changes the selection process to improve the diversity preservation and aid the search process [8] [9]. NSGAIII was implemented using the python library DEAP (Distributed Evolutionary Algorithms in Python) [10]. The algorithim parameters chosen for the optimization were those used in the original NSGAIII paper with the exception of the reference points and population size. The reference points were created with two layers using the approach described in the paper the outer layer with p=4 and the inner layer with p=3 [8]. The population size was then set to 120. This optimization was run for 100 generations.

The injector was simulated using the accelerator code ASTRA [11]. The particle count was set to 4096 which is relatively low. The requirement for 12,000 individual ASTRA runs means that the particle count and space charge grid needed to be set as a compromise between accuracy and keeping the run time of the optimization reasonable. The intial thermal emittance of the bunch was determined using the FD_300 emission model and assuming a Cs_3Sb photocathode illuminated with a 532 nm laser.

OPTIMIZATION RESULTS

The result of the optimization is a 5d pareto front of equivalently optimal solutions. This front can be used to understand how the different objectives trade off against each other and what values of the objectives are achievable. The final solution can then be selected from the pareto front using this information. Two 2d projections of the pareto front have been plotted to show how two different objectives trade off against each other. The first of these shows how transverse and longitudinal emittance trade off against each other and can be seen in Fig. 2.

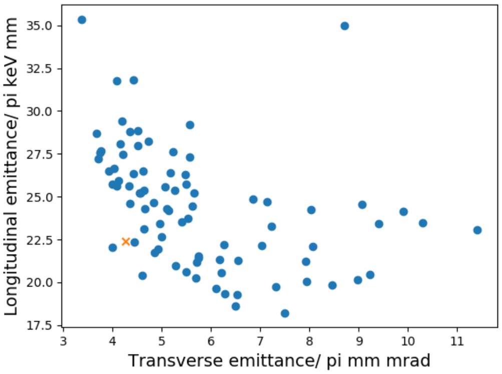

Figure 2: The 2d projection of the 5d pareto front showing how transverse emittance and longitudinal emittance trade off. The chosen solution is marked with an orange x.

The second plotted trade off shows the transverse emittance against the longitudinal halo parameter This can be seen in Fig. 3.

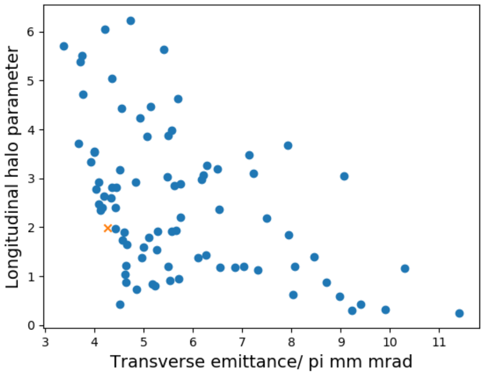

Figure 3: The 2d projection of the 5d pareto front showing how transverse emittance and longitudinal halo parameter trade off. The chosen solution is marked with an orange x.

The selected solution is not the lowest emittance solution in the pareto front. Instead the decision was made to sacrifice some performance in transverse emittance for improved longitudinal parameters. The lower transverse emittance solutions had significantly larger longitudinal halo parameters. This manifested itself in the form of significantly larger slice energy spread in the tail of the bunch. This could potentially cause problems with halo formation later in the ERL.

CHOSEN SOLUTION

The chosen solution was adjusted by hand to achieve an exact final energy of 7 MeV and to minimise the correlated energy spread. It was then re-run at the higher particle count of 32768 to get a more accurate result.

The beam parameters at booster exit for the chosen solution can be seen in Table 5. These parameters in general meet the PERLE specification.

Table 5: The Parameters of the Chosen Solution after It Has Been Re-Run at Higher Particle Count

Parameters of the chosen solution	
RMS transverse normalized emittance, mm·mrad	4.0
RMS longitundinal normalized emittance, keV·mm	25.1
Bunch length, mm	3
Beam energy, MeV	7

The rms horizontal transverse beam size and the bunch length along the injector can be seen in Fig. 4.

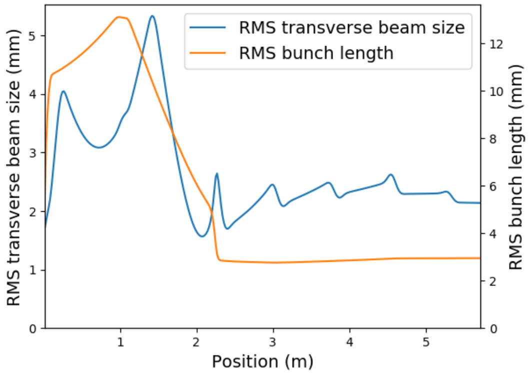

Figure 4: The variation of rms transverse beam size in blue and the rms bunch length in orange along the injector.

The transverse beam size is well controlled below the target value of 6 mm. The bunch length increases rapidly after emission due to the space charge but it never grows above the point where the 401 MHz buncher would introduce significant non-linearities. The bunching is primarly done by the buncher cavity but there is some bunching in the first cell of the booster. After that the bunch length is held constant at the target value of 3 mm rms.

The transverse and longitudinal emittances can be seen in Fig. 5. The transverse emittance is compensated down to a value of 4 mm·mrad at the booster exit which is below the required specification of less than 6 mm·mrad. This is greater than the thermal emittance indicating either imperfect compensation or some slice emittance growth.

The average bunch energy and rms energy spread can be seen in Fig. 6.

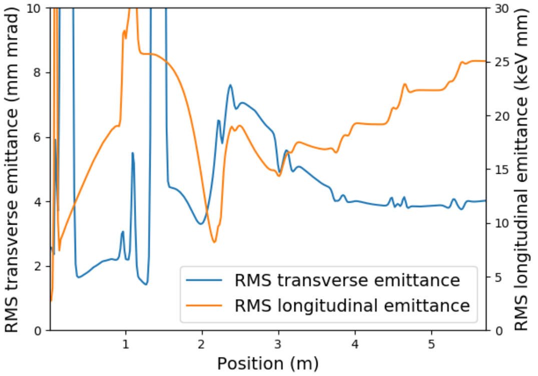

Figure 5: The variation of rms transverse normalized emittance in blue and the rms longitudinal emittance in orange along the injector.

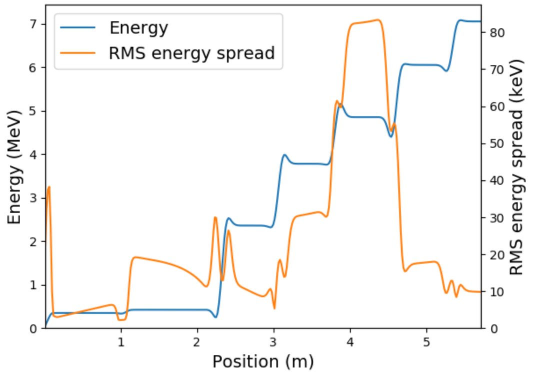

Figure 6: The variation of average beam energy in blue and the rms energy spread in orange along the injector.

The energy gain is most significant in the first booster cavity but after that is fairly consistent ending at the specified value of 7 MeV. The final cavity can be used to adjust the chirp on the beam which may important for the longitudinal match of the main ERL loop. However at present the requirements on the chirp of the injected bunch are not well defined.

The transverse phase space and bunch distributions in space and momentum can be seen in Fig. 7. From the transverse phase space it can be seen that in general the emittance is well compensated but that the tail is poorly compensated. The transverse bunch phase space may be considered as satisfactory.

The longitudinal phase space and longitundinal bunch distributions can be seen in Fig. 8. The longitundinal phase space is not as linear as would be desired. The biggest issues being at the head and tail of the bunch which is due to space charge effect at injection. Prior to the booster entrance there was a clear third order non-linearity due to space charge. The current longitudinal phase space shape began to emerge in the first cell of the booster.

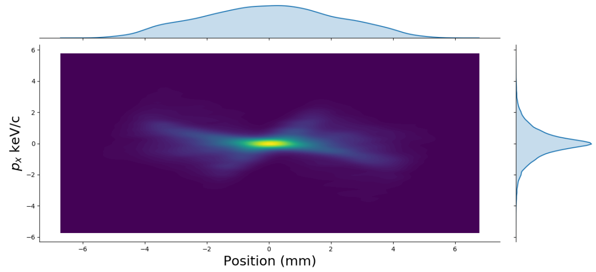

Figure 7: The transverse phase space at the exit of the booster. At the top is the bunch distribution in space while on the right is the distribution in momentum.

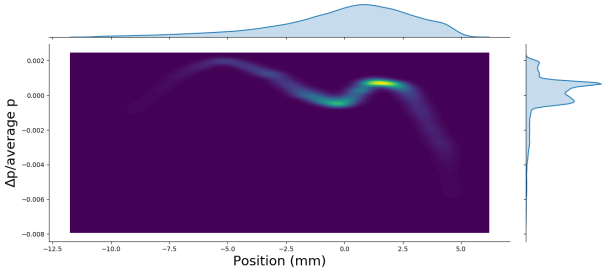

Figure 8: The longitudinal phase space at the exit of the booster. At the top is the bunch distribution in space while on the right is the distribution in momentum.

CONCLUSION

The chosen injector solution satisfies the PERLE specification at the booster exit. The longitundinal phase space may need to be improved and the possbility of linearization will be investigated. The next step towards a complete injector design is selection of the scheme and optimization of the merger. The beam dynamics will be investigated and optimised to the start of the first spreader section at the exit of the linac. Once a complete injector design has been obtained tolerance studies will need to be performed.

REFERENCES

[1] W. Kaabi *et al.*, “PERLE: A High Power Energy Recovery Facility”, *in Proc. 10th Int. Particle Accelerator Conf. (IPAC’19)*, Melbourne, Australia, May 2019. `doi:10.18429/JACoW-IPAC2019-TUPGW008`

[2] C. Gerth and F. E. Hannon.“Injector design for the 4GLS energy recovery linac prototype,” in *Proc. EPAC 2004*, Lucerne, Switzerland, 2004. paper: MOPKF056

[3] A. Bartnik *et al.*, “Operational experience with nanocoulomb bunch charges in the Cornell photoinjector”, in *Physical Review Special Topics-Accelerators and Beams* 18.8 (2015), p. 083401. `doi:10.1103/PhysRevSTAB.18.083401`

[4] B. L. Militsyn *et al.*, “Design of an Upgrade to the ALICE Photocathode Electron Gun”, in *Proc. 11th European Particle Accelerator Conf. (EPAC’08)*, Genoa, Italy, Jun. 2008, paper MOPC073, pp. 235–237.

[5] B. Hounsell *et al.*, “Re-optimization of the ALICE gun upgrade design for 500 pC bunch charge requirements for PERLE ”, in Proc. 10th Int. Particle Accelerator Conf. (IPAC’19), Melbourne, Australia, May 2019, paper TUPTS066. `doi:10.18429/JACoW-IPAC2019-TUPTS066`

[6] Bazarov, I. V. and Sinclair, C. K., “Multivariate optimization of a high brightness dc gun photoinjector”, in . *Physical Review Special Topics-Accelerators and Beams* 8(3), (2005), p. 034202. `doi:10.1103/PhysRevSTAB.8.034202`

[7] C. K. Allen and T. P. Wangler, “Parameters for quantifying beam halo ”, in Proceedings of the 2001 Particle Accelerator Conference (PACS2001) (Cat. No.01CH37268), Chicago, IL, USA, 2001, pp. 1732-1734 vol.3. `doi:10.1109/PAC.2001.987164`

[8] K. Deb and H. Jain, “An Evolutionary Many-Objective Optimization Algorithm Using Reference-Point-Based Nondominated Sorting Approach, Part I: Solving Problems With Box Constraints”, in *IEEE Transactions on Evolutionary Computation*, vol. 18, no. 4, pp. 577-601, Aug. 2014. `doi:10.1109/TEVC.2013.2281535`

[9] H. Jain and K. Deb, “An Evolutionary Many-Objective Optimization Algorithm Using Reference-Point Based Nondominated Sorting Approach, Part II: Handling Constraints and Extending to an Adaptive Approach,” in *IEEE Transactions on Evolutionary Computation*, vol. 18, no. 4, pp. 602-622, Aug. 2014. `doi:10.1109/TEVC.2013.2281534`

[10] Félix-Antoine Fortin, François-Michel De Rainville, Marc-André Gardner, Marc Parizeau and Christian Gagné, "DEAP: Evolutionary Algorithms Made Easy", *Journal of Machine Learning Research*, vol. 13, pp. 2171-2175, jul 2012. `http://www.jmlr.org/papers/v13/`

[11] K. Floettmann (1997), “ASTRA: A Space Charge Tracking Algorithm”, `http://www.desy.de/~mpyflo/`

ISBN: 978-3-95450-217-2 doi:10.18429/JACoW-ERL2019-WEPNEC21

Decoupling Cathode and Lattice Emittance Contributions from a 100 pC, 100 MeV Electron Injector System

N.P. Norvell*, SLAC National Accelerator Lab, Menlo Park and UC Santa Cruz, CA USA
M.B. Andorf, I.V. Bazarov, J.M. Maxson, C. Gulliford
Center for Bright Beams, Cornell University, Ithaca NY, USA

Abstract

We present simulation results to decouple the emittance contributions that are intrinsic from the injector lattice versus emittance contributions due to the quality of the cathode out of a 100 MeV electron injector system. Using ASTRA driven by the NSGA-II genetic algorithm, we optimized the LCLS-II injector system with a zero emittance cathode. We then imposed FEL specific energy constraints and show how the Pareto Front solution shifts. Lastly, we reoptimized at various cathode emittances to map out the dependence of cathode emittance versus final emittance out of the injector system. We then determined the cathode quality needed to hit a 0.1 mm mrad 95% rms transverse emittance specification out of the current LCLS-II injector system.

SIMULATION MOTIVATION

SLAC National Accelerator Lab is currently constructing a MHz repetition rate Free Electron Laser (FEL), the Linac Coherent Light Source II, to follow up the success of the 120 Hz LCLS. LCLS-II will initially run with a 4 GeV superconducting linac but plans are underway to upgrade the linac further to accelerate electrons to 8 GeV for LCLS-II HE (High Energy), increasing the maximum deliverable x-ray energy up to almost 15 keV[1]. Even after the upgrades to the LCLS-II facilities, FEL users would still like a higher photon range from the LCLS-II complex. At higher electron energies, the x-ray energy range becomes throttled by emittance if the number of undulator magnets are not increased[1]. Emittance directly determines how efficiently the electron beam microbunches, which is required to start the exponential growth of x-ray production in the undulators[2]. Currently, LCLS-II expects a transverse normalized emittance of 0.4 mm-mrad at the first undulator for a 100 pC electron beam. As shown in Fig. 1, simulations predict that decreasing the normalized emittance at the undulators from 0.4 to 0.1 mm-mrad with an 8 GeV electron beam would expand LCLS-II HE x-ray energy upper bound from 15 keV to 22 keV. The benefit from lower emittance is even more drastic for FELs driven with higher electron energies with a similar undulator hall.

The quality of the electron beams produced in an accelerator facility is inherently limited by the emittance of the beam produced in the injector system. We define the injector system as the beamline that takes the beam from a cathode to around 100 MeV, when space charge effects are no longer a concern. The current LCLS-II injector system simulations predict transverse emittances around 0.3 mm-mrad out of the injector, indicating that injector improvements are necessary and the correct place to start looking to improve the emittance [3]. In these proceedings, we investigate the emittance benefits for the LCLS-II injector we could expect from improving the cathode quality and determine how much we would have to improve the cathode by to deliver a beam with a 0.1 mm mrad 95% rms transverse emittance for the LCLS-II HE project.

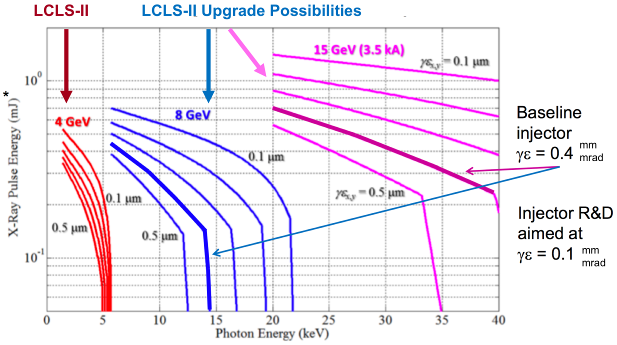

Figure 1: Expectations for how the emittance will effect the photon range for the LCLS-II and potential upgrades for various linac energies. The curves are predicted from the Ming Xie equations that numerically find the power gain length for x-ray generation[1].

OPTIMIZATION METHODOLOGY

We started with the optimization end point from the original LCLS-II optimization[4][5]. We used the particle tracking code ASTRA[6] driven by the multi-objective genetic algorithm NSGA-II [7] to compute and optimize two competing quantities, bunch length σ_z and the 95% rms horizontal emittance[8]. We get a set of solutions, called a Pareto Front, that visually documents the trade off between these two competing variables. We used a population size of 80 and ran all simulations with a bunch charge of 100 pC.

The first study documented the Pareto Front limit of an injector system. To isolate the lattice emittance contributions that are due to space charge, we turned off the cathode emittance by using ASTRA's generator program to create a radially uniform beam emerging from a zero longitudinal and transverse emittance source.

We imposed constraints to guide the optimizer to rea-

---

* nnorvell@slac.stanford.edu

Table 1: Parameters that were varied for the injector system. Zero degrees is defined as on crest for max acceleration and the field gradients are the value of the maximum field in the field file.

Knob	Variable Range
Transverse rms at cathode	0.05 - 2 mm
Bunch length at cathode	5 - 50 ps
Gun gradient	20.04 MV/m
Gun phase	-45 - 10 deg.
Solenoid 1 field	0.01- 0.2 T
Capture cavity gradient	0 - 2 MV/m
Capture cavity phase	-120 - 0 deg.
Solenoid field	0 - 0.2 T
Cavity 1 field	0 - 32 MV/m
Cavity 2 field	0 MV/m
Cavity 4 field	0 - 32 MV/m
Cavity 1 phase	-90 - 90 deg.
Cavity 4 phase	-90 - 90 deg.

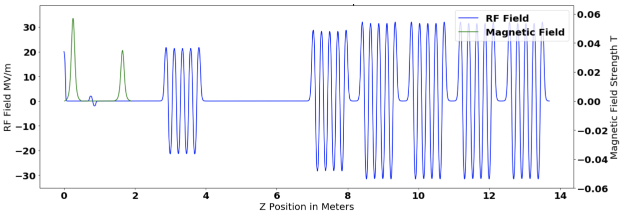

Figure 2: The field layout for the LCLS-II injector with the APEX gun.

sonable solutions. Constraints are binary conditions where configurations are initially ranked on the number of constraints violated. We required: a) The end energy is $>$ 90 MeV, b) rms bunch length is less than 1.5 mm, c) 100% rms emittance is less than 1.0 mm mrad, d) Final energy spread $<$ 500 keV, e) Higher Order (HO) Energy spread $<$ 50 keV, f) The average $x_{pos}x_{angle}$ is negative so we have a converging beam. HO energy spread is calculated by fitting a second order polynomial to the energy spread and finding an rms energy spread after subtracting out the polynomial of best fit.

We obtained a suitable front with a zero emittance cathode and then imposed more stringent energy constraints to determine how the Pareto Front would shift. First, we tightened the overall energy spread constraint from 500 keV to 200 keV. The 200 keV value matches previously performed LCLS-II optimization work and was imposed to ensure a sufficiently small energy spread at the undulator hall[5]. To save computing time, we seeded the NSGA-II algorithm with the final population from the zero emittance cathode run with looser energy constraints. We then continued optimizing for sufficient generations to get a satisfactory Pareto Front with the harder constraint.

We then took the end population with the tightened energy spread constraint and further tightened the higher order energy spread constraint from 50 keV to 5 keV.

We kept in the 200 keV energy spread and 5 keV HO energy spread constraints and started the next phase of the experiment to quantify how cathode emittance effects the Pareto Front. We set the cathode quality by specifying an emittance for the initial beam profile. We selected an isotropic momentum distribution, or radially uniform emission angles into a half sphere, to describe the beam off the cathode and realistically couple the initial transverse and longitudinal momentum spreads [9]. To help mitigate the legitimate problem of getting stuck in a local minimum, we started the cathode portion of the study with an unseeded, fresh run with a cathode having a thermal emittance (Temit) of 1 μm/ mm rms or a Mean Transverse Energy (MTE) of 510 meV. We filled in intermediary cathode emittances by seeding with population members from both the zero emittance cathode population with stricter energy constraints and the 1 μm/ mm rms cathode baseline.

CATHODE UPGRADE RESULTS

LCLS-II is using the 187 MHz gun developed for the Advanced Photoinjector Experiment (APEX)[10]. Past simulation results used a conservative cathode thermal emittance estimate of 1 μm/ mm rms [5] and we present results from the LCLS-II injector to show the emittance improvements we could expect if we were able to improve the thermal emittance. Accordingly, we froze the positions of the components of the beamline to correspond to the injector that is currently being built at SLAC. The knobs we varied and the layout of the LCLS-II injector are shown in Table 1 and Fig. 2. The Pareto Fronts achieved are displayed in Fig. 3.

ANALYSIS

LCLS-II is interested in a beam with a longitudinal bunch length around 1 mm at the end of the injector so we manually picked the lowest emittance population member in the 0.9-1.2 mm range to compare here (see Table 2). All displayed results are with 10,000 ASTRA particles with 100 pC. However, there is typically a 10% emittance reduction when 200,000 ASTRA particles are used with finer meshing. We plot the energy spread, 95% rms transverse emittance and the bunch length as a function of the injector position, Z, to show which variables had to change to accommodate either a harder constraint value, or more spot size dependent emittance off of the cathode.

Reaching the 200 keV energy spread specification was immediate. Achieving the 5 keV HO energy spread constraint was more difficult. No configuration initially met the HO constraint and the only populations that could survive had a smaller cathode spot size and shorter initial bunch lengths. The HO energy spread was then mostly fixed by adjusting the cavity 4 phase as visually show in the energy spread plot in Fig. 4. Because the HO energy spread constraint already necessitated the smaller spot size, the knobs did not change very much when the cathode

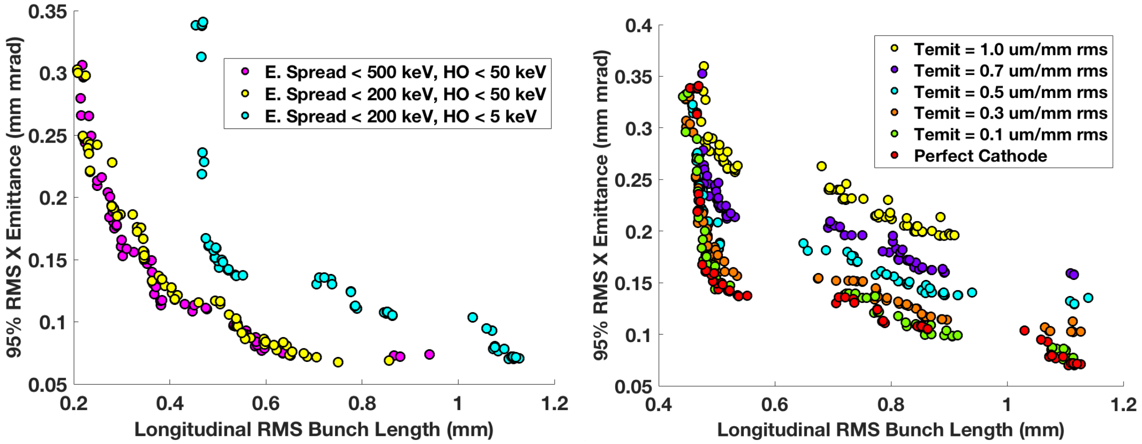

Figure 3: Pareto Fronts that show the impact of FEL specific energy constraints with a zero emittance cathode (left) and the dependence of the cathode emittance on the final emittance (right)

Table 2: Upgrade Emittance Table. All configurations were evaluated with 10,000 ASTRA particles

APEX Configuration	Emit. at Cathode mm mrad	100 % X Emit mm mrad	95 % X Emit mm mrad	Long. Size mm	E.Spread keV
E. Spread < 500 keV, HO < 50 keV	0	0.111	0.074	0.94	296.7
E. Spread < 200 keV, HO < 50 keV	0	0.108	0.069	0.86	157.7
E. Spread < 200 keV, HO < 5 keV	0	0.113	0.070	1.11	66.6
Thermal Emit = 0.1 $\frac{\text{mm mrad}}{\text{mm rms}}$	0.017	0.122	0.076	1.1	104
Thermal Emit. = 0.3	0.054	0.152	0.103	1.07	131.9
Thermal Emit. = 0.5	0.087	0.181	0.130	1.12	77.2
Thermal Emit. = 0.7	0.122	0.215	0.158	1.12	76.9
Thermal Emit. = 1.0	0.16	0.261	0.196	0.91	185.4

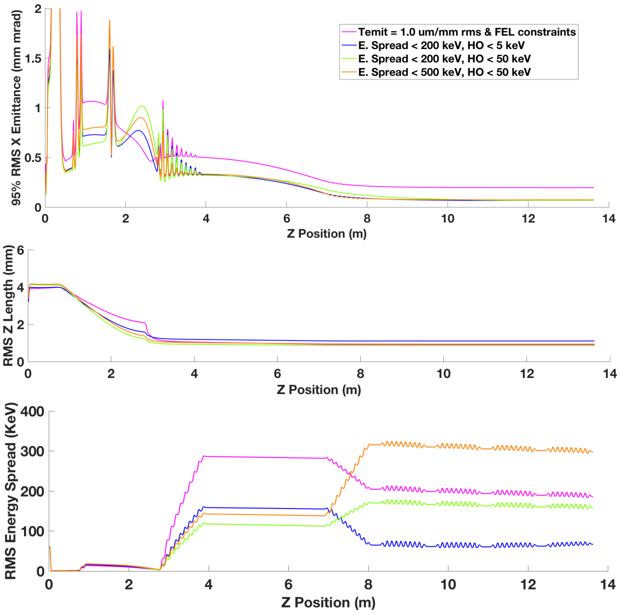

Figure 4: Emittance, bunch length and energy spread comparisons for a population with an end bunch length around 1 mm. The blue, orange, and green plots are all with a zero emittance cathode.

emittance was added back in.

CONCLUSION

We seek to understand the individual cathode and lattice emittance contributions towards the final injector emittance. The Pareto Fronts start documenting the benefits from further cathode research for the LCLS-II injector system. Keeping in mind that the 95% rms transverse emittance reliably decreases around 10% when 200,000 ASTRA particles are used, the results with the current LCLS-II injector indicate we would need a cathode around 0.3 μm/ mm rms to feasibly achieve 0.1 mm mrad 95% emittance at the end of the injector.

The main limitation of this study is that there is no way to definitively know that the Pareto Fronts are truly the global optimum. We played with the mutation and crossover parameters, but a perfect recipe of number of generations, algorithm parameters and ASTRA particle size that prevents getting in local minimum with reasonable computation time is still elusive.

REFERENCES

[1] T. Raubenheimer, “LCLS-II-HE FEL Facility Overview”. Workshop on Scientific Opportunities for Ultrafast Hard X-rays at High Rep. Rate. Sept. 2016, SLAC.

`https://portal.slac.stanford.edu/sites/conf_public/lclsiihe2016/Pages/default.aspx`

[2] Z. Huang, K.J. Kim. “Review of x-Ray Free-Electron Laser Theory” *Phys. Rev. ST Accel. Beams*, vol. 10 (3), p. 034801, 2007. `doi:10.1103/PhysRevSTAB.10.034801`

[3] F. Zhou *et al.*, “LCLS-II Injector Physics Design and Beam Tuning”, in *Proc. IPAC’17*, Copenhagen, Denmark, May 2017, pp. 1655–1658. `doi:10.18429/JACoW-IPAC2017-TUPAB138`

[4] C. F. Papadopoulos *et al.*, “RF Injector Beam Dynamics Optimization for LCLS-II”, in *Proc. IPAC’14*, Dresden, Germany, Jun. 2014, pp. 1974–1976. `doi:10.18429/JACoW-IPAC2014-WEPRO015`

[5] C. Mitchell *et al.*, “Beam Dynamics Optimization in High-Brightness Electron Injectors”, presented at FEL’17, Santa Fe, NM, USA, Aug. 2017. paper: THB01, unpublished.

[6] K. Floettmann, “ASTRA: A Space Charge Tracking Algorithm”, user’s manual available at `http://www.desy.de/~mpyflo/`

[7] D. Kalyanmoy *et al.*, “Fast and Elitist Multiobjective Genetic Algorithm: NSGA-II”. IEEE Transaction on Evolutionary Computation, vol. 6, no. 2, Apr. 2002, pp. 182-197. `doi:10.1109/4235.996017`

[8] K. Floettmann, “Some Basic Features of the Beam Emittance”, *Phys. Rev. ST Accel. Beams*, 6, p. 034202 (2003). `doi:10.1103/PhysRevSTAB.6.034202`

[9] T. Rao, and D. Dowell. “An Engineering Guide to Photoinjectors”. CreateSpace Independent Publishing, 2013. `arXiv:1403.7539[physics.acc-ph]`

[10] F. Sannibale *et al.*, “Status of the APEX Project at LBNL”, in *Proc. IPAC’14*, Dresden, Germany, Jun. 2014, pp. 727–729. `doi:10.18429/JACoW-IPAC2014-MOPRI054`

ISBN: 978-3-95450-217-2 doi:10.18429/JACoW-ERL2019-WEPNEC22

BEAM IMPEDANCE STUDY ON A HARMONIC KICKER FOR THE CCR OF JLEIC

Gunn Tae Park, Jiquan Guo, Shaoheng Wang, Robert Rimmer,
Frank Marhauser, and Haipeng Wang
Thomas Jefferson National Laboratory, Newport News, VA 23606, USA

Abstract

The design of a high power prototype of the harmonic kicker cavity for the Circulator Cooler Ring (CCR) of Jefferson Lab's proposed Electron-Ion Collider (JLEIC) is complete and fabrication is underway. In this report we present some of the impedance studies assuming a high beam current of the JLEIC (~ 0.76 A average) to estimate the HOM power dissipation and RF power requirement.

INTRODUCTION

A harmonic kicker cavity has been developed as a device that rapidly injects/extracts electron bunches into/out of the CCR of JLEIC [1], [2]. The engineering design of a high power prototype cavity based on a quarter wave resonator (QWR) is complete (See Fig, 1) [3], [4]. The cavity optimization took into consideration the higher order mode (HOM) impedance spectrum so that the HOM power induced by passing electron bunches is relatively low. In this report, we demonstrate that the beam-induced power due to the HOM's is below ~ 15 W within a ± 10 mm transverse beam offset from the ideal orbit. Consequently, HOM dampers are not strictly needed. This analysis was carried out employing both analytical calculation with the knowledge of impedance of discrete eigenmodes and via a wake field simulation using CST-MWS and CST-PS respectively [5]. In addition, we estimated the required power from the RF source needed to maintain a constant kick voltage with five deflecting harmonic modes.

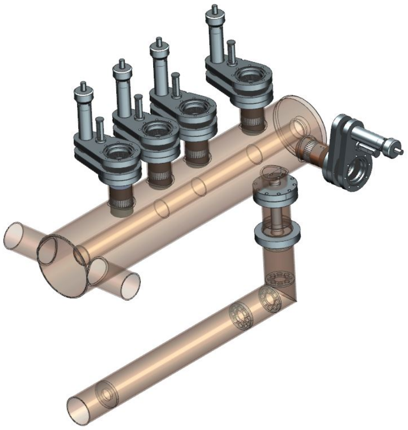

Figure 1: CAD model of the harmonic kicker cavity.

HOM POWER

The induced HOM power dissipated in the cavity can be evaluated in two ways. One is based on eigenmodes of the cavity computed numerically by the eigensolver of CST-MWS. Then the power associated with each eigenmode can be calculated analytically. The other is taking into account that the cavity modes are continuously fed by the beam bunch train. Therefore, the broadband coupling impedance spectrum (up to the first cutoff frequency of the beam pipe) has been evaluated using the wake field solver of the CST-PS, which allows to compute its power spectrum.

Time Structure of Beam Current in the CCR

The beam current in the CCR (for the parameters, see [6]) comes in a series of bunch trains with a gap (empty bucket) between the trains as shown in Fig. 2a. In addition to the periodicity of the bunch at a repetition rate of (f_b = 476.3 MHz), there is another periodicity arising from bunch train i.e., f_p = 1.4 MHz, which is very close to the CCR revolution frequency. The beam current can be expanded in a Fourier series, i.e.:

$$I(t) = \sum_m I_m e^{im\omega_p t} = c + id, \tag{1}$$

where
$$c(t) = \sum_m I_m \cos(m\omega_p t),$$
$$d(t) = \sum_m I_m \sin(m\omega_p t),$$

where I_m and $m\omega_p$ with $\omega_p = 2\pi f_p$ are the amplitude and angular frequency of each mode of the current. The Fourier spectrum of the current is shown in Fig. 2b.

Power Evaluation via Eigenmodes

For each eigenmode, the induced voltage with beam current as given in the CCR can be written as

$$\begin{aligned} V_{b,n,\parallel}(t) &= \int_{-\infty}^{t} dt'\, I(t') \frac{\omega_n R_{n,\parallel}}{2Q_{n,0}} e^{(i\omega_n - 1/\tau_n)(t-t')} \\ &= \frac{R_{n,\parallel}}{Q_{n,0}} Q_{n,L}\Big(a + ib\Big), \end{aligned} \tag{2}$$

where
$$a(t) = \sum_m \frac{I_m}{\sqrt{1+\zeta_m^2}} \cos(m\omega_p t - \psi_m),$$
$$b(t) = \sum_m \frac{I_m}{\sqrt{1+\zeta_m^2}} \sin(m\omega_p t - \psi_m),$$
$$\zeta_m = 2Q_L\left(\frac{m\omega_p}{\omega_n} - 1\right), \quad \psi_m = \tan^{-1}\zeta_m.$$

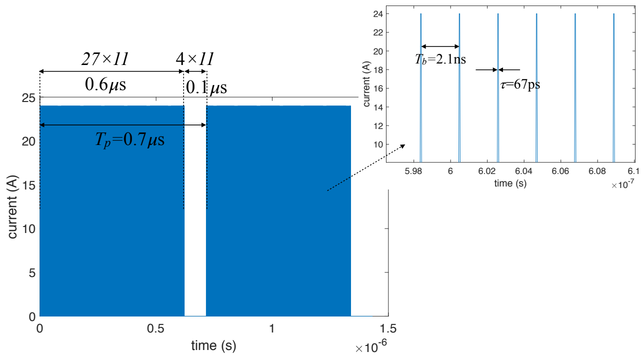

(a) The temporal profile. There are 27 × 11 bunches and 4 × 11 empty buckets (gaps) in a bunch train.

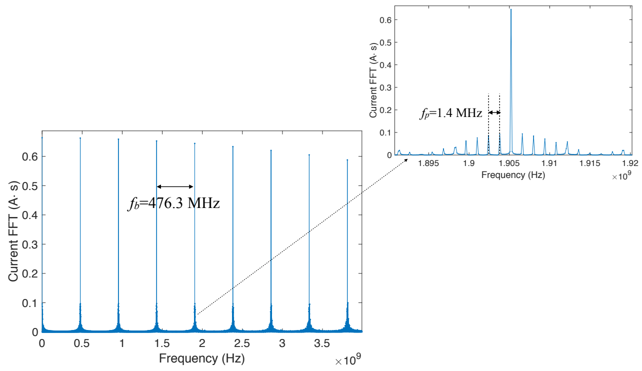

(b) The frequency spectrum.

Figure 2: The profiles of the beam current of the CCR

In Eq. (2), $I(t)$ is beam current, ω_n is a nth angular eigenfrequency of the cavity, $R_{n,\parallel}/Q_{n,0}$ is a longitudinal shunt impedance of the cavity, and $\tau_n = 1/Q_{n,L}$ with $Q_{n,L}$ being loaded quality factor is the natural decay time of the mode. Note that this is a voltage profile in time domain. From Eq. (2), the steady state induced power is computed straightforwardly according to

$$P_{ind,n} = \lim_{t\to\infty} P_{ind,n}(t) = \lim_{t\to\infty} \frac{|V_{b,n,\parallel}(t)|^2}{R_n}. \tag{3}$$

For a harmonic kicker, we add up the contribution from all the relevant eigenmodes to estimate the total power loss of the cavity, i.e., the ones that are confined within the cavity with the eigenfrequencies lower than TE_{11} cutoff frequency of the beam pipe (2.5 GHz). Because the eigenmodes are orthogonal modes to each other, we have

$$P_{tot} = \sum_{n}^{f_n<2.5GHz} P_{n,ind} \tag{4}$$

Here added n in the subscript refers to nth eigenmode. All the parameters needed in Eq. (2) and Eq. (5) were obtained from the CST eigensolver (up to 2.5 GHz). The power spectrum covering more than 100 eigenmodes (up to 2.5 GHz) is shown in Fig. 3. The summation of Eq. (4) yields $P_{tot} \sim 3.4$ W.

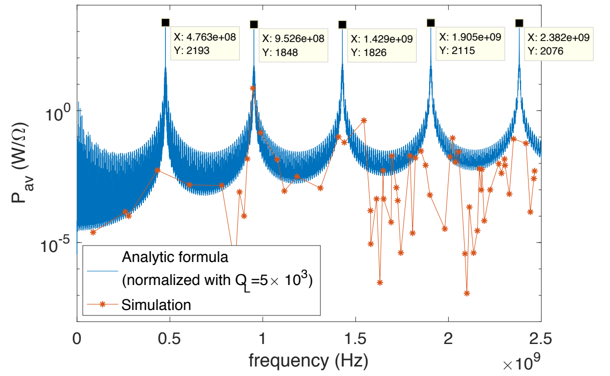

Figure 3: The power spectrum based on eignmode calculation. The red stars are the discrete spectrum of power while blue curve is continuous spectrum with a generic Q_L.

Power Evaluation via Impedance Spectrum

To take into account transient modes for power estimation, we use wakefield solver of the CST-PS to obtain the full. First, the cavities' wake potential has been computed as excited by a single bunch of Gaussian shape (line current) passing on the beam axis (The induced power is dominated by monopole modes). Then the wake potential is Fast Fourier transformed (FFT) to result in the broadband impedance spectrum using a customized FFT [7], which can resolve the peaks more accurately than via CST's embedded post-processing (up to a factor of 3 compared to the results (R/Q_0) of eigenmodes at resonance). In Fig. 4a, the real part of the longitudinal impedance spectrum $Z_\parallel$ is shown. By combining $Z_\parallel$ with the current spectrum shown in Fig. 2b, the beam-induced power can be calculated via

$$P(\omega) = \int_0^{\omega_c} d\omega\, I^2(\omega) Z_\parallel(\omega), \tag{5}$$

The resulting power spectrum is shown in Fig. 4b. The spectral density sums up to $P_{tot} = 3.6$ W (slightly more than the one based on eigenmode results). In addition, longitudinal loss factor has been calculated resulting in $k = 0.003$ V/pC.

Wake Fields by Dipole Charge

In addition to the HOM power excited by monopole modes, one would need to know the power induced by the beam traveling off-axis through the cavity, while this could also affect the transverse beam dynamics. But the effect on the beam dynamics is limited by a small number (11 turns) of circulation for each bunch. This aspect has been addressed by computing the transverse coupling impedance due to a dipole excitation, i.e., the electron bunches were offset vertically by a certain amount r_s from the beam tube axis. According to the Panofsky-Wenzel theorem, the transverse impedance at r_0 is related to the longitudinal impedance according to

$$Z_\perp(r_0,\omega) = \frac{c}{\omega r_s}\nabla_\perp Z_\parallel(r,\omega)\Big|_{r=r_0}, \tag{6}$$

ISBN: 978-3-95450-217-2 doi:10.18429/JACoW-ERL2019-WEPNEC22

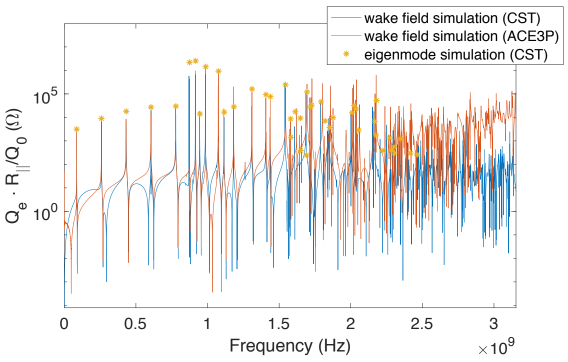

(a) The longitudinal impedance spectrum.

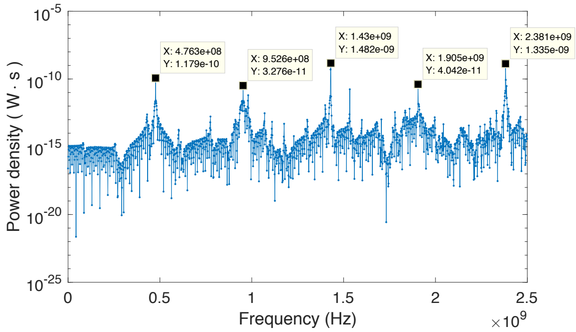

(b) The power spectrum by monopole excitation.

Figure 4: The impedance spectrum by monopole excitation.

We used a rather larger bunch length (= 6 cm) in the simulation than actual beam bunch length in the CCR, but this is small enough to reach 2.5 GHz. The wake potential is calculated up to 2.5 km in order to resolve within the bandwidth of each resonance.

where r_s is the distance of the driving charge from the beam axis. By setting $r_0 = 0$, longitudinal impedance $Z_\parallel$ can be Taylor-expanded as

$$Z_\parallel(r,\omega) = Z_\parallel(0,\omega) + \frac{\omega r_s}{c} Z_\perp(0,\omega) r + \mathcal{Z}(\omega) r^2 + \cdots, \quad (7)$$

where the coefficient of the linear term was fixed by making use of Eq. (6). With Eq. (7) and $Z_\parallel(0)$ obtained from the monopole excitation, one can evaluate $Z_\parallel$ at an arbitrary offset up to the linear term (dipole contribution) by evaluating $Z_\perp(0)$. To obtain a spectrum exclusively comprised by dipole modes, we setup a pair of oppositely charged bunches at opposite offsets, which cancels all the even-multipoles including $\mathcal{Z}$. In Fig. 5a, the resulting dipole impedance spectrum is shown. Utilizing the impedances plotted in Fig. 4a and 5a, and Eq. (7) and Eq. (5), the computed HOM power at an arbitrary offset up to linear order term, which resulted in $P(r) = (3.6 + 904.5r)$ W (with r in units of eter [m]). E.g. at an offset $r = \pm 1$ mm, the expected power is 3.6 ± 0.9 W.

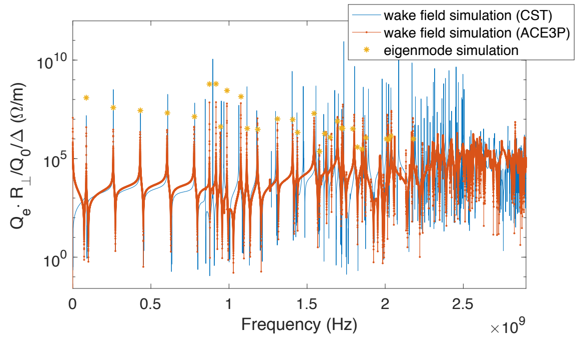

(a) The transverse impedance spectrum.

Figure 5: The impedance spectrum by dipole excitation.

DEFLECTING MODE POWER

Unlike the parasitic HOM's, the operating deflecting modes are excited by the RF generator as well as the beam. Because the resonant frequencies of the harmonic kicker are incommensurate with the bunch repetition rate of the CCR beam current, the phase relation between the generator mode and induced mode is dynamical, i.e., changes in time. The longitudinal kick voltage $V_{c,n\parallel}$ associated with the nth resonant mode in the cavity with phase ϕ_n can be written as

$$V_{c,n,\parallel} e^{i(\tilde{\omega}_n t + \phi_n)} = \tilde{V}_{g,n,\parallel}(t) + \tilde{V}_{b,\parallel}(t), \quad (8)$$

where $\tilde{V}_{g,n,\parallel}(t), \tilde{V}_{b,\parallel}(t)$ are complex voltages of the generator and beam induced mode, respectively. $V_{g,n,\parallel}(t)$ is adjusted so that $V_{c,n,\parallel}$ remains constant in time. The induced voltage by a train of $\mathcal{N}$ bunches with the period of $1/f_b$ is given via Eq. (2) as

$$\tilde{V}_{b,n,\parallel} = V_{b,n,\parallel} \left\{ \sum_{k=1}^{\mathcal{N}} e^{ik\tilde{\omega}_n/f_b} - \frac{1}{2} \right\} \quad (9)$$

$$= V_{b,n,\parallel} \left\{ \left(\frac{1 - e^{i\mathcal{N}\tilde{\omega}_n/f_b}}{1 - e^{i\tilde{\omega}_n/f_b}} \right) - \frac{1}{2} \right\}, \quad (10)$$

where $V_{b,n,\parallel}$ is the induced voltage by a single bunch. With $\mathcal{N} = 11$, the first term in the curly bracket of Eq. (10) vanishes with $11\omega_n = 4\pi n f_b$ for any n. A factor of half integer in the curly bracket is due to the voltage seen by the electron due to beam loading. This implies that the contribution from the beam loading remains at a few bunch-to-bunch fluctuations, which are negligible. Accordingly, the total power would be very close to ~ 7.4 kW as evaluated previously without beam loading in ref. [3].

CONCLUSION

The impedance study for a high power prototype of the harmonic kicker for the CCR of JLEIC has been completed. The results based on two different methods are consistent and yield HOM power levels lower than 20 W. This is insignificant compared to the RF power dissipated in the cavity walls for the operating, deflecting modes, for which we have designed a proper water cooling layout. Consequently we do not contemplate using HOM dampers. Also the required additional RF power due to beam loading is not significant compared to the cavity wall loss.

REFERENCES

[1] Y. Huang, H. Wang, R. A. Rimmer, S. Wang, and J. Guo, "Multiple harmonic frequencies resonant cavity design and half-scale prototype measurements for a fast kicker", *Phys. Rev. Accel. Beams*, vol. 19 (12), 122001 (2016). `doi:10.1103/PhysRevAccelBeams.19.122001`

[2] Y. Huang, H. Wang, R. A. Rimmer, S. Wang, and J. Guo, "Ultrafast harmonic rf kicker design and beam dynamics analysis for an energy recovery linac based electron circulator cooler ring", *Phys. Rev. Accel. Beams*, vol. 19, 084201 (2016). `doi:10.1103/PhysRevAccelBeams.19.084201`

[3] G. Park, H. Wang, R. A. Rimmer, S. Wang, and J. Guo, "The Development of a New Fast Harmonic Kicker for the JLEIC Circulator Cooling Ring", in *Proc. IPAC'18*, Vancouver, Canada, 2018. `doi:10.18429/JACoW-IPAC2018-TUPAL068`

[4] G. Park, H. Wang, R. A. Rimmer, S. Wang, F. Marhauser, J. Henry, M. Marchlik, and J. Guo, "Status Update of a Harmonic Kicker Development for JLEIC", in *Proc. IPAC'19*, Melbourne, Australia, 2019. `doi:10.18429/JACoW-IPAC2019-WEPRB099`

[5] CST, simulation packages, `http://www.cst.com`

[6] S. Benson *et al.*, "Development of a Bunched-Beam Electron Cooler for the Jefferson Lab Electron-Ion Collider", in *Proc. IPAC'18*, Vancouver, Canada, 2018. `doi:10.18429/JACoW-IPAC2018-MOPMK015`

[7] F. Marhauser, R.A. Rimmer, K. Tian, and H. Wang, "Enhanced method for cavity impedance calculations", *Proceedings of PAC09*, Vancouver, BC, Canada, paper: FR5PFP094.

RESEARCH ON ALKALI ANTIMONIDE PHOTOCATHODE FABRICATION RECIPE AT PKU

D.M.Ouyang, X.K. Zhang, S. Zhao, H.M. Xie†, L.W. Feng, S. Huang, S.W. Quan, K.X. Liu,
Institute of Heavy Ion Physics & State Key Laboratory of Nuclear Physics and Technology Physics and Technology, Peking University, Beijing 100871, China

Abstract

Low emittance, high QE and long lifetime photocathode is widely studied for X-ray Free Electron Laser (XFEL) and Energy Recovery Linacs (ERL) applications. A deposition system for alkali antimonide photocathode (K_2CsSb, Cs_3Sb etc.) is being commissioned at Peking University. In this paper, we present our experimental results on alkali antimonide photocathode with this deposition system. We successfully fabricated Cs_3Sb photocathode on oxygen free copper, p-type Si (100) and Mo substrates with QE of 1.4%, 2.6% and 2.6% respectively.

INTRONDUCTION

XFEL, ERL and electron cooling demand low emittance, high QE and long lifetime photocathode. The alkali antimoide photocathode has high QE (4~10%) at green light, low intrinsic emittance (~0.5 μm/mm) and long lifetime [1]. DC-SRF injector was stable operation to generating CW electron beams in 2014 at PKU [2]. Now, a low emittance DC-SRF photocathode injector (DC-SRF-II) is under construction for XFEL at PKU. In order to meet the requirement of the upgraded version of DC-SRF-II injector (bunch charge 100 pC, lower emittance < 1μm and repetition rate ~1MHz) [3-4], we choose the alkali antimonide photocathode.

In this paper we present our alkali antimonide photocathode deposition system and experimental results on fabricating Cs_3Sb photocathode at PKU. We also measured its spectral response and dark lifetime on the UHV system.

ALKALI ANTIMONIDE PHOTOCATHODE DEPOSITION SYSTEM

We have developed an alkali antimonide deposition system which consists of a deposition chamber, a transport chamber, a suitcase chamber, a spectral response measurement system, an intrinsic emittance measurement system (under construction based on LBNL design [5]), and four manipulators to transfer the sample. The substrate was initially kept in the suitcase chamber, and then transferred to the transport chamber by two manipulators. Utilizing another manipulator, the substrate can be moved to the deposition chamber. When the photocathode was prepared, it can be transported to injector by suitcase or though the transport chamber. Three sources, Cs, K and Sb were mounted on the deposition chamber and alkali sources were separated from each other and from the chamber by ultrahigh-vacuum (UHV) gate valves. A sputtering ion pump (400L/s) and SAES NEG pumps (3500L/s and 2000L/s) can provide pressure 10^{-9} Pa in deposition chamber and transport chamber. We employed a quartz crystal monitor to record the thickness of the film during evaporation and a residual gas analyser (RGA) was utilized to analyse the partial pressure of gases in the deposition chamber (see Fig. 1). The photocathode was irradiated by a 520 nm, power adjustable laser and we employed a Keithley 6485 picoammeter to monitor the photocurrent leaving the photocathode.

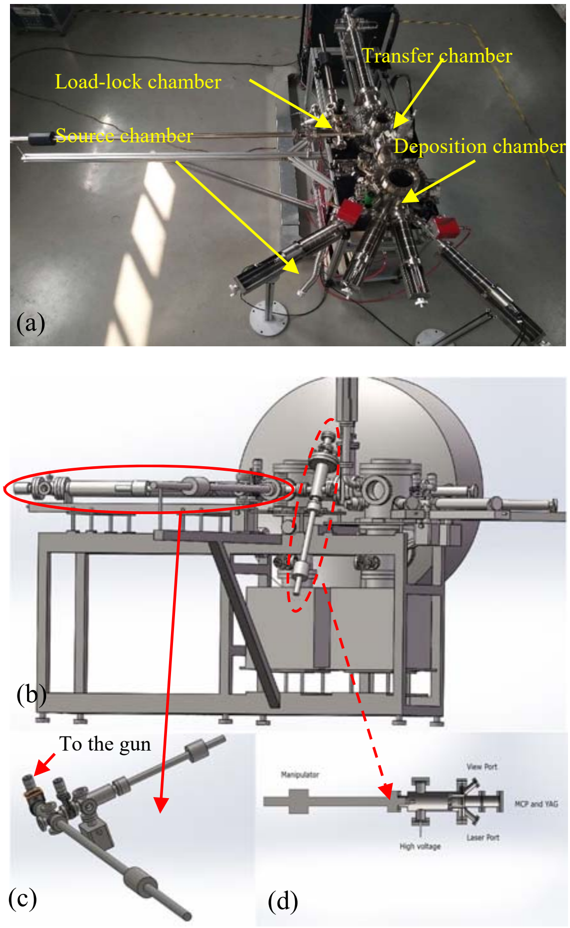

Figure 1: (a) Photograph and (b) schematic diagram of alkali antimonide photocathode deposition system. (c)Suitcase. (d)The intrinsic emittance measurement system.

---

† hmxie@pku.edu.cn

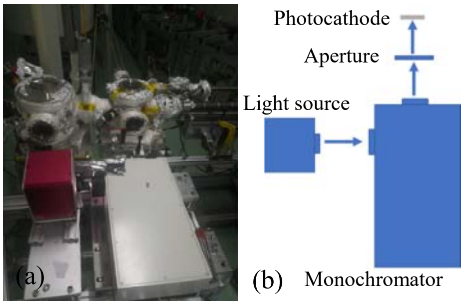

Figure 2: (a) Photograph and (b) schematic diagram of spectral response measurement system.

The spectral response measurement system consists of light source (Xenon and Mercury-Xenon Short-Arc Sources: 240 - 2400 nm), a monochromator (200-2500 nm) and an aperture (see Fig. 2). We can use the spectral response measurement system to research the work function and band structure of photocathode, especially when the photocathode is in low-temperature environment. The spectral response system can be used to measure the work function of the photocathode. And the temperature dependence of the spectral response can also be derived when the cathode is cooled by liquid nitrogen.

Cs_3Sb PHOTOCATHODE FABRICATION AND DISCCUSION

We have fabricated Cs_3Sb on Cu, Mo and p-type Si (100) substrates to research the recipe .The following will introduce our experiments and results.

Cs_3Sb Photocathode on Cu Substrate

The Cu substrates were electropolished in solution of phosphoric acid and N-butanol and then was passivated in sulfamic acid (see Fig.3). Then the substrate was ultrasonic reinsed in alcohol and dried with flowing N_2 gas.

Figure 3: (a) Cu substrate after EP. (b) Cs_3Sb photocathode on Cu substrate.

The recipe of Cs_3Sb photocathode on Cu substrate is as following:

- The Cu substrate was degassed in UHV chamber @ 400 °C for about two hours.
- Deposit Sb film about 13nm~16nm at 140°C.
- Start Cs activation after Sb film is deposited. The Cs activation stopped when the photocurrent reaches a plateau. The substrate is cooled naturally.

We can see the whole process of Cs_3Sb cathode growth from Fig. 4(The peaks of the chamber pressure curve corresponds to the movement of sample holder, source arms and crystal monitor in the deposition and transferring chamber). The fresh QE of Cs_3Sb on Cu could reach 1.4% (#20190616) at 520 nm laser. The 1/e dark lifetime is about 2 weeks. The QE map of the photocathode was also measured.

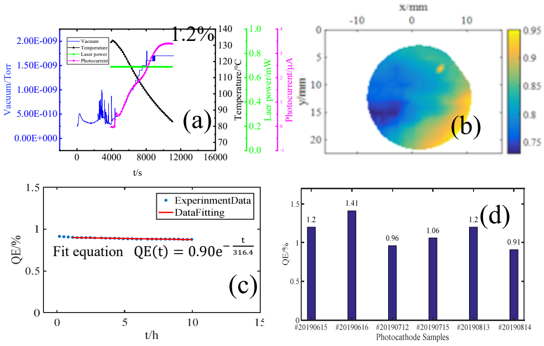

Figure 4: (a) The fabrication process of Cs_3Sb photocathode #20190813. (b)QE map of Cs_3Sb photocathode #20190813. (c)Dark lifetime of Cs_3Sb photocathode #20190813. (d)QE of Cs_3Sb on Cu substrates.

Cs_3Sb Photocathode on Mo Substrate

Mo is widely used as the substrate for photocathode deposition accounting for its chemical stability worldwide [6]. The Mo substrate was polished with sandpaper from 1500# to 7000# and diamond paste (see Fig. 5). The cleaning procedures were similar as Cu.

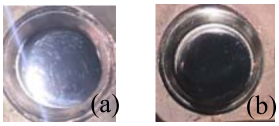

Figure 5: (a)Mo substrate after polished by sandpaper and diamond paste. (b)Cs_3Sb photocathode on Mo substrate.

As we can see in Fig. 6, the fresh QE of Cs_3Sb on Mo substrate was ~ 2.6% incident by 520nm laser.

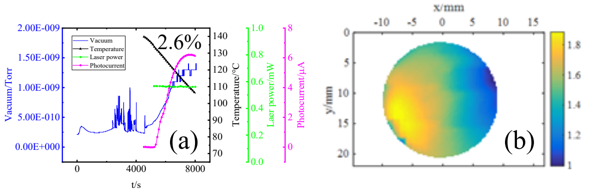

Figure 6: (a)The activation process of Cs_3Sb photocathode #20190909. (b)QE map of Cs_3Sb photocathode #20190909.

From Fig. 3 and Fig. 5, the Cu and Mo substrates were not optical polished. The surface was rough and it may also influence the film growth and the emittance of the photocathode [7].

Cs_3Sb Photocathode on Si Substrate

The Si substrate surface was smooth and no processing was needed. We also fabricated Cs_3Sb on p-type Si substrate with recipe in Table 1. The Si wafer has a resistivity of 0.001~0.009 and was cleaned by 2% HF solution for 5 min. Then the wafer was reinsed in alcohol and dried with flowing N_2 gas (see Fig. 7).

Table 1: Recipe of Cs_3Sb on Si Substrate

Photocathode	Recipe
#20190714	Sb film: 13-16nm 140°C Cs: 140°C
#20190811	Sb film: 13-16nm 140°C Cs: 140°C
#20190906	Sb film: 13-16nm 120°C Cs: 120°C

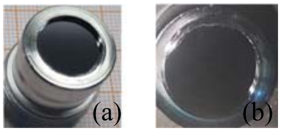

Figure 7: (a)Si substrate after cleaning. (b)Cs_3Sb photocathode on Si substrate.

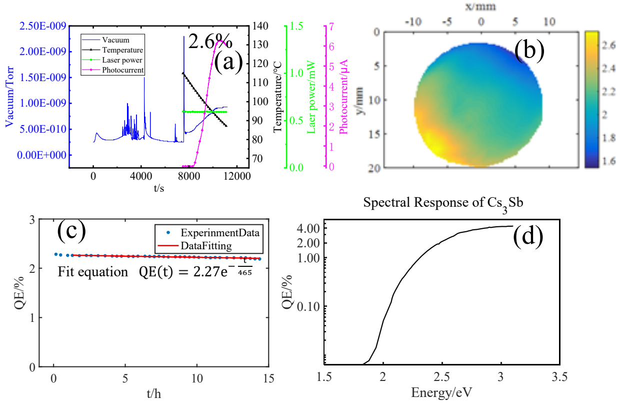

Figure 8: (a) The Cs_3Sb photocathode fabrication process of #20190906. (b)QE map of #20190906. (c)Dark lifetime of #20190906. (d)Spectral response measurement of #20190906.

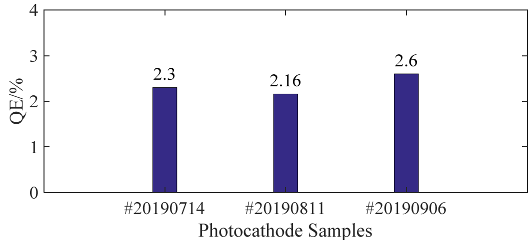

Figure 9: QE of Cs_3Sb on Si substrates.

The fresh QE of Cs_3Sb on Si substrate could reach 2.6% and the dark lifetime was about 3 weeks (see Fig. 8 & Fig. 9). From the QE map of #20190906, the QE of most area could achieve more than 2%.

In order to optimize the recipe, the morphology of the Sb film on Si substrate was investigated with SEM. The thickness of the Sb film is about 13nm. As shown in Fig.10, the Sb islands were separate which means that the Sb film might be too thin. So the Cs_3Sb could not crystallize fully and the QE was lower. Also, the reason that the quality of #20190906 was better than #20190714 and #20190811 might be the Sb film of #20190906 was thicker, because the lower temperature may be beneficial to Sb films deposition.

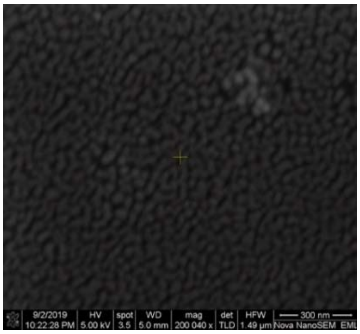

Figure 10: The morphology of Sb film on Si substrate.

CONCLUSION

We successfully fabricated Cs_3Sb photocathode on oxygen free copper, Mo and p-type Si (100) substrates with QE of 1.4%, 2.6% and 2.6% respectively.

In the future, the recipe will be further optimized and bialkali photocathode will also be fabricated and tested in the DC-SRF injector at PKU. The cryogenic effect on QE and intrinsic emittance of alkali antimonide photocathode will also be investigated.

REFERENCES

[1] H. M. Xie *et al.*, “Research on Fabrication Recipe of High Quantum Efficiency K_2CsSb Photocathode”, *Vacuum*, vol. 54(1), pp.63-66, 2017. `doi: 10.13385/j.cnki.vacuum.2017.01.16`

[2] K. X. Liu *et al.*, “Experimental Study on the Electron Superconducting Linac and its Application”, *in Proc. 13th Symposium on Accelerator Physics (SAP'17),* Jishou, China, Aug. 2017. `doi:10.18429/JACoW-SAP2017-MOBH1`

[3] S. Zhao, S. Huang, K. X. Liu, Y. Q. Liu, and D. M. Ouyang., “Performance Optimization of Low-Emittance DC-SRF Injector Using Cs2Te Photocathode”, *in Proc. 39th Int. Free Electron Laser Conf. (FEL'19)*, Hamburg, Germany, Aug. 2019, paper WEP057.

[4] Y. Q. Liu *et al.*, “Engineering Design of Low-Emittance DC-SRF Photocathode Injector”, *in Proc. 39th Int. Free Electron Laser Conf. (FEL'19)*, Hamburg, Germany, Aug. 2019, paper WEP056.

[5] J. Feng *et al.*, “A novel system for measurement of the transverse electron momentum distribution from photocathodes”, *Rev. Sci. Instrum.* , vol. 86, p. 015103, 2015. `doi:10.1063/1.4904930`

[6] Martin A. H. Schmeißer *et al.*, “Towards the operation of Cs-K-Sb photocathodes in superconducting rf photoinjectors”, *Phys. Rev. Accel. Beams*, vol. 21, p. 113401, Nov. 2019. `doi:10.1103/PhysRevAccelBeams.21.113401`

[7] G. Gevorkyan *et al.*, “Effects of physical and chemical surface roughness on the brightness of electron beams from photocathodes”, *Phys. Rev. Accel. Beams*, vol. 21, p. 093401, Sep. 2018. `doi:10.1103/PhysRevAccelBeams.21.093401`

ISBN: 978-3-95450-217-2 doi:10.18429/JACoW-ERL2019-WECOYBS04

COMMISSIONING OF THE bERLinPro DIAGNOSTICS LINE USING MACHINE LEARNING TECHNIQUES*

B. Kuske†, Helmholtz-Zentrum für Materialien und Energie, Berlin, Germany,
A. Adelmann, Paul Scherrer Institut, Villigen, Switzerland

Abstract

bERLinPro is an Energy Recovery Linac (ERL) project currently being set up at HZB, Berlin. It is intended as an experiment in accelerator physics, to pioneer the production of high current, low emittance beams in a fully super-conducting accelerator, including SRF gun, booster and linac. RF-Commissioning of the gun is planned in mid 2020, [1]. HZB triggered and partially supported the development of release 2.0 of the particle tracking code OPAL [2]. OPAL is set up as an open source, highly parallel tracking code for the calculation of large accelerator systems and many particles. Thus, it is destined for serving attempts of applying machine learning approaches to beam dynamic studies, as demonstrated in [3]. OPAL is used to calculate hundreds of randomized machines close to the commissioning optics of bERLinPro. This data base is used to train a polynomial chaos expansion, as well as a neural network, to establish surrogate models of bERLinPro, much faster than any physical model including particle tracking. The setup of the sampler and the sensitivity analysis of the resulting data are presented, as well as the quality of the surrogate models. The ultimate goal of this work is to use machine learning techniques during the commissioning of bERLinPro.

INTRODUCTION

As any linear accelerator, an ERL is an initial value problem: without exact knowledge of the initial parameters of the beam, a later understanding and characterization of the beam parameters is difficult. Therefore, a thorough understanding of the gun is indispensable. Before the gun is assembled and tested, many ambiguities exist, starting from the actual energy of the beam, i.e. the gun field reachable with tolerable field emission, over the bunch parameters, to the system parameters leading to successful acceleration. As the system is heavily space charge dominated with bunch charges of 77 pC, tracking calculations including space charge take minutes to hours, depending on the size of the considered structure, the number of particles and the grid size, even with a highly parallized code like OPAL. It is tempting to try to replace the tracking calculations by surrogate models, that deliver answers very close to tracking results in much shorter time, in the order of milliseconds. That would enable 'online modeling' in the control room, where the surrogate model is fed by machine parameter read-backs and would deliver expectation results for beam measurements. The paper presents first steps in setting up surrogate models for the diagnostics line of bERLinPro, where the gun is characterized. It makes strong use of earlier work and experience, published in [3] and [4]. It is intended to use surrogate models to ease and to speed up commissioning.

DIAGNOSTICS LINE

The diagnostics line consists of the 1.3 GHz, 1.4 cell, single cavity SRF gun, providing up to 3 MeV electrons with a design bunch charge of 77 pC. The gun module also hosts two corrector coils (H/V) and a cold solenoid. The booster, hosting three two-cell cavities can boost the energy up to 6.5 MeV. The first cavity imprints a chirp on the bunch for velocity bunching, while the other two cavities are run on crest for acceleration. Further elements are 6 quadrupoles, a transverse deflecting cavity, a spectrometer followed by a 300 W Faraday cup, or, straight ahead, a 35 kW beam dump, Fig. 1. Optics were developed including the booster (6.5 MeV) and with three booster replacement quadrupoles (taken from the recirculator) and 2.7 MeV. Four beam position monitors (BPM) and two screens (FOM) are available for diagnostics.

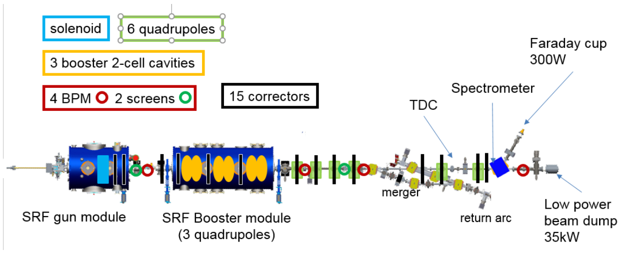

Figure 1: The diagnostics line is intended for the characterization of gun and booster and initial beam parameters.

Independent Modeling Parameters

The ambiguities in the gun parameters, prior to commissioning, are caused by:

- production uncertainties like cavity geometry and field flatness, i.e. the gun field
- changes during cool down of SRF structures (f.e. cathode retraction position)
- ambiguities before first use (f.e. achievable max. gun field amplitude).

In addition, the cathode laser pulse length, spot size and intensity, the solenoid strength, the phases and amplitudes of three booster cavities and the field of the six quadrupoles in the beam line will determine the bunch properties. The transverse beam size can be measured on the two screens and four BPMs. The transverse deflecting cavity (TDC) and the spectrometer in combination enable the measurement of

---

* Work supported by German Bundesministerium für Bildung und Forschung, Land Berlin and grants of the Helmholtz Association

† bettina.kuske@helmholtz-berlin.de

the full, 6D phase space. The emittance will be determined by quadrupole scans using the first three merger quadrupoles. See Fig. 2, where the 19 independent parameters are indicated. In order to predict the expected bunch properties for all possible combinations of set points of the independent parameters, huge scans would be necessary. Even using only three set points for each parameter, $3^{19} = 1.16 \times 10^9$ possible combinations arise.

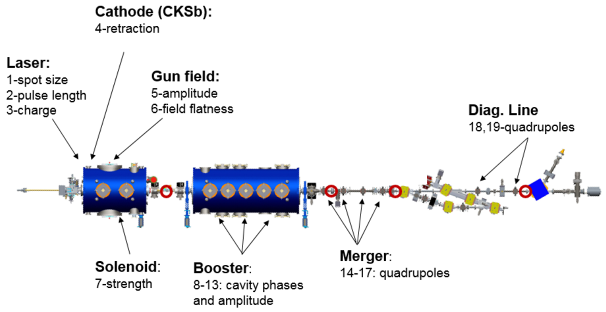

Figure 2: The most relevant 19 parameters contributing to the physics model of the diagnostics line of bERLinPro.

Therefore, there is a strong need to minimize the number of independent parameters to ease commissioning and enable modeling. In order to thread the beam successfully through the diagnostics line and enable first bunch measurements, the following restrictions can be taken:

- Bunch charge, current: During commissioning, the current will be limited to ≈ 1 µA defined by the tolerable load on the screens. Measurements can be taken by much lower currents, down to nA. Calculations show, that the limit for the bunch charge to eliminate space charge effects in the reference optics is about 0.1 pC corresponding to 1 µA in single bunch mode at 10 Hz. Low bunch charge also eliminates the dependance on the laser intensity.
- Quadrupole setting: The quadrupoles in front of the screen in the merger can be set in a way to produce a round beam on the screen. This is easily controllable. Without space charge, the settings can be linearly scaled to the achieved energy.
- Booster amplitudes and phases: We assume, that these parameters can be well measured and keep them fixed in the simulations.
- The two last quadrupoles serve to adjust the transverse beam size into the dump. They are located behind the diagnostics elements and need not be part of the modeling.

This leaves six independent variables for the first commissioning phase. The expected variation range and set points used in the sampling run, are listed in Table **??**. The five cathode retreat positions and three field flatnesses are encoded in 15 CST field files.

OPAL

OPAL is one of the few tracking codes, that includes a 3D space charge routine, coherent synchrotron radiation effects and is open source. OPAL was planned from the beginning as a highly parallelized tracking code for the calculation of large accelerator systems and many particles, and its underlying structure has been developed by computer scientists and mathematicians. HZB triggered and partially supported the development of release 2.0 of OPAL, as no other code was available at the time, that was suitable for the modeling of a high current, low energy ERL, such as bERLinPro. OPAL can now cope with with specifics like double passage through elements, and thus is a very adequate tool to study this type of machines.

Table 1: Range and Number of Equidistant Set Points of the Six Independent Parameters

Parameter	Range	Set point
Laser pulse length	± 10%	3
Laser spot size	± 10%	3
Gun field flatness	100, 113, 130%	3
Cathode retreat	0.5-1.5mm	5
Gun voltage	15-17MV/m	5
Solenoid field	0.035-0.065T/m	7
combinations		4725

OPAL also offers a sampler option: in a single run it allows for random, raster or mixed sampling of parameters with different distribution functions. The results are stored in a separate directory. This is a big advantage compered to other optimization procedures, like swarm calculations or generic optimizers, where most of the calculated data is deleted and not accessible for later studies. Using the sampler, a set of 4725 different realizations of the diagnostics line has been calculated over the complete length of 14 m. The calculations included space charge (to cover cases with unintended beam waists) and 100.000 particles. On the PSI cluster the run took 5 h, using 320 cores. It should be mentioned, that this computational effort has to be invested only once. The derived surrogate model, though, can be used for further optimization and as an on-line model. Once the data is available, it can be used in versatile ways:

- Data mining
- Polynomial chaos expansion
- Neural networks
- Other boost or regression algorithm

The latter three all create a surrogate model, that approximates the parameters of interest, but is MUCH faster than the under-lying tracking calculations.

RESULTS

Data Mining

Data mining is a rich source for understanding the basic mechanisms of the system, especially, if expectations based on accelerator physics knowledge can be retrieved in the data. As an example, one can look at the cases where particles get lost in the diagnostics line. From optics development it is known, that the rf focusing of the booster is strong, and the transverse beam size at the booster entrance is a critical parameter. Figure 3 shows the number of stable particles at 10 m (left) and at 14 m (right) as a function of the rms beam size at the beginning of the booster (round beam). Clearly, all beams with transverse sizes larger than 1.5 mm will loose particles before reaching the dump.

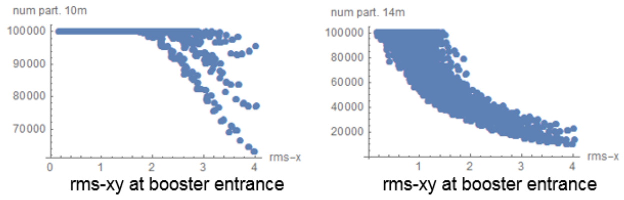

Figure 3: Number of stable particles at 10 m, left, and at 14 m, right. There is a clear dependance on the transverse beam size at the booster entry.

The correlation between four of the independent input parameters and the beam size at the beginning of the booster is displayed in Fig. 4. The distinct set values are visible. Surprisingly, the cathode position has a larger impact on the transverse beam size, than the laser spot size (within the ranges studied). In order to reach transverse beam sizes ≤1.5 mm at the entrance of the booster and secure particle transport into the dump, the setting of the solenoid is the most critical parameter. It has not been expected, that setting the solenoid field to 0.055 T/m guarantees adequate beam sizes for all other cases (red line). Selecting only cases with the optimal solenoid setting, expectation values can now be extracted for other beam parameters.

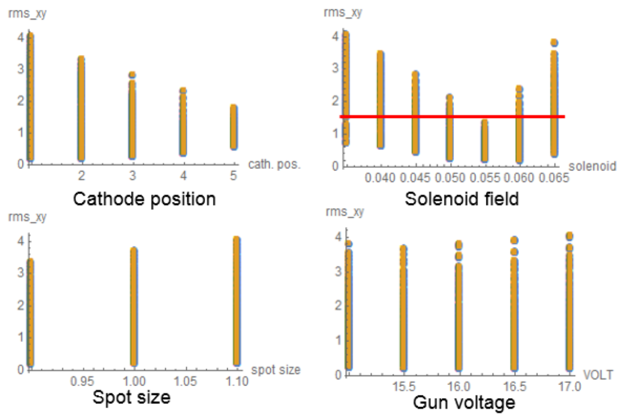

Figure 4: The transverse beam size at the entrance to the booster is displayed as a function of the cathode position, the solenoid setting, the laser spot size and the gun voltage. The red line indicates the goal of $\sigma \leq 1.5$ mm.

Polynomial Chaos Expansion

Polynomial chaos expansion (PCE) and its application in accelerator physics is explained in detail in [4]. PCE is applicable, whenever system parameters with a given uncertainty or distribution are mapped by a physical model or evolution, onto quantities of interest (QoI), that depend on these system parameters. As f.e. the laser pulse length entering tracking calculations will lead to beam parameters like the bunch length, that depend on the pulse length and will have a distribution, that will depend of the distribution of the laser pulses, Fig. 5.

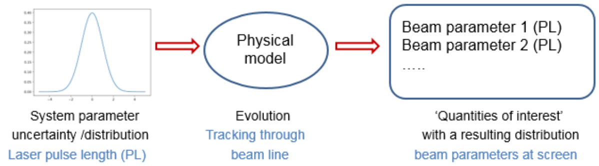

Figure 5: Polynomial Choas Expansion is a method to determine evolution in dynamical systems, when there is probabilistic uncertainty in the system parameters.

It can be shown, that:

- the distribution space of the QoI always has an orthonormal polynomial basis, i.e. every element in the QoI space can be represented as a polynomial sum
- the kind of polynomials to be used depends on distribution of the independent variables (uniform ⇔ Lagrange, Gaussian ⇔ Hermite, …)
- the determination of the sum coefficients reflects the model involved (regression technique)
- PCE is applicable in multi-dimensions and for mixed distributions

The mathematics behind PCE is conveniently wrapped up in the python package 'chaospy', [5].

The PCE will always be trained with a subset of the available samples, in order to check the results with the left over testing samples. The quality of the PCE model can be represented by plotting the results for a single QoI calculated by tracking and calculated by PCE against each other. For a perfect model all points would lie on the diagonal. Figure 6 shows the results for the horizontal emittance for different sizes of training sets. While the prediction of the model for the training samples is quite independent of the number of samples used, the results for the testing samples differ strongly. 1500 training samples were found to be sufficient, no further improvement was found for more samples.

A further optimization parameter is the order of the polynomials used in the expansion. Figure 7 compares the results for the horizontal rms beam size at the screen in the merger for third and sixth order polynomials. Blue dots represent the results for the training data and red dots that for testing samples. Sixth order polynomials show sufficient accuracy.

The accuracy of the PCE model might differ for different parameters. This reflects the sensitivity of the QoI in the system. The beam size in Fig. 7 is taken at the screen in the merger. The beam goes through a waist close to the screen for many samples. The position of the waist, and thus the beam size measured on the screen, is sensitive to small changes in all focusing parameters. For comparison, the results for the bunch length (left) and the energy (right) are shown in Fig. 8. While the energy is perfectly matched independent of the polynomial order, the bunch length profits from using sixth order polynomial (blue dots).

ISBN: 978-3-95450-217-2 doi:10.18429/JACoW-ERL2019-WECOYBS04

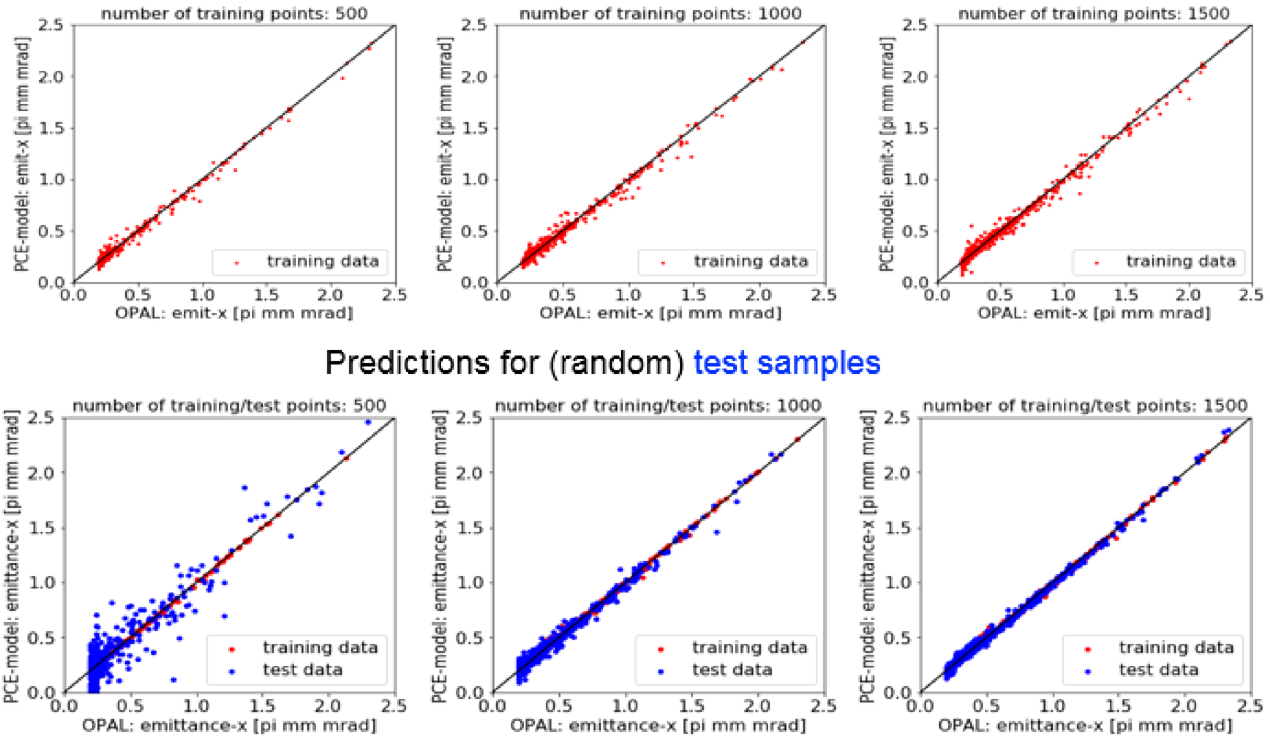

Figure 6: Results for the horizontal emittance calculated by the surrogate model and by tracking. 500 (left), 1000 (center), and 1500 (right) training samples (top) and the same number of testing samples (bottom) were used. 1500 training samples seek best results.

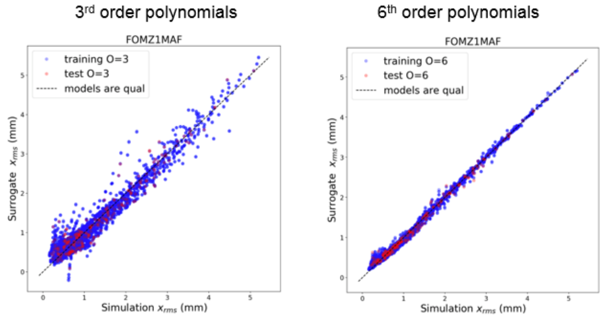

Figure 7: Results for the horizontal beam size, using third (left) and sixth order (right) polynomials. Red dots display the results for test particles, blue dots that of the training particles.

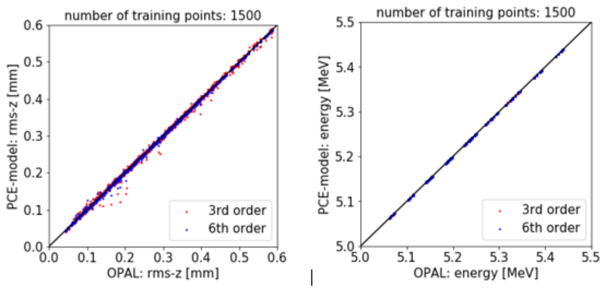

Figure 8: Results for the bunch length (left) and the energy (right). Third order polynomial expansion is shown in red, sixth order in blue.

Uncertainty Quantification

Having developed a PCE from calculated or measured samples, it is straight forward to calculate Sobol's indexes, for details refer to [4]. The first order PC-based Sobol's indexes represent the individual effects of a single random input parameter on the variability of the output. Figure 9 shows the uncertainty quantification for eight quantities of interest and six independent input parameters, taken at the end of the diagnostics line. Many dependencies are expected from accelerator physics knowledge: the dependence of energy on the field flatness or the importance of the solenoid field for the beam size and emittance. The dominant importance of the gun voltage for the bunch length, is less obvious. Higher gun voltage and higher field flatness lead to increased bunch length and increased energy spread at the exit of the gun. The dependance is enhanced by velocity bunching in the booster, see Fig. 10, and diminishes slightly towards the end of the line.

The seemingly obvious impact of the laser pulse length on the bunch length turns out to be negligible. Due to the lack of space charge effects in the sampling data, the bunch length is dominated by the velocity difference due to varying fields after emission from the cathode. The change in field flatness (100 – 130 %) has a larger influence on the particle

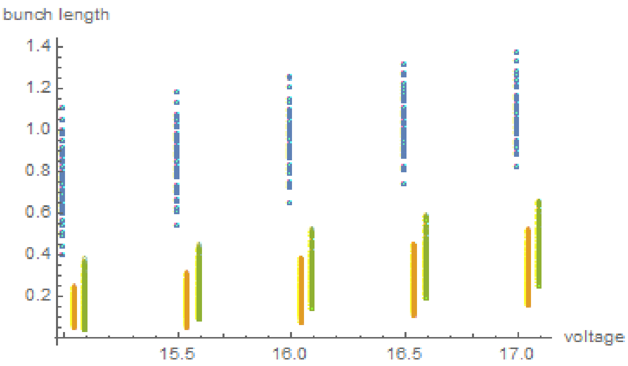

Figure 9: Sensitivity analysis of 4725 samples evaluated at the end of the diagnostics line. Blue: field flatness; light blue: cathode position; orange: laser pulse length; green: solenoid field; light green: laser spot size; red: gun voltage.

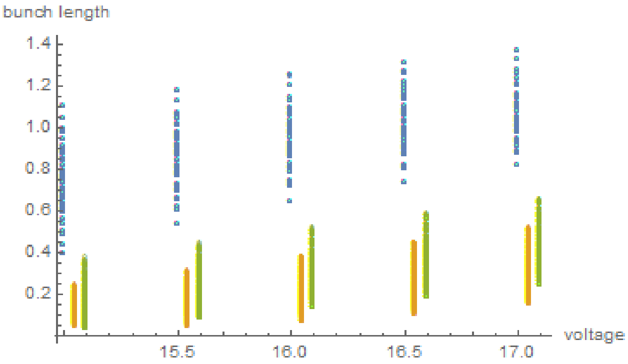

Figure 10: The dependence of the bunch length on the gun voltage. Behind the gun (blue), after compression in the booster (orange) and at the end of the line (green).

energy, than the variation of the gun voltage between 15 and 17 MV/m. After warm measurements of the field flatness, this ambiguity can be largely decreased. Sensitivity quantification helps to sort the importance of machine parameters, when trying to achieve specific bunch parameters. It is important to note, that the sensitivities can vary over the beam line.

Neural Network

A four layer, fully connected artificial neural network has been trained on the same sample data. The results for training data (left), as well as for the test data (right), at the screen in the merger, are displayed in Fig. 11, for the horizontal emittance. Both approaches seek qualitatively good results. For the training data, the mean average error (MAE) between both models, PCE and ANN, and OPAL is 0.5 %. For the testing data, there is a small advantage for the ANN, with an error of again 0.5 %, compared to PCE with an error of 0.6 %. No sensitivity analysis is available, though, when using ANNs.

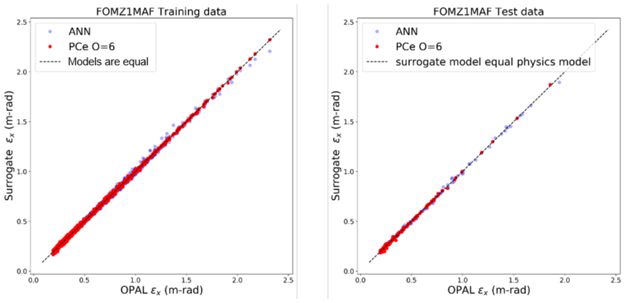

Figure 11: Comparison between PCE

CONCLUSION

This article concentrated on showing that the application of statistical learning (PCE) or machine learning (ANN) in commissioning has manifold advantages:

- The data necessary to perform PCE/ANN in itself is a rich source of information, that can reveal helpful dependencies.
- Uncertainty quantification, a side product of PCE, gives a quick overview of dependencies of QoI on machine parameters.
- Surrogate models are fast. They can be implemented in the control room and can translate machine settings online into expectation values for beam parameters.
- Surrogate models can speed up optimizations. When approximating measured data or finding new working points, genetic optimizers can be run much faster using the surrogate model.
- The surrogate model prepared for commissioning on theoretical data can be easily improved by including measured date, when it is available.
- Ultimately, one could build a model exclusively on measured data.

Both approaches will be applied to ease the commissioning of bERLinPro. Different samples will be prepared to serve different stages and questions during commissioning, where the understanding of the gun plays the mayor role. Validation tests have to be performed for each model. The effect of increasing bunch charge is of central concern and will be studied in detail. Fortunately, bERLinPro, designed to serve accelerator physics rather than being a user facility is the ideal testbed to study this new approach.

REFERENCES

[1] M. Abo-Bakr et al., "The Berlin Energy Recovery Linac Project bERLinPro – Status, Plans and Future Opportunities", presented at ERL'19, Berlin, Germany, Sep. 2019, paper: MOCOXBS04, this conference.

[2] `https://gitlab.psi.ch/OPAL/Manual-2.0/wikis/home`

[3] Auralee Edelen, Nicole Neveu, Yannick Huber, Mattias Frey, Christopher Mayes, Andreas Adelmann, "Machine Learning for orders of magnitude speedup in multi-objective optimization of particle accelerator systems", `https://arxiv.org/abs/1903.07759`

[4] Andreas Adelmann, "On non-intrusive uncertainty quantification and surrogate model construction in particle accelerator modelling", *SIAM/ASA Journal on Uncertainty Quantification*, 7(2), (2019), `doi:10.1137/16M1061928`

[5] `https://chaospy.readthedocs.io/en/master/`

SYSTEM IDENTIFICATION PROCEDURES FOR RESONANCE FREQUENCY CONTROL OF SC CAVITIES*

S. Orth†, H. Klingbeil, Institut für Teilchenbeschleunigung und Elektromagnetische Felder,
Accelerator Technology Group, TU Darmstadt, Germany

Abstract

Energy Recovery Linacs promise superior beam quality—smaller emittance and higher intensity. To reach these goals, resonance frequency control of the superconducting RF cavities has to be optimized.

To ensure stability of the resonance frequency the helium pressure inside the cryomodules is measured and stabilized. In order to improve the performance of the applied controller, i. e. for optimizing its parameters, one has to obtain the system's transfer function by means of physical modelling or system identification techniques. In this work the latter approach is presented. Special constrictions are the necessity to run the system in closed-loop mode and using data obtained during normal machine operation.

The results of system identification procedures conducted at the helium-pressure stabilizing system of the S-DALINAC's cryomodules (Institute for Nuclear Physics, TU Darmstadt, Germany) and first results of a test with improved control parameters are shown.

MOTIVATION

Due to their narrow bandwidth SC cavities are very sensitive to changes in their geometry. A 1 mbar pressure change of the helium in the cryomodules for example can cause a change in the resonant frequency of 20 to 50 Hz. Resonance frequency control with e. g. piezo tuners can be used to counteract this [1]. Another approach can be eliminating the sources of some disturbances, like decoupling the cryomodules from mechanically vibrating components such as vacuum pumps. Nevertheless, if there is for example a sudden heat intake, maybe due to turning on the RF power delivery to the cavities (or vice versa, lesser heat intake if one has to turn them off), this can cause more helium to evaporate (or less, respectively) and thus resulting in fluctuations of the helium pressure that have to be damped by the controller by increasing (or decreasing) the pump's speed.

Figure 1 shows a typical measurement of the helium pressure when such a disturbance occurs. The system is operated in closed-loop mode so that the controller damps the disturbance to reach the steady state. At the S-DALINAC this process can take up to three hours, as on can see in Fig.1.

Although this is a rather slow process it causes drifts that have to be compensated by the piezo tuners. Since these feedback loops rely on the measurement of the RF phase, they can have problems detecting such slow changes and sometimes manual corrections to the RF phase are applied by the operators who recognize e. g. a drift in the beam energy. To improve long-term stability of the beam quality and to ease the operation of the machine, an improvement of the helium pressure stabilizing controller was desired.

There have been some tests modifying the controller's parameters—it's a standard PID controller with $P = 250,\ I = 3\,\mathrm{s},\ D = 0\,\mathrm{s}$:

$$U(t) = PE(t) + \frac{1}{I}\int_0^t E(t')\mathrm{d}t' + D\frac{\mathrm{d}E(t)}{\mathrm{d}t}. \qquad (1)$$

Especially the D-component was slightly increased to speed up the system, but no results were found in the tested parameter range. To ensure stable operation this range was chosen very narrow.

With the model obtained from system identification an improved set of control parameters was suggested and successfully tested.

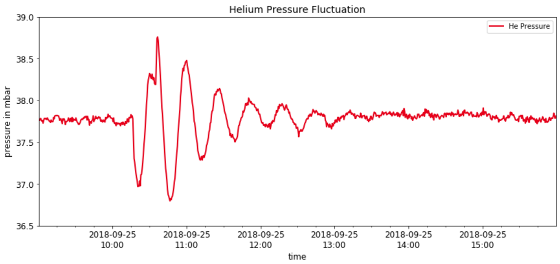

Figure 1: Helium pressure fluctuation in a cryomodule after a disturbance.

This system identification was also intended to serve as a prove of principle for closed-loop system identification procedures that are planned to be applied to other components as well. To make this transfer more convenient a generalized description of the system will be given in the next section followed by an overview over different closed-loop system identification techniques and a their advantages and disadvantages. Then, the results of such an identification process applied to the helium pressure stabilizing system and simulations with improved control parameters are shown. These predictions have been tested and first measurement results are presented.

BLOCK DIAGRAM AND SYSTEM EQUATIONS

The block diagram of a closed-loop system is depicted in Fig. 2. Note that for an open-loop system identification there is no feedback of the system's output y and in many cases the identification directly uses the system's input u. Also

---

* Work supported by DFG: GRK 2128 "AccelencE"

† orth@temf.tu-darmstadt.de

for closed-loop system identification one can make use of an exiting signal r_1 that directly acts on the plant. In normal operation this signal r_1 typically is not present.

Measurements of u and y are mandatory, while exact knowledge of r_1 or r_2 or knowledge of C is not required in general but can be necessary for some identification schemes.

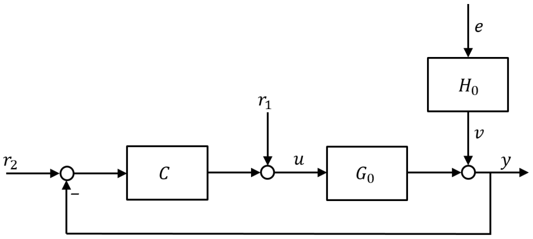

Figure 2: Block diagram of a closed-loop system with a controller C, the plant G_0, reference signals r_1 and r_2 and noise v.

The system's output $Y(t)$ is assumed to be digitally sampled with a constant sampling time T with $Y_k := Y(kT)$, $k = 0, 1, \ldots$ and hence the system is described in its z-transform with z being the forward shift operator,

$$Y_k \circ\!\!-\!\!\bullet\; y(z) \tag{2}$$

$$Y_{k+1} \circ\!\!-\!\!\bullet\; z \cdot y(z). \tag{3}$$

Following [2] the exciting signals are combined to

$$r = r_1 + C(z) r_2. \tag{4}$$

The noise v is modelled as filtered white noise,

$$v = H_0(z) e, \tag{5}$$

where $H_0(z)$ has to be stable and stably invertible. The noise disturbance will be assumed to be uncorrelated with the signals r_1 and r_2. The system's sensitivity function is

$$S_0 = (1 + G_0 C)^{-1} \tag{6}$$

where the argument is omitted for better readability.

This results in the following system equation and feedback law:

$$y = S_0 G_0 r + S_0 H_0 e, \tag{7}$$

$$u = S_0 r - S_0 C H_0 e. \tag{8}$$

CLOSED-LOOP SYSTEM IDENTIFICATION

The aim of the identification process is to obtain a model (an estimate) of the plant G_0 and possibly also the noise filter H_0 or also the controller C. When one already knows the controller C knowledge of the set-point signal r_1 and extra input r_2 brings no additional information if u is measured [3] and vice versa. In practice however, delimiters and other nonlinearities can occur and thus the controller won't have the simple form one could assume if e. g. the PID parameters are known. Thus even for seemingly simple controllers it can be beneficial to identify them as well.

In this contribution the focus will be on parametric system estimation. Since there is an important difference to the open-loop case, it shall be mentioned that while in the open-loop case a non-parametric (spectral) estimate $\hat{G}(e^{j\omega})$ can be obtained from the spectra of the input and output data, $\hat{G}(e^{j\omega}) = \frac{\hat{\Phi}_y}{\hat{\Phi}_u}$, this is no longer valid when the loop is closed and will result in a weighted average between G_0 and $-\frac{1}{C}$ [2]. To avoid this, one has to provide an external excitation via r and use the cross-spectra to obtain an unbiased estimate via

$$\hat{G}(e^{j\omega}) = \frac{\hat{\Phi}_{yr}}{\hat{\Phi}_{ur}}. \tag{9}$$

In parametric spectrum estimation the closed-loop case is rearranged in such a way that open-loop methods can be applied. Different approaches are often grouped into the so-called direct and indirect methods, but it can be shown [3] that from the estimator's point of view they differ only in the parametrization of the noise model. Nevertheless this distinction is useful to understand the advantages and restrictions that come with the different approaches.

In the following we will only consider rational transfer functions of the form

$$G(z) = \frac{b_{n-1} z^{-1} + \ldots + b_0 z^{-n}}{1 + a_{n-1} z^{-1} + \ldots + a_0 z^{-n}} = \frac{A(z^{-1})}{B(z^{-1})} \tag{10}$$

($H(z)$ analog) with polynomials $A(z^{-1})$, $B(z^{-1})$, ..., with a priori known order n and without delay. The parameters a_i, b_i, ... are combined into a parameter vector θ.

Direct Identification

The most simple solution is to "ignore" the fact that the feedback path is closed and identify a transfer function from u to y by defining the equation error

$$\tilde{\epsilon}(\theta) := y - G(z, \theta) u \tag{11}$$

and minimizing

$$J = \tilde{\epsilon}^{\mathrm{T}} \tilde{\epsilon} \tag{12}$$

to obtain $\hat{\theta}$, which is a least squares problem. This method generally works if the noise v (present in y) is uncorrelated with u. For closed-loop systems this is not the case and thus in general a very high signal-to-noise ratio (SNR) at the plant input u is required to mitigate the bias. In the special ARX-case, i. e. when the noise filter is given as $H(z) = \frac{1}{A(z^{-1})}$, then $G(z, \hat{\theta})$ will be a bias-free and consistent estimator (a Python package that implements system identification algorithms for the ARX- and also the more general ARMAX-case is SIPPY [4]).

To overcome this restriction one can use the *prediction error* instead of the equation error,

$$\epsilon(\theta) := H^{-1}(z, \theta)\,(y - G(z, \theta) u) \tag{13}$$

and minimize

$$V = \epsilon^{\mathrm{T}} \epsilon \tag{14}$$

to obtain $\hat{\theta}$. This method results in estimates $G(z, \hat{\theta})$ for the plant and $H(z, \hat{\theta})$ for the noise which will be bias-free and consistent if the whole system $S := (G_0, H_0)$ is present in the chosen model set $\mathcal{M} := \{(G(z,\theta), H(z,\theta)),\ \theta \in \Theta\}$. This means, a rich model set has to be chosen, especially for modelling the noise and thus this method is not suitable if one is interested in reduced-order (approximate) model identification.

Note that the direct identification methods described above do not require knowledge of the controller C but also they do not benefit from knowing C.

Indirect Identification

The general idea behind the indirect identification methods is to identify the closed-loop system's transfer function $G_{\mathrm{cl}} = \frac{G_0}{1+G_0C}$ or the system's sensitivity function $S_0 = \frac{1}{1+G_0C}$ and to extract the plant's transfer function from these estimates. Whether G_{cl} or S_0 is to be identified, in either case the identification makes use of the signal r instead of the plant's input u and thus benefits from the fact that r and the noise v are uncorrelated. Using e. g. the prediction error method one can estimate G_{cl} from

$$y = G_{\mathrm{cl}}(z,\theta) r + H_{\mathrm{cl}}(z,\theta) e \tag{15}$$

and with knowledge of C an estimate for G_0 is obtained as

$$G(z,\hat{\theta}) = \frac{\hat{G}_{\mathrm{cl}}}{C(1-\hat{G}_{\mathrm{cl}})}. \tag{16}$$

Equation (16) typically results in a high-order model and exact knowledge of C is required. For lower-order models special parametrizations of the estimated transfer functions can be chosen to avoid the calculation of Eq. (16). One possibility to do so is the coprime factor identification [2].

If one wants to ensure that the identified model will definitely be stabilized by the given controller C one can chose the dual Youla-Kučera parametrization [2].

To identify the system without knowledge of C and for precise control of the desired model order the two-stage methods can be applied [2]. In this approach one rewrites the system's equation (7) and the control law Eq. (8) introducing a *noise-free* input $u_r := S_0 r$ ending up with

$$y = G_0 u_r + S_0 v, \tag{17}$$

$$u = u_r - S_0 C v, \tag{18}$$

$$u_r = S_0 r. \tag{19}$$

The first step is then to identify the system's sensitivity function S_0 from

$$u = S(z,\beta) r_1 + W(z,\beta) e \tag{20}$$

(in the case where r_2 is used instead of r_1 the function $S(z,\beta)$ estimates CS_0 and the result is the same [2]) applying open-loop techniques like the prediction error method or simple least squares with the equation error (since r_1 and e are uncorrelated the estimator will be bias-free and consistent). With $S(z,\hat{\beta})$ one can simulate the noise-free input $\hat{u}_r$ with Eq. (19).

In the second step G_0 can be estimated from Eq. (17) again with e. g. the prediction error method with

$$\epsilon(\theta) = K^{-1}(z,\theta)\,(y - G(z,\theta)\hat{u}_r)\,, \tag{21}$$

benefitting from the fact that u_r and noise v in Eq. (17) are uncorrelated. One finally obtains the estimates

$$\hat{G}_0 = G(z,\hat{\theta}), \tag{22}$$

$$\hat{H}_0 = K(z,\hat{\theta}) S^{-1}(z,\hat{\beta}). \tag{23}$$

The estimators will be bias-free and consistent if S_0 lies within the chosen model set for $S(z,\beta)$, so a high-order estimate should be used to find an unbiased estimate $\hat{S}_0$ [3].

The high-order estimate of $\hat{S}_0$ will not result in a high-order estimate of $\hat{G}_0$ because since there are no constraints on $G(z,\theta)$ in Eq. (21) the model order is fully under control [2].

Additionally, no knowledge of C is required.

IDENTIFICATION OF THE HELIUM PRESSURE STABILIZING SYSTEM

Based on the helium pressure fluctuations after an impulse-shaped disturbance an indirect identification scheme based on reconstructing $\hat{G}_0$ from Eq. (16) was performed. To avoid high-order estimates the system was set up as a PT2 system with one zero to allow for the jump that was present in the data. The controller C was modelled as standard PID controller.

With these assumptions the transfer function of the plant in the Laplace-domain (complex variable $s = \sigma + j\omega$) is

$$\hat{G}_{\mathrm{He}}(s) = \frac{3.988 \cdot 10^{-5} s}{s^2 - 9.034 \cdot 10^{-3} s + 2.901 \cdot 10^{-6}}. \tag{24}$$

Simulation and Controller Improvement

Figure 3 shows a comparison of the measured data (red curve) and the simulated response of the system consisting of the controller C with the parameters $P = 250$, $I = 3\,\mathrm{s}$, $D = 0\,\mathrm{s}$ and $\hat{G}_{\mathrm{He}}$ from Eq. (24) in closed-loop operation (green curve) to an impulse-shaped disturbance. Additionally Fig. 3 includes a prediction of the system's response to the same impulse-shaped disturbance if a set of improved control parameters, $P = 300$, $I = 3\,\mathrm{s}$, $D = 1000\,\mathrm{s}$, is applied (blue curve). Using the D-part of the controller significantly increases the system's response time allowing it to return to steady-state in 20 % of the time it took before.

Since the D-part of the controller acts proportional to the frequency it also amplifies high frequency noise. To estimate the impact of the improved parameters Fig. 4 shows a simulation of the system's response to noisy input with the estimated response with the old parameters in green and with

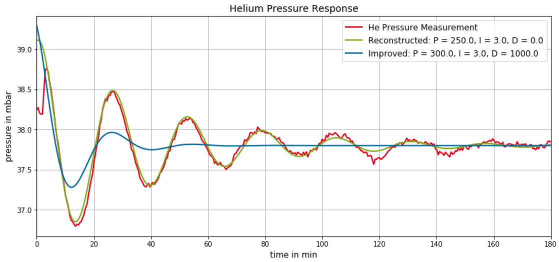

Figure 3: Comparison of the measured response of the helium pressure to an impulse-shaped disturbance (red), a simulation of the identified system to an accordingly modelled disturbance (green) and the simulated response of this model when improved control parameters are set (blue).

the new ones in blue. The red lines indicate that the peak values stay in the same range for both options and only the average noise power is higher. Note that the absolute value of the amplitude is much higher than in normal operation, but since the system is linear it can be scaled without distortion.

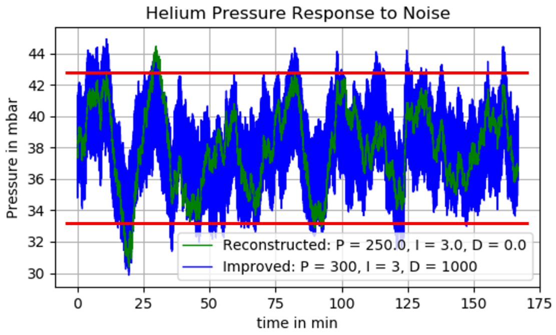

Figure 4: Simulation of consequences of the increased D-value for the system's reaction to noise. The red lines indicate that the amplitude stays within the same range.

MEASUREMENT RESULTS

To benchmark the simulation results it was planned to apply the improved control parameters to the system just before the maintenance shut-down in December 2018. Due to the warm-up process being already in preparation the helium-level inside the cryomodules was lower than during normal operation and three pumps running at idle reduced the pressure well below the set-point. To bring the system back to the working point one pump was turned off at 07:39 a.m., see Fig. 5. This disturbance caused an oscillation as was expected but since the controller still was set with the old parameters this oscillation should have been damped. As Fig. 5 shows, this wasn't the case, probably due to the mentioned circumstances. Nevertheless we decided to apply the improved parameters at 10:31 a.m. and with these new parameters a significant reduction in the amplitude of the oscillation was achieved.

So far, no further tests during normal operation were conducted.

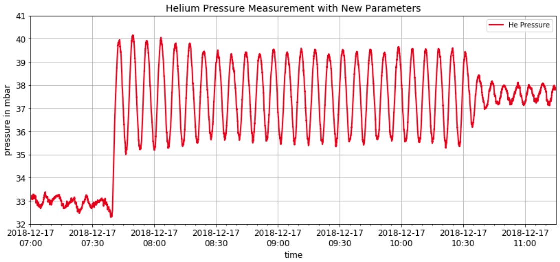

Figure 5: Measured helium pressure change when one of three running pumps is turned off (07:39 a.m.) and when the new control parameters are applied (10:31 a.m.). The remaining oscillation is still under investigation but is supposed to originate from the already very low Helium level due to the running shut-down process.

SUMMARY AND OUTLOOK

In this work different methods for closed-loop system identification have been summarized. They can be distinguished as direct and indirect methods, where direct methods make use of the plants in- and output u and y while indirect methods need an external reference signal r and the plant's output y. The choice between these methods is depending on knowledge of the controller C and the demands on the model orders of the plant and also the noise filter.

An indirect approach with assumed second order plant transfer function was carried out for the helium pressure stabilizing system of the S-DALINAC and simulations showed possible improvements for the PID controller's parameters. First tests with those parameters conducted just before the last maintenance shut-down gave promising results.

In the future, extended tests shall be carried out, including the application of different reference signals to be able to compare and benchmark the different approaches and to justify the assumptions.

Furthermore, these closed-loop system identification schemes can also be applied to more low-level RF components with data taken during normal operation. Thus, no beam time has to be omitted for testing and data generation.

REFERENCES

[1] C. W. Burandt, "Optimierung und Test der digitalen Hochfrequenzregelung und Entwicklungen für das EPICS-basierte Beschleunigerkontrollsystem am S-DALINAC", Ph.D. Thesis, TU Darmstadt, Germany, 2017.

[2] P. Van den Hof, "Closed-loop issues in system identification", *Annual Reviews in Control*, Vol. 22, 1998. doi:10.1016/S1367-5788(98)00016-9

[3] U. Forssell and L. Ljung, "Closed-loop identification revisited", *Automatica*, vol. 35, 1999. doi:10.1016/S0005-1098(99)00022-9

[4] G. Armenise, R. Bacci di Capaci, G. Pannocchia and M. Vaccari, “An open-source system identification package for multivariable processes”, in *Proc. 12th International Conference on Control (CONTROL)*, Sheffield, UK, 5-7 Sept 2018. doi:10.1109/CONTROL.2018.8516791

63th ICFA Advanced Beam Dynamics Workshop on Energy Recovery Linacs ERL2019, Berlin, Germany JACoW Publishing
ISBN: 978-3-95450-217-2 doi:10.18429/JACoW-ERL2019-THCOWBS06

BEAM BREAKUP LIMIT ESTIMATIONS AND HIGHER ORDER MODE CHARACTERISATION FOR MESA*

C. P. Stoll†, F. Hug, Institut für Kernphysik der JGU Mainz, Germany

Abstract

MESA is a two pass energy recovery linac (ERL) currently under construction at the Johannes Gutenberg-University in Mainz. MESA uses two 1.3 GHz TESLA type cavities with 12.5 MV/m of accelerating gradient in a modified ELBE type cryomodule in c.w. operation. One potential limit to maximum beam current in ERLs is the transverse beam breakup (BBU) instability induced by dipole HOMs. These modes can be excited by bunches passing through the cavities off axis. Following bunches are then deflected by the HOMs, which results in even larger offsets for recirculated bunches. This feedback can even lead to beam loss. To measure the quality factors and frequencies for the dressed as well as undressed cavities improves the validity of any current limit estimation done.

MESA

The Mainz Energy-recovering Superconducting Accelerator (MESA) is a small-scale, multi-turn, double-sided recirculating linac with vertical stacking of the return arcs currently being built at the Johannes Gutenberg Universität Mainz [1]. The operation modes planned are a thrice recirculating external beam mode (EB) with 150 µA current and 155 MeV particle energy for precision measurements of the weak mixing angle at the P2 Experiment or a twice recirculating energy recovering mode (ER) with 1 mA and later 10 mA current at a beam energy of 105 MeV where 100 MeV of beam energy can be recovered from the beam and fed back into the cavities. A windowless gas target as part of the MAGIX experiment will enable electron scattering experiments with different atoms. An overview of the MESA facilities is given in fig. 1. The electron source (STEAM) provides up to 1 mA of polarized beam at 100 keV. It is followed by a spin manipulation system containing two Wien filters. A chopper system with a collimator and two buncher cavities prepares the longitudinal phase space of the bunches for the normal conducting milliampere booster (MAMBO), which accelerates them to 5 MeV. A 180° injection arc delivers the beam to the first cryomodule. Depending on the operation mode the beam is either twice or thrice recirculated. This paper focusses on the high current twice recirculating ERL operation, where the beam passes each cavity 4 times and is then dumped at 5 MeV in the ERL beam dump.

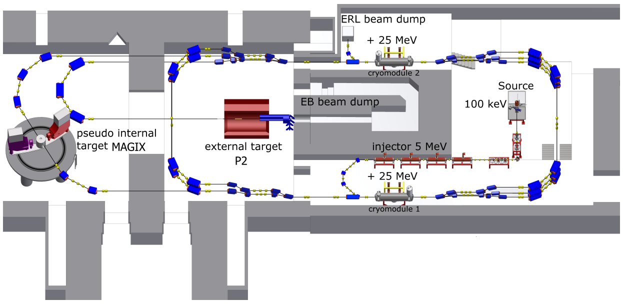

Figure 1: Overview of the MESA layout as used in this work.

SRF CAVITIES AND CRYOMODULES

For the MESA main accelerator two ELBE-type cryomodules were chosen [2] and modified for ERL operation [3]. Each module contains two 9-cell superconducting radio frequency (SRF) cavities of the TESLA-type. These cavities will provide a gradient of 12.5 MeV at $Q_0 = 1.25 \times 10^{10}$ while being operated at 1.8 K and 1.3 GHz. A CAD model of the full cavity string is provided in fig. 2. Besides the wanted accelerating π-mode, also unwanted HOMs with high quality factors exist in the cavity. As the TESLA-type cavities are elliptical cavities, dipole modes naturally occur in pairs of two with polarisations separated by approximately 90° and very small differences in frequency. For a simulation of the threshold current at least two HOMs have to be present in one cavity.

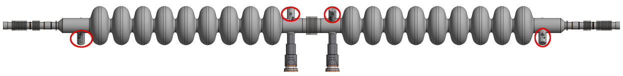

Figure 2: CAD Model of the MESA cavity string. In the bottom center the two HF power couplers can be seen, the four other ports (red circles) are the HOM couplers.

As can be seen in fig. 2 two HOM ports, which allow for the measurement of HOMs for each cavity, are present.

DIPOLE HIGHER ORDER MODES

In [4] a dedicated study of HOMs in TESLA type cavities including the effects of fundamental power couplers and higher order mode couplers was presented. A total of 86 dipole HOMs is presented. Each dipole HOM has a polarisation, a quality factor Q and a shunt impedance R/Q. In fig. 3 an example of the field distribution in a dipole HOM can be seen. As part of the quality control and site acceptance tests the HOM spectra were measured first in the vertical cold test, not yet tuned to the fundamental mode, and a second time for each cavity in the fully assembled string in the cold cryomodule tuned to the 1.3 GHz fundamental mode.

---

* This work has been supported by DFG through the PRISMA+ cluster of excellence EXC 2118/2019 and Research Training Group GRK 2128 and by the European Union's Horizon 2020 Research and Innovation programme under Grant Agreement No 730871.

† stollc@uni-mainz.de

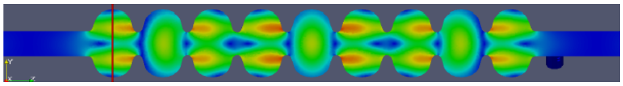

(a) Electric field of a dipole HOM in a TESLA cavity.

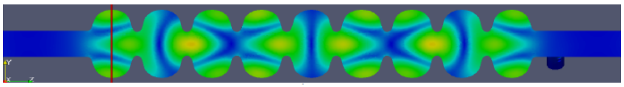

(b) Magnetic field of a dipole HOM in a TESLA cavity.

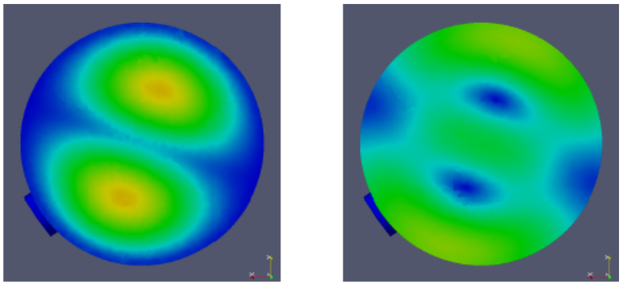

(c) Cut view of electric field (left) and magnetic field (right) at the red line indicated in fig. 3a and 3b

Figure 3: Example of a dipole HOM in a TESLA cavity taken from [4].

TRANSVERSE BBU

Electron bunches that enter a SRF cavity with a small deviation from the reference orbit excite dipole (quadrupole, sextupole, etc.) HOMs in above-mentioned cavity. Due to their potentially high Q_0, these modes can persist until the next bunch arrives at the cavity. The magnetic field of an excited mode deflects the following bunches that do not travel on the reference orbit. The kick induced by the dipole HOM translates into a transverse displacement at the cavity after recirculation.

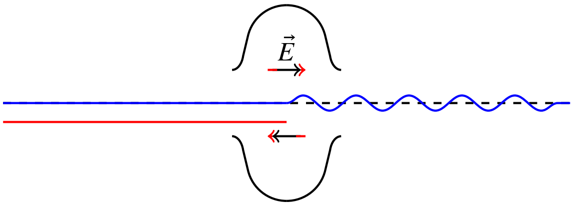

Figure 4: Simplified picture of the transverse BBU instability. A bunch (blue) gets deflected by the magnetic field of the dipole HOM and a bunch travelling off axis (red) can exchange energy with the elctric field of the HOM further powering the instability.

The recirculated beam induces a HOM voltage, depending on the magnitude and direction of the beam displacement. This can lead to a periodic unstable growth of the HOM voltage, which finally results in loss of the beam and depends strongly on the bunch charge and thereby the average beam current [5]. The maximum current that can be recirculated before BBU occurs is called threshold current. For multiturn ERLs with a number of passes N_p, this was described by Hoffstaetter et. al. in [6]:

$$I_{\text{th}} = -\frac{2c^2}{e\left(\frac{R}{Q}\right)_\lambda Q_\lambda \omega_\lambda}\,\frac{1}{\sum_J^{N_p}\sum_I^{N_p}\frac{1}{p_I}\sin(\omega_\lambda[t^I - t^J])T^{IJ}},$$

where I_{th} is the threshold current, $(R/Q)_\lambda$ and Q_λ the shunt impedance and quality factor of the HOM, ω_λ the frequency of the HOM, p the particle momentum and:

$$T^{IJ} = T_{12}^{IJ}\cos^2(\theta) + \frac{1}{2}(T_{14}^{IJ} + T_{23}^{IJ})\sin(2\theta) + T_{34}^{IJ}\sin^2(\theta),$$

is the transport line parameter from the end of one cavity to the end of the next, where θ is the polarisation of the HOM. In general, it is expected to find the threshold current limited by a single HOM, if the frequency deviation between neighbouring modes is in the order of ≈ 1 MHz. In the presence of multiple polarized HOMs, as it is the case in elliptical cavities, this assumption does no longer hold [7]. Consequently, in the simulation of the threshold currents at least 2 HOMs were analysed in each cavity.

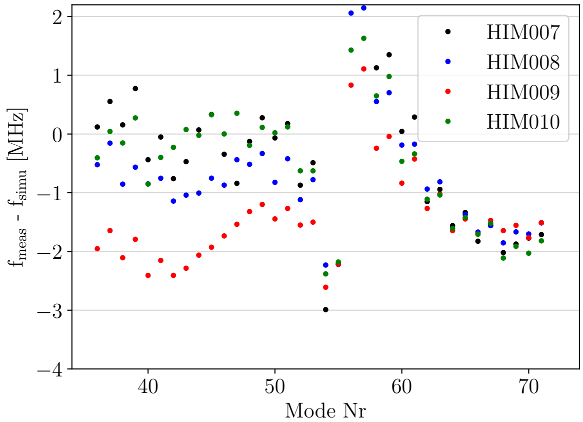

Figure 5: Deviation of the measured HOM frequency from the simulated frequencies for the first two passbands of dipole HOMs as measured at Helmholtz Institute Mainz.

In reality, each cavity is produced with certain manufacturing tolerances and tuned to the fundamental mode. Since the frequencies of HOMs in a cavity depend on the geometry of the cavity, every cavity can have slightly different HOM frequencies, as can be observed in the comparison of the results measured at Helmholtz Institute Mainz (HIM) shown in fig. 5. This can significantly increase the achievable threshold currents since there is less crosstalk between cavity HOMs as was investigated for example for the Cornell-Brookhaven 4-Pass ERL [8] or for MESA in [9].

SIMULATIONS WITH BI

The code bi [10] uses tracking of point-like bunches through a 6×6 transfer matrix representation of the lattice. It calculates the beam position as a function of time and determines the threshold current by variation of the beam current.

The transfer matrices were taken from a simulation of the MESA ERL-lattice with ELEGANT starting right behind the 5 MeV injection arc. For simulations of the achievable threshold current for MESA, measured Q-values and frequencies of the 4 cavities cold tests at DESY Hamburg [11] as well as measured data from horizontal tests obtained at the Helmholtz Institut Mainz (HIM) were combined with polarisation and R/Q data from simulation [4]. In total, the Q values and frequencies (first two passbands) of up to 36 dipole HOMs were measured for each cavity. In fig. 6 a comparison of the measured and simulated Q values is shown. A difference between the measurement at DESY and HIM was expected, since the assembly of the cryomodule with 2 cavities and the tuning to the fundamental mode changes the geometry of the cavity and thus its HOM frequencies and bandwidths which impacts the Q values. The larger Q spread for the two different polarisations in each cavity can be explained by a deviation from the elliptical shape as compared to the simulated geometry. The overall higher Q factor results from a deviation of the HOM coupler gap width as compared to the simulated geometry [12].

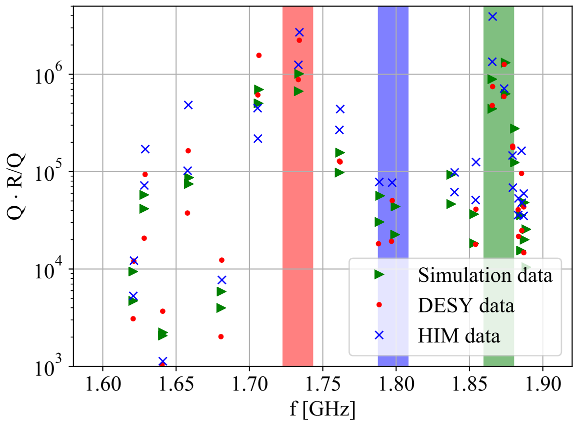

Figure 6: Comparison of measured and simulated Q · R/Q values shown for cavity 7. The cavities are numbered from 7 to 10 with cavity 7 and 8 in one module and 9 and 10 in the other one.

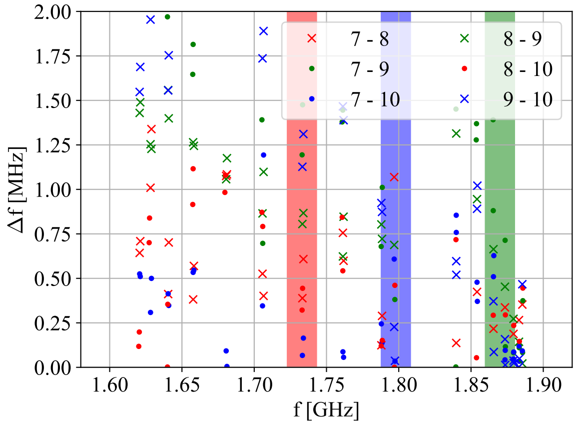

Figure 7: Comparison of absolute frequency deviation between cavity HOMs as measured at HIM.

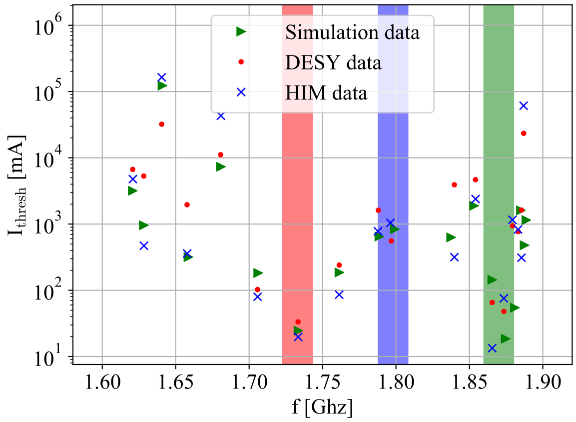

Figure 8: Simulation of threshold current values for different data sets. Red: All values from simulated data, blue: Q and f values from vertical cold test measurements at DESY and green: Q and f values measured in the cryomodule tuned to 1.3 GHz.

Figure 7 shows the absolute frequency deviation between the 4 cavities as presented in [13]. It varies between 0 and 1.955 MHz with an average of 0.59 MHz. Three regions of interest can be noticed here, one around 1.73 GHz, the second around 1.78 GHz and the last one around and above 1.87 GHz. In all three of these areas, frequency spread is considerably smaller then anywhere else. Considering the same areas in fig. 6 and fig. 8 a pattern is visible. Relatively high Q values and low frequency spread coincide with low threshold currents as was also expected from theory. In the second area this is negated by the smaller Q values and above 1.87 GHz by very small shunt impedances R/Q of the modes. In fig. 8 the threshold current for the first two passbands of HOMs is shown. For the measured HOMs in the dressed and tuned MESA cryomodules a threshold current of 19.8 mA in region 1 (red) is expected and a threshold current of 13.4 mA in region 2 (green). Both values exceed the 10 mA design current for MESA stage 2.

CONCLUSION AND OUTLOOK

Transverse BBU will not limit the MESA stage 1 operation with 1 mA. For stage 2 a perfectly aligned machine with no steering errors could achieve 10 mA in a 4-pass ERL configuration. Investigation of alignment errors of the magnets and their impact on the beam parameters and BBU limits will further be conducted. Future studies need to investigate the heating of the HOM antennas with respect to beam current as HOM antenna quenching could be another limiting factor. Afterwards ultimate beam current limits for MESA using the presented cryomodule can be derived.

REFERENCES

[1] F. Hug, K. Aulenbacher, R.G. Heine, B. Ledroit, and D. Simon. "MESA - an ERL Project for Particle Physics Experiments". In *Proc. LINAC'16*, Lansing, MI, USA, Sep. 2016.. `doi:10.18429/JACoW-LINAC2016-MOP106012`

[2] F. Schlander, A. Arnold, K. Aulenbacher, R.G. Heine, and D. Simon. "Investigation of Cryomodules for the Mainz Energy-recovering Superconducting Accelerator MESA". In *Proc. IPAC'14*, Dresden, Germany, 2014. `doi:10.18429/JACoW-IPAC2014-WEPRI013`.

[3] T. Stengler et al. "Status of the Superconducting Cryomodules and Cryogenic System for the Mainz Energy-recovering Superconducting Accelerator MESA". In *Proc. IPAC'16*, Busan, Korea, 2016. `doi:10.18429/JACoW-IPAC2016-WEPMB009`.

[4] W. Ackermann, H. De Gersem, C. Liu, and T. Weiland. "Eigenmode calculations for the tesla cavity considering wave-propagation losses through fundamental and higher-order mode couplers". 2015. `http://bib-pubdb1.desy.de/record/289143`.

[5] E. Pozdeyev, C. Tennant, J. J. Bisognano, M. Sawamura, R. Hajima, and T. I. Smith. "Multipass beam breakup in energy recovery linacs". *Physical Review Special Topics - Accelerator and Beams*, 557 (1), 2006. `doi:10.1016/j.nima.2005.10.066`.

[6] Georg. H. Hoffstätter and Ivan V. Bazarov. "Beam-breakup instability theory for energy recovery linacs". *Physical Review Special Topics - Accelerator and Beams*, 7(054401):13, 5 2004. `doi:10.1103/physrevstab.7.054401`.

[7] Georg. H. Hoffstaetter, Ivan V. Bazarov, and Changsheng Song. "Recirculating beam-breakup thresholds for polarized higher-order modes with optical coupling". *Physical review special topics - Accelerators and Beams*, 10(4), 044401, 2007. `doi:10.1103/PhysRevSTAB.10.044401`.

[8] W. Lou and G.H. Hoffstaetter. "Beam-breakup studies for the 4-pass cornell-brookhaven energy-recovery test accelerator". *Journal of Physics: Conf. Series* 1067(2018) 062014, 2018. `doi:10.1088/1742-6596/1067/6/062014`.

[9] C.P. Stoll, F. Hug, and D. Simon. "Beam Break Up Simulations for the MESA Accelerator". In *Proc. 59th ICFA Advanced Beam Dynamics Workshop (ERL'17)*, Geneva, Switzerland, June 18-23, 2017. `doi:10.18429/JACoW-ERL2017-MOPSPP009`.

[10] Ivan V. Bazarov. "bi - beam instability bbu code". `http://www.lepp.cornell.edu/~ib38/bbucode/src`.

[11] T. Stengler, K. Aulenbacher, F. Hug, T. Kürzeder, and D. Simon. "Cryomodule Fabrication and Modification for High Current Operation at the Mainz Energy Recovering Superconducting Accelerator MESA". In *Proc. SRF'17*, number 18 in International Conference on RF Superconductivity, pages 297–300. `doi:10.18429/JACoW-SRF2017-MOPB101`.

[12] L. Xiao, C. Adolphsen, V. Akcelik, A. Kabel, K. Ko, L. Lee, Z. Li, and C. Ng. "Modeling imperfection effects on dipole modes in TESLA cavity". In *2007 IEEE Particle Accelerator Conference (PAC)*, pages 2454–2456, June 2007. `doi:10.1109/PAC.2007.4441281`.

[13] C.P. Stoll and F. Hug. "Beam Breakup Simulations for the Mainz Energy Recovering Superconducting Accelerator MESA". In *Proc. 10th International Particle Accelerator Conference (IPAC'19)*, Melbourne, Australia, 19-24 May 2019, `doi:10.18429/JACoW-IPAC2019-MOPGW025`.

DEVELOPMENT OF HOM COUPLER WITH C-SHAPED WAVEGUIDE FOR ERL OPERATION

M. Sawamura†, R. Hajima, QST, Tokai, Ibaraki 319-1195 Japan
Masato Egi, Kazuhiro Enami, Takaaki Furuya, Hiroshi Sakai, and Kensei Umemori,
KEK, Tsukuba, Ibaraki 305-0801 Japan

Abstract

We are developing the higher-order mode (HOM) attenuators for superconducting cavity for high current beam operation. We propose new type of HOM coupler using C-shaped wave guide (CSWG). The CSWG has good features of high-pass filter, easy cooling of the inner conductor, and compactness. The measured and calculated results of the CSWG type HOM coupler installed to TESLA type cavity model showed good properties of high external Q-value for the accelerating mode and low external Q-values for HOMs. Since CSWG becomes long to get high external Q-value for accelerating mode, bending CSWG type HOM coupler is practical considering the cryomodule design. The bent CSWG type HOM coupler showed similar properties to the straight CSWG.

INTRODUCTION

The superconducting accelerator projects such as International Linear Collider (ILC) or Energy-Recovery Linac (ERL) are pushed forward all over the world. The superconducting cavity has an advantage of high Q-value due to few wall losses. This leads to a disadvantage that beam acceleration easily grows up higher-order modes (HOMs). Since HOMs excited in a cavity increase with beam current and cause beam instability [1], the performance of HOM attenuators finally limits cavity performance.

Desirable properties of the HOM attenuators so as not to deteriorate the cavity performance are as follows.

i. Ability to install near the cavity not to decrease the effective accelerating field.
ii. Effective cooling to avoid the temperature rise leading to breaking superconductivity for high power of HOMs.
iii. Separation of RF absorbers such as ceramics and ferrites from the cavity vacuum which might be sources of outgas and dust.
iv. Compactness to reduce the cryomodule size.

We developed the C-shaped wave guide (CSWG) as shown in Figure 1 [2]. The CSWG has the cutoff frequency determined by an inner diameter, an outer diameter, and a connection plate thickness since the CSWG is topologically similar to the rectangle wave guide. Furthermore, since the inner conductor connected with the outer conductor through the connection plate, the CSWG has an advantage of easy cooling of the inner conductor. Applying the CSWG to the HOM coupler satisfies the above requests.

The present paper describes the measured and calculated results of the CSWG type HOM coupler properties.

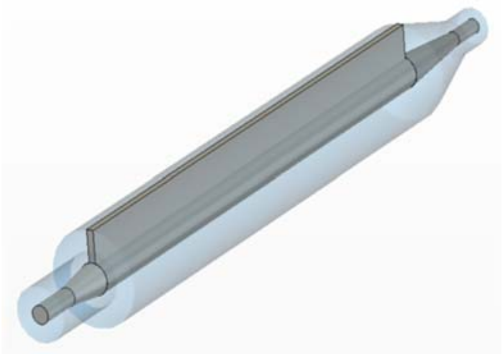

Figure 1: Schematic view of CSWG connected with coaxial lines at both ends.

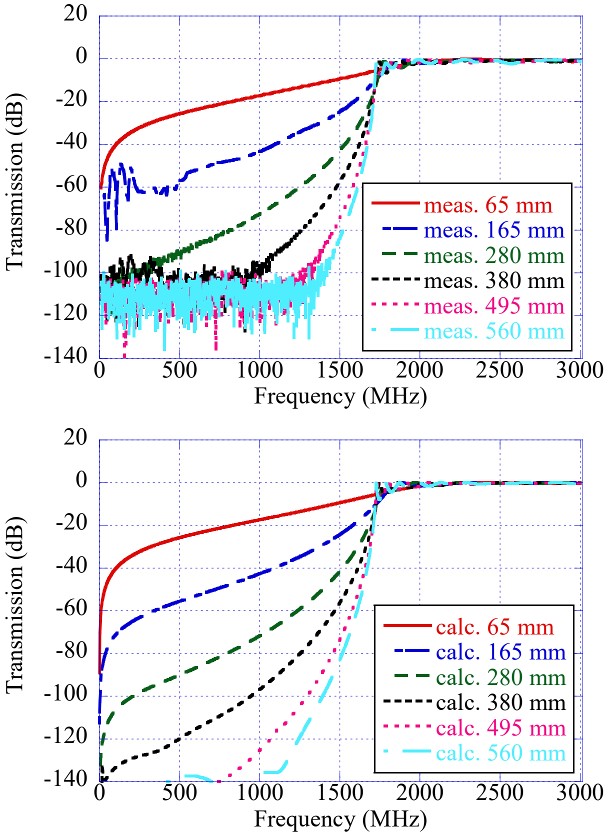

Figure 2: Measured (top) and calculated (bottom) transmission coefficients through CSWG for different CSWG length.

CSWG MODEL

The aluminium CSWG models were fabricated to measure the RF properties. The inner and outer diameters were 18 mm and 42 mm, respectively. The CSWG length can be varied from 65 mm to 560 mm. The coaxial-N

---

† email address: sawamura.masaru@qst.go.jp

type connector converters were attached to the both ends and transmission coefficients were measured with a network analyzer. The calculations were also done for the same shape as the models with CST Microwave Studio.

The transmission coefficients through the CSWG for different CSWG length and for different connection plate angles are shown in Figure 2 and 3, respectively When the CSWG length increases, the attenuation below cutoff frequency becomes large and the transmission above the cutoff frequency is almost same. When the angle of the connection plate increases, the cutoff frequency increases. Measurements well agree with calculations in both cases.

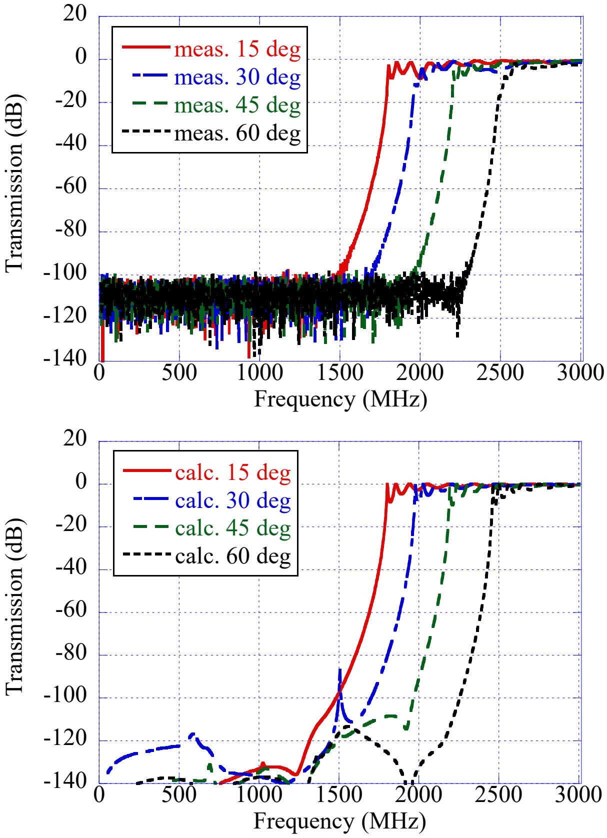

Figure 3: Measured (top) and calculated (bottom) transmission coefficients through CSWG for different connection plate angle.

CSWG TYPE HOM COUPLER

The schematic view of the CSWG type HOM coupler is shown in Figure 4. The CSWG type HOM coupler can be divided into three roles. The first is the coaxial line extended from the CSWG to couple with the cavity RF. The second is the CSWG through which the HOMs above the cutoff frequency transmit and the fundamental mode below the cutoff frequency is reflected. The third is the coaxial line to extract the HOM power outside of the HOM coupler.

The aluminium CSWG type HOM coupler model was fabricated to measure the RF properties. The inner diameters of CSWG type HOM coupler were 18, 21, 25.8 and 30 mm, the outer diameter was 42 mm, and the thickness of connection plate was 4 mm for all types of the inner diameters. The CSWG length can be varied from 65 mm to 560 mm. The CSWG length is defined as the center line length of the inner conductor connected with the connection plate. The end of connection plate for cavity side was located 27 mm outside from the beam pipe. In order to couple with the cavity RF a cylindrical rod was connected to the inner conductor of CSWG. The insertion length is defined as the length from the beam pipe to the tip of the coaxial line. The positive value means the tip is inside of the beam pipe.

The CSWG type HOM coupler was installed to the TESLA type cavity model. The TESLA cavity is designed to install the antenna type HOM couplers. The HOM coupler port is located 40 mm away from the cell end at the beam pipe. Though installing HOM couplers near the cavity does not require extra beam pipe which decreases the effective accelerating field, the high-pass filter structure is essential so as not to affect the accelerating mode. The CSWG type HOM coupler can be replaced with antenna type HOM couplers owing to the cutoff frequency of the CSWG.

The cavity model has three cells to reduce the number of HOMs to be measured and calculated as shown in Figure 4. The TESLA type cavity model is made of copper. The diameter of the beam pipe was 78 mm. The input port for measurement was installed at the end cell. The RF connectors of the input coupler and the CSWG type HOM coupler were connected to the network analyzer to measure the RF transmission and reflection coefficients.

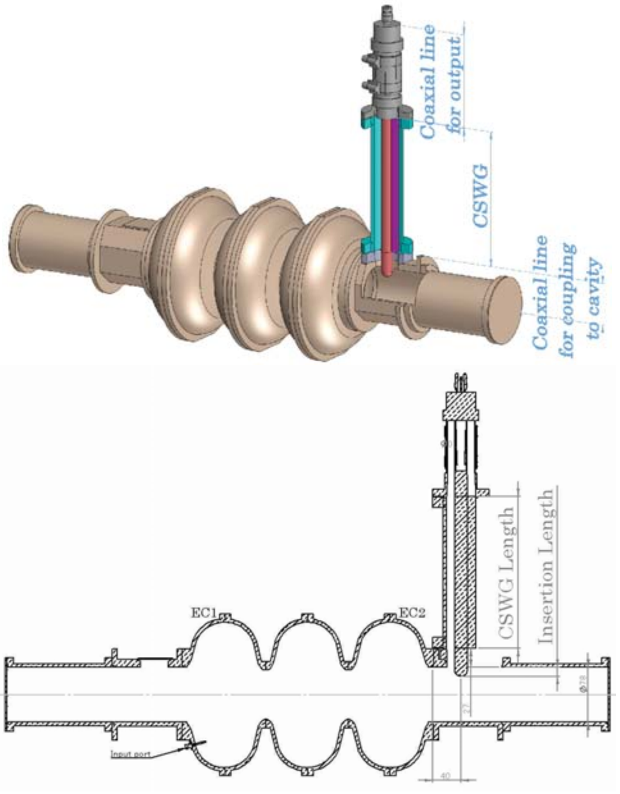

Figure 4: Schematic view (top) and cross section (bottom) of CSWG type HOM coupler installed to the TESLA type cavity model.

ISBN: 978-3-95450-217-2 doi:10.18429/JACoW-ERL2019-THCOXBS02

RESULTS

The external Q-values of the CSWG type HOM coupler were measured and calculated by changing the CSWG length and the insertion length. The measured and calculated external Q-values for the accelerating mode are shown in Figure 5 as a function of the CSWG length. Increasing the external Q-values for accelerating mode with the CSWG length means that the accelerating mode below the cutoff frequency could not transmit through the CSWG. On the contrary the external Q-values of the HOMs above the cutoff frequency were almost same regardless to the CSWG length as shown in Figure 6. These mean that the HOMs could transmit through the CSWG to be damped.

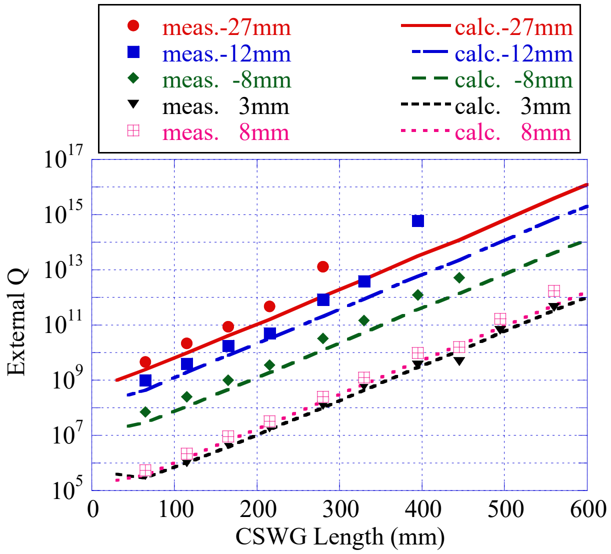

Figure 5: Measured and calculated external Q-values of the accelerating mode as a function of CSWG length for different insertion length.

The CSWG length increases the external Q-value for the accelerating mode and is independent of that of HOM. The insertion length decreases the external Q-values for the accelerating mode and HOMs. When the parameters of CSWG type HOM coupler are decided, first select insertion length for external Q-values of HOMs to be small enough, and then select CSWG length for external Q-values of accelerating mode to be large enough.

The TESLA cavity has two different shapes of the end cells, endcap 1 (EC1) and endcap 2 (EC2), to enhance the field amplitude of the trapped mode in one end cell [3]. The distribution of the external Q-values with the CSWG type HOM coupler installed at either EC1 or EC2 side is shown in Figure 7. Since the asymmetric end cell shapes enhances HOM amplitude to either side of the end cell, some degraded HOMs show high Q-values. The HOM coupler installed at either EC1 side or EC2 side can lower the external Q-values less than 10^{6} at least, while the external Q-values for the accelerating mode can be kept more than 10^{11}.

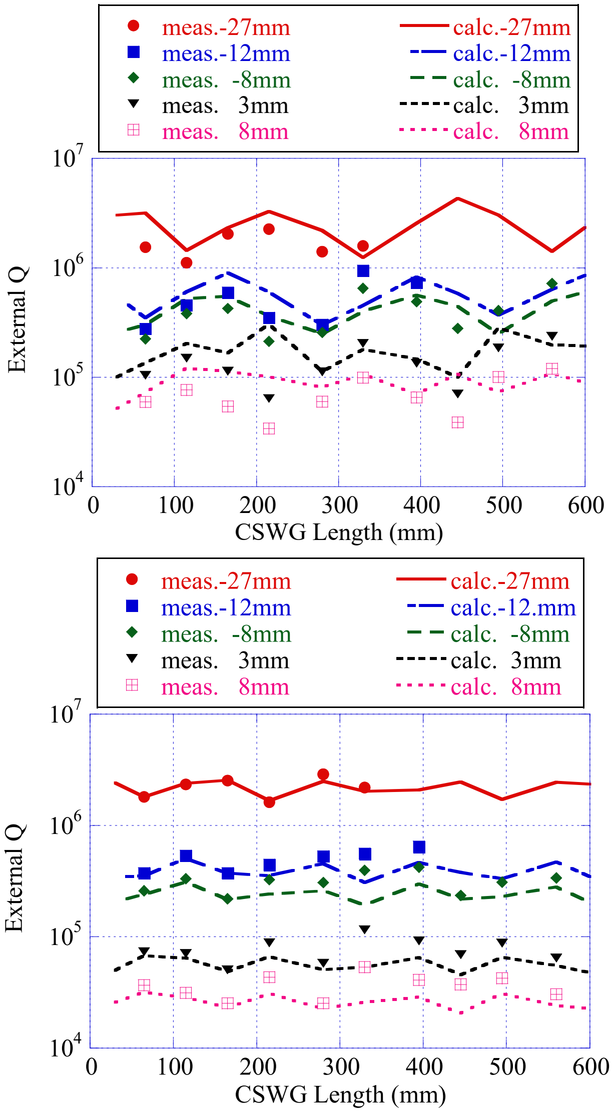

Figure 6: Measured and calculated external Q-values of TE111-pi/3 mode (top) and TM110-pi mode (bottom) as a function of CSWG length for different insertion length.

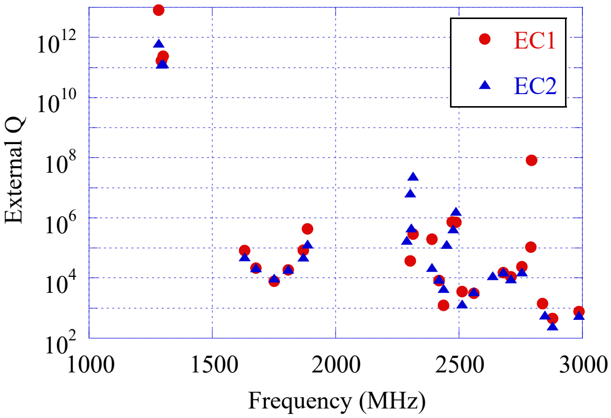

Figure 7: The distribution of measured external Q-values for CSWG HOM coupler of either EC1 or EC2 side.

BENDING CSWG TYPE HOM COUPLER

The CSWG type HOM coupler requires a long pipe so as not to affect the accelerating mode when it is installed near the cavity. Since no bending of the CSWG type HOM coupler requires large radial size of a cryomodule, the bent CSWG type HOM coupler is practical as shown in Figure 8. The effects to the RF properties for bending the CSWG type HOM coupler were investigated. The CSWG type HOM coupler was bent at 90 degrees to be parallel to the beam axis with a quarter regular polygon. The bending angle is defined as the exterior angle of the regular polygon. The direction of the connection plate is defined as “inside” when it is located in the inside of the bending section.

Figure 9 shows the measured external Q-values with CSWG type HOM coupler of bending angle of 45 degrees for three directions of connection plate. Outside connection plate direction is preferable for the accelerating mode because of higher external Q-value. According to the HOMs, suitable connection plate directions vary, but the differences are little.

Figure 8: Bent CSWG HOM coupler of bending angle of 45 degrees installed to TESLA type cavity model.

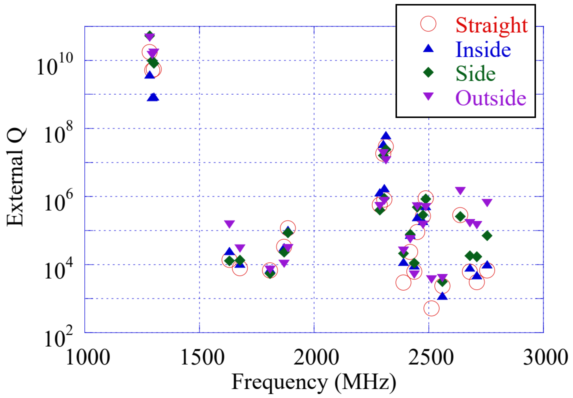

Figure 9: Measured external Q-values with bent CSWG type HOM coupler of bending angle of 45 degrees with three directions of connection plate.

CONCLUSION

The CSWG has good features for HOM attenuator such as high-pass filter, easy cooling of inner conductor, easy conversion to coaxial-line, and compactness. With these features the CSWG type HOM coupler realizes good attenuation properties of high external Q-value for accelerating mode and low external Q-values for HOMs.

Bending the CSWG type HOM coupler is practical for considering the cryomodule design. The external Q-values are almost same as those of straight CSWG regardless of bending angle except for the 90-degree bending of the inside connecting plate.

The structure of bent CSWG type HOM coupler is complicated and fabrication process is under investigation

REFERENCES

[1] E. Pozdeyev *et al.*, “Multipass beam breakup in energy recovery linacs”, *Nucl. Instrum. and Methods in Phys. Res.*, A 557 (2006) p. 176. `doi:10.1016/j.nima.2005.10.066`

[2] M. Sawamura, *et. al.*, “Properties of the RF Transmission Line of a C-Shaped Waveguide”, *Nucl. Instrum. and Methods in Phys. Res.*, A 882 (2018) p.30. `doi:10.1103/PhysRevLett.114.050511`

[3] B. Aune *et al.*, “Superconducting TESLA cavities”, *Physic. Rev. Special Topics – Acc. and Beams*, vol. 3, 092001 (2000). `doi:10.1103/PhysRevSTAB.3.092001`

ISBN: 978-3-95450-217-2 doi:10.18429/JACoW-ERL2019-THCOYBS01

METAL AND SEMICONDUCTOR PHOTOCATHODES IN HZDR SRF GUN

R. Xiang†, A. Arnold, P. Murcek, J. Teichert, HZDR, 01328 Dresden, Germany
J. Schaber, TU Dresden & HZDR, 01328 Dresden, Germany

Abstract

Quality of photocathode in a photoinjector is one of the critical issues for the stability and reliability of the whole accelerator facility. In April 2013, the IR FEL lasing was demonstrated for the first time with the electron beam from the SRF gun with Cs_2Te at HZDR [1]. Cs_2Te photocathode worked in SRF gun-I for more than one year without degradation. Currently, Mg photocathodes with QE up to 0.5% are applied in SRF Gun-II, generating CW beams with bunch charge up to 300 pC and sub-ps bunch length for the high power THz radiation. It is an excellent demonstration that SRF guns can work reliably in a high power user facility.

INTRODUCTION

As well known, the quality of photocathodes is a key part to improve the stability and reliability of the photoinjectors. For SRF guns at HZDR, metal cathodes (copper, magnesium) and semiconductor photocathode (Cs_2Te) are chosen as photocathode materials.

The design is shown in the Fig. 1. The metal plug (ϕ 10mm, 7 mm long) can be photoemission material or the substratum with a deposited photoemission layer. The copper stem is used to cool down the plug to LN2 temperature, which is realized by cotact the conus area to a liquid N2 reservoir. The bayonet and spring can fix the cathode body on to the cold reservoir. The whole cathode is isolated to the SRF cavity, so that a bias can be loaded on the cathode to suppress the multipacting around cathode stem or reduce the dark current from the cathode [2].

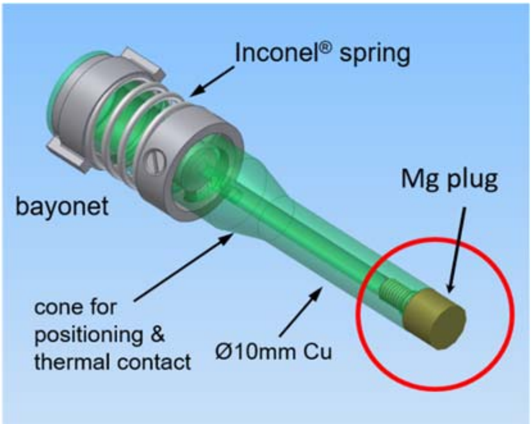

Figure 1: Design of photocathode in the SRF gun II.

Copper is used as commissioning cathode in SRF Gun-II. But the work function of Cu (4.6 eV) is rather high and its QE of 1×10^{-5} at 260 nm is too low for the regular beam production. Magnesium is a metal with low work function of 3.6 eV, and its QE can reach 0.5% after ps UV laser cleaning. Although it has lower QE than Cs_2Te, Mg has the advantage of long life time, reliable compatibility, good QE and little risk of contamination to niobium cavity.

Driven with UV laser Cs_2Te (with band gap 3.3 eV + electron affinity 0.2 eV) has shown good QE and long life time in the SRF gun-I. After we solve the problems of field emission and overheating during the last tests of Cs_2Te on Mo in SRF gun-II, it will be applied again with Cu substratum for the medium current generation.

CU CATHODE IN SRF GUN II

During the assembling of SRF gun cavity in the cleanroom, an oxygen free copper plug was installed in the cavity. The copper plug had been polished with diamond suspension, and then cleaned with alcohol in ultrasonic bath. Figure 2 is the photo of this copper cathode after use. The pattern on surface is believed from the flash during the rf commissioning.

Figure 2: The copper cathode after used in the SRF gun II. A radius of 0.3mm is used to reduce the field enhancement on the sharp edge. The pattern on surface is believed from the flash during the rf commissioning.

This Cu cathode helped to finish the successful commissioning for first beam [3]. There was no obvious multipacting problem with copper cathode. The maximum field on cathode surface is 14.6 MV/m, and the dark current from cathode was 53 nA. Difference parameters of SRF gun were measured with this cathode. A low transverse emittance of 0.4 mm·mrad for 1 pC bunch charge was achieved with this cathode.

Copper cathode is proved being safe for SRF gun. But the work function of Cu (4.6 eV) is rather high and its QE of 1×10^{-5} at 260 nm is too low for the regular beam production.

MG CATHODES IN SRF GUN II

As metallic photocathode, Mg is a safe choice for SRF gun. There have been several Mg photocathodes stably working in SRF Gun II since 2016. Figure 3 shows the QE measurement of the Mg #216 in the SRF gun II. A record

---

† email address: r.xiang@hzdr.de

QE of 0.5% is achieved with this cathode. The photoemission of Mg cathode in the SRF gun is dominated by space charge effect and Schottky effect. Fig. 4 plots the extracted photoelectron bunch charge as the function of the launch phase (gun phase). In the case of low bunch charge, the Schottky effect plays the main role, and the bunch charge is ascending in the plateau range. But with increased laser pulse energy, the space charge effect becomes stronger in the photoemission process.

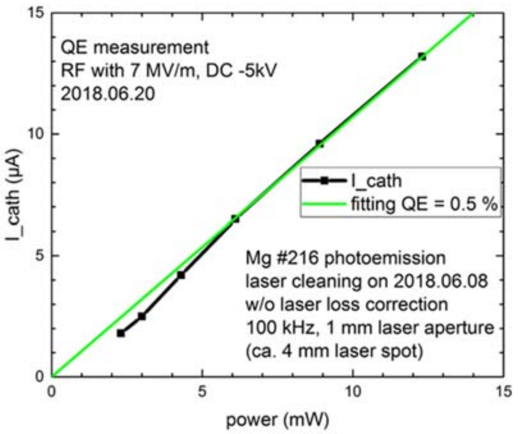

Figure 3: The image of Mg photocathode inserted into the cavity back wall. The bright circle is the opening of cathode hole, and inside this ring is the plug with spots induced by laser cleaning.

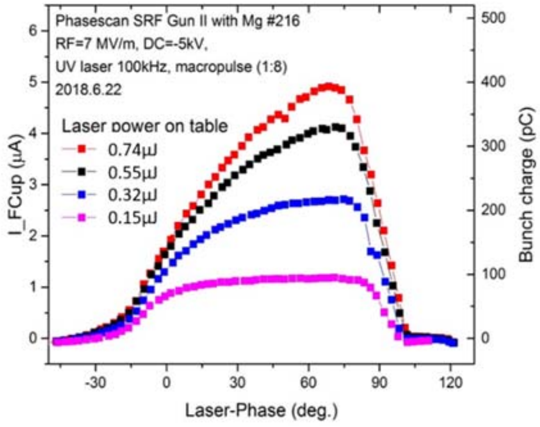

Figure 4: Bunch charge versus laser arriving phase. Max. bunch charge can reach 400 pC.

A key technology for good Mg cathode is the laser cleaning. The Mg cathode is a Φ 10 mm bulk plug of pure magnesium. The plug was mirror-like polished with different sizes diamond compound. And the polished cathode with a mean roughness of ca. 10 nm was de-oxided, cleaned and blown with filled N2, then installed in the cathode transport chamber, where cathodes can be laser cleaned and stored.

Because after the chemical de-oxide process, the Mg plugs are shortly exposed in air, the QE of new Mg cathode was only 1.8×10^{-5} in our measurement. In order to reach clean Mg surface and reduce the surface work function, treatments in vacuum have to been performed.

Photocathode drive Laser has been used to burn off the MgO insulator layer in transport chamber. The laser is a UV laser with 263 nm (4.7 eV) wavelength, repetition rate of 100 kHz and ultra-short pulses of 3 ps. For the cleaning, the mean power was set to 100 mW. With a movable focusing lens the laser spot size on the cathode can be accurately adjusted down to 30 μm radius. The power intensity of 2 W/mm^2 was found the best for cleaning. The cleaned surface has a shining silver color. Also the microscope view demonstrated the surface structure change (Fig. 5). Virgin part is the polished mirror-like surface, and the cleaned part shows period wave structure induced by the scanned laser beam [4].

Figure 5: surface structure changes after cleaned with high intensity laser.

The cleaning process can be very well repeated, and one Mg photocathode is possible to be cleaned for several times. Figure 6 shows the results of the QE measured in transport chamber with DC bias. Cleaned Mg is very sensitive. It kept stable in transport chamber (with 10^{-10} mbar vacuum) and also during the SRF gun operation. Another experiment showed that cleaned a Mg cathode in 10^{-8} mbar vacuum lost 60% of its QE in one day.

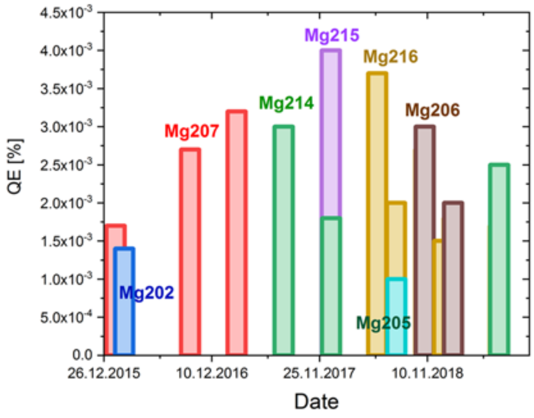

Figure 6: The statistic of the Mg cathodes at HZDR. Measured with DC bias in transport chamber.

CS$_2$TE PHOTOCATHODES

HZDR has long history of preparing Cs$_2$Te [5]. For the Cs$_2$Te cathode, the plug in Fig. 1 is changed to Molybdenum, and Cs$_2$Te is deposited on the tip of Mo plug, which is screwed on the cathode body.

Up to now more than 40 Cs_2Te photo cathodes have-been produced at HZDR photocathode laboratory. The typical QE of the fresh cathodes are from 8% to 15%. Before 2014, there were 8 cathodes ever worked in the SRF gun I. The QEs in the gun are normally about 1%, and the life time can be months. For example, cathode #17.04.2012 Cs_2Te had fresh QE of 8.5%, and the QE dropped down to 0.6% after it was transferred to gun. Nevertheless, it provided beam time more than 2100 h ours, totally extracted charge more than 264 C.

However, in 2016 we tried twice Cs_2Te photocathodes in SRF gun II. Both cathodes ran well in the first two weeks and delieved good beams. But then the cathode lost QE suddenly. At the same time, the field emission from cavity increased dramatically and camera showed the Cs_2Te layer disappeared, which means the temperature of plug surface was over 300ºC at that moment (see Fig.7). The shift of resonant frequency of cavity also gave clue that the cathode position changed in those events.

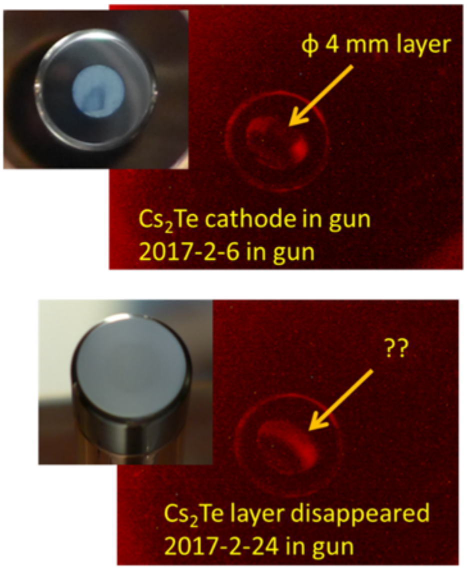

Figure 7: One Cs_2Te cathode lost film in the SRF gun-II due to overheating. Top: the Mo plug with Cs_2Te layer in center. Bottom: the layer disappeared in the gun and lost photoemission.

A systematic study has been performed since 2016. Through CST simulation and experiments on test bench, the main reason the screw connection method between the Mo plug and Cu stem, which have different thermal expansion coefficient (Cu: 16 m/(m·K), Mo: 5 m/(m·K),). During the cathode preparation, the cathodes were heated up to 400ºC for surface cleaning and 120ºC for deposition. And the same cathodes were cooled down to LN2 temperature in SRF gun. This temperature difference makes big deformation of the thread structure, leading the bad thermal transfer from plug to copper cooling body.

One solution to solve the thermal problem is to use the same materials for the plug and cathode stem. So the next Cs_2Te will be deposited on Cu instead of Mo substratum.

CONCLUSION

The metallic photocathodes provide us a safe solution for SRF guns, especially Mg cathode for medium bunch charge application. From our experience, Mg cathode is safe for the niobium cavity and can produce up to 300 pC bunch charge. Laser cleaning produces QE as high as 0.5 %, but it induces rough surface on the cathodes.

For high bunch charge and high current operation, Cs_2Te photocathode will be used in SRF Gun II. The next step is to demonstrate the deposition of Cs_2Te on copper plug and finally to provide a safe semiconductor photocathode for SRF Gun II at HZDR.

ACKNOWLEDGEMENT

We would like to thank the whole ELBE team for their help and assistance with this project. The work is supported by the German Federal Ministry of Education and Research (BMBF) grant 05K12CR1 and Deutsche Forschungsgemeinschaft (DFG) project (XI 106/2-1)

REFERENCES

[1] J. Teichert *et al.*, "Free-electron laser operation with a superconducting radio-frequency photoinjector at ELBE", *Nucl. Instr. Meth. A*, vol. 743, pp. 114-120, 2014. `doi:10.1016/j.nima.2014.01.006`

[2] A. Arnold *et al.*, "Development of a superconducting radio frequency photoelectron injector", *Nucl. Instr. Meth. A*, vol. 577, pp. 440-454, 2007. `doi:10.1016/j.nima.2007.04.171`.

[3] J. Teichert *et al.*, "First beam characterization of SRF gun II at ELBE with a Cu photocathode", *Proceedings of ERL2015*, Stony Brook, USA, 2015 `doi:10.18429/JACoW-ERL2015-TUIDLH1038`

[4] R. Xiang *et al.,* "Improvement of the Photoemission Efficiency of Magnesium Photocathodes", *proceedings of IPAC2017*, Copenhagen, Denmark, 14-19 May 2017, p. 500. `doi:10.18429/JACoW-IPAC2017-MOPIK003`

[5] R. Xiang *et al.,* "Recent improvement of Cs2Te photocathodes at HZDR", *Proceedings of IPAC'14*, June 15-20, 2014, Dresden, Germany. `doi: 10.18429/JACoW-IPAC2014-MOPRI025`

HIGH CHARGE HIGH CURRENT BEAM FROM BNL 113 MHZ SRF GUN*

I. Pinayev†, I. Ben-Zvi, J.C. Brutus, M. Gaowei, T. Hayes, Y. Jing, V.N. Litvinenko[1], J. Ma, K. Mihara[1], G. Narayan, I. Petrushina[1], F. Severino, K. Shih[1], J. Skaritka, E. Wang, G. Wang, Y.H. Wu[1],
Brookhaven National Laboratory, Upton NY, U.S.A.
[1]also at Stony Brook University, Stony Brook NY, U.S.A.

Abstract

The 113 MHz superconducting gun is used an electron source for the coherent electron cooling experiment. The unique feature of the gun is that a photocathode is held at room temperature. It allowed to preserve the quantum efficiency of Cs_2KSb cathode which is adversely affected by cryogenic temperatures. Relatively low frequency permitted fully realize the accelerating field gradient what in turn helps to achieve 10 nC charge and 0.3 microns normalized emittance. We present the achieved performance and operational experience as well.

GUN DESIGN

The injector is an essential part of any accelerator, and the quality of the produced beams completely relies on its performance. Among the well-known electrostatic (DC) and normal-conducting (NC) RF photo-guns, the injectors based on an SRF cavity are rapidly gaining popularity in the generation of the high-brightness high-quality beams.

The idea of utilizing the SRF technology brings advantages and challenges [1, 2]. The biggest advantage is the reduced power losses (orders of magnitude lower compared to a NC cavity) which allow for reliable operation in continuous wave (CW) regime and generation of beams with high average current, providing a higher accelerating gradient. Another advantage is an excellent vacuum conditions inside the cavity which serves ad huge cryopump.

However, introduction of a photocathode into the SRF environment causes several complications: since the photocathode has to be replaced throughout the operation of the gun, the area around the cathode creates a condition for RF power leakage which has to be taken care of. To keep the power within the cavity, an RF choke filter has to be designed for this purpose.

Moreover, the cathodes are generally kept at room temperature creating an additional heat leak between the cold surface of the cavity and the warm cathode.

We utilized quarter-wave resonator (QWR) based geometry for our gun. The QWR cavities are specifically suitable for operation at low frequencies which allow for a generation of long bunches. This fact is beneficial for the reduction of the space charge effect in the initial stages of the beam generation, allowing to achieve higher charge per bunch. The accelerating gap in such a cavity is relatively short compared to the wavelength, which makes the field distribution in the gap close to constant. To a degree, such SRF guns are similar to DC guns but offer both high accelerating gradient and higher beam energy at the gun exit. The main RF parameters of the gun can be found in Table 1.

Table 1: RF Parameters of the Gun

Parameter	**Value**
Frequency, MHz	113
Quality factor w/o cathode	3.5×10^9
R/Q, Ω	126
Geometry factor, W	38.2
Operating temperature, K	4.2
Accelerating voltage, MV	1.25 (1.7)

The geometry of the SRF gun is shown in Fig. 1. The cavity body is made of bulk Nb, and, as all of the QWR geometries, has “outer conductor” and “inner conductor” parts due to the nature of this type of a cavity. The “inner conductor” is hollow and accommodates the system of the cathode insertion and extraction. The accelerating electric field is concentrated between the front wall of the cavity and the rounded part of the “inner conductor,” which we denote as the cavity “nose”. The inset in the Fig. 1 shows in detail the location of the cathode puck in the cavity nose.

The necessary half-wavelength RF choke for the reduction of the power leakage incorporates a hollow stainless-steel cathode stalk which allows insertion of a cathode puck [3, 4]. The cathode stalk is coated with layers of copper and gold to reduce heat emission into the 4 K system. It is kept at room temperature by circulating water in the channel soldered to the stalk.

The stalk does not have direct physical contact with the cold center conductor of the cavity, thus reducing the leakage of heat into the cavity only allowing the exchange of the radiated heat. The stalk is shorted at the far end to serve as a choke filter. The choke reduces the penetration of the RF field, and minimizes the voltage drop between the cathode and the cavity's center conductor. The gap between the stalk and the cavity nose at the entrance of the cavity is only 3.56 mm. The length of the stalk was shortened to account for the capacitance created by this small gap. The impedance transformer in the middle of the stalk is used to reduce the current through the short, which includes a coated bellow.

A pick-up antenna for measuring the RF voltage is located outside of the gun cryostat and is weakly coupled to the choke. The axial position of the stalk tip and, therefore, the photocathode surface with respect to the cavity nose can be manually adjusted. The latter provides us with an opportunity to optimize the initial focusing of the electron beam.

---

* Work supported by Brookhaven Science Associates, LLC under Contract No. DE-AC02-98CH10886 with the U.S. Department of Energy.
† pinayev@bnl.gov

ISBN: 978-3-95450-217-2 doi:10.18429/JACoW-ERL2019-THCOYBS02

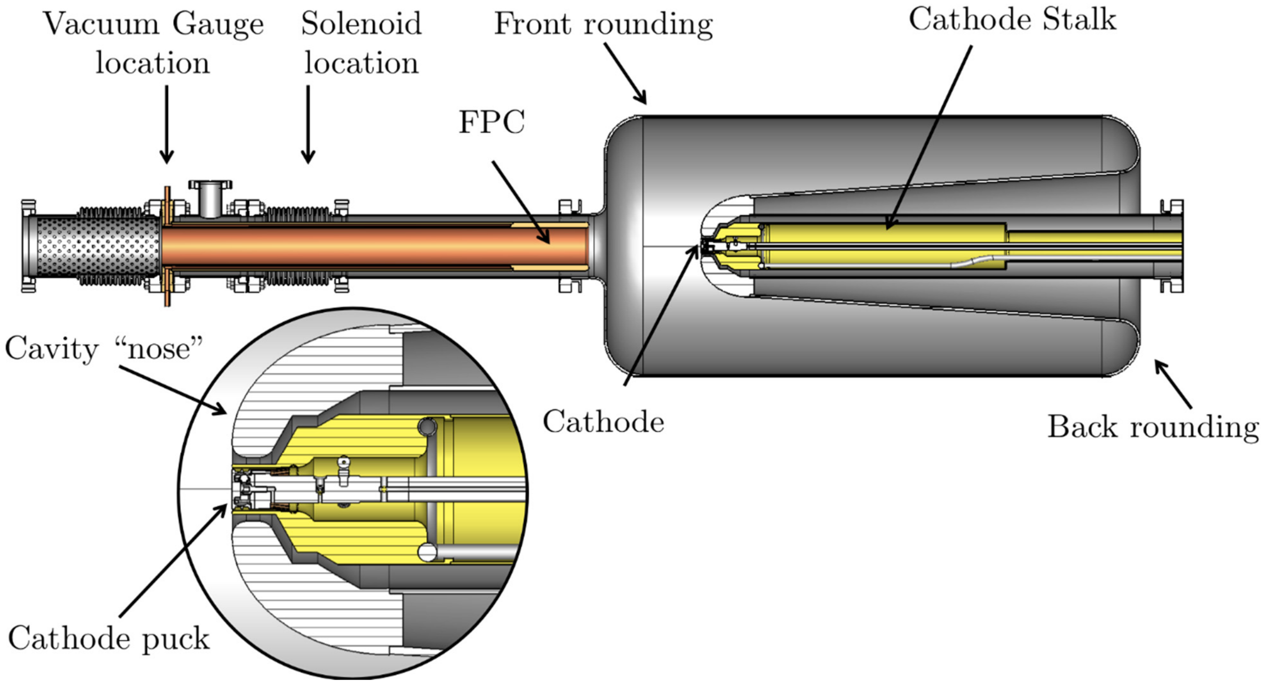

Figure 1: Cross-section of the SRF gun. The cathode is inserted through the opening inside of the cathode stalk with long manipulator. The cathode stalk serves as a field pick-up for the cavity control. The electron and laser beams are passing inside of the FPC. Electron beam focusing is done with a solenoid placed around FPC over the bellows.

The coarse tuning of the cavity frequency is provided by the two manual tuners, while the fine frequency tuning and the Low-Level RF (LLRF) feedback loops utilize the fundamental power coupler (FPC). The coaxial FPC with water cooling is incorporated in the front side of the cavity and is hollow in order to allow for the electron and laser beams propagation. The FPC is placed on a motorized translation stage, so its position can be adjusted by about 40 mm, which allows us to tune the coupling and the gun frequency. Coarse tuning range is 80 kHz and fine tuning range is 6 kHz.

The RF power to the gun is provided by a 4-kW solid-state amplifier. The first focusing element, which we denote as the gun solenoid, is located 65 cm downstream of the cathode surface and encapsulates the bellow of the FPC section. This section is followed by the laser cross which delivers the green drive laser beam to the cathode surface. The drive laser can generate up to 0.5 µJ pulse at 532 nm wavelength. The pulse duration is variable from 100 ps to 1 ns and the maximal repetition rate is 78 kHz. These laser pulses are amplified to the desirable level by a regenerative amplifier. The time structure of the delivered laser pulses is controlled by a set of Pockels cells and can provide the following configurations: single pulses, pulse trains of various duration, and CW mode. The laser pulse intensity is controlled by the cross-polarizers.

A small, 20 mm-diameter, cathode puck, shown in Fig. 2, is made of molybdenum. A high quantum efficiency (QE) CsK_2Sb photoemission coating with diameter of 8 to 10 mm is deposited in the center of its polished front surface. Small photoemissive surface contributes to less beam halo and reduces number of multipacting events.

The important feature in the design of the SRF gun is the capability of in-situ cathode puck replacements using an ultra-high vacuum (UHV) manipulator system. The UHV portable transport system ("garage") has a built-in QE measuring system. Up to three cathode pucks can be stored and transported in such a "garage" without any significant loss of QE. The garage is attached to the gun's manipulator system via a bakeable load-lock unit and is used for storing cathodes for months. Cathodes can be exchanged between the gun and the garage in about one hour, with most of the time used to slowly move the manipulators to avoid friction-driven vacuum pressure rise. Two grooves on the side of the puck allow us to insert and extract it using forks of the in-vacuum manipulators. The manipulator arm has three centering standoffs with rolling ceramic wheels, which prevent damage to the cathode during the insertion and limit the generation of particulates. The gold-plated RF spring finger contacts connect the puck with the inner surface of the stalk ensuring that the electromagnetic field does not propagate inside the cathode stalk.

ISBN: 978-3-95450-217-2 doi:10.18429/JACoW-ERL2019-THCOYBS02

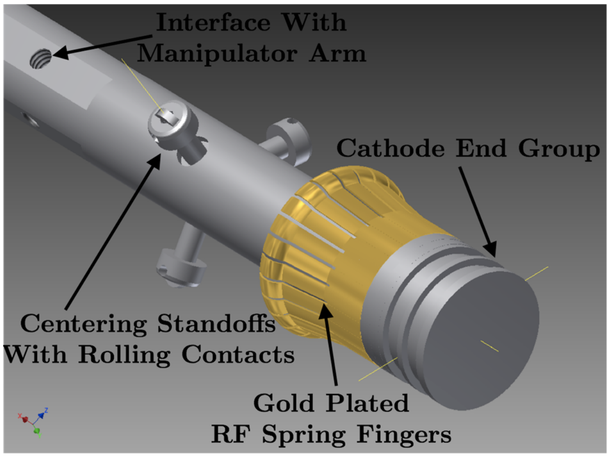

Figure 2: Cathode end assembly.

MEASUREMENT OF THE GUN PARAMETERS

Cathode Recess

The field distribution was evaluated using CST Microwave Studio (MWS) [5] with tetrahedral mesh. To reduce the computational time, an H-plane was utilized based on the symmetry of the fundamental mode field distribution. Axial symmetry of the gun allowed to 2D solver for calculating axial fields such as Poisson SUPERFISH [6]. The electric field profiles for different cathode recess (cathode position vs. nose tip) are shown in Fig. 3.

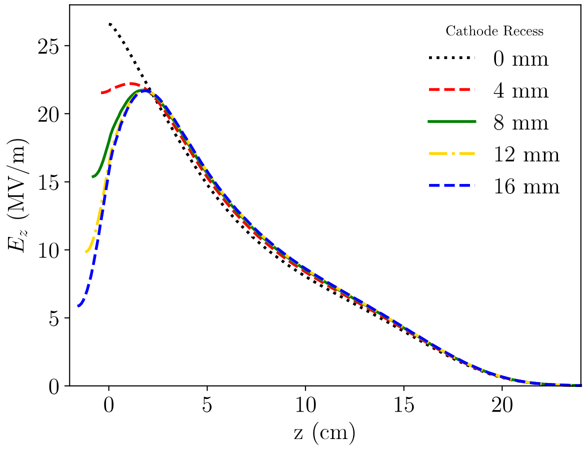

Figure 3: Electric field distribution along the gun axis for various values of the cathode recess.

As one can see the cathode position substantially changes accelerating field profiles and, hence, focusing field of the gun. With zero recess the field at the cathode is maximal but there is no focusing component. With cathode withdrawn the focusing is strong but cathode field is low and significant charges cannot be extracted due to the space charge.

The location of the cathode can be fixed relatively to the stalk but the position of the latter is not well defined due to the cavity contraction after cool down. We have developed procedure for the measuring the cathode position in the cavity based on the focusing properties of the gun cavity. For this purpose, laser spot was set to smallest value (0.25 mm) and laser intensity was reduced to suppress electron beam divergence due to the space charge forces. Under such conditions it is possible to observe the electron beam on the first profile monitor without additional focusing by solenoids. The laser spot was scanned on the cathode surface and beam position on the profile monitor was measured. From this measurement magnification factor, ratio of electron beam displacement to the laser spot displacement was found and cathode position was found from the calibration curve shown in Fig. 4.

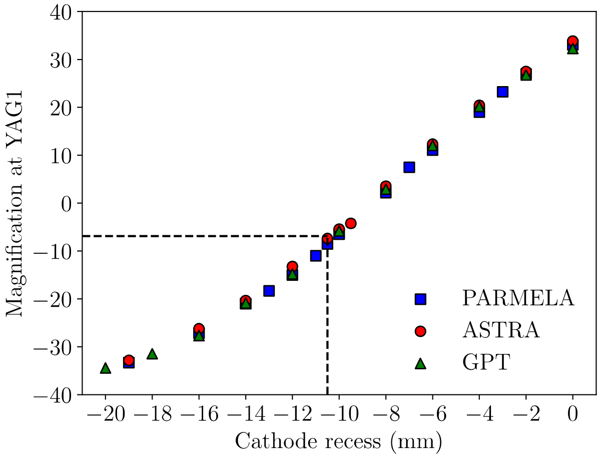

Figure 4: Magnification factor of beam displacement on the first profile monitor obtained with different tracking codes. Positive values correspond to the electron beam displacement in the same direction as laser spot motion and negative ones to the opposite direction.

Electrical Axis of the Gun

In the axially symmetric system the electron beam generated on the center of the cathode leaves gun without transverse momentum. However, manufacturing imperfections change the field distribution within the cavity. In order to determine the electrical axis of the gun, we changed the beam rigidity by scanning the gun voltage and measured the position of the electron beam on the first profile monitor. The beam position has linear dependence on the inverse beam rigidity as shown in Fig. 5.

Extrapolating the line to the infinity beam energy (inverse rigidity equal to zero) on can find coordinates of the electrical axis at the observation point and, hence, its tilt. For these measurements all of the solenoids were turned off. To guarantee that the beam stays on the screen the trajectory was adjusted two times, that is why we have three lines. But intercept for each line is approximately the same (the infinitely rigid beam is not steered by correctors).

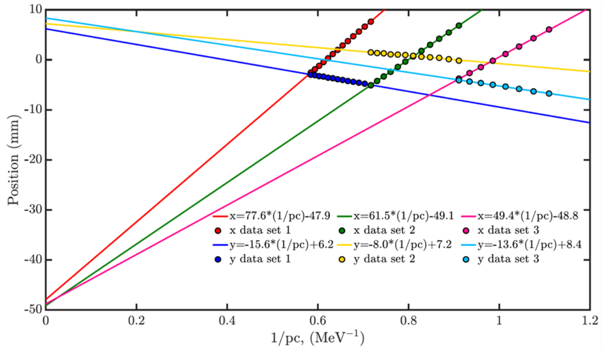

Figure 5: Horizontal and vertical position of the beam center as function of the inverse beam rigidity for three different trim sets. The intercept values and distance from the gun to profile monitor (4.27 m) give horizontal angle of -11.1±0.1 mrad and vertical angle of +1.6 ±0.2 mrad.

BEAM PARAMETERS

The first operation after insertion of a new cathode is phase scan either a drive laser or gun voltage. The result of the laser phase scan is shown in Fig. 6. The shape of the curve is trapezoidal not a triangular commonly observed in the high frequency RF guns. Moreover, the width at baseline exceeds 180 degrees due to the non-zero laser pulse length.

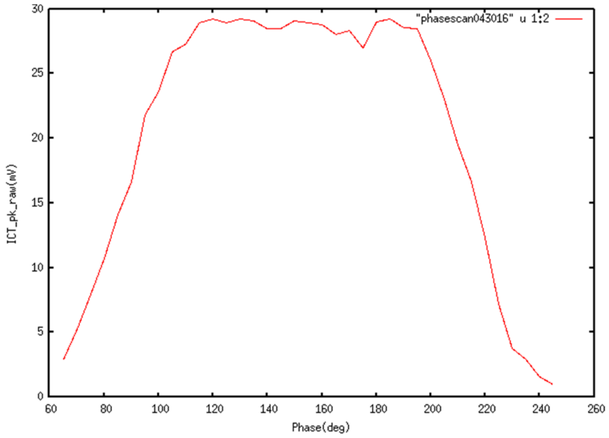

Figure 6: Dependence of the extracted charge vs. drive laser phase. The laser pulse is 0.5 nanoseconds long.

Fig. 7 shows the bunch charge dependence on the laser pulse power. The saturation becomes visible for the charges above 4 nC. In this figure we do not observe saturation but the observed maximal charge is 10.7 nC as shown in Fig. 8.

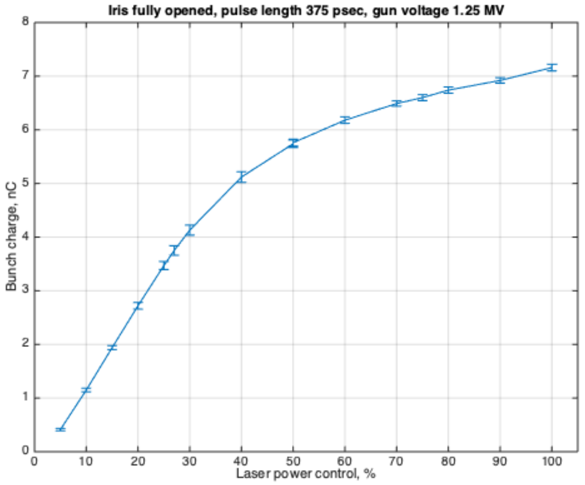

Figure 7: Dependence of the bunch charge vs laser power. Gun voltage is 1.25 MV, cathode recess is -10.5 mm, laser pulse length is 375 psec, laser spot diameter is 6 mm.

We have not tried to propagate the beam with charge close to the maximum to the high-power dump. The experiment utilized maximal charge of 1.5 nC and maximal current observed is 120 µA (repetition rate 78 kHz).

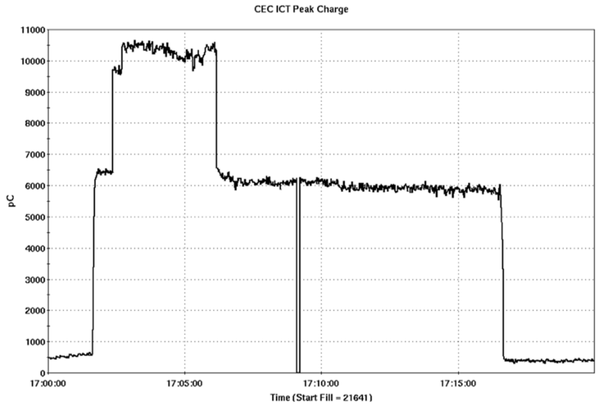

Figure 8: History of the gun charge during test.

Important beam parameter is its emittance. While we have a system of slits it is not very suitable for measurement of small emittances. Therefore, we used the solenoid scan. The dependence of the beam size on the profile monitor vs. solenoid current is shown in Fig. 9. To account for the space charge forces with tracking code to simulate the observed values. And beam parameters obtained in simulations were used actual values.

Typically, cathode lifetime in the gun was 2-3 weeks and we have cathode that was utilized for two months. Long cathode lifetime we attribute to the high vacuum in the SRF gun which serves as cryogenic pump and absence of the substantial ion bombardment. We never observed specific dip in the cathode QE in the center which is reported in most DC guns.

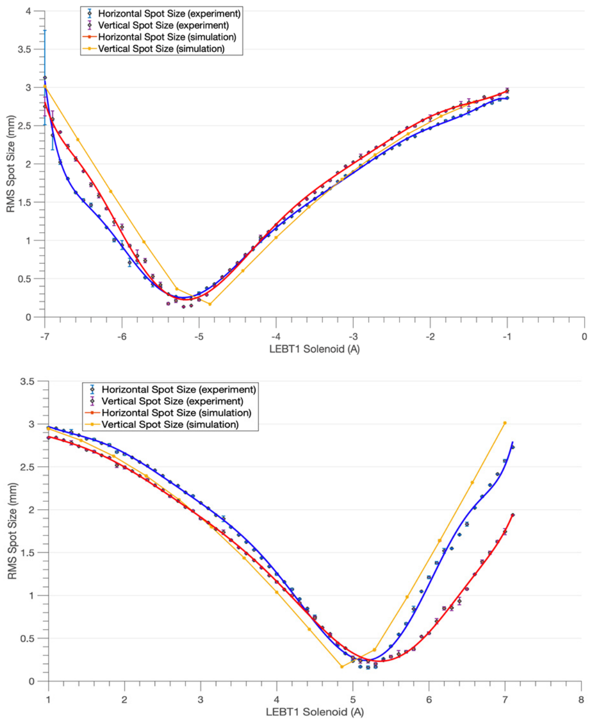

Figure 9: Dependence of the electron beam size vs solenoid current (negative on the top and positive on the bottom). Blue lines represent horizontal beam size, red lines – vertical beam size, yellow – round beam size in the simulation. Laser spot diameter was 3.3 mm, bunch charge 600 pC, bunch length 400 psec. The projected normalized emittance is 0.57 mm mrad, normalized core emittance is 0.35 mm mrad.

CONCLUSION

The low-frequency superconducting RF gun allows to generate electron bunches with record parameters both in charge and transverse emittance. Low frequency allows to generate electron beam close to conditions in DC gun but avoid QE degradation due to the ion bombardment.

High vacuum inside the SRF vacuum provides for the cathode's long lifetime.

SRF gun is an attractive electron source for the free-electron lasers and high-energy electron coolers.

REFERENCES

[1] A. Arnold and J. Teichert, "Overview on superconducting photoinjectors", *Phys. Rev. ST Accel. Beams*, vol. 14, p. 024801, Feb. 2011. `doi:10.1103/PhysRevSTAB.14.024801`

[2] S. Belomestnykh, "Survey of SRF Guns", *in Proc. 15th Int.Conf. RF Superconductivity (SRF'11),* Chicago, IL, USA, Jul. 2011, paper MOIOB04, pp. 23-26.

[3] J. Harris, K. Ferguson, J. Lewellen, S. Niles, B. Rusnak, R. Swent, W. Colson, T. Smith, C. Boulware, T. Grimm, *et al.*, "Design and operation of a superconducting quarter-wave electron gun", *Phys. Rev. ST Accel. Beams,* vol. 14, no. 5, p. 053501, 2011. `doi:10.1103/PhysRevSTAB.14.053501`

[4] J. Bisognano *et al.*, "Wisconsin SRF Electron Gun Commissioning", *in Proc.North American Paricle Acceleratro Conf. (NAPAC'13)*, Pasadena, CA, USA, Sep.-Oct. 2013, paper TUPMA19, pp. 622-624.

[5] `http://www.cst.com`

[6] M. Menzel and H. K. Stokes, "Users guide for the POISSON/SUPERFISH group of codes", Los Alamos National Lab., Los Alamos, NM, USA, LA-UR-87-115, Jan. 1987, `doi:10.2172/101`

ESSENTIAL INSTRUMENTATION FOR CHARACTERIZATION OF ERL BEAMS*

N. Banerjee†, A. Bartnik, K. Deitrick, J. Dobbins, C. Gulliford, G. Hoffstaetter,
Cornell Laboratory for Accelerator-Based Sciences and Education, Ithaca, USA
J. S. Berg, S. Brooks, R. Michnoff,
Brookhaven National Laboratory, Upton, USA

Abstract

The typical requirement of Energy Recovery Linacs to produce beams with high repetition rate and high bunch charge presents unique demands on beam diagnostics. ERLs being quite sensitive to time of flight effects necessitate the use of beam arrival time monitors along with typical position detection. Being subjected to a plethora of dynamic effects, both longitudinal and transverse phase space monitoring of the beam becomes quite important. Additionally, beam halo plays an important role determining the overall transmission. Consequently, we also need to characterize halo both directly using sophisticated beam viewers and indirectly using radiation monitors. In this talk, I will describe the instrumentation essential to ERL operation using the Cornell-BNL ERL Test Accelerator (CBETA) as a pertinent example.

INTRODUCTION

The unique diagnostic requirements for beams produced in Energy Recovery Linacs (ERLs) stem from the hybrid nature of these accelerators which combine aspects of both Linacs and storage rings. Just like their Linac counterparts, ERLs produce very bright beams with typical normalized transverse emittance of a few microns. On the other hand, the requirements on longitudinal distribution of the beam depends on particular applications. A survey of beam parameters [1] of different ERL projects around the world reveals bunch lengths from less than a pico-second for light sources, up to 50 ps for the Coherent electron Cooler proposed for eRHIC. Just like storage rings, ERLs are CW high current machines with large beam power. However, beam is continuously produced in ERLs while rings can only hold a finite amount of charge inside. This difference is very important in the context of machine protection. Consequently, the list of diagnostics essential to ERL beam operations must include monitoring of all these aspects.

Apart from the distinguishing features of the beams, ERLs are sensitive to time of flight errors and losses. The time of flight of the beam in the return loop needs to be within the target value with narrow tolerances in order to ensure correct arrival phase in the accelerating cavities. This in turn establishes correct beam energies and zero average beam loading [2], which is crucial for sustaining high currents. In this way, ERLs are operationally time of flight spectrometers. [3] Further, ERLs are designed for high average beam power up to mega-watts, so even modest losses can result in large radiation and thermal load on machine components. Consequently halo characterization and bunch arrival time measurements are crucial for high current operations along with the usual measurement of the core and the transverse position of the beam.

The Cornell-BNL ERL Test Accelerator (CBETA) [4] is a 4-turn superconducting ERL which has been constructed under the collaboration of Cornell University and Brookhaven National Laboratories and is currently being commissioned. With a target injection current of 40 mA and the top energy of 150 MeV, the diagnostics used in this accelerator serves as a representative example of essential instrumentation crucial to ERL operation. In the next section, we describe how we measure the beam centroid in CBETA. Then we explain various methods of observing the phase space distribution of the core of the beam. After this, we list instrumentation to detect beam halo and loss, including the equipment protection system. Finally we describe other miscellaneous diagnostics.

BEAM CENTROID

Beam Position Monitors (BPMs) detect the position of the centroid of the bunch both in space and time. In terms of hardware, BPMs can be broadband devices such as button BPMs and striplines such as the ones used in CBETA, or they may work as resonant cavities which are narrowband. In the case of broadband monitors, the image charges induced by the bunches are electrically coupled to pickups and the relative amplitudes and phases of the detected impulses can be used to measure beam position. On the other hand cavity BPMs work by measuring the amplitudes and phases of specific resonant modes excited by the beam and can be used for very precise measurements. [5] ERLs pose an additional requirement on BPMs to be able to detect multiple beams at the same time, which is especially true in CBETA which has a Non Scaling Fixed Field Alternating (NS FFA) [6] return loop hosting 7 beams at the same time.

We use both time and frequency domain techniques for signal processing on broadband BPMs in CBETA. The time domain technique first uses a custom low pass filter with a cut off frequency at 800 MHz to broaden and smooth the incoming wideband signal from the buttons. Then after a programmable gain, we digitize the signal using a 400 MSPS ADC, after which a FPGA processes the data. We acquire

---

* This work was supported by the New York State Energy Research and Development Authority.

† nb522@cornell.edu

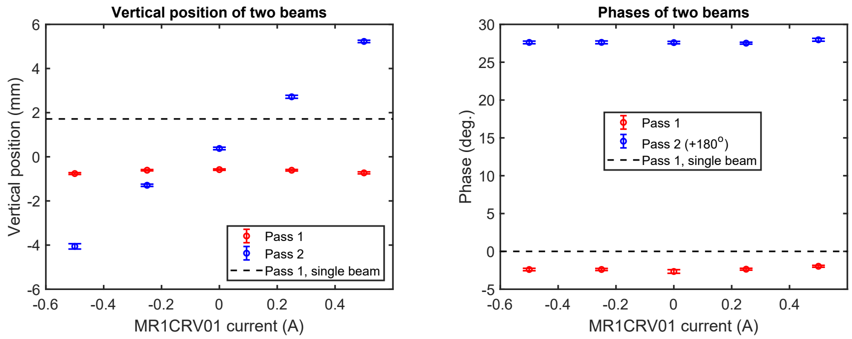

Figure 1: First tests on a dual frequency BPM just before the main linac in CBETA. The plots show the vertical position (left) and phase of the beam (right) as a function of corrector magnet setting in the recombiner line. The red points represent the injected beam going through the merger unaffected by the vertical corrector while the blue points represent the recirculated beam about to enter the main linac. The dashed lines are the baseline measurements with only the injected beam in the pipe.

the position information of separate beams by synchronizing on to the arrival times of different energy bunches, the details of which are documented elsewhere. [7] We obtain a typical transverse measurement jitter of 0.1 mm using 5 pC bunches with a 20 Hz repetition rate, while bunch arrival times can't be measured using this system.

The frequency domain technique is used to both measure position and arrival time of both accelerating and decelerating bunches in the splitter/recombiner and merger sections of CBETA. The button signals are split into two parts and processed through bandpass filters of 1.3 GHz and 2.6 GHz which are the CBETA RF frequency and it's second harmonic respectively. These are then mixed down to intermediate frequency signals which are digitized so that we can obtain their in-phase (I) and quadrature (Q) components with respect to the RF clock. We are going to document the details of this technique in a future paper. The results from initial testing are depicted in Fig. 1. The single shot measurement jitter of this system is 0.3 mm and 0.1° with one train of 10-20 5 pC bunches.

PHASE SPACE

The phase space distribution of beams must meet specifications set by particular applications. Apart from the use of conventional viewscreens which help us measure the transverse distribution of charge at different places in the accelerator, we also need instrumentation dedicated to measuring transverse and longitudinal phase space. At CBETA, we use a multi-slit system [8], with scanning coils and a Faraday cup in a separate diagnostic line to measure the transverse emittance and twiss parameters of the injected beam as it enters the main linac. Figure 2 shows the measured transverse phase space at a bunch charge of 5 pC. Full 4D phase space measurement have been explored elsewhere [9] using tomographic techniques which rely on rotating the phase space using quadrupole magnets and measuring the resulting projections. Both these techniques need a dedicated diagnostic line and are not in-situ measurements.

The design of the longitudinal phase space of ERL beams depend on particular applications. On one hand, light sources require very short bunches while electron coolers need very long bunches up to 50 ps with small energy spread of 10^{-4}. Applying a time dependent transverse kick using deflector cavities placed in dedicated diagnostic lines is a widely used technique. At CBETA, we use a pulsed copper cavity [10] in conjunction with slits and a Faraday cup to map the longitudinal distribution of charge as shown in Fig. 3. Other groups have demonstrated measurement of slice emittance along the longitudinal position of the bunch using tomographic projection in conjunction with deflector cavities. [11] Coherent Transition Radiation (CTR) is yet another method of measuring the longitudinal distribution, where the beam goes through a metal foil and the radiation is measured using an interferometer. [12] These are all destructive methods and we can only use them in special low current diagnostic modes of the machine. Non-destructive methods of measuring the longitudinal distribution include interferometric techniques on synchrotron radiation [13] and electro-optic modulation of laser pulses using the electric field generated by the bunch. [14]

HALO AND LOSSES

The beam halo plays an important role in operation of ERLs. While characterizing the charge distribution in the core of the beam is important for various applications, the halo determines how much unwanted radiation the machine produces which in turn constrains the beam current. Halo measurement requires devices capable of high dynamic range, typically more than 10^6. At CBETA we have used conventional BeO viewscreens to measure transverse halo of the injected beam. We boosted the dynamic range of measurement by averaging multiple frames and acquiring the averaged frames at multiple exposure times. Then we weighted each averaged frame with the inverse of the exposure time and subtracted a background image with the beam turned off. The result of this process is shown in Fig. 4. To rule out effects of lens flare, reflections and spurious light we scanned an upstream quadrupole magnet to verify that the halo also changes shape along with the core of the beam. Extensions of this technique include using Charge Injection

ISBN: 978-3-95450-217-2 doi:10.18429/JACoW-ERL2019-FRCOWBS04

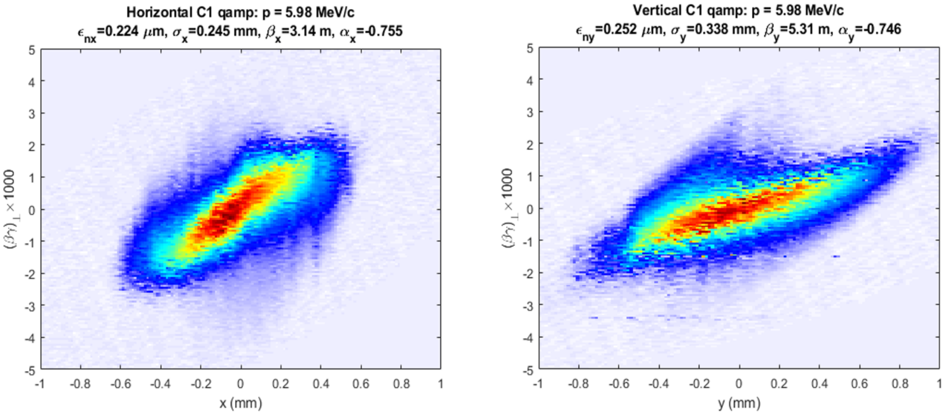

Figure 2: Measured transverse phase space of the injected beam in CBETA with a 5 pC bunch charge.

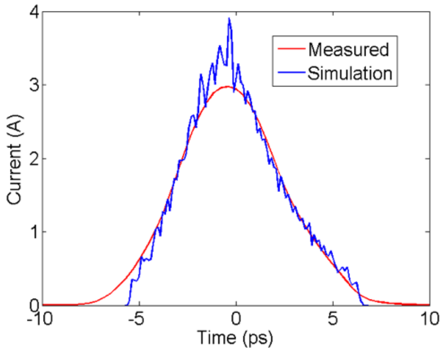

Figure 3: Longitudinal charge distribution of a 20 pC test bunch at the CBETA injector.

Device (CID) cameras and selective masking of different areas of the beam spot using micro mirror arrays. [15] Besides viewscreens, wirescanners achieve high dynamic range by introducing an intercepting monitor through the beam and recording the resulting radiation. [16]

The ionizing radiation generated during ERL operations constrain the maximum sustainable beam power and is very important from a equipment protection point of view. Scraping of beam halo on the vacuum chamber generates a steady field of radiation throughout the machine. We must measure and constrain this beam loss to make sure enough energy is recovered and sensitive equipment, for example the permanent magnet return loop in CBETA is not damaged. The amount of current lost can be measured directly using beam current monitors. In CBETA, slow monitors based on CsI scintillators coupled to PiN photodiodes provide calibrated time averaged radiation dose information primarily to monitor dose to our permanent magnets. On the other hand, we use plastic scintillating fibers coupled to photo-multiplier tubes placed all around the machine to detect catastrophic beam loss and turn off the machine within 1 µs.. An exhaustive view of machine protection has been presented in a different talk at this workshop. [17]

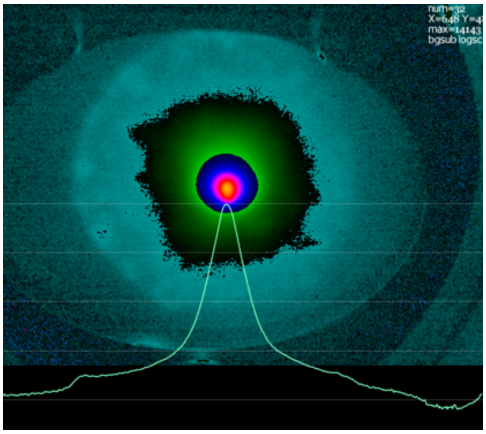

Figure 4: Halo measured at the CBETA injector using a viewscreen. The area intensity of the halo is 3×10^{-4}, while it accounts for 3% of the total charge.

MISCELLANEOUS

Besides instrumentation dedicated to beam diagnostics, other components of the accelerator may also provide important information about the beam. At CBETA, we have used the main linac cavities to measure net transmission through our return loop. Figure 5 shows the beam loading on all six cavities of the main linac as functions of injected beam current. In the situation of perfect energy recovery, the beam loading should be independent of current, however the blue data points representing the energy recovered beam shows a small slope on all cavities. Since the beam reached the main beam stop with the nominal orbit in all cases, the residual beam loading represents net beam loss in the return loop of the machine. We measured a transmission efficiency of 99.6 ± 0.1 % from the fitted slopes. Cavities can also be used to detect the onset of Beam Breakup Instability (BBU) and characterize the excited Higher Order Mode (HOM) which is responsible. [18]

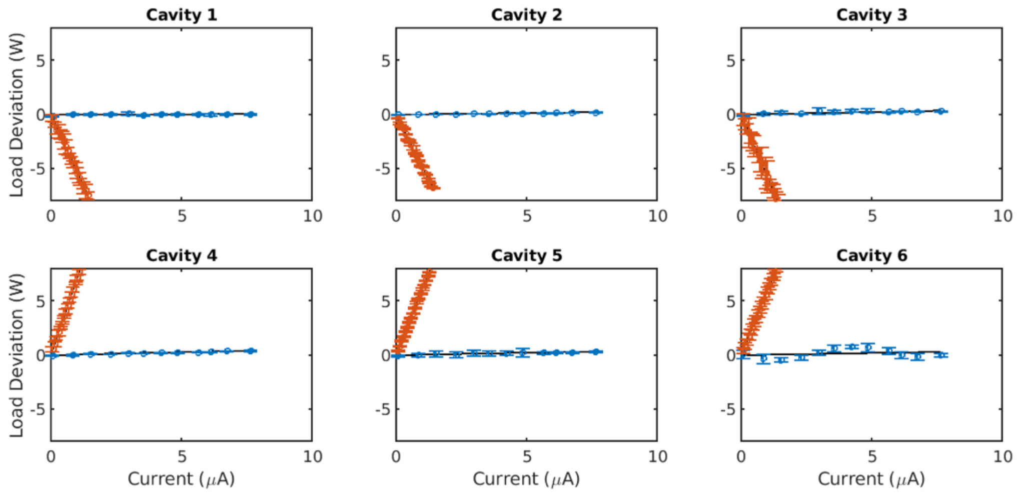

Figure 5: Beam loading as a function of injected current in the CBETA main linac cavities. The red data points represent a situation where cavities 4, 5 and 6 accelerated the beam while 1, 2 and 3 decelerated it. The blue points represent data collected during energy recovery operation.

CONCLUSION

ERLs produce high power bright CW beams while being very sensitive to time of flight deviations and beam losses in the return loop. This necessitates an unique set of minimal diagnostics combining requirements of high power CW beams in storage rings and precise phase space measurement of linac beams. Since ERLs operate as time of flight spectrometers, we need to measure the centroid of the beam both in space and time sometimes for multiple beams in the same pipe. At CBETA, we have developed both time and frequency domain approaches to obtain this information. Besides the centroid, measurement of the transverse and longitudinal distributions is important to match with various applications. Most methods use a dedicated diagnostic line with slits, deflector cavities and associated optics and may only be used in special diagnostic modes of the machine as in CBETA. Interferometric methods which detect synchrotron radiation and electro-optic methods which detect electric field generated by bunches are non-destructive techniques for longitudinal measurement. Scraping of the beam halo with the vacuum chamber generates unwanted radiation which can be detrimental in ERLs due to the very high currents involved. Measuring halo requires a device with high dynamic range which may be achieved by controlling exposure times on viewscreens as is done for CBETA or using intercepting wire monitors. While we can use beam current monitors to directly measure current loss, radiation monitors are crucial for machine protection and are employed in CBETA to protect its permanent magnets. Finally, cavities are also important diagnostic tools capable of measuring net transmission and diagnosing BBU.

ACKNOWLEDGEMENTS

We would like to thank David Burke, Yulin Li and Karl Smolenski for designing and managing the fabrication of the vacuum system including all diagnostic hardware components for CBETA. We want to acknowledge Ivan Bazarov for extensive help in setting up the injector diagnostic system. We would also like to highlight the contributions of Malida Hecht, who validated the design of our fast loss monitor system. CBETA is a collaboration between between CLASSE and Brookhaven National Laboratories, supported by the New York State Energy Research and Development Authority. CLASSE facilities are operated with major support from the National Science Foundation.

REFERENCES

[1] International Organizing Committee, ERL Workshop, "List of ERL worldwide facilities". `https://www.helmholtz-berlin.de/media/media/spezial/events/erl2019/erl-facilitysummary-january2018.xlsx`

[2] Koscica, Rosalyn *et al.*, "Energy and rf cavity phase symmetry enforcement in multiturn energy recovery linac models". *Phys. Rev. Accel. Beams*, 22, 091602, 2019. `doi:10.1103/PhysRevAccelBeams.22.091602`

[3] D. Douglas, "Beam physics issues encountered during the operation of CW SRF ERLs", presented at the Electron Ion Collider User Group Meeting (EIC 2014), Newport News, Virginia, USA, March 2014, unpublished.

[4] G. H. Hoffstaetter *et al.*, "CBETA, the 4-Turn ERL with SRF and Single Return Loop", in *Proc. 9th Int. Particle Accelerator Conf. (IPAC'18)*, Vancouver, Canada, Apr.-May 2018, pp. 635–639. `doi:10.18429/JACoW-IPAC2018-TUYGBE2`

[5] Inoue, Yoichi *et al.*, "Development of a high-resolution cavity-beam position monitor". *Phys. Rev. ST Accel. Beams*, 11, 062801, 2008. `doi:10.1103/PhysRevSTAB.11.062801`.

[6] W. Lou *et al.*, "The Beam Optics of the FFAG Cell of the CBETA ERL Accelerator", in *Proc. IPAC'18*, Vancouver, BC, Canada, Apr. 4,, pp. 3000–3003, `doi:10.18429/JACoW-IPAC2018-THPAF023`

[7] R.J. Michnoff, J. Dobbins, and R.L. Hulsart, "The CBETA Beam Position Monitor (BPM) System Design and Strategy for Measuring Multiple Simultaneous Beams in the Common Beam Pipe", in *Proc. IPAC'19*, Melbourne, Australia, May 2019, pp. 2736–2738, `doi:10.18429/JACoW-IPAC2019-WEPGW104`

[8] I. Bazarov, *et al.*, "Benchmarking of 3D space charge codes using direct phase space measurements from photoemission high voltage dc gun". *Phys. Rev. ST Accel. Beams*, 11, 100703, 2008. `doi:10.1103/PhysRevSTAB.11.100703`.

[9] V. Yakimenko, *et al.*, "Electron beam phase-space measurement using a high-precision tomography technique". *Phys. Rev. ST Accel. Beams*, 6, 122801, 2003. `doi:10.1103/PhysRevSTAB.6.122801`.

[10] S. Belomestnykh, *et al.*, "Deflecting cavity for beam diagnostics at Cornell ERL injector", Nucl. Instrum. Meth. A 614, no. 2, 179 (2010). `doi:10.1016/j.nima.2009.12.063`.

[11] E. Prat, *et al.*, "Emittance measurements and minimization at the SwissFEL Injector Test Facility". *Phys. Rev. ST Accel. Beams*, 17, 104401, 2014. `doi:10.1103/PhysRevSTAB.17.104401`.

[12] P. Evtushenko *et al.*, "Electron Beam Diagnostics of the JLab UV FEL", in *Proc. 24th Particle Accelerator Conf. (PAC'11)*, New York, NY, USA, Mar.-Apr. 2011, paper WEOCN4, pp. 1446–1448.

[13] P. Evtushenko *et al.*, "Bunch length measurements at the JLab FEL using coherent transition and synchrotron radiation", *AIP Conf. Proc.* 868, 193 (2006). `doi:10.1063/1.2401405`.

[14] X. Yang, *et al.*, "Electron bunch length monitors using spatially encoded electro-optical technique in an orthogonal configuration". *Appl. Phys. Lett.*, 95, 231106, 2009. `doi:10.1063/1.3266919`

[15] K. Wittenburg, "Beam Diagnostics for the Detection and Understanding of Beam Halo", in *Proc. 54th ICFA Advanced Beam Dynamics Workshop on High-Intensity and High-Brightness Hadron Beams (HB'14)*, East Lansing, MI, USA, Nov. 2014, paper TUO2AB03, pp. 183–186.

[16] A. Freyberger, "Large Dynamic Range Beam Profile Measurements", in *Proc. 7th European Workshop on Beam Diagnostics and Instrumentation for Particle Accelerators (DIPAC'05)*, Lyon, France, Jun. 2005, paper ITMM04, pp. 12-16.

[17] S. Seletskiy *et al.*, "Design and Commissioning Experience with State of the Art MPS for LEReC Accelerator", presented at the 63rd Advanced ICFA Beam Dynamics Workshop on Energy Recovery Linacs (ERL'19), Berlin, Germany, Sep. 2019, paper FRCOWBS02, this conference.

[18] D. R. Douglas *et al.*, "Experimental investigation of multibunch, multipass beam breakup in the Jefferson Laboratory Free Electron Laser Upgrade Driver". *Phys. Rev. ST Accel. Beams*, 9, 064403, 2006. `doi:10.1103/PhysRevSTAB.9.064403`.

BEAM DYNAMICS SIMULATIONS FOR THE TWOFOLD ERL MODE AT THE S-DALINAC*

F. Schließmann†, M. Arnold, M. Dutine, J. Pforr, N. Pietralla, M. Steinhorst
Institut für Kernphysik, Darmstadt, Germany

Abstract

The recirculating superconducting electron accelerator S-DALINAC at TU Darmstadt is capable to run as a onefold or twofold Energy Recovery Linac (ERL) with a maximum kinetic energy of approximately 34 or 68 MeV in ERL mode, respectively. The onefold ERL mode has already been demonstrated, the twofold ERL mode not yet. In conjunction with the first test phase of the twofold ERL mode, simulations have been performed to study the beam dynamics. Acceptance studies for individual beamline sections were carried out and the influence of phase slippage on the energy recovery efficiency during the entire acceleration/deceleration process was examined. The latter is crucial, since the maximum kinetic energy for the twofold ERL mode at injection is less than 8 MeV ($\beta < 0.9982$) while multi-cell cavities are used in the main accelerator that are designed for $\beta = 1$.

INTRODUCTION

The S-DALINAC at TU Darmstadt is a superconducting electron accelerator with a maximum energy gain of 130 MeV in conventional acceleration (CA) mode [1]. This energy gain is achieved by recirculating the beam three times in order to pass the main linac four times. The second of these recirculation beamlines houses a path length adjustment system (PLAS) that offers the possibility to change the phase of the beam relative to the accelerating cavities by up to 360° [2]. In this way, the S-DALINAC can be used as an Energy Recovery Linac (ERL) which requires a phase shift of roughly 180° [3]. By realizing such a phase shift, the electrons arrive at the cavities of the main linac at a time when a decelerating electric field is present. The electrons will then lose a part of their kinetic energy, which will be stored in the electromagnetic field in the cavities and can then be used to accelerate subsequent electrons. Due to the energy recovery, the acceleration process in the main linac exhibits a high power efficiency. In 2017, the onefold ERL mode was realized at the S-DALINAC [3,4]. In this case, the electron beam was accelerated once, recirculated and decelerated. The next step is to realize the twofold ERL mode, i.e. accelerating the electrons, recirculating, accelerating again, recirculating, decelerating, recirculating and decelerating a second time. Figure 1 shows the floor plan of the S-DALINAC and schemes for the onefold and twofold ERL mode. The maximum energy gain in the onefold or twofold ERL mode is 34 MeV or 68 MeV, respectively, instead of 130 MeV as in the CA mode. Linked with the first test phase of the twofold ERL mode, beam dynamics simulations have been performed using the *elegant* tracking code [5]. An acceptance study of the recirculation beamlines provides the shape of the maximum phase space which can be guided through the individual beamlines. Furthermore, the negative impact of phase slippage on the ERL efficiency was investigated, if one optimizes on the first linac transit using an on-crest acceleration.

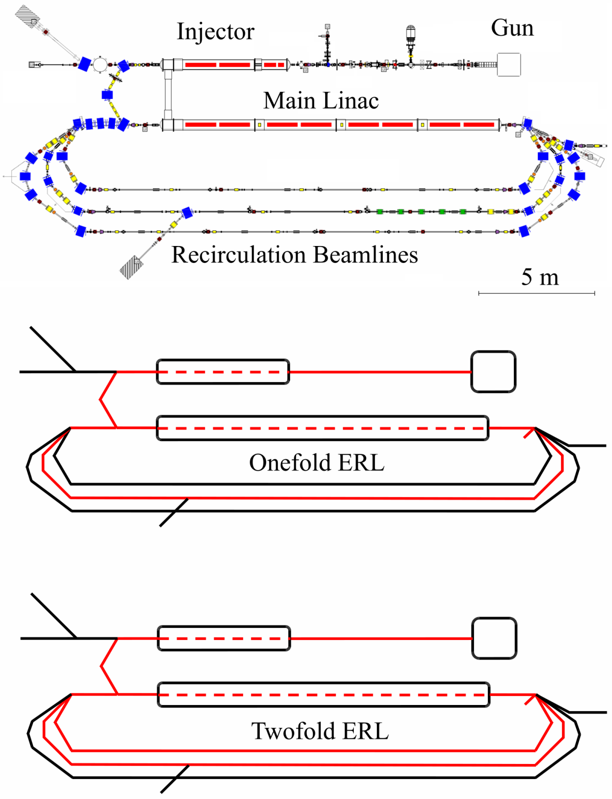

Figure 1: Floor plan of the S-DALINAC and schemes for the onefold and twofold ERL mode.

ACCEPTANCE STUDY OF THE FIRST RECIRCULATION BEAMLINE

In order to guide the beam without beam losses through the entire accelerator, it is important to know the acceptance of the beamlines. While an acceptance study of the entire accelerator is significantly influenced by the settings of all individual beam guiding devices, acceptance studies of several individual sections, which are examined independently, provide the necessary acceptance information to guide the

---

* Work supported by the BMBF through grant No. 05H18RDRB2 and by the DFG through GRK 2128.

† fschliessmann@ikp.tu-darmstadt.de

ISBN: 978-3-95450-217-2 doi:10.18429/JACoW-ERL2019-FRCOXBS03

Table 1: Target momenta and corresponding speed ratios at crucial locations during the acceleration/deceleration process at the first test phase of the twofold ERL mode.

	momentum p in MeV/c	**speed ratio** $\beta = v/c$
injection/extraction	3.85	0.991...
after 1st/3rd linac pass	19.25	0.9996...
after 2nd linac pass	34.65	0.9998...

beam step-by-step. The acceptance of an individual section is of high interest, if the beam could already be guided through all upstream-located sections.

Of crucial interest is the first recirculation beamline (FRB) since two beams will be guided through this beamline at the same time: the once accelerated and the once decelerated beam. Furthermore, this beamline has sections with narrow beampipe diameters where nonzero transverse dispersions exist. In order to investigate the acceptance of this beamline, electrons with deviations from the design particle have been tracked through the beamline. For the acceptance studies for every individual beamline, the tracking has been performed for deviations in the following quantities: transverse positions x and y, transverse divergences x' and y', momentum p and longitudinal position l relative to the design particle. For the FRB, a deviation of l is not relevant since it houses only beam guiding devices which are independent of the longitudinal position relative to the design particle. Of interest is not only the shape of the phase space with all the particles which can be guided through the section, but also the resulting quantities at the end of the section, depending on the initial deviations. Figure 2 shows two cross sections of the acceptance phase space of the FRB. The resulting divergence x' at the end of the FRB can be determined from the contour plot. In particular, the results show that small absolute values for the divergence at the end of the beamline result if the particle is within the acceptance, which is consistent to the possibility of subsequent beam guiding.

IMPACT OF PHASE SLIPPAGE

Relating to the ERL operation, it is of particular interest in which way the electron beam suffers from phase slippage, especially if the acceleration process is optimized on the first main linac transit using the on-crest acceleration, which is sufficient for the CA mode. Phase slippage is an issue because the electrons fly with low momenta (see Table 1) which leads to speeds which differ significantly from speed of light and since up to eight 20-cell cavities are used in the main accelerator that are designed for $\beta = 1$. Therefore, 6D beam dynamics simulations were performed in order to verify if a beam guiding is still possible in this case.

Figure 3 shows the resulting momenta due to the acceleration/deceleration process in the case that the main linac is optimized on the first transit using on-crest acceleration. As visualized in this figure, an asymmetric setting of energy

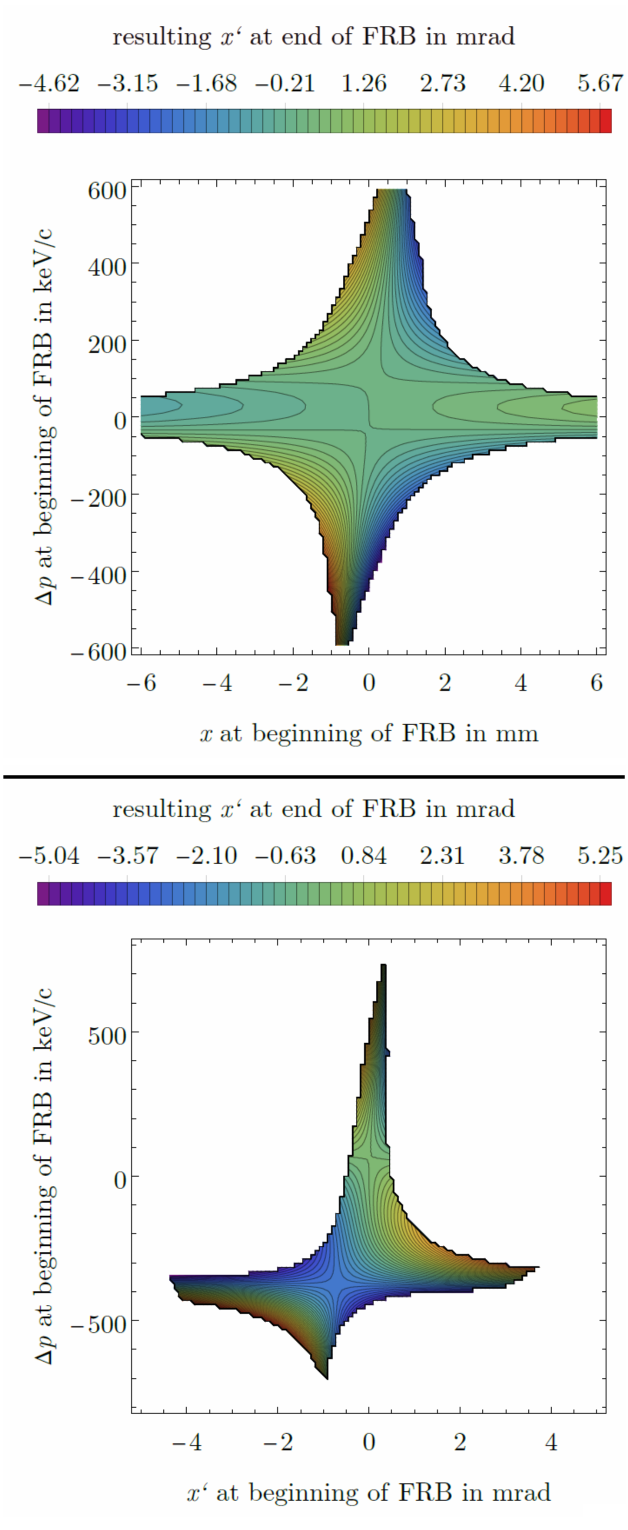

Figure 2: Two cross sections of the acceptance phase space of the first recirculation beamline (FRB). The variables are deviations at the beginning of the FRB, the values of the contour plot represent the resulting divergence x' at the end of the FRB.

ISBN: 978-3-95450-217-2 doi:10.18429/JACoW-ERL2019-FRCOXBS03

gradients was used for the simulations which is identical to the one used at the first test phase of the twofold ERL mode. The asymmetric setting of energy gradients had to be used due to several temporary restrictions and have led to the reduced target values for this test phase listed in Table 1. In the case of optimizing on the first transit using on-crest acceleration, only the PLAS of the FRB can be used to optimize on the second main linac transit. Due to the low momenta (see Table 1) the electrons suffer from phase slippage and the resulting momentum after the second main linac pass differs from the target value by -185 keV/c (-0.53 %) as visualized in Fig. 3. Using the PLAS of the second recirculation beamline (SRB) in order to optimize on the first deceleration process, a relaxation of the deviation from the target momentum can be achieved and the difference is only +7 keV/c (+0.04 %). Since the beam then has to travel again through the FRB, the beam passes the last main linac transit in such a way, that the electrons with low momentum (due to the first deceleration) suffer strongly from the phase slippage and can not be completely decelerated to injection momentum; the momentum of the final beam is +947 keV/c (+24.6 %) too large. Thus, there is an insufficient efficiency of the twofold ERL mode, if the beam is tuned as described.

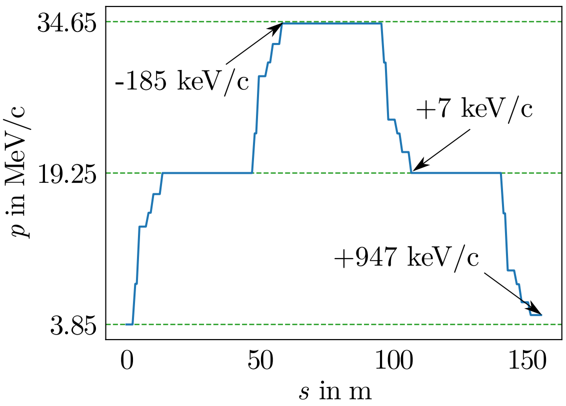

Figure 3: The acceleration/deceleration process is visualized for the case of a beam tracking with optimization on the first main linac transit, operating on-crest. The used energy gradients are identical to the ones used at the first test phase of the twofold ERL mode. Due to phase slippage, the acceleration/deceleration is not optimal for the subsequent main linac transits. The mentioned values are the deviations from the target momenta.

As visualized in Fig. 4, the beam can be guided four times through the main linac (twice accelerating, twice decelerating). That is, a twofold ERL mode is possible with an impaired efficiency, due to phase slippage caused by the low momenta (as shown in Fig. 3). Since the final momentum differs strongly from the injection momentum, which is also the necessary momentum to deposit the electrons in the intended dump, the particles will be lost in the last deflection section (see Fig. 4).

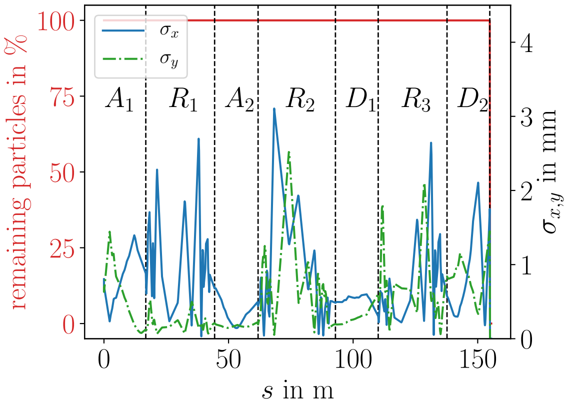

Figure 4: Beam losses and envelopes in the case of a beam tuning with optimization on the first main linac transit, operating on-crest. Highlighted sections: (A)cceleration, (R)ecirculation, (D)eceleration. Due to imperfect deceleration, the electrons can not be guided into the intended beam dump, but are lost during the last deflection due to beam rigidity.

The results expound that it is of crucial importance to optimize the entire acceleration/deceleration process in order to get a high efficiency. In particular, it shows that a suitable setting for the cavities' phases and amplitudes (resulting in off-crest acceleration/deceleration) as well as for the both PLAS have to be found.

CONCLUSION

In 2017, it was demonstrated that the S-DALINAC is capable to run in the onefold ERL mode. Currently, preparations are made to operate the S-DALINAC also in the twofold ERL mode. Acceptance studies have shown, what limits exist and what minimum requirements on the beam quality have to be fulfilled in order to guide the beam without losses through the machine in the twofold ERL mode. It was also examined whether a simplified beam tuning (optimization on first main linac transit, working on-crest) will lead to a successful twofold ERL operation. Although this mode is possible, an unsatisfactory recovery efficiency results and the electrons will not be dumped at the intended cup due to beam rigidity. Therefore, investigations on the optimization of the entire acceleration/deceleration process with the focus on high recovery efficiency and the control of phase slippage are currently performed.

REFERENCES

[1] N. Pietralla, "The Institute of Nuclear Physics at the TU Darmstadt", *Nuclear Physics News*, vol. 28, pp. 4–11, 2018. doi:10.1080/10619127.2018.1463013

[2] M. Arnold *et al.*, "First ERL Operation of S-DALINAC and Commissioning of a Path Length Adjustment System", in *Proc. 9th Int. Particle Accelerator Conf. (IPAC'18)*, Vancou-

ver, Canada, Apr.-May 2018, pp. 4859–4862. `doi:10.18429/JACoW-IPAC2018-THPML087`

[3] M. Arnold *et al.*, “ERL Mode of S-DALINAC: Design and Status”, in *Proc. 59th Advanced ICFA Beam Dynamics Workshop on Energy Recovery Linacs (ERL’17)*, Geneva, Switzerland, Jun. 2017, pp. 40–44. `doi:10.18429/JACoW-ERL2017-MOIDCC006`

[4] M. Arnold *et al.*, “First operation of the superconducting Darmstadt linear electron accelerator as an energy recovery linac”, submitted for publication.

[5] M. Borland, "elegant: A Flexible SDDS-Compliant Code for Accelerator Simulation," Advanced Photon Source LS-287, September 2000. `doi:10.2172/761286`

STATUS OF THE CONTROL SYSTEM FOR THE ENERGY RECOVERY LINAC bERLinPro AT HZB*

Thomas Birke†, Pablo Echevarria, Dan Eichel, Roland Fleischhauer, Ji-Gwang Hwang,
Guido Klemz, Roland Müller, Christoph Schröder, Ervis Suljoti, Andriy Ushakov
Helmholtz-Zentrum Berlin für Materialien und Energie GmbH, Berlin, Germany

Abstract

bERLinPro is an energy recovery linac (ERL) demonstrator project built at HZB. It features CW SRF technology for the low emittance, high brightness gun, the booster module and the recovery linac. Construction and civil engineering are mostly completed. Synchronized with device integration, the EPICS based control system is being set-up for testing, commissioning and finally operation. In the warm part of the accelerator, technology that is already operational at BESSY and MLS (e.g. CAN-bus and PLC/OPC UA) is used. New implementations like the machine protection system (MPS) and novel major subsystems (e.g. Low Level RF (LLRF), photo cathode laser) need to be integrated. The first RF transmitter has been tested and commissioned. For commissioning and operation of the facility the standard set of EPICS tools form the back-bone. A set of generic Python applications already developed at BESSY/MLS will be adapted to the specifics of bERLinPro. Scope and current project status are described in this paper.

INTRODUCTION

The goal of bERLinPro is the production of high current, high brightness, low emittance CW beams and to demonstrate energy recovery at unprecedented parameters [1]. The three stage acceleration consists of an SRF photo electron gun, an SRF booster linac with an extraction energy of 6.5 MeV and an SRF main linac module equipped with three 7-cell HOM damped cavities. All magnets and the vacuum system of the low energy injector and dump line are installed. Commissioning of the diagnostic line and the low energy part of the machine, i.e. gun / booster / linac replacement straight / dump line, the *banana* (see eponymous shape in Fig. 1) is planed for 2020,

bERLinPro is designed to show energy recovery for high current (100 mA) beams. The damping of higher order modes in the SRF linac is demanding and led to a new design of the HOM damping waveguids [2]. Availability of a proper linac module is critical.

The MESA project (Johannes Gutenberg Universität, Mainz, Germany) is planned for 1 % of the bERLinPro current, with a possible upgrade to 10 mA. For HOM-damping, the same technology as used at ELBE (HZDR) and XFEL (DESY) is in operation. Intermediate installation of the MESA linac module into bERLinPro allows to proceed towards recirculation with beam at 32 MeV and some mA at bERLinPro [3].

OPERATIONAL MODES

Unlike cERL and cBETA, bERLinPro features numerous different use cases. These comprise the photo-electron-source only, straight diagnostic beamline, *banana* path and recirculation with and without energy recovery (see Fig. 1). Available modes also differ in beam power, bunch charge, acceleration voltage and bunch train pattern as well as methods to increase beam current. All of these and the individual operation states of accelerating units, booster and linac modules will have immediate impact and consequences on a challenging set of soft- and hardware machine protection systems and set-ups.

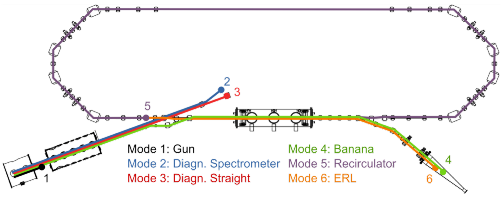

Figure 1: Basic bERLinPro layout and planned operation modes.

DEVICE INTEGRATION

The source part, consisting of an SRF photo electron gun, has already been set up in GunLab [4], where precision control of the laser guide system and the timing is presently in the works. With the beginning of installation in the bERLinPro bunker, integration of major functional blocks (e.g. laser) will be realized by remote control of 3rd party subsystems.

In March 2018 the first vacuum components for the *banana* path have been delivered, pumps and sensors are made available and are logged in the already running archiver [5] as they are installed. Similarly RF power conditioning and cryo system surveillance of cold compressors, warm vacuum pumps and the module feed boxes are well known and progress smoothly.

The various sub components of the booster and linac cryo modules are about to be addressed. At this point competing requirements for BESSY VSR [6] generate synergies, but also challenging working conditions.

IT-Infrastructure

Operator consoles as well as servers are strictly Linux-based. To be monitored and controlled, all relevant components need to be interfaced using an EPICS-I/O Controller (IOC) providing a Channel Access (CA) server.

---

* Work funded by BMBF and Land Berlin
† thomas.birke@helmholtz-berlin.de

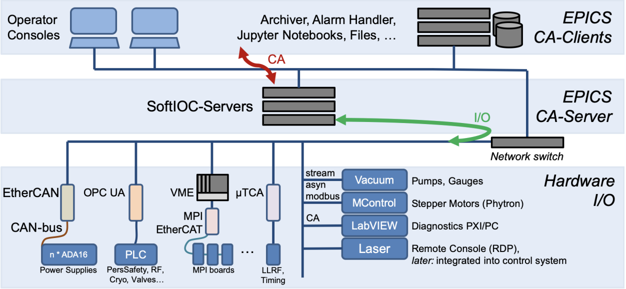

Figure 2: Simplified control-system structure.

Besides operator consoles and server-infrastructure (EPICS CA-client layer), all CA-servers run as SoftIOCs and perform their device-I/O via the control system network (see Fig. 2).

The network-connected I/O modules and variants differ by device-class or application.

Standard Components

Power Supplies of the beam guiding component are BESSY-standard, partly even re-used, so the control system integration follows the lines at BESSY and MLS. At the device-level, they are interfaced via ADA16 analog/digital I/O cards with an embedded controller and CAN-bus is used as a field-bus. A major difference to the setup at BESSY and MLS is, that, with the only exception of the MPS system, there are no VME-IOCs involved anymore. All CAN-I/O is performed through EtherCAN modules connected to the control system network.

PLC based systems RF systems as well as the cryo systems and the personnel safety system are all implemented using Siemens-PLCs. Communication with these systems is realized using OPC UA (OPC Unified Architecture). The SoftIOCs are communicating via the control system network to OPC UA servers that are either built into the PLC or realized as separate modules.

Vacuum System Vacuum gauges and ion getter pump power supplies are interfaced directly using serial I/O and Modbus. The various getter pumps are controlled by Cosylab microIOC - LOCO boards with actual ion getter pump currents converted to pressure equivalents.

All valves are controlled by Siemens PLCs and also interfaced via OPC UA. Switching outputs of gauges fire when configured limits of vacuum gauge readbacks are exceeded. They are connected to the PLC, which then closes surrounding valves and hence form a vacuum interlock system.

Stepper Motors All stepper motors (except of those at the SRF cavitiy tuners) are uniformly powered by Phytron motor controllers and controlled using the standard EPICS motor record.

TIMING SYSTEM AND TRIGGER DISTRIBUTION

RF Synchronization

Ultra low phase noise RF synchronization between the photocathode laser and LLRF subsystems is mandatory at bERLinPro, in order to provide stable electron bunches of variable length from 2 ps down to ~100 fs. Therefore RF generation was a challenging task with intensive effort to design and specify the best solution for bERLinPro master oscillator (MO).

Taking into consideration the shortest bunch length of ~100 fs, the arrival time jitter of the laser bunch through the approx. 35 m long transfer line into the photocathode SRF Gun and the phase stability better than 0.1 deg of the field in the SRF cavity required by the LLRF subsystem, a customized state of the art master oscillator unit has been developed by AXTAL GmbH [7] and commissioned in the timing laboratory. This 19 inch/1 U compact unit, featured with ULN OCXOs and SAW filter and delivers three phase coherent RF signals to the following subsystems:

- 10 MHz → diagnostics
- 50 MHz → laser control and diagnostics
- 1.3 GHz → RF systems, LLRF and laser

The last one is the most important frequency imposing the highest requirement in terms of phase noise and RMS jitter (0.1 deg ~ 200 fs, see Tab. 1).

Table 1: Measured Parameters of AXTAL Master Oscillator

Reference Signal	Short RMS Phase Jitter	Max RMS Phase Jitter	Integration Region
10 MHz	60 fs	70 fs	1 Hz~1 MHz
50 MHz	60 fs	70 fs	1 Hz~10 MHz
1.3 GHz	50 fs	60 fs	1 Hz~100 MHz

A network of Cellflex® 3/8” coax cables with an excellent phase drift stability of 1 ppm @ 25 °C [8], will distribute the RF signals through the facility. The longest link of about 40 m is the one from MO rack to the diagnostics patch panel. In order to cope with slow phase drift of the RF signals due to temperature change, coax cables have been distributed through thermally insulated pipes. A network of calibrated temperature and humidity measurementss based on OneWire sensors will be installed every 5 m along the coax cable pipes. A StreamDevice based EPICS device support has been already implemented for the OneWire to Ethernet Bridge and running already at BESSY on a SoftIOC (see Fig. 3). By knowing the temperature at each sensor, the exact distance between the temperature sensors and the phase drift characteristic of the coax cable, phase drift of the RF signals can be predicted [9] and fed into the LLRF control loop. Sensitive electronics such as the MO, LLRF-Controls and Laser-Controls will be installed in temperature stabilized racks.

Trigger Distribution

As bERLinPro is preparing the road to fulfillment of the high demanding requirements of BESSY VSR [6], doors have been opened also towards the evaluation of novel state of the art trigger distribution systems (TDS). The decision to build bERLinPro TDS on Micro Research Finland (MRF) [10] EVG/EVR-300 event products and µTCA was mainly because of three reasons: high scalabilty of the MRF TDS, which is a key issue at BESSY VSR, the elimination of the VME hardware platform due to high maintenance costs and the very mature EPICS device support provided by the EPICS community.

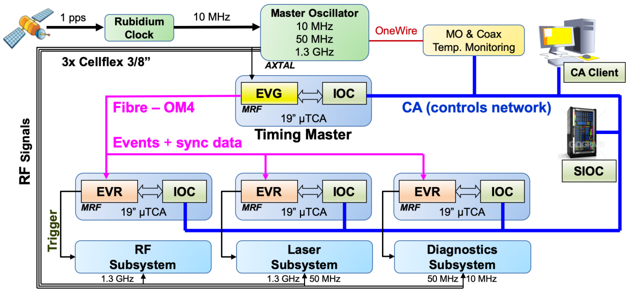

Figure 3: Schematic of timing system with master oscillator, RF distribution and trigger distribution system.

One master event generator (EVG) IOC will send trigger events at 125 MHz, clocks and data to three event receivers (EVR) IOCs through an OM4 optical fiber network in a tree topology (see Fig. 3). Through active delay compensation featured by MRF-300 series, slow phase drifts of the optical link due temperature changes are detected and compensated. Because of the three commissioning phases of bERLinPro (single bunch, burst and CW) and 6 operational modes, the trigger specification table is too complex to be shown and out of scope of this paper.

LOW LEVEL RF

For Low Level RF (LLRF) control, the same system developed and used at XFEL's gun (DESY), ELBE (HZDR) and MESA (JG|U) has been chosen [11] and a prototype installation has been set up with help of colleagues from DESY. Each LLRF system consists of a µTCA crate containing the following components:

1. A CPU running Ubuntu Linux providing the slow control algorithms and a communication layer translating the internal DOOCS controls into EPICS using ChimeraTK [12, 13] on a locally running SoftIOC
2. An FPGA board for amplitude and field control and
3. An FPGA board for tuner control (motors and piezos)

All six SRF cavities (1×gun, 3×booster and 2×linac) as well as the normal conducting transverse deflecting cavity in the diagnostics line will be supplied with these LLRF controllers.

Minor changes to the EPICS-IOC are being made to translate the DOOCS signal names into EPICS PV names that are compliant to the BESSY/HZB device naming convention. So far, only the amplitude and phase control servers are implemented and running on the µTCA based CPU, but in the near future, the tuners' motor control will be installed. Moreover, new firmware is currently being developed to control microphonics using a Kalman filter observer [14] and to detect quenches of the SRF cavities [15]. As a preliminary step to connect these two new features, µTCA Matlab and python bindings will be use to control them and connect them to the EPICS control system.

BEAM DIAGNOSTICS

In the recirculator of bERLinPro, various types of diagnostics have been developed in order to cover a wide range of operating modes in terms of bunch charge, repetition rate, and lateral as well as spatial distributions. Basically, there are fast and slow diagnostics - categorized according to the speed of data acquisition and data transfer. In the early commissioning phase with low beam-current, the slow detectors such as screen monitors and a synchrotron-light-based halo and profile monitor are most important. These diagnostics mainly use slow CCD cameras as data acquisition devices and LabVIEW for processing of the images. Processed data like internal gain, shutter speed and trigger mode of CCD camera as well as analysis results such as lateral size and center of mass will then be transmitted to the control system.

Since it is not allowed to insert any destructive monitors when the average beam current in the recirculator is higher than 50 µA, the status of the screen monitors is also monitored carefully as a part of machine protection system.

On the contrary, the fast diagnostics such as stripline beam position monitors (BPMs), Faraday-cups, DC- and Fast-current transformers (CTs) and beam loss monitor system are non-destructive devices. Particularly, the operable current of the stripline BPMs and CTs is higher than with the screen monitor. Therefore, it is necessary to put effort into optimizing the diagnostics system during early stages of the commissioning phase.

The analog processing unit for adjusting a signal magnitude suited for the digitizer is needed to control for covering a wide dynamic range with the requested resolution.

All diagnostic data acquisition is performed using LabVIEW systems (either PC- or PXI-based) operating independently and transferring processed data to the EPICS control system.

The diagnostics setups have been tested in the laboratory to examine the limitations of stability, resolution, and accuracy for different operation modes. The installation is now underway in the bERLinPro bunker.

PERSONNEL SAFETY AND RADIATION PROTECTION SYSTEM

The personnel safety system is based on Siemens safety PLCs according to all relevant machinery safety regulations of the EU. It consists of a master-PLC and 4 decentralized I/O-blocks with ~250 I/O-points. The PLCs are communicating via dedicated Ethernet/Profibus lines.

The connection to the EPICS control system is realized using a OPC UA-Client on a Linux-SoftIOC communicating with an OPC UA-server built into the master-PLC.

The installation of sensors and hardware has been finished. Tests and commissioning of the personnel safety system is currently in process with ~70% finished. A final acceptance test is planned for the end of 2019.

The same PLC-based technology is also used for the laser-interlock to prevent laser operation if any of the preconditions is violated. Shutters at the laser-hutch as well as at the photocathode-gun are closed and locked if areas are in a possibly insecure state. Hutch-doors are monitored and locked and warning-signs are controlled.

Next steps are to connect further RF-transmitters as well as the air conditioning system to the personnel safety system.

MACHINE PROTECTION SYSTEM

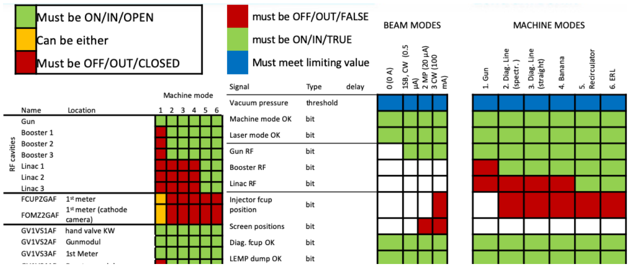

🟩 Must be ON/IN/OPEN
🟨 Can be either
🟥 Must be OFF/OUT/CLOSED

	Name	Location	Machine mode 1	2	3	4	5	6
RF cavities	Gun		🟩	🟩	🟩	🟩	🟩	🟩
	Booster 1		🟥	🟩	🟩	🟩	🟩	🟩
	Booster 2		🟥	🟩	🟩	🟩	🟩	🟩
	Booster 3		🟥	🟩	🟩	🟩	🟩	🟩
	Linac 1		🟥	🟥	🟥	🟥	🟩	🟩
	Linac 2		🟥	🟥	🟥	🟥	🟩	🟩
	Linac 3		🟥	🟥	🟥	🟥	🟩	🟩
	FCUPZGAF	1st meter	🟨	🟥	🟥	🟥	🟥	🟥
	FOMZ2GAF	1st meter (cathode camera)	🟨	🟥	🟥	🟥	🟥	🟥
	GV1VS1AF	hand valve KW	🟩	🟩	🟩	🟩	🟩	🟩
	GV1VS2AF	Gunmodul	🟩	🟩	🟩	🟩	🟩	🟩
	GV1VS3AF	1st Meter	🟩	🟩	🟩	🟩	🟩	🟩

🟥 must be OFF/OUT/FALSE
🟩 must be ON/IN/TRUE
🟦 Must meet limiting value

			BEAM MODES				MACHINE MODES					
Signal	Type	delay	0 (0 A)	1SB, CW (0.5 µA)	2 MP (20 µA)	3 CW (100 mA)	1. Gun	2. Diag. Line (spectr.)	3. Diag. Line (straight)	4. Banana	5. Recirculator	6. ERL
Vacuum pressure	threshold		🟦	🟦	🟦	🟦	🟦	🟦	🟦	🟦	🟦	🟦
Machine mode OK	bit		🟩	🟩	🟩	🟩	🟩	🟩	🟩	🟩	🟩	🟩
Laser mode OK	bit		🟩	🟩	🟩	🟩	🟩	🟩	🟩	🟩	🟩	🟩
Gun RF	bit			🟩	🟩	🟩	🟩	🟩	🟩	🟩	🟩	🟩
Booster RF	bit						🟥	🟩	🟩	🟩	🟩	🟩
Linac RF	bit						🟥	🟥	🟥	🟥	🟩	🟩
Injector fcup position	bit					🟥		🟥	🟥	🟥	🟥	🟥
Screen positions	bit				🟥	🟥						
Diag. fcup OK	bit		🟩	🟩	🟩	🟩	🟩	🟩	🟩	🟩	🟩	🟩
LEMP dump OK	bit		🟩	🟩	🟩	🟩	🟩	🟩	🟩	🟩	🟩	🟩

Figure 4: Snippet of table of various operation conditions and constraints.

The machine protections system (MPS) is needed to ensure safe non-destructive operation of the machine in the different operation modes (see Fig. 1 and 4). Beam may only be extracted from the cathode if all necessary conditions are met and further extractions have to be prevented within 1 µs if any condition is violated.

To achive this, an EtherCAT based system of EtherCAT master, MPS-mainboards and MPS-I/O-boards (the latter two forming an MPS Unit) has been developed. Core components of the MPS are shown in Fig. 5:

EtherCAT Master

The EtherCAT Master is the single controlling instance of the MPS. It is connected via streamdevice socket-I/O to an EPICS SoftIOC that reflects current state and allows for switching operation modes. The EtherCAT Master distributes configurations and active mode via EtherCAT to the connected MPS Mainboard. Activation of a new mode on all boards is achieved within.

MPS Mainboard

An MPS Mainboard is the FPGA board evaluating the programmed logic. It processes all MPS-inputs, drives the MPS-outputs and is programmed over the EtherCAT line. Current status of this MPS Unit is also posted to the EtherCAT Master and communicated to the EPICS control system.

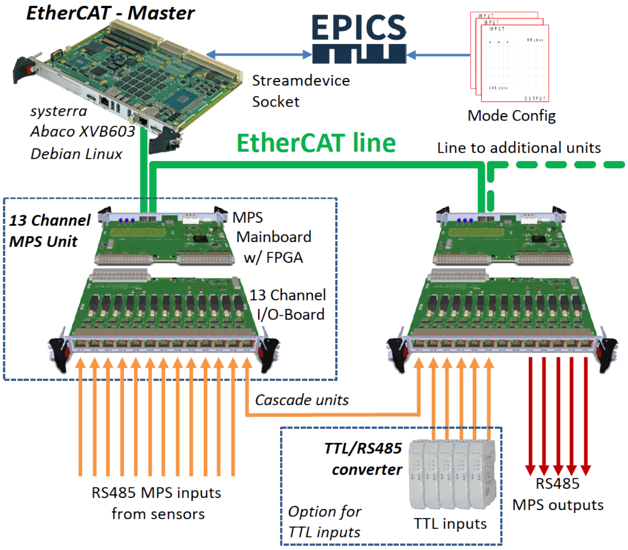

Figure 5: Machine Protection System core components.

13 Channel MPS I/O Board

converts from/to up to 13 RS485 input or output signals. A complete cycle (input conversion, FPGA processing and output conversion) takes ~120 ns. The I/O Board is equipped with reliable RS485 line-break detection to properly ensure safe operation.

MPS Units may be cascaded to form a hierarchical MPS with a maximum of 65535 MPS Mainboards (limited only by 16-bit IDs with ID=0 being a special case).

Inputs or outputs can optionally be equipped with TTL↔RS485 converters, if applicable.

For bERLinPro, the reaction time of the complete MPS including signal delays due to cable lengths, RS485↔TTL conversions, cascading and FPGA processing time can be assured to be well below the required 5 µs.

PHOTOINJECTOR LASER AND LASER BEAM TRANSFER LINE

The laser for operation of the RF-photoinjector has been developed and will also be installed by the Max-Born-Institute (MBI). In the end it will be fully embedded into the accelerator infrastructure and therefore be controlled by the machine control system and EPICS. This includes a concept by MBI for tight synchronicity with the RF-master oscillator already proven at accelerators of XFEL and ELBE. In addition, precautions are made to account for a slow phase drift between the RF-field in the gun-cavity and the arrival time of a laser pulse which might have accumulated along the path of the rf-waveguides and the approx. 35 m long laser beam transfer line.

The laser beam is transferred to the photo injector via an imaging system to counteract diffractive broadening and distortion. A substantial fraction of this transfer line is contained in a vacuum tube including bending mirrors and two piezomotor-driven remote controlled lenses with closed-loop linear alignment along three orthogonal axes. These are commercial systems controlled and monitored by EPICS.

The entire transfer line allows for control of laser beam spot size, -position, -position stability and the generated bunch charge at the photo-cathode and its according diagnostic.

Stepper- and servo motors will be used as actuators for mirrors, lenses and irides. End-switches, several CCD-cameras along the laser beam path and special devices for measuring laser pulse duration and pulse energy represent the main detectors.

It will be managed by one GUI displaying a summary of the laser parameters at the photo-cathode. From here further GUI's dedicated to individual parameters of the transfer line and the laserspot can be opened.

OPERATION PROGRAMS

The toolset that is standard for EPICS environments at HZB is easily adapted as the project proceeds. I.e. engineering screens become available as the device integration is deployed, data monitoring is well covered by the EPICS Archiver Appliance and alarm handling is realized with *alh* while alarm-logs will be accessible via the elastic stack. At a later point, the aging motif based alarm-handler *alh* will be superseded by the CSS/phoebus alarm-server.

Program launchpad and machine operation parameter save/restore/compare are already adapted from the BESSY instances and is extended with ongoing installation and commissioning of components.

BERLinPro is not planned as a user-facility and hence is not operated by the BESSY/MLS operator crew. The main ”users” of the bERLinPro control-room will be scientists and engineers commissioning the machine and pursuing new goals in accelerator physics. Therefor, the typical routine tasks performed at a production user facility are not applicable to bERLinPro.

Novel Developments from the Community

For controls and applications, this is a unique chance to evaluate and establish newer tools and techniques like

EPICS version 7 - a major upgrade to the EPICS version 3 control system suite currently in use at BESSY and MLS. After several years of development, the most recent development branch of EPICS V3 and the new development (used to be named EPICS V4) merged into what is now named EPICS 7. The new communication protocol *pvAccess* together with the underlying *pvDatabase* or any other 3rd party service layer, enables the transition from a controls framework to a physics framework [16].

CSS/phoebus is following the paradigm of the eclipse-based Control System Studio [17] but with a streamlined lightweight implementation. CSS/phoebus [18] will, once integrated into the operator environment, provide operator displays, alarm monitoring and retrieval and plotting of archived as well as live data.

PyDM, caQtDm, ... For day one, all operator displays will be created with the same tools that have already been in use at BESSY and MLS for many years. Since the aging display managers *dm2k* and *edm* are both well established, they are nevertheless based on outdated software environments and not easily portable to other system platforms. Establishing a replacement display manager like PyDM or caQtDm requires a transition in user experience as well as deployment strategy and hence takes time and will be started when bERLinPro has entered the commissioning phase.

Commissioning Software Environment

Commissioning will further be supported by several scripting environments (MATLAB, Jupyter notebook, etc.) as well as by a number of software stacks (Bluesky/ophyd [19], ocelot, transitions...) to provide a uniform testbed and production environment for developers and scientists.

Simulation programs (elegant, OPAL) get their configuration files from a reference database. In a later phase the project will certainly benefit from the OPAL capabilities to describe space charge effects and take advantage of machine learning procedures [20].

To loosen potential dependencies to and/or conflicts within the operating system environment of the operator consoles, all these supported application will be deployed in dedicated software ans OS environments using Singularity [21] containers.

SUMMARY

Setting up bERLinPro as a test facility has numerous consequences for controls. It has to be very flexible and easy to adapt. Temporary units like the MESA LINAC module or components on development path like the SRF gun variants are demanding w.r.t. timely installation and replacement.

On the other hand requirements to availability, reliability and maintainability of the controls installation are relaxed compared to a light source in production. Software tools and automation inventory need not to be operator ready.

These relaxed requirements open the possibility to also experiment with novel software and establish new systems that, at a later time, could also broaden and renovate the control room computing environment at BESSY and MLS.

ACKNOWLEDGEMENTS

Thanks to the bERLinPro team, the accelerator controls groups and all other HZB staff and external colleagues, that helped realizing this project.

REFERENCES

[1] M. Abo-Bakr *et al.*, "Status Report of the Berlin Energy Recovery Linac Project BERLinPro", in *Proc. IPAC'18*, Vancouver, Canada, Apr.-May 2018, `doi:10.18429/JACoW-IPAC2018-THPMF034`

[2] A. Neumann *et al.*, "Final Design for the bERLinPro Main Linac Cavity", in *Proc. LINAC'14*, Geneva, Switzerland, 2014. paper:MOPP070

[3] W. Anders *et al.*, "Incorporation of a MESA Linac Module into bERLinPro", in *Proc. IPAC'19*, Melbourne, Australia, `doi:10.18429/JACoW-IPAC2019-TUPGW023`

[4] Gun Cavity & Module Development / GunLab & Photocathode Development @ HZB, `https://www.helmholtz-berlin.de/projects/berlinpro/bpro-groups/gun_en.html`

[5] T. Birke, "EPICS Archiver Appliance - Installation and Use at BESSY/HZB", in *Proc. ICALEPCS'19*, New York, NY, USA. paper:WEPHA014

[6] A. Jankowiak *et al.*, eds., "BESSY VSR – Technical Design Study", Helmholtz-Zentrum Berlin für Materialien und Energie GmbH, Germany, June 2015, `doi:10.5442/R0001`

[7] Advanced XTAL Products, `https://www.axtal.com/cms/iwebs/download.aspx?id=113581`

[8] K. Czuba, D. Sikora, "Temperature Stability of Coaxial Cables". Acta Physica Polonica A. 119. `doi:10.12693/APhysPolA.119.553`

[9] S. Simrock Stefan *et al.*, "Performance of the new master oscillator and phase reference system at FLASH", in *Proc. PAC2007*, Albuquerque, New Mexico, USA, 2007. `doi:10.1109/PAC.2007.4440154`

[10] Micro-Research Finland Oy, `http://www.mrf.fi/`

[11] P. Echevarria *et al.*, "First LLRF Tests of BERLinPro Gun Cavity Prototype", in *Proc. IPAC'16*, Busan, Korea, May 2016, `doi:10.18429/JACoW-IPAC2016-TUPOW035`

[12] Chimera TK Github, `https://github.com/ChimeraTK/`

[13] M. Killenberg *et al.*, "Abstracted Hardware and Middleware Access in Control Applications", in *Proc. ICALEPCS2017*, Barcelona, Spain, 2017. `doi:10.18429/JACoW-ICALEPCS2017-TUPHA178`

[14] A. Ushakov, P. Echevarria, A. Neumann, "Developing Kalman Filter Based Detuning Control with a Digital SRF CW Cavity Simulator", in *Proc. IPAC'18*, Vancouver, BC, Canada, 2018. `doi:10.18429/JACoW-IPAC2018-WEPAK012`

[15] P. Echevarria *et al.*, "Simulation of Quench Detection Algorithms for Helmholtz Zentrum Berlin SRF Cavities", in *Proc. IPAC'19*, Melbourne, Australia, May 2019. `doi:10.18429/JACoW-IPAC2019-WEPRB016`

[16] G. White, *et al.*, "The EPICS Software Framefork Moves from Controls to Physics", in *Proc. IPAC'19*, Melbourne, Australia, `doi:10.18429//JACoW-IPAC-2019-TUZZPLM3`

[17] Control System Studio, `http://controlsystemstudio.org/`

[18] "Phoebus" - the lastet update of Control System Studio (CS-Studio), `https://controlssoftware.sns.ornl.gov/css_phoebus/`

[19] Bluesky Data Collection Framework and Ophyd Device Abstraction, `http://nsls-ii.github.io/bluesky/`, `https://nsls-ii.github.io/ophyd/`

[20] L. Vera Ramirez *et al.*, "Adding Machine Learning to the Analysis and Optimization Toolsets at the Lightsource BESSY II", in *Proc. ICALEPCS'19*, New York, USA, 2019. paper:TUCPL01

[21] Singularity - A secure, single-file based container format, `https://sylabs.io/`

ISBN: 978-3-95450-217-2 doi:10.18429/JACoW-ERL2019-FRCOXBS05

ADJUSTING bERLinPro OPTICS TO COMMISSIONING NEEDS*

B. Kuske†, M. McAteer, Helmholtz-Zentrum für Materialien und Energie, Berlin, Germany

Abstract

bERLinPro is an Energy Recovery Linac (ERL) project being set up at HZB, Berlin. During the turn of the project, many adaptations of the optics to changing hardware realities and new challenges were necessary. Exemplary topics are chosen for each of the three different machine parts: the diagnostics line, the Banana and the recirculator. In the diagnostics line, the need to seek a quick understanding of the machine during commissioning and the low energy are the central concern. In the Banana, unwanted beam will dominate the performance. Commissioning of the recirculator will be realized with the super-conducting linac module fabricated for the Mainz ERL project MESA, as the bERLinPro linac is delayed. The Mainz linac will supply 60 % of the energy planned. While the adopted optics shows similar parameters as the original 50 MeV optics, studies of longitudinal space charge and coherent synchrotron radiation show that the lower energy leads to large emittance blow up due to micro bunching and CSR effects.

INTRODUCTION

bERLinPro is an Energy Recovery Linac project close to completion at HZB, Berlin, Germany, [1]. It is intended as an experiment in accelerator physics, to pioneer the production of high current, low emittance beams in a fully super-conducting accelerator, including SRF gun, booster and linac. The machine, with a length of roughly 80 m consists of three different independent sub-parts: the diagnostics line, straight forward from the SRF gun and booster; the low energy part, including injector, merger, linac straight, splitter and dump line. This is called the Banana. In presence of a linac module, the beam would run through the recirculator and be energy recovered before being led to the dump line, Fig. 1. Over the turn of the project different boundary conditions asked for optics adjustments and new challenges had to be met. The paper describes examples of this work for each machine part.

DIAGNOSTICS LINE

The diagnostics line consists of the 1.3 GHz, 1.4 cell, single cavity SRF gun, providing up to 3 MeV electrons with a design bunch charge of 77 pC. The gun module also hosts two corrector coils (H/V) and a cold solenoid. The booster, hosting three two-cell cavities can boost the energy up to 6.5 MeV. The first cavity imprints a chirp on the bunch for velocity bunching, while the other two cavities are run on crest for acceleration. Further elements are 6 quadrupoles, a transverse deflecting cavity, a spectrometer followed by a 300 W Faraday cup, or, straight ahead, a 35 kW beam dump, Fig. 2.

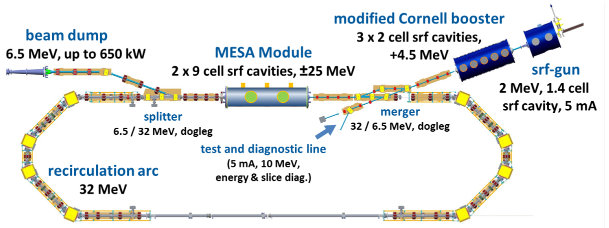

Figure 1: Layout of bERLinPro with the diagnostics line in straight continuation of the gun, the low energy part (Banana) from gun to dump, and the recirculator with the MESA module.

Optics were developed including the booster (6.5 MeV) and with three booster replacement quadrupoles (taken from the recirculator) and 2.7 MeV. Four beam position monitors (BPM) and two screens (FOM) are available for diagnostics. Two laser systems are available: a 50 MHz laser providing single bunches at frequencies between 1 Hz and 100 kHz, corresponding to 77 pA to 8 µA, or up to 4 mA cw; and a 1.3 GHz laser providing macro pulses from 1 Hz to 1 kHz, 6 nA to 20 µA, or up to 100 mA cw.

As any linear accelerator, an ERL is an initial value problem: without exact knowledge of the initial parameters of the beam, a later understanding and characterization of the beam parameters is difficult. Therefore, a thorough understanding of the gun is indispensable. The gun enables the low emittance and the stability of the complete machine due to the laser- and RF stability and the synchronization between the two. Most of the unwanted beam, from laser effects to field emission at 30 MV/m will originate in the gun and the machine up time is determined by the cathode life time. Finally, the goal of producing 100 mA is achieved in the gun (although with a second version, utilizing high power couplers).

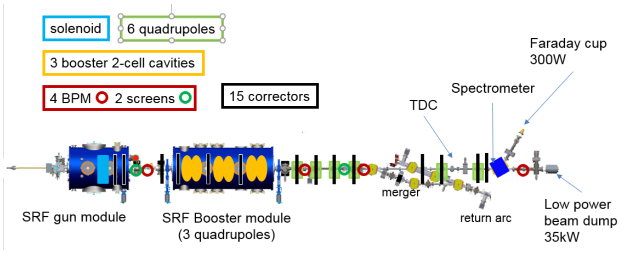

Figure 2: Diagnostics line: Intended for the characterization of gun and booster and initial beam parameters.

Before the gun is assembled and tested, many ambiguities arise, starting from the actual energy of the beam, over the bunch parameters, to the system parameters leading to successful acceleration. It is intended to use machine learning

---

* Work supported by German Bundesministerium für Bildung und Forschung, Land Berlin and grants of the Helmholtz Association

† bettina.kuske@helmholtz-berlin.de

or statistical learning to ease commissioning, see [2]. In addition, the number of independent parameters necessary to thread the beam successfully through the diagnostics line, should be minimized. Using the samples (tracking results of the diagnostics line for different machine parameters) produced for the machine learning attempts, dependencies can be identified via 'data mining'. Fig. 3 shows the example of the solenoid field setting, that leads to a comparable beam transport through the diagnostics line (black dots). It can be derived from the maximal gun field on axis and the cathode position (yellow surface). Here, cathode position '0' refers to no cathode retraction and position '6' means a recess of 2.5 mm.

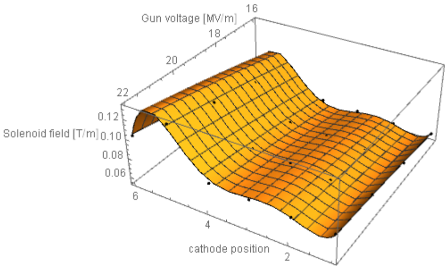

Figure 3: The solenoid field adequate to transport the beam through the beam line can be expressed as a function of cathode position and gun field.

Another option is to define the quadrupole settings, as to produce round beams on the screens for easier detection. For low currents, where the bunch is not space charge dominated, the set values can be simply scaled with energy.

Low energy beam

Analytic estimations of the influence of the earth magnetic field on the low energy beam from the gun indicate, that the trajectory might be influenced by external magnetic fields. Therefore, the magnetic field has been measured prior to the installation of magnets and girders in the subterranean hall. A 3D Hall-probe, installed on a small wagon at beam height, was moved along the future path of the electrons. The result is shown in Fig. 4. The strong, and strongly varying, vertical field (blue dots) of up to ± 1 G is caused by the reinforcement iron in floor and ceiling of the hall. The total height of the hall is only 3 m and the beam height is 1.2 m. Due to the larger distance from the side walls of the hall, the horizontal field is relatively stable between 0.2 G and 0.4 G. The step function indicates the realization of the field in the tracking code OPAL, [3]. After the installation of the girders and the lower half of the magnets, strong local magnetization was observed, partly due to remanent fields in the half-magnets, but also in the iron girders. After the completion of the installation and cycling of the magnets a third measurement will be carried out.

When the measured magnetic field was included in tracking studies, the beam got lost at the vacuum aperture 7 m behind the cathode. For comparison, no particle loss was detected during extensive error studies performed for the complete machine, [4], [5]. Trajectory corrections using singular value decomposition of the response matrix revealed, that although more than sufficient corrector magnets are installed (except for inside the booster), we run short of BPMs in the diagnostic line, as well as in the Banana. As a consequence of these investigations, corrector coils are now also included in the booster module. Residual trajectory offsets of up to 7 mm in the horizontal plane remain after correction. Workarounds including beam based alignment, or the usage of calibrated response matrices, including the optics as well as the magnetic fields, have to be used to establish better corrections.

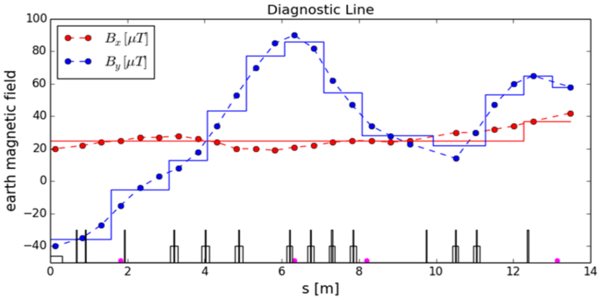

Figure 4: The magnetic field measured along the electron path in the diagnostics line, prior to the installation of magnets and girders.

BANANA

In the low energy section of the machine, the 'Banana', the beam, after acceleration in the booster, passes through the merger chicane, through the straight section with three quadrupoles replacing the linac, and is then deflected into the dump line to the 650 kW beam dump, see Fig. 5. A single collimator is located in the merger at highest dispersion. In the Banana, the merger optics, the emittance compensation scheme, and the bunch compression will be verified. Halo studies can be performed.

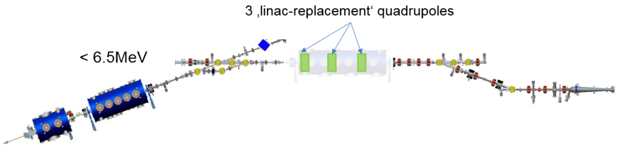

Figure 5: The layout of the low energy part of the machine (without linac).

It is expected that, for the operation of high current ERLs, the limit for beam halo at the entrance to the linac is in the order of 10^{-7} to 10^{-8} A thorough understanding of sources of unwanted beam is therefore indispensable, so intense studies of 'unwanted beam' have been performed for the injector [6].

There are two major sources of unwanted beam: field emission from cavity and cathode surfaces, and laser-related effects. The magnitude of each source is installation-dependent and only quantifiable after the start of operation. Predictions of possible transport of unwanted beam are based on Astra tracking studies.

Laser-related effects

The longitudinal tails of the laser pulse, transverse tails due to diffraction at the window where the laser pulse enters the cryomodule, and stray light that scatters off of imperfections in mirrors in the laser transport system all generate unwanted beam. Much of the beam from the longitudinal tails of the laser pulse can be collimated in the merger. The beam from transverse tails of the laser pulse will mostly pass through the merger and contribute to beam halo. About 20% of the electrons from stray light on the cathode (modeled as a uniform distribution in space and time of photons hitting the cathode) will have the correct energy to pass through the merger, and so will contribute to beam halo in the Banana or linac.

In addition, when operating in single-bunch or pulsed mode, there will be ”ghost bunches” (low-charge electron bunches from incompletely-blocked laser pulses) between the full-charge electron bunches. The design extinction ratio for blocked laser pulses is 10^{-8}, but achieving that level of extinction is challenging and higher extinction ratio in the real machine is possible. These bunches will have different beam dynamics from full-charge bunches due to the reduced space charge effects. They will be critical in diagnostic mode, especially when the single-bunch rep rate is low, where they might spoil bunch measurements.

Field emission

The effects of ”dark current” from field emission were studied in Astra tracking simulations. The simulations assumed a uniform distribution of emitters on the surface of the gun and booster cavies, on the cathode surface, and around the edge of the cathode plug.

Of the field emission electrons from the cathode and plug, most are lost on the aperture in the injector and merger. 5-10% of emitted electrons travel back to strike the cathode surface, which may reduce cathode lifetime. Several percent pass through the merger.

Of the electrons emitted from the gun cavity surface, the vast majority is lost within the cavity. A few percent strike the cathode surface, and a very small amount (around one permil) passes through the merger.

Of the electrons emitted from the booster surface, the vast majority is lost within the cavities or within the booster cryomodule. A very small amount (a couple permil) travels upstream to strike the cathode. Electrons that escape the cryomodule travelling downstream are lost in the merger.

RECIRCULATOR

The bERLinPro recirculator consists of two 180 ° arcs with four 45 ° rectangular dipoles each. The two central dipoles and the central quadrupole in each arc are moveable to enable path length adaptions. Two dipole chicanes, merger and splitter, compensate for the kick necessary to deflect the low energy beam onto the linac axes and into the dump. The linac straight has a free length of 5.8 m.

The bERLinPro linac, Fig. 6, is planned with three five-cell cavities and elaborate wave guide HOM absorbers for high currents. It can boost the energy to 50 MeV. Due to the prioritization of a competing project at HZB, BESSY-VSR, the production of the linac had to be postponed.

The ERL project MESA, at the Mainz University, has the opposite problem: the linac module is delivered, but the civil construction plans had to be altered, and no building will be available to host the machine before 2022. A collaboration between the two projects has been established, that consists of testing the MESA module with beam at bERLinPro, [7]. The MESA module, Fig. 7, hosts two nine-cell Tesla-type cavities. It is shorter than the bERLinPro module and capable to boost the energy to 30 MeV. The MESA project suffices with low currents so the HOM dampers consist of a notch-filter and a coupling antenna. HOMs will probably limit the current when running the module in bERLinPro to a few mA. The changes necessary in bERLinPro to host the MESA linac module have been described in detail in [7]. Geometrical differences were the different length and beam height. Technical differences like the He-supply from the side, as opposed to the top (MESA), or the cooling with

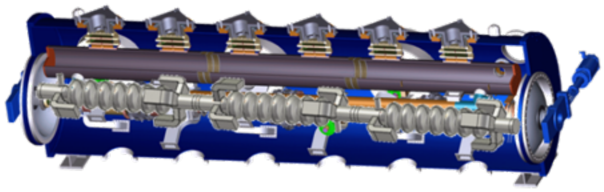

Figure 6: The layout of the bERLinPro linac module with elaborate wave guide HOM absorbers.

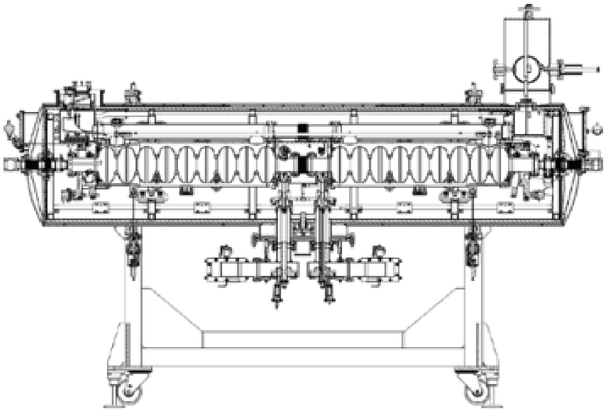

Figure 7: The layout of the MESA linac module with two Tesla-type cavities.

liquid nitrogen, not foreseen for bERLinPro, are manageable. The path length changes by 7.7 mm due to the lower energy, lies just within the range of the path length adaption of bERLinPro. The larger beam offset in the merger and splitter chicane of 55 mm lies well within the aperture of 80 mm. Two effects have to be accounted for, when adjusting the optics to the lower energy: the reduced RF focusing of the MESA linac due to the lower peak field of 23 MV/m on axis (compared to 35 MV/m) and the enhanced focusing of the chicane dipoles, where the dipole field is set by the injection/dump energy, but the edge focusing is determined by the energy of the accelerated beams. Both could be compensated by linear retuning of the standard bERLinPro optics. The bERLinPro project goal parameters, mainly the emittance of well below $1 \times 10^{-6}\,\pi$ mm mrad and the bunch length of 2 ps in the straight section, could be reached also with the MESA linac, without adjusting the emittance compensation scheme, the sextupole configuration or the chirp imprinted in the linac cavities, Fig. 8. Differences do arise though, as the optics is now space charge dominated from cathode to dump, and micro bunching and coherent synchrotron radiation (CSR) effects dominate the emittance.

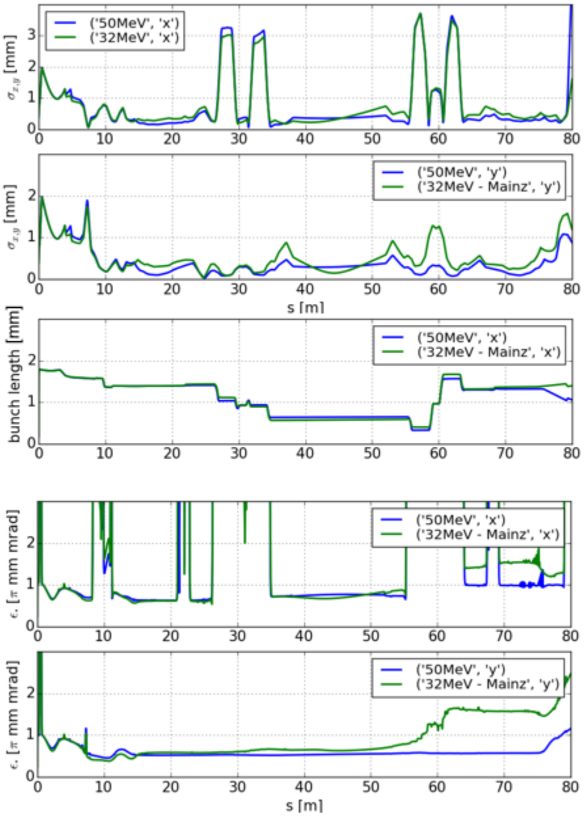

Figure 8: The optics for both linacs achieve the bERLinPro project goals in the straight section.

Micro bunching and CSR effects

Micro bunching structures can occur on the longitudinal current distribution. First, shot noise from the cathode laser leads to density modulations in the particle distribution. In combination with space charge forces these density modulations are transferred to energy modulations, which, in combination with R56, turn into micro bunching structures or might also be diluted. The bunching factor is defined as the Fourier transform of the current distribution, and given by

$$b(\lambda) = \frac{1}{Nec} \int I(z) e^{\frac{-i2\pi z}{\lambda}} dz; \tag{1}$$

Fig. 9 shows the longitudinal phase space for the bERLinPro optics (left) and the optics with the MESA linac (right) at the beginning of the straight section. The enhanced energy modulations in the MESA case are clearly visible. Fig. 10 shows the according bunching factor of both bunches. There is a 50 to 100 % increase in bunching between 30 and slightly above 100 µm wavelengths for the MESA optics. To detect these micro bunching structures and investigate to which extent they cause bunch degradation due to CSR radiation, intensive tracking simulations are necessary. The grid size for space charge calculations has to resolve the bunching wavelengths, and the number of tracked electrons has to chosen accordingly. In the tracking code OPAL, [3], we use a grid of 2^{21} in different combinations, depending on the bunch form, and 2.4×10^6 particles. Using 64 cores on the HZB cluster, tracking 1 m through bERLinPro roughly only takes 30 min, due to the efficient parallelization of OPAL.

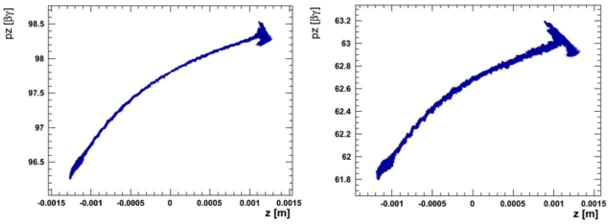

Figure 9: Longitudinal phase space at the beginning of the straight section. Left: bERLinPro optics. Right: optics with MESA linac. The enhanced energy modulation is clearly visible.

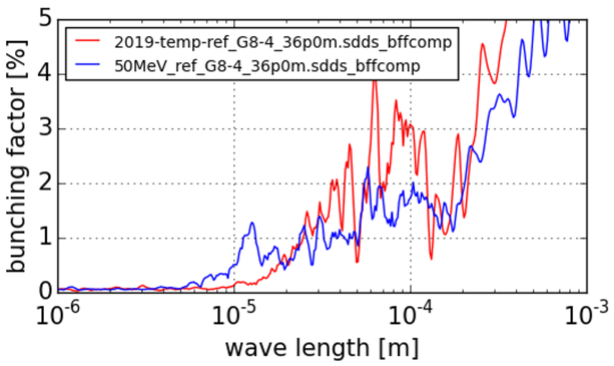

Figure 10: The bunching factor of the MESA bunch exceeds that of bERLinPro by 50 to 100 %.

No enhancement of micro bunching due to CSR radiation could be observed in either case. But CSR effects do cause a loss of energy of 10 keV in both cases. They also deteriorate the emittance in both cases, although much stronger for the optics with the MESA linac. It should be noticed, that due to the enhanced grid size and the vast amount of particles, the emittance already increases by 15 % for both optics, compared to the standard grid of 32^3 and 10^5 particles. The increase due to space charge, and due to the combination of space charge and CSR is listed in Table 1. The emittance blow up due to space charge exceeds that due to CSR by almost a factor of three. While for the bERLinPro case the emittance values stay within the project goals, at reduced energy, the horizontal emittance is doubled. This could not be seen in the standard tracking calculations with a decent number of grid cells and particles.

Table 1: Increase of the Horizontal Emittance after First Arc

E [MeV]	Emittance [π mm mrad] space charge	 space charge and CSR
50	0.778 (+18%)	0.837 (+6%)
30	1.420 (+101%)	2.050 (+44%)

The longitudinal space charge impedance is a property of the vacuum chamber of the dipoles and reflects the frequency range, where matching frequencies in the current profile of the bunch could potentially be enhanced according to $V(\ ) = I(\ ) \cdot Z(\ )$, with I, the Fourier transform of the current profile of the bunch, Z, the impedance, and V, the resulting frequency dependent voltage. Following the approach of Venturini, [8], who takes a 3D shot noise model into account for an analytic expression of the longitudinal space charge impedance, one can derive the space charge impedance for both optics, considering the different particle energies and different average radii of the bunches, as shown in Fig. 11.

The impedance is shifted towards shorter wavelengths for higher energies. For identical bunch radii, higher energy leads to a reduction of the amplitude of the impedance. For the average radii in the first arc of 0.5 mm in the 30 MeV MESA optics, compared to 0.3 mm in the 50 MeV bERLinPro optics, the amplitude of the impedance is similar. This agrees well with the result of the tracking studies. Fig. 12 shows the gain of the first arc, i.e. the ratio between the bunching at the end of the arc and the bunching at the beginning. We see the same signature as in the analytic formula. The wavelength of maximum increase of bunching is shifted towards shorter wavelength for higher energy and the amplitude for the lower energy but larger bunch radius is only slightly smaller. The independence of the gain of the initial particle distribution is shown in Fig. 13.

CONCLUSION

During the turn of the project bERLinPro many different adaption of the optics to changing hardware realizations had to be handled and different challenges had to be met. Examples were given for each of the three parts of the machine: the diagnostics line, the Banana and the recirculator. The measurement of the magnetic field in the accelerator hall led to the installation of corrector coils in the booster module. Ways to correct the trajectory in the diagnostics line and the Banana despite the lack of sufficient BPMs have to be developed. The sources of unwanted beam in the injector have been studied, and sources of halo leading to emittance dilution have been identified. In the recirculator it was found that the employment of the MESA linac module will prohibit to achieve the project goal of seeking an emittance of below 1×10^{-6} π mm mrad in the straight section, due to space charge and CSR effects, that were of no concern with the higher energy foreseen for the bERLinPro linac.

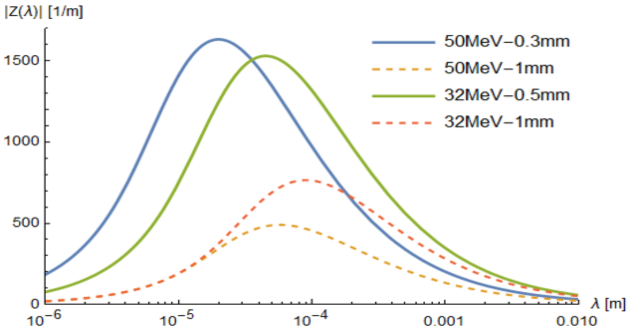

Figure 11: Longitudinal space charge impedance model for two energies and different radii.

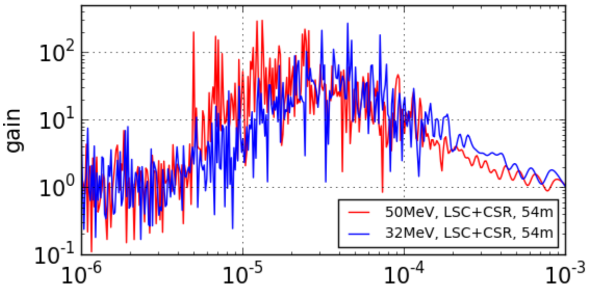

Figure 12: The gain as a function of the wavelength calculated by tracking follows the same dependencies on energy and beam radius as predicted by the analytical formula.

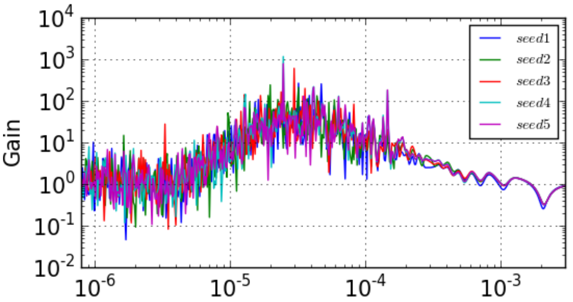

Figure 13: Gain in first arc calculated for 5 different seeds.

ISBN: 978-3-95450-217-2 doi:10.18429/JACoW-ERL2019-FRCOXBS05

REFERENCES

[1] M. Abo-Bakr et al., “The Berlin Energy Recovery Linac Project bERLinPro – Status, Plans and Future Opportunities”, presented at ERL’19, Berlin, Germany, Sep. 2019, paper: MOCOXBS04, this conference.

[2] B. Kuske, A. Adelmann, “Commissioning of the bERLinPro Diagnostics Line using Machine Learning Techniques”, presented at ERL’19, Berlin, Germany, Sep. 2019, paper: WECOYBS05, this conference.

[3] `http://amas.web.psi.ch/docs/opal/opal_user_guide-2.0.0.pdf`

[4] B. Kuske, J. Rudolph, “Beam Positioning Concept and Tolerance Considerations for bERLinPro”, TUPRO038, in *Proc. IPAC’14*,Dresden, Germany, 2014. `doi:10.18429/JACoW-IPAC2014-TUPRO038`

[5] B. Kuske, Ch. Metzger-Kraus, “Start-to-end Calculations and Trajectory Correction for bERLinPro”, in *Proc. IPAC’16*,Busan, Korea,2016. `doi:10.18429/JACoW-IPAC2016-THOBA03`.

[6] M. McAteer, “Dark current and halo tracking in ERLs”, presented at ERL’17, Geneva, Switzerland, Jun 2017, paper THIACC002, unpublished.

[7] W. Anders, K. Aulenbacher, F. Hug, A. Jankowiak, B. Kuske, A. Neumann, T. Stengler, C.P. Stoll, “Incorporation of a MESA Linac Modules into bERLinPro”,in *Proc. IPAC’19*, Melbourne, Australia, May 2019, pp. 1449–1452, `doi:10.18429/JACoW-IPAC2019-TUPGW023`

[8] M. Venturini, “Models of longitudinal space - charge impedance for microbunching instability”, *Phys. Rev. ST Accel. Beams*, vol. 11, p. 034401 (2008). `doi=10.1103/PhysRevSTAB.11.034401`

ISBN: 978-3-95450-217-2 doi:10.18429/JACoW-ERL2019-FRCOYBS01

WORKING GROUP SUMMARY: ERL FACILITIES

Michael Abo-Bakr, Helmholtz-Zentrum Berlin, Berlin, Germany
Michaela Arnold, Technische Universität Darmstadt, Darmstadt, Germany

Abstract

The Workshop on Energy Recovery Linacs 2019 was held in September 2019 at Helmholtz Zentrum Berlin, Germany. Working Group 1 (WG1), named "ERL Facilities", focused on ERLs around the world being in operation, under construction or in planning. In total seven invited oral presentations have been held and one poster contribution was presented. This report summarizes the main aspects of the presentations and introduces an overview on the ERL landscape.

INTRODUCTION

Fig. 1 shows a scattering plot of maximum beam energy vs beam current for of all ERL facilities around the world. Those are assigned into five categories: "operational ERL facilities" (purple), "past ERL facilities" (red), "planned ERL facilities" (green), "potential future ERL facilities" (blue) and "NC ERL facilities" (black). Diagonally running lines are added to the plot, representing "iso-lines" for selected virtual beam power values between 100 W and 10 GW.

All these facility data are collected in the "ERL facilities list", an EXCEL file generated on the ERL workshop in 2017 and updated in 2019. An according version is available in the proceedings of both workshops [1, 2]. The present version will be hosted and updated at HZB [3].

At present only four ERL facilities are in operation worldwide:

- Novosibirsk ERL at BINP in Russia (normalconducting)
- cERL at KEK in Japan (superconducting)
- S-DALINAC ERL at TU Darmstadt in Germany (superconducting)
- CBETA at Cornell in USA (superconducting)

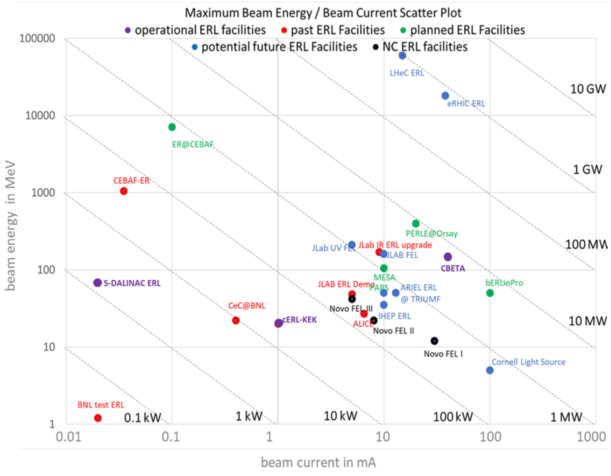

Figure 1: The ERL landscape is shown in maximum beam energy / beam current scatter plot. The status of the different facilities is indicated by colour code.

The Novosibirsk ERL is operated in multi-turn mode as the first multi-turn ERL world-wide. For the superconducting ERLs multi-turn ERL operation was not achieved up to now. CBETA (Cornell) and S-DALINAC (TU Darmstadt) are closest to success at the current time.

ERLS IN OPERATION

CBETA (Cornell)

As part of the development effort for a potential eRHIC design, the Cornell-BNL Energy recovery linac Test Accelerator (CBETA) [4], a 4-pass, 150 MeV SRF based ERL utilizing a Non-scaling Fixed Field Alternating-gradient (NSFFA) permanent magnet return loop with large energy acceptance (factor ~ 4), is currently under construction at Cornell University through the joint collaboration of Brookhaven National Lab (BNL) and the Cornell Laboratory for Accelerator based Sciences and Education (CLASSE).

In 2018 already the first beam was sent thorough the SRF chain, one separator and the first installed FFA unit. This spring, installation of the lowest energy splitter line after the linac and permanent magnet FFA loop was completed, allowing the beam to be passed nearly all the way back to the linac. In parallel to construction, beam commissioning was

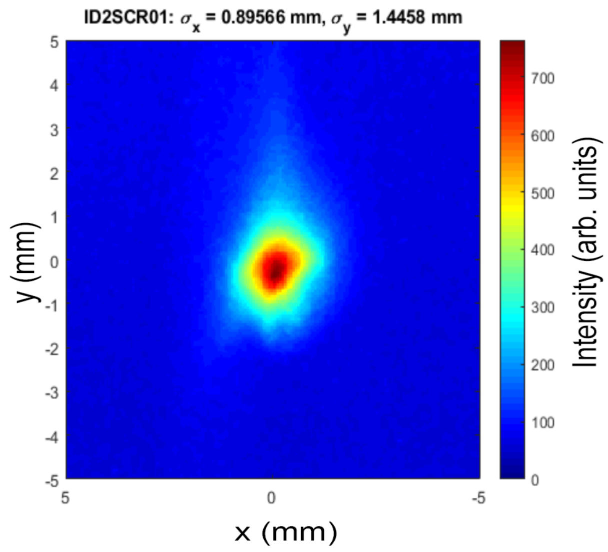

Figure 2: CBETA - recirculated beam on first view screen in the dump line ($E \approx 6.1$ MeV, $E_0 = 6.0$ MeV, $Q_b = 5$ pC).

continued in March with the initial tune up of the injector for 5 pC bunches, as well as the recommissioning of the main linac, yielding a desired energy gain of 36 MeV.

In June 2019 the successful threading of the beam through the FFA permanent magnet return loop was achieved, with a very good transmission rate of 99.6% on the corrected orbit, see Fig. 2. By measuring the load deviation in the linac cavities the recovery efficiency was estimated to be larger than 99.8% at beam currents up to 8 μA.

Several important measurements of energy, emittance, tunes, orbit etc. have been performed accompanied by simulation to improve both the machine understanding and the virtual model.

The full 4-turn construction is underway now by installing the remaining higher energy spreader lines so that starting from 2020, CBETA will be available for R&D on high power beams. More details can be found in [5].

cERL (KEK)

The cERL is a superconducting linac based accelerator with a recirculation loop for the energy recovery at KEK [6]. It has been commissioned between 2013-15 with increasing currents up to 1 mA with cw operation and recovery. In 2016 the KEK future light source was decided to be based on a high-performance storage ring. However the importance of the R&D for industrial application based on ERL technologies has been pointed out, so that ERL activities were continued on a reduced level, now with the focus on potential industrial applications like ERL based EUV-FELs for lithography, high intense laser Compton Scattering sources, brilliant THz sources or rare isotope factories [7]. As these applications require a high bunch charge, high average current electron beam (target of cw current: 10 mA) with small emittance, pulses length and energy spread the operation of cERL could be restarted in 2017 with a high bunch charge operation phase (40 - 60 pC) to develop beam handling methods towards a high average current FEL.

In June 2018 an operation block followed, where once more stable 1 mA cw operation could be demonstrated, although the accelerating linac voltage had to be reduced to control field emission, see Fig. 3. The key to achieve stable cw operation was an optics fine tuning in order to reduce losses of beam halo and other sources of unwanted beam. Important tuning items were the transverse beam optics, R_{56}, the achromatic condition of the second arc as well as the deceleration and dump line tuning. Finally, the careful collimator setting was very important. In this machine setup emittances close to design values were measured and a 100% (within measurement accuracy) recovery efficiency was reached.

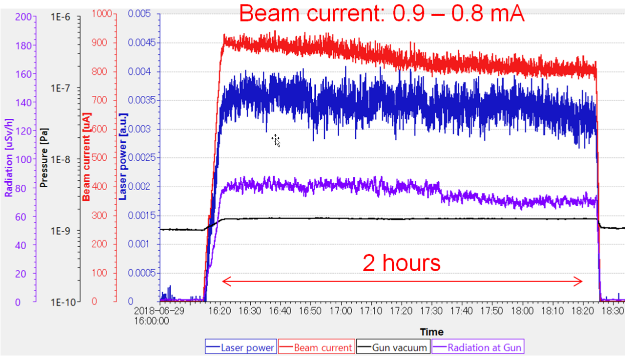

Figure 3: cERL - 1 mA beam operation with 2 hours of stable beam current, trajectory and radiation level, $V_{gun} = 500\,\text{kV}$ (DC), $E = 17.6\,\text{MeV}$, $Q_b = 0.77\,\text{pC}$).

Future planing go for a next test phase in 2020, aiming to reach stable 10 mA beam current operation. That run will give measurement opportunities to better understand the mechanisms of beam halo generation and mitigation, to study the wake fields caused by the collimators and to test the reproducibility of beam loss tuning and collimator setting. Also the observed cathode QE degradation of the GaAs photo-cathodes will be investigated. More details can be found in [8].

S-DALINAC ERL (TU Darmstadt)

The S-DALINAC, a 3 GHz superconducting electron linac, is in operation since 1991 at Technische Universität Darmstadt [9]. It was built as a recirculating linac. During a major upgrade in 2015/2016 a third recirculating beam line was installed [10]. This beam line houses a path length adjustment system being capable of a phase shift of up to 360° and thus the change to ERL operation. A commissioning phase followed the modification of the machine, where all six possible operation schemes have been or will be operated:

- Injector operation
- Single pass mode (one passage through the main linac)
- Once-recirculating mode (two passages through the main linac)
- Thrice-recirculating mode (four passages through the main linac)
- Once-recirculating ERL mode (one accelerating and one decelerating passage through the main linac)
- Twice-recirculating ERL mode (two accelerating and two decelerating passages through the main linac), not demonstrated yet

In August 2017 a once-recirculating ERL operation was demonstrated. The measurement is separated into four phases:

1. No beam in the main accelerator (red).
2. Single pass: one beam is accelerated in the main accelerator (grey).
3. Once-recirculating mode: two beams are accelerated in the main accelerator (blue).
4. ERL mode: one beam is accelerated, another beam is decelerated in the main accelerator (green).

Figure 4 summarizes the results. The change in forward (black curve) and reverse (orange curve) radio-frequency (RF) power of the first main accelerator cavity was monitored. During the ERL phase (green shading) the beam loading cancels nearly out. For one or two accelerated beams (grey and blue shading) the beam loading increases correspondingly. The beam current on the ERL beam dump (ERL-Cup, green curve) and on the extraction beam dump (E0F1-Cup, blue curve) was measured as further evidence of the operation mode.

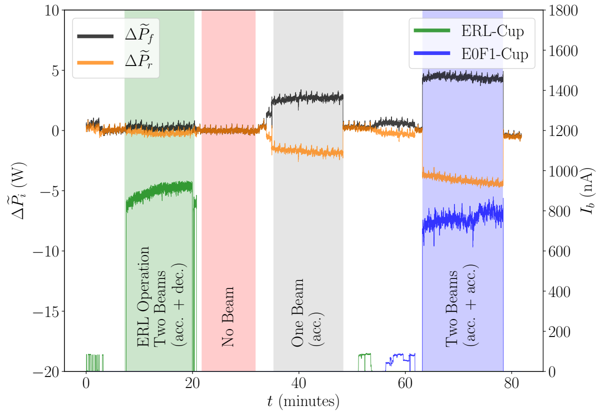

Figure 4: During four different settings (ERL: green, no beam: red, single pass: grey, twice accelerating: blue) the changes in forward (black curve) and reverse (orange curve) RF power of the first main accelerating cavity (A1SC01) have been monitored. The beam current on the corresponding faraday cups (ERL-Cup: green, E0F1-Cup: blue) was measured [11].

During this measurement the RF recovery effect for the first main accelerator cavity, the RF power gained back during deceleration, amounted to $(90.1 \pm 0.3)\%$. Additionally an analytical model was found for forward and reverse power. An analytical prediction of the reverse power was achieved after curve-fitting to the data of the forward power. More details can be found in [11, 12].

Novosibirsk ERL (BINP)

The Novosibirsk FEL Facility at Budker Institute for Nuclear Physics, based on a normal-conducting, 180 MHz accelerating system, has been the first multi-turn ERL in the world [13]. Since 2004 the facility has been operating for users of terahertz radiation. Constructed with a rather compact footprint of about (6 x 40) m^2 three modes of the magnetic system are now in operation, providing beams to drive three FELs in the wavelength range from 8 to 240 μm (see Fig. 5 and Table 1). 11 workstations are in operation and two more are currently under construction.

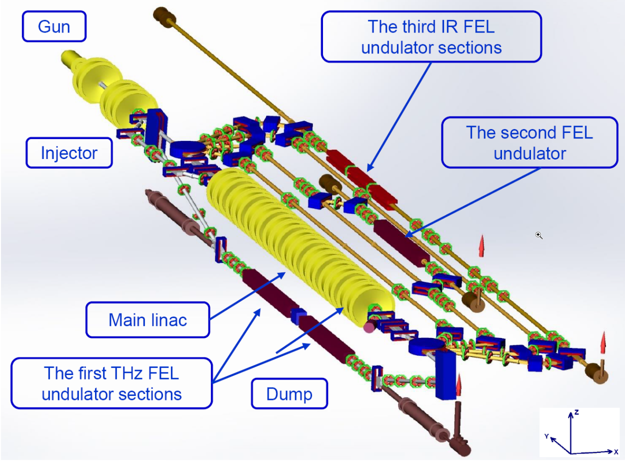

Figure 5: Footprint of the Novosibirsk ERL.

Table 1: NovoERL FEL modes. FEL 1 and FEL 2 are the world's most powerful (in terms of average power) sources of coherent narrow-band (less than 1%) radiation in their wavelength ranges.

	FEL 1	**FEL 2**	**FEL 3**
Energy / MeV	12	22	42
Current / mA	30	10	3
Wavelength / μm	90-240	37-80	8-11
Radiation power / kW	0.5	0.5	0.1
Pulse rep-rate / MHz	5.6 or 11.2	7.5	
Peak power / MW	1	1	

To further increase the FEL output power in addition to the existing DC electron gun with the grid thermionic cathode a high current, RF cw gun has been designed, constructed and also installed and commissioned in 2019 [14]. Also an option for user defined, fast changes of the average FEL power has been developed and is in operation now [15]. More details can be found in [16].

ERLS UNDER CONSTRUCTION

bERLinPro (HZB)

bERLinPro [17] is an Energy Recovery Linac Project, currently under construction at the Helmholtz-Zentrum Berlin (HZB), Germany. The layout is shown in Fig. 6.

The bERLinPro injector, consisting of an SRF photo injector cavity (1.4 cell), followed by a Booster module containing three Cornell design, SRF cavities (2 cells), generates a high brilliant beam with an energy of 6.5 MeV. The beam from the injector is merged into the linac section to be accelerated and is then send through a racetrack magnetic lattice to be recirculated in order to demonstrate effective energy recovery.

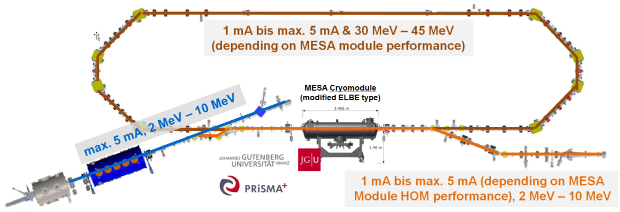

Figure 6: bERLinPro - with a MESA module as main linac.

After deceleration the beam is sent into the dump line with a high power beam stop at its end. Space in the return arc is provided to install future experiments or insertion devices to demonstrate the potential of ERLs for user applications.

Recently a major descope of the project became necessary. On the one hand, the high current gun, planned for up to SI100mA beam operation was canceled, so that bERLinPro will be operated with a medium current gun only, expected to generate a maximum current of about SI5mA, limited by the installed TTF III RF power couplers. On the other hand the main linac can not be purchased anymore. However, acceleration and energy recovery is still planned in bERLinPro, due to a collaboration with the Johann Gutenberg University Mainz. With the so called MESA option the temporal test operation of one of the two MESA project main linacs will give the chance to characterize the MESA module with beam and to accelerate the beam in bERLinPro to an energy of about 32 MeV (compared to 50 MeV with the dedicated bERLinProlinac) and to demonstrate energy recovery.

Due to a variety of mostly externally caused delays the initially planned stage-wise installation is not longer possible within the remaining project time, running until the end of 2022. For that the installation of the whole machine including Gun, Booster & MESA module and the recirculator vacuum system will be firstly completed, before bERLinPro commissioning and beam operation will start in mid of 2021. More details can be found in [18].

MESA (JGU Mainz)

The MESA ERL Project [19] is a based on a double sided recirculation design with a normal-conducting injector and two superconducting main linacs running at different operation modes:

External beam operation (three recirculations): a polarized beam of up to 150 μA at 155 MeV will serve the P2/BDX experiment (weak mixing angle, dark sector searches),

ERL operation (two recirculations): a (un)polarized beam up to 1 (10) mA at 105 MeV will be provided for the MAGIX experiment (proton radius, dark photons, astrophysics, etc).

A footprint is shown in Fig. 7.

Construction of the extended MESA hall will run until 2021, afterwards the construction of accelerator and experiments will start. Many of the accelerator parts have been ordered or even built already. The electron source and first parts of the low energy beam transfer system are currently tested. First MESA beam was existing already (up to 150 keV) and a maximum beam current of 10 mA has been achieved.

The MAMBO linac parts are ordered and will be at Mainz in fall 2020. Afterwards setup and commissioning can start.

The cryo module tests started in June 2018. One module was accepted (April 2019), the second module is under re-treatment and will be tested again at the end of 2019. One module is planned to be tested with beam at HZB in 2021/2022. MESA operation with first beam to experiments is expected in 2023. More details can be found in [20].

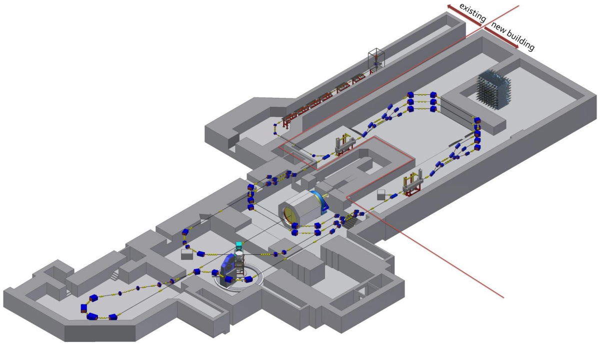

Figure 7: Footprint of MESA in the extended hall.

ERLS IN PREPARATION

PERLE (Orsay)

PERLE is a planned energy recovery linac facility to be hosted at Orsay-France, covering the 10 MW power regime [21]. It is planned as a compact multi pass ERL based on SRF technology, to serve as test bed for validation and testing a broad range of accelerator phenomena and technical choices for future projects, especially on SRF, for the Large Hadron Electron Collider (LHeC).

The PERLE main parameter are listed in Table 2, a footprint is shown in Fig. 8.

Table 2: PERLE Main Parameters

target parameter	value
injection energy / MeV	7
electron beam energy / MeV	500
normalised emittance $\varepsilon_{x,y}$ / mm mrad	6
average beam current / mA	20
bunch charge / pC	500
RF frequency / MHz	801.58

A DC photo-cathode gun will be used as electron source as it can produce the required high current as well as po-

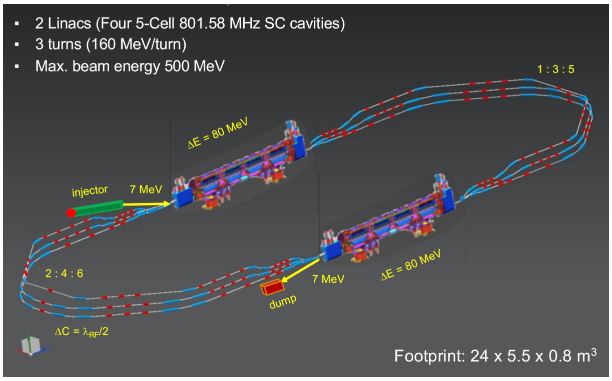

Figure 8: Schematics of the PERLE facility.

larised beams, needed for specific experiments. For that the design of the PERLE electron source will initially be based on the eXtra High Vacuum (XHV) DC photocathode gun previously used on the ALICE ERL / Daresbury and now transferred to Orsay. The significantly higher bunch charge of PERLE compared to ALICE requires a complete, ongoing re-optimisation of the gun electrode system.

For the linac the cryomodule layout developed by IPN Orsay and CERN for the Superconducting Proton Linac (SPL) with four 5-cell cavities has been choosen.

Cavity prototype and design activities to optimize a bare fine grain, high-RRR, 801.6 MHz five-cell Nb cavity design, to build a prototype and to validate the design in a vertical test at 2K helium temperature have been successfully completed at JLAB in 2018: an accelerating field slightly above 30 MV/m was reached with still $Q > 10^{10}$.

Beside the hardware activities mentioned, gun & injector optimization as well as magnet & lattice optimization of the recirculation have been performed. More details on the project can be found in [22].

CONCLUSION

The talks and discussions showed the current state on ERL facilities. Common goals are to achieve superconducting multi-turn operation and going to higher beam powers. This developments are important for potential future ERLs like LHeC ERL or eRHIC ERL.

REFERENCES

[1] Proceedings of ERL17, the 59th ICFA Advanced Beam Dynamics Workshop on Energy Recovery Linacs, Geneva, Switzerland, June 2017, `http://accelconf.web.cern.ch/AccelConf/erl2017/`

[2] Proceedings of ERL19, the 63rd Advanced ICFA Beam Dynamics Workshop on Energy Recovery Linacs, Berlin, Germany, Sep. 2019, `http://accelconf.web.cern.ch/AccelConf/erl2019/`

[3] List of ERL Facilities Worldwide, EXCEL file hosted and updated on the HZB website, `https://www.helmholtz-berlin.de/projects/berlinpro/index_de.html`

[4] C. M. Gulliford *et al.*, “CBETA Beam Commissioning Results”, in *Proc. 10th Int. Particle Accelerator Conf. (IPAC’19)*, Melbourne, Australia, May 2019, pp. 748–750. `doi:10.18429/JACoW-IPAC2019-MOPRB076`

[5] G. H. Hoffstaetter, “CBETA, a 4-turn ERL Based on SRF Linacs: Construction and Commissioning”, presented at the 63rd Advanced ICFA Beam Dynamics Workshop on Energy Recovery Linacs (ERL’19), Berlin, Germany, Sep. 2019, paper MOCOWBS01, this conference.

[6] S. Sakanaka *et al.*, “Recent Progress and Operational Status of the Compact ERL at KEK”, in *Proc. IPAC’15*, Richmond, VA, USA, May 2015, pp. 1359–1362. `doi:10.18429/JACoW-IPAC2015-TUBC1`

[7] Y. Morikawa *et al.*, “New Industrial Application Beamline for the cERL in KEK”, in *Proc. 10th Int. Particle Accelerator Conf. (IPAC’19)*, Melbourne, Australia, May 2019, pp. 3475–3477. `doi:10.18429/JACoW-IPAC2019-THPMP012`

[8] T. Miyajima, “Compact ERL (cERL), Stable 1 mA Operation with a Small Beam Emittance at KEK”, presented at the 63rd Advanced ICFA Beam Dynamics Workshop on Energy Recovery Linacs (ERL’19), Berlin, Germany, Sep. 2019, paper MOCOWBS02, this conference.

[9] N. Pietralla, “The Institute of Nuclear Physics at the TU Darmstadt”, in *Nuclear Physics News*, vol. 28, no. 2, p. 4-11, 2018. `doi:10.1080/10619127.2018.1463013`

[10] M. Arnold, C. Eschelbach, R. Grewe, F. Hug, T. Kürzeder, M. Lösler, J. Pforr, N. Pietralla, “Construction and Status of the Thrice Recirculating S-DALINAC”, *Proc. IPAC 2017*, Copenhagen, Denmark, May 2017, pp. 1384-1387. `doi:10.18429/JACoW-IPAC2017-TUPAB030`

[11] M. Arnold, J. Birkhan, F. Hug, J. Pforr, N. Pietralla, F. Schließmann, M. Steinhorst, “First operation of the superconducting Darmstadt linear electron accelerator as an energy recovery linac”, submitted for publication.

[12] M. Arnold *et al.*, “ERL Operation of S-DALINAC”, presented at the 63rd Advanced ICFA Beam Dynamics Workshop on Energy Recovery Linacs (ERL’19), Berlin, Germany, Sep. 2019, paper MOCOXBS02, this conference.

[13] N.A. Vinokurov *et al.*, “First lasing at the high-power free electron laser at siberian center for photochemistry research”, *Nuclear Instruments and Methods in Physics Research A*, vol. 528, p. 15–18, 2014. `doi:10.1016/j.nima.2004.04.009`

[14] V. Volkov *et al.*, “Bench Test Results of CW 100 mA Electron RF Gun for Novosibirsk ERL based FEL”, presented at the 63rd Advanced ICFA Beam Dynamics Workshop on Energy Recovery Linacs (ERL’19), Berlin, Germany, Sep. 2019, paper WECOXBS03, this conference.

[15] O. A. Shevchenko *et al.*, “Electronic Modulation of the FEL-Oscillator Radiation Power Driven by ERL”, presented at the 63rd Advanced ICFA Beam Dynamics Workshop on Energy Recovery Linacs (ERL’19), Berlin, Germany, Sep. 2019, paper FRCOXBS01, this conference.

[16] N. A. Vinokurov, “Status of Novosibirsk ERL”, presented at the 63rd Advanced ICFA Beam Dynamics Workshop on Energy Recovery Linacs (ERL’19), Berlin, Germany, Sep. 2019, paper MOCOXBS03, this conference.

[17] M. Abo-Bakr *et al.*, “Status Report of the Berlin Energy Recovery Linac Project BERLinPro”, in *Proc. 9th Int. Particle Accelerator Conf. (IPAC’18)*, Vancouver, Canada, Apr.-May 2018, pp. 4127–4130. `doi:10.18429/JACoW-IPAC2018-THPMF034`

[18] A. Jankowiak *et al.*, “The bERLinPro Project - Status and Perspectives”, presented at the 63rd Advanced ICFA Beam Dynamics Workshop on Energy Recovery Linacs (ERL’19), Berlin, Germany, Sep. 2019, paper MOCOXBS0, this conference.

[19] F. Hug, D. Simon, T. Stengler, C. P. Stoll, S. D. W. Thomas, and K. Aulenbacher, “MESA: The Mainz Energy Recovering Superconducting Accelerator”, presented at the 19th Int. Conf. RF Superconductivity (SRF’19), Dresden, Germany, Jun.-Jul. 2019, paper MOFAB1.

[20] F. Hug *et al.*, “Status of the MESA ERL Project”, presented at the 63rd Advanced ICFA Beam Dynamics Workshop on Energy Recovery Linacs (ERL’19), Berlin, Germany, Sep. 2019, paper MOCOXBS05, this conference.

[21] W. Kaabi *et al.*, “PERLE: A High Power Energy Recovery Facility”, in *Proc. 10th Int. Particle Accelerator Conf. (IPAC’19)*, Melbourne, Australia, May 2019, pp. 1396–1399. `doi:10.18429/JACoW-IPAC2019-TUPGW008`

[22] W. Kaabi, “PERLE: A High Power Energy Recovery Facility at Orsay”, presented at the 63rd Advanced ICFA Beam Dynamics Workshop on Energy Recovery Linacs (ERL’19), Berlin, Germany, Sep. 2019, paper MOCOYBS01, this conference.

ISBN: 978-3-95450-217-2 doi:10.18429/JACoW-ERL2019-FRCOYBS04

WORKING GROUP SUMMARY: SUPERCONDUCTING RF

F. Gerigk, CERN, Geneva, Switzerland
P. McIntosh, STFC, Daresbury, United Kingdom

Abstract

16 talks were presented in Working Group 4, which are divided into four main themes. These themes along with their talks will be listed and summarized in the following.

ERL SRF SYSTEMS SPECIFICATIONS, DEVELOPMENT, FABRICATION, COMMISSIONING AND PERFORMANCE

This theme includes 5 talks [1-5] reporting on 2 different cryomodules and on tests with 2 dual-axis cavities for ERL applications.

The MESA ERL at KPH Mainz employs 2 cryomodules, which were ordered as turn-key modules from industry. The performance goal of 12.5 MV/m at a Q_0 of 1.25×10^{10} was readily achieved in vertical tests at DESY. The first assembled module was accepted after a cold module test at Mainz, while the second module did not achieve specifications and will be sent back to the manufacturer. This failure was most likely caused by the undefined state of a valve during transport, which may have produced particles that travelled into the cavity volume. Nevertheless, this experience shows that vendors have accumulated enough technical know-how to deliver complete turn-key cryomodules. As the MESA facility is still under construction a collaboration with bERLinPro was created to make beam test with the qualified MESA module at bERLinPro. There, the construction is more advanced but funds are currently lacking for the procurement of a cryomodule. Beam tests are foreseen in 2021 at bERLinPro. The module will then be shipped back to Mainz and MESA plans first operation in 2022.

A report on operational experience with 2 ERL cryomodules came from cERL at KEK. The required phase and amplitude stability (< 0.01% and < 0.01 deg) was achieved by damping microphonics from rotary pumps with simple rubber feet. The modules suffer from increasing field emission during operation, which is probably related to contamination, but also to a high ratio of peak surface fields to accelerating fields of the particular cavities used. An unexplained vacuum burst event in 2017 further degraded performance of one module, which could so far not be recovered by high power pulsed processing.

Dual-axis cavities where already discussed at ERL 2017 [6] where a recommendation for was given for more R&D on this type of cavity. The cold test results reported by ODU [4] of a twin-axis cavity showed that the expected gradient of 15 MV/m could be surpassed, however only for one of the 2 cavities. Due to a welding defect Cavity 2 only reached 5 MV/m. Nevertheless, the suppression of multipacting by design was successful as well as the chemical treatment and processing.

Prototyping and warm tests of multi-cell dual axis cavities with bridge couplers were reported in [5] and showed good agreement between simulations and measurements.

HIGH LOADED Q CAVITY OPERATION (MICROPHONICS, LLRF, RF POWER SYSTEMS, TRANSIENT BEAM LOADING)

This theme comprised 6 talks [7-12] reporting on various types of RF control systems, encompassing both low-level and high-power technologies, as well as fundamental development of a HOM damped cavity solution.

Analysis of the microphonics characteristics of the two, cERL main linac cavities at KEK [7], has identified that the stability of the first cavity (ML1) has deteriorated over the past 5-years, whilst the second cavity (ML2) has remained stable. Further investigation has shown a cavity field-level dependency threshold of ~3MV/m for this limiting cavity, which is most likely related to a quench limit level. A transfer function characterisation has been developed for the cavity with its piezo tuner system, with future plans being made to optimise the cavity control more effectively utilising this analysis.

Three reports identified specific RF technology control processes employed for microphonics diagnostic and control for ERL operation. First single turn ERL operation was demonstrated at S-DALINAC in August 2017 with a new FPGA-based LLRF system [8], supporting a beam current of 1 µA to achieve up to 90% transmission efficiency for 6 out of 8 of the 20-cell S-band cavities. RF stability measurements showed a negligible phase control impact for beam currents <1 µA, however amplitude errors were much larger than expected and require further optimisation. A beam disturbance at 52 Hz was identified, which was assumed to originate from a gun-induced modulation, but this also requires further investigation to confirm. A new RF power measurement system has been developed and is ready for use with an optimization algorithm for improved RF Control.

Also at TU Darmstadt, system identification procedures for resonance frequency control of SRF cavities have been developed [9], driven by the primary motivation to overcome the impact of helium pressure transients and their effect on RF stability. By incorporating a 2-stage, least-square, close-loop transient analysis and integrating a suitable PID controller, optimised control parameters have been defined, which can effectively replicate the measured responses observed on the S-DALINAC accelerator. Reconfiguring the PID parameters with considerably increased differential gain has enabled the closed-loop re-

ISBN: 978-3-95450-217-2 doi:10.18429/JACoW-ERL2019-FRCOYBS04

sponse to be improved by approximately a factor of 3. Further investigations are planned in order to validate the control parameters against variable excitation errors.

As ERLs operate with low to zero beam loading, SRF linacs can operate with high loaded Q-factors (~10^8), which makes the cavities very sensitive to microphonics. Passive control of mechanical vibrations can include clamping and absorbing supports of mounting frames, waveguide components, vacuum and water pumps, cryogenic transfer lines and compressor systems. By analysing the mechanical eigenmodes of all components of the cryomodule, potential cryogenic instabilities can be identified which may become major microphonics drivers. Such drivers can be cryogenic pressure waves which induce thermoacoustic oscillations or otherwise turbulent cryogenic flow induced by transfer restrictions in distribution pipes and/or valves. Active control measures can complement passive processes, which invariably employ fast-tuner technologies and feedback techniques which can compensate for microphonic detuning. Utilisation of advanced Least Mean Square techniques, incorporating band-pass detection processes can considerably improve microphonics detection and correction. By using narrowband Active Noise Control (ANC), keeping the cavity phases in a stable region even when the cavity transfer function changes, resulted in impressive cavity isolation and reduced detuning levels by a factor of 2 for the CBETA main linac cavities [10].

Advances in ferroelectric ceramics has opened up possibilities for the development of fast reactive tuners for SRF cavity applications. Ceramic response times are now very fast, achieving < 10 ns capability. CERN has recently acquired and tested a Proof of Principle Ferro Electric Fast Reactive Tuner (FE-FRT), which was built by Euclid Techlabs with input from BNL [11] and which incorporates such materials. A 400 MHz cavity test has been successfully conducted at CERN at 4.5 K and 2 K, showing that the FE-FRT could react within 50 µs, considerably faster than the cavity filling time. Multi-application scenarios are envisaged utilising this technology i.e. for high beam loaded machines, the FE-FRT can directly be used to supress microphonics and for low beam-loaded machines (i.e. ERLs), the FE-FRT can be used to significantly reduce the RF power required. An 800 MHz estimate for PERLE, with a 3 x 10^8 Q_{ext}, can reduce the forward power requirement by a factor of 15!

For the High Energy Photon Source (HEPS) in Beijing, a 116 MHz main storage ring RF frequency is proposed by IHEP [12]. The SRF cavity design requires HOM damping (Q_{L} < 1000), so that the 5 x QWR structures are able to stably operate with 200 mA and 6 GeV electron beams. A first proof-of-principle cavity has been designed, fabricated and tested, exceeding the 12.5 MV/m and 1 x 10^9 target performance levels at 4 K. Further development of cavity ancillaries i.e. coupler, tuner and helium tank designs identified a field leakage issue with the cavity forward power coupler, requiring an elongation of the coupler tube and improved outer conductor cooling to reduce the dynamic losses, whilst also increasing the helium tank volume to improve 4 K operation stability. HOM power is extracted through large aperture beam-pipes which enables effective damping of dangerous monopole and dipole modes. A HOM coupler is also incorporated which extracts power through a C-shaped waveguide (see later session), which provides an effective high-pass filtering of the broadband power. The design optimisation is ongoing in order to achieve the required damping performance.

HOMS, HOM DAMPING AND HIGH-CURRENT OPERATION

Being able to extract HOM power efficiently from SRF cavities, without introducing potential breakdown weaknesses is a significant challenge for high current ERL linacs. Two talks in this session identified techniques for HOM management using i) waveguide HOM loads for high current operation [13] and ii) a C-shaped waveguide HOM coupler optimisation [14]. New broadband ceramic and ferrite absorbing materials are providing improved power handling capabilities. HOM load solutions at 1.3 GHz and 1.5 GHz [13], utilising a high thermal-conductivity AlN and SiC composite, have been developed by JLAb and HZB for BerlinPro and BESSY VSR respectively, each demonstrating good damping performance capabilities. Having overcome brazing challenges for this material, it is anticipated that such technology solutions can also be applicable for the JLEIC electron-ion collider in the future.

Efficient extraction of HOM power above the fundamental operating frequency, using a compact and easy to cool coupler has been innovatively developed at KEK [14]. The technique employs a C-shaped coaxial waveguide, which can be precisely tuned to maximise high-pass filtered RF power extraction from the SRF cavity. Due to its configuration, the central coax is much easier to cool and its conversion to a conventional coaxial transmission line is also much simpler than the standard coax-waveguide alternative. In addition, the physical size of the coupler can be reduced whilst providing excellent fundamental-mode isolation and effective damping of HOM impedances in the SRF cavity. Further developments are underway to be able to qualify its capability at high power levels.

At Mainz University, Beam Break-Up threshold estimations have been conducted [15], utilising comparative analysis of HOM measurements of single 1.3 GHz cavity tests performed at DESY and 2-cavity characterisation measurements performed at HIM for the integrated MESA cryomodule. Whilst the cavity HOM trends were similar, frequency deviations are observed because of fundamental mode tuning variations, the frequency spread differences between cavities is most likely due to fabrication tolerances and the larger Q-spread observed is most likely due to mechanical deviations from the cell elliptical shapes. A BBU threshold current limit of 13.4 mA is estimated, and whilst further MESA lattice optimisation is being performed, it is anticipated this threshold can be increased further.

HIGH Q0 CAVITY PERFORMANCE

The focus of this session was not on discussing the latest recipes or procedures to push the Q-value or the accelerating gradient. The purpose was rather to look at day-to-day operational issues or procedures, which may limit cavity performance. Both talks under this heading described real-life issues of i) cold testing SC cavities in a vertical test stand [16], and of ii) operating a SC CM in an ERL [17]. Both talks highlighted once more the importance of cleanliness during cavity testing, cryomodule assembly and also the effects of contamination during operation, which can yield performance degradation over time. Degrading operation was reported for the cERL main linac modules [1] as well as for the cERL injector module. Both modules also suffered from a certain performance degradation between vertical tests and tests of the assembled modules. In case of the cERL injector module, the performance can be recovered by applying plasma processing systematically before each run.

The fact that the performance degrades over time probably implies a slow contamination by the surrounding warm beam line elements. In case of the cERL injector module the situation is further complicated by the acceleration of field-emitted electrons hitting surrounding beam line elements (Faraday Cup or the photocathode gun) thereby producing X-rays. In large machines containing dozens or hundreds of cryomodules one usually has the luxury of having long distances in the order of several metres between cold and warm beam line elements. In small ERLs with 1 or 2 cryomodules this space cannot be afforded, which means that the cleanliness requirements for the warm machine parts should be as strict as for the cold parts and that cold traps should be employed to minimise cross-contamination once the cryomodules are cold.

REFERENCES FROM ERL 2019

[1] H. Sakai, “KEK ERL SRF Operational Experience“, TUCOYBS01, this conference.

[2] S. Thomas, “Integration of the MESA modules to bERLinPro for high power beam tests”, TUCOYBS04, this conference.

[3] F. Hug, “Cryomodules for the Mainz Energy-Recovering Superconducting Accelerator (MESA)”, TUCOZBS06, this conference.

[4] H. Park, “Superconducting Twin-Axis Cavity for ERL Applications”, TUCOYBS03, this conference.

[5] Y. Shashkov, “Asymmetric SRF Dual Axis Cavity for ERLs: Studies and Design for Ultimate Performance and Applications”, WECOYBS05, this conference.

[6] I. Ben-Zvi and F. Gerigk, „ERL 2017, Summary of WG4, Superconducting RF”, ERL 2017, CERN, Switzerland, `doi:10.18429/JACoW-ERL2017-FRIBCC004`

[7] F. Qiu, “Characterization of Microphonics in the cERL Main Linac Superconducting Cavities”, TUCOZBS04, this conference.

[8] M. Steinhorst, “LLRF ERL Experience at the S-DALINAC”,TUCOZBS05, this conference.

[9] S. Orth, “System Identification Procedures for Resonance Frequency Control of SC Cavities”, THCOWBS03, this conference.

[10] N. Banerjee, “Passive and Active Control of Microphonics at CBETA and elsewhere”, THCOWBS07, this conference.

[11] A. Macpherson, “A Ferroelectric Fast Reactive Tuner (FRT) to Combat Microphonics”, TUCOZBS02, this conference.

[12] P. Zhang, “The Development of HOM-Damped 166.6 MHz SRF Cavities for High Energy Photon Source in Beijing”, THCOWBS05, this conference.

[13] J. Guo, “Waveguide HOM Loads for High-Current Elliptical Cavities”, THCOXBS01, this conference.

[14] M. Sawamura, “Development of HOM Coupler with C-Shaped Waveguide for ERL operation”, THCOXBS02, this conference.

[15] C. Stoll, “Beam Breakup Limit Estimations and HOM Characterisation for MESA”, THCOWBS06, this conference.

[16] A. Macpherson, “High Q 704 MHz Cavity Tests at CERN”, THCOXBS05, this conference.

[17] E. Kako, “Degradation and Recovery of Cavity Performance in Compact ERL Injector Cryomodule at KEK”, THCOXBS06, this conference.

List of Authors

Bold papercodes indicate primary authors; ~~crossed out~~ papercodes indicate 'no submission'

Institutes List

BINP
Novosibirsk, Russia

- Choporova, Y.

BINP SB RAS
Novosibirsk, Russia

- Arbuzov, V.S.
- Bykov, E.V.
- Chernov, K.N.
- Davidyuk, I.V.
- Deichuli, O.I.
- Dementyev, E.N.
- Dovzhenko, B.A.
- Getmanov, Ya.V.
- Kenzhebulatov, E.
- Knyazev, B.A.
- Kolobanov, E.I.
- Kondakov, A.A.
- Kozak, V.R.
- Kozyrev, E.V.
- Krutikhin, S.A.
- Kulipanov, G.N.
- Kuper, E.A.
- Kuptsov, I.V.
- Kurkin, G.Y.
- Matveev, A.S.
- Medvedev, L.E.
- Motygin, S.V.
- Murasev, A.A.
- Osipov, V.N.
- Ovchar, V.K.
- Petrov, V.M.
- Pilan, A.M.
- Popik, V.M.
- Repkov, V.V.
- Salikova, T.V.
- Scheglov, M.A.
- Sedlyarov, I.K.
- Serednyakov, S.S.
- Shevchenko, O.A.
- Skrinsky, A.N.
- Tararyshkin, S.V.
- Tcheskidov, V.G.
- Tribendis, A.G.
- Vinokurov, N.A.
- Volkov, V.

BNL
Upton, New York, USA

- Altinbas, Z.
- Ben-Zvi, I.
- Berg, J.S.
- Brooks, S.J.
- Bruno, D.
- Brutus, J.C.
- Cannizzo, L.
- Cen, J.
- Costanzo, M.R.
- Drees, K.A.
- Fedotov, A.V.
- Gaowei, M.
- Gassner, D.M.
- Gu, X.
- Hammons, L.R.
- Hayes, T.
- Hock, J.
- Hulsart, R.L.
- Inacker, P.
- Jamilkowski, J.P.
- Jing, Y.C.
- Kayran, D.
- Kewisch, J.
- Lehn, D.
- Liaw, C.J.
- Litvinenko, V.
- Liu, C.
- Ma, J.
- Mapes, M.
- Méot, F.
- Mernick, K.
- Mi, C.
- Michnoff, R.J.
- Mihara, K.
- Miller, T.A.
- Minty, M.G.
- Narayan, G.
- Paniccia, M.C.
- Pekrul, W.E.
- Petrushina, I.
- Pinayev, I.
- Ptitsyn, V.
- Rao, T.
- Roser, T.
- Sandberg, J.
- Schoefer, V.
- Seletskiy, S.
- Severino, F.
- Shih, K.
- Shrey, T.C.
- Skaritka, J.
- Smart, L.
- Smith, K.S.
- Sukhanov, A.
- Than, R.
- Thieberger, P.
- Trbojevic, D.
- Tsoupas, N.
- Tuozzolo, J.E.
- Walsh, J.
- Wang, E.
- Wang, G.
- Willeke, F.J.
- Wu, Y.H.
- Xu, W.
- Zhao, H.
- Zhao, Z.

Ceramics Ltd.
St. Petersburg, Russia

- Nenasheva, E.

CERN
Meyrin, Switzerland

- Bastard, J.
- Brüning, O.S.
- Charles, T.K.
- Coly, M.R.
- Gerigk, F.
- Jensen, E.
- Macpherson, A.
- Shipman, N.C.
- Stapley, N.

Cockcroft Institute
Warrington, Cheshire, United Kingdom

- Bailey, I.R.
- Hounsell, B.
- Jones, L.B.
- Juarez-Lopez, D.P.
- Militsyn, B.L.
- Muratori, B.D.
- Noakes, T.C.Q.
- Soomary, L.A.J.
- Welsch, C.P.
- Williams, P.H.

Cockcroft Institute, Lancaster University
Lancaster, United Kingdom

- Perez-Segurana, G.

COMPAEC e.G.
Rostock, Germany

- Pöplau, G.

Cornell University (CLASSE), Cornell Laboratory for Accelerator-Based Sciences and Education
Ithaca, New York, USA

- Andorf, M.B.
- Bae, J.
- Banerjee, N.
- Bartnik, A.C.
- Bazarov, I.V.
- Cultrera, L.
- Deitrick, K.E.
- Dobbins, J.
- Franck, C.
- Galdi, A.
- Gulliford, C.M.
- Hoffstaetter, G.H.
- Ikponmwen, F.
- Koscica, R.M.
- Liepe, M.
- Lou, W.
- Maxson, J.M.
- Premawardhana, G.T.
- Quigley, P.
- Sagan, D.
- Smolenski, K.W.

DESY Zeuthen
Zeuthen, Germany

- Huck, H.

Douglas Consulting
York, Virginia, USA

- Douglas, D.

Euclid TechLabs, LLC
Solon, Ohio, USA

- Jing, C.-J.
- Kanareykin, A.

GSI
Darmstadt, Germany

- Aulenbacher, K.

HIM
Mainz, Germany

- Aulenbacher, K.
- Friederich, S.

HU Berlin
Berlin, Germany

- Kamps, T.

HZB
Berlin, Germany

- Abo-Bakr, M.
- Al-Saokal, N.
- Anders, W.
- Bergmann, Y.
- Birke, T.
- Bürkmann-Gehrlein, K.
- Bundels, A.
- Böhlick, D.
- Büchel, A.B.
- Bürger, M.
- Dirsat, M.
- Echevarria, P.
- Eichel, D.
- Fleischhauer, R.
- Frahm, A.
- Glock, H.-W.
- Glöckner, F.
- Göbel, F.
- Heling, S.
- Hwang, J.G.
- Janke, K.
- Jankowiak, A.
- Kalus, C.
- Kamps, T.
- Klauke, S.
- Klemz, G.
- Knobloch, J.
- Kolbe, J.
- Kourkafas, G.
- Kühn, J.
- Kugeler, O.
- Kuske, B.C.
- Kuszynski, J.
- Leuschner, N.
- Matveenko, A.N.
- McAteer, M.
- Meseck, A.
- Mistry, S.

- Müller, R.
- Neumann, A.
- Ohm, N.
- Ott, K.
- Panofski, E.
- Pflocksch, F.
- Pichl, L.
- Plötz, H.
- Rahn, J.
- Rotterdam, S.
- Schmeißer, M.A.H.
- Schröder, C.
- Schüler, O.
- Schuster, M.
- Stein, H.
- Suljoti, E.
- Tamashevich, Y.
- Ullrich, J.
- Ushakov, A.
- Vélez, A.V.
- Völker, J.

HZDR
Dresden, Germany

- Arnold, A.
- Evtushenko, P.E.
- Ma, S.
- Murcek, P.
- Schaber, J.
- Teichert, J.
- Xiang, R.
- Zwartek, P.Z.

IHEP
Beijing, People's Republic of China

- Dai, J.
- Ge, R.
- Han, R.
- Huang, T.M.
- Li, S.P.
- Li, Z.Q.
- Lin, H.Y.
- Ma, Q.
- Mi, Z.H.
- Wang, Q.Y.
- Zhang, P.
- Zhang, X.Y.

IKP
Mainz, Germany

- Aulenbacher, K.
- Friederich, S.
- Heil, P.
- Kempf, R.F.K.
- Matejcek, C.

IMP/CAS
Lanzhou, People's Republic of China

- Yang, J.C.
- Zhang, Z.M.
- Zhao, H.W.
- Zhao, Q.T.

INFN-Ferrara
Ferrara, Italy

- Cardarelli, P.
- Gambaccini, M.
- Paternò, G.
- Taibi, A.

INFN-Milano
Milano, Italy

- Bacci, A.
- Cialdi, S.
- Drebot, I.
- Faillace, L.
- Giannotti, D.
- Rossetti Conti, M.
- Rossi, A.R.
- Serafini, L.
- Statera, M.
- Torri, V.

INFN-Napoli
Napoli, Italy

- Sarno, A.

INFN/LASA
Segrate (MI), Italy

- Bosotti, A.
- Broggi, F.
- Giove, D.
- Michelato, P.
- Monaco, L.
- Paparella, R.
- Sertore, D.

INFN/LNF
Frascati, Italy

- Esposito, A.
- Gallo, A.
- Vaccarezza, C.

International Tomography Center, SB RAS
Novosibirsk, Russia

- Fedin, M.V.
- Veber, S.L.

JAI
Oxford, United Kingdom

- Konoplev, I.V.
- Topp-Mugglestone, M.E.

JLab
Newport News, Virginia, USA

- Adderley, P.A.
- Benesch, J.F.
- Benson, S.V.
- Bogacz, S.A.
- Bullard, D.B.
- Grames, J.M.
- Guo, J.
- Hannon, F.E.
- Hansknecht, J.
- Hernandez-Garcia, C.
- Kazimi, R.
- Krafft, G.A.

- Mamun, M.A.
- Marhauser, F.
- Park, G.-T.
- Park, H.
- Poelker, M.
- Rimmer, R.A.
- Seryi, A.
- Suleiman, R.
- Tennant, C.
- Tiefenback, M.G.
- Wang, H.
- Wang, S.
- Wang, Y.W.
- Zhang, S.
- Zhang, Y.

KAERI
Daejon, Republic of Korea
- Vinokurov, N.A.

KEK
Ibaraki, Japan
- Arakawa, D.A.
- Aryshev, A.
- Egi, M.
- Enami, K.
- Furuya, T.
- Honda, Y.
- Kako, E.
- Katagiri, H.
- Kato, R.
- Konomi, T.
- Matsumoto, T.
- Michizono, S.
- Miura, T.
- Miyajima, T.
- Nakamura, N.
- Obina, T.
- Qiu, F.
- Ryukou, R.
- Sakai, H.
- Shimada, M.
- Takai, R.
- Tanaka, O.A.
- Uchiyama, T.
- Umemori, K.
- Yamamoto, N.

KPH
Mainz, Germany
- Aulenbacher, K.
- Heine, R.G.
- Hug, F.
- Meseck, A.
- Simon, D.
- Stengler, T.
- Stoll, C.P.
- Thomas, S.D.W.

Lancaster University
Lancaster, United Kingdom
- Bailey, I.R.
- Burt, G.
- Castilla, A.

LANL
Los Alamos, New Mexico, USA
- Smedley, J.

MEPhI
Moscow, Russia
- Bulygin, A.M.
- Samarokov, N.Yu.
- Shashkov, Ya.V.

MIT
Cambridge, Massachusetts, USA
- Donnelly, T.W.
- Friščić, I.
- Milner, R.

NSTU
Novosibirsk, Russia
- Tribendis, A.G.

NSU
Novosibirsk, Russia
- Davidyuk, I.V.
- Gerasimov, V.V.
- Getmanov, Ya.V.
- Knyazev, B.A.
- Kozyrev, E.V.
- Matveev, A.S.
- Serednyakov, S.S.
- Vinokurov, N.A.

ODU
Norfolk, Virginia, USA
- Delayen, J.R.
- Park, H.

PKU
Beijing, People’s Republic of China
- Feng, L.W.
- Huang, S.
- Liu, K.X.
- Ouyang, D.M.
- Quan, S.W.
- Xie, H.M.
- Zhang, X.K.
- Zhao, S.

POLIMI
Milano, Italy
- Galzerano, G.

Politecnico/Milano
Milano, Italy
- Puppin, E.

PSI
Villigen PSI, Switzerland
- Adelmann, A.

QST
Tokai, Japan
- Hajima, R.
- Sawamura, M.

SBU
Stony Brook, New York, USA
- Shih, K.

SLAC
Menlo Park, California, USA
- Mayes, C.E.
- Norvell, N.P.
- Stupakov, G.

Sokendai
Ibaraki, Japan
- Kako, E.
- Konomi, T.
- Matsumoto, T.
- Miura, T.
- Qiu, F.
- Sakai, H.
- Umemori, K.

Sokendai - Hayama
Hayama, Japan
- Egi, M.
- Michizono, S.

STFC/DL/ASTeC
Daresbury, Warrington, Cheshire, United Kingdom
- Angal-Kalinin, D.
- Jones, L.B.
- McIntosh, P.A.
- Militsyn, B.L.
- Muratori, B.D.
- Noakes, T.C.Q.
- Williams, P.H.

Stony Brook University
Stony Brook, USA
- Litvinenko, V.

SUNY SB
Stony Brook, New York, USA
- Petrushina, I.
- Wu, Y.H.

TEMF, TU Darmstadt
Darmstadt, Germany
- Boine-Frankenheim, O.
- Khan, A.
- Klingbeil, H.
- Orth, S.

The University of Liverpool
Liverpool, United Kingdom
- Hounsell, B.
- Juarez-Lopez, D.P.
- Klein, M.
- Soomary, L.A.J.
- Welsch, C.P.

The University of Melbourne
Melbourne, Victoria, Australia
- Charles, T.K.

TRIUMF
Vancouver, Canada
- Alcorta, M.
- Ames, F.
- Chapman, E.
- Fong, K.
- Humphries, B.
- Kester, O.K.
- Kishi, D.
- Koscielniak, S.R.
- Laxdal, R.E.
- Ma, Y.
- Planche, T.
- Rowe, M.
- Rädel, S.D.
- Verzilov, V.A.

TU Darmstadt
Darmstadt, Germany
- Arnold, M.
- Bahlo, T.
- Dutine, M.
- Grewe, R.
- Hanten, J.H.
- Jürgensen, L.E.
- Pforr, J.
- Pietralla, N.
- Schließmann, F.
- Steinhorst, M.
- Weih, S.

TU Dresden
Dresden, Germany
- Schaber, J.

UMAN
Manchester, United Kingdom
- Crone, J.
- Owen, H.L.

UNIFE
Ferrara, Italy
- Gambaccini, M.

UniNa
Napoli, Italy
- Mettivier, G.
- Russo, P.

Universita’ degli Studi di Milano & INFN
Milano, Italy
- Petrillo, V.
- Prelz, F.

University of Science and Technology of Korea (UST)
Daejeon, Republic of Korea
- Vinokurov, N.A.

Université Paris-Saclay, CNRS/IN2P3, IJCLab
Orsay, France
- Hounsell, B.
- Kaabi, W.

UST
Daejeon City, Republic of Korea
- Vinokurov, N.A.

Participants List

— A —

Abo-Bakr, Michael
Helmholtz-Zentrum Berlin

Al-Saokal, Nawar
Helmholtz-Zentrum Berlin

Anders, Wolfgang
Helmholtz-Zentrum Berlin

Andre, Kevin
CERN

Angal-Kalinin, Deepa
STFC

Arnold, Michaela
IKP, TU Darmstadt

Arpacioglu, Cansu
Helmholtz-Zentrum Berlin

— B —

Banerjee, Nilanjan
Cornell University

Benson, Stephen
Jefferson Lab

Birke, Thomas
Helmholtz-Zentrum Berlin

Bogacz, Alex
Jefferson Lab

— C —

Choporova, Yulia
Budker INP

Crone, Joe
University of Manchester

Cultrera, Luca
Cornell University

— D —

Debes, Markus
PINK GmbH

Delayen, Jean
ODU

Drebot, Illya
INFN-Milan

— E —

Echevarria, Pablo
Helmholtz-Zentrum Berlin

Ehmler, Hartmut
Helmholtz-Zentrum Berlin

Eichhorn, Ralf
Xelara Research

Evtushenko, Pavel
HZDR

— F —

Frii, Ivica
MIT - LNS

— G —

Gaowei, Mengjia
Brookhaven National Laboratory

Gerigk, Frank
CERN

Getmanov, Yaroslav
Budker INP

Gu, Xiaofeng
BNL

Guo, Jiquan
Jefferson Lab

— H —

Hoffstaetter, Georg
Cornell

Hounsell, Benjamin
Cockcroft Institute/
University of Liverpool/LAL

Hug, Florian
JGU Mainz

Hwang, Ji-Gwang
Helmholtz-Zentrum Berlin

— J —

Jankowiak, Andreas
Helmholtz-Zentrum Berlin

Jensen, Erk
CERN

Jing, Yichao
BNL

Jones, Lee
STFC Daresbury Laboratory

— K —

Kaabi, Walid
LAL-CNRS

Kako, Eiji
KEK

Kamps, Thorsten
Helmholtz-Zentrum Berlin

Kayran, Dmitry
BNL

Khan, Aamna
TEMF, TU Darmstadt

Klemz, Guido
Helmholtz-Zentrum Berlin

Knobloch, Jens
Helmholtz-Zentrum Berlin

Konomi, Taro
KEK

Koscica, Rosalyn
Cornell University

Kühn, Julius
Accelerator Physics

Kuske, Bettina
Helmholtz-Zentrum Berlin

— L —

Lederer, Sven
DESY

Lou, William
Cornell University

— M —

Macpherson, Alick
CERN

Matveenko, Alexander
Helmholtz-Zentrum Berlin

McAteer, Meghan
Helmholtz-Zentrum Berlin

McIntosh, Peter
STFC

Meseck, Atoosa
HZB/JGU

Militsyn, Boris
UKRI STFC ASTeC

Mistry, Sonal
Helmholtz-Zentrum Berlin

Miyajima, Tsukasa
KEK

— N —

Neumann, Axel
Helmholtz-Zentrum Berlin

Norvell, Nora
SLAC

— O —

Orth, Sebastian
TEMF

Ott, Klaus
Helmholtz-Zentrum Berlin

Ouyang, Dongming
Peking University

— P —

Park, Gunn
Jefferson Lab

Park, HyeKyoung
Jefferson Lab

Peggs, Steve
BNL

Pérez Segurana, Gustavo
Lancaster University

Perrot, Luc
IPNO

Petenev, Yuriy
Helmholtz-Zentrum Berlin

Pietralla, Norbert
TU Darmstadt

Pinayev, Igor
BNL

Pöplau, Gisela
Universität zu Lübeck

— Q —

Qiu, Feng
KEK

— R —

Rädel, Stephanie
TRIUMF

— S —

Sakai, Hiroshi
KEK

Sawamura, Masaru
QST

Schabardin, Roswitha
Helmholtz-Zentrum Berlin

Schließmann, Felix
IKP, TU Darmstadt

Seletskiy, Sergei
BNL

Sharples, Emmy
Helmholtz-Zentrum Berlin

Shashkov, Yaroslav
MEPhI

Shevchenko, Oleg
BINP

Shi, Liangliang
Helmholtz-Zentrum Berlin

Shimada, Miho
KEK

Smedley, John
LANL

Smolenski, Karl
Cornell University

Steinhorst, Manuel
IKP, TU Darmstadt

Stoll, Christian
KPH Mainz

— T —

Tamashevich, Yegor
Helmholtz-Zentrum Berlin

Tanaka, Olga
KEK

Thomas, Sebastian
Institut für Kernphysik

Trbojevic, Dejan
Brookhaven National Laboratory

— V —

Velez, Adolfo
Helmholtz-Zentrum Berlin

Völker, Jens
Helmholtz-Zentrum Berlin

Volkov, Vladimir
BINP

— W —

Wang, Erdong
BNL

Williams, Peter
Daresbury

— X —

Xiang, Rong
HZDR

Xie, Huamu
Peking University

— Z —

Zhang, Pei
IHEP, CAS

Zhao, Quantang
IMP, CAS